Distribution Of Baryonic And Dark Matter In Spiral And Irregular Nearby Galaxies

Distribution de la matière baryonique et noire dans les galaxies spirales et irrégulières

Marie Korsaga

Thèse en cotutelle présentée pour obtenir le grade de:
A thesis submitted in fulfilment for the degree of:

Thèse de doctorat
Docteur d'Aix-Marseille Université
Ecole Doctorale de Physique et Sciences de la Matière
Spécialité: Astrophysique et Cosmologie

&

Doctor of Philosophy (Astronomy)
University of Cape Town

March 2019

Supervisors: Philippe Amram (Aix-Marseille Université)
Claude Carignan (Cape-Town University)
Benoit Epinat (Aix-Marseille Université)

Contents

Résumé

Ma thèse de doctorat vise à comprendre la distribution de la matière noire (MN) et de la matière lumineuse dans les galaxies spirales et irrégulières. L'étude de cette matière pourrait clairement améliorer nos connaissances sur la formation et l'évolution des galaxies. Alors que la description globale du contenu baryonique des galaxies est désormais bien connue, il est crucial de comprendre la distribution de la MN dans les galaxies et donc d'étudier leur dynamique. Pour ce faire, j'étudie la distribution de la matière lumineuse et noire dans les galaxies proches. L'étude consiste à utiliser l'échantillon GHASP (Gassendi HAlpha survey of SPirals) qui me permet d'investiguer la distribution des halos de MN dans les regions centrales des galaxies, en combinant les données cinématiques obtenues à partir des observations optiques aux données photométriques disponibles dans la littérature. Après avoir résumé les propriétés globales de la matière lumineuse et noire des galaxies, je présente les instruments basés sur la technique de l'interféromètre de Fabry-Perot utilisés pour observer l'échantillon GHASP. Je présente également les données photométriques (en bande infrarouge et optique), ainsi que les modèles utilisés pour déterminer la distribution de la matière lumineuse et noire dans les galaxies.

Au chapitre 2, nous présentons les données cinématiques et les données de photométrie infrarouge disponibles dans la littérature utilisées pour faire les modèles de masse. Pour les données cinématiques, nous utilisons des courbes de rotation de l'échantillon GHASP. Pour les données photométriques, nous utilisons le profil de lumière de l'infrarouge moyen W1 et W2 (3.4 et 4.6 μm) de WISE (Wide-field Infrared Survey Explorer), qui détecte l'émission provenant des vielles populations stellaires. Le profil de lumière est décomposé si nécessaire en plusieurs composantes (bulbe, disque, barre, bras spirale, etc.). La combinaison des données cinématiques

optiques avec les données en photométrie infrarouge nous permet de determiner la distribution de masse d'un échantillon de 121 galaxies couvrant des types morphologiques de S0 à Irr, et donc de comprendre comment le halo de MN est distribué dans les galaxies spirales de type précoce comparé aux galaxies de type tardif. Nous utilisons deux principaux modèles pour décrire le comportement des halos de MN dans les galaxies: le profil de densité pseudo-isotherme, uniforme dans le centre du halo des galaxies et le profil de densité cuspide Navarro-Frenk-White. Nous permettons aux rapports masse-sur-luminosité du disque et le cas échéant du bulbe de varier et nous les fixons par la couleur (W1-W2). Nous explorons aussi l'hypothèse du disque maximal pour le modèle pseudo-isotherme. Nous trouvons que les deux profils de densité décrivent bien les courbes de rotation bien que le modèle pseudo-isotherme donne de meilleurs résultats. Nous trouvons que les relations entre les paramètres du halo de MN et la luminosité des galaxies dépendent des types morphologiques (présence de bulbe ou non dans les galaxies).

Au chapitre 3, nous présentons la distribution de masse de 100 galaxies irrégulières et spirales de type précoce et tardif en combinant les données cinématiques (courbes de rotation Hα) avec la photométrie en bande visible R_c disponible dans la littérature. Nous utilisons les même méthodes et description données au chapitre 2. Le rapport masse-sur-luminosité est maintenant fixé par la couleur (B - V). Nous comparons les résultats obtenus utilisant la photométrie en bande visible R_c à ceux avec la photométrie dans la bande W1. Nous trouvons des résultats similaires pour les paramètres du halo de MN mais des valeurs plus élevées pour les rapports masse-sur-luminosité dans la bande R_c que W1. Cependant, la dispersion dans les paramètres du modèle est plus petite et, comme les masses stellaires sont mieux définies, la photométrie en bande infrarouge devrait être préférée, si possible, à l'optique.

Les courbes de rotations HI sont essentielles pour étudier la distribution de la MN dans les régions internes et externes des galaxies. Au chapitre 4, nous construisons en un premier temps la distribution de masse de 31 galaxies en utilisant les courbes de rotation Hα et les données de photométrie dans l'infrarouge moyen utilisées au chapitre 2 avec l'ajout de la contribution de la composante de gas HI. Deuxièmement, la distribution de masse est déterminée avec la même photométrie

et composante gazeuse mais cette fois en utilisant des courbes de rotation hybrides étendues (Hα et HI). Enfin, la distribution de masse est déterminée en utilisant uniquement des courbes de rotation HI. L'objectif principal est de comprendre comment les paramètres de la matière lumineuse et de la MN peuvent varier quand on utilise différentes données cinématiques. Pour construire les modèles de masse, nous utilisons les mêmes méthodes et descriptions données au chapitre 2. Nous trouvons que la relation entre les paramètres de la MN est fonction des données cinématiques utilisées.

Abstract

My PhD research is focused on the dark matter (DM) and luminous matter distribution in spiral and irregular galaxies. Studying this matter could clearly improve our knowledge on the formation and evolution of galaxies. While the overall description of the baryon content of galaxies is now well known, we will now use the kinematics to understand the distribution of DM, especially in the inner parts of galaxies. To do this, I study the distribution of the luminous and DM in nearby galaxies. The study consists of using the GHASP (Gassendi HAlpha survey of SPirals) sample which allows me to investigate the distribution of the DM halos in the inner regions of galaxies, by connecting the kinematical data from the optical observations to the photometry data available in the literature. After summarizing the global properties of the luminous and DM of galaxies, I present the instruments based on the Fabry-Perot interferomter used to observe the GHASP survey. I also present the different photometry (infrared and optical bands) data, and models used to determine the distribution of luminous and DM inside galaxies.

In chapter 2, we present the kinematical data and the infrared photometry data available in the literature used to construct galaxy mass models. For the kinematical data, we use rotation curves from the GHASP survey. For the photometry data, we use the luminosity profile of the mid-infrared W1 and W2 (3.4 and 4.6 μm) of WISE (Wide-field Infrared Survey Explorer), which probes the emission from the old stellar population. The radial profile is decomposed if necessary to multiple components (bulge, disc, bar, spiral arm, ect.). Combining the optical kinematical data with the infrared photometry data allows us to determine the mass distribution of the sample of 121 galaxies covering morphological types from S0 to Irr, and therefore to understand how the DM halo is distributed in early type spiral compared

to late type spiral and irregular galaxies. We use two main models to describe the shape of the DM halos in galaxies: the pseudo-isothermal core density profile and the Navarro-Frenk-White cuspy density profile. We allow the mass-to-light ratios of the disc and if necessary the bulge to vary and we keep them fixed by the colour (W1-W2). We also explore the maximum disc for the pseudo-isothermal model. We find that the two profiles describe well the rotations curves while the pseudo-isothermal model gives better results. In order, to understand how the DM is distributed, we study relations between the parameters of the DM and the luminosity of galaxies. We find that the relations between the DM halo parameters and the luminosity of galaxies depend on the morphological types (presence of bulge or not in galaxies).

In chapter 3, we present the mass distribution of 100 early and late type spiral and irregular galaxies by combining the kinematical data (Hα rotation curves) with the optical R_c band photometry data available in the literature. We use the same methods and descriptions given in Chapter 2. The mass-to light ratios are now fixed using the (B - V) colour. We compare the results obtained using the optical R_c band photometry to the W1 band photometry. We find similar results on the DM halo parameters but the values are higher for the mass-to-light ratios in the R_c band than in the W1. However the dispersion in the model parameters is smaller and because stellar masses are better defined, the infrared photometry should be preferred, when possible, to the optical band.

The HI rotation curves are crucial in studying the distribution of the DM in the inner and outer regions of galaxies. In chapter 4, we first construct the mass distribution of 31 galaxies using the Hα rotation curves and mid-IR photometry data used in chapter 2 with the addition of the contribution from the HI gas component. Secondly, the mass distribution is determined with the same photometry and gas component but using hybrid (Hα and HI) extended rotation curves. Lastly, the mass distribution is constructed using HI kinematical data. The main goal is to understand how the luminous and DM parameters may vary when using the different kinematical data. We use the same models to construct the mass models and the fitting procedures as described in chapter 2. We find that the relation between the parameters varies from one dataset to the other.

Acknowledgements

It is a real pleasure to thank my supervisor Professor Claude Carignan at the University of Cape Town (UCT), for giving me an opportunity to do my thesis between Aix-Marseille University and University of Cape Town. Because of this joint guardianship, I interacted and acquired a lot of knowledge in two different worlds and raise my level in English. I do not intend to praise you but sincerely you are someone special with a big heart, always listening and present when I need you despite your busy schedule. Thank you for believing in me, working with you is a great happiness and a pride for me. I would also like to thank Dr Monique Mujawamariya for her generosity and her joy of living that she shares around her, thank you for the numerous discussion that we had.

I would like to extend my gratitude to my supervisor Professor Philippe Amram at the Laboratoire d'Astrophysique de Marseille (LAM) , a big man with a full of humour and sympathy. Always dynamic and kind, always listening and helping me in both professionally and personally. I remain admiring of your passion for the job of researcher.

I also wish to extend my thank you to my supervisor Dr Benoit Epinat at LAM for his great help. Thank you for the help, advices and encouragements. You are someone nice and very respectful, working with you is a real pleasure.

A special thanks to my family for all the love and support, encouragements that make me proud of myself today. Thank you to my parents, brothers and sisters Arsène, Eric, Pélagie and Martine, to my grandmother Gilga for her help and blessings. I love you all. I extend my thank you to my bigger family for the love and support.

Another special thank you to my friend Françoise Maxant and her daughter Laurène Maxant, you are a second family for me at Marseille.

I would like to say a big thank you to Sylvie Imbert for her generosity, Jean Luc

Stara, Melodie Didier, Cristina Gonzalez for their friendship. Melodie, we had a great time together in Marseille, thank you for the swimming pool sessions.

My deepest gratitude to astronomers Maurice Imbert, George Compte, Michel Marcelin, Tom Jarrett, you have always been there for me when I had needed professional supports even personal too.

I am grateful to the administration and informatique team at LAM for their help and listening. Many thanks to Vincent and Adrien for giving me a helping hand when I had technical issues with my computers.

Thank you to the administrative team at UCT, Roslyn and Carol for the sympathy and help.

My gratitude to Stephane Courteau for the discussions about my work during my stay in Montreal. It was a pleasure to discuss astronomy with you.

I would also like to thank you Professor Jean Koulidiati of the University of Ouagadougou for his encouragements and advices. I extend my thanks to Mr Pierre Sanon alias "Tonton Pierre" who is like a second father for me, Dr. Kam Zacharie, Dr. Issa Ouattara, Dr Issouf Kafando for your supports.

My final thank you goes to PhD students at LAM and UCT. Special thanks to Amidou, Marc, Julien, Blaise, Zara, you made my stay in Cape Town full of nice memories.

"Alone we go faster, together we go further." African proverb.

To my family.

Declaration of Authorship

The work presented in this thesis was done in collaboration with my supervisors together with various people who provided some of the data. This thesis contains research that has already been published or submitted for publication:

1. Chapter 2 (Paper I) entitled "GHASP: an Hα kinematical survey of spiral galaxies. XI. Distribution of luminous and dark matter in spiral and irregular nearby galaxies using WISE photometry" has been published in the Monthly Notices of the Royal Astronomical Society Journal; **M. Korsaga**, C. Carignan, P. Amram, B. Epinat, T. H. Jarrett, 2018, MNRAS 478, 50-68.

   We present the mass distribution of luminous and dark matter within the optical disc of 121 nearby galaxies using the kinematical and the infrared photometry data. For the kinematical data, we use the Hα rotation curves selected from the GHASP (Gassendi HAlpha Survey of Spirals) survey, which were observed using the Fabry-Perot interferometer around the emission line Hα. For the photometry data, we use the mid-infrared W1(3.4μm) and W2(4.6μm) of WISE surface brightness profiles. We use two main models with different fitting procedures to determine the shape of the dark matter halos in galaxies: the pseudo-isothermal core density profile and the Navarro-Frenk-White cuspy density profile. This study allow us to find that the relations between the dark matter halo parameters and the luminosity of galaxies depend on the morphological types (the presence of bulge or not in galaxies).

2. Chapter 3 (Paper II) entitled "GHASP: an Hα kinematical survey of spiral galaxies. XII. Distribution of luminous and dark matter in spiral and irregular nearby galaxies using R_c-band photometry" has been published in the Monthly Notices of the Royal Astronomical Society Journal; **M. Korsaga**, P. Amram, C. Carignan, B. Epinat, 2019, MNRAS 482, 154-174.

In this paper, we present the mass distribution of the baryonic and dark matter halo within the optical disc of 100 nearby galaxies using the Hα rotation curves from GHASP survey and the optical R_c-band surface brightness profiles available in the literature. We use the same methods as described in Chapter 2 to determine the mass models of the galaxies. We compared the results with the results obtained using the 3.4μ photometry data in order to investigate if the earlier results derived from optical photometry are still valid or we need to replace them with the new recent results obtained with infrared photometry.

3. Chapter 4 (Paper III) entitled " Distribution of luminous and dark matter in spiral and irregular nearby galaxies using hybrid rotation curves and WISE photometry" has been submitted to the Monthly Notices of the Royal Astronomical Society Journal; **M. Korsaga**, C. Carignan, P. Amram, B. Epinat, A. Sorgho, P. Adamczyk, MNRAS, submitted.

   We show the mass distribution of the baryonic and dark matter of 31 galaxies using different datasets: Hα rotation curves from the GHASP survey, HI rotation curves from the literature and hybrid rotation curves (combined Hα rotation curves with HI rotation curves extending beyond the optical disc). We also use the 3.4μm of WISE photometry data with the contribution of the HI gas component. This allows us to observe if the contribution of the neutral gas component has an influence on the mass-to-light ratios and the dark matter halos parameters and also to see how the dark matter is distributed outside the optical disc of the galaxies.

I confirm that I have been granted permission by the University of Cape Town's Doctoral Degrees Board to include the following publications in my PhD thesis, and where co-authorships are involved, my co-authors have agreed that I may include the publications:

1. **M. Korsaga**, C. Carignan, P. Amram, B. Epinat, T. H. Jarrett, " GHASP: an Hα kinematical survey of spiral galaxies. XI. Distribution of luminous and dark matter in spiral and irregular nearby galaxies using WISE photometry", 2018, MNRAS 478, 50-68.

2. **M. Korsaga**, P. Amram, C. Carignan, B. Epinat, "GHASP: an Hα kinematical survey of spiral galaxies. XII. Distribution of luminous and dark matter in spiral and irregular nearby galaxies using R_c-band photometry", 2019, MNRAS 482, 154-174.

3. **M. Korsaga**, C. Carignan, P. Amram, B. Epinat, A. Sorgho, P. Adamczyk, "Distribution of luminous and dark matter in spiral and irregular nearby galaxies using hybrid rotation curves and WISE photometry" (submitted to MNRAS).

SIGNATURE: M. K. **DATE: March 2019**

STUDENT NAME: Marie Korsaga **STUDENT NUMBER:**

Plagiarism Declaration

I, Marie Korsaga, know the meaning of plagiarism and declare that all of the work in the document, save for that which is properly acknowledged, is my own.

List of Figures

List of Tables

Chapter 1

Introduction and literature review

1.1 General Overview

Dark Matter (DM) remains one of the most investigated topics in modern astronomy. In early 20th century, our picture of the Universe was made only of our own Galaxy, the Milky Way, which comprised the solar system surrounded by millions of stars. The Universe was believed to end at the edge of our Galaxy, and nothing was meant to exist beyond. Fortunately, one question was continuously haunting astronomers: was the Milky Way the only entity that constituted the Universe, or could there exist other galaxies beyond? The birth of the Mount Wilson telescope in early 1900s would change forever our knowledge of the Universe, by expanding the limits of the cosmos thanks to the discovery of another galaxy. In 1923, Edwin P. Hubble took a plate of the Andromeda Galaxy (M31) and discovered the first Cepheid variable star in the galaxy M31 and therefore concluded that M31 was a separate galaxy from our Milky Way. This discovery pushed back the frontier of the cosmos, which was previously only made of the mere Milky Way. It also opened doors to the discovery of numerous subsequent galaxies which were observed to be moving away from each other. Their respective rotation velocities were furthermore measured to be higher than expected in the outer parts of galaxies. These facts triggered the idea that the Universe contained some unseen matter other than the usual ordinary one revealed by direct observations (e.g. stars and gas). Nowadays, the matter in the Universe is thought to be approximately distributed as follows: 68% of “Dark Energy", 26% of DM and 5% of baryonic (or ordinary) matter (Schumann 2014). To understand the Universe, it is therefore crucial to understand its principal constituents such as the DM and the Dark Energy (Peebles & Ratra 2003).

DM does not interact (or very weakly) with ordinary (baryonic) matter. This property makes it hard to detect and has only been theoretically predicted so far. On the other hand, the Dark Energy is a component that opposes to the gravitational force on large scales, and is associated with the accelerating expansion of the Universe that makes galaxies move faster apart. The present thesis is concerned by the DM distribution in the inner regions of galaxies. Throughout this work we will extensively use models and observations of visible matter to investigate the distribution of the DM inside galaxies, especially in their inner parts.

1.1.1 Different types of galaxies

1.1.1.1 Introduction

Immediately after the Big Bang, the Universe is made up of unstructured matter and radiation were first radiation and then matter dominate. Following this phase, under the effect of the gravitational force, the matter (essentially composed of simple atoms and molecules) collapses to form stars and the temperatures of the stellar cores will increase until nuclear fusion reactions begin. Still under the influence of the gravitational force, the stars are bound into DM potential wells to form galaxies and a large fraction of galaxies in turn become bound into clusters. Then the observable universe is approximatively constituted of one hundred billion galaxies and each galaxy is composed of a hundred billion of stars and contain gas, dust and large amounts of DM.

The exact nature of the galaxies was not known until the beginning of the XX century. Although the formation and evolution of these objects was not really known, this did not stop the astronomers to classify them according to their aspect. Galaxies have a structured form, differentiated by their size, shape and composition (Hubble 1926). The two main morphological types of galaxies observed in the local universe, namely elliptical and spiral galaxies, can be explained as follows: elliptical have a prolate or oblate elliptical morphology with a stellar population resulting from a major star formation and a passive evolution; the late-type galaxies may be spiral-shaped or completely irregular with a high rate of stellar formation. To do this, astronomers classify them into three main types, (see Figure 1.4) that we will briefly explore together. Edwin Hubble was the first to propose a classification of galaxies in 1926, a more detailed description of the morphological types is given by de Vaucouleurs (1959).

1.1.1.2 Elliptical Galaxies

They are mainly composed of red and old stars and are more or less devoid of young and massive stars. They represent only about 15 % of the galaxies (Dressler 1980). Elliptical galaxies contain only a very small amount of gas and dust, and therefore a relatively non-existent interstellar medium because gas is the necessary ingredient of star formation. If the gas is absent, new stars can not be formed and all the stars

present were formed at the time when interstellar gas was still available, hence the presence of little massive stars, young and blue. In these type of galaxies, the stars are supported against gravity by their velocity dispersion. Elliptical galaxies are shaped like a spheroid, or elongated sphere. The elliptical galaxies are denoted E, scaling a range of numbers from 0 to 7 according to the elongation of the elliptical shape drawn on the sky by the galaxy (Hubble 1926). For example a galaxy of classification of E0 (see an example of M87 in the left panel of Fig. 1.1) appears to be perfectly circular compared to the others (see in the right panel an example of NGC 4473 which corresponds to E5 classification).

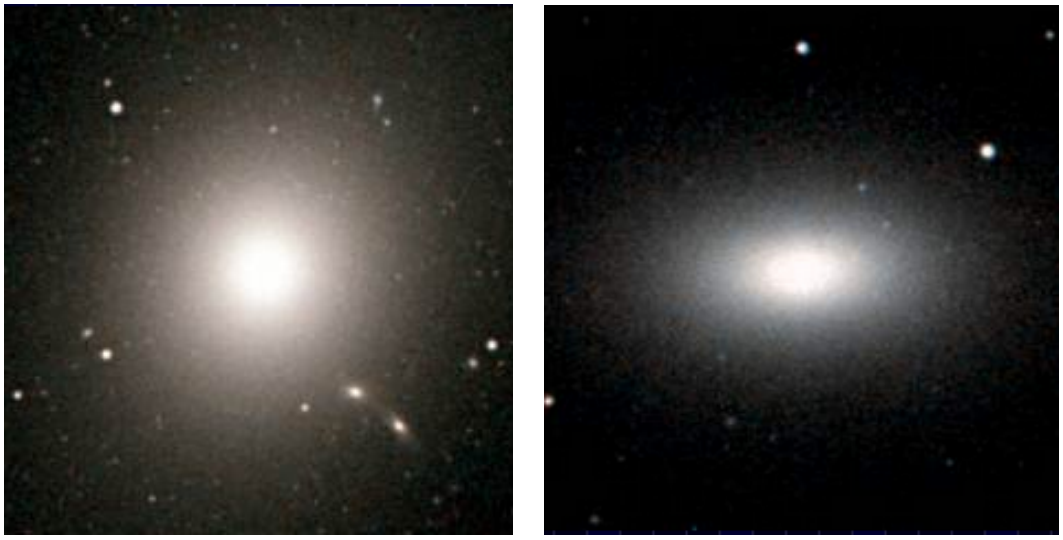

Figure 1.1: Right panel: Image of M87. Left panel: NGC 4473. Credit: Altas.

1.1.1.3 Spiral Galaxies

Unlike ellipticals, spiral galaxies contain a large amount of gas and dust, and new stars still form in today. They are therefore made up of stars of all ages and all masses. My thesis sample has a large proportion of spiral galaxies, especially due to the presence of large amount of gas within it that will allow us to observe the ionised gas emission coming from the galaxy using the Hα emission line. The galaxies perform a rotational movement around the center, which are at the original of most of their structure like for instance the spiral arms creation. The arms are mainly made up of hydrogen, especially in its molecular form. This is illustrated by the CO emission map and velocity field of M51 shown in Fig. 1.2 from Koda et al. (2009).

The spiral galaxies are subdivided into two main groups: the normal spirals, where the arms develop directly from the nucleus, are classified as Sa to Sm according to the nature of the spiral arms and the importance of the bulge. The barred spirals which have a large central bar whose extremities are the starting point of the arms and are marked SB (this is the case of our galaxy, the Milky Way). The spiral arms are believed to be high density regions (Grabelsky et al. 1987, Engargiola et al. 2003, Holwerda et al. 2005), this can be explained in the sense that when stars and interstellar matter cross an arm, they slow down and therefore create a higher density. The overall rotation of the galaxy is responsible for the flattening of the whole and the formation of the disc, this same rotation also prevents the gravitational collapse of the stars towards the center. The younger stars with a shorter lifetime are located in the spiral arms as traced by the Hα emission (e.g, Calzetti et al. 2005) while the old stars with a longer lifetime are more concentrated in the bulge and the stellar halo. Note also that between the spirals and ellipticals are the lenticular galaxies. Lenticular galaxies have huge bulge and faint disc, but they don't have spiral arms like spirals and have a poor interstellar medium. Lenticular galaxies are usually known as S0. The light of the spirals' discs usually follow an exponential radial decrease (Freeman 1970a).

1.1.1.4 Irregular Galaxies

These galaxies are for the most part deformed, and have no particular shape. The shape is defined by the bright HII regions (see Fig. 1.3) but the underlying profile is often very regular (Carignan & Beaulieu 1989) and similarly to the spiral galaxies' disc, usually is exponential. Irregular galaxies contain both old and young Pop I stars and significant amounts of gas and dust. Having a lot of gas and dust means a lot of star formation. This can make these galaxies very bright. Only a few of the extreme seem to be without a possible older stellar component, but the exact nature of this older population and the number of past generations of stars are not specific (Searle & Sargent 1972, Thuan 1983). Usually, irregular galaxies are found to be smaller and less massive than spiral and elliptical galaxies; in the optical bands, they also appear to be fainter because of their relatively high content of neutral hydrogen not yet converted into stars.

A variety of physical processes may be responsible for the structures of irregular galaxies Gallagher & Hunter (see review by 1984): first, their intrinsic projected

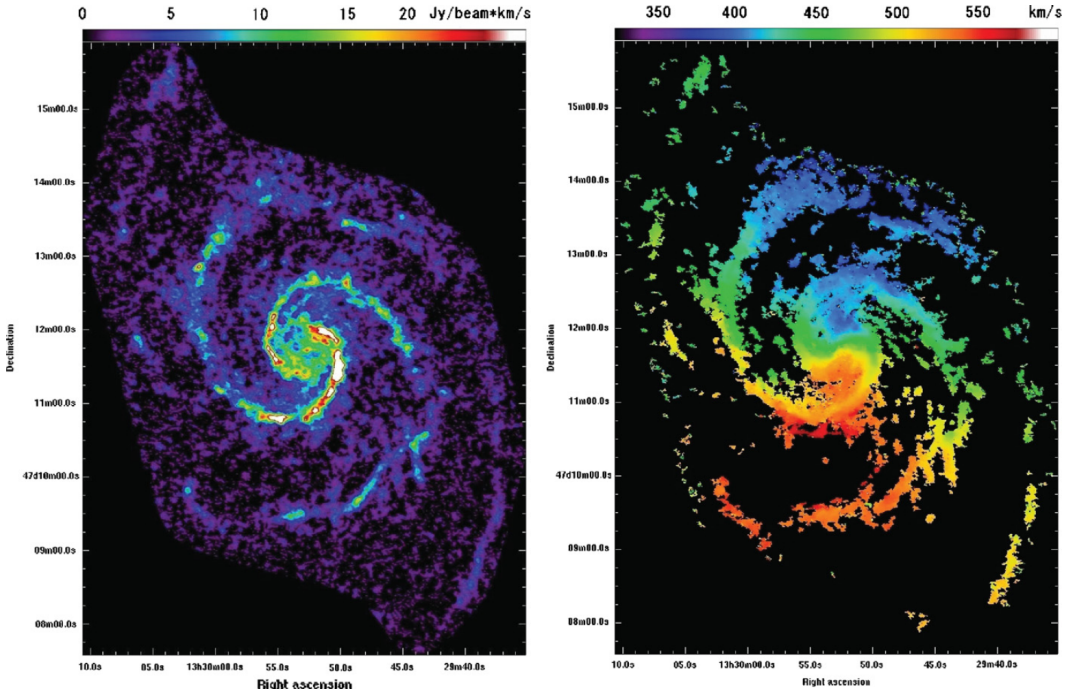

Figure 1.2: Left picture represents the integrated intensity map of $CO(J = 1 - 0)$ emission of M51. The right picture relates the velocity field. Credit: Koda et al. (2009).

Figure 1.3: Example of irregular galaxy DDO 155. Credit: www.lowell.edu

stellar mass distribution may undergo a disturbance, resulting in a non-symmetrical stellar distribution. Secondly, the dense interstellar gas in galaxies may be distributed in such a way that dark filaments are produced across the 2-dimensional optical image of the galaxies. Lastly, if a galaxy site of recent star formation is dominated by young, low mass-to-light ratios, massive stars, these regions may stand out against the rest of the galaxy's stellar regions, thus disrupting its symmetry. Irregular galaxies are also part of my thesis sample.

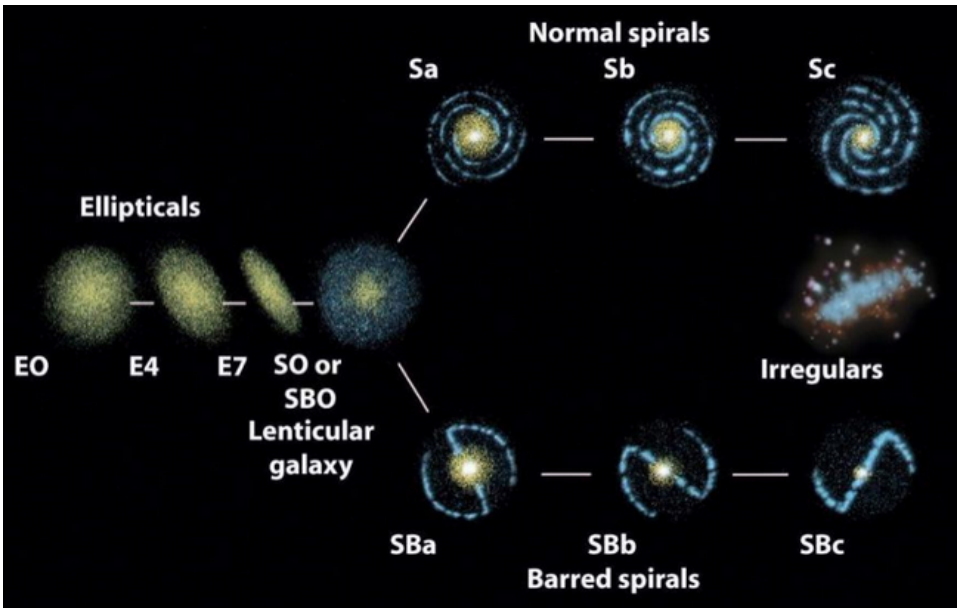

Figure 1.4: Hubble classification scheme of galaxies. Credit: www.physast.uga.edu

1.1.1.5 Influence of bulges and bars in galaxies

1.1.1.5.a *Bulges*

Most spiral galaxies contain a central bulge. Bulges are spherical structures basically made of stars that tend to be older than those in the disc and that can be explained in the sense that their formation would be made in the very early epoch of galaxy formation (Zoccali & Valenti 2016). A large fraction of our sample consists of bulgeless galaxies, they are irregular and late-type spiral (Sd to Sm) galaxies. The distribution of stars in the galactic bulge can be represented by a $r^{1/4}$ de Vaucouleurs profile, a Sersic profile and sometimes even by an exponential profile. Galaxy bulges are classified into two categories: classical bulges or pseudo-bulges (Kormendy &

Freeman 2004). Classical bulges would be spheroids mainly formed by external accretion during minor or major mergers (Bournaud et al. 2005, Katz 1992). Pseudo-bulges are noticed by the presence of bars in the innermost regions and originated from disc instabilities due to the presence of bars boosting the accretion of gas in the inner regions of the discs (Athanassoula 2005).

1.1.1.5.b *Bars*

The presence of bars has a strong influence on the galactic structures in affecting the stellar orbits and the angular momentum distribution in the galaxy including also the DM halo. The bar spins at a specific angular rate called pattern speed and the presence of a bulge influences the slowdown rate of the bar, in the sense that the pattern speed of bars decreases faster in the presence of a bulge than without it (Athanassoula 2003). The strong-barred galaxies show lower star formation activity and older stellar populations, with respect to weak-barred and unbarred disc objects (Vera et al. 2016). There is also a clear dependance found between the bar length and the morphological type of galaxies, the early-type disc galaxies have longer bars than late types (Elmegreen & Elmegreen 1985). However, the growth of the bar is not necessarily the same over time, sometimes, the bar strength can decrease up to total disappearance in the case of the interaction with a nearby galaxy. The gas inside galaxies is normally moving on circular orbits but for barred galaxies, the gas is moving along the bar and not in circular orbits. The non-circular orbits of gas in barred galaxies can affect their rotation curves and make them be non-axisymmetric (Randriamampandry et al. 2015). To understand the effect of the bar on the observed rotation curves, Randriamampandry et al. (2016) compared the bar properties from the simulations with the observations. They showed that gas bar and stellar bar have similar bar lengths. However, they found that gas bars are stronger.

1.1.2 Existence of the Dark Matter

It all began in 1933 when Fritz Zwicky studied the motion of a sample of galaxies in the Coma cluster and found that their radial velocities were much higher than predicted by the laws of physics; the gravitational force exerted by the cluster's baryonic matter was insufficient to keep the galaxies from moving apart. Zwicky then predicted the presence of some matter with a mass higher than that of the

cluster's visible matter (Zwicky 1933). It would not be until almost 40 years later that Vera Rubin, in 1970, studied the Andromeda galaxy's rotation curve and noticed that stars located in the outer parts of the galaxy were moving at roughly than stars in the central regions (Rubin & Ford 1970). This is in contradiction with the stellar light distribution, which requires that objects farther away from most of the mass move slower than objects closer to most of the mass in stars and gas. In 1970 also, Freeman wrote about the HI rotation curve of NGC 300 obtained with Parkes: "If the HI rotation curve is correct, then there must be undetected matter beyond the optical extent of NGC 300; its mass must be at least of the same order as the mass of the detected galaxy" (Freeman 1970b).

For objects in the outer parts of the galaxy to move this fast, there has to be an important mass that keeps the whole system gravitationally bound together. The respective conclusions of Zwicky, Rubin and Freeman will allow to shed a light on the existence of some halo of invisible matter whose presence is only "felt" by its gravitational effect : the famous "Dark Matter". Ever since astronomers got the idea of the existence of the DM, several devices were developed in hope to detect it, but every effort has thus far been vain. No DM particle has yet been detected. Numerous hypotheses regarding its composition were formulated and explored, its study being fuelled by the fact that the matter is a key component in the evolution of the universe. Without the DM, the formation of stars, galaxies, the solar system and life on Earth would have been improbable.

Several experimental methods describe the presence of DM on different scales.

1. On the cosmological scale, the DM is detected thanks to the observations of the Cosmic Microwave Background (CMB, see e.g, Komatsu et al. 2011). Being made of photons emitted when the Universe was much younger (380 000 year old) with a homogeneous and isotropic plasma and a temperature of 3000 K, the detection of the CMB gives us an image of the Universe at a much earlier epoch and is therefore essential to understand the state of the matter as it was just $\sim$ 400 000 years after the formation of the Universe. The CMB anisotropies is decomposed into a strong spectrum providing the existence of DM and dark energy (Hložek et al. 2016). The first peak represents the density of the baryonic matter and the third peak shows mostly the density of the DM.

2. The method of gravitational lensing where DM creates gravitational lenses that distort background galaxies. These results in a deviation of light rays by massive objects and therefore a distortion of the image of a galaxy when a massive galaxy or cluster of galaxies happens to be on the line of sight (Brainerd et al. 1996). This technique of gravitational lensing allows us to not only determine the mass of DM distribution in massive objects, but also its distribution therein. Thus, by analysing the distortions on a cluster, one can obtain, from the mass of visible matter, the distribution of DM on large regions of the sky.

3. The Chandra observations of the Bullet cluster (Markevitch et al. 2004), a collision between two galaxy clusters may provides evidence on the existence of the DM. Therefore, during the interaction, the gas particles become more hot due to the high energy of the collision and emit an intense observable X-ray. However, the distribution of the total mass of the cluster does not correspond to the distribution of the gas, a large part of the mass seems to be invisible. Therefore the famous "bullet cluster" has been presented as a direct evidence for the existence of DM (Clowe et al. 2006).

4. Lastly, on galactic scales with the method of the mass models (which is extensively used in the present work), which allow to determine the mass distribution of the DM in galaxies from their rotation curves and the distribution of their visible components. This technique was developed by Rots (1975), Carignan (1983). Numerous studies were carried on the subject with interesting results on the distribution of the DM halo of galaxies (e.g, de Blok & Bosma 2002, Blais-Ouellette et al. 2001, de Blok et al. 2008, Spano et al. 2008, Randriamampandry & Carignan 2014, Bottema & Pestaña 2015, Lelli et al. 2016).

All these models will allow us to better understand the distribution of the DM halo and the baryonic matter in galaxies, and also determine the best suited model to describe the DM inside discs of nearby galaxies.

However, DM could be baryonic or non-baryonic. For the baryonic DM (protons, neutrons, electrons), the most probable candidates are the brown dwarfs, dust particles, molecular hydrogen (H_2) clouds, black holes. But we know that on large scales (e.g, clusters of galaxies) there is not enough baryonic DM in the universe,

so a large part of the DM should be non-baryonic. The non-baryonic DM such as neutrinos, the Weakly Interactive Massive Particles (WIMPs) which, by definition, are massive particles weakly interacting with ordinary matter. WIMPs are made of hypothetic particles such as neutralinos, axions and photinos.

Another solution to solve the DM puzzle is to rethink the laws of gravity on large scales in order to conceive a universe without DM, as suggested in 1983 by Milgrom (1983b;a) with his theory of MOND (MOdified Newtonian Dynamics). The theory of MOND is as follows: according to Newton's laws of gravitation, an object of mass M attracting a smaller object of mass m at a distance r away is described by

$$a = \frac{GM}{r^2} \tag{1.1}$$

where a represents the acceleration of the smaller object and G the Newton's gravitational constant. Milgrom wrote the above equation with an extra factor $\mu(\frac{a}{a_0})$ where a_0 is a scale constant and

$$\mu a = \frac{GM}{r^2}. \tag{1.2}$$

1.2 Instrumentation and GHASP survey

1.2.1 Introduction

The rotation curves presented in this thesis were obtained by using a special instrument which consists of the Fabry-Perot (FP) interferometer within a focal reducer installed on the 1.93m telescope at the OHP (Observatoire de Haute-Provence) in France. It is an ideal instrument for the spectral study of low luminosity extended objects such as galaxies and nebulae. It allows us to make the kinematical study of our sample because it makes it possible to measure with precision the radial velocities of the ionised regions of interstellar hydrogen. I will give a brief overview of the instrument. More informations can be found in Garrido et al. (2003) and Epinat et al. (2008b).

Developed in 1896 by Charles Fabry and Alfred Perot in order to measure width variations in metrology, the Fabry-Perot etalon was used in astronomy for the first time in 1914 by Buisson et al. (1914), to kinematically study the ionized gas of the Orion nebula, with the 80cm Foucault telescope of the *Observatoire de Marseille*.

Over fifty years later, in 1972, Courtes used the FP interferometer to study HII regions in the Galaxy and in other nearby galaxies.

The ordinary FP instrument used for observing until 1970 was made of etalon for which the distance between the plates was fixed, which did not allow to cover the whole velocity range; this type is called FP etalon. The FP interferometer, which has a varying distance between the plates, was developed in 1970 with the ability to scan the velocity range. Ever since, the interferometer has been widely used throughout the world by various astronomers at the LAM and other research institutes (Boulesteix et al. 1987, Laval et al. 1987, Marcelin et al. 1987, Amram et al. 1991, Plana & Boulesteix 1996, Russeil et al. 1998, Gach et al. 2002, Garrido et al. 2003, Epinat et al. 2008b). The whole sample of the GHASP survey was observed using the FP interferometer, which allows us to obtain data cubes made of spectra for every bidimensional image; GHASP is, to date, the largest sample ever observed with a FP interferometer.

1.2.2 Focal reducer

The focal reducer is composed of a field lens, a collimator and a camera lens. Its goal is to reduce the telescope's focal length, and thus decrease the aperture ratio F/D, which is proportional to the ratio F/f of the collimator's (F) and lens's (f) focal lengths (Courtès 1960). Thus, the observed field is larger and the detection power of extended, low brightness sources by the telescope increases given that the intensity of the incoming light on the detector is inversely proportional to the squared focal length. The path followed by an incoming light ray as it crosses the focal reducer is showed in Figure 1.5. An incoming light ray falling on the focal reducer first encounters the field lens; this will broaden the field of view and increase the detection power of the light source and channel the outer rays towards the collimator. The latter allows light rays coming from a same point of the telescope's focal plane, i.e from a same region of the observed galaxy, to come out parallel to each other and fall on the focal plane with the same angle. The light rays coming out of the focal plane form interference rings at infinite, hence the importance to make use of a lens to re-focus the image on the receiver.

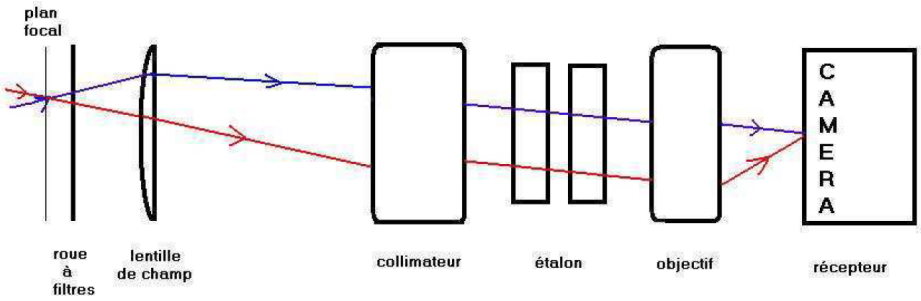

Figure 1.5: The focal reducer used by the GHASP survey, mounted on the Cassegrain system of the OHP 193cm telescope, and the trajectory of light rays coming out of the secondary mirror. Credit: Garrido Ph.D. Thesis, 2003.

1.2.3 Fabry-Perot interferometer and interference filter

The interferometer is composed of two semi-reflecting blades of transmissivity τ_1, τ_2, of reflexivity ρ_1, ρ_2, of width e and index n ($n = 1$ in the air); the electric field of a two-dimensional wave contained in an incident beam of inclination θ with respect to the FP's optical axis is written

$$\mathrm{E}(\lambda) = \mathrm{U}\mathrm{e}^{-\mathrm{iwt}+\mathrm{i}\phi_\mathrm{o}} \tag{1.3}$$

where $\mathrm{w} = 2\pi\mathrm{c}\lambda$ is the angular frequency, U is the wave's amplitude and ϕ_0 the phase at the origin. The difference of optical path between the blades l_1 and l_2 is given by

$$\delta = l1 - l2 = 2ne\cos(\theta) \tag{1.4}$$

For a given position, several waves of different wavelengths are transmitted. To avoid a superposition of these different wavelengths, one uses interference filters (see figure 1.7). These filters block all wavelengths but the desired ones, resulting in a final beam only spanning a narrow spectral range. This allows one to reduce the contamination of the galaxy's signal by eventual undesired continuum sources or any other source. The resulting image therefore only contains the light corresponding to the conditions of the FP's peak transmission.

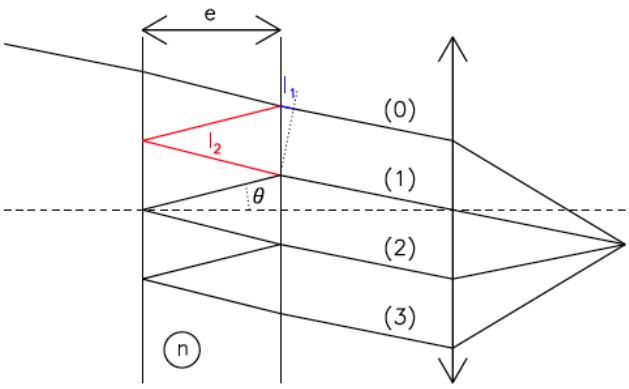

Figure 1.6: Path of the light ray inside the FP cavity and the image construction by the camera lens at infinite. Credit: Epinat Ph.D. Thesis, 2008

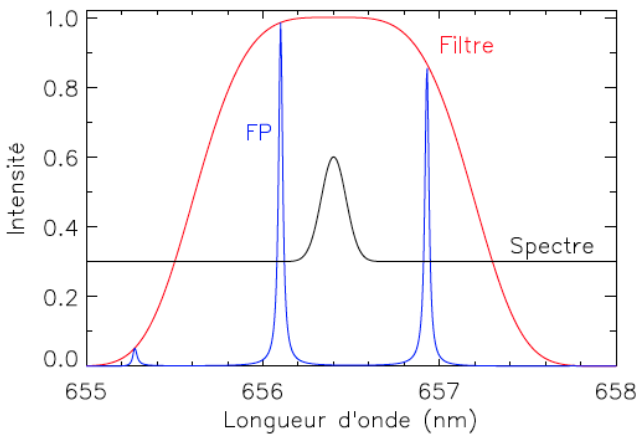

Figure 1.7: FP's Airy function modulated by the interference filter's response. Credit: Epinat Ph.D. Thesis, 2008

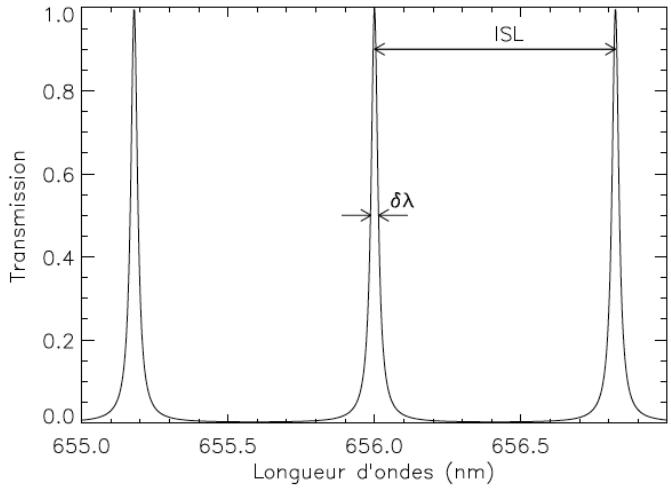

Figure 1.8: Airy function with a reflection of 0.9 and working at an order of 798 for the Hα line (656.3 nm). Credit: Epinat Ph.D. Thesis, 2008

The Airy function I(λ, θ) represented in the figure 1.8 is given by:

$$\mathrm{I}(\lambda, \theta) = \mathrm{I_o} \left(\frac{\tau}{1-\rho} \right)^2 \frac{1}{1 + \frac{\mathrm{AF}^2}{\pi^2} \sin^2(\frac{\phi}{2})} \tag{1.5}$$

with $\mathrm{I_o} = |\mathrm{U}|^2$

$\tau = \tau_1 \tau_2$

$\rho = \rho_1 \rho_2$

F the finesse, $\mathrm{F} = \frac{\pi\sqrt{\rho}}{1-\rho}$ and $\phi = \frac{4\pi ne \cos i}{\lambda}$ is the phase shift

I(λ, θ) is a 2π periodic function of ϕ.

The fundamental relationship expressing the wavelength of order p for a FP of index n and blade spacing e is :

$$\lambda p = 2ne \cos\theta \tag{1.6}$$

with $P \in \mathbb{N}$.

When observing an extended monochromatic light source with the FP of intensity

I, we observe the existence of interference rings in the interferograms. This is illustrated in figure 1.9. This figure shows the 3D data cube obtained from varying the spacing between the FP plates; that means a 2D (x,y) image associate at a 1D (z) spectra.

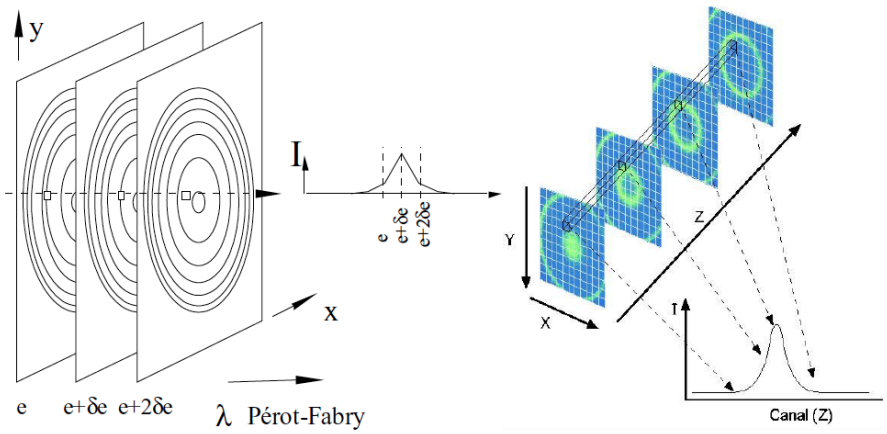

Figure 1.9: Formation of the recovered information when varying the spacing between the FP plates. Credit: Le Coarer HDR, 2005.

1.2.4 The Hα emission line

In astronomy, the Hα line is used to trace the ionised hydrogen content in gas clouds. This emission line, of red colour is located in the visible part of the electromagnetic spectrum at a wavelength of 656.3 nm. It is the main line of the Balmer series and is emitted during the transition of an hydrogen atom from a $n = 3$ energy level towards a $n = 2$ energy level. This line is used to determine the shape and the size of clouds. Within the optical disc, the Hα line is the most used to get the motions in galaxies because it is intense and predominant in nebulae.

1.3 GHASP Survey and kinematical data

The GHASP (Gassendi HAlpha survey of SPirals) survey is composed of 203 spiral and irregular galaxies that were observed with the 1.9m telescope of the OHP using the Hα line with Fabry-Perot techniques and leading to the construction of data cubes (Garrido et al. 2002; 2003; 2004; 2005, Epinat et al. 2008b;a). The exposure

time is approximatively 2 hours per galaxy. The candidates of the survey were selected by giving a priority to the isolated galaxies without companions; however, because such objects are not very common among local galaxies (within 0.5Mpc), some galaxies with companions were included in the sample. The sample has been chosen from the catalog WHISP (Westerbork survey of H1 in SPiral galaxies) which contains about 400 galaxies mapped with neutral hydrogen (van der Hulst et al. 2001). The GHASP survey selection have been made following several criteria (absolute magnitude, morphological type, inclination, systemic velocity ...) as indicated on the figure 1.10. More details about the selections criteria and the GHASP objectives are shown in Garrido et al. (2003).

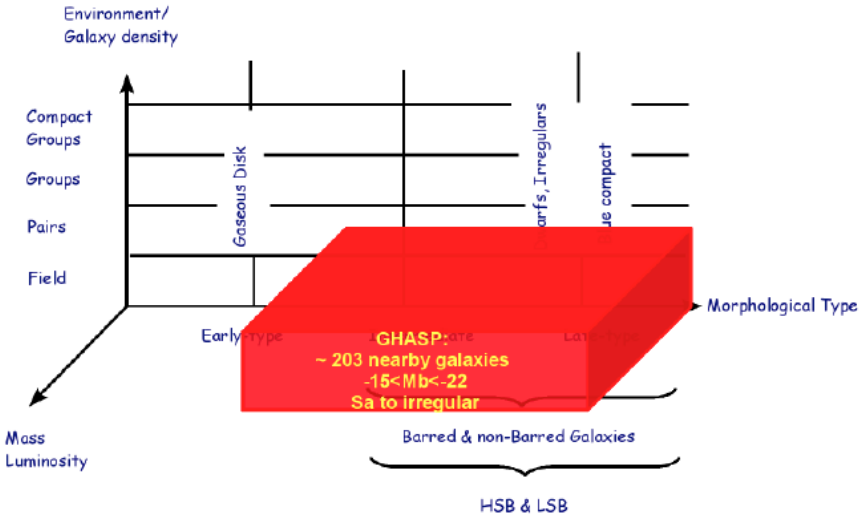

Figure 1.10: Local reference sample of GHASP .

The sample has been obtained using a 256×256 Imaging Photon Counting System (IPCS) until 2000 March with run numbers from 1 to 4 and pixel scales of 0.96 arcsec and since 2000 October by using a 512×512 IPCS with run numbers from 5 to 14 and a pixel scale of 0.68 arcsec (Epinat et al. 2008b). The Ghasp sample is the largest Fabry-Perot survey today, but there was other Fabry-Perot interferometer projects (SINGS, Virgo, GHαFAS samples) using the same set-up, such as BHαBAR (Hernandez et al. 2005), SINGS (Daigle et al. 2006), Virgo (Chemin et al. 2006) and GHαFAS (Hernandez et al. 2008). Using GHASP allows us to get accurate disc kinematics studies and then to determine the visible matter and the dark matter halo distribution covering all morphological types (early to late

type galaxies). The rotation curves and kinematical parameters (systemic velocity, position of the center, position angle, inclination and rotation velocity) of these galaxies were already derived and published and also can be found on the following website https://cesam.lam.fr/fabryperot/.

The objective of my thesis is to combine kinematical data with the photometry data already available in the literature to get the mass models and then to determine the DM distribution in the inner parts of the galaxies . Since knowledge of the distribution of the DM in galaxies is one of the keys to understanding the formation and evolution of these objects, this study allows us to bring one more element to the knowledge on galaxies at low redshifts.

The kinematical data of 170 galaxies from a total sample of 203 local galaxies have been used in this document, we just made our study on 170 galaxies in the sense that some rotation curves have very low quality and high dispersions and difficult to be used to fit correctly with mass models and also we selected galaxies having photometric profile in the optical R_c band and the infrared W1 (3.4 μm) of WISE.

We extended our rotation curves as far as possible beyond the optical edge with HI data available in the literature to derive hybrid rotation curves. We found 31 HI rotation curves from the literature: 15 have been taken from van Eymeren et al. (2011) and the remaining 16 from Lelli et al. (2016) can be accessed at SPARC website.

1.4 Photometry data and decomposition

As I have already mentioned, we have worked with photometry in the optical R_c and the infrared W1 of WISE which are available in the literature. These bands are much more representative of the stellar mass than bluer bands. The luminosity of the spiral galaxies are dominated by young and blue stars, therefore of population I whereas the bulges are rather dominated by stars of population II (old and red) consequently rich in metal (Peletier & Balcells 1996). Combining the photometry of the visible and infrared band will allow us to better understand the stellar distribution and then get better constrains on the parameters of the different components (i.e. the M/L ratio) in the inner regions of the galaxies and to better know the distribution of the DM halo in the inner parts and beyond the disc. I will start to discuss first the photometric data in the R_c and after the photometric data in the infrared band W1

of WISE.

1.4.1 R_c band photometry

The surface photometry in the R_c band of 100 galaxies of our sample is available in the literature. This photometric sample is built from two different sources; the first one is composed of 73 luminosity profiles and have been observed over many years by using the R_c band at the Observatoire de Haute-Provence (OHP) and the second one contains 27 $ugriz$ luminosity profiles derived from the public Sloan Digital Sky Survey (SDSS) data. The 1σ limits of the images are $u = 22.0$, $g = 22.2$, $r = 22.2$, $i = 21.3$ and $z = 20.5$; these values depend on the seeing and the sky brightness (Abazajian et al. 2004). The data observed using the R_c band at OHP goes about half a magnitude deeper than the SDSS one (Barbosa et al. 2015). The R_c band images of the sample of 73 galaxies have been obtained with the 1.2 m telescope at OHP using the single CCD with array of 1024×1024 pixels, a pixel size of 0.685 arcsec and a field of view of 11.7 arcmin $\times$ 11.7 arcmin. The Point Spread Function (PSF) has been modeled using the IRAF PSFMEASURE task by selecting bright, unsaturated stars across the fields and modeling their light profiles with a circular Moffat function given by:

$$\mathrm{PSF(r)} = \frac{\beta - 1}{\pi\alpha^2}[1 + (\frac{\mathrm{r}}{\alpha})^2]^{-\beta} \tag{1.7}$$

where the radial scale length α and the slope β are free parameters (Barbosa et al. 2015) with the full-width at half-maximum, $\mathrm{FWHM} = 2\alpha\sqrt{2^{\frac{1}{\beta}} - 1}$ (Trujillo et al. 2001).

The 27 SDSS $ugriz$ photometry images coming form the SDSS DR7 (Abazajian et al. 2009) have been transformed to the R_c band (Barbosa et al. 2015) using this relation:

$$\mu_{\mathrm{R}}(\mathrm{r}) = 0.42\mu_{\mathrm{g}}(\mathrm{r}) - 0.38\mu_{\mathrm{r}}(\mathrm{r}) + 0.96\mu_{\mathrm{i}}(\mathrm{r}) - 0.16 \tag{1.8}$$

with μ(r) the surface brightness profile at the radius r in the passband indicated in the subscripts.

To test the accuracy of this equation, the comparison of OHP R_c band surface brightness profiles and profiles derived from the SDSS *ugriz* bands has been made on a sample of 54 galaxies for which the geometric parameters are similar for both data sets. This comparison can be found in Figure 1.11 which shows the difference between the R_c surface brightness profiles for OHP and SDSS versus the OHP surface brightness profile relative to the sky level. In Figure 1.11, the red dash line indicate that the error coming from the procedure of the transformation between the photometric systems is $\sim$ 0.08 mag.arcsec^{-2} in the regions brighter than the sky level, $\sim$ 0.15 mag.arcsec^{-2} for the regions two magnitudes lower, and $\sim$ 0.4 mag.arcsec^{-2} for the regions with 5 magnitudes lower than the sky level.

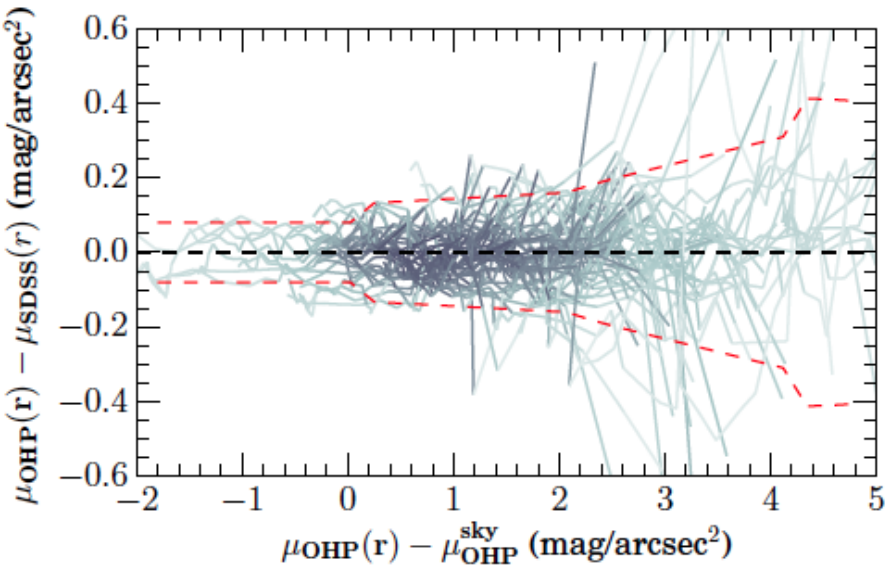

Figure 1.11: Difference between R_c band surface brightness profiles for OHP and SDSS data obtained using the relation of the equation 3.1 for 54 galaxies in common for both samples as a function of the OHP surface brightness profile relative to the sky level. Each blue line represents the difference in the surface brightness profiles of a single galaxy profile comparison and the dash red lines the running RMS difference between the profiles. Credit: Barbosa et al. (2015).

The decomposition of 73 R_c band galaxies of OHP has been done by Barbosa et al. (2015) and the 27 R_c band galaxies from SDSS have been decomposed by us. We used the same method used by Barbosa et al. (2015) to decompose the 27 R_c band

galaxies from SDSS. The central parts of the observed rotation curves are explained by scaling up the stellar contributions (disc and bulge). The limit surface brightness restriction is 24.5 mag arcsec^{-2}. The early-type galaxies of our sample have an important bulge. However, many galaxies have very little or no bulge component (specifically late type and irregular galaxies). In that case, the luminosity profiles were not decomposed, we took the observed surface brightness profile and called it disc component to make our mass models. For the galaxies with the presence of a bulge, we used a parametric profile fitting procedure to separate the photometric components like bulge, disc, bar, spiral arm, ring. The aim of using this method of decomposition is to obtain an accurate bulge component in the central part of the observed surface brightness profile.

For the Type I galaxies that means with a simple disc, we used the exponential disc function to obtain the disc component by this equation:

$$I_d(r) = I_o exp(-\frac{r}{h}) \tag{1.9}$$

where I_o is the central intensity of the disc and h the disc scale length and the total apparent magnitude is :

$$m_{disc} = -2.5log(2\pi I_o h^2 \frac{b}{a}) \tag{1.10}$$

with $\frac{b}{a} = 1 - \epsilon$ the minor to major axis ratio for the galaxy.

For the Type II or downbending (meaning discs with downward truncations) and Type III or upbending (discs with upward bends) we used the following equation to describe the disc component:

$$I_d(r) = SI_o exp(-\frac{r}{h_i}).\{1 + exp[\alpha(r - r_b)]\}^{\frac{1}{\alpha}(\frac{1}{h_i} - \frac{1}{h_o})} \tag{1.11}$$

with I_o the central intensity of the disc, h_i the inner disc scale length, h_o the outer disc scale length, r_b the break radius and α the sharpness of the disc transition between the inner and the outer region. The scaling factor S is given by :

$$S = [1 + \exp(-\alpha r_b)]^{-\frac{1}{\alpha}(\frac{1}{h_i} - \frac{1}{h_o})} \tag{1.12}$$

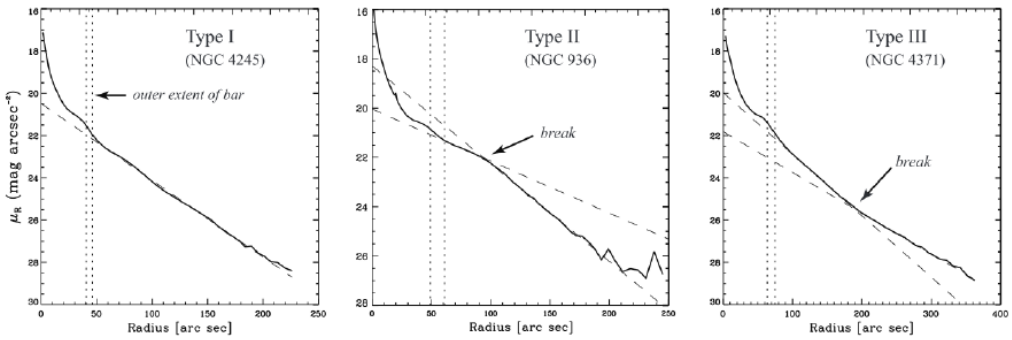

Figure 1.12: Surface brightness profiles for three galaxies with the three different disc types. From left to right panel, we have respectively the Type I, the Type II and the Type III. Credit: Peschken Ph.D. Thesis, 2016.

The other components like bulge, bar, spiral arm, ring have been determined by using the Sérsic function given by :

$$I_b(r) = I_e \exp\left(-b_n\left[(\frac{r}{r_e})^{\frac{1}{n}} - 1\right]\right) \tag{1.13}$$

where r_e is the effective radius, I_e is the intensity at the effective radius, n is the Sersic shape parameter and b_n the scaling $\gamma(b_n, 2n) = \frac{1}{2}\Gamma(2n)$, with γ the incomplete function and Γ the complete function. The total apparent magnitude is :

$$m_{sersic} = -2.5\log\left(\frac{2\pi I_e r_e^2 \exp^{b_n} n\Gamma(2n)}{b_n^{2n}}\frac{b}{a}\right) \tag{1.14}$$

with $\Gamma(x)$ the complete function of a variable x.

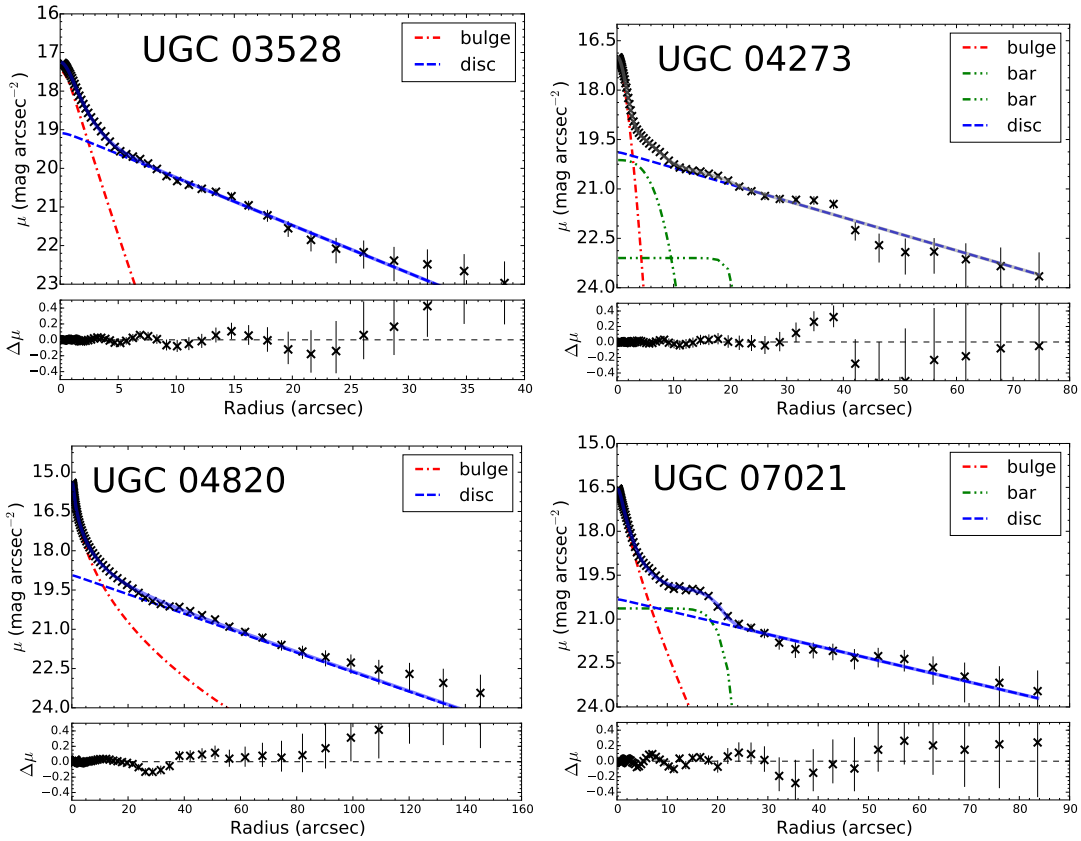

Figure 1.13: Example of the structural decomposition for 4 galaxies in the R_c band: UGC 3528, 4273, 4820, 7021. For each galaxy, the upper panel shows the surface brightness profile (black cross) and the different components (dash line) , the bottom panel represents the fitting residuals.

To built our mass models we assume that the luminous parts are composed of two principal components; we disentangle spherical components (bulges) from planar components (disc, bar, spiral arm, ring, etc.) that we call disc in the mass models. Therefore, we used this disc component and the bulge component to do our mass models because the total luminosity profile at each point in a galaxy is a superposition of light coming from the bulge and disc. When the surface brightness profile cover a smaller part of the galaxy than the rotation curve, we extrapolated the last points of the SB profile by fitting them in order to extend the radius to a value higher than the last radius value of the rotation curve. This extrapolation is only useful for the disc component and not for the bulge because the SB of bulges falls much faster. The advantage for doing the extrapolation is to obtain a smooth disc contribution at the outer radius. This prevents having a truncation blip in our mass profiles (Casertano 1983).

1.4.2 Photometry in the 3.4 μm infrared band

We used the infrared photometry of 121 galaxies in the W1 (3.4 μm) band of WISE (Wide-field Infrared Survey Explorer) already available in the literature. WISE is a NASA-funded Medium-Class Explorer mission, which consists of a 40 cm primary-mirror space infrared telescope mapping the entire sky at the infrared wavelengths W1(3.4 μm), W2(4.6 μm), W3(12 μm) and W4(22 μm) with minimum 5σ sensitivities of 0.08, 0.11, 0.8 and 6 mJy, respectively. The science instrumentation includes a 1024×1024 pixel Si:As and HgCdTe array, each band covers a field of view of 47arcmin × 47arcmin with an angular resolution of 6 arcsec in the short bandpasses and 12 arcsec in the longest bandpass. W1 is the most sensitive for almost all types of galaxies and has the larger isophotal radius, the adopted 1σ elliptical isophotal radius corresponding to the 1σ isophotal surface brightness equal to 23.0 mag arcsec^{-2} (Vega; and 25.7 mag arcsec^{-2} in AB) for W1 and 21.8 mag arcsec^{-2} for W2 (Jarrett et al. 2013). Optimal profile (PSF) fitting has been used to measure the fluxes of stars and the calibration zero-point magnitude is derived from these measurements of calibration stars (Jarrett et al. 2013). We used the photometric profile of 121 galaxies which corresponds to the galaxies for which we have a good resolution and low dispersion rotation curves. The decomposition has been made by using the same method that we used to decompose the 27 R_c band photometry if needed from SDSS.

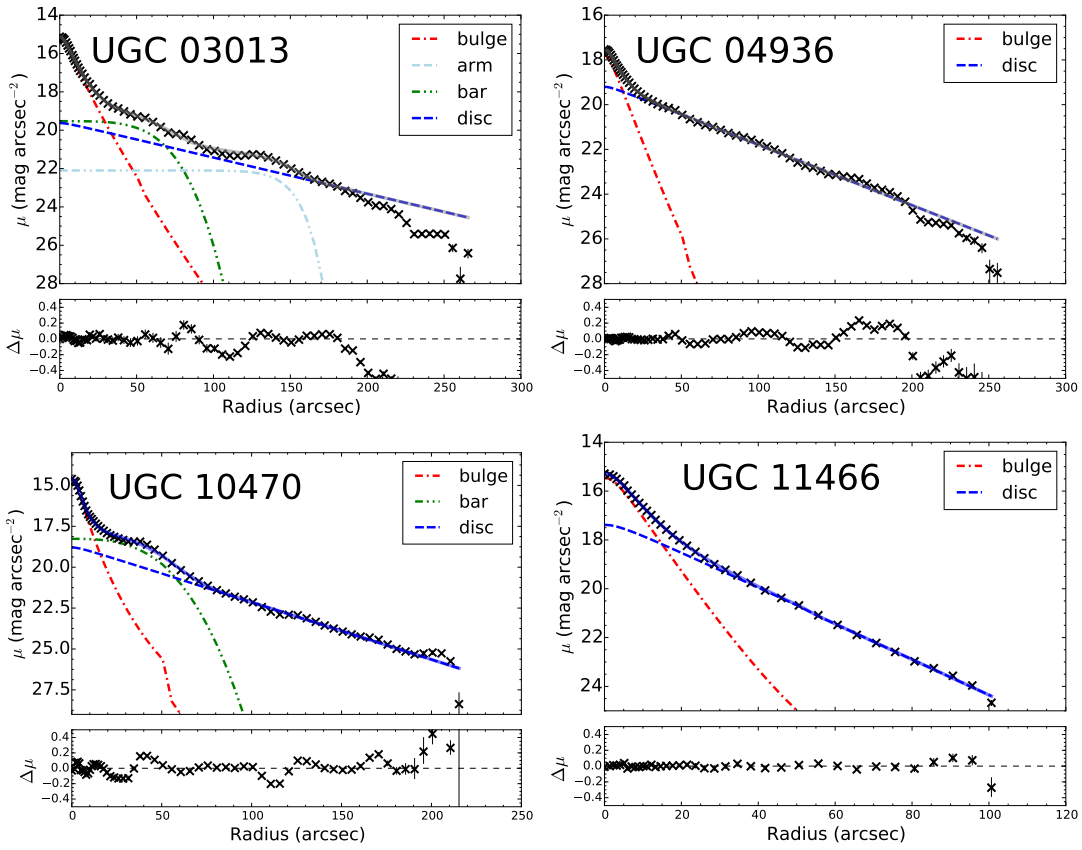

Figure 1.14: Example of the structural decomposition for 4 galaxies in the W1 band: UGC 3013, 4936, 10470, 11466. For each galaxy, the upper panel shows the surface brightness profile (black cross) and the different components (dash line) , the bottom panel represents the fitting residuals.

1.5 Mass models

To describe our rotation curves we used two main DM halo models. The first model is called the pseudo isothermal sphere (ISO) or observational model which assumes a core density halo in the center and the second one called the NFW halo, which predicts a cuspy density halo. The luminous matter distribution depends mainly on the M/L ratio. For our mass models distribution, all the luminous matter is derived from the R_c and infrared photometry bands. We extend some hight resolution Hα rotation curves with the HI when available in the literature. The mass models showed in this document are all made by using a new python code built by us. The rotational velocities from all the contributions are then added and compared to the rotation curves using a χ^2 (chi-square) minimization. The equations are shown below:

$$V_{\rm rot}(r) = \sqrt{V^2_{\rm disc} + V^2_{\rm bulge} + V^2_{\rm halo}} \tag{1.15}$$

$$\chi^2 = \sum_i \left(\frac{\rm X_i - \mu_i}{\sigma_i} \right)^2 \tag{1.16}$$

with $i \in N$ and $\rm X_i$ the observations, μ_i the rotational velocities from all the components (disc, bulge, gas, DM halo) , σ_i the errors from the observations.

The reduced χ^2 is obtained by $\chi^2_{\rm red} = \chi^2/(\rm N_p - N_d)$, with $\rm N_p$ the number of points in the rotation curve, $\rm N_d$ the number of degrees of freedom in the fits.

1.5.1 Pseudo Isothermal Profile

The dark halo density distribution can be described by assuming that the density profile follows a symmetric and spherical distribution and has a flat core in the center (Begeman 1987, Kravtsov et al. 1998, Jimenez et al. 2003). The DM halo can be model either by an isothermal sphere (Blais-Ouellette et al. 1999) or a pseudo isothermal sphere (acronym ISO) (de Blok & McGaugh 1996). Since, the density distribution of the isothermal sphere need to be calculated numerically, we use in

this work the ISO model for which the density has the simple analytic form. This density distribution $\rho_{\rm iso}(r)$ is given by :

$$\rho_{\rm iso}(r) = \frac{\rho_0}{\left[1 + \left(\frac{r}{r_0}\right)^2\right]} \tag{1.17}$$

with the corresponding rotation curve $V_{\rm iso}(r)$ by:

$$V_{\rm iso}(r)^2 = 4\pi G\rho_0 r_0^2 \left[1 - \frac{r_0}{r}\arctan\left(\frac{r}{r_0}\right)\right] \tag{1.18}$$

which is an increasing function of r, asymptotically reaching $V_{\rm max} = V(r = \infty) = \sqrt{4\pi G\rho_0 r_0^2}$
where ρ_0 is the central density of the DM, r_0 is the scale radius.

As we already know that the mass-to-light ratio (M/L) defines the galactic disc contribution, better constraints on this value help us to derive better dark halo parameters. To reach this, we decided to used three different technics based on the M/L ratio to study the shape of the halo distribution; the best fit model, the maximum disc fit, the M/L calculated as a function of the colours.

1.5.2 ΛCDM density profile (NFW)

The formation of galaxies is a non-linear process and then the direct computation through N-body numerical simulations is required. These numerical simulations predict cuspy halo profiles peaked in the centre (Navarro et al. 1996). This model is also called the universal profile or Navarro-Frenk-White profile (NFW) profile. The density profile is given by:

$$\rho_{\rm NFW}(\mathrm{r}) = \frac{\rho_{\rm i}}{\left(\frac{\mathrm{r}}{\mathrm{r_s}}\right)\left(1 + \frac{\mathrm{r}}{\mathrm{r_s}}\right)^2} \tag{1.19}$$

where ρ_i is the density of the universe at the time of collapse and r_s is a scale radius. The density and radius are strongly correlated with the mass of the halo and the density tends to r^{-1} at small radius.

The rotation curve is given by

$$V^2_{NFW}(r) = V^2_{200}\left[\frac{\ln(1+cx) - cx/(1+cx)}{x[\ln(1+c) - c/(1+c)]}\right] \tag{1.20}$$

where V_{200} is the velocity at the virial radius R_{200}, $c = R_{200}/R_s$ gives the concentration parameter of the halo and x is defined as R/R_s. The relation between V_{200} and R_{200} is given by:

$$V_{200} = \frac{R_{200} \times H_0}{100} \tag{1.21}$$

where H_0 is the Hubble constant in km s^{-1} Mpc^{-1}. For the model NFW, we use two techniques to describe the mass models: the best fit model and the M/L calculated as a function of the colours (see equations 3.5 and 1.23).

The two density profiles used in this document to describe the halo distribution are shown in the following Figure 1.15.

1.5.3 Fitting procedures

To model the mass distribution of the DM, we used different fitting strategies to deal with the mass-to-light ratio (M/L).

1.5.3.1 The Best Fit Model

The best fitting model (BFM) is obtained by minimizing the χ^2 with three free parameters ($(M/L)_{disc}$, ρ_0, r_0) for no bulge galaxies and four free parameters if we added the $(M/L)_{bulge}$ for galaxies with a bulge.

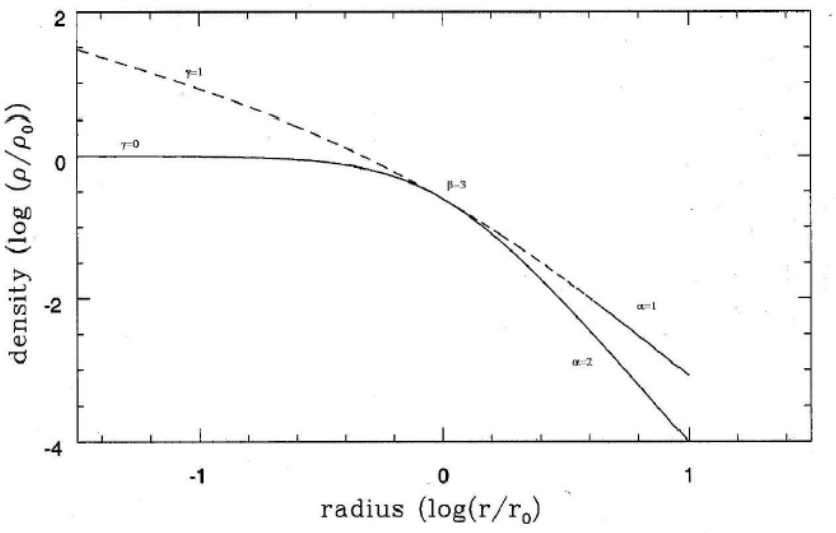

Figure 1.15: Density profiles for the ISO profile and NFW profile respectively in full and dash line. Credit: Garrido Ph.D. Thesis, 2003.

1.5.3.2 The Maximum disc Fit

The Maximum disc Model (MDM) assumes a maximum contribution of the luminous components to the rotation curve, without exceeding it by minimizing the dark halo contributions and therefore gives an upper limit on the mass surface density in stellar discs. The maximum disc fit allows us to conclude if the galaxies are dominated by DM. This technique was used (Swaters 1999) on dwarf late type galaxies and they found that dwarf galaxies are not necessarily dominated by DM into the inner regions but outside the optical disc, the DM is dominating. Kent (1987) and Bottema & Pestaña (2015) also used the MDM to fit spiral galaxies and find good agreement between models and data. The M/L of the MDM is obtained using the following procedure: we first run the BFM to estimate the M/L ratio corresponding to the minimal $\chi^2_{\rm BFM}$. We therefore require the M/L of the disc to be higher than that obtained with the BFM but letting the χ^2 to increase up to $1.3 \times \chi^2_{\rm BFM}$. This limit is chosen from the intrinsic dispersion of the data and from the degeneracy of the fits.

1.5.3.3 The colour M/L relationships

To constrain the stellar mass distribution, we used the colour M/L relationships in the sense that the stellar population models predict a strong correlation between the optical colour of the population and its M/L ratio. The relative quantities of DM and luminous matter is strongly depended of the M/L ratio. The M/L values for their colours increase faster for late type galaxies than early type galaxies meaning that late type galaxies (means galaxies with tiny or no bulge) are more dominated by the DM (Tinsley 1981). In the case of using the M/L with W1 − W2, we just have the halo parameters (ρ_0, r_0) as free parameters and we fixed the $(M/L)_{disc}$ and $(M/L)_{bulge}$. The M/L ratio value depends on the band used.

For the R_c band, the stellar M/L ratio is calculated as a function of their colours (Bell & de Jong 2001) and the relation is given by :

$$\log(M/L_R) = -0.660 + 1.222(B - V) \tag{1.22}$$

We used the (B − V) colours corrected for extinction in the RC3 catalogue when available. We completed these with values found by using the relation between (B − V) and morphological types for the whole RC3 catalogue spanning morphological types range from 0 to 10.

For WISE W1, the stellar M/L values can be calculated for galaxies as a function of their colours (Cluver et al. 2014))and the relation M/L ratio is given by :

$$\log(M_{stellar}/L_{W1}) = -2.54(W_{3.4\mu m} - W_{4.6\mu m}) - 0.17 \tag{1.23}$$

where the value $(W_{3.4\mu m} - W_{4.6\mu m})$ corresponds to the rest-frame colour of the source. Our sample has the values $(W_{3.4\mu m} - W_{4.6\mu m})$ between -0.1 and 0.3 .

1.6 Structure of this thesis

The aim of this thesis is twofold: at first we investigate the distribution of the DM and luminous matter of galaxies using mass models based on two different models (ISO, NFW); from that, we try to understand the variability of the DM halo as a function of the luminosity of galaxies based on the morphological type. To reach this goal, this work is divided into three parts:

In chapter 2, I present the mass distribution of DM and luminous matter in 121 galaxies using the Hα rotation curves and the WISE 3.4μm photometry data (Korsaga et al. 2018). The aim is to understand how the DM is distributed in the optical disc of galaxies and which model between ISO and NFW describes better the DM halos in galaxies. The luminosity profiles of galaxies are decomposed if needed to eventual components (bulge, disc, bar, spiral arm, etc.) using a 2D fitting routine. To simplify the construction of the mass models, I minimise the number of parameters to fit; I assume only two components: a spherical one containing the bulge that I call the bulge component and a planar one containing the disc and eventually other components embedded within the disc such as bar(s), spiral arm(s) and ring(s), that I call normal disc component.

I developed a python pipeline in order to construct the mass models using the pseudo-isothermal core profile (ISO) and the Navarro-Frenk-White cuspy profile (NFW) and the fitting procedures such as the Best Fit Model, the Maximum disc fit and the Fixed M/L ratio. I study the relations between the halos parameters derived from the mass models and the luminosity of galaxies. To test the strength of the results, I study the relations between the DM parameters by taking into account the effect of the bar, and the quality of the rotation curves. I also check that the results are not affected by the fact that we only consider optical rotation curves. For that, I determine the mass distribution of the sample of Randriamampandry & Carignan (2014) by limiting their HI rotation curves to the optical radius.

Chapter 3 shows the mass distribution of DM and luminous matter in 100 galaxies using the Hα rotation curves and the optical R_c band photometry data (Korsaga et al. 2019). I use the same models and fitting procedures as described in chapter 2 to construct the different mass models. Using the optical photometry, it should be possible to verify if the optical photometry is still valid to describe the baryonic distribution in galaxies, and if the DM halo parameters are very different when using the optical band compared to infrared band.

To compare the stellar distribution, I study the correlations between the photometric parameters obtained from the R_c and the 3.4 μm bands. To evaluate if the results derived from the mass models, mainly based on optical photometry, are still valid or superseded by the infrared photometry, I construct different figures which

show the comparison of the M/L ratios and the DM parameters as a function of the absolute B-magnitude of galaxies derived from the two bands (R_c and 3.4 μm photometries). To analyse the impact of the band used in the correlations found between the DM halo parameters and the luminosity of galaxies, I use the magnitudes in the W1-band and compared the results found with the absolute B-magnitude. In order to test if the DM halo models depend on the local light distribution rather than on the global light distribution, I therefore use an exponential disc instead of normal disc to construct the mass distribution of the galaxies and compared the results obtained with the results using the normal disc component.

In chapter 4, I study the mass distribution of 31 galaxies using different datasets. For that, I first construct the mass models using the Hα rotation curves and mid-IR photometry data used in chapter 2 with the addition of the contribution from the HI gas component. Secondly, the mass distribution is determined with the same photometry and gas component but using extended hybrid (Hα and HI) extended rotation curves. Lastly, the mass distribution is constructed using HI kinematical data. The main goal is to understand how the luminous and DM parameters may vary when using the different kinematical data.

Finally, a general summary of the different studies and future prospects are given in Chapter 5.

Bibliography

Abazajian K., et al., 2004, AJ, 128, 502

Abazajian K. N., et al., 2009, ApJS, 182, 543

Amram P., Boulesteix J., Marcelin M., 1991, in Combes F., Casoli F., eds, IAU Symposium Vol. 146, Dynamics of Galaxies and Their Molecular Cloud Distributions. p. 182

Athanassoula E., 2003, MNRAS, 341, 1179

Athanassoula E., 2005, MNRAS, 358, 1477

Barbosa C. E., et al., 2015, MNRAS, 453, 2965

Begeman K. G., 1987, PhD thesis, , Kapteyn Institute, (1987)

Bell E. F., de Jong R. S., 2001, ApJ, 550, 212

Blais-Ouellette S., Carignan C., Amram P., Côté S., 1999, AJ, 118, 2123

Blais-Ouellette S., Amram P., Carignan C., 2001, AJ, 121, 1952

Bottema R., Pestaña J. L. G., 2015, MNRAS, 448, 2566

Boulesteix J., Georgelin Y. P., Lecoarer E., Marcelin M., Monnet G., 1987, A&A, 178, 91

Bournaud F., Jog C. J., Combes F., 2005, A&A, 437, 69

Brainerd T. G., Blandford R. D., Smail I., 1996, ApJ, 466, 623

Buisson H., Fabry C., Bourget H., 1914, ApJ, 40

Calzetti D., et al., 2005, ApJ, 633, 871

Carignan C., Beaulieu S., 1989, ApJ, 347, 760

Casertano S., 1983, MNRAS, 203, 735

Chemin L., et al., 2006, MNRAS, 366, 812

Clowe D., Bradač M., Gonzalez A. H., Markevitch M., Randall S. W., Jones C., Zaritsky D., 2006, ApJ, 648, L109

Cluver M. E., et al., 2014, ApJ, 782, 90

Courtès G., 1960, Annales d'Astrophysique, 23, 115

Daigle O., Carignan C., Amram P., Hernandez O., Chemin L., Balkowski C., Kennicutt R., 2006, MNRAS, 367, 469

Dressler A., 1980, ApJ, 236, 351

Elmegreen B. G., Elmegreen D. M., 1985, ApJ, 288, 438

Engargiola G., Plambeck R. L., Rosolowsky E., Blitz L., 2003, ApJS, 149, 343

Epinat B., et al., 2008a, MNRAS, 388, 500

Epinat B., Amram P., Marcelin M., 2008b, MNRAS, 390, 466

Freeman K. C., 1970a, in Becker W., Kontopoulos G. I., eds, IAU Symposium Vol. 38, The Spiral Structure of our Galaxy. p. 351

Freeman K. C., 1970b, ApJ, 160, 811

Gach J.-L., et al., 2002, PASP, 114, 1043

Gallagher III J. S., Hunter D. A., 1984, ARA&A, 22, 37

Garrido O., Marcelin M., Amram P., Boulesteix J., 2002, A&A, 387, 821

Garrido O., Marcelin M., Amram P., Boissin O., 2003, A&A, 399, 51

Garrido O., Marcelin M., Amram P., 2004, MNRAS, 349, 225

Garrido O., Marcelin M., Amram P., Balkowski C., Gach J. L., Boulesteix J., 2005, MNRAS, 362, 127

Grabelsky D. A., Cohen R. S., Bronfman L., Thaddeus P., May J., 1987, ApJ, 315, 122

Hernandez O., Carignan C., Amram P., Chemin L., Daigle O., 2005, MNRAS, 360, 1201

Hernandez O., et al., 2008, PASP, 120, 665

Hložek R., Marsh D. J. E., Grin D., Allison R., Dunkley J., Calabrese E., 2016, preprint, (arXiv:1607.08208)

Holwerda B. W., González R. A., van der Kruit P. C., Allen R. J., 2005, A&A, 444, 109

Hubble E., 1926, Contributions from the Mount Wilson Observatory / Carnegie Institution of Washington, 324, 1

Jarrett T. H., et al., 2013, AJ, 145, 6

Jimenez R., Verde L., Oh S. P., 2003, MNRAS, 339, 243

Katz N., 1992, ApJ, 391, 502

Kent S. M., 1987, AJ, 93, 816

Koda J., et al., 2009, ApJ, 700, L132

Komatsu E., et al., 2011, ApJS, 192, 18

Kormendy J., Freeman K. C., 2004, in Ryder S., Pisano D., Walker M., Freeman K., eds, IAU Symposium Vol. 220, Dark Matter in Galaxies. p. 377

Korsaga M., Carignan C., Amram P., Epinat B., Jarrett T. H., 2018, MNRAS, 478, 50

Korsaga M., Amram P., Carignan C., Epinat B., 2019, MNRAS, 482, 154

Kravtsov A. V., Klypin A. A., Bullock J. S., Primack J. R., 1998, ApJ, 502, 48

Laval A., Boulesteix J., Georgelin Y. P., Georgelin Y. M., Marcelin M., 1987, A&A, 175, 199

Lelli F., McGaugh S. S., Schombert J. M., 2016, preprint, (arXiv:1606.09251)

Marcelin M., Lecoarer E., Boulesteix J., Georgelin Y., Monnet G., 1987, A&A, 179, 101

Markevitch M., Gonzalez A. H., Clowe D., Vikhlinin A., Forman W., Jones C., Murray S., Tucker W., 2004, ApJ, 606, 819

Milgrom M., 1983a, ApJ, 270, 365

Milgrom M., 1983b, ApJ, 270, 371

Navarro J. F., Frenk C. S., White S. D. M., 1996, ApJ, 462, 563

Peebles P. J., Ratra B., 2003, Reviews of Modern Physics, 75, 559

Peletier R. F., Balcells M., 1996, AJ, 111, 2238

Plana H., Boulesteix J., 1996, A&A, 307, 391

Randriamampandry T. H., Carignan C., 2014, MNRAS, 439, 2132

Randriamampandry T. H., Combes F., Carignan C., Deg N., 2015, MNRAS, 454, 3743

Randriamampandry T. H., Deg N., Carignan C., Combes F., Spekkens K., 2016, A&A, 594, A86

Rots A. H., 1975, A&A, 45, 43

Rubin V. C., Ford Jr. W. K., 1970, ApJ, 159, 379

Russeil D., Georgelin Y. M., Amram P., Georgelin Y. P., Laval A., Marcelin M., 1998, PASA, 15, 9

Schumann M., 2014, Brazilian Journal of Physics, 44, 483

Searle L., Sargent W. L. W., 1972, ApJ, 173, 25

Spano M., Marcelin M., Amram P., Carignan C., Epinat B., Hernandez O., 2008, MNRAS, 383, 297

Swaters R., 1999, in Merritt D. R., Valluri M., Sellwood J. A., eds, Astronomical Society of the Pacific Conference Series Vol. 182, Galaxy Dynamics - A Rutgers Symposium. (arXiv:astro-ph/9811010)

Thuan T. X., 1983, ApJ, 268, 667

Tinsley B. M., 1981, MNRAS, 194, 63

Trujillo I., Aguerri J. A. L., Cepa J., Gutiérrez C. M., 2001, MNRAS, 328, 977

Vera M., Alonso S., Coldwell G., 2016, A&A, 595, A63

Zoccali M., Valenti E., 2016, PASA, 33, e025

Zwicky F., 1933, Helvetica Physica Acta, 6, 110

de Blok W. J. G., Bosma A., 2002, A&A, 385, 816

de Blok W. J. G., McGaugh S. S., 1996, ApJ, 469, L89

de Blok W. J. G., Walter F., Brinks E., Trachternach C., Oh S.-H., Kennicutt Jr. R. C., 2008, AJ, 136, 2648

de Vaucouleurs G., 1959, Handbuch der Physik, 53, 275

van Eymeren J., Jütte E., Jog C. J., Stein Y., Dettmar R.-J., 2011, A&A, 530, A29

van der Hulst J. M., van Albada T. S., Sancisi R., 2001, in Hibbard J. E., Rupen M., van Gorkom J. H., eds, Astronomical Society of the Pacific Conference Series Vol. 240, Gas and Galaxy Evolution. p. 451

Chapter 2

GHASP: an Hα kinematical survey of spiral galaxies - XI. Distribution of luminous and dark matter in spiral and irregular nearby galaxies using WISE photometry

This chapter has been published in the Monthly Notices of the Royal Astronomical Society (MNRAS): M. Korsaga, C. Carignan, P. Amram, B. Epinat and T. H. Jarrett, MNRAS 478, 50-68 (2018)

Abstract

We present the mass distribution of a sample of 121 nearby galaxies with high quality optical velocity fields and available infrared *Wide-field Infrared Survey Explorer (WISE)* 3.4 μm data. Contrary to previous studies, this sample covers all morphological types and is not biased toward late-type galaxies. These galaxies are part of the Fabry-Perot kinematical *Gassendi HAlpha survey of SPirals (GHASP)* survey of spirals and irregular nearby galaxies. Combining the kinematical data to the *WISE* surface brightness data probing the emission from the old stellar population, we derive mass models allowing us to compare the luminous to the dark matter halo mass distribution in the optical regions of those galaxies. Dark matter (DM) models are constructed using the isothermal core profile and the Navarro-Frenk-White cuspy profile. We allow the mass-to-light ratio (M/L) of the baryonic disc to vary or we keep it fixed, constrained by stellar evolutionary models (*WISE* W_1-W_2 colour) and we carry out best fit (BFM) and pseudo-isothermal maximum disc (MDM) models. We found that the MDM provides M/L values four times higher than the BFM, suggesting that disc components, on average, tend to be maximal. The main results are: (i) the rotation curves of most galaxies are better fitted with core rather than cuspy profiles; (ii) the relation between the parameters of the DM and of the luminous matter components mostly depends on morphological types. More precisely, the distribution of the DM inside galaxies depends on whether or not the galaxy has a bulge.

2.1 Introduction

Current ΛCDM models teach us that baryonic matter evolved within large dark matter (DM) halo cocoons. It is known since the beginning of the 1970s (Freeman 1970), and 1980s (Bosma 1981) that, without the presence of this dark halo, rotation curves of galaxies should be rapidly decreasing after a peak located around 2.2 disc scale lengths of the baryonic matter located in an exponential disc. Except if we consider alternative models like MOdified Newtonian Dynamics (MOND), which postulates that gravity deviates from a pure Newtonian force at very low acceleration, DM halos are thus mandatory to explain the shape of the rotation curves of galaxies, which remain usually more or less flat in the outer regions out to the edge of the HI disc.

Different predictions are classically used to describe the shape of the central density profiles. One family of models supposes that the central core density of the halo is almost constant within the first kpc or so. Those models show that the DM halo density distribution can be described by an isothermal (Carignan & Freeman 1985) or pseudo-isothermal sphere (van Albada et al. 1985), this last one being used to avoid a central divergence of the density observed when a singular isothermal sphere profile is used. The other family of models, coming from ΛCDM simulations (Navarro et al. 1996b), supports that DM halos should display cuspy central density distributions. Unfortunately, the sensitivity of the rotation curves to the exact density profile of the halos is quite low and one must use the highest sensitivity and the highest resolution possible to arrive at useful comparisons (Blais-Ouellette et al. 1999).

Understanding the formation and evolution of galaxies requires a fine knowledge of the nowadays luminous and dark matter distribution within local galaxies. One problem in the debate between the cuspy or core density profiles is that numerical simulations predict the shape of the halo density profile at the time of formation while galaxies are observed after many Gyr of evolution. Internal dynamics and interaction between the DM halo, the luminous disc and the environment may have modified the shape of the halo density profile. Despite this debate, studies using the two predictions produced acceptable results about the distribution of the DM halo of galaxies (e.g, Blais-Ouellette et al. 2001, Salucci 2001, de Blok & Bosma 2002, Gentile et al. 2004, Spano et al. 2008).

Kormendy & Freeman (2004) suggest that there are clear scaling laws between the DM halos parameters and the optical parameters (e.g. M_B) of the parent galaxies. For example, as suggested in previous studies (e.g, Carignan & Freeman 1988), halos in less luminous galaxies tend to have smaller core radius r_0 and higher central density ρ_0.

To disentangle the central mass distribution of the DM halos, high spatial resolution rotation curves are requested in the inner disc. Such data are commonly provided by Hα observations. This has been done by several authors (e.g. Blais-Ouellette et al. 1999; 2001, Spano et al. 2008). In the last few years, two different approaches have been used to try to discriminate between those two families of DM halos. The first one by Bottema & Pestaña (2015) was to limit the study to a small number of very well determined rotation curves, with very well known distances and

spanning an as broad range of luminosities as possible ($\sim$ 2.5 orders of magnitude). For their observed high quality and extended rotation curves, four different schemes, each with two free parameters, were used. For the "maximum disc fits", the authors found that the rotation curves could be well matched, although this required a large scatter in the M/L values of the individual galaxies in their sample. Interestingly, they found that the rotation curves of low mass galaxies could not be reproduced when assuming the Navarro-Frenk-White cuspy profile, implying that one should prefer cores over cusps. They used a combination of the pseudo-isothermal sphere with a universal M/L ratio to successfully describe the observed rotation curves, leading to "sub maximum disc" mass contributions. Similar conclusions had been reached a year before by Randriamampandry & Carignan (2014) using 3.6 μm mid-IR photometry instead of R band data.

The second approach of Lelli et al. (2016) was to use a large sample of 175 nearby galaxies (the SPARC sample) from previous HI and Hα kinematical studies, combined with 3.6 μm (Spitzer) photometry. Using a unique M/L ratio of 0.5 for the whole sample, their main result is that the disc component is nearly maximal for high-mass, high-surface-brightness galaxies while it contributes less to the total mass in low-mass, low-surface-brightness galaxies. A mean value of M/L $\gtrsim$ 0.7 is statistically ruled out because it implies an over-maximum baryonic contribution in high surface brightness and high mass galaxies.This study gives a good idea of what to expect from a sample with well resolved rotation curves in the inner parts and with stellar mass distribution well traced using mid-infrared bands. Following the study of Lelli et al. (2016), Katz et al. (2017) used almost the same SPARC sample to study the inner density profile dependence on the ratio of stellar to DM mass. They confronted the SPARC data to cosmological N-body simulations (Di Cintio et al. 2014a;b) and found an agreement between DM halo profiles modified by baryonic processes and the Λ-Cold Dark Matter cosmology. They also showed that these halo profiles describe galaxy rotation curves better than halo models which do not account for baryonic physics.

Bottema & Pestaña (2015) used a sample of 12 galaxies for which three out of four Hα rotation curves have been computed from 2D Hα velocity fields. Kormendy & Freeman (2004) used a sample of 55 galaxies taken from the literature, extending results already published in other conference reviews. Lelli et al. (2016) used a sample of 175 galaxies for which 15 out of 56 Hα rotation curves have been

computed from 2D Hα velocity fields. The last relatively large sample (36 galaxies) using 2D kinematics was studied in Spano et al. (2008). However, most of those studies (e.g, Kormendy & Freeman 2004, Bottema & Pestaña 2015, Spano et al. 2008) were focused on late rather than early morphological types galaxies. In the present work, we study mass models for a sample of 121 galaxies using high resolution Hα rotation curves computed from 2D Hα velocity fields. The sample covers morphological types ranging from Sa to Im types and the stellar component is modelled using mid-infrared photometry.

This paper is organised as follows. In section 3.2, we present the sample and the data used to constrain mass models. Section 3.3 describes the decomposition of the infrared luminosity profiles. In section 2.4 the mass models are presented and the results of the fits are described in section 3.4.2. Section 2.6 presents the discussion of the DM halo parameters and section 3.6 gives a summary and the general conclusions. Appendix 1 lists the global properties and mass models parameters for the 121 galaxies. In Appendix 2, we present the photometry, the luminosity profiles and the mass models of the sample. In Appendix 3, we compare the mass models derived from HI and optical rotation curves limited to the solid body rising parts for 15 galaxies (taken from Randriamampandry & Carignan 2014). Throughout this paper, we assume a Hubble constant $H_0 = 75$ km s^{-1} Mpc^{-1}.

2.2 Data and Sample Selection

We aim at studying a large galaxy sample, spanning a wide range in mass and morphological types, for which accurate constraints can be provided on mass models in the inner regions of the galaxies. We therefore need accurate optical rotation curves and photometry representative of the bulk of the stellar mass.

2.2.1 Data

Our parent sample is the *GHASP* (acronym for Gassendi HAlpha survey of SPirals) sample, which contains 203 spiral and irregular galaxies observed with the 1.93m telescope of the Observatoire de Haute Provence (France). The Hα line was scanned with a Fabry-Perot (FP) interferometer in photon-counting mode providing both high spectral and spatial resolution 3-D data cubes over a large field of view (~

6×6 arcmin^2). The typical spatial resolution is around 2 arcsec full width at half maximum and the spectral resolution is around 10000 with a spectral sampling corresponding to $\sim$ 15 km s^{-1}. Velocity fields were derived from these data cubes before extracting $\sim$ 5 km s^{-1} accurate rotation curves from the full 2D information for 170 galaxies. Those data have been published in several papers (Garrido et al. 2002; 2003; 2004; 2005, Epinat et al. 2008a;b). In the present paper, we use the rotation curves published in Epinat et al. (2008b), who also provide a global view on the full *GHASP* sample. Those rotation curves were extracted using the method detailed in Epinat et al. (2008a).

We use photometry from the *Wide-field Infrared Survey Explorer (WISE)*. *WISE* is a NASA-funded Medium-Class Explorer mission consisting in a 40 cm primary-mirror. This space infrared telescope mapped the entire sky in the following mid-infrared bands: W_1 (3.4 μm), W_2 (4.6 μm), W_3 (12 μm) and W_4 (22 μm). The science instrumentation includes a 1024×1024 pixels Si:As and HgCdTe array and each band covers a field-of-view of 47×47 arcmin^2 with an angular resolution of 6 arcsec in the short bandpass and 12 arcsec in the longest one (Jarrett et al. 2012). In the present study, we use the W_1 band luminosity profiles to describe the baryonic component in our mass models (cf. section 2.3.1).

2.2.2 Sample Selection

We use a sample of 121 spiral and irregular nearby galaxies for which accurate Hα rotation curves, derived from 2D velocity fields, and *WISE* infrared surface photometry were available.

From the whole *GHASP* sample of 203 galaxies, 147 galaxies have both available Hα rotation curves and *WISE* photometric data in the W_1-band (3.4 μm). A quality flag was attributed to each galaxy to describe the quality of the rotation curve: 1 for very high, 2 for high and 3 for low quality. This flag is reported in column (14) of Table B.1. In order to compute mass models with good constraints, we restricted our analysis to galaxies with flags 1 or 2, reducing the sample to 121 galaxies. In brief, we excluded 26 galaxies having ill-defined rotation curves due to various reasons: existence of a strong bar, strong signs of galaxy interaction, too high inclination (>75^o) or another peculiarity (e.g. strong lopsidedness) and/or very low SNR data.

The final sample of 121 galaxies we defined is not complete in volume but it samples the main galaxies parameters space. Indeed, as illustrated by Fig. 3.1,

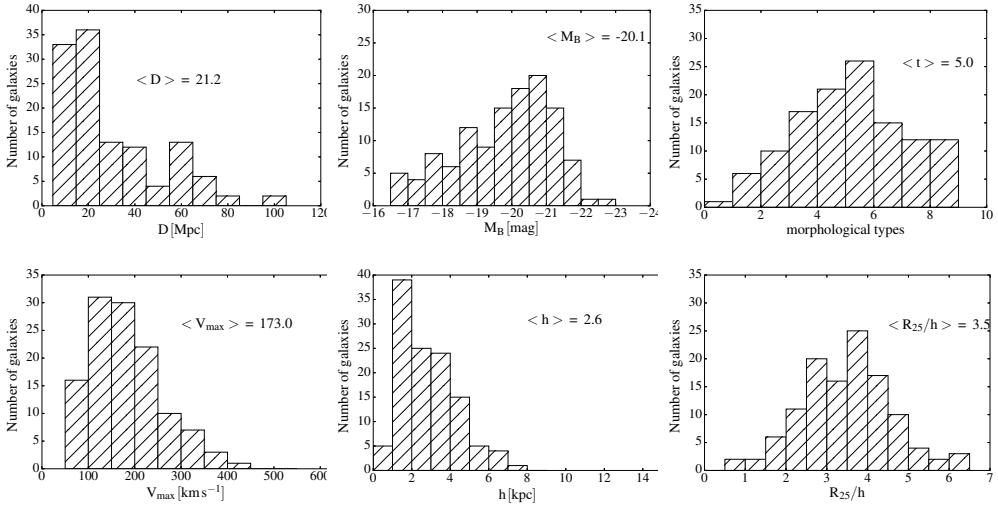

Figure 2.1: Properties of our sample. First line; from left to right, we have respectively the distance of the galaxies, the absolute magnitude and the morphological type. Second line; from left to right, we have respectively the maximum rotational velocity, the disc scale length and the ratio of the isophotal radius R_{25} to the disc scale length. The median of each parameter is shown in the middle of each plot.

it samples *(i)* nearby galaxies (from 5 to 100 Mpc with a median distance of 21.2 Mpc); *(ii)* M_B absolute blue magnitude ranging from -16 to -23 (with a median value of -20.1); *(iii)* morphological types from Sa to Irregular (the median value of t is 5.0, i.e. *Sc* galaxies); *(iv)* maximum rotation velocity from 50 to 400 $\mathrm{km\,s^{-1}}$ (the median velocity is 173.0 $\mathrm{km\,s^{-1}}$, a tail in the distribution is observed toward high mass galaxies), i.e. dynamical masses ranging from 0.5 to 2.5 10^{11} $M_\odot$ and finally *(v)* galaxy sizes, represented by their optical diameters R_{25}, which corresponds to the isophotal radius at the limiting surface brightness of 25 mag $\mathrm{arcsec^{-2}}$, or by their disc scale lengths, ranging from 1 to 10 kpc (median value of 2.6 kpc). The disc scale lengths are discussed in section 2.3.4. The distances and velocities used in this work are taken from Epinat et al. (2008a).

2.3 The WISE surface brightness photometry

2.3.1 Stellar population in the near/mid infrared

According to observations and stellar population models, the light coming from discs is usually dominated by Population I stars (blue and young stars) and bulges by

Population II stars (red and old stars) but the majority of the stellar mass is provided by red stars, both from the disc (old Pop I) and bulge, better seen in the near and mid-infrared bands. Those bands map the bulk of stellar masses and thus provide the most representative stellar mass distribution. We therefore use mid-infrared bands to model the stellar populations.

Luminosity profiles were extracted from the *WISE* photometry (Jarrett et al. 2013). Optimal profile Point Spread Function fitting has been used to measure the fluxes of stars and the calibration zero-point magnitude is derived from the measurements of calibration stars (Jarrett et al. 2013). The adopted 1 σ elliptical isophotal radius corresponding to the 1 σ isophotal surface brightness is equal to 23.0 mag arcsec^{-2} (Vega; and 25.7 mag arcsec^{-2} in AB) for W_1 (as shown in Fig. 4.3) and to 21.8 mag arcsec^{-2} for W_2 (Jarrett et al. 2013). Because W_1 is the shortest wavelength band of *WISE* and the most sensitive for almost all types of galaxies, yielding the largest isophotal radius, we use the 3.4 μm luminosity profile to describe the baryonic component in our mass models. The central surface brightness of the luminosity profiles are given in Table B.1, column (4).

2.3.2 Photometric mass-to-light ratio

The *WISE* photometry can be used to infer the mass-to-light (M/L) ratio of galaxies in our sample. Indeed, infrared bands are the best suited to constrain the values of the M/L ratio of the luminous matter. In addition, population synthesis models show that the relation between light and mass is more nearly constant in the near/mid-infrared than in the UV and in the optical (de Denus-Baillargeon et al. 2013). Indeed, recent star formation mainly visible in the UV and in the optical produces large amount of light from little mass during short times, which impacts the M/L ratio of a galaxy. This is also observed in Tully-Fisher relations for which the scatter decreases from blue to near infrared bands (e.g., Verheijen 2001).

For each galaxy, the stellar M/L ratio can be calculated as a function of the mid-infrared colour using the following relation from Cluver et al. (2014):

$$\log(M_{\rm stellar}/L_{W1}) = -2.54(W_1 - W_2) - 0.17 \quad (2.1)$$

where L_{W1} is the inband luminosity in the W_1 band and where W_1 and W_2 correspond to magnitudes in the W_1 and W_2 bands respectively. W_1-W_2 corresponds to the rest-

frame colour of the source and ranges between -0.1 and 0.3 in our sample. We will refer to this M/L ratio as the photometric M/L ratio and we will note it fixed M/L.

2.3.3 Radial Profile Decompositions

Since we aim at studying the inner distribution of dark matter halos, we need to constrain the contribution of stars to the dynamical potential in the inner parts of galaxies with care.

Among the 121 galaxies included in our final sample, the median morphological type is Sc-type galaxies, i.e. that 52 galaxies have a morphological type earlier than Sc, 29 are Sc's and 40 are of later types than Sc. Galaxies with a morphological type earlier than or equal to Sc potentially display a significant bulge in their radial profiles. Indeed 81 galaxies requested a decomposition into multiple components while the remaining 40 did not. Nevertheless we did not decide from the morphological type if the profile requested or not a decomposition but instead by visual inspection of each profile not to be subject to misclassification, which could happen for the most distant objects.

To transform the radial light profiles into radial mass profiles we need to disentangle the different components because their distribution, hence their impact on circular velocities, is different. Indeed, material in a plane (gas and stellar disc) globally follows circular orbits in the plane of the disc while material in spherical-like structures (stellar bulge) displays random motions. The geometry of the mass distribution has an impact on the kinematics which has to be taken into account in mass models. For instance, for a given mass, at a given radius, the rotational velocity expected for a flat component is higher than the one expected for a spherical component of the same mass. Even if the material (stars or gas) orbiting along bars, within spiral structures or in rings presents strong deviations from circular motions, that should be taken into account. To simplify the model and to minimise the number of free parameters, we only disentangle spherical components (bulges) from planar components (disc, bar, spiral arms, rings, etc.) that we call disc in the mass models.

In principle, the subtraction of the bulge component from the observed profile should provide a bulge-free profile. In practice, it only works if the galaxy does not contain any additional structure such as a bar and/or a ring. If the profile contains a bar or a ring, this method fails and produces strong residuals in the very center. Thus, in order to minimise the residuals values in the central regions, we have to proceed

to a full decomposition in modelling all the components together to end up with the different components used for the mass models. It is illustrated by Fig. 2.2 for the galaxy UGC 8900 where strong residuals are visible when a bulge only is subtracted (top panel), while residuals within the uncertainties are obtained when the bar and the bulge have been modelled together. However, for galaxies with very little or no bulge (specifically late types or irregular galaxies), the luminosity profiles were not decomposed, the disc component is then directly the observed surface brightness profile. Furthermore, we used a parametric profile fitting procedure to separate the photometric components: bulges, discs, bars, arms and rings.

The surface brightness profile were decomposed by using the method described in Barbosa et al. (2015).

The disc is modelled with an exponential profile defined by:

$$I_d(r) = I_0 \exp\left(-r/\mathrm{h}\right) \tag{2.2}$$

with I_0 the central intensity of the disc and h the disc scale length. The other components like bulges, bars, rings, lenses are determined by using a Sérsic function given by :

$$I_b(r) = I_e \exp\left(-b_n\left[(r/r_e)^{1/n} - 1\right]\right) \tag{2.3}$$

where r_e is the effective radius, I_e is the intensity at the effective radius, n is the Sérsic shape parameter and b_n a Sérsic index function due to the parametrization of the function at the effective radius. The total apparent magnitude is :

$$m_{\mathrm{sersic}} = -2.5 \log\left(\frac{2\pi I_e\, r_e^2\, \mathrm{e}^{b_n}\, n\, \Gamma(2n)}{b_n^{2n}} \frac{b}{a}\right) \tag{2.4}$$

with $\Gamma(x)$ the complete gamma function of a variable x.

Examples of parameters of the bulge and disc components are shown in Table B.1. This table represents only a fraction of our sample. The full table is provided online. The figures showing the disc and bulge components for the whole sample are also displayed online (see an example on the right top panel of Fig. 4.3).

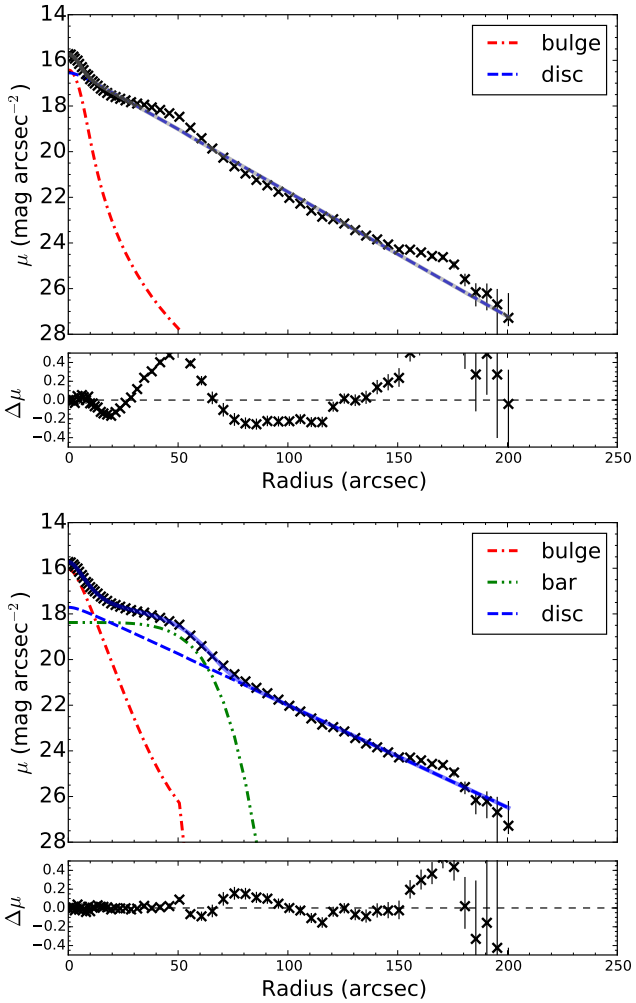

Figure 2.2: Example of the structural decomposition of UGC 8900 in the W_1 band without including a bar component (top panel) and including a bar component (bottom panel). The observed surface brightness profile in plotted using black cross and the different components bulge, disc, bar (bottom panel) in red, blue and green dash lines respectively. The lower subpanel represents the fitting residuals, which are obviously reduced when a bar is included in the model.

2.3.4 Disc and Bulge Parameters

In Figs. 2.3 and 2.4, we illustrate several correlations between the photometric parameters displayed in Table B.1.

The top panel of Fig. 2.3 shows, as expected, that the brightest bulge central surface brightnesses are observed for the brightest disc central surface brightnesses, which are preferentially early type spirals while fainter later type galaxies display the weakest central surface brightnesses. The same trend is seen in the first middle panel where the strongest bulges (largest effective radius $r_{e,b}$) tend to display larger discs (larger disc scale lengths h). The $y = x$ line of this plot emphasises that discs are on average brighter than bulges. The second middle panel of Fig. 2.3 shows that there is a correlation between the disc central surface brightnesses and the disc scale lengths only for the earliest type (Sa-Sab), for which large discs correspond to high central surface brightness, or for the latest type (Sdm-Im), for which small discs exhibit low central surface brightness, while for the intermediate types (Sb-Sd) there is no straightforward correlation, the central surface brightness does not depend on the disc scale length. The bottom panel of Fig. 2.3 and the last panel of Fig. 3.1 show a clear average relation between the isophotal radius R_{25} and the disc scale length h. The median value of R_{25}/h is 3.5.

The two top panels of Fig. 2.4 show that discs have slightly increasing luminosities from Sa to Sc before decreasing toward later types while bulges see their luminosity decreasing from early to late types, which is not surprising since this is one of the important criteria being used for morphological classification. A wide luminosity dispersion is noted within each morphological type meaning that we sample galaxies with different luminosities, sizes and thus masses. In order to compare and to quantify the light coming from the disc and the bulge, the third panel shows the ratio of luminosity between the two components. Most of the galaxies have their disc brighter than their bulge ($\log\ L_D/L_B > 0$) with only 7 galaxies being bulge-dominated. The dispersion in those three panels also points out that morphological classification should be taken with care when comparing only the disc to the bulge components. Later morphological types might have stronger bulges than earlier types. For instance, a $\log\ L_D/L_B \sim 0.5$ can be observed from Sa (t=1) to Sd (t=8) galaxies; some t=6-7 galaxies might have a bulge almost as luminous as the disc. This justifies the fact that disc/bulge decomposition has been done independently of the galaxy morphological type. The bottom panel shows that, while the disc central

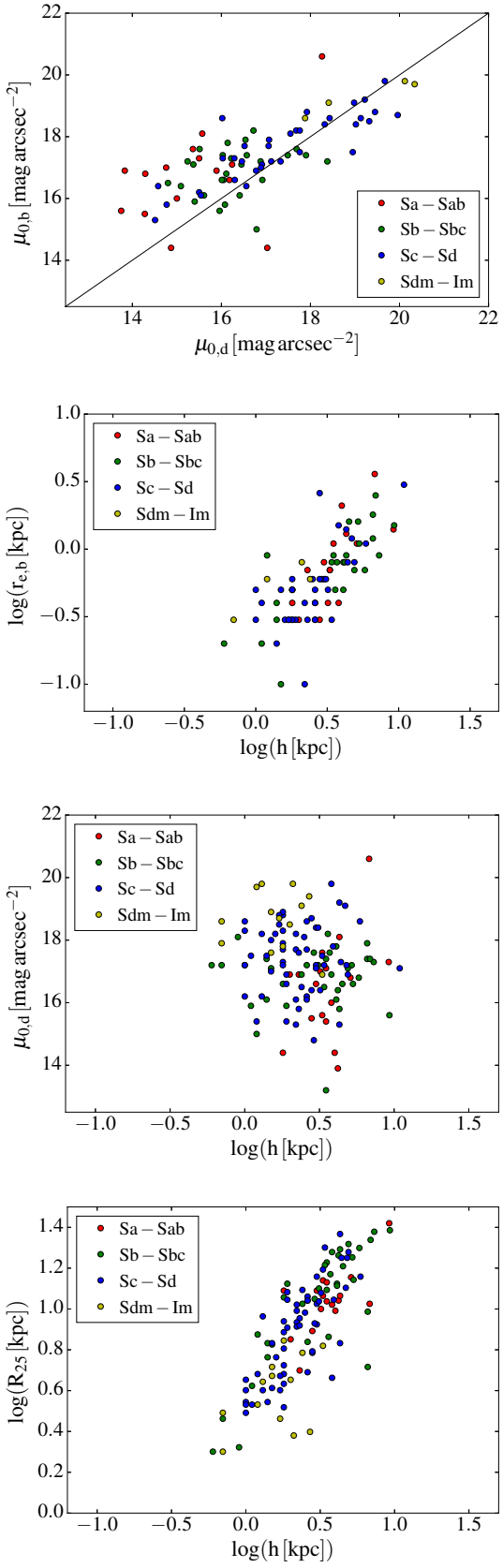

Figure 2.3: Correlations between parameters derived from the W1 profiles. The top panel shows the bulge central surface brightness versus the disc central surface brightness. The two middle panels represent the bulge effective radius and the disc central surface brightness versus the disc scale length respectively. The bottom panel shows the isophotal radius R_{25} versus the disc scale length.

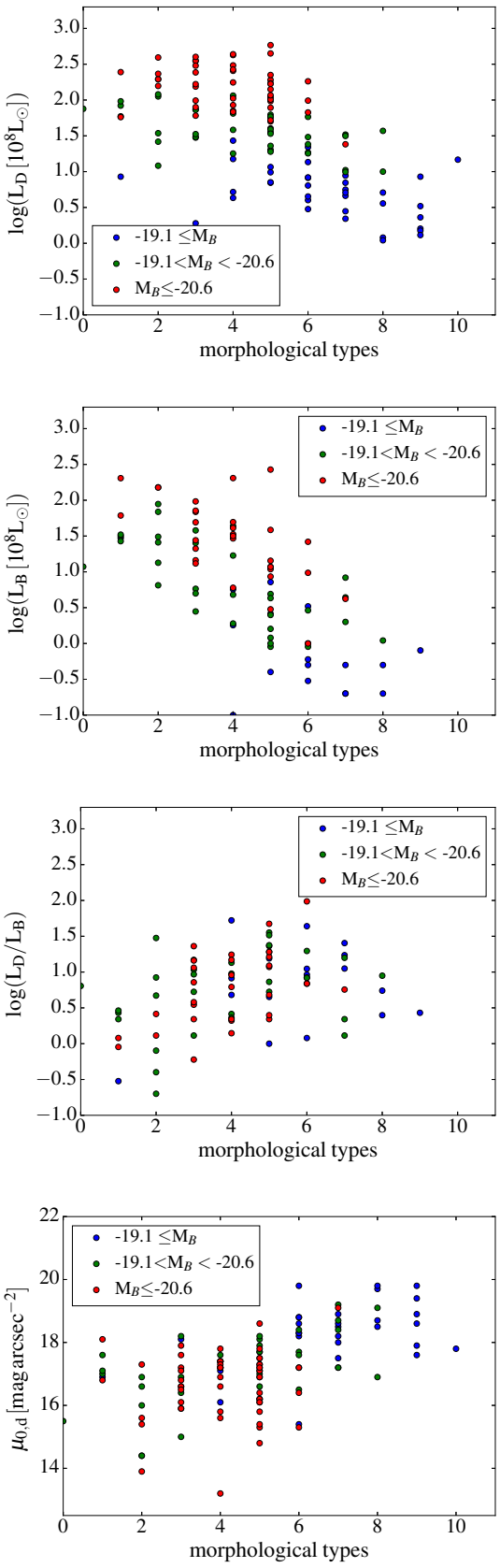

Figure 2.4: From the top to the bottom panel: disc luminosity, bulge luminosity, ratio of disc-to-bulge luminosity and the central disc surface brightness versus the morphological types.

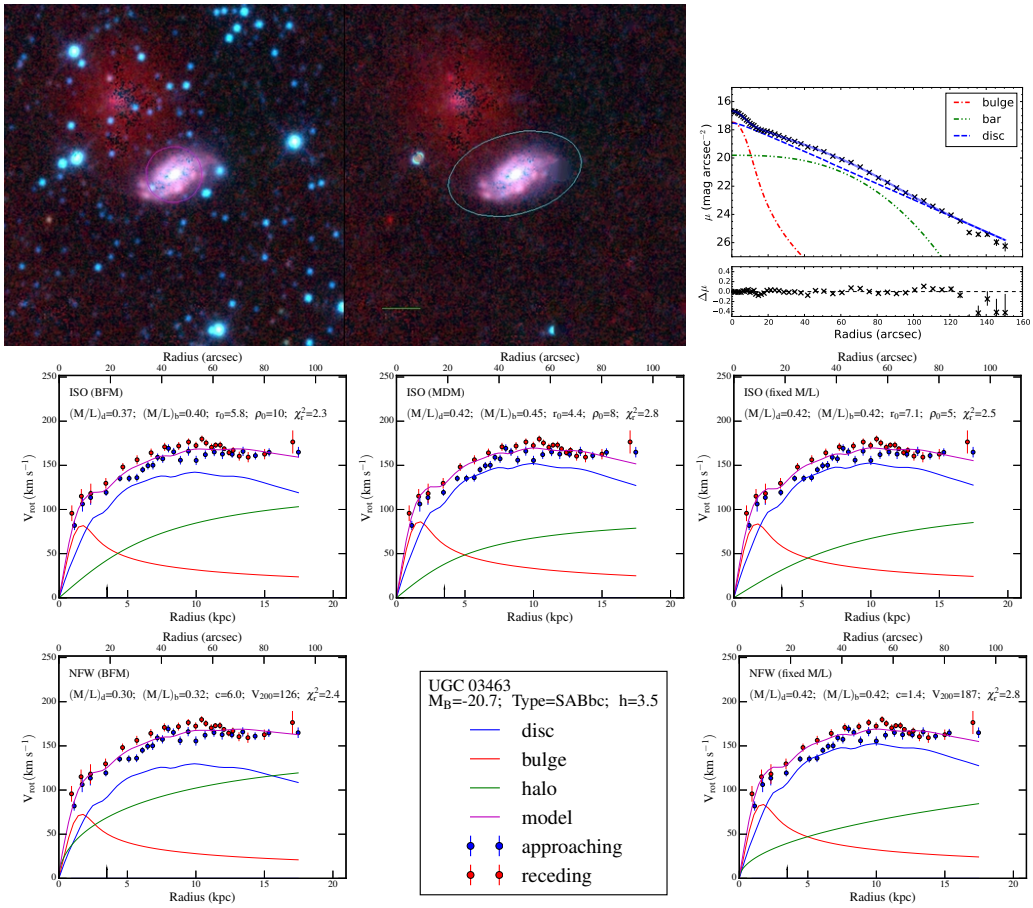

Figure 2.5: Example of surface brightness profile decomposition and mass models for the galaxy UGC 3463. First line - (Left panel) *WISE* surface brightness image at 3.4 μm. Left side: image showing the field and the galaxy. Right side: image after the stars are removed; the circle represents the 1 σ isophotal ellipse, used for integrated photometry and the green line shows 1 arcmin in length. (Right panel) Luminosity profile decomposition corresponding to the left image. Lines 2 and 3 - Mass models. Second line: pseudo-isothermal sphere density profiles (ISO). Third line: Navarro, Frenk & White density profiles (NFW). First column: Best Fit Model (BFM). Second column: Maximum disc Model (MDM) for line 2 (ISO model). Third column: Mass-to-Light ratio M/L fixed using *WISE* W_1-W_2 colour. The name of the galaxy, its B-band absolute magnitude, morphological type and disc scale length have been indicated in the insert located line 3-column 2. For each model, the fitted parameters and the reduced χ^2 have been indicated in each sub-panel.

surface brightness stay more or less constant for the early-types, it decreases with from types Sc to Sm.

2.4 Mass Models

Rotation curves of spiral and irregular galaxies need a DM halo component to be fitted (e.g, Carignan & Freeman 1985, van Albada et al. 1985) and this is even mandatory to model the mass distribution in the outskirts of the HI disc. In the present study, we do not consider the HI gas component (densities and velocities), which are not available for a large part of the galaxies in our sample. This will be done in a following paper. This nevertheless does not prevent us from studying the inner mass distribution in spiral and irregular galaxies. Indeed, even if rotation curves within the optical size of galaxies are largely dominated by the stellar components (e.g, Kalnajs 1983, Kent 1986), it has already been shown in previous works (e.g, Carignan & Freeman 1985, Blais-Ouellette et al. 2001, Spano et al. 2008) that a dark halo is nevertheless often also mandatory to fit high resolution rotation curves limited to the stellar disc, meaning that not all discs are maximal.

From the theoretical side, a dark halo component can be necessary to prevent discs having bar instabilities, as can be seen in analytic calculations and in numerical simulations of stellar discs with initially exponential mass distribution (e.g, Hohl 1971, Ostriker & Peebles 1973). Amongst other considerations, it has also been shown that the presence of a bar might decrease the halo central density distribution (Weinberg & Katz 2002). In summary, observational and theoretical reasons justify that we can limit this study to optical rotation curves. Nevertheless, when rotation curves are not defined to sufficiently large radii, rotation curves could sometimes be modelled using disc-only or disc+bulge-only systems, without the need for DM (Kalnajs 1983). In such cases, those galaxies will be taken out of the final sample that will be used to study the relations between the dark halos' parameters and optical parameters.

We use two different models of dark matter distributions: the pseudo-isothermal sphere (ISO) distribution (section 2.4.1), which is observationally motivated and that predicts a cored density profile, and the Navarro-Frenk-White (NFW) one (section 2.4.2), which is theoretically motivated (cosmological numerical simulations) and that features a cuspy halo density profile. These two distributions assume that the

DM distribution is spherically symmetric.

In these models, we include two components for the luminous matter (disc and bulge, if present) and one for the DM halo. The final rotation curve is the quadratic sum of the individual contributions of these components:

$$V_{\rm cir}(r) = \sqrt{V_{\rm disc}^2 + V_{\rm bulge}^2 + V_{\rm halo}^2} \tag{2.5}$$

$$\tag{2.6}$$

where $V_{\rm cir}$ is the circular velocity, $V_{\rm disc}$ and $V_{\rm bulge}$ are the velocity of the disc and bulge components respectively and $V_{\rm halo}$ is the DM halo velocity.

We will end the section by presenting the different strategies used to fit the different profiles (section 2.4.3).

2.4.1 Pseudo-Isothermal density profile (ISO)

This profile features a flat core in the center (Begeman 1987, Kravtsov et al. 1998, de Blok et al. 2001). The density distribution $\rho_{\rm iso}(r)$ of this DM halo is given by:

$$\rho_{\rm iso}(r) = \frac{\rho_0}{\left[1 + \left(\frac{r}{r_0}\right)^2\right]} \tag{2.7}$$

where ρ_0 is the central density of the DM, r_0 is the scaling radius. The corresponding velocity contribution $V_{\rm iso}(r)$ is given by:

$$V_{\rm iso}(r)^2 = 4\pi G\rho_0 r_0^2 \left[1 - \frac{r_0}{r}\arctan\left(\frac{r}{r_0}\right)\right] \tag{2.8}$$

which is an increasing function of r, asymptotically reaching $V_{\rm max} = V(r = \infty) = \sqrt{4\pi G\rho_0 r_0^2}$.

This model has two parameters to describe its rotation curve, the central density ρ_0 and the scale radius r_0.

2.4.2 ΛCDM density profile (NFW)

The formation of galaxies is a non-linear process and therefore a direct computation through N-body simulations is required. Those simulations predict cuspy halo profiles, peaked in the center (Navarro et al. 1996b, Cole & Lacey 1996, Moore et al. 1998). The density distribution of the NFW halo is given by:

$$\rho_{\rm NFW}(r) = \frac{\rho_i}{\left(\frac{r}{r_s}\right)\left(1+\frac{r}{r_s}\right)^2} \tag{2.9}$$

where ρ_i is the density of the universe at the time of collapse and r_s is a scale radius. The resulting circular velocity is:

$$V^2_{\rm NFW}(r) = V^2_{200}\left[\frac{\ln(1+cx)-cx/(1+cx)}{x[\ln(1+c)-c/(1+c)]}\right] \tag{2.10}$$

where V_{200} is the velocity at the virial radius R_{200}, $c = R_{200}/r_s$ is the concentration parameter of the halo and x is defined as r/r_s. The relation between V_{200} (km s^{-1}) and R_{200} (kpc) is given by:

$$V_{200} = \frac{R_{200} \times {\rm H}_0}{100} \tag{2.11}$$

where $\rm H_0$ is the Hubble constant in km s^{-1} Mpc^{-1}.

In order to describe the velocity contribution associated to the NFW profile, we use the two following parameters: the concentration c and the velocity V_{200} at the virial radius.

2.4.3 Fitting strategies

It is usual to model the rotation curves of spiral and irregular galaxies with multi-components mass models consisting of discs (stellar and gaseous), bulge (if present) and dark halo components. The M/L ratio of the stellar components (disc and bulge) can be estimated from the stellar light distributions (see section 2.3.2). The faint radial colour gradients and low thickness variations observed in galaxies allow to use a radially constant M/L ratio (de Jong & van der Kruit 1995) in the red, near-infrared

and mid-infrared bands. At the opposite, colour index is an imperfect tool to assign masses in bluer bands, i.e. to young stellar populations (de Denus-Baillargeon et al. 2013). In this section, we describe the three different strategies used to deal with M/L: Best Fit Model (BFM), Maximum disc Model (MDM) and M/L fixed by colours.

The MDM consists in maximising the disc component, and therefore to use the highest M/L ratio and the shallower dark halo component, allowing a reasonable fit of the rotation curve. It has been very successful in reproducing the inner features due to spiral arms or bars observed along the rotation curves of galaxies (e.g, Buchhorn 1992, Amram et al. 1996). For optical rotation curves, the "maximum disc" solution is favoured in several previous studies (e.g, de Denus-Baillargeon et al. 2013, Spano et al. 2008). The Tully-Fisher relation obviously indicates that the stellar luminosity alone seems to determine the rotation velocity of spiral galaxies, favouring the maximum disc solution. Nevertheless, compared to the Tully-Fisher empirical evidences, models based on dark halo contraction due to adiabatic infall of baryons lead to the need of a major dark halo contribution in the central regions (Courteau & Rix 1999, Dutton et al. 2005). In addition "maximum discs" do not provide good solutions when NFW-like profiles are used. In summary we do not know yet if discs are maximum or not. This is why we still have to consider alternatives like BFM or M/L ratio fixed using additional constrains like colours.

2.4.3.1 Best Fit Model (BFM)

The most open way to fit the different components of a mass model is to let all the parameters free. This gives the same weight to all the parameters. The M/L ratio(s) is(are) the free parameter(s) of the stellar component(s). For galaxies without a bulge, only the M/L ratio of the disc is considered and it is supposed to be independent of the galacto-centric distance, assumption that cannot be made in the optical (de Denus-Baillargeon et al. 2013). For galaxies with a bulge, we have to consider the M/L ratio of the bulge as a second baryonic free parameter. We nevertheless set the constraint that the bulge M/L ratio has to be equal to or larger than that of the disc since bulges have older stellar populations and their stars are on average fainter. In addition to the baryonic free parameter(s), the various models (ISO and NFW) have additional free parameters. The best fit model (BFM) technique consists of selecting the set of free parameters that minimises the χ^2.

Its main advantage is that it does not need any prior but its main inconvenient is the degeneracy of the solutions (see e.g. Fig. 4 of Carignan et al. 1990 or Fig. 13 of Jobin & Carignan 1990, where different combinations of the free parameters can give equally acceptable solutions). It is indeed well known that the disc-halo decomposition is affected by the degeneracy of the possible solutions and for some galaxies, possible mass model solutions could range from "the minimum disc" to the maximum disc solutions (van Albada et al. 1985). The "minimum disc" solution means that in fact "no stellar disc" component is necessary. It could be used e.g. for modelling low surface brightness galaxies where the stellar component is negligible with respect to the cold gas disc and the dark halo components (Carignan & Freeman 1988). This is not the case for most of the galaxies presented in the present sample.

We use the BFM technique for the two models. This leads to three/four free parameters for both the ISO (r_0, ρ_0 and M/L_{disc}, M/L_{bulge} for bulgeless/bulge galaxies) and NFW (c, V_{200} and M/L_{disc}, M/L_{bulge} for bulgeless/bulge galaxies) models. To avoid some non physical values, we fixed minimal values on the parameters; the M/L ratio of the disc and bulge are limited at 0.1.

2.4.3.2 Maximum disc Models (MDM)

The definition of a MDM is somewhat confusing. We expect that a MDM provides a maximum rotation velocity for the disc that is comparable to the maximum rotation velocity of the observed rotation curve. In that case, an operational definition for the maximum disc hypothesis could be, for instance, that the stellar disc provides 85% ± 10% of the total rotational support of the galaxy at a radius equal to 2.2 disc scale lengths (Sackett 1997). However, this definition cannot be used for fitting rotation curves. Indeed, the disc rotation curve, computed using a model from the stellar light distribution, must match the observed rotation curve and not overestimate it. But in practice the constraint comes from the rising part of both rotation curves, where they must match. If the rising shape of the disc rotation curve is steeper than the rising shape of the observed rotation curve, the maximum rotation velocity of the stellar disc could be much smaller than the maximum velocity of the rotation curve (see for instance UGC 2800, 10075, 11466, 11861), despite the fact that the disc rotation curve is literally scaled to its highest amplitude.

For the MDM, the disc M/L ratio is obtained using the following procedure: we first run the BFM to estimate the M/L ratio corresponding to the minimal χ^2_{BFM}.

Then, we impose the disc M/L ratio to be higher than that obtained with the BFM but letting the χ^2 to increase up to $1.3 \times \chi^2_{\rm BFM}$. We chose this limit from the intrinsic dispersion of the data and from the degenerescence of the fits. For bulge galaxies, the final model is the one having the highest disc M/L ratio and the bulge M/L ratio which provides the lowest χ^2 while remaining equal or larger than that of the disc.

The MDM technique was used for the ISO model only, with three or four free parameters (r_0, ρ_0 and $\mathrm{M/L_{disc}}$, $\mathrm{M/L_{bulge}}$) depending if galaxies are bulgeless or have a bulge. We also ran but do not present the MDM in the case of the NFW profile because both the baryonic and the cuspy dark halo components tend to be equally maximised in the rising part of the rotation curve, furthermore the BFM is almost identical to the MDM in the case of the NFW dark halo.

2.4.3.3 M/L ratio fixed by the colours

The third method we used in this paper consists in constraining the stellar M/L ratio using the photometry, as described in section 2.3.2. Like the MDM, the M/L ratio estimated from spectrophotometric evolution models give an upper limit to the baryonic mass (e.g, Carignan & Freeman 1985, Bell & de Jong 2001, Kassin et al. 2006a;b). Because the spectrophotometric models does not allow to disentangle a different M/L ratio for the disc and for the bulge, we use the same M/L ratio for the disc and for the bulge. We refer to this method as the fixed M/L ratio method.

This method was used for the two models. It leads to two free parameters for both ISO (r_0 and ρ_0) and NFW (c and V_{200}) models.

2.5 Results of the mass models

In this section, we present the mass models using the two DM profiles, ISO and NFW. We have applied the various decompositions and mass models described in section 3 and 4 on our sample of 121 galaxies. As described in section 3.2, our sample of nearby galaxies covers a broad range of morphological types (from Sa to Im) and luminosities (masses). An example illustrating the mass models is shown in Fig. 4.3 for the galaxy UGC 3463. For this case, all models give equivalently reasonable good fits. The profile decompositions and the different mass models for each galaxy are given in Appendix 2. The whole catalogue is available online.

When looking at the results and comparing with similar studies in the literature, one has to be careful and compare between themselves similar models. For example, ISO models can vary a lot from one author to the other. In the earlier models (e.g, Carignan & Freeman 1985), a nonsingular isothermal sphere model was used, charaterized by the core radius r_c, while later (e.g, van Albada et al. 1985) a pseudo-isothermal sphere model having a scaling radius r_0 was used, where e.g. $r_c \simeq 3r_0/\sqrt{2}$. Spano et al. (2008), who also modeled *GHASP* FP data, used a Hubble-modified density profile to model the DM halo, which means we cannot directly compare our results with theirs. Indeed, the shape of the Hubble-modified and of the ISO profiles do not have the same behaviour before and beyond their scaling radius (Kormendy & Freeman 2004, Binney & Tremaine 2008).

In what follows, we will compare our results to the ISO results of Kormendy & Freeman (2004) and of Randriamampandry & Carignan (2014), who used exactly the same formalism. In addition, as we will see, we will only be able to compare bulgeless galaxies since the sample of Kormendy & Freeman (2004) is limited to late-type galaxies from Sc to Irr, while our sample covers the whole range from Sa to Irr.

2.5.1 Pseudo-isothermal models (ISO)

For the luminous disc, Lelli et al. (2016) found that when modeling galaxies, the values of M/L in the 3.6 μm band are in the range of 0.2 to 0.7 $M_\odot/L_\odot$. As seen in Fig. 2.6, we find a median value of M/L = 0.1 when using the BFM (left); 0.4 for the MDM (center) and also 0.4 for the fixed M/L (right). The values of the latter two models are in the range of Lelli's results. Recently, (Kettlety et al. 2018) found that the M/L can be fixed at a value of 0.65 when using the W1 band of WISE, this is close to the average value we found for the fixed M/L and the MDM. We note that the average M/L ratio for the BFM is four times smaller than for the MDM, meaning that the BFM does not provide maximum disc solutions. Despite the fact that their M/L distribution are quite different, it is noticeable that the MDM gives the same average M/L value than the models for which the M/L ratios are fixed by the *WISE* colours. This would suggests that discs tend, on average, to be maximal, as defined in Sec. 2.4.3.2.

For the ISO models, we observe in Fig. 4.6 a clear anti-correlation between the central halo density and the halo core radius for the three models (BFM, MDM,

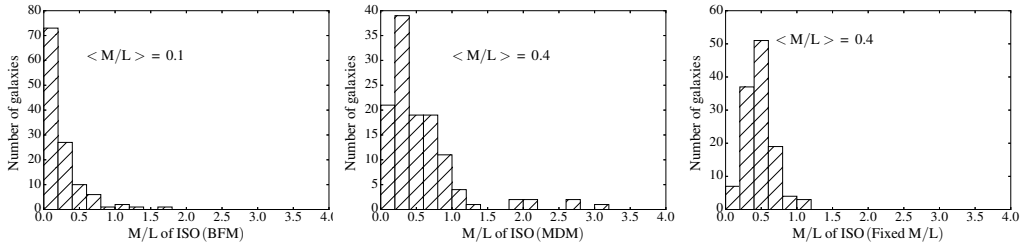

Figure 2.6: Mass-to-light ratio distribution from the pseudo isothermal sphere model (ISO). From left to right: for the best fit model (BFM), for the maximum disc model (MDM) and for the M/L fixed using the *WISE* colour (W_1-W_2). The median <M/L> values are indicated in the plots for each case.

Fixed M/L). This means that higher central density dark halos have smaller core radius. We show the results for the full sample (top panel) and for the sub-sample of galaxies which had no profile decomposition (middle panel) and those for which we did a profile decomposition (bottom panel). The points are for the BFM but we overlay the results for the 3 models. The different linear regressions found for the different models and for the full sample are:

$$\begin{aligned} \log\ \rho_0 &= (-1.14 \pm 0.09)\ \log\ r_0 - (0.51 \pm 0.06) \qquad \text{[BFM]} \\ \log\ \rho_0 &= (-1.03 \pm 0.12)\ \log\ r_0 - (0.83 \pm 0.08) \qquad \text{[MDM]} \\ \log\ \rho_0 &= (-1.10 \pm 0.08)\ \log\ r_0 - (0.59 \pm 0.08) \qquad \text{[fixed M/L]} \end{aligned} \tag{2.12}$$

The results for the sub-sample with no decomposition (middle: later types) and the sub-sample with decompositions (bottom: earlier types) give very similar results, but with different zero points. If we compare with the litterature for authors using the same ISO formalism, we find:

$$\begin{aligned} \log\ \rho_0 &= -1.10\ \log\ r_0 - 1.05 \qquad \text{[BFM : R\&C2014]} \\ \log\ \rho_0 &= -1.21\ \log\ r_0 - 1.10 \qquad \text{[MDM : K\&F2004]} \end{aligned} \tag{2.13}$$

Kormendy & Freeman (2004) used MDM models while Randriamampandry & Carignan (2014) used BFM models. Overall, our relations are closer for our sub-sample with no decomposition (later types) than for the sub-sample with decomposition. The fact that the relations found are similar to those of the literature, with a similar slope but slightly different zero points, could come from using different datasets. In the case of Kormendy & Freeman (2004), their sample covers only

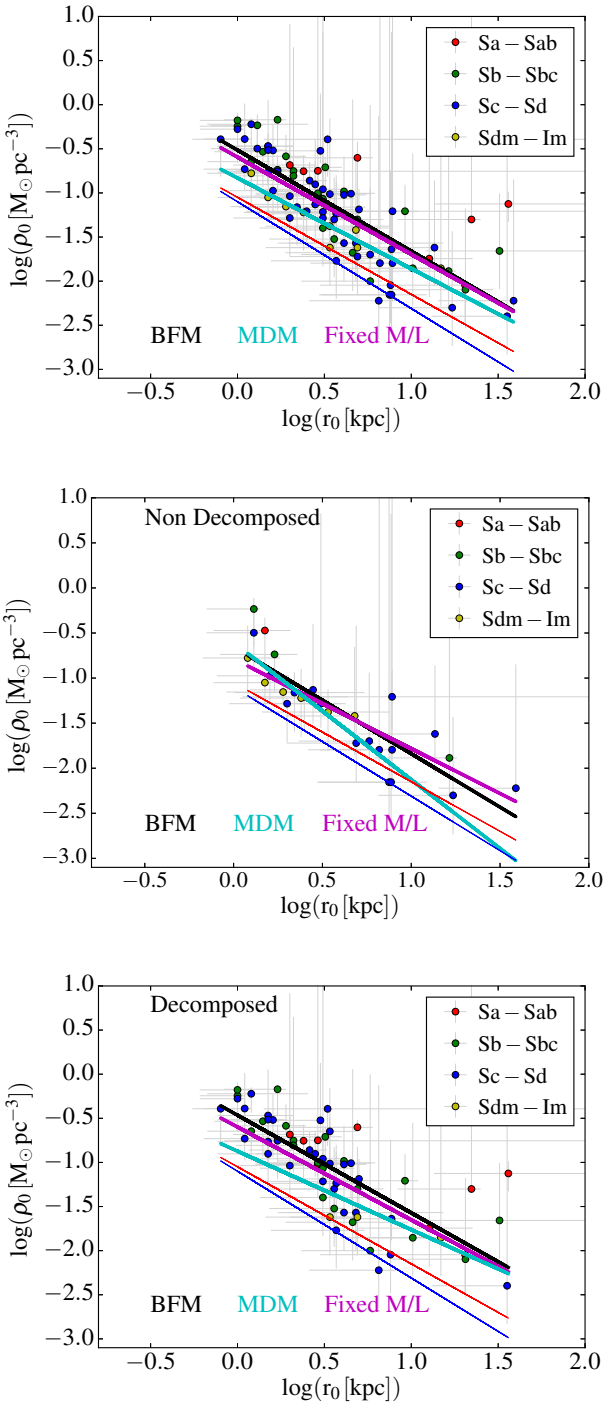

Figure 2.7: Central halo density versus halo core radius for the ISO best fit models (BFM), maximum disc models (MDM) and fixed M/L models. It is given for the whole sample at the top, for the galaxies with no luminosity profile decomposition (later types) in the middle and for the galaxies for which we did a profile decomposition (earlier types) at the bottom. The thin dark blue and red lines represent respectively the fits found by Kormendy & Freeman (2004) and Randriamampandry & Carignan (2014)

late-type galaxies (Sc to Irr) while we cover all morphological types and they are using mainly B-band photometry. For Randriamampandry & Carignan (2014), their results are based on extended HI data while we mainly model the inner parts with our optical FP data but using also mid-infrared photometry. All those different approaches make direct comparisons very difficult.

Fig. 2.8 shows the halo parameters (halo core radius and central density) as a function of the B-band luminosity M_B. To avoid crowding or multiple figures, we do not plot symbols representing individual galaxies for the MDM and the fixed M/L but only the fit to the data points of these models: a cyan line for the MDM and a magenta line for the fixed M/L model. Running BFM without fixing any lower limit for the core radius (r_0) and higher limit for the core density (ρ_0) show that 10 galaxies have a core radius $r_0 < 1$ kpc and 7 galaxies have a core density $\rho_0 > 0.75$ $M_\odot kpc^{-3}$. In addition, core densities $\rho_0 > 0.75$ $M_\odot kpc^{-3}$ are only obtained where core radius r_0 are lower than 1.5 kpc. The combination of very small r_0 and high ρ_0 leads to DM halo with constant rotation velocities at all radius (except in the very center of the galaxies). They add a kind of offset to the disc component(s). In all cases, the MDM shows that a DM halo is not necessary to fit the rotation curves. Therefore, we found 25 galaxies for which we do not need halos parameters (shown with an asterisk in Appendix B.2). These galaxies are obviously best fitted by a maximum disc model until almost the end of the optical radius (no DM halo) and those are removed in the fits between the core radius and the central density, and the core radius or the central density as a function of M_B. On the other hand, only dwarf galaxies having a dynamical mass less than $2 \times 10^9 M_\odot$ and a rotation velocity smaller than 40 km/s might eventually have core radius lower than 1 kpc (e.g, Holmberg I and II, DDO 53, Oh et al. 2011) and our sample does not contain such low mass galaxies. Furthermore we do not allow BFM to have core radius lower than 0.5 kpc and a core density larger than 0.75 $M_\odot kpc^{-3}$, we do not take into account galaxies which reach the lower value 0.5 kpc or the upper value 0.75 $M_\odot kpc^{-3}$ to fit the halos parameters. Typically no clear correlation is found between the core radius or the central density and M_B but the dispersion is rather high (0.50 dex and 0.75 dex respectively) around the average of $\sim$ 3 kpc and $\sim$ 0.1 $M_\odot.pc^{-3}$.

We do not confirm previous studies suggesting that less luminous dwarf galaxies tend to have smaller halo core radius and larger central density (e.g, Carignan & Freeman 1988). However, we observe a weak correlation between the core radius

and the luminosity, less luminous galaxies tend to have smaller core radius. At the opposite, a weak correlation between the central density and the luminosity is observed: the less luminous galaxies tend to have shallower central density than brighter galaxies. Similarly, we note again that the mean central halo density is lower for the fixed M/L than for the BFM and the MDM models.

In order to understand the impact of the quality of the rotation curves on the lack of correlation, we have separated the higher quality rotation curves (flag 1) from the lower quality ones (flag 2) in Fig. 2.9. The weak trends we found are not a result of the quality of the data. This will be discussed further in section 2.6.

2.5.2 NFW dark matter halos

Cosmological numerical simulations (e.g., Navarro et al. 1996c) show a strong correlation between the velocity at the virial radius (i.e V_{200}) and its concentration in the sense that low mass halos are more concentrated. de Blok et al. (2008) emphasised that large values of the concentration parameter c indicate a larger collapse factor while $c = 1$ indicates no collapse. Due to the fact that concentration c lower than unity makes no sense in the CDM context (de Blok et al. 2008), we do not allow $c < 1$. This naturally lead to the fact that 4 and 31 galaxies have a concentration equal to the lower limit $c = 1$, respectively for the BFM and fixed M/L model. Examples of parameters obtained for the NFW fits are listed in Table B.4 and the full table can be found online.

In Fig. 2.10, we plot the distribution of log c as a function of log V_{200}. For the BFM, the correlation between c and V_{200} is given by:

$$\log\ c = (-1.01 \pm 0.09)\ \log\ V_{200} + (3.27 \pm 0.22) \tag{2.14}$$

We find an average value of concentration c = 8.71 ± 1.71, which iagrees within the error with the values usually found in the literature (e.g. c ≃ 10, Bullock et al. 2001) and with the value of $c = 6.9$ derived by Noordermeer (2006) for a sample of early-type galaxies.

When the M/L ratio is calculated using *WISE* colours, the correlation found between c and V_{200} is:

$$\log\ c = (-0.83 \pm 0.09)\ \log\ V_{200} + (2.79 \pm 0.20) \tag{2.15}$$

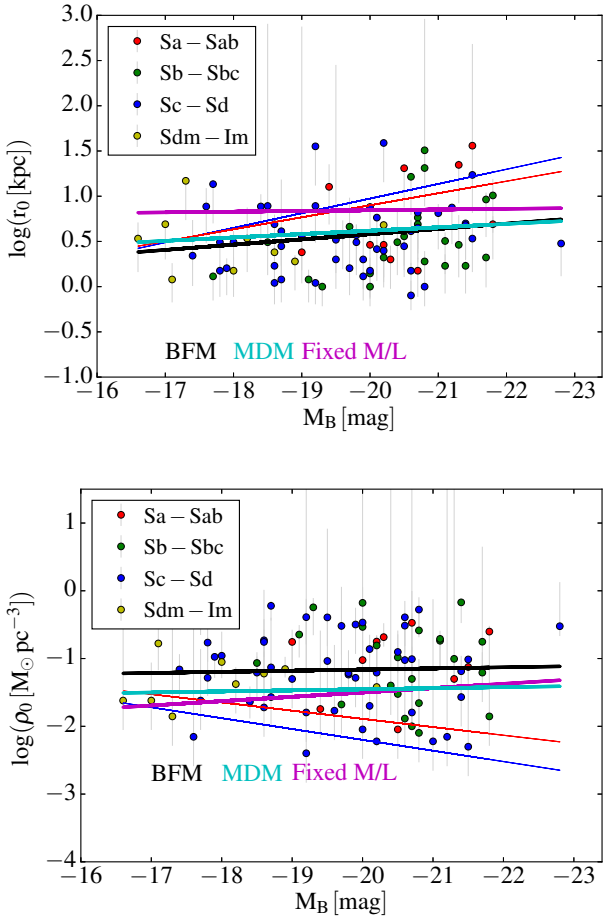

Figure 2.8: Halo scaling radius (top panel) and central halo density (bottom panel) versus the absolute magnitude for the whole sample from the pseudo-isothermal (ISO) models. The black, cyan and magenta lines are the best fit (BFM), the maximum disc (MDM) and the fixed M/L models respectively. The thin blue and red lines represent respectively the fit found by Kormendy & Freeman (2004) and Randriamampandry & Carignan (2014).

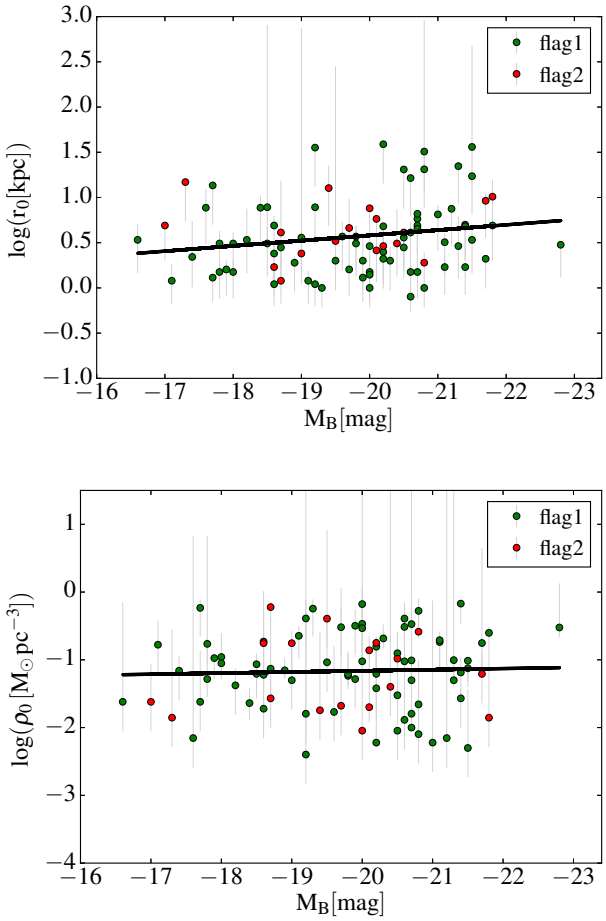

Figure 2.9: Halo scaling radius (top panel) and central halo density (bottom panel) versus the absolute magnitude for all the sample from the ISO (BFM) models. The green symbols represent the higher quality rotation curves (flag 1) while the red circles show the lower quality rotation curves (flag 2). The black line linearly fits the dots.

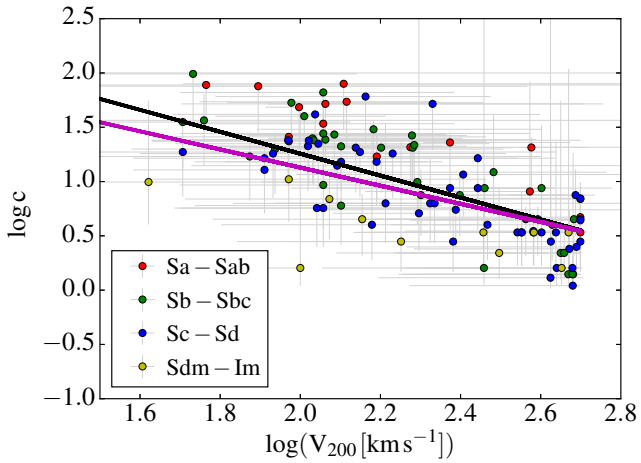

Figure 2.10: Distribution of log c as a function of log V_{200} for the NFW best fit models (BFM) points. The black and magenta lines represent respectively the best fit model (BFM) and the fixed M/L models.

we find an average value c = 6.46 ± 1.59, closer to the results of Noordermeer (2006).

The mean concentration derived from the BFM is slightly higher than the one found using fixed M/L ratio, meaning that baryons may be responsible for the lower concentration inferred in the later case. More interestingly, the slope of the linear regression linking log c to log V_{200} is also shallower in the later case, indicating that the concentration parameter is less dependent on the velocity at the virial radius when the M/L ratio is set by the baryonic content of the galaxy. However, this is a very small effect. More importantly, Fig. 2.10 shows that late-type galaxies tend to be located below the best fit line and the early type galaxies above, pointing out that early-type galaxies tend to display a more concentrated halo than later-type ones in the NFW paradigm. The same trend is also observed when M/L is fixed.

2.5.3 ISO vs NFW profiles

Fig. 2.11 shows that, on average, smaller χ^2 values are found for the ISO fits than for NFW models. It can been seen in Tables B.2 to B.4 listing all the parameters that, for a majority of galaxies, the observed rotation curves are better fitted by an ISO than by a NFW halo profile. Confirming previous works, our sample is thus better represented by a central cored than a cuspy DM density profile.

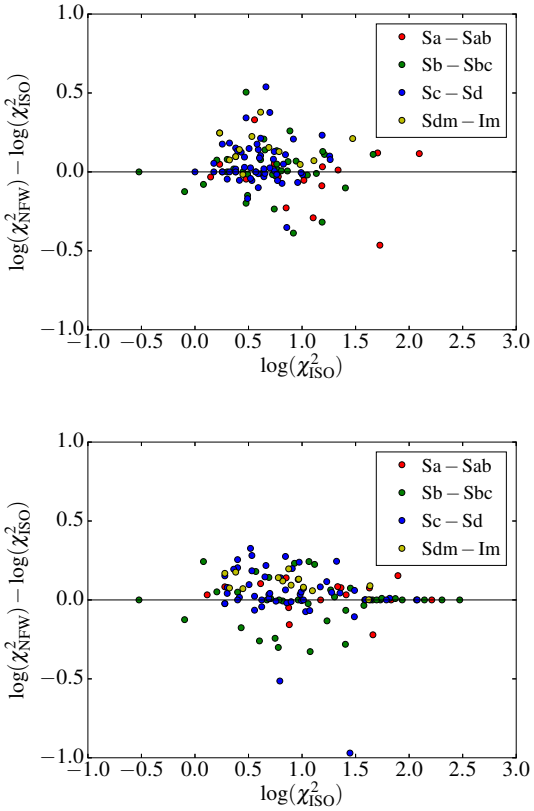

Figure 2.11: The top panel presents the comparison between the reduced χ^2 of NFW and ISO for the best fit model (BFM). The bottom panel shows the comparison between the reduced χ^2 of NFW with fixed M/L and ISO with fixed M/L.

2.6 Discussion

The presence of a bulge or of a bar may have an influence on the derived halo contribution.

The previous studies on the mass distribution from high-resolution rotation curves, described earlier in this paper, have focused on late-type galaxies where the absence of a bulge makes these objects easier to analyse. We have here a sample that allows us to tackle the problem of earlier types bulge galaxies.

The presence of a bar is also a major difficulty as it induces non-circular motions due to the streaming of the gas along the bar. If a bar is perpendicular to the major axis of a galaxy, the measured rotational velocities are overestimated and underestimated if the bar is parallel to the major axis (Dicaire et al. 2008, Randriamampandry et al.

2015), which may impact the mass models.

2.6.1 Bulge influence

Probably the most interesting scaling laws proposed by the previous studies (first by Kormendy & Freeman 2004) is the fact that the product $\rho_0 \times r_0$ appears to be independent of luminosity. To understand the bulge influence on this result, we split our sample in two parts based on the luminosity profile decomposition presented in section 2.3.3: a first sample of 40 is composed of galaxies with very little or no bulge such that no decomposition was performed and the second set of 81 galaxies is composed of bulge galaxies for which we did a proper decomposition. The first group is essentially composed of the late type and irregular galaxies, but not only (see Fig. 2.4, third panel). Using this classification scheme, we reproduce $\rho_0 \times r_0$ as a function of luminosity in Fig. 2.12. The galaxies with no decomposition (top) agree well with what was found before. However, if we take the whole sample including the early-type galaxies (bottom), this relation does not hold anymore and even less when using the galaxies for which we did a decomposition (middle).

In order to investigate this further, we used a slightly different approach to separate late and early types than the one used above, based on decomposing or not the luminosity profiles. We produced two sub-samples: (i) a *bulgeless* sample defined as the galaxies with $L_{bulge}/L_{total} < 0.02$ and (ii) a *bulge* sample with $L_{bulge}/L_{total} > 0.07$. So, the first sub-sample is mainly composed of late-type spirals while the second of earlier types galaxies. The advantage of this approach is that it better quantifies the bulge relative importance and enables to have two extreme classes with a comparable sample sizes, the bulgeless and bulge sub-samples having respectively 34 and 54 galaxies.

A comparison of the DM halo parameters with the absolute magnitudes is presented in Fig. 2.13 for the BFM. Differences occur between bulgeless and bulge galaxies when we compare the 2 parameters characterising the dark halo (scaling radius r_0 and central density ρ_0) to the absolute magnitudes M_B. The bulgeless galaxies show a clearer correlation between r_0 and M_B (left panel, green line) than bulge early-type spirals (left panel, black line). The main difference is found for ρ_0 that is anticorrelated to M_B for bulgeless galaxies (right, green line), contrary to the correlation observed for the bulge galaxies (right, black line). Both trends for r_0 and ρ_0 for bulgeless galaxies were already found by Kormendy & Freeman (2004) and

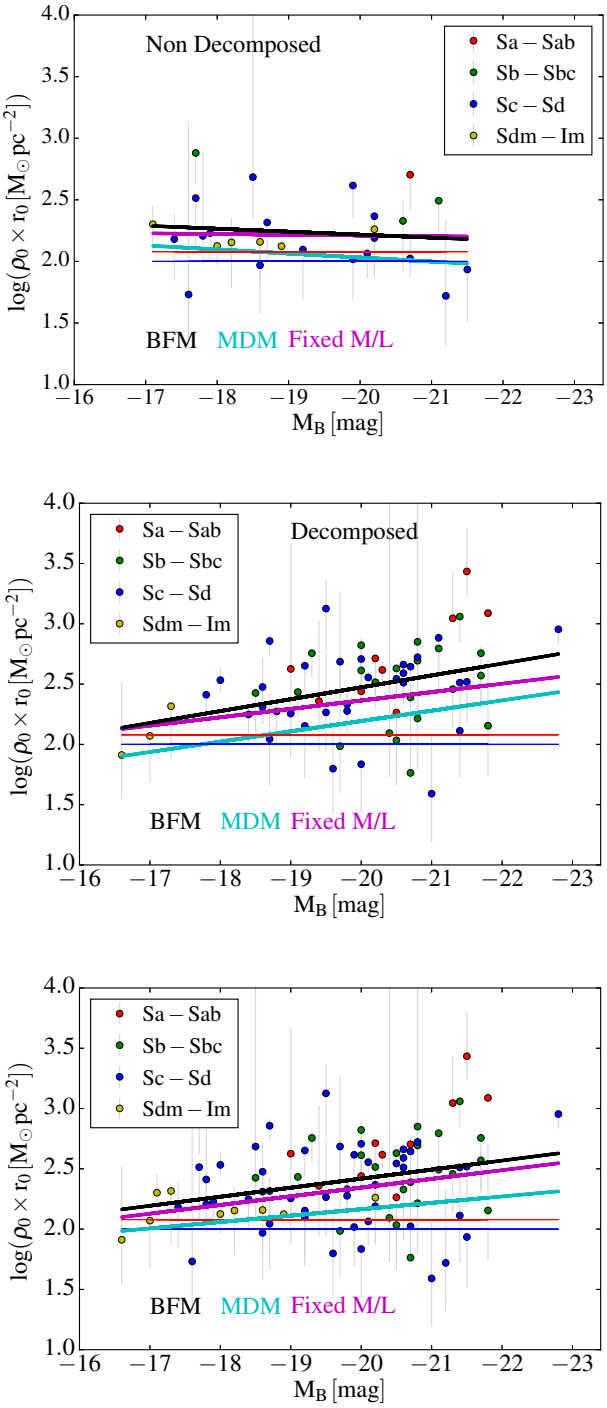

Figure 2.12: $\rho_0 \times r_0$ as a function of M_B. The black, cyan and magenta lines represent the fit using the BFM, the MDM and the fixed M/L respectively. The thin blue and red lines represent respectively the fits found by Kormendy & Freeman (2004) and Randriamampandry & Carignan (2014) respectively. Top panel for galaxies with no luminosity profile decomposition (later types), middle for the galaxies for which we did a profile decomposition (earlier types) and the bottom panel for the whole sample.

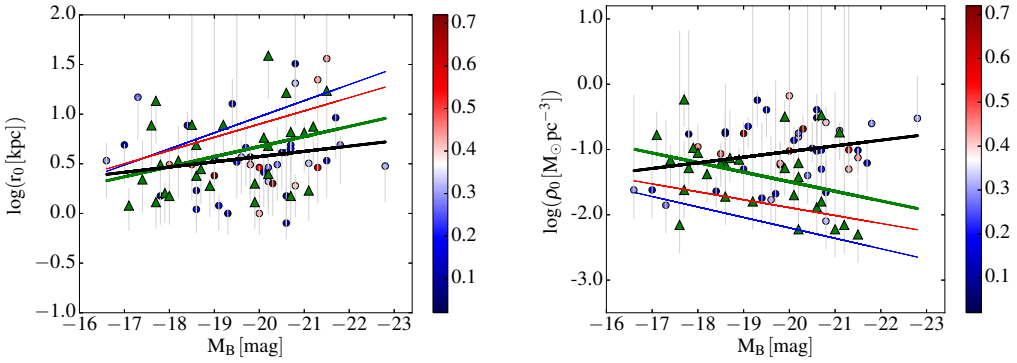

Figure 2.13: Halo parameters (scaling radius on the left and central density on the right) versus absolute magnitude for the bulgeless (triangles) and bulge (dots) subsamples. The colours of the dots represent the importance of the bulge (see colour bar on the right). The thin blue and red lines represent respectively the fit found by Kormendy & Freeman (2004) and Randriamampandry & Carignan (2014), mainly for late-type galaxies.The thick green line represents the fit for the bulgeless and the thick black line for the bulge galaxies.

Randriamampandry & Carignan (2014). This shows that we should not generalize the scaling relations found previously to all morphological types. Clearly, DM is not distributed similarly in bulgeless and bulge systems. This either indicates intrinsic differences in the way DM is distributed in early-types and late-types or a problem in taking into account the luminous matter distribution of the bulge and the disc or a combination of both. Another possibility is that, in this work we are mainly probing the inner parts while many of the other studies were based on extended HI rotation curves.

In order to better understand the impact of using only optical rotation curves to constrain mass models rather than both optical and HI rotation curves, which generally extend well beyond the optical radius $D_{25}/2$, we have used the HI rotation curves, published in Randriamampandry & Carignan (2014) and have artificially limited these rotation curves to their optical radius. As shown in Appendix 3, the optical rotation curves provide a good estimate of the mass model parameters when the plateau is reached, which is the case for 9 out of 15 galaxies: IC 2574, NGC 2403, NGC 2841, NGC 3031, NGC 3621, NGC 55, NGC 7331, NGC 7793, NGC 925. The mass models offer a less satisfactory agreement when the optical curves are limited to their solid body rising part, which is the case for 6 out of 15 galaxies: DDO 154, NGC 2366, NGC 247, NGC 300, NGC 3109 , NGC 3198. The tuning

is particularly good when the constraints of the rotation curve come from internal regions (eg NGC 2403, NGC 7331, NGC 7793, NGC 925) and it is even the case to a lesser level when the plateau of the rotation curve is barely achieved (eg NGC 55, NGC 3621) or when it is not fully achieved (e.g. NGC 247). The case of NGC 3621 is interesting because the plateau is reached although the rotation curve is still slightly increasing beyond the optical radius. In addition, galaxies with decreasing rotation curves already observed within the optical radius show very good agreement (eg NGC 2841, NGC 3031, NGC 7331, NGC 7793). Indeed, decreasing rotation curves are generally observed for early-type galaxies, whose central regions are dominated by the presence of a bulge that optical data can constrain well.

2.6.2 Bar influence

To study the effect of the bar, we split the sample in non-barred (SA), moderately barred (SAB) and barred (SB) galaxies: the first sample of 31 is composed of galaxies with no bar, the second set of 46 galaxies is composed of systems with moderate bars and the third sample of 28 barred galaxies. In Fig. 2.14, we show the correlations between the halo core radius r_0 (top) or the central halo density ρ_0 (bottom) and the M_B using different colours for non-barred galaxies (SA, blue), moderately barred galaxies (SAB, red) and barred galaxies (SB, black). These plots show that these correlations do not depend on the fact that a galaxy has developed a bar or not; the scatter around the fits is roughly identical for the three categories of galaxies.

2.7 Summary and Conclusion

In this work, we have studied mass models using Hα rotation curves and mid-infrared photometry on a sample of 121 galaxies which cover all morphological types. Luminosity profiles have been decomposed using a flat (disc, bar, etc.) and a spherical (bulge) component. We used a pseudo-isothermal sphere (ISO) and a Navarro-Frenk-White model (NFW) to describe the dark matter halos and used various fitting strategies: a best fit model (BFM), a maximum disc model (MDM) and a M/L fixed using colours.

The two BFM models (ISO and NFW) used to describe the distribution of the

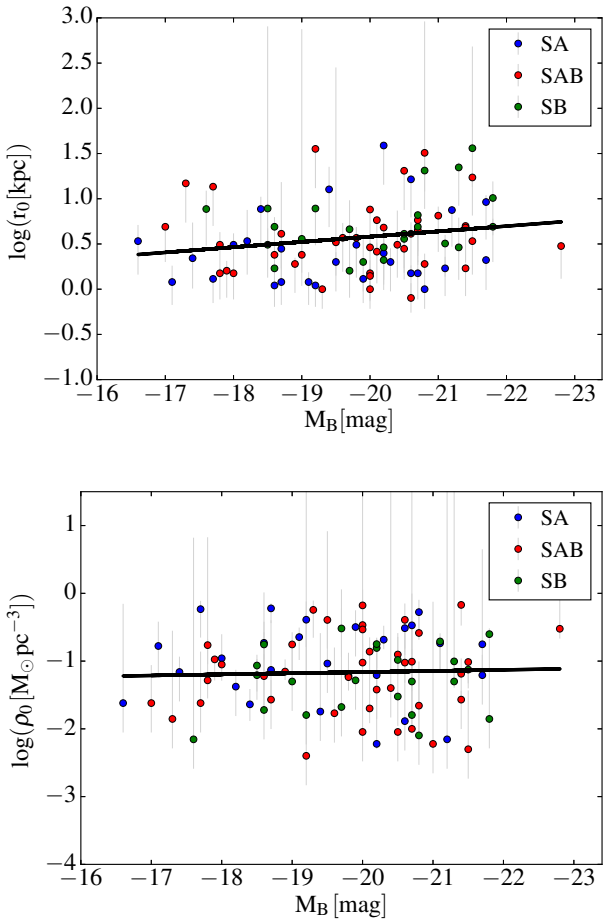

Figure 2.14: Halo core radius (top) and central halo density (bottom) versus the absolute magnitude for the whole sample. The blue dots indicate non barred galaxies (SA); the red dots represent moderately barred galaxies (SAB) and the green dots display barred galaxies (SB).

DM halo within the visible discs are both acceptable, with ISO giving somewhat better results. For ISO with maximum disc fit, the M/L values are similar to the M/L obtained from the (W_1-W_2) colour. This suggests that discs tend to be "maximum". The ISO (MDM), ISO and NFW with M/L fixed from colours give also reasonable fits for almost all galaxies.

Previous works considered in this paper for comparison were carried on samples of galaxies mainly composed of late morphological types. This difference in galaxy populations with our sample, which covers all morphological types, may explain the disagreement between our results and those published in the literature. For the ISO model, the trend between the dark halo parameters and the absolute magnitude found for no bulge galaxies in this paper (less luminous galaxies tend to have smaller core radius and higher central density) is in agreement with previous works (Kormendy & Freeman 2004, Randriamampandry & Carignan 2014) but not the relations found for bulge galaxies. For bulge galaxies, less luminous galaxies tend to have smaller core radius and smaller central density. However, we find that the trend between ρ_0 and r_0 does not depend on morphological types. For the NFW profile, we can see that the halo is more concentrated for early type galaxies than for late type galaxies whatever technique is used (BFM or fixed M/L), again showing a difference in DM properties between early and late morphological types. Therefore, the relation between the dark halo parameters and the luminosity of the galaxies seems dependent on the morphological types. We also checked whether the presence of a bar could impact the observed DM correlations and found not convincing trend.

In order to ensure that our results are not affected by the fact that we only consider optical rotation curves, we have analyzed the sample of Randriamampandry & Carignan (2014) by truncating their HI rotation curves to the optical radius. We found that mass models are in good agreement when the plateau is (barely) reached within this radius, which is usually the case for the relatively early types of galaxies.

While the effect of adiabatic contraction of the halo by the disc is to steepen cores into cusps (Dutton et al. 2005), observations continue to argue that dark matter profiles are more core-like. Stellar feedback at high redshift may flatten the cusps in the less massive galaxies by removing low angular momentum material leading to potential fluctuations decreasing the central density (Navarro et al. 1996a) but those processes are not effective enough for massive galaxies with deeper potential well (Mac Low & Ferrara 1999).

2.8 Acknowledgments

We thank Carlos Barbosa for the methods of the decomposition of surface brightness profiles. Most of the research of MK was done while she was having a PhD Scholarship from the Science faculty of the University of Cape Town. CC's work is based upon research supported by the South African Research Chairs Initiative (SARChI) of the Department of Science and Technology (DST), the Square Kilometer Array South Africa (SKA SA) and the National Research Foundation (NRF). We acknowledge financial support from "Programme National de Cosmologie et Galaxies" (PNCG) funded by CNRS/INSU-IN2P3-INP, CEA and CNES, France.

Bibliography

Amram P., Balkowski C., Boulesteix J., Cayatte V., Marcelin M., Sullivan III W. T., 1996, A&A, 310, 737

Barbosa C. E., et al., 2015, MNRAS, 453, 2965

Begeman K. G., 1987, PhD thesis, , Kapteyn Institute, (1987)

Bell E. F., de Jong R. S., 2001, ApJ, 550, 212

Binney J., Tremaine S., 2008, Galactic Dynamics: Second Edition. Princeton University Press

Blais-Ouellette S., Carignan C., Amram P., Côté S., 1999, AJ, 118, 2123

Blais-Ouellette S., Amram P., Carignan C., 2001, AJ, 121, 1952

Bosma A., 1981, AJ, 86, 1825

Bottema R., Pestaña J. L. G., 2015, MNRAS, 448, 2566

Buchhorn M., 1992, PhD thesis, , Australian National Univ., (1992)

Bullock J. S., Kolatt T. S., Sigad Y., Somerville R. S., Kravtsov A. V., Klypin A. A., Primack J. R., Dekel A., 2001, MNRAS, 321, 559

Carignan C., Freeman K. C., 1985, ApJ, 294, 494

Carignan C., Freeman K. C., 1988, ApJ, 332, L33

Carignan C., Charbonneau P., Boulanger F., Viallefond F., 1990, A&A, 234, 43

Cluver M. E., et al., 2014, ApJ, 782, 90

Cole S., Lacey C., 1996, MNRAS, 281, 716

Courteau S., Rix H.-W., 1999, ApJ, 513, 561

Di Cintio A., Brook C. B., Macciò A. V., Stinson G. S., Knebe A., Dutton A. A., Wadsley J., 2014a, MNRAS, 437, 415

Di Cintio A., Brook C. B., Dutton A. A., Macciò A. V., Stinson G. S., Knebe A., 2014b, MNRAS, 441, 2986

Dicaire I., et al., 2008, MNRAS, 385, 553

Dutton A. A., Courteau S., de Jong R., Carignan C., 2005, ApJ, 619, 218

Epinat B., et al., 2008a, MNRAS, 388, 500

Epinat B., Amram P., Marcelin M., 2008b, MNRAS, 390, 466

Freeman K. C., 1970, ApJ, 160, 811

Garrido O., Marcelin M., Amram P., Boulesteix J., 2002, A&A, 387, 821

Garrido O., Marcelin M., Amram P., Boissin O., 2003, A&A, 399, 51

Garrido O., Marcelin M., Amram P., 2004, MNRAS, 349, 225

Garrido O., Marcelin M., Amram P., Balkowski C., Gach J. L., Boulesteix J., 2005, MNRAS, 362, 127

Gentile G., Salucci P., Klein U., Vergani D., Kalberla P., 2004, MNRAS, 351, 903

Hohl F., 1971, ApJ, 168, 343

Jarrett T. H., et al., 2012, AJ, 144, 68

Jarrett T. H., et al., 2013, AJ, 145, 6

Jobin M., Carignan C., 1990, AJ, 100, 648

Kalnajs A., 1983, in Athanassoula E., ed., IAU Symposium Vol. 100, Internal Kinematics and Dynamics of Galaxies. pp 87–88

Kassin S. A., de Jong R. S., Pogge R. W., 2006a, ApJS, 162, 80

Kassin S. A., de Jong R. S., Weiner B. J., 2006b, ApJ, 643, 804

Katz H., Lelli F., McGaugh S. S., Di Cintio A., Brook C. B., Schombert J. M., 2017, MNRAS, 466, 1648

Kent S. M., 1986, AJ, 91, 1301

Kettlety T., et al., 2018, MNRAS, 473, 776

Kormendy J., Freeman K. C., 2004, in Ryder S., Pisano D., Walker M., Freeman K., eds, IAU Symposium Vol. 220, Dark Matter in Galaxies. p. 377

Kravtsov A. V., Klypin A. A., Bullock J. S., Primack J. R., 1998, ApJ, 502, 48

Lelli F., McGaugh S. S., Schombert J. M., 2016, preprint, (arXiv:1606.09251)

Mac Low M.-M., Ferrara A., 1999, ApJ, 513, 142

Moore B., Governato F., Quinn T., Stadel J., Lake G., 1998, ApJ, 499, L5

Navarro J. F., Eke V. R., Frenk C. S., 1996a, MNRAS, 283, L72

Navarro J. F., Frenk C. S., White S. D. M., 1996b, ApJ, 462, 563

Navarro J. F., Frenk C. S., White S. D. M., 1996c, ApJ, 462, 563

Noordermeer E., 2006, PhD thesis, Groningen: Rijksuniversiteit

Oh S.-H., de Blok W. J. G., Brinks E., Walter F., Kennicutt Jr. R. C., 2011, AJ, 141, 193

Ostriker J. P., Peebles P. J. E., 1973, ApJ, 186, 467

Randriamampandry T. H., Carignan C., 2014, MNRAS, 439, 2132

Randriamampandry T. H., Combes F., Carignan C., Deg N., 2015, MNRAS, 454, 3743

Sackett P. D., 1997, ApJ, 483, 103

Salucci P., 2001, MNRAS, 320, L1

Spano M., Marcelin M., Amram P., Carignan C., Epinat B., Hernandez O., 2008, MNRAS, 383, 297

Verheijen M. A. W., 2001, ApJ, 563, 694

Weinberg M. D., Katz N., 2002, ApJ, 580, 627

de Blok W. J. G., Bosma A., 2002, A&A, 385, 816

de Blok W. J. G., McGaugh S. S., Bosma A., Rubin V. C., 2001, ApJ, 552, L23

de Blok W. J. G., Walter F., Brinks E., Trachternach C., Oh S.-H., Kennicutt Jr. R. C., 2008, AJ, 136, 2648

de Denus-Baillargeon M.-M., Hernandez O., Boissier S., Amram P., Carignan C., 2013, ApJ, 773, 173

de Jong R. S., van der Kruit P. C., 1995, VizieR Online Data Catalog, 410

van Albada T. S., Bahcall J. N., Begeman K., Sancisi R., 1985, ApJ, 295, 305

Chapter 3

GHASP: an Hα kinematics survey of spiral galaxies - XII. Distribution of luminous and dark matter in spiral and irregular nearby galaxies using R_C-band photometry

This chapter has been published in the Monthly Notices of the Royal Astronomical Society (MNRAS): M. Korsaga, P. Amram, C. Carignan, and B. Epinat, MNRAS 482, 154 (2019)

Abstract

Mass models of 100 nearby spiral and irregular galaxies, covering morphological types from Sa to Irr, are computed using Hα rotation curves and R_c-band surface brightness profiles. The kinematics was obtained using a scanning Fabry-Perot interferometer. One of the aims is to compare our results with those from Korsaga et al. (2018), which used mid-infrared (MIR) WISE W1 (3.4 μm) photometric data. For the analysis, the same tools were used for both bands. Pseudo-Isothermal (ISO) core and Navarro-Frenk-White (NFW) cuspy models have been used. We test Best Fit Models (BFM), Maximum Disc Models (MDM) and models for which M/L is fixed using the B - V colours. Similarly to what was found in the MIR 3.4 μm band, most of the observed rotation curves are better described by a central core density profile (ISO) than a cuspy one (NFW) when using the optical R_c-band. In both bands, the dispersion in the (M/L) values is smaller for the fixed M/L fits. As for the W1 photometry, the derived DM halos' parameters depend on the morphological types. We find similar relations than those in the literature, only when we compare our results for the bulge-poor sub-sample because most of previous results were mainly based on late-type spirals. Because the dispersion in the model parameters is smaller and because stellar masses are better defined in that band, MIR photometry should be preferred, when possible, to the optical bands. It is shown that for high-z galaxies, sensible results can still be obtained without full profile decomposition.

3.1 Introduction

The Λ-Cold Dark Matter (ΛCDM) model has a great deal of success in replicating large-scale structures such as the cosmic microwave background (e.g. Planck's results), baryonic and dark matter (DM) mass distributions in galaxy cluster using weak lensing, or structure growing through the ages (e.g. Springel et al. 2006). However, the ΛCDM model still struggles to explain galactic scale structures like, e.g. the cusp-core problem. Indeed, the cusp-core controversy, which consists of observing that inner galaxy rotation curves rise less steeply than expected from pure DM structure formation in ΛCDM simulations (e.g. Flores & Primack 1994), is far from being closed as a large number of studies show it continuously. In order to illustrate it, we will only mention two very recent works reaching pretty puzzling

opposite conclusions. For a recent review, see e.g. Bullock & Boylan-Kolchin (2017).

On the one hand, Read et al. (2018) studied the central DM density profile of the Draco dwarf spheroidal galaxy that is supposed to be a prime candidate for hosting a pristine DM cusp, unaffected by stellar feedback during galaxy formation. These authors found that Draco has an inner DM density consistent with a ΛCDM cusp. On the other hand, Carleton et al. (2018) concluded that ultra-diffuse Galaxies which suffer a dramatic reduction in surface brightness due to tidal stripping and heating, are remarkably well modelled if they reside in cored halos. Their semi-analytic simulations show that galaxies in cored dark-matter halos expand significantly in response to tidal stripping and heating in agreement with observations, whereas galaxies embedded in cuspy halos experience limited evolution.

Spiral and Irregular galaxies request a substantial amount of DM to model their mass distribution in the flat outer parts of their rotation curves (RCs) (e.g. Carignan & Freeman 1985, van Albada & Sancisi 1986). Because of the higher spatial resolution of Hα 2D velocity fields, the kinematics derived from those high spectral and spatial resolution data cubes allow to accurately construct the RCs that are best suited to derive the shape of the DM halo in the central part of the galaxies. Indeed, the rising inner regions of the RC actually constrain the parameters of the mass models (Blais-Ouellette et al. 1999), including the Mass-to-Light ratio (M/L) of their luminous components and the shape and parameters of the DM halo component. Therefore, high resolution RCs derived from 2D velocity fields allow to obtain accurate correlations between the dark halo properties and the optical properties of the galaxies (Blais-Ouellette et al. 2001). The stellar mass distribution is the hardest parameter to constrain, and the ill-defined stellar M/L ratios translate into degeneracies. To tackle this problem, the high resolution RCs observed by the Gassendi Hα survey of Spirals (GHASP) will be used (Epinat et al. 2008a;b).

A serious complication comes from the fact that the baryonic matter is not monotonically distributed in a single component. The presence of a bulge component usually makes the rotational velocities rise rapidly thus impacting the solid body shape of the RC. The latter reaches a plateau in the central regions and one needs to disentangle the contributions of the bulge and of the disc by assigning different spatial distribution (sphere vs disc) and different M/L ratios to each component since they are gravitationally supported by different mechanisms (velocity dispersion and

velocity rotation respectively) and have different stellar populations, the stars being on average older in bulges than in discs and therefore $(M/L)_{bulge} > (M/L)_{disc}$.

One goal of this paper is to test baryonic and DM mass distributions from early to late morphological types to account for galaxies with a bulge. In this study, the distribution of the DM profile is defined by either a pseudo-isothermal sphere (ISO) with a core density profile, as suggested by most of the observations (Begeman 1987, Kravtsov et al. 1998) or by a cuspy dark halo density profile, as suggested by cosmological numerical simulations (Navarro et al. 1996). Cuspy profiles describe well the DM distribution of steeply rising RCs while the core profiles give a better representation of slowly rising RCs (Blais-Ouellette et al. 2001, de Blok et al. 2001, Swaters et al. 2003, Gentile et al. 2004). Most previous work based on late type and low surface brightness galaxies mentioned that the constant core density profile rather than the cuspy profile describes better the mass distribution in the inner parts of the galaxies (Gentile et al. 2004, Spano et al. 2008, Bottema & Pestaña 2015).

To represent the stellar luminous mass distribution, prior to the development of good IR detectors that were developed to be used in space, earlier studies on galaxy mass distribution have been using optical bands (B-band or preferentially R-band, see e.g. Kormendy & Freeman 2004) while most of the recent studies used MIR data, either the 3.6μm band of Spitzer (see e.g. Lelli et al. 2016) or the 3.4μm band of WISE (see e.g. Korsaga et al. 2018). One of the main reason to revisit the R_c-band in this paper is to study if the derived DM halo parameters are very different when using an optical band compared to a MIR-band, which sample different stellar populations. If this is the case, one would have to forget about most of the earlier results and concentrate only on recent studies.

In a previous study by Korsaga et al. (2018), the mass distribution was derived using a sample of 121 galaxies by combining the optical Hα kinematical and the mid-infrared (MIR) WISE photometric data. Two different techniques were used for each model; the best fit model and the one with the M/L calculated from the MIR colour index (W1-W2); pseudo-isothermal maximum disc models were also derived. Korsaga et al. (2018) found that (i) most rotation curves were better described by core rather than cuspy profiles; (ii) the relation between the DM parameters and the luminosity of galaxies depends on morphological types and (iii) the value of the M/L provided by the maximum disc models is ∼4 times higher and the one given by the (W1-W2) colour is ∼3 higher than the M/L for the best fit model.

The same fitting procedure to construct the mass models was used in both photometric bands, such that we should be able to see how the DM parameters vary when using optical photometry instead of MIR for a similar sample of galaxies. In addition, this work gives us an excellent opportunity to compare the core and cuspy density profiles for both early and late type galaxies since our sample covers all morphological types and not only late-types, which was often the case in earlier studies. Our main objective is thus to trace the relation between the DM parameters (central density and the scaling radius) and the luminosity of galaxies covering all morphological types in order to study if the R_c results are comparable with the MIR results found in Korsaga et al. (2018). We also want to study the distribution of the scale radius and of the central halo density as a function of the optical disc scale length, see how the M/L is distributed when using the optical R_c- and MIR W1-bands and test which band provides correlations with the smallest dispersion.

This paper is organized as follows. In section 3.2 we present the sample and the selection criteria for the Hα RCs. Section 3.3 describes the decomposition of the R_c-band luminosity profiles, analyses the R_c-band scale relations and compares them with the MIR ones. In Section 3.4, we describe the formalism of the different mass models and present the results. In Section 3.5, we compare the results obtained using optical R_c and MIR W1 photometry. A summary and the main conclusions are given in Section 3.6. Appendix 1 lists the global properties and mass models parameters of the sample. In Appendix 2, we present the mass models of the 100 galaxies. We use a Hubble constant $H_0 = 75$ km s^{-1} Mpc^{-1} throughout this paper.

3.2 Sample selection

We use a sample of 100 spiral and irregular nearby galaxies with high resolution Hα rotation curves (RCs), derived from 2D velocity fields, and the optical R_c-band photometry: 73 from surface brightness photometry obtained at the Observatoire de Haute Provence (OHP) (Barbosa et al. 2015) and 27 from SDSS DR7 (Abazajian et al. 2009) archival data. The RCs of this sample are selected from the GHASP survey, which contains 203 galaxies observed with the 1.93 m telescope of the OHP using a Fabry-Perot interferometer scanning around the Hα emission line with high spectral and spatial resolutions. The spectral resolution is $\sim$ 10000 and the spatial resolution is $\sim$ 2 arcsec over a large field of view of $\sim 6 \times 6$ arcmin^2. The GHASP

objects are mostly isolated to reduce the perturbative effects of neighbours. The GHASP data have been published in several previous papers (Garrido et al. 2002; 2003; 2004; 2005, Epinat et al. 2008a;b).

The present study combines the Hα rotation curves and the optical R_c-band photometry. We apply the following selection criteria to define the sample of 100 galaxies. Firstly, we began with 124 galaxies, which have both Hα rotation curves and optical R_c-band photometric data. Secondly, we assigned a quality flag to the rotation curve of each galaxy, ranging from 1 to 3 (see column 15 of Table B.1): -1- for very high, -2- for high and -3- for low quality. To construct mass models with good constraints, we therefore selected only galaxies with flag -1- and -2- which reduced the sample to 100 galaxies. We discarded 24 galaxies which were attributed a flag 3 for various reasons: too high inclination (>75^o), presence of a strong bar, signs of galaxy interaction, strong lopsidedness or very low SNR data.

The overall properties of our sample are shown in Fig. 3.1. The sample spans a range in (i) distances (D) from 5 to 100 Mpc with a median value of 20.2 Mpc; (ii) absolute blue magnitudes M_B, from -16 to -23 with a median value of -20; (iii) morphological types (t) from t=0 to t=10 with a median value of t=5.0 (S_c); (iv) maximum rotation velocities (V_{max}), from 50 to 500 $\mathrm{km\,s^{-1}}$with a median value of 170.5 $\mathrm{km\,s^{-1}}$; (v) disc scale lengths (h), from 1 to 8 kpc with a median value of 2.7 kpc and (vi) isophotal radii at the limiting surface brightness of 25 mag $\mathrm{arcsec^{-2}}$ (r_{25}), such that r_{25}/h ranges from 1 to 6 with a median value of 3.2, which is identical to the value of 3.2 found by Freeman (1970) in the B-band for most spiral galaxies.

3.3 R_c-band surface photometry

3.3.1 The luminosity profile

It is well known that, within the optical range, the R_c-band surface brightness photometry describes better the old stellar population which represents the bulk of the stellar mass than, for instance, the B-band from which a lot of analysis has been based on in the past. Therefore, we used 73 photometric R_c-band data obtained on the OHP 1.2 m telescope and completed the sample with homogeneous available data in archives which consists of 27 $g + r + i$-bands profiles derived from the Sloan Digital Sky Survey (SDSS) archival data. This leads us to a total of 100 galaxies.

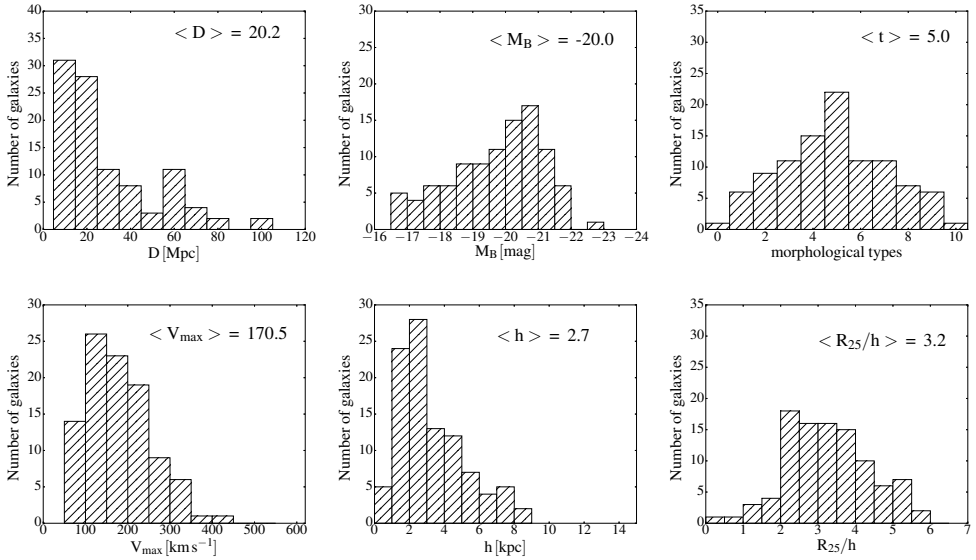

Figure 3.1: Properties of the sample. First line: from left to right, distribution of the galaxies' distances, of the absolute magnitudes and of the morphological types, respectively. Second line: from left to right, distribution of the maximum velocities, of the disc scale lengths and of the ratios of the isophotal radius R_{25} to the disc scale length, respectively. The median of each parameter is shown in the respective panel.

The OHP images have a field of view of 11.7' × 11.7' and were taken with a single 1024 × 1024 CCD having a pixel size of 0.68 arcsec^{-1}. The isophotal level used as reference is 23.5 mag arcsec^{-2}. The OHP surface brightness profiles are taken from Barbosa et al. (2015). The SDSS data are taken from SDSS DR7 (Abazajian et al. 2009), which provides imaging and calibration in the *ugriz* pass bands. The R_c surface brightness profiles were computed by using the multi-band scaling relation (Barbosa et al. 2015) to transform the SDSS *ugriz*-bands into R_c-band:

$$\mu_R(r) = 0.42\mu_g(r) - 0.38\mu_r(r) + 0.96\mu_i(r) - 0.16 \tag{3.1}$$

where μ(r) is the surface brightness profile at radius r. The surface brightness profiles were computed by using the IRAF task ELLIPSE, which gives the parameters that describe the luminosity of the galaxy as a function of the semi-major axis, the position angle, the ellipticity and the curve of growth that quantify the total apparent magnitude present in each isophote.

3.3.2 The light profile decomposition

The radial profile decomposition of the 73 OHP R_c-band data has been done by Barbosa et al. (2015). We utilize exactly the same method for the 27 remaining galaxies for which we used SDSS data. The different luminosity profiles are shown in Appendix 2. The surface brightness profiles were decomposed, when needed, into multiple components (disc, bulge, bar, spiral arm, ring, lens, ...) by using a 2D fitting Python routine. Type I discs were modelled by using a simple exponential disc:

$$I_d(r) = I_0 \exp\left(-\frac{r}{\mathrm{h}}\right) \tag{3.2}$$

with I_0 being the central intensity of the disc and h its scale length. Type II and Type III discs, which correspond respectively to discs with downward truncations and discs with upward bends, were modelled using broken exponential disc profiles:

$$I_d(r) = SI_0 \exp\left(-\frac{r}{\mathrm{h_i}}\right).\{1+\exp[\alpha(r-r_b)]\}^{\frac{1}{\alpha}(\frac{1}{\mathrm{h_i}}-\frac{1}{\mathrm{h_0}})} \tag{3.3}$$

where $\mathrm{I_0}$ is the central intensity of the disc, h_i and $\mathrm{h_0}$ the inner and outer disc scale length respectively, r_b is the break radius, α is the sharpness of the disc transition between the inner and the outer region, and S is a scaling factor, S= $[1+\exp(-\alpha r_b)]^{-\frac{1}{\alpha}(\frac{1}{\mathrm{h_i}}-\frac{1}{\mathrm{h_0}})}$. Bulges, bars, rings, lenses components were determined by using a Sérsic function given by :

$$I_b(r) = I_e \exp\left(-b_n\left[(r/r_e)^{1/n}-1\right]\right) \tag{3.4}$$

We show an example of decomposition in multiple components in Fig. 3.2. This example illustrates two general trends: (i) MIR-band profiles are more extended than R_c-band profiles, the arms components are also detected further away in MIR than in R_c; (ii) the bulge is more cuspy in R_c than in MIR, this cuspiness is nevertheless mainly linked to the difference in spatial resolutions (seeing ~2-3" for R_c versus a resolution of 6" for W1 in the case of the space mission WISE). Fig. 3.2 provides a simple example for which only three components were needed (bulge, exponential disc and spiral arms) but decompositions usually request more components.

Spherical and flat components do not provide, for the same given mass, the same rotational velocity, thus we have to disentangle them. On the other hand, in order to simplify the construction of our mass models, we aim to minimise the number

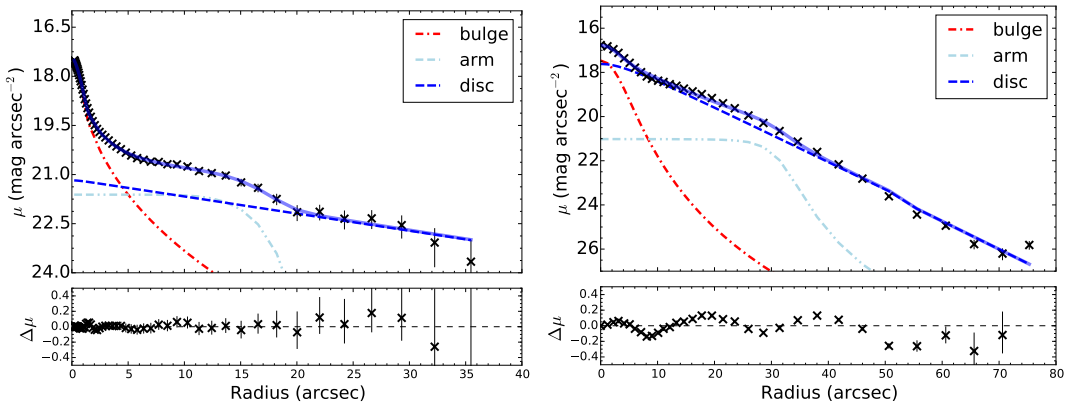

Figure 3.2: Examples of surface brightness decomposition for the galaxy UGC 5045. The bottom panel of each plot represents the difference between the observed surface brightness distribution and the model displayed in light blue in the top panels. Left panels are for the R_c-band and right panels for the W_1 band.

of parameters to fit. Furthermore we assume only two components: a spherical one containing the bulge that we call the bulge component and a planar one containing the disc and eventually other components embedded within the disc such as bar(s), spiral arm(s) and ring(s), that we call disc component. The different parameters of the bulge and disc components for all the sample are shown in Table B.1.

When the last radius of the surface brightness profile of the disc is smaller than the one of the rotation curve, we extrapolate the last points of the profile using the decomposition parameters in order to extend the radius to a value larger than the last radius of the rotation curve to avoid creating a truncation bump. It was never necessary to extend bulge surface brightness profiles since bulges are less bright than discs at large radii because their luminusoty decreases rapidly at small radius.

3.3.3 Mass-to-light ratio

To obtain the stellar mass density profiles, we used the R_c-band luminosity profiles. The transition between the photometry and the dynamics is based on the estimation of the stellar mass-to-light ratio (M/L). The stellar M/L values can be calculated as a function of their colour, based on stellar population models (Bell & de Jong 2001). The correlation between the stellar M/L and the optical colour is rather tight, especially for galaxies with smooth star formation histories. Those relations between the colour index and the M/L do not allow allocating masses to young

stellar populations due to the fact that, at low colour index, all bands are affected by a degeneracy (e.g. de Denus-Baillargeon et al. 2013). However, a general trend is expected between colour and M/L in the sense that younger populations have lower M/L and are relatively bluer compared to older populations which have higher M/L ratio. It is thus important to understand the stellar populations distribution. The relation between the M/L in the R_c-band and the (B − V) colour (Bell & de Jong 2001) is given by :

$$\log(M/L_R) = -0.660 + 1.222\,(B - V) \tag{3.5}$$

We used the colour corrected for extinction designated as $(B - V)^0_T$ in the RC3 catalogue when available. We found these $(B - V)^0_T$ values for 62 galaxies of our sample. To estimate the values for the remaining 38 galaxies, we selected the 1706 galaxies of the RC3 (out of the 23011 galaxies) having a tabulated $(B - V)^0_T$ value and a morphological types spanning the range from 0 to 10. We plotted in Fig. 3.3, $(B - V)^0_T$ as a function of the morphological types for those galaxies. As expected $(B-V)^0_T$ decreases with morphological types. To derive a relation between $(B - V)^0_T$ and morphological types, we binned the morphological types (bin size=1) and choose the average value within each bin, these are the magenta dots showed in the figure and the blue line is the fit to those dots taking the error bars into account. We therefore used the relation found when using the fit to derive the remaining $(B - V)^0_T$. This relation is :

$$(B - V)^0_T = (-0.032 \pm 0.004) \times t + (0.73 \pm 0.02) \tag{3.6}$$

where t is the morphological type. The $(B-V)^0_T$ are shown in column (4) of Table B.1 and those marked with an asterisk correspond to the values derived from equation 3.6.

3.3.4 Scale parameters and light distribution of discs and bulges

From Figs. 3.4 to 3.7 we display the correlations between the photometric parameters obtained for the R_c-band photometry and we compare those trends with the ones obtained using the MIR 3.4 μm of WISE photometry presented in Korsaga et al. (2018). The resulting parameters corresponding to those figures are also listed in

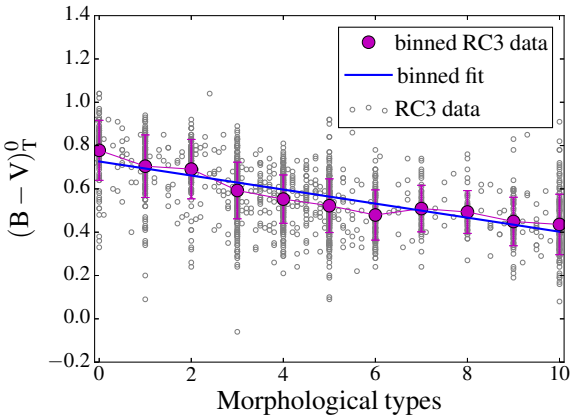

Figure 3.3: $(B-V)^0_T$ colours as a function of the morphological types. The gray dots represent the RC3 data and the magenta dots represent the RC3 binned data which are obtained by binning the data in morphological types with a bin size of 1, and these points are connected with a magenta line. The blue line shows the fit of the binned data.

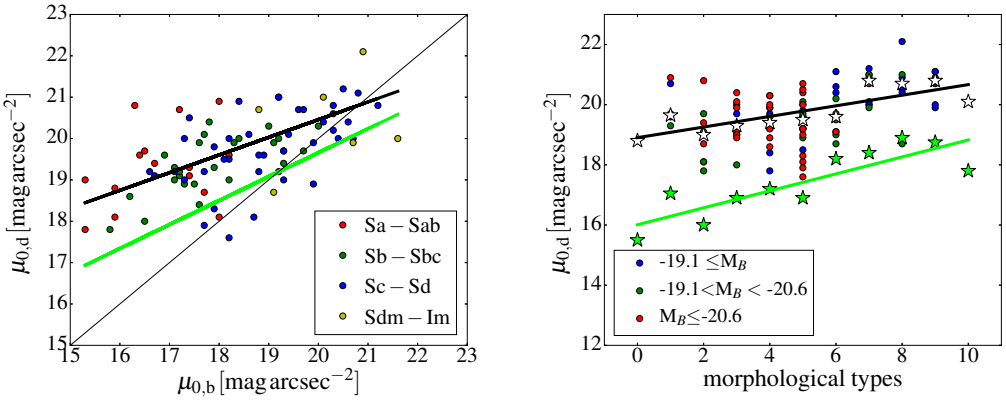

Figure 3.4: The left panel shows the disc central surface brightness versus the bulge central surface brightness by morphological type. The thin black line represents the y=x relation. Thick black and lime lines represent the fit of Rc and W1 bands respectively. The right panel shows the disc central surface brightness versus morphological type. The open black stars represent the median in morphological types and the thick black line is the fit of the median data for the R_c-band; the lime stars show the median in morphological types and the thick lime line is the fit of the median data for the W1-band.

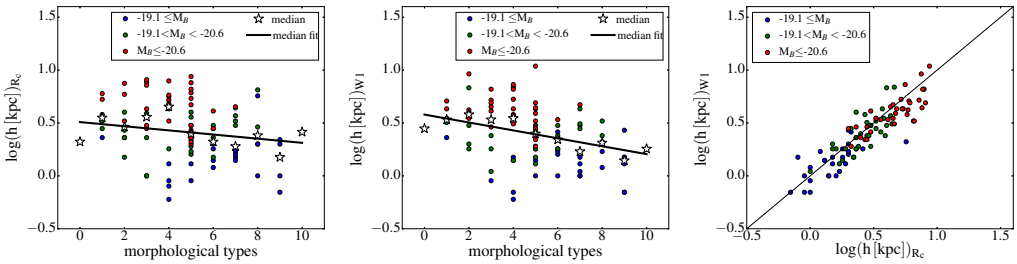

Figure 3.5: The left and middle panels show respectively the disc scale lengths in the R_c-band and in the W1-band versus morphological types. The open black stars represent the median in morphological types. The thick black line is the fit of the median data. The right panel represents the disc scale length in the W1-band versus the disc scale length in the R_c band. The thin black line shows the y=x relation.

Table B.1.

Surprisingly, the left panel of Fig. 3.4, the top panel of Fig. 3.6, the middle and bottom panels of Fig. 3.7, show several late-type Sdm/Im galaxies displaying a faint bulge structure.

The y=x line of Fig. 3.4, left panel clearly shows, as expected, that for most of the cases, bulge central surface brightnesses are brighter than disc central surface brightnesses. The slope of this correlation is almost identical in the MIR, this means that both bands lead to roughly the same bulge-to-disc decompositions. The zero point is about one magnitude lower in the MIR than in the R_c-band and closer to the y=x line, which means that the stellar populations of the bulge and of the disc are closer in the MIR than in the R_c-band. However, one has to be careful since this shift of one magnitude could be partially due to beam smearing effects (seeing): the spatial resolution being higher in the R_c-band (ranging from $\sim$ 1.5 to 3 arcsec, depending on the seeing) than in the MIR WISE W1-band (limited at 6 arcsec by the pixel sampling). As expected, the right panel of Fig. 3.4 shows a correlation between disc central surface brightness and morphological types. The slope is again similar in both bands.

The left and middle panels of Fig. 3.5 show that disc scale lengths in the R_c-band are less correlated to the morphological types than the ones in the MIR-band. The scatter of those relations being very high, the slope difference in the trend is maybe not significant. As expected, for a given morphological type (from t = 0 to $\sim$7) disc scale lengths are larger/smaller for bright/faint galaxies as it is underlined by the median fit lines. The right panel of Fig. 3.5 compares the disc scale lengths in

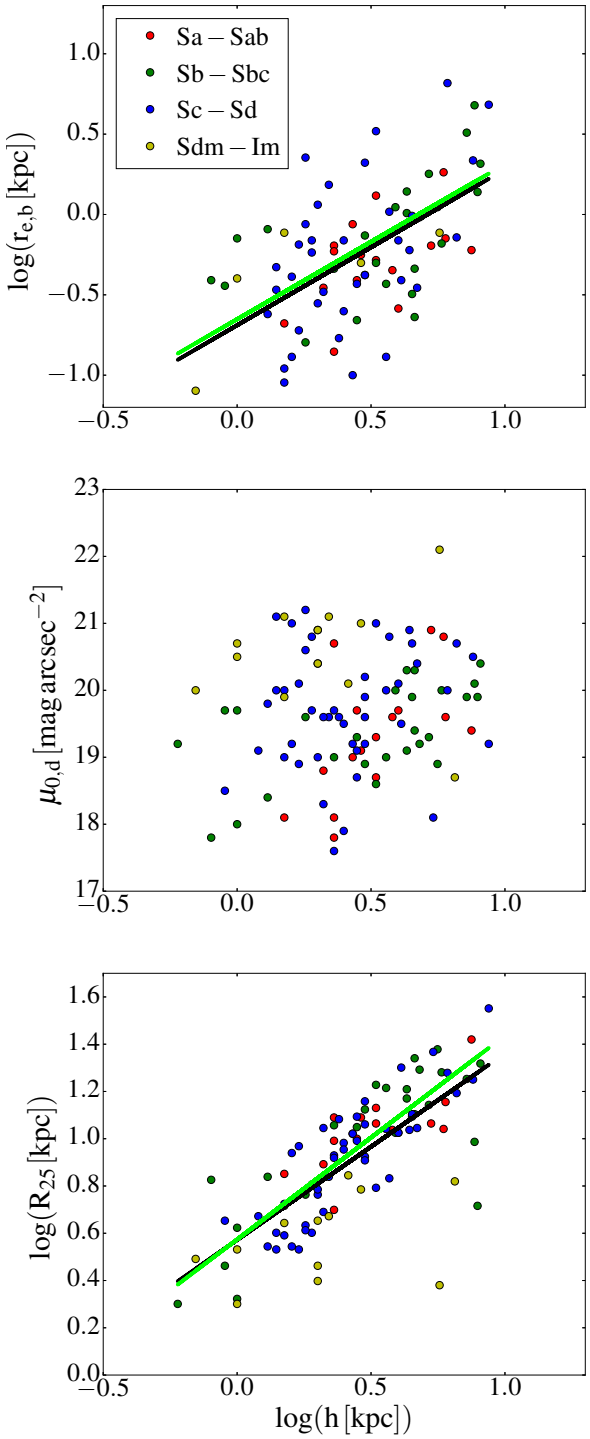

Figure 3.6: Correlations between the parameters derived from the R_c luminosity profiles. From top to bottom: the bulge effective radius, the disc central surface brightness and the isophotal radius R_{25} versus the disc scale length respectively. The thick black and lime lines represent the fits of the Rc and W1 band respectively. The legends for the three panels are shown in the top panel.

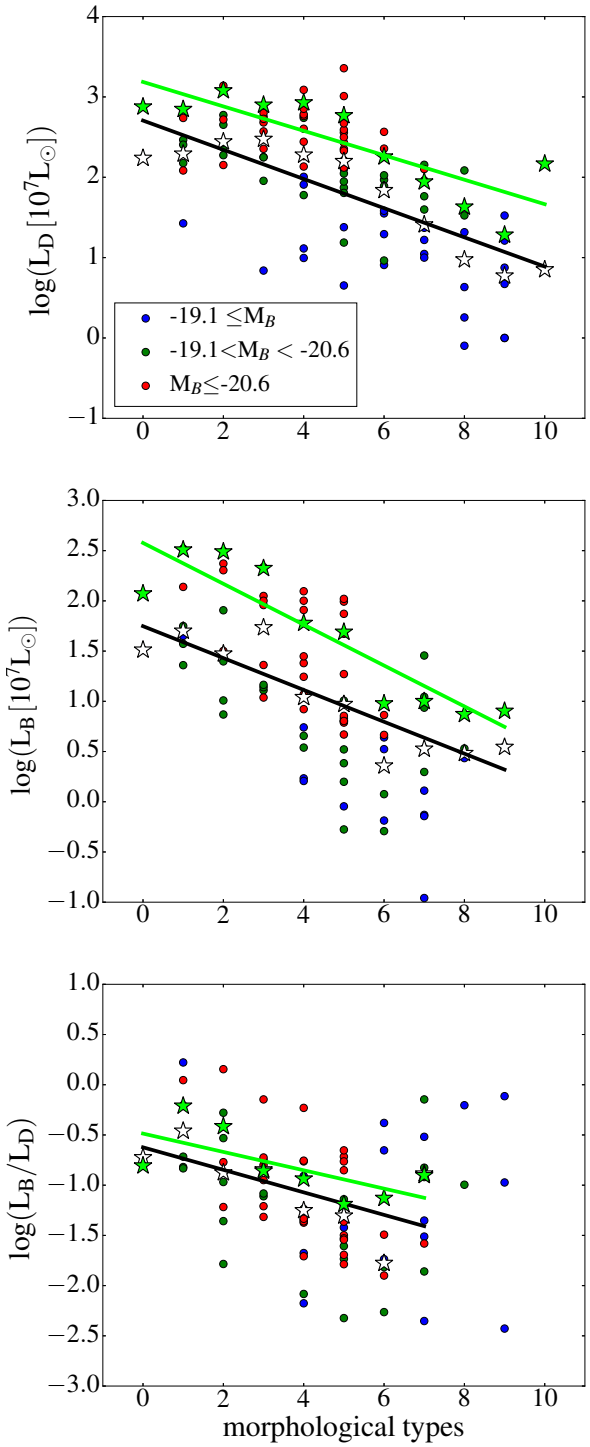

Figure 3.7: From top to bottom: disc luminosity, bulge luminosity and ratio of disc-to-bulge luminosity versus the morphological types. The open black stars represent the median in morphological types for the R_c-band and the thick black line is the fit of the median data. The lime stars represent the median in morphological types for the W1 band and the thick lime line is the fit of the median data. The legends for the three panels are shown in the top panel.

the MIR- and in the R_c-bands, which follow well the y=x line and as expected faint galaxies have smaller disc scale lengths than bright ones, which seems to support the fact that the difference of slope observed in the left and middle panels is not significant.

Despite the large dispersion, the top panel of Fig. 3.6 shows some correlation between the disc scale length and the bulge effective radius; galaxies with small/large disc scale lengths (h) tend to display small/large bulge effective radius ($r_{e,b}$). This correlation is the same as the one observed in the MIR.

The middle panel of Fig. 3.6 displays a large scatter between discs scale lengths and central surface brightnesses. As expected, early type galaxies (Sa − Sab) tend to have larger disc scale lengths and late type galaxies (Sdm − Im) fainter central surface brightness but we do not see any correlation between central surface brightness and disc scale length or the morphological type from Sb to Sd galaxies. The correlation found in the top panel and the absence of correlation observed in the middle panel mean that the characteristic sizes of the disc and of the bulge are identically correlated in R_c- and in MIR-bands while their central surface brightnesses may differ. As expected, the bottom panel of Fig. 3.6 shows a clear correlation between isophotal radii R_{25} in the B-band and discs scale lengths h_R in the R_c-band. For spiral galaxies, the 25 mag arcsec^{-2} isophote is, on averaged, reached at 3.2 h_B, where h_B is the disc scale length in the B-band (Freeman 1970). Bottom-right panel of Fig 3.1 provides an average value of 3.2±1.2 h for this ratio. This value is smaller than the value of 3.5±1.2 h found in the MIR (Korsaga et al. 2018) but the scatters are rather large.

As expected, the top and middle panels of Fig. 3.7 show that both discs and bulges luminosities are clearly anti-correlated with morphological types and that early morphological type galaxies show more luminous discs and bulges than later type galaxies. These plots demonstrate that the slope of the correlation is almost the same in the MIR than in the R_c-band, which means that the M/L in both bands will display the same trend with respect to the morphological type. The bottom panel of Fig. 3.7 quantifies the bulge–to–disc ratio versus the morphological type, which decreases, as expected. We nevertheless note a large scatter in this relation but here again, consistently with the two previous plots, the slope of the anti-correlation is the same for both bands (MIR- and R_c-bands) from morphological type t=0 (S0) to t=7 (Sd). One should note that most bulge-to-disc ratios of t=8 (Sdm) and t=9 (Im) galaxies are quite large and do not fit the general trend observed for earlier

types. This is not due to their bulge luminosity that fits the general trend (Fig. 3.7, middle panel) but to the faint disc luminosity (Fig. 3.7, top panel). From the whole sample of 100 galaxies, only 6 of them are pure discs, i.e. their profiles do not exhibit any bulge, bar(s), ring(s), lense(s) or spiral arm(s) components, thus have not been decomposed. Among the 100 galaxies, only 17 do not exhibit a bulge component. Surprisingly, among the 83 galaxies with a bulge, 13 of them are Sdm or Im galaxies. In addition, the mean L_b/L_d (0.32) of those 13 galaxies is greater that the mean L_b/L_d (0.09) of the 45 Sc and Sd galaxies. This is explained by the fact that, on average, in our sample, the difference of the luminosity between Sdm/Im and Sc/Sd galaxies is larger for the disc than for the bulge. Indeed, the mean disc luminosity decreases from $\simeq 199\times10^8$ for Sc/Sd galaxies to $\simeq 17\times10^8$ for Sdm/Im. Meanwhile the bulge luminosity drops only from $\simeq 14\times10^8$ to $\simeq 3\times10^8$. Thus the luminosity disc ratio between Sc/Sd and Sdm/Im is $\simeq 12$ while the bulge ratio is $\simeq 5$.

In conclusion of this section 3.3.4, the scale relations and light distributions observed between the different photometric parameters of discs and bulges are not dependant on the photometric band used, from the optical R_c to the MIR 3.4 μm bands.

3.4 Mass Models

3.4.1 Methods

We use Hα rotation curves in combination with R_c-band photometry to construct the mass models of the 100 galaxies. The mass models are constructed using an improved version of the python routines used for Korsaga et al. (2018). We performed two main models to describe the mass distribution of the DM halo; the pseudo-isothermal core density profile (ISO) (Begeman 1987) and the ΛCDM cuspy density profile (NFW) (Navarro et al. 1996). The total circular velocity is given by:

$$V_{\rm cir}(r) = \sqrt{V^2_{\rm disc} + V^2_{\rm bulge} + V^2_{\rm halo}} \tag{3.7}$$

where $V_{\rm cir}$ is the circular velocity, $V_{\rm disc}$ and $V_{\rm bulge}$ are the velocity of the disc and bulge components respectively and $V_{\rm halo}$ is the DM halo velocity.

For the pseudo-isothermal sphere (ISO) model, the density profile is given by:

$$\rho_{\rm iso}(r) = \frac{\rho_0}{\left[1 + \left(\frac{r}{r_0}\right)^2\right]} \tag{3.8}$$

and the corresponding velocity by:

$$V^2_{\rm iso}(r) = 4\pi G\rho_0 r_0^2 \left[1 - \frac{r_0}{r}\arctan\left(\frac{r}{r_0}\right)\right] \tag{3.9}$$

which is an increasing function of r , asymptotically reaching $V_{\rm max} = V(r = \infty) = \sqrt{4\pi G\rho_0 r_0^2}$
where ρ_0 is the central density of the DM halo and r_0 its scaling radius.

The Navarro-Frenk-White (NFW) model derived from ΛCDM numerical simulations generates a cuspy halo where the density profile is given by:

$$\rho_{\rm NFW}(r) = \frac{\rho_i}{(\frac{r}{r_s})(1 + \frac{r}{r_s})^2} \tag{3.10}$$

where ρ_i is the density of the universe at the time of collapse and r_s is a scale radius.

The velocity is given by:

$$V^2_{\rm NFW}(r) = V^2_{200}\left[\frac{\ln(1 + cx) - cx/(1 + cx)}{x[\ln(1 + c) - c/(1 + c)]}\right] \tag{3.11}$$

where V_{200} is the velocity at the virial radius, c is the concentration parameter of the halo and $x = r/r_s$. The scale radius r_s can be inferred from V_{200} and c:

$$r_s = \frac{V_{200}}{10c \times {\rm H}_0} \tag{3.12}$$

where $\rm H_0$ is the Hubble constant.

For the different models, we use the same fitting procedures used and discussed in Korsaga et al. (2018). For the ISO fit, we used three different techniques. The first one is the best fit model (BFM), which lets all the parameters free to be fitted finding the best values corresponding to the minimal χ^2. This leads to three free parameters for galaxies with no bulge ($\rm r_0$, ρ_0 and $\rm M/L_{\mathit{disc}}$) or four free parameters for galaxies with a bulge ($\rm r_0$, ρ_0, $\rm M/L_{\mathit{disc}}$, $\rm M/L_{\mathit{bulge}}$). Note that $\rm M/L_{\mathit{bulge}}$ is constrained to be equal or larger than $\rm M/L_{\mathit{disc}}$ to account for the older stellar populations in the

bulge than in the disc (see section 3.3.3). The second technique is the maximum disc fit (MDM) that minimises the halo contribution by maximising the stellar disc (and bulge when present) contribution. We used also three or four free parameters (r_0, ρ_0, M/L_{disc}, M/L_{bulge}) depending if the galaxy is has a bulge or not. For the MDM, we allow the χ^2 to increase up to 1.3 times the χ^2 derived from the BFM and the M/L_{disc} is constrained to be higher than the one used for the BFM. The last technique considers a value of M/L (fixed M/L) derived from the (B − V) colour as described in section 3.3.3. For this technique, we used the same value of M/L for the disc and the bulge due to the fact that the spectrophotometric models do not allow to disentangle them. We are thus left with only the two free parameters of the DM halo (r_0, ρ_0). To avoid non physical values, a minimal limiting value of $r_0 = 0.5$ kpc was imposed. For the NFW model, we use two techniques: the BFM and the fixed M/L. The fitting procedures are the same as explained for the ISO model. For all models, we imposed a minimal M/L value of the disc and bulge at 0.1 $M_\odot/L_\odot$. In Fig. 3.8, we show the different mass models of the galaxy UGC 3463. In this special case, all models give equivalent good fits.

3.4.2 Results

Most of our observed rotation curves are better described by a central core density profile (ISO) than a cuspy one (NFW). This is clearly represented in Fig. 3.9 for which the smallest χ^2 values correspond to the ISO fits (70 galaxies have higher χ^2 values for NFW compared to ISO for BFM and 66 galaxies for Fixed M/L). The detail of the parameters is shown in Tables B.2 and B.4. As mentioned in other studies, the cuspy central density does not describe well most of the faint galaxies (de Blok et al. 2003, Gentile et al. 2004).

In Fig. 3.10, we show the variation of (M/L) as a function of morphological types for the three ISO models: BFM, MDM and fixed M/L. These plots represent the disc M/L values. As expected, M/L is getting smaller when going from early to late types. (Faber & Gallagher 1979). The smallest dispersion is obtained for the fixed (by colour) M/L models. The distributions of (M/L)s for the different ISO models are shown in Fig. 3.11 (black). We find the expected results where the smaller M/Ls are found for the BFM, the larger for the MDM and intermediate values for the fixed M/L. The M/L median value of the ISO (BFM) is 0.39 $M_\odot/L_\odot$; this value is ~ 3 time larger than the one computed for NFW (BFM) which is equal

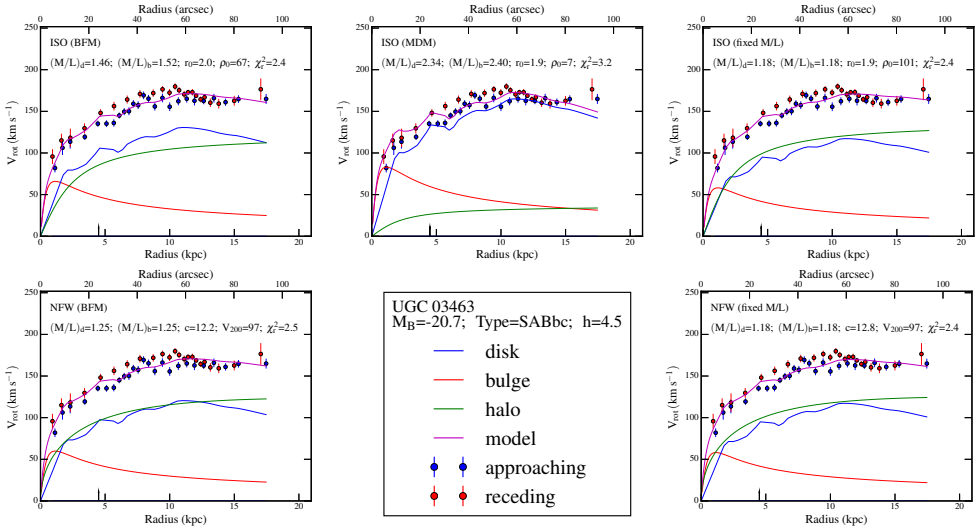

Figure 3.8: Example of mass models for the galaxy UGC 3463. First line: pseudo-isothermal sphere density profiles (ISO). Second line: Navarro, Frenk & White density profiles (NFW). First column: Best Fit Model (BFM). Second column: Maximum disc Model (MDM) for line 1 (ISO model). Third column: Mass-to-Light ratio M/L fixed using the optical (B − V) colour. The name of the galaxy, its B-band absolute magnitude, morphological type and disc scale length have been indicated in the insert located line 2-column 2. For each model, the fitted parameters and the reduced χ^2 have been indicated in each sub-panel.

to 0.15 $M_\odot/L_\odot$ (50% hit the 0,1 $M_\odot/L_\odot$ lower boundary). These low M/L values for NFW profiles are expected (Navarro et al. 1997); this is due to the intrinsically steeper mass distribution of the cuspy profile which replaces the contribution from the stellar disc in the inner parts (e.g. de Blok et al. 2008).

Scaling laws between the DM halos parameters (r_0 and ρ_0) and between the DM halos parameters and the absolute B-magnitude of galaxies are found in Kormendy & Freeman (2004) and Randriamampandry & Carignan (2014). More precisely, Kormendy & Freeman (2004) studied the properties of DM halos in late type and dwarf irregular galaxies and found that high ρ_0 tend to have smaller r_0, and also less luminous galaxies tend to have smaller r_0 and higher ρ_0. Similar conclusions had been found by Randriamampandry & Carignan (2014) who also worked on a sample mostly composed of late type galaxies. In order to check if these scaling laws are still the same whatever the morphological types of galaxies, we plot the DM halos parameters using our sample which covers early type and late type spiral and irregular galaxies.

In Fig. 3.12, we plot the relation between the central halo density (ρ_0) and the scaling radius (r_0) for ISO, which shows a clear anti-correlation meaning that high ρ_0 corresponds to smaller r_0 for the three techniques (BFM, MDM and fixed M/L). We choose to make the plots using the points of the BFM and overlay the results for the 3 techniques (BFM, MDM and Fixed M/L) to avoid over-crowding. The thick black line is for the BFM, the cyan is for the MDM and the magenta for the fixed M/L. To do the fit of the ISO DM parameters, we excluded galaxies with r_0 equal or smaller to 0.5 which corresponds to the minimal limiting value (see Table 3.2). We also excluded galaxies for which a DM halo is not needed to describe the observed rotation curves. In this case, a MDM model describes better the observed rotation curves with only the baryonic matter, without the need of DM. These galaxies (26 galaxies in total) are marked with an asterisk in Table B.2. The general relation between ρ_0 and r_0 is:

$$\log\ \rho_0 = (a \pm \delta a)\ \log\ r_0 + (b \pm \delta b) \tag{3.13}$$

where the parameters a, δa, b and δb are shown in Table 4.3.

Fig. 3.13 presents the variation of the DM halo parameters r_0, ρ_0 and $\rho_0 \times r_0$, as a function of the galaxies absolute magnitude in the B-band. For our total

sample, r_0 seems independent of the luminosity while brighter galaxies tend to have larger central densities and less luminous galaxies tend to have smaller $\rho_0 \times r_0$. This seems at odd with previous results by Kormendy & Freeman (2004) and Randriamampandry & Carignan (2014), which predicted smaller DM scaling radius and higher central density for the weaker dwarf galaxies. The difference between our results and theirs will be explained in section 3.5.2.

In order to study the impact of the band used in the correlations found with the DM halo parameters, we used the magnitudes in the W1-band (see Fig. 3.14). Interestingly, we found the same trends compared to those found using the absolute B-band magnitude, which means that the different trends with the luminosity do not depend on the band used. In this work, we have used the luminosity in the B-band, because we want to compare our results with the previous authors who used the B-band luminosity.

It is interesting to look also at the relation between the DM halo parameters r_0 and ρ_0 as a function of the optical size characterized by the scale length h. This is shown in Fig. 3.15, where both parameters seem quite independent of h for all morphological types.

In Fig. 3.16, we plot the halos parameters found by using the NFW (BFM) points, that is, the concentration c as a function of the velocity at the virial radius (i.e V_{200}). We fitted the following linear relation to the BFM and Fixed M/L:

$$\log\ c = (a \pm \delta a)\ \log\ V_{200} + (b \pm \delta b) \tag{3.14}$$

The parameters are provided in Table 4.3. These fits are represented in thick black and magenta lines respectively. To do the fit, we excluded galaxies (8 galaxies in total) with $c \leq 1$ and $V_{200} \geq 500\ \mathrm{km\,s^{-1}}$ because these values are not physical in the CDM context (de Blok et al. 2008). The different parameters are shown in Table B.4. We find that low mass halos are more concentrated than high mass halos. The halos are slightly more concentrated when using the BFM than the fixed M/L. Indeed, the average concentration is $c = 13.80 \pm 2.29$ and $c = 12.02 \pm 1.66$ for the BFM and the fixed M/L respectively (see Table 3.3). We also notice that early type spirals tend to be located above the best fit line and late type galaxies below. A similar trend is found when using the fixed M/L.

To search of possible bias in the analysis, we describe in this paragraph the

three tests we did. In order to understand if the mass distribution of baryonic and DM halos depends or not on the method used to determine the disc component, we made two tests for which we constructed new mass models: (1) using pure exponential discs and (2) including the bulge light distribution into the disc light distribution. For the first test (1), we decomposed each surface brightness profile, if requested, into a disc and a bulge component, as we did previously but we fit a theoretical exponential disc (see equation 3.2) instead of the actual light distribution accounting for wiggles due to non-circular motions (spiral arms, bars, ...). This test allowed to check that the disc and halo's parameters we computed previously are not affected by irregular light distributions within the discs. This is illustrated on the example of the disc M/L for ISO (MDM) by the top panel of Fig. 3.17 where we plot the difference between the M/L values obtained using the modelled exponential disc and the actual disc. The median difference is close to zero and the scatter is small and does not depend much on the absolute magnitude, meaning that M/L is not strongly affected by non-circular motions. We found for the ISO models the same trends between the scaling radius and the central halo density, and for the scaling radius or the central halo density as a function of the luminosity, whichever disc is used. For the NFW models, the same trend is found between the halo concentration and the velocity at the virial radius whichever disc is used but the halo is more concentrated when using the exponential disc. In the case of the second test (2), we selected the nine galaxies of the sample having the strongest bulge, using the criterium $L_B/L_D > 0.2$. For those galaxies we do not decompose the surface brightness distribution into two distinct components, a disc and a bulge, even if it is obviously requested by the light distribution. Instead, we use the raw surface brightness profile and consider that all the the stellar contribution lie within the disc component. This test, canceling the bulge component, reduces the number of degrees of freedom of the model and overcomes a possible dependence on the method used to decompose the light profile. We find very similar trends for the DM parameters to what was found when considering the bulge and disc decomposition. It is well-known that for a given galaxy mass the rotation curve is expected to peak at a velocity ~1.3 times larger if the whole mass is in a flat disc rather than in a spherical bulge component. This means that the M/Ls of the bulges are typically 1.3^2 ~1.7 times larger in that case. Meanwhile the bulge mass distribution is slightly shifted toward larger radii in the spherical case with respect to the disc case. Consequently,

this affects very weakly the halo parameters because these two effects cancel each other and therefore the central slopes and core radii of the halos do not change significantly. This is illustrated by the middle panel of Fig. 3.17, in the case of ISO (BFM), by the difference between the log of the product $\rho_{0,d} \times r_{0,d} \times (M_{\odot}pc^{-2})$ when it is computed without profile decomposition into two distinct components and the log of the product $\rho_{0,b+d} \times \times r_{0,b+d}$ $(M_{\odot}pc^{-2})$ obtained when the profiles are decomposed into a disc and a bulge. This second test implies that when one does not have sufficient spatial resolution to disentangle the bulge from the disc component as is the case for high redshift galaxies, we can nevertheless probe the luminous-to-dark matter distribution by fitting the surface brightness profile with, for instance, a single exponential disc. Finally, we made a third test: (3) we checked that the different correlations are not artefacts resulting from incorrect galaxy inclinations as it could be the case if the inclinations were not correctly estimated in the mass models or even in the rotation curves. Indeed, the M/L disc ratios and the halo parameters depend on the maximum rotation velocities, which depend on the sinus of the inclination and, to transform the projected surface brightness distribution into baryonic circular velocity distribution in the plane of the galaxy, one has also to account for the inclination of the galaxy. This is illustrated for the ISO (MDM) on the bottom panel of Fig. 3.17 that clearly shows that the M/L ratios are randomly distributed and thus are not biased by a possible incorrect inclination.

3.5 Discussion

3.5.1 Comparison between R_c and W1

In this section, the results obtained using optical R_c photometry are compared to the results using MIR W1 photometry. Because some improvements were done to the mass model package since Korsaga et al. (2018), we reran the models using the W1 band photometry before doing the comparison with the R_c band photometry. In this way, it should be possible to evaluate if early mass modelling results, mainly based on optical photometry, are still valid or if they are superseded by more recent results using MIR photometry.

		a	δ a	b	δ b
R_c-band: ρ_0 vs r_0 (ISO)	BFM	-1.18	0.10	-0.42	0.06
	MDM	-1.12	0.15	-0.78	0.09
	fixed M/L	-1.30	0.12	-0.41	0.06
	MDM (K&F2004)	-1.21	—	-1.10	—
	BFM (R&C2014)	-1.10	—	-1.05	—
W1-band: ρ_0 vs r_0 (ISO)	BFM	-1.48	0.14	-0.38	0.07
	MDM	-0.81	0.12	-0.95	0.08
	fixed M/L	-1.07	0.10	-0.62	0.08
R_c-band: c vs V_{200} (NFW)	BFM	-0.98	0.11	+3.29	0.26
	fixed M/L	-1.11	0.12	+3.52	0.26
W1-band: c vs V_{200} (NFW)	BFM	-1.15	0.14	+3.63	0.31
	fixed M/L	-1.28	0.12	+3.85	0.28

Table 3.1: Relation between the DM halo parameters for ISO and NFW models. K&F2004: Kormendy & Freeman (2004) and R&C2014: Randriamampandry & Carignan (2014).

	BFM (1)	MDM (2)	Fixed M/L (3)
ISO (R_c)	6	26	26
NFW (R_c)	12	-	20
ISO (W1)	10	32	24
NFW (W1)	16	-	28

Table 3.2: Number of galaxies for which a DM halo component is not needed for ISO and NFW using the R_c and W1-band photometry. Columns (1), (2) and (3) show respectively the BFM, the MDM and the Fixed M/L.

c	BFM (1)	Fixed M/L (2)
NFW (R_c)	13.80 ± 2.29	12.02 ± 1.66
NFW (W1)	11.22 ± 1.78	8.32 ± 1.58

Table 3.3: Values of the average concentration c using the R_c and W1-band photometry. Columns (1) and (2) represent the values of BFM and Fixed M/L respectively.

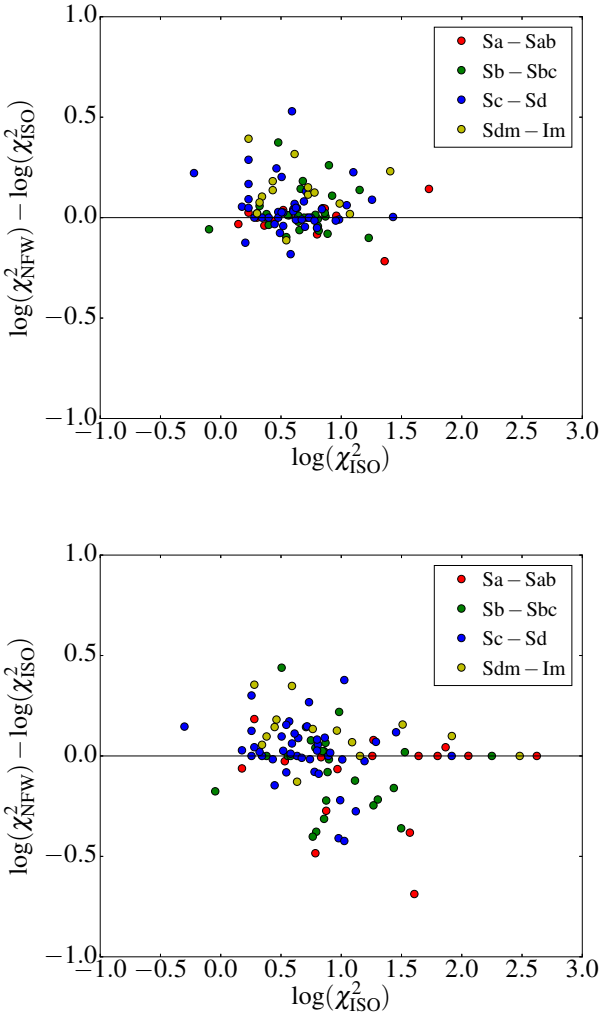

Figure 3.9: Comparison between the reduced χ^2 of NFW and ISO for the best fit model (BFM) (top panel) and for the fixed M/L (bottom panel).

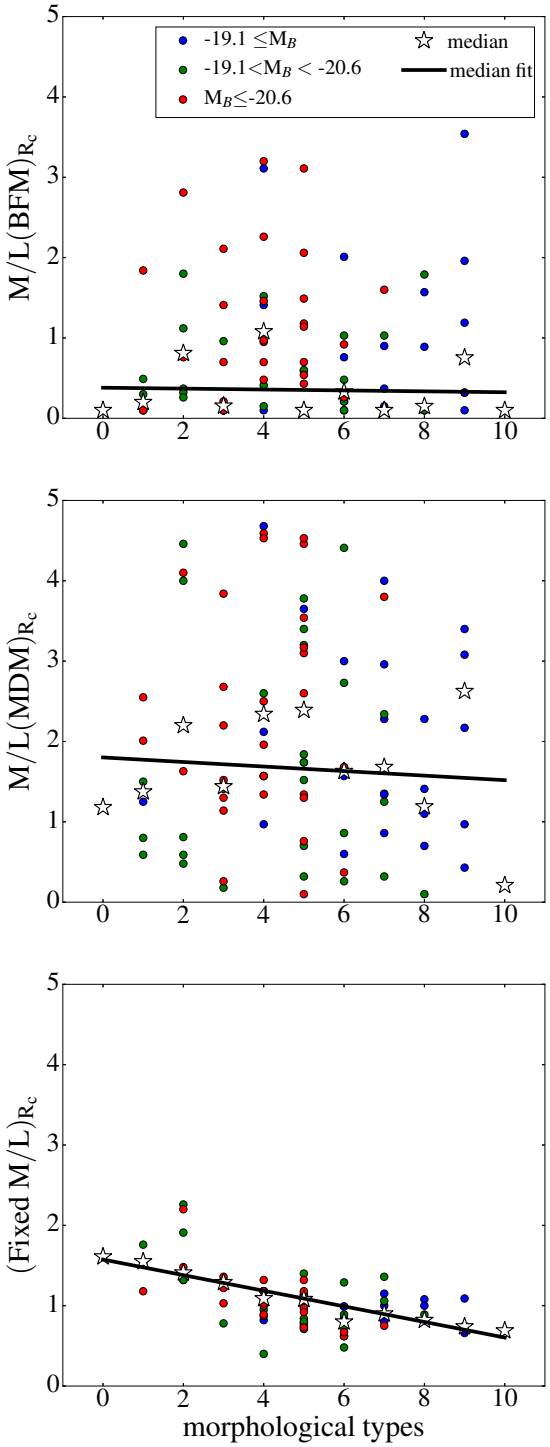

Figure 3.10: Top to bottom panels: respectively the M/L of ISO (BFM), the M/L of ISO (MDM) and the fixed M/L versus morphological types using the R_c-band. These plots represent the disc M/L values. The open black stars represent the median in morphological types. The thick black line is the fit of the median data. The legends for the three panels are shown in the top panel.

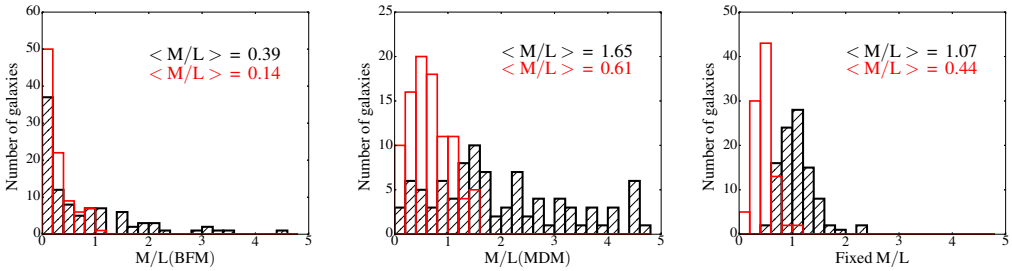

Figure 3.11: Mass-to-light ratio distribution for the isothermal sphere model (ISO) using the R_c-band in black and the W_1-band in red. The median values are noted in each panel using the same colour code. From left to right: best fit model (BFM), maximum disc model (MDM) and value calculated using the optical (B − V) and MIR ($W_1 - W_2$) colours respectively.

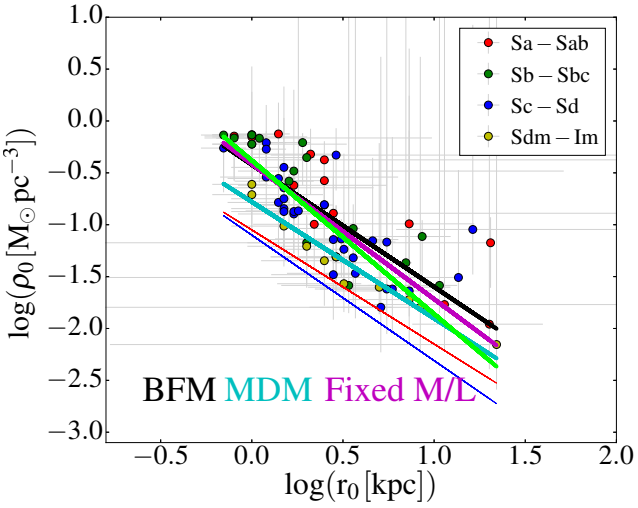

Figure 3.12: Central halo density versus halo core radius for the ISO best fit models (BFM) for the whole sample. The thick black, cyan and magenta lines represent the fit for BFM, MDM and fixed M/L models respectively. The thick lime, thin blue and thin red lines represent respectively the fit of the BFM found using the W1-band, Kormendy & Freeman (2004) and Randriamampandry & Carignan (2014).

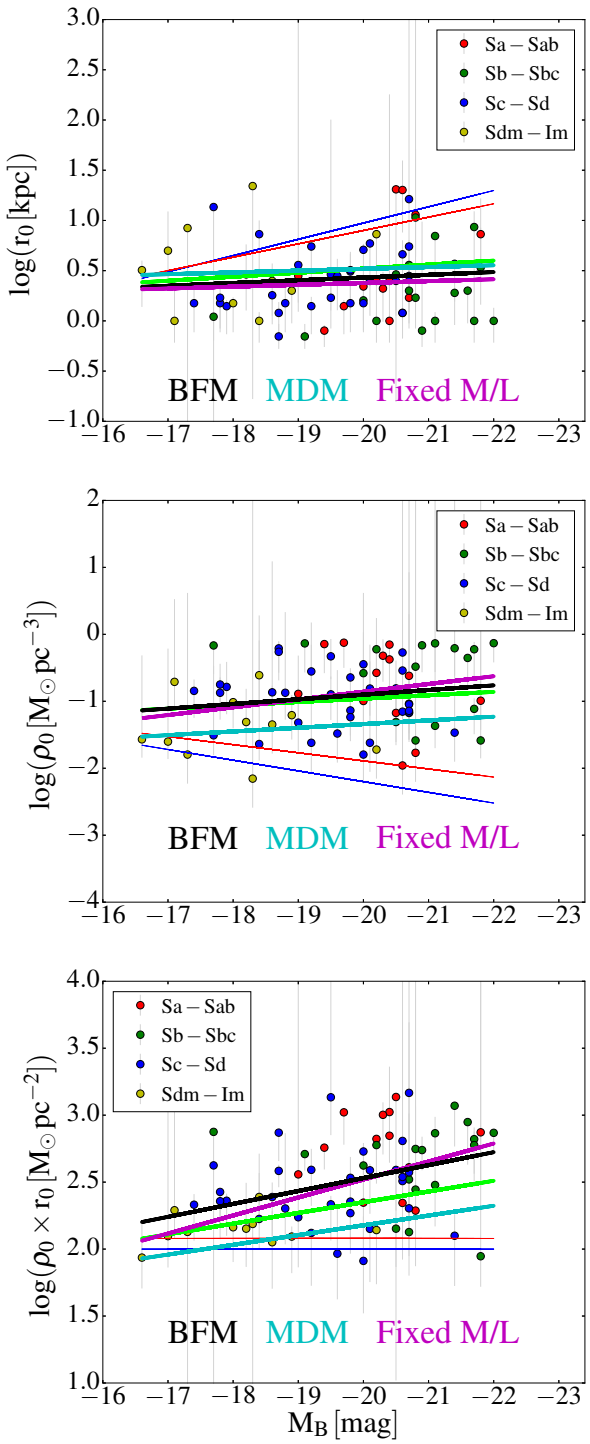

Figure 3.13: Halo scaling radius (top panel), central halo density (middle panel) and the product of the central halo density with the scaling radius versus the absolute B-band magnitude for the whole sample for ISO (BFM) points. The thick black, cyan and magenta lines are the best fit (BFM), the maximum disc (MDM) and the fixed M/L models respectively. The thick lime, thin blue and thin red lines represent respectively the fit found using the W1-band, Kormendy & Freeman (2004) and Randriamampandry & Carignan (2014).

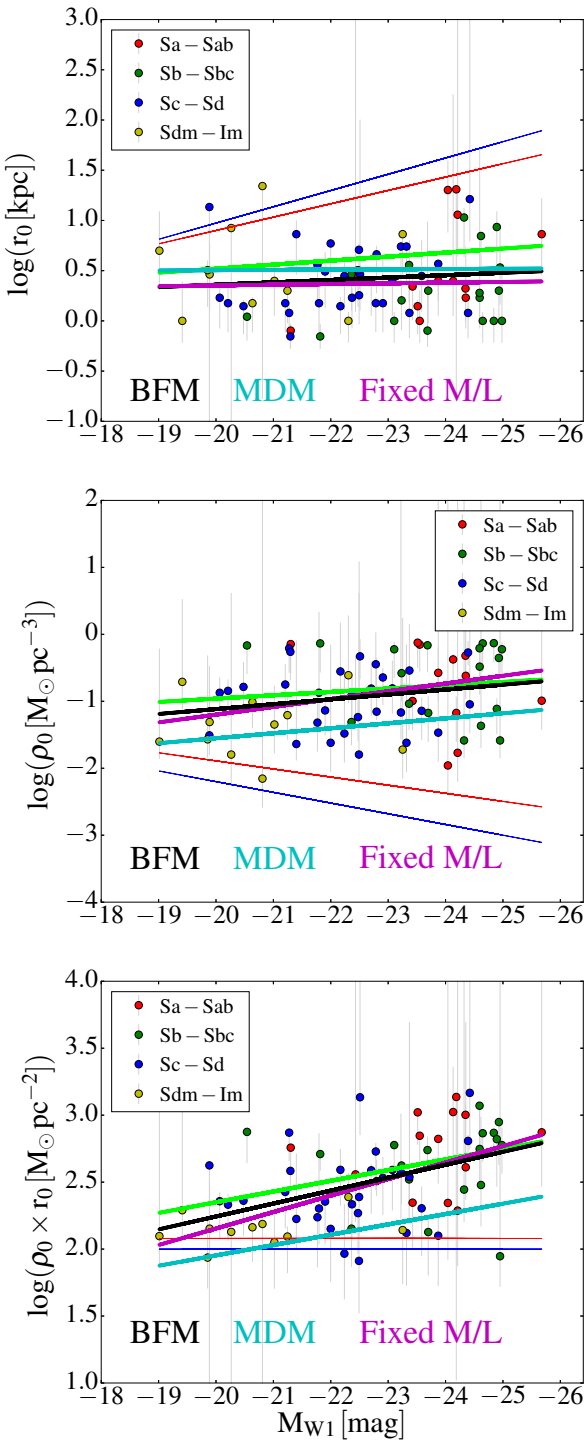

Figure 3.14: Halo scaling radius (top panel), central halo density (middle panel) and the product of the central halo density with the scaling radius versus the magnitude in W1-band for the whole sample for ISO (BFM) points. The thick black, cyan and magenta lines are the best fit (BFM), the maximum disc (MDM) and the fixed M/L models respectively. The thick lime, thin blue and thin red lines represent respectively the fit found using the W1-band, Kormendy & Freeman (2004) and Randriamampandry & Carignan (2014).

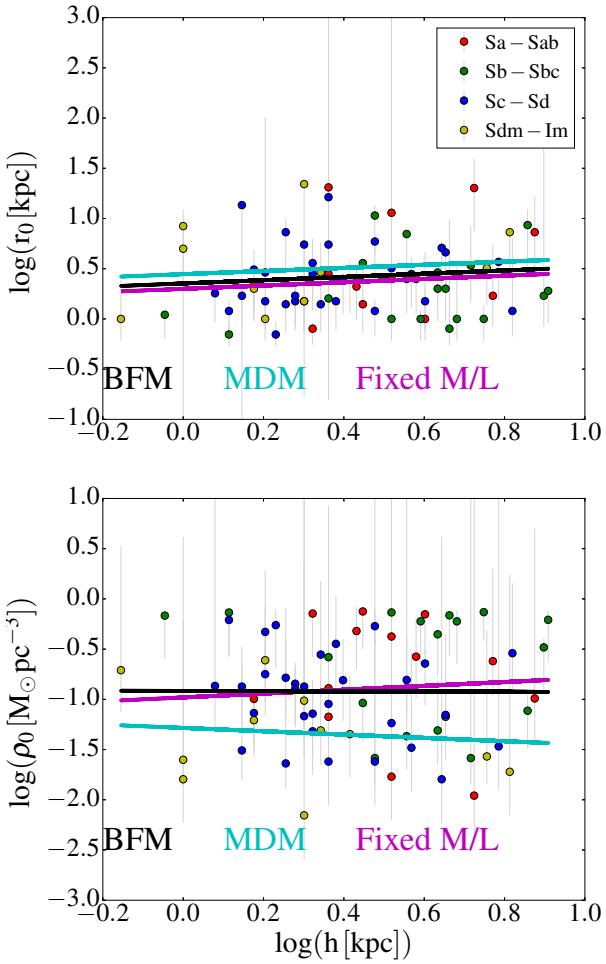

Figure 3.15: Halo parameters as a function of the disc scale length for the whole sample for the ISO (BFM) points. Top and bottom panels show respectively the scale radius and the central halo density as a function of the disc scale length. The thick black, cyan and magenta lines are the best fit (BFM), the maximum disc (MDM) and the fixed M/L models respectively. The legends for the two panels are shown in the top panel.

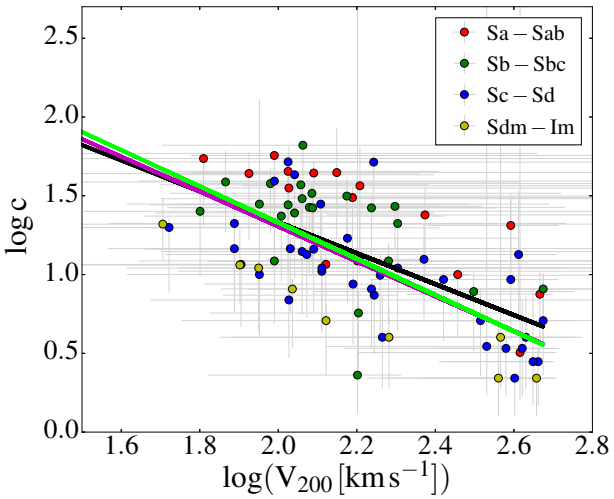

Figure 3.16: Distribution of log c as a function of log (V_{200}) for NFW best fit model (BFM). The thick black and magenta lines represent respectively the fit for BFM and fixed M/L. The thick lime line shows the fit for the BFM found using the W1-band.

3.5.1.1 Photometry

If we look at the photometry, we found in Figs. 3.4 right panel and 3.7 the same trends for the photometric parameters as a function of morphological types. Probably the most interesting one is in Fig. 3.4 (right) where we see clearly, in both bands, that the central surface brightnesses of the discs are far from being constant but show a clear trend where early type discs are brighter and late-type discs fainter. The distribution of the baryonic matter is characterized by the adopted M/L ratios. Fig. 3.11 shows that the median values of the M/L ratios in the R_c-band (0.39, 1.65 and 1.07 $M_\odot/L_\odot$ respectively for BFM, MDM and fixed M/L) are, as expected, higher than the values found in the MIR (0.14, 0.61 and 0.44). The distributions in both bands are however quite similar. The MDM maximises the contribution from the discs; the M/Ls obtained using the MDM method are indeed ∼4 times larger than the BFM model ones.

The dispersion in the M/L values are smaller in the MIR than in the optical for BFM and MDM and fixed M/L. This can be seen in Table 3.4 (see columns 3 and 6) and Fig. 3.18, where the M/L values range from 0 to 5 in the R_c-band and from 0 to 1.6 in the W1-band. Nevertheless, in order to compare those dispersions with

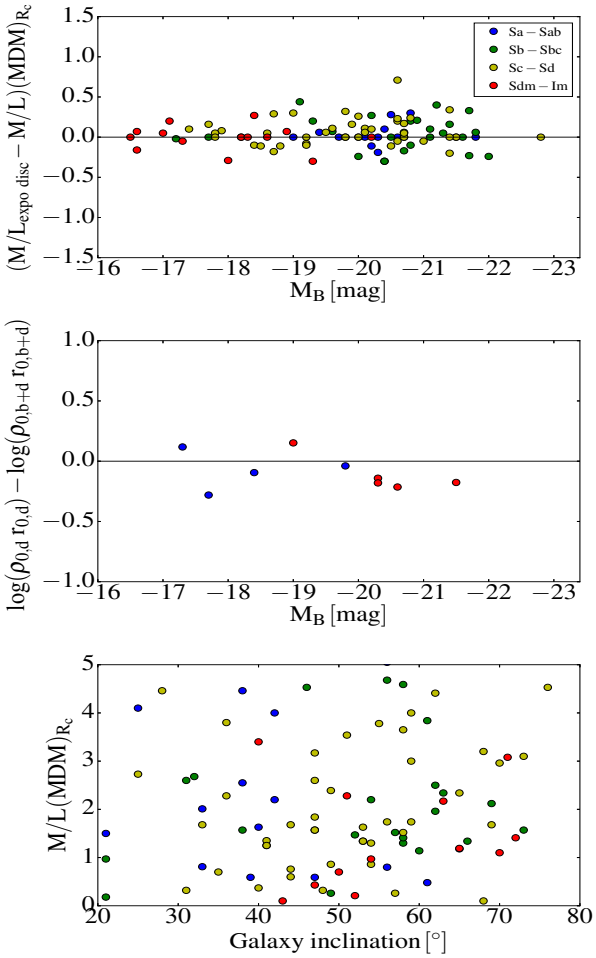

Figure 3.17: The three plots are obtained using the R_c-band surface brightness photometry. Top panel: difference between the M/L values obtained using the modelled exponential disc and the actual disc as a function of the absolute M_B magnitude for the ISO (MDM). Middle panel: difference between the log of the product $\rho_{0,d}\times r_{0,d}$ ($M_\odot pc^{-2}$) computed without profile decomposition into two distinct components and the log of the product $\rho_{0,b+d} \times r_{0,b+d}$ ($M_\odot pc^{-2}$) obtained when the profiles are decomposed into a disc and a bulge as a function of M_B for the ISO (BFM). Bottom panel: M/L of disc versus the galaxy inclination for the ISO (MDM). The colour code represents the morphological type and is the same than for the top panel.

M/L	R_c			W1		
$M_\odot/L_\odot$	Med	σ	σ_N	Med	σ	σ_N
(1)	(2)	(3)	(4)	(5)	(6)	(7)
BFM	0.39	0.99	2.54	0.14	0.26	1.86
MDM	1.65	1.29	0.78	0.61	0.37	0.61
Fixed M/L	1.07	0.33	0.31	0.44	0.18	0.41

Table 3.4: Values of the M/L for the BFM, MDM and fixed M/L. Columns (2) to (4) show respectively the median value of M/L, the dispersion and the normalized dispersion for the R_c- band. Column (5) to (7) show the same description using the W1- band.

respect to the median M/L value for each band, we have to consider the normalized dispersions. Table 3.4 (see columns 4 and 7) shows that the normalized dispersion is also higher in the optical than in the MIR for BFM and MDM while it is smaller in the optical than in the MIR when M/L is fixed. This is probably due to the relation used to calculate the M/L as a function of colour. In the W1 band, they used the relation described by Cluver et al. (2014) while in the R_c band, we used the relation shown in equation 3.5. Using the fixed M/L, we found that 19 galaxies have non physical M/L values and do not provide good fit (the model is higher than the observed rotation) for W1 while we found only 9 such galaxies in the R_c-band.

3.5.1.2 Mass models

The anti-correlation found in Fig. 3.12 between ρ_0 and r_0 is comparable to that found using the 3.4 μm surface brightness (which is represented by a thick lime line and corresponds to the fit of the BFM. This relation is slightly different from the one published in Korsaga et al. (2018) because the sample contains here 100 galaxies instead of 121. The values of the different parameters for ISO (BFM, MDM and fixed M/L) are shown in Table 4.3. These parameters are very similar to those found in the R_c-band. The different weak trends found in the top and middle panels of Fig. 3.13 for ISO, where no clear correlation is found between the scaling radius and the luminosity of galaxies while less luminous galaxies tend to have smaller central halo densities, are in agreement with Korsaga et al. (2018). However, previous authors found that less luminous dwarf galaxies tend to have smaller scaling radii and higher central densities (e.g, Carignan & Freeman 1988).

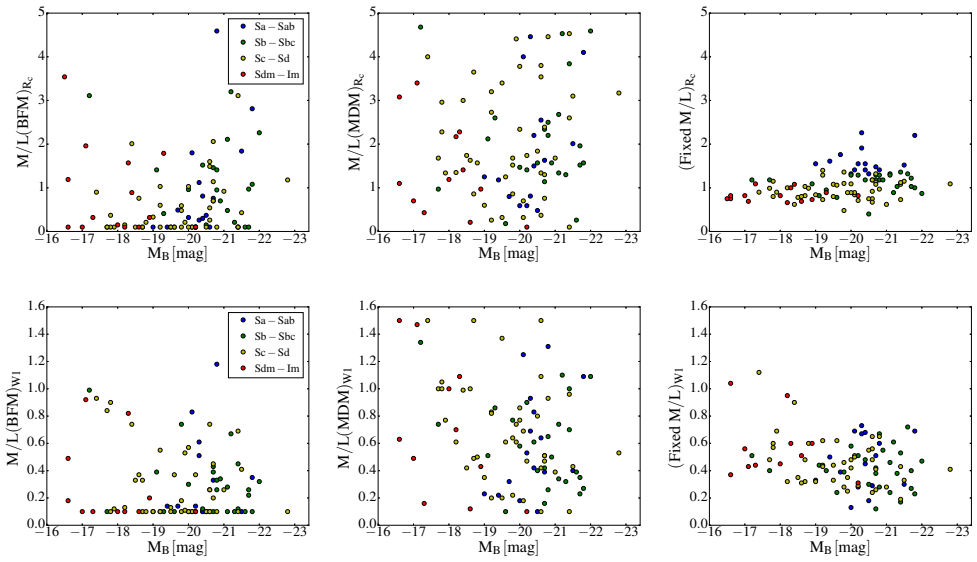

Figure 3.18: M/L ratio versus absolute magnitude M_B using the R_c-band (top) and the W1-band (bottom). From left to right: M/L of ISO (BFM), M/L of ISO (MDM) and fixed M/L. The legends are shown in the left panels.

Korsaga et al. (2018) explored the reasons of the discrepancy with the literature by splitting the sample either into (i) very high and acceptable quality rotation curves, (ii) barred (SB), moderately barred (SAB) and no-barred galaxies (SA), or into (iii) bulge-poor and bulge-rich galaxies. They concluded that the difference is due to the presence of bulge-rich galaxies for which the bulge has an influence on the derived halo contribution.

In the bottom panel of Fig. 3.13, less luminous galaxies tend to have smaller $\rho_0 \times r_0$, which is consistent with the results found in the W1-band (thick lime line). In order to understand if the various trends we found between the halo scale radius and the central density as a function of M_B are also due to bulges, we defined two sub-samples like Korsaga et al. (2018) did with the W1-band photometry: a bulge-poor sample composed of galaxies with $L_{bulge}/L_{total} < 0.02$ (mostly composed of late-type spiral galaxies) and a bulge-rich sample with $L_{bulge}/L_{total} > 0.07$ (composed of early type spirals). The DM halo parameters of these sub-samples are plotted as a function of M_B in Fig. 3.19. The top panel of this figure shows the scaling radius as a function of M_B; a clear correlation appears for bulge-poor galaxies (thick green line) while we notice a very weak correlation for bulge-rich galaxies (thick black line). The middle panel of Fig. 3.19 represents the central density of the halo as

a function of the luminosity M_B where an anti correlation is found for bulge-poor galaxies (thick green line) and a correlation for bulge-rich galaxies (thick black line). The bottom panel shows $\rho_0 \times r_0$ as a function of M_B; we found no correlation for bulge-poor galaxies (thick green line) while a clear correlation is seen for bulge-rich galaxies (thick black line). All the trends we found in this work for bulge-poor and bulge-rich galaxies are similar to those found in W1-band (represented by thin green and black lines respectively for bulge-poor and bulge-rich galaxies). Those results seem to point out that the results of the mass models are quite independent of the photometric band used.

For the NFW model, the average concentration values found are c = 13.80 ± 2.29 and c = 12.02 ± 1.66 for the BFM and the fixed M/L respectively. These values are higher than what found using the 3.4 μm luminosity profile (c = 11.22 ± 1.78 and 8.32 ± 1.58 for BFM and fixed M/L respectively). As seen in Fig. 3.16, an anti-correlation is found between c and V_{200} showing that high concentrations trend to have smaller mass halos. Similar results are seen in the W1-band.

In Fig. 3.21, the top panel shows the comparison between r_0 for the two bands R_c and W1 using ISO (BFM); we notice that the scaling radius are smaller in the R_c-band than in the W1-band. The bottom panel represents the comparison between ρ_0 for R_c and W1 bands, ρ_0 are higher in the R_c-band. When looking at the NFW models (Fig. 3.22), it can be seen that the concentration c are higher and V_{200} smaller in the R_c-band compared to the results obtained in the W1 band. This could be due to the fact that those two bands are probing different stellar populations. Most specifically, the difference between the M/L ratios of bulges and discs may be more important for the Rc-band than for the W1-band because the Rc-band is more sensitive to blue stars. Therefore, if the M/L ratio of the bulge and disc becomes similar, we might have a larger contribution of the bulge in the W1-band which might lead to a lower concentration. Indeed, the rise of the rotation curve grows as the central concentration c, thus when the contribution of the bulge decreases, the contribution of the DM halo is expected to increase in the inner regions of the galaxies.

Alternatively, this could be the result of the minimal value allowed for the M/L ratio. The median of M/L is 3 times larger for the Rc-band than for the W1-band (see Table 3.4) but the M/L lower limit allowed for both bands are identical (M/L = 0.1). Thus we expect that more galaxies reach this lower limit for the W1-band than

for the Rc-band and that this limit corresponds to a larger contribution of the stellar components for the W1-band.

3.5.2 Comparison with previous works

According to Swaters et al. (2011), the M/L ratio is usually high (up to 15 in the R-band) when using the maximum-disc fits of HI rotation curves for gas-rich irregular galaxies; these high values imply that irregular galaxies are dominated by DM at all radii (Zibetti et al. 2009). As can be seen in Fig. 3.18, such large values are surely not seen in this study where the largest values we find are even less than 5. This difference could be partly explained by the fact that the HI resolution is lower than in the optical, thus the constraints are lower in the optical regions. Moreover, Lelli et al. (2014)'s study on dwarf galaxies revealed that M/L is ∼1.5 in the R_c-band, mostly for the blue compact dwarfs (BCDs); this value is close to the one found in this paper when using the ISO (MDM). As expected, the median values of the M/L ratio found in this work (0.39, 1.65 and 1.07 $M_\odot/L_\odot$ respectively for BFM, MDM and fixed M/L) are higher than the previous works which used the MIR photometry band (e.g. McGaugh & Schombert 2015, Richards et al. 2016, Lelli et al. 2016, Richards et al. 2018, Korsaga et al. 2018).

In this work, we find no clear correlation between the scaling radius and the luminosity of the galaxies for the whole sample and less luminous galaxies tend to have smaller central halo densities (see top and middle panels of Fig. 3.13). However, our results are not in agreement with previous studies made by Kormendy & Freeman (2004) and Randriamampandry & Carignan (2014) represented by the thin blue and red lines respectively in Fig. 3.13. They found that less luminous dwarf galaxies tend to have smaller scaling radii and higher central densities. In the bottom panel of Fig. 3.13, we find that less luminous galaxies tend to have smaller $\rho_0 \times r_0$ which is not in agreement with previous studies (Kormendy & Freeman 2004, Randriamampandry & Carignan 2014, thin blue and red lines respectively) which suggest that $\rho_0 \times r_0$ does not depend on the luminosity. When comparing the correlations found using the sub-samples in Fig. 3.19 with previous authors (Kormendy & Freeman 2004, Randriamampandry & Carignan 2014, thin blue and red lines respectively) who mostly worked on late type galaxies, we find a consistency for bulge-poor galaxies only but not for bulge-rich galaxies. We conclude that the distribution of the DM as a function of the absolute luminosity depends on the

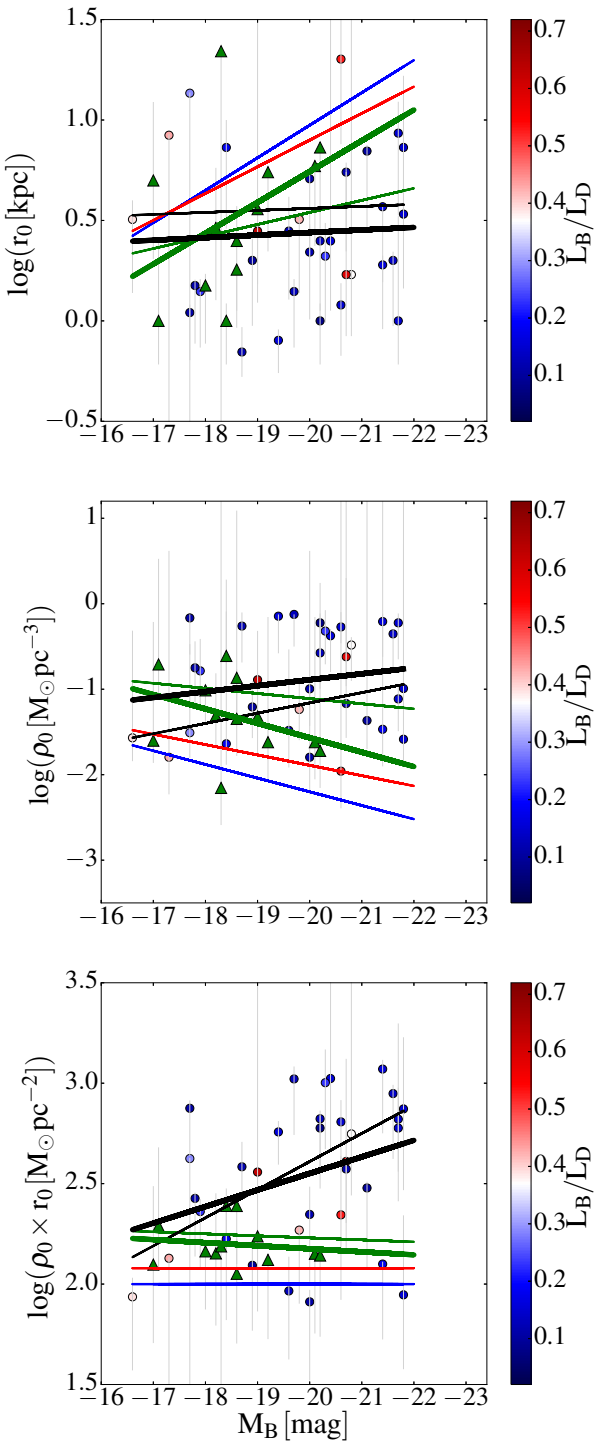

Figure 3.19: Halo parameters (scaling radius at the top, central density in the middle and $\rho_0 \times r_0$ at the bottom) for ISO (BFM) versus absolute magnitude for the bulge-poor (triangles) and bulge-rich (dots) sub-samples. The colours of the dots represent the importance of the bulge (see colour bar on the right). The thick green line represents the fit for the bulge-poor galaxies, which corresponds to $L_{bulge}/L_{total} < 0.02$ and the thick black line for the bulge-rich galaxies which corresponds to $L_{bulge}/L_{total} > 0.07$. The thin blue and red lines represent respectively the fit found by Kormendy & Freeman (2004) and Randriamampandry & Carignan (2014), mainly for late-type galaxies. The thin green line represents the fit for the bulge-poor and the thin black line for the bulge-rich galaxies found using the W1-band.

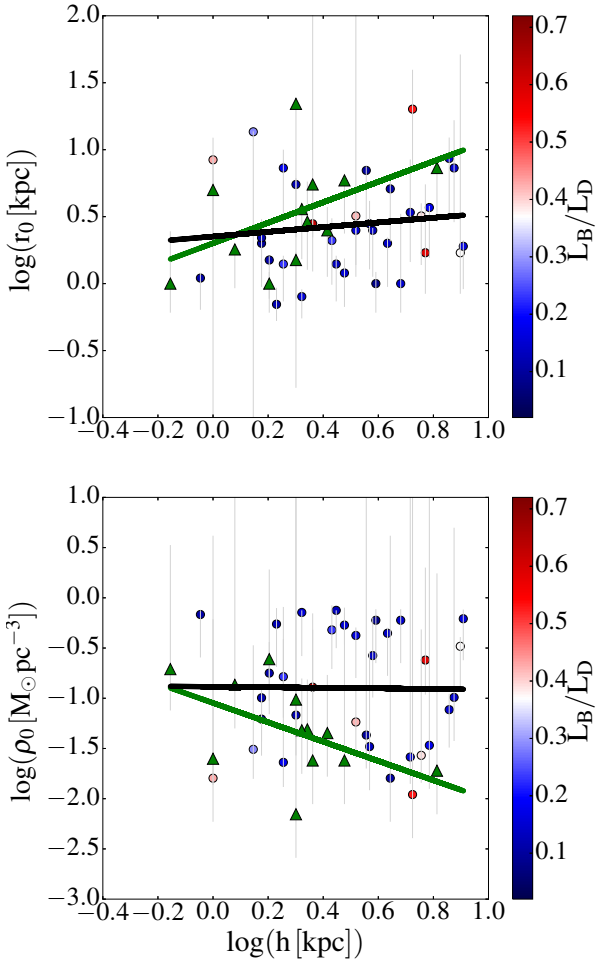

Figure 3.20: The top and bottom panels show respectively the scale radius and the central halo density as a function of the disc scale length for ISO (BFM). The colours and symbols are the same as used in Fig. 3.19. The thick green line represents the fit for the bulge-poor and the thick black line for the bulge-rich galaxies.

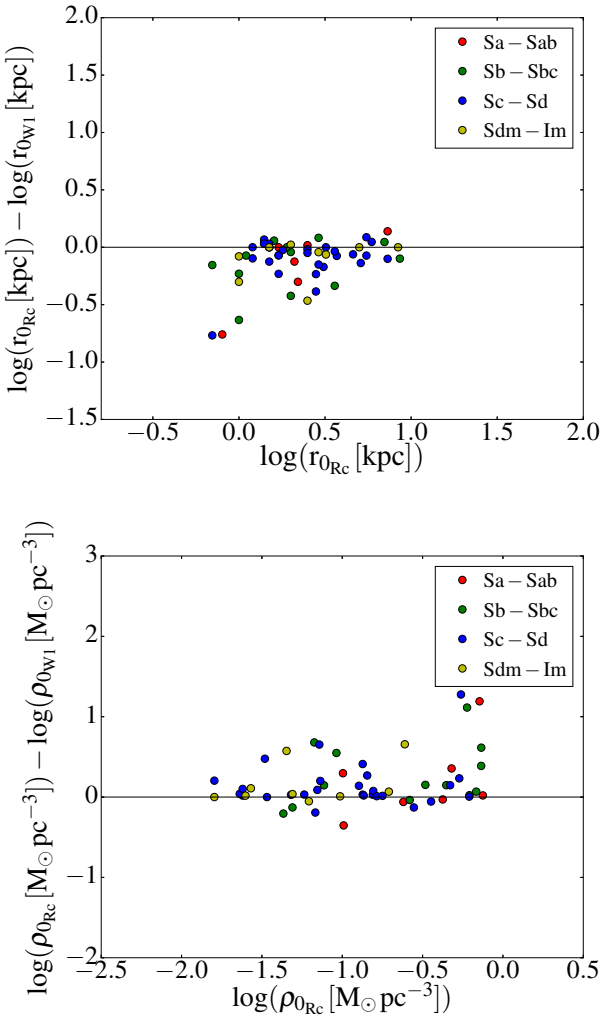

Figure 3.21: Comparison of the results obtained for ISO (BFM) using the optical R_c and MIR W1 bands. Top panel: scaling radius r_0. Bottom panel: central density ρ_0.

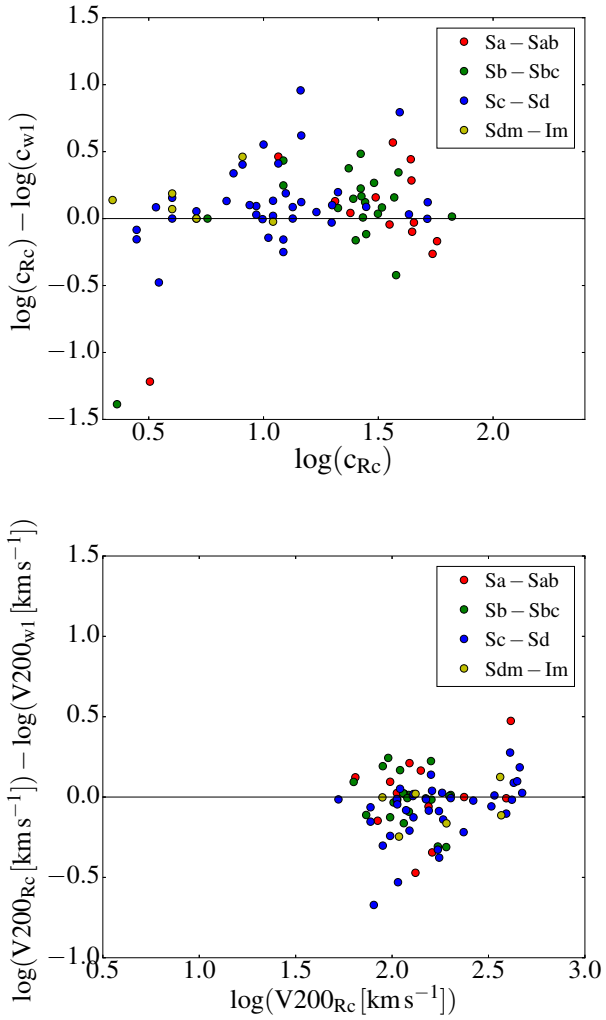

Figure 3.22: Comparison of the results obtained for NFW (BFM) using the optical R_c and MIR W1 bands. Top panel: concentration c. Bottom panel: velocity at the virial radius V_{200}.

morphological type of the galaxy which means that we cannot expect to have the same trend when working with bulge-poor or bulge-rich galaxies.

The average concentration values c = 13.80 ± 2.29 and c = 12.02 ± 1.66 for the NFW (BFM) and NFW (fixed M/L) respectively in this study are higher than the standard value found by Bullock et al. (2001) which is c = 10 but in the range of the values found by Martinsson et al. (2013) which are between 10 and 20. Noordermeer (2006) used this standard value to model mass distributions and concluded that NFW fits with c = 10 remain comparable to the minimal χ^2 of the isothermal fits. The anti-correlation between the concentration and the mass halos for NFW (BFM) and NFW (fixed M/L) found in Fig. 3.16 is also found by Wechsler et al. (2002), Barnes et al. (2004), Noordermeer (2006), Martinsson et al. (2013).

As already mentioned in section 3.4.2, we do not find a clear correlation between r_0 and ρ_0 as a function of the disc scale length represented in Fig. 3.15. This is not in agreement with previous studies (e.g. Côté et al. 2000, Donato et al. 2004) who used a sample composed of mostly late type galaxies and found that galaxies with a small disc scale length h tend to have a small r_0 and a high ρ_0. However, when we use the sub-samples in Fig. 3.20 (top and bottom panels), we find that bulge-poor galaxies (thick green line) with a small h tend to have a small r_0 and a high ρ_0. This correlation is in agreement with the previous authors mentioned. No clear correlation is found for the bulge-rich galaxies (thick black line). Once again, we conclude that the relation between the halo parameters and the optical disc scale length depends on the presence or not of a bulge.

3.6 Summary and Conclusions

This paper presents the study of mass models using Hα rotation curves and optical R_c-band photometry for a sample of 100 galaxies covering morphological types from Sa to Irr. The high resolution rotation curves are used to understand the stellar mass distribution and the shape of dark halo density distribution. Therefore, we used two main models to describe the DM distribution; the pseudo-isothermal sphere (ISO) and the Navarro-Frenk-White model (NFW) with different fitting procedures (a best fit model (BFM), a maximum disc model (MDM) and a M/L calculated using the colours (fixed M/L)).

(i) Using only optical rotation curves, galaxy mass models request a DM halo

for two third of the sample for the ISO (MDM) models, this fraction rises to 87% for BFM and to 78% for the fixed M/L. For NFW models, a DM halo is requested for 89%, 78% of the galaxies for BFM and fixed M/L respectively. Kalnajs (1983) showed more than 30 years ago that many galaxies do not need DM halos to model their RCs when only optical kinematics is available (e.g. M33, NGC 7793). For those galaxies, the need to add a DM halo only arise when HI kinematics going further out is added.

(ii) For the ISO (BFM), the model describes very well the inner and outer part of the rotation curves for both low and high luminosity galaxies. The ISO (MDM) also procures good fits to the observed rotation curves with large values of M/L ratios. The fixed M/L provides acceptable fits but we sometimes found some non-physical fits when using this technique (e.g.: UGC 2045, 2855, 6118). The M/L values found for ISO (MDM) are ~4 times higher and for ISO (fixed M/L) ~3 times higher than the M/L ratio values of the ISO (BFM). The M/L dispersion is higher when using the R_c-band compared to the W1 band for all models.

(iii) Isothermal models suggest that smaller scaling radius (r_0) tend to have higher central halo density (ρ_0) (Fig. 3.12). This correlation does not depend on the morphological types (presence of bulge or not) because the same trend is seen when we compare our results with previous studies which used mostly late type spiral galaxies. A correlation is found between ρ_0 and $\rho_0 \times r_0$ as a function of the luminosity when using the whole sample; less luminous galaxies tend to have smaller ρ_0 and smaller $\rho_0 \times r_0$ while no clear correlation is found between r_0 and the luminosity. We need to be careful with these relations in the sense that our work contains galaxies covering all morphological types (from early to late type spirals and irregulars) which means the presence of bulge-rich galaxies.

(iv) For that, we divided the sample in two sub-samples (bulge-poor and bulge-rich galaxies). For bulge-poor galaxies, we found that less luminous galaxies tend to have smaller r_0 and higher ρ_0, and an independent relation is found between $\rho_0 \times r_0$ and the luminosity. For the bulge-rich galaxies, the correlations found are in agreement with those found using the whole sample. We found no clear correlation between r_0 and ρ_0 and the optical disc scale length (h). However, a clear correlation is found for bulge-poor galaxies; smaller h corresponds to smaller r_0 and higher ρ_0. Once again, for bulge-rich galaxies, the correlations found are in agreement with the whole sample.

In conclusion, we can say that the relations between the halo parameters and the luminosity depend on morphological types, which means that we do not find the same relation when using galaxies with or without a bulge. The same conclusion is also found between the halo parameters and the optical disc scale length. The fact that we found similar correlations when using the whole sample and when using the sub-sample of bulge-rich galaxies is due to the presence of a large number of bulge-rich galaxies in the sample. It is worthwhile to note that these relations are independent of the band used: the same results are being observed when using the B-band and the W1-band luminosities.

(v) In order to test the strength of the previous results we have modelled the observed disc with an exponential disc. Indeed, one might expect that the disc - DM halo models depend on the local light distribution rather than on the global light distribution. The correlations discussed in item (ii) remain basically the same. This means that high-z galaxies, for which it is too challenging to measure the detailed light distribution as a function of the galacto-centric distance, could be modelled by an exponential disc. In other words, the knowledge of the disc scale length should be enough for high-z galaxies.

(vi) In the case of NFW (BFM), the rotation curves can be well explained with this model especially for high luminosity galaxies, but for less luminous galaxies, the fit becomes inconsistent. The fixed M/L ratio provides acceptable fits for most galaxies while the model gives non physical fits for some galaxies. For cuspy profile density, we found that low mass halos are more concentrated than high mass halos. We concluded that our rotation curves are better described by core than cuspy density profiles whatever we use BFM or fixed M/L techniques, as shown in Fig. 3.9.

(vii) When we compare the M/L ratios and the halo distribution in R_c-band with W1-band, we notice that the dispersion of the M/L values is higher for the optical R_c-band than the W1 band; and the halo is more concentrated when using R_c-band than the MIR 3.4μm band for ISO and NFW models.

Acknowledgements

We thank the referee for useful comments that helped in improving the paper. Most of the research of MK was done while she was having a PhD Scholarship from the Science faculty of the University of Cape Town. CC's work is based upon research

supported by the South African Research Chairs Initiative (SARChI) of the Department of Science and Technology (DST), the Square Kilometre Array South Africa (SKA SA) and the National Research Foundation (NRF). We acknowledge financial support from “Programme National de Cosmologie et Galaxies” (PNCG) funded by CNRS/INSU-IN2P3-INP (Centre national de la recherche scientifique/Institut national des sciences de l’Univers - Institut national de physique nucleaire et de physique des particules - Institut de physique), CEA (Commissariat à l’Energie atomique et aux Energies alternatives) and CNES (Centre national d’etudes spatiales) in France.

Bibliography

Abazajian K. N., et al., 2009, ApJS, 182, 543

Barbosa C. E., et al., 2015, MNRAS, 453, 2965

Barnes E. I., Sellwood J. A., Kosowsky A., 2004, AJ, 128, 2724

Begeman K. G., 1987, PhD thesis, , Kapteyn Institute, (1987)

Bell E. F., de Jong R. S., 2001, ApJ, 550, 212

Blais-Ouellette S., Carignan C., Amram P., Côté S., 1999, AJ, 118, 2123

Blais-Ouellette S., Amram P., Carignan C., 2001, AJ, 121, 1952

Bottema R., Pestaña J. L. G., 2015, MNRAS, 448, 2566

Bullock J. S., Boylan-Kolchin M., 2017, ARA&A, 55, 343

Bullock J. S., Kolatt T. S., Sigad Y., Somerville R. S., Kravtsov A. V., Klypin A. A., Primack J. R., Dekel A., 2001, MNRAS, 321, 559

Carignan C., Freeman K. C., 1985, ApJ, 294, 494

Carignan C., Freeman K. C., 1988, ApJ, 332, L33

Carleton T., Errani R., Cooper M., Kaplinghat M., Peñarrubia J., 2018, preprint, (arXiv:1805.06896)

Cluver M. E., et al., 2014, ApJ, 782, 90

Côté S., Carignan C., Freeman K. C., 2000, AJ, 120, 3027

Donato F., Gentile G., Salucci P., 2004, MNRAS, 353, L17

Epinat B., et al., 2008a, MNRAS, 388, 500

Epinat B., Amram P., Marcelin M., 2008b, MNRAS, 390, 466

Faber S. M., Gallagher J. S., 1979, ARA&A, 17, 135

Flores R. A., Primack J. R., 1994, ApJ, 427, L1

Freeman K. C., 1970, ApJ, 160, 811

Garrido O., Marcelin M., Amram P., Boulesteix J., 2002, A&A, 387, 821

Garrido O., Marcelin M., Amram P., Boissin O., 2003, A&A, 399, 51

Garrido O., Marcelin M., Amram P., 2004, MNRAS, 349, 225

Garrido O., Marcelin M., Amram P., Balkowski C., Gach J. L., Boulesteix J., 2005, MNRAS, 362, 127

Gentile G., Salucci P., Klein U., Vergani D., Kalberla P., 2004, MNRAS, 351, 903

Kalnajs A., 1983, in Athanassoula E., ed., IAU Symposium Vol. 100, Internal Kinematics and Dynamics of Galaxies. pp 87–88

Kormendy J., Freeman K. C., 2004, in Ryder S., Pisano D., Walker M., Freeman K., eds, IAU Symposium Vol. 220, Dark Matter in Galaxies. p. 377

Korsaga M., Carignan C., Amram P., Epinat B., Jarrett T. H., 2018, MNRAS, 478, 50

Kravtsov A. V., Klypin A. A., Bullock J. S., Primack J. R., 1998, ApJ, 502, 48

Lelli F., Verheijen M., Fraternali F., 2014, A&A, 566, A71

Lelli F., McGaugh S. S., Schombert J. M., 2016, AJ, 152, 157

Martinsson T. P. K., Verheijen M. A. W., Westfall K. B., Bershady M. A., Andersen D. R., Swaters R. A., 2013, A&A, 557, A131

McGaugh S. S., Schombert J. M., 2015, ApJ, 802, 18

Navarro J. F., Frenk C. S., White S. D. M., 1996, ApJ, 462, 563

Navarro J. F., Frenk C. S., White S. D. M., 1997, ApJ, 490, 493

Noordermeer E., 2006, PhD thesis, Groningen: Rijksuniversiteit

Randriamampandry T. H., Carignan C., 2014, MNRAS, 439, 2132

Read J. I., Walker M. G., Steger P., 2018, preprint, (arXiv:1805.06934)

Richards E. E., et al., 2016, MNRAS, 460, 689

Richards E. E., et al., 2018, MNRAS, 476, 5127

Spano M., Marcelin M., Amram P., Carignan C., Epinat B., Hernandez O., 2008, MNRAS, 383, 297

Springel V., Frenk C. S., White S. D. M., 2006, Nature, 440, 1137

Swaters R. A., Madore B. F., van den Bosch F. C., Balcells M., 2003, ApJ, 583, 732

Swaters R. A., Sancisi R., van Albada T. S., van der Hulst J. M., 2011, ApJ, 729, 118

Wechsler R. H., Bullock J. S., Primack J. R., Kravtsov A. V., Dekel A., 2002, ApJ, 568, 52

Zibetti S., Charlot S., Rix H.-W., 2009, MNRAS, 400, 1181

de Blok W. J. G., McGaugh S. S., Bosma A., Rubin V. C., 2001, ApJ, 552, L23

de Blok W. J. G., Bosma A., McGaugh S., 2003, MNRAS, 340, 657

de Blok W. J. G., Walter F., Brinks E., Trachternach C., Oh S.-H., Kennicutt Jr. R. C., 2008, AJ, 136, 2648

de Denus-Baillargeon M.-M., Hernandez O., Boissier S., Amram P., Carignan C., 2013, ApJ, 773, 173

van Albada T. S., Sancisi R., 1986, Philosophical Transactions of the Royal Society of London Series A, 320, 447

Chapter 4

Distribution of luminous and dark matter in spiral and irregular nearby galaxies using Hα and HI rotation curves and WISE photometry

This chapter has been submitted in the Monthly Notices of the Royal Astronomical Society (MNRAS): M. Korsaga, C. Carignan, P.Amram, B. Epinat, A. Sorgho and P. Adamczyk

Abstract

We present the mass models of 31 spiral and irregular nearby galaxies obtained using hybrid rotation curves combining high resolution Hα and extended HI rotation curves, 3.4 μm WISE (Wide-field Infrared Survey Explorer) photometry data and the neutral hydrogen surface density profiles to account for the atomic gas component. The Hα rotation curves were selected from the GHASP (Gassendi HAlpha survey of SPirals) survey. The aim is to compare the dark matter halo parameters in different cases: using only Hα rotation curves with the effect of including and excluding the contribution of the neutral gas component to the circular velocity profile, HI rotation curves with the neutral gas component, and hybrid rotation curves with the neutral gas component. Two different models are used to determine the shape of the dark matter halos: the pseudo-isothermal (ISO) core profile and the Navarro-Frenk-White (NFW) cuspy profile. We use three fiducial fitting procedures: best fit models (BFM), models with M/L fixed from the W1-W2 colour and maximum disc models (MDM) for the pseudo-isothermal profile only. When using hybrid rotation curves, we find that the M/L values are higher and that the dark matter halos are less concentrated than when using purely Hα kinematics. The correlations between the dark matter halo parameters remain the same whatever rotation curve is used. Clearly, the differences between the fitting procedures are larger than between the different datasets.

4.1 Introduction

Since ~50 years, it is well observed that there is a large discrepancy between the luminous mass and the dynamical mass of galaxies (see e.g. Freeman 1970, Bosma 1978). This is usually explained by adding a more or less spherical halo of dark matter (DM) to the visible baryonic mass composed of stars and gas (see e.g. Carignan & Freeman 1985). The DM can be distributed using a theoretical or an empirical density profile. Therefore, in the literature, several density profile models are used to determine the DM distribution. The two most commonly used models are the pseudo-isothermal sphere (ISO: Begeman 1987) with a core density profile and the ΛCDM cuspy density profile from Navarro–Frenk–White (NFW: Navarro et al. 1996; 1997).

In the last ~10 years, 2D-kinematics of large samples of nearby galaxies have

been obtained either in the optical using Fabry-Perot interferometry of the Hα line (see e.g. the GHASP sample of ~200 galaxies, Epinat et al. 2008), at radio wavelength using aperture synthesis of the HI line (see e.g. the WHISP sample, a homogenous survey of ~300 spiral and irregular galaxies with the Westerbork Synthesis Radio Telescope -WSRT- in Swaters et al. 2002, Noordermeer et al. 2005, van Eymeren et al. 2011 or the THINGS sample of ~35 galaxies observed with the Very Large Array -VLA- in de Blok et al. 2008) or a combination of those two types of data (see e.g. the SPARC sample of ~175 galaxies in Lelli et al. 2016). At present, Hα kinematics has ~1-2" spatial resolution, limited by the seeing, as compared to radio (e.g. WSRT or VLA) 15-30" resolution. Naturally, the new radio interferometers, with longer baselines, will improve on this and eventually get comparable resolutions. In the near future, large sample of more distant galaxies will be obtained using UV-optical-NIR emission lines with IFUs on large optical/IR telescopes or HI on the new generation of large radio interferometers such as MeerKAT for nearby galaxies and in a more distant future with the SKA for thousands of distant galaxies. It is thus important to compare the results we get for nearby galaxies using either optical Hα, radio HI or hybrid (optical + HI) datasets and understand properly the effects of different spatial resolutions. When analyzing the mass distribution of galaxies, it is also important to know if the derived parameters of both the luminous and dark components are affected by using those different datasets.

The main difference is expected to come from the spatial resolution of today's data because of the great sensitivity of the mass distribution parameters to the central part of the galaxies' rotation curves (Blais-Ouellette et al. 2001), where the velocity gradient is maximal. It is that part of the rotation curve that will constrain the free parameter of the luminous disc, namely the M/L ratio, which necessarily also has an impact of the parameters of the DM component. Many other studies have shown that the parameters of the DM distribution are very sensitive to the inner part kinematics as observed using emission line Hα observations (see e.g. Amram et al. 1992, Spano et al. 2008).

Korsaga et al. (2018) in their work, used 121 Hα rotation curves combined to WISE W1-band photometry data to determine the DM halo distribution. Another study was also done using a sample of 100 Hα rotation curves combined with optical R_c-band photometry data (Korsaga et al. 2019). The main aim was to see

if the luminous and DM parameters were dependant of the photometric band used (optical vs IR), since they are dominated by different stellar populations. In this paper, we aim to first construct the mass distribution of 31 galaxies using the same rotation curves and mid-IR photometry data mentioned earlier and considering the effect of including the contribution from the HI gas component. Secondly, the mass distribution is determined with the same photometry and gas component but using extended hybrid rotation curves (Hα in the inner parts extended with HI data in the outer parts). This will also be compared to purely HI kinematical data. The main goal here is to study how luminous and DM parameters depend on the dataset used to derive the rotation curves (RCs).

The galaxy sample is presented in Section 4.2. In Section 4.3, we present the mass models and the results of the fits are described in Sections 4.4 and 4.5. A discussion on the results obtained with the different types of RCs is done in Section 4.6 and Section 4.7 presents a summary and the general conclusions. In Appendix A , we present the mass models of all the galaxies.

4.2 Sample

4.2.1 Rotation curves

Our sample consists of 31 nearby galaxies selected from the GHASP survey (which contains 203 galaxies) and having HI rotation curves and 3.4μm photometry data. The GHASP survey produced high spectral ($\sim$ 10 000) and spatial ($\sim$ 2 arcsec) resolution Hα rotation curves. The Hα line was scanned using a Fabry-Perot interferometer at the 1.93 m telescope of the Observatoire de Haute Provence (OHP) (Garrido et al. 2002, Epinat et al. 2008). As we already applied a selection criteria on the quality of the Hα rotation curves in a previous study (Korsaga et al. 2018), we use the same Hα rotation curves which have both W1-band photometric data and HI rotation curves available in the literature.

For the HI rotation curves, 15 galaxies were taken from van Eymeren et al. (2011) and the remaining 16 from Lelli et al. (2016), which can be accessed on the SPARC website*. The HI rotation curves are derived by fitting tilted-ring models to the observed velocity fields and the errors on the rotation velocities are based on the

*http://astroweb.cwru.edu/SPARC/

difference between the approaching and the receding sides of the galaxy (Begeman 1987, Swaters et al. 2009, Lelli et al. 2016). Because the HI and Hα data have different sources, a correction of the galaxy radii and velocities for the distance and inclination of the galaxy was required before the hybrid rotation curves could be derived. In other words, we multiplied the HI radii by the ratio between the Hα and HI distances of the galaxy. The HI velocity is instead corrected by multiplying by the ratio between the sinus of Hα inclination and HI inclination of the galaxy. The different parameters and the references of the HI rotation curve for each galaxy are shown in Table 1.

4.2.2 Photometric data

The infrared surface photometry provides smaller dispersion for the M/L ratios compared to the optical photometry (Korsaga et al. 2019). Several models also predict that the values of the M/L ratios are approximatively constant when using the near infrared photometry (Bell & de Jong 2001, Lelli et al. 2016). Because our first step is to better constrain the M/L ratio, the W1-band (3.4 μm) from the Wide-field Infrared Survey Explorer (WISE; Jarrett et al. 2013) is suitable due to its weaker sensitivities to star formation activities and dust. The field of view is 47×47 arcmin^2 with an angular resolution of 6 arcsec. The decomposition of the surface brightness profiles into multiple components (bulge, disc, bar, spiral arm, ring, etc.) was already performed in Korsaga et al. (2018). From the whole sample of 31 galaxies, 11 did not need a decomposition (faint bulge) while the remaining 20 galaxies were decomposed. In order to reduce the number of parameters, we disentangle spherical components (bulges) from planar components (disc, bar, spiral arm, etc.) that we call disc in the mass models (Korsaga et al. 2018). The sample covers the morphological types (early type to late spiral and irregular galaxies) from Sa to Im. We have 10 Sa-Sbc, 15 Sc to Sd and 6 Sm-Im. The stellar mass contribution is obtained by scaling the M/L ratio. We first use the M/L ratio as a free parameter in mass models corresponding to the minimal χ^2 value; secondly, we constrained the M/L to have a maximum stellar contribution, so higher than the M/L derived from the minimal χ^2 and lastly, we consider the M/L as a constant parameter calculated as a function of the colour index (W1-W2) using the following

UGC	D_{HI}	$D_{H\alpha}$	i_{HI}	$i_{H\alpha}$	t	flag	HI beam	ref
(1)	(2)	(3)	(4)	(5)	(6)	(7)	(8)	(9)
01913	9.3	9.3	53.65	48	SABd	d	30	VE11
02080*	13.7	13.7	27.64	25	SABcd	d/b	30	VE11
02800	20.6	20.6	61.87	52	Im	d	30	VE11
02855***	17.5	17.5	61.49	68	SABc	d/b	30	VE11
03574	21.8	21.8	31.20	19	SAcd	d/b	30	VE11
03734	15.9	15.9	21.61	43	SAc	d/b	30	VE11
04284	9.8	9.8	61.67	59	SAcd	d/b	30	VE11
04325**	9.6	10.9	41.0	63	SAm	d	30	SW09, SW02
04499	12.50	12.2	50.0	50	SABdm	d/b	30	SW09, SW02
05251	21.5	21.5	64.50	73	Sbc	d/b	30	VE11
05253	22.90	21.1	37.0	40	SAab	d	11.6	No07, No05
05414	9.40	10.0	55.0	71	IABm	d	30	SW09, SW02
06537	18.00	14.3	53.0	47	SAB(r)c	d/b	12	VS01, SV98
06778	18.0	15.5	49.0	49	SABc	d/b	12	VS01, SV98
07323*	8.0	8.1	47.0	51	SABdm	d	30	SW09, SW02
07766*	9.00	13.0	67.0	69	SABcd	d/b	17	Ba05
08334	9.90	9.8	55.0	66	SAbc	d	28	Bt06, Bl04
08490	4.65	4.7	50.0	40	SAm	d	30	SW09, SW02
09179	7.06	5.7	51.0	36	SABd	d/b	20	Bl99, Sa96, Co91
09649*	7.7	7.7	56.56	54	SBb	d	30	VE11
09858	38.2	38.2	69.98	75	SABbc	d/b	30	VE11
09969	39.70	36.0	60.0	61	SAB(r)b	d/b	14	Bl04, Br92
10075	17.00	14.7	60.0	62	SAcd	d	13	VM97
10359	16.0	16.0	43.82	44	SBcd pec	d/b	30	VE11
10470	21.2	21.2	36.78	34	SBbc	d/b	30	VE11
11012	6.26	5.3	74.0	72	SAcd	d	30	Be91, Be87
11597*	5.52	5.9	38.0	40	SABcd	d/b	12	Bo08
11670	12.7	12.8	67.34	65	SA(r)0 − a	d/b	30	VE11
11852*	80.0	80.0	46.03	47	SBa	d/b	30	VE11
11914***	16.90	15.0	31.0	33	SA(r)ab	d/b	10.5	No07, No05
12754	8.9	8.9	49.46	53	SBcd	d/b	30	VE11

Table 4.1: Global properties of galaxies. (1) Name of the galaxy in the UGC catalogue. Column (2) and (4) represent respectively the distance in Mpc and the inclination for HI data. (3) and (5) show the distance in Mpc and inclination for Hα data taken from Epinat et al. (2008). (6) shows the morphological type from the RC3 catalogue. (7) represents the baryonic components that have been used (d: for disc only; d/b: for disc and bulge). (8) shows the HI beam for the HI rotation curves in arcsec. (9) shows the HI data references (VE11: van Eymeren et al. (2011); SW09: Swaters et al. (2009); SW02: Swaters et al. (2002); No07: Noordermeer et al. (2007); No05: Noordermeer et al. (2005); VS01: Verheijen & Sancisi (2001); SV98: Sanders & Verheijen (1998); Ba05: Barbieri et al. (2005); Bt06: Battaglia et al. (2006); Bl04: Blais-Ouellette et al. (2004); Bl99: Blais-Ouellette et al. (1999); Sa96: Sanders (1996); Co91: Cote et al. (1991); Br92: Broeils (1992); VM97: Verdes-Montenegro et al. (1997); Be91: Begeman et al. (1991); Bo08: Boomsma et al. (2008)). Galaxy names marked with asterisks mean galaxies for which we do not need DM to describe their rotation curves: 1 asterisk when using only Hα RC, 2 asterisks for hybrid rotation curves and 3 asterisks when it is the same case when using Hα and hybrid rotation curves.

relation given by Cluver et al. (2014).

$$\log(M_{\rm stellar}/L_{W_1}) = -2.54(W_1 - W_2) - 0.17 \tag{4.1}$$

where L_{W_1} is the inband luminosity in the W1 band and where W1 and W2 correspond to magnitudes in the W1 and W2 bands respectively.

4.2.3 HI density

To trace the mass of the galaxy at larger radii, the contribution of the neutral gas component is necessary, especially for late-type galaxies where HI can become an important (if not dominant) part of the luminous mass. As already mentioned in section 4.2, from the whole sample of 31 galaxies, 15 galaxies were taken from van Eymeren et al. (2011) and the remaining 16 from Lelli et al. (2016). However, the HI density profiles for 15 galaxies were not available in van Eymeren et al. (2011). For those, we use the total HI maps of the galaxies at the 30 arcsec resolution from the WHISP (Westerbork observations of neutral Hydrogen in Irregular and SPiral galaxies) website. We derive the surface density profiles of the neutral hydrogen using the GIPSY* task ELLINT and the tilted ring geometric parameters (de Blok et al. 2008). To take into account the presence of Helium, the surface densities are corrected by a factor of 1.33. The rotation curves associated with those surface densities are derived by assuming an infinitely thin gas disc.

To check the consistency of the HI surface brightness profiles with those collected from the literature, we run the software BBarolo Di Teodoro & Fraternali (2015) on our sample. This software fits a 3D tilted ring model directly on an observed emission-line datacube. For each datacube, we compute the RC in determining the parameters for each ellipse of the tilted ring model and we derive the HI surface brightness profiles. We compute the HI surface mass density profiles using the total HI mass M_{HI} of the galaxy that was derived from the total flux using

$$M_{HI} = 2.36\ 10^5\ D^2\ \int F(v)dv \tag{4.2}$$

where M_{HI} is in solar units, D is the distance of the galaxy in Mpc, and $\int F(v)dv$ is the total flux in Jy km s^{-1}.

*The Groningen Image Processing SYstem

4.3 Mass Models

We used the extended hybrid rotation curves (Hα extended with the HI rotation curves) of 31 galaxies to study the mass distribution. Therefore, two main models are used to quantify the distribution of the DM within the galaxies: the observation motivated pseudo-isothermal sphere (ISO) with a constant central density core profile (Begeman 1987) and the Navarro-Frenk-White (NFW) cuspy central density profile derived from the Λ-CDM N-body simulations (Navarro et al. 1996). The total rotation velocity $V_{\rm rot}$ is the quadratic sum of the individual contributions of stellar disc, bulge, gas disc and DM halo. The expression is :

$$V_{\rm rot}(r) = \sqrt{V^2_{\rm disc} + V^2_{\rm bulge} + V^2_{\rm gas} + V^2_{\rm halo}} \tag{4.3}$$

where $V_{\rm disc}$ and $V_{\rm bulge}$ are respectively the stellar disc and bulge contribution, $V_{\rm gas}$ is the gas disc contribution and $V_{\rm halo}$ the contribution of the DM halo. $V_{\rm gas}$ is derived in Section 4.2.3.

The core central density profile of the ISO model is given by

$$\rho_{\rm iso}(r) = \frac{\rho_0}{\left[1 + \left(\frac{r}{r_0}\right)^2\right]} \tag{4.4}$$

and the corresponding circular velocity is

$$V^2_{\rm iso}(r) = 4\pi G\rho_0 r_0^2 \left[1 - \frac{r_0}{r}\arctan\left(\frac{r}{r_0}\right)\right] \tag{4.5}$$

which is an increasing function of r, asymptotically reaching $V_{\rm max} = V(r = \infty) = \sqrt{4\pi G\rho_0 r_0^2}$
where ρ_0 is the central density of the DM and r_0 is the scaling radius.

The cuspy density profile of the NFW model is given by

$$\rho_{\rm NFW}(r) = \frac{\rho_i}{(\frac{r}{r_s})(1 + \frac{r}{r_s})^2} \tag{4.6}$$

where ρ_i is the density of the universe at the time of collapse and r_s the characteristic

radius of the halo.

The velocity is given by:

$$V^2_{\rm NFW}(r) = V^2_{200}\left[\frac{\ln(1+cx) - cx/(1+cx)}{x[\ln(1+c) - c/(1+c)]}\right] \tag{4.7}$$

where V_{200} is the velocity at the virial radius, $c = R_{200}/r_s$ is the concentration parameter of the halo and $x = r/r_s$. The relation between V_{200} (km s^{-1}) and R_{200} (kpc) is given by:

$$V_{200} = \frac{R_{200} \times \mathrm{H_0}}{100} \tag{4.8}$$

where $\mathrm{H_0}$ is the Hubble constant in km s^{-1} Mpc^{-1}. We assume $\mathrm{H_0}$=75 km s^{-1} Mpc^{-1}.

We assume the two parameters such as the concentration c and the velocity V_{200} at the virial radius to describe the velocity contribution associated to the NFW profile.

Because the density of points of the Hα rotation curves is different from that of HI rotation curves, we do not have the same radial weighting for Hα and HI velocities. To construct the mass models with the hybrid rotation curves, we optimised an equal radial weighting for both Hα and HI data points when fitting the rotation curves. Therefore, for the new Hα error-bars, we consider the average error on the approaching and receding Hα rotation curves. For the new HI error-bars, we multiply the existing HI error-bars values by the ratio of the new Hα error-bars and the median value of the existing HI error-bars. To obtain the same weight, the new HI error-bars are multiplied by the ratio of the number of Hα and HI rotation curve points. This method allows the model to describe the hybrid rotation curves in the inner and outer regions using optimized uncertainties for the rotational velocities. Note that when we construct the mass model with the hybrid rotation curves without optimizing the weights, the model does not fit well the outer parts of the rotation curves where the HI points are, because of their smaller spatial sampling (see Fig. 4.1).

The mass models are built using the same fitting procedures as used in Korsaga et al. (2018). We use two techniques for ISO and NFW models: (i) the best fit model (hereafter BFM) with a minimum χ^2 value, for which, all the parameters are free. This leads to three (or four if presence of a bulge) free parameters for both ISO ($\mathrm{r_0}$, ρ_0, and $\mathrm{M/L}_{disc}$, and $\mathrm{M/L}_{bulge}$ if presence of a bulge) and NFW (c, $\mathrm{V_{200}}$, and $\mathrm{M/L}_{disc}$, and $\mathrm{M/L}_{bulge}$ if presence of a bulge); (ii) the fixed M/L ratio for which

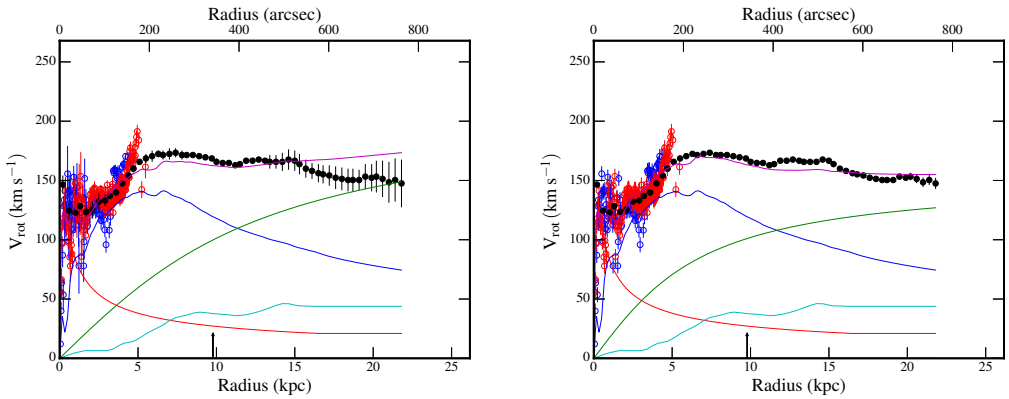

Figure 4.1: Example of mass model using ISO (BFM) with the hybrid rotation curve of a galaxy UGC 10597. Left panel corresponds to the model without optimizing the same weight of Hα and HI points. The right panel shows the model after applying the same weight for the Hα and HI points. For each panel, the open blue and red circles corresponds respectively to the approaching and receding points of the Hα rotation curve, the full black dots are the HI rotation curve. The blue, red, cyan, and green lines correspond respectively to the disc, bulge, gas and DM halo components. The magenta line is the model of the fit. The arrow represents the disc scale length of the galaxy.

the value of M/L is derived from the (W1-W2) colour described in section 4.2.2. In this case, the M/L is considered as a fixed parameter, which leaves us with two free parameters for both ISO (r_0 and ρ_0) and NFW (c and V_{200}). For this technique, the same value of M/L for the disc and the bulge is used because the spectrophotometric models do not allow to disentangle them. We also look at the maximum disc model (hereafter MDM) for ISO models. This technique allows to maximise the baryonic contribution by minimising the DM halos contribution. The M/L value for the MDM is constrained to be higher than the M/L value of the BFM and the χ^2 is allowed to increase up to 1.3 times the minimal χ^2 value. Minimal values were imposed to the parameters to avoid some unphysical values; M/L = 0.1 $M_\odot/L_\odot$, r_0 = 0.5 kpc and c = 1. The value 0.1 $M_\odot/L_\odot$ is imposed as a minimum value because we do not find a value of M/L below 0.1 $M_\odot/L_\odot$ when using the colour index to calculate the M/L shown in equation 4.1.

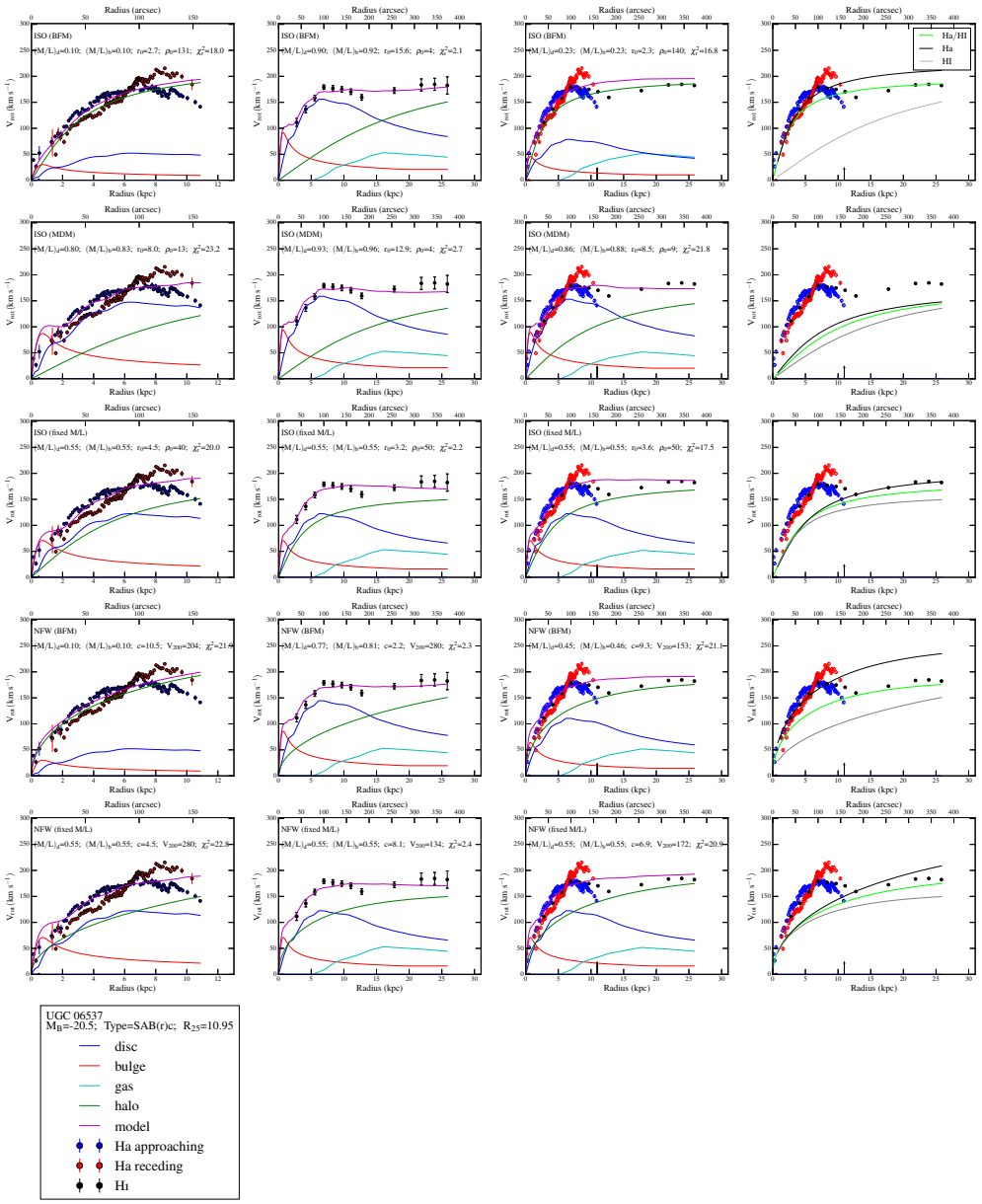

Figure 4.2: Example of mass models for the galaxy UGC 6537. Lines 1-3: pseudo-isothermal sphere density profiles (ISO). Lines 4-5: Navarro, Frenk & White density profiles (NFW). First line: Best Fit Model (BFM). Second line: Maximum disc Model (MDM). Third line: Mass-to-Light ratio M/L fixed using W1 - W2 colour. Fourth line: Best Fit Model (BFM). Fifth line: Mass-to-Light ratio M/L fixed using W1 - W2 colour. The name of the galaxy, its B-band absolute magnitude, morphological type and optical radius in kpc have been indicated in the insert located at line 6. Column 1: Models using Hα rotation curves and no neutral gas distribution. Column 2: Models using HI rotation curves. Column 3: Models using the hybrid Hα/ HI rotation curves. Column 4: We show the halo derived from the different rotation curves. The arrow represents the isophotal radius R_{25} of the galaxy in kpc. For each model, the fitted parameters and the reduced χ^2 have been indicated in each sub-panel.

4.4 Analysis of the mass models for individual galaxies

Different datasets are being used to build the mass models of the galaxies from the GHASP sample. In previous papers, the mass distribution was first determined using Hα rotation curves with the stellar mass component (disc and bulge, if presence of a bulge). We looked at the differences when using the mid-IR W1 photometric band (Korsaga et al. 2018) vs the optical R_c band (Korsaga et al. 2019) data. Since we found in those studies that it was better to use mid-IR photometry, WISE W1 data will be used in the rest of this study.

In this paper, we also add the contribution of the neutral gas component, which was not considered in previous papers (Korsaga et al. 2018; 2019), to the total circular velocity. We first use Hα rotation curves. Secondly, we use the HI rotation curves. Finally we use hybrid (Hα / HI) extended rotation curves with the stellar and the neutral gas contributions. The different models and methods used for the three datasets are given for the whole sample in the Appendix. An example of mass models for the galaxy UGC 6537 is shown in Fig. 4.2.

In this section we review the main properties and conclusions we can draw from a detailed examination of individual RC and mass models. We discuss the shape and the flat parts of the RCs; the consequence of limited spatial coverage and spatial resolution in HI RCs; the behaviour of intermediate and outer RCs; the constraints driven by the M/L estimates using stellar population models and we conclude by discussing the galaxies with a bar and with a bulge.

4.4.1 Shapes of Hα and HI rotation curves

Hα RCs display larger wiggles, asymmetries when comparing both sides, and other irregularities, than HI RCs. In the inner regions, Hα RCs are more affected than HI RCs by non-circular motions due to bars and by larger central rotation velocity peaks due to bulge components (e.g. UGC 11670). Outside the central kpc where the bar and the bulge usually dominate, Hα RCs display larger wiggles than HI RCs due to the presence of warm star forming HII regions, expanding bubbles/supernova remnants and gas acceleration/deceleration when crossing spiral arms (e.g. UGC 1913, 6537).

4.4.2 Flat parts of the rotation curves

The flat part of the RCs is clearly reached in Hα for 16/31 galaxies (UGC 1913, 2080, 2800, 4284, 4325, 4499, 5251, 5414, 6778, 7323, 8490, 9179, 9649, 10359, 11597, 11852). In some cases, the flat part in Hα does not seem to be reached while in fact it is, when comparing to the HI RC (UGC 6778, 8490, 10359, 11597, 11852). This brings to 20/31 the number of galaxies for which the flat part is reached even if the Hα data alone do not allow to estimate this fraction. In other cases, we can estimate that the flat part is reached even if the RC is still very slowly rising (e.g. UGC 3734).

14/31 Hα RCs do not reach the optical radius (UGC 1913, 2800, 4325, 5251, 5253, 7766, 8334, 8490, 10075, 11012, 11597, 11670, 11852, 11914) meaning that the other 17/31 reach it. Nevertheless only 3/31 Hα RCs do not reach 0.72 R_{opt} (UGC 1913, 8334, 11597). Among the 17 Hα RCs that reach the optical radius, only 4/17 do not reach the flat part. Surprisingly, the HI RC of UGC 11914, which is an early-type with its HI in a ring, does not reach the optical radius while the Im galaxy UGC 5414 barely reached it.

When the flat part is not reached within the optical disc, the halo parameters are generally not well modelled using the Hα data alone (e.g. UGC 2800, 4284, 4325, 4499, 6537, 6778, 8490, 11012, 11597, 11852). Exceptions to this rule are noted when a minimum disc model (M/L=0.1) is used to fit all the datasets (e.g. UGC 1913, 11670).

Even when the flat part is reached or almost reached in Hα, the halo parameters strongly depend on the extension of this flat part; a small variation of the stellar M/L may considerably change the halo parameters in the case of the Hα data alone while they do not impact so much the halo parameters in the case of the HI or hybrid RCs (e.g. UGC 2080, 3734, 4284, 4499, 6778, 9858, 9969, 12754).

When the flat part is never reached, neither in Hα nor in HI, the halo parameters obtained using the Hα RCs differ from those obtained with HI or hybrid RCs, which provides consistent results (e.g. UGC 5251, 8490, 10359, 11597, 11852).

In summary, the flat part of the RC as well as the optical radius are reached in Hα for two third of the sample even if it is sometimes barely reached. If the flat part is not reached within the optical disc, the halo parameters are poorly constrained using the Hα data alone but if the flat part is almost reached or even reached in Hα, the halo parameters strongly depend on the extension of this flat part. When the flat

part is never reached, neither in Hα nor in HI, the halo parameters are similar using HI or hybrid RCs but are different from those obtained using Hα RCs.

4.4.3 Spatial coverage and spatial resolution in the galaxy inner regions

The M/L of the stellar component (disc and/or bulge) and the halo parameters are poorly estimated in HI when the HI RC do not provide a sufficient spatial coverage or when the spatial resolution is too low to correctly sample the inner 0 to ~3 kpc of the RC (e.g. UGC 9858, 10470, 11914, 12754). In some cases, the Hα models give a RC that is less steep than the one fitted by the model when HI data are missing in the inner regions (e.g. UGC 9969, 10075) and in those cases, the M/L deduced from the HI data alone are obviously overestimated by the model.

The stellar M/L components could be identical using the 3 sets of data just by chance when the central density increases to compensate the core (e.g. UGC 1913, 2800, 2855, 4499, 9858, 10359, 10470, 11597, 11670). Even when the 3 datasets probe about the same spatial extension, i.e. when $R_{HI} \leq$ 1.2 - 1.4 R_{Ha}, the halo parameters may differ due to the difference of slope in the inner regions (e.g. UGC 2855, 7323, 9858, 11914, 12754).

When the baryonic components (disc alone or bulge plus disc) dominate the optical RC, the halo parameters are difficult to estimate from the Hα data alone; it could be overestimated for the ISO model (e.g. UGC 2080, 2800, 4284, 6778, 7323, 11012) or at the opposite underestimated for the NFW model (e.g. UGC 2080). When the RC is slightly rising both in Hα and HI, the NFW dark matter profiles provide a poorer fit to the data than the ISO ones.

In summary, the M/L of the stellar component and the halo parameters are weakly estimated in HI when the HI RC does not provide sufficient constraints in the inner regions. As a consequence, the halo parameters depend on the inner slope of the RC. The only way to estimate them correctly is to use high resolution Hα RC. If the baryonic components dominate the optical RC, the halo parameters tend to be over/under-estimated for the ISO/NFW models respectively.

4.4.4 Intermediate and outer galaxy regions

As expected, HI RCs extend further out than Hα RCs for 30/31 galaxies at the last measured velocity point. For a third of the sample HI RCs are 1 to 1.5 times more extended than the Hα RCs; for another third of the sample the HI RCs are more than 2.5 times more extended than the Hα RCs. The mean, median and standard deviation of the ratio between the HI and Hα radii, is 2.4, 2.1 and 1.5 respectively. These values are similar for early-type galaxies (i.e. galaxies below the median morphological type), for which we get respectively 2.3, 2.1 and 1.3 and for late-type galaxies (i.e. galaxies above this median), for which we measured 2.1, 1.9 and 1.1, respectively. We reach the same conclusion when studying this ratio as a function of the stellar mass and luminosity. This indicates that, on average, the HI RC extension is correlated to the Hα ones, regardless of the morphological type, the stellar mass or the luminosity of the galaxies.

Among the 31 galaxies, 12 RCs show a decrease (UGC 1913, 2080, 2855, 4284, 5253, 6778, 8334, 9179, 9969, 11597, 11852, 12754), 10 are flat (UGC 3574, 4325, 6537, 7766, 8490, 9858, 10075, 11012, 11670, 11914) and 9 are rising (UGC 2800, 3734, 4499, 5251, 5414, 7323, 9649, 10359, 10470). The case of UGC 11914 is particularly interesting: it shows a decreasing Hα RC and increasing HI RC and when mixing both sets of data in the hybrid dataset, the RC becomes finally flat. None of the HI decreasing RCs show a Keplerian decline. None of the Hα RCs is decreasing except UGC 11914 mentioned just before and UGC 9858 that exhibits 3 velocity measurements much lower than the HI velocity points at the same radius; 7/31 are flat (UGC 2855, 3574, 5253, 8334, 9969, 10470, 11670). Among those 7 flat HI RCs, 4 are finally decreasing in the outer regions in HI.

Outside the first kpc, usually smoothed out by beam smearing effects in HI (except in a few cases e.g. UGC 10470), HI and Hα RC match fairly well up to the optical radius or up to the last Hα data points in the case where the Hα RC does not reach the optical radius (e.g. UGC 11597). For very extended and decreasing HI RCs, the halo parameters deduced from extended Hα data alone match those deduced from HI and hybrid RCs, essentially because galaxies with decreasing RCs are massive galaxies showing a fast-rising inner RC, even in HI (e.g. 5253, 8334). For solid-body RC or even for rising RCs, when the HI RC does not extent further out than the Hα RC, the halo parameters match fairly well regardless of the model or of the dataset (e.g. 5414, 7323).

In summary, the HI RCs presented here are on average a little more than twice as extended than the Hα ones, nevertheless with a large standard deviation around this median value. In addition, this HI over Hα radius ratio do not strongly depend neither on the morphological type, the stellar mass, nor on the luminosity. About a third of the galaxies show HI decreasing RC, another third flat ones and the last third increasing ones. Nevertheless, none the Hα RCs is decreasing (except maybe UGC 3574). At radii for which HI RCs are not affected by beam smearing effects, HI and Hα RCs match reasonably well up to the last Hα data points if those are within the optical radius. The three datasets lead to similar halo parameters in two cases: for large galaxies displaying decreasing HI RCs and for rising RCs when the three datasets provide RCs having about the same extension.

4.4.5 M/L computed from the colour index

When the M/L are fixed by the colour index, the stellar RC (disc and/or bulge) is higher than the Hα RC at least within the first kpc for 10/31 galaxies (UGC 1913, 2800, 2855, 3734, 5253, 6537, 8334, 10470, 11597, 11670). When HI RCs are used, this happens for 13/31 galaxies (UGC 1913, 2800, 2855, 3734, 5251, 5253, 5414, 6537, 8334, 9858, 11597, 11670, 11852). It should be noted that the lack of constraints in HI results in the stellar RC does not overestimating the HI RC while it does in Hα (UGC 10470). This means that for about 2/3 of our sample of 31 galaxies, M/L fixed by the colour indices provides a possible way for mass modelling and this is not significantly different in Hα or HI.

The M/L fixed by the colour index gives larger values than those computed using ISO/MDM for 11/31 galaxies when using Hα RCs (UGC 1913, 2800, 2855, 4325, 4499, 5251, 5253, 8334, 10470, 11597, 11670) and for 15/31 galaxies when using HI RCs (UGC 1913, 2800, 2855, 4325, 4499, 5251, 5414, 7323, 7766, 8334, 9858, 10359, 11597, 11670, 11914) or even 17/31 galaxies if we consider UGC 5253 and UGC 10470 for which HI is missing in the first 5 and 3 kpc respectively and thus unable to constrain the disc.

In summary, the M/L values estimated from the colour index overestimate the disc component in one third and one half of the cases using Hα and HI RCs respectively.

4.4.6 Bulgy galaxies

20 galaxies among the 31 have a bulge component. Constrained by the physics of stellar evolution, we force the M/L of the bulge to be larger or at minimum equal to the M/L of the disc. This has some impacts on the mass distribution since the bulge component dominates the very inner central regions and furthermore minimizes the M/L of the disc, the halo central density and increases the halo core radius. Regarding the difference of inner slope in Hα and HI RCs and regarding the spatial coverage at both wavelengths this have different consequences. If the HI spatial coverage is not good in the central regions, the M/L of the bulge could be larger with respect to the constraints imposed by the high spatial coverage of Hα RC (e.g. UGC 4284, 6537, 9179, 9969, 10470, 11852, 11914, 12754) or alternatively smaller (e.g. UGC 3574, 6778, 9858, 10359, 11670). This can also be seen for galaxies with an important bulge component (L_{bulge}/L_{disc}>0.2; UGC 3574, 3734, 6778, 9858, 10470, 11852) or not (L_{bulge}/L_{disc}<0.2; e.g. UCG 9969, 10359). In addition, due to beam smearing smoothing, Hα RCs are usually steeper than the HI RCs in the inner regions, thus the bulges tend to have lower M/L with HI data than with Hα or hybrid datasets (e.g. UGC 2080, 3574, 5251, 6778, 7766, 9858).

Regarding the halo of bulgy galaxies, the halo shape at large radius is almost the same regardless of the datasets but this could be just by chance. Indeed, due to the lack of constraint in the central HI RC, the high M/L for the bulge observed in the case of steep Hα RC becomes smaller using lower resolution HI RC but this effect is compensated by a larger central halo density without significantly changing the core radius (e.g. UGC 3574, 7766).

In summary, the presence of a bulge usually leads to lower both the stellar M/L and the halo central mass density, and to increase the halo core radius. Nevertheless, it could lead to very different trends if the inner RC is affected by beam smearing or low spatial coverage because the bulge component can thus be respectively lower or higher than what it should be.

4.4.7 Barred-galaxies

22 galaxies among the 31 have a bar which is consistent with the expected ratio in the MIR. Due to non-circular motions, when the bar is aligned with the major axis position angle (PA), the slope of the RC is artificially lowered by radial motions

along the bar while, at the contrary, this slope increases when the bar is aligned with the minor axis position angle (MA) (Dicaire et al. 2008, Randriamampandry et al. 2015). If the bar ranges around the median of these two axes, the bar does not affect the slope of the RC that traces in this case only circular motions. 16 galaxies among 22 have their bar located at 20° or less from the PA and 2 have their bar located at 25° or less from the MA; the 4 others range in between.

We verify this effect by comparing the inner slopes of the RC and of the stellar RC computed from the surface density profile distribution. Among the 16 having a bar within 20° from the PA, the slope of the stellar RC overestimates the Hα RC for 10 galaxies (UGC 1913, 2800, 2855, 4284, 4499, 5251, 6537, 6778, 7323, 9969, 10470). For 6 cases they overestimate one side of the RC only. This is even worse for HI RCs: the stellar RCs overestimate the HI RC for 13 cases over 16. None of the 15 remaining galaxies shows a stellar RC overestimating the Hα RC. This could be true as well for the HI RC, nevertheless the inner constraints are often not strong enough to discard some cases. Beam smearing observed on HI RCs has the same effect than a bar aligned with the PA or diminish the effect of a bar aligned with the MA while a lack of coverage in the inner RC does not allow to observe the shape induced by the bar.

In summary, the presence of a bar changes the inner shape of RCs that are better constrained with Hα or hybrid RCs than with HI RCs.

4.5 Results

In the previous section we reviewed the main properties on individual cases. In this section we study the global properties. The aim of using different datasets to construct the mass distribution is to study how the DM halo parameters may vary when including the neutral gas component or using a hybrid rotation curve or only Hα or HI kinematics.

4.5.1 Mass models – Hα + stars

The mass distribution is determined by combining the Hα rotation curves with the W1-band photometric data for the stellar component (Korsaga et al. 2018). The distribution of the baryonic matter is characterised by the M/L ratios (Table 4.2). For

the ISO model, we find median values of 0.16, 0.55 and 0.50 $M_\odot/L_\odot$ respectively for BFM, MDM and fixed M/L. These values are consistent with Lelli et al. (2016) who found M/L minimum and maximum values of $\sim$ 0.2 and $\sim$0.7 $M_\odot/L_\odot$ respectively. The median value of the fixed M/L (0.5 $M_\odot/L_\odot$) is similar to the fixed M/L assumed by Lelli et al. (2016) and Richards et al. (2018), who used 3.6 μm photometric data. The M/L value obtained using the MDM model is $\sim$4 times higher than the value of the BFM.

For the ISO model, we study how the DM parameters (r_0, ρ_0) are distributed. The general relation between ρ_0 in $\times 10^{-3}$ $M_\odot pc^{-3}$ and r_0 in kpc is:

$$\log\ \rho_0 = (a \pm \delta a)\ \log\ r_0 + (b \pm \delta b) \tag{4.9}$$

where the parameters a, δa, b and δb are shown in Table 4.3.

Before doing the study, we exclude galaxies for which DM is not needed to build the mass models, the rotation curves are well modelled with only the contribution of the baryonic matter when using the ISO MDM (these galaxies are marked with an asterisk in Table 4.1). We find an anti-correlation between the two parameters where smaller r_0 tend to have higher ρ_0, which is in agreement with previous studies made by Kormendy & Freeman (2004), Randriamampandry & Carignan (2014). However, when looking at the relation between the DM parameters and the luminosity of the galaxies, we find no clear correlation between r_0 and the luminosity, which is not in agreement with Kormendy & Freeman (2004), Randriamampandry & Carignan (2014). As we already explained in Korsaga et al. (2019), the difference between our results and the previous authors is due to the fact that their studies were based mostly on late type galaxies (mostly composed of bulge-poor galaxies), while we cover all morphological types.

For NFW models, we can look at the relation between the concentration parameter c and the velocity at the virial radius (V_{200}). Before doing the fit, we exclude galaxies for which $c \leq 1$ and $V_{200} \geq 500$ $km\,s^{-1}$ because these values are non physical in the CDM context (de Blok et al. 2008). We find that low mass halos are more concentrated. We find a median value of $c = 9.30 \pm 1.69$ which is in agreement with the value of c = 10 found by Bullock et al. (2001) for BFM and $c = 6.60 \pm 1.58$ for fixed M/L, meaning that the halo is more concentrated for BFM compared

to fixed M/L. The general relation between c and V_{200} is:

$$\log\ c = (a \pm \delta a)\ \log\ V_{200} + (b \pm \delta b) \tag{4.10}$$

where the parameters a, δa, b and δb are shown in Table 4.3.

4.5.2 Mass models – Hα + stars & gas

The mass models are constructed in this case using Hα rotation curves, W1-band photometric data and the neutral gas component from radio HI observations. The reason for including the gas component is to check if the presence of this component could change the distribution of the luminous and DM in galaxies. For the ISO models, we find median values of M/L equal to 0.15, 0.53 and 0.50 $M_\odot/L_\odot$ respectively for BFM, MDM and fixed M/L. We see that despite a slightly smaller value for the BFM and MDM (0.15 vs 0.16 and 0.53 vs 0.55), the M/L values for fixed M/L are the same with or without considering the gas component. This may not be completely surprising since the M/L is a parameter for the stellar disc, which is in the inner parts while HI is more abundant in the outer parts.

Similarly, the relation between ρ_0 and r_0 and between the DM parameters and the luminosity of the galaxies are very similar. This is why, in the rest of the paper, we will not discuss those models anymore. As for the NFW models, we find slightly more concentrated halos with the median values of the concentration c equal to 10.0 ± 1.77 and 8.13 ± 1.62 respectively for BFM and fixed M/L.

4.5.3 Mass models – Hybrid Hα / HI + stars & gas

It is well known that HI rotation curves are well suited to study DM in the outer parts of galaxies. However, mass models parameters are very sensitive not only in the outer regions but also to the exact velocity gradient in the inner parts of the rotation curves (Blais-Ouellette et al. 2001), where the HI data can be affected by beam smearing. Therefore, the best combination is to use the high spatial resolution Hα rotation curve which probes the inner regions and extends it with the HI rotation curve in the outer parts.

To construct the mass models, we use those hybrid rotation curves, W1-band photometric data, and the neutral gas component from radio HI observations. Using

the hybrid rotation curves will allow us to see how the DM is distributed in the inner and outer regions of galaxies and also to compare the results with those obtained using only Hα (Sec. 4.5.1) and only HI (Sec. 4.5.4) kinematics. We find median values of the baryonic M/L ratio equal to 0.30, 0.57 and 0.5 $M_\odot/L_\odot$ for BFM, MDM and fixed M/L respectively. Naturally, the fixed M/L value will always remain the same. While the values of M/L using the MDM are very similar ($\sim$ 1.2 times larger) those for the BFM are around twice as large as when using only the Hα kinematics.

For the NFW models, the median value of the concentration parameter c is equal to 12.20 $\pm$ 1.64 and 10.50 $\pm$ 1.64 for BFM and fixed M/L respectively. While between 30%-50% higher than when using only the Hα kinematics, these values are still in the range $10 \leq c \leq 20$ defined by Martinsson et al. (2013). The halo is more concentrated for BFM than for fixed M/L.

4.5.4 Mass models − HI + stars & gas

The mass models are constructed in this case using the 21cm HI rotation curves, the W1-band photometry and the neutral gas component. Even, when it is already known that the HI rotation curves may suffer from beam smearing in their central parts, we decide to use these data as is in order to compare these results with what we find using only Hα kinematics (Sec. 4.5.1) or the hybrid (Hα / HI) rotation curves (Sec. 4.5.3). For the baryonic matter, we find median values of M/L corresponding to 0.26, 0.49 and 0.5 $M_\odot/L_\odot$ for BFM, MDM and fixed M/L respectively. Curiously, those values are closer to what was obtained using Hα only than using the hybrid rotation curves. For the NFW model, we find as usual that galaxies with a low V_{200} tend to have a higher concentration. The median values of the concentration c is 10.25 $\pm$ 1.99 for BFM and 9.60 $\pm$ 2.14 for fixed M/L. Those values are intermediate between what was found for Hα only and for the hybrid rotation curves.

A detailed comparison of the results for the different datasets will be presented in Sec. 4.6.

4.6 Comparison between the different datasets

The main aim of this paper is to compare the results of mass models, both for the luminous disc and for the DM halo components, using rotation curves (RCs)

Table 4.2: Median, average and standard deviation values of the M/L for ISO models.

	M/L ($M_\odot/L_\odot$) (1)	Median (2)	Average (3)	δ (4)
	BFM	0.16	0.37	0.09
Hα:	MDM	0.55	0.77	0.14
	fixed M/L	0.50	0.52	0.04
	BFM	0.26	0.44	0.08
HI:	MDM	0.49	0.62	0.09
	fixed M/L	0.50	0.52	0.04
	BFM	0.30	0.41	0.08
Hα/HI:	MDM	0.57	0.84	0.14
	fixed M/L	0.50	0.52	0.04

derived from the three different datasets: 1- using Hα kinematics only; 2- using HI kinematics only and 3- using hybrid RCs combining the high spatial resolution optical data in the inner parts to the more extended radio data in the outer parts. There are many ways to compare those results. In the first 2 papers of this series (Korsaga et al. 2018; 2019), we studied the different parameters as a function of the photometric band used.

In this paper, with the 3 datasets mentioned above, we use 2 different halo shapes (ISO and NFW), 3 different methods (BFM, MDM, fixed-M/L), 4 free parameters per model for BFM and MDM (ρ_0 the central halo mass density, r_0 the halo core radius and the disc and bulge M/L ratios) for the 20 galaxies with a bulge, 3 free parameters per model for the 11 disc-only galaxies and finally 2 or 3 free parameters for disc-only and bulge galaxies respectively for the fixed (by colour) M/L models. So, the number of free parameters to explore per galaxy ranges from 48 for disc-only galaxies to 66 for galaxies with a bulge. This is because of this huge number of free parameters that we force the M/L of the disc and of the bulge to be the same for the fixed M/L model.

Naturally, it is not possible to present here a systematic search of the whole parameter space. Instead, we tabulate some key mean values and illustrate the most important relations in different plots. In this section, we study the correlations

between the DM parameters of ISO and NFW models (Table 4.3 & Figs. 4.3 to 4.7) and in Table 4.4, we discuss the values of those parameters.

For the ISO models, let us first concentrate on the first 3 rows of Table 4.3 and on Fig. 4.3. We see that the agreement is very good for the three datasets for the BFM, especially between the Hα only and the HI only, as compared to the hybrid RCs. On the other hand, the best agreement is between Hα & hybrid RCs for the MDM and hybrid RCs & HI for the fixed M/L models. Clearly, the relation between the parameters of the ISO model varies from one dataset to the other depending on the fitting technique used. So, the relation between the parameters of the ISO functional form (ρ_0 & r_0) vary by $\sim 20\%$ and eq. 4.9 becomes:

$$\log\ \rho_0 = (-1.45 \pm 0.25)\ \log\ r_0 - (0.60 \pm 0.15) \tag{4.11}$$

Figs.4.4 to 4.6 explore the relations between the ISO DM parameters and the absolute galaxy luminosity M_B. There is no clear trend of those parameters as a function of the luminosity. There may however exist a trend with morphological types but a larger sample would be necessary to confirm this. This was already suggested in Korsaga et al. (2018; 2019).

Table 4.4 allows us to examine the physical values of the DM parameters. For ISO (r_0 & ρ_0), it can be seen that the three datasets give similar estimates of the parameters with the BFM having the more concentrated halos (2.54 ± 0.15 kpc & 75 ± 25 $\times 10^{-3}$ $M_\odot pc^{-3}$), followed by the fixed M/L (3.05 ± 0.25 kpc & 35 ± 4 $\times 10^{-3}$ $M_\odot pc^{-3}$), and finally, by the MDM (4.05 ± 0.25 kpc & 26.5 ± 3.0 $\times 10^{-3}$ $M_\odot pc^{-3}$). Naturally, the result for the MDM is expected by definition since maximizing the M/L necessarily minimize the halo by pushing it out. Clearly, the differences between the fitting procedures are larger than between the different datasets.

It is interesting to note in the last 3 rows of Table 4.3 and in Fig. 4.7, that the relation between the parameters of the NFW functional form (c & V_{200}) is less affected by either different datasets (Hα, HI or hybrid) or fitting techniques (BFM or fixed M/L), which is quite different from the situation with ISO models. The parameters of the relation vary by less than 10% and eq. 4.10 becomes:

$$\log\ c = (-1.16 \pm 0.12)\ \log\ V_{200} + (3.46 \pm 0.30) \tag{4.12}$$

This suggests that Hα kinematics in the inner parts is sufficient to characterize a

NFW halo. As for the value of the concentration parameter c, we get from all the datasets and fitting techniques c = 10 ± 2, which is exactly the value found by Bullock et al. (2001), who did Λ-CDM N-body simulations and had a statistical sample of ∼ 5000 halos in the range $10^{11}-10^{14}h^{-1}M_{\odot}$.

Figs. 4.8 & 4.9 show the variation of the NFW parameters (c & V_{200}) as a function of the luminosity (M_B). We can see that c is nearly constant. However, while V_{200} seems also to be constant when using only Hα kinematics, HI and hybrid RCs suggest that it increases with luminosity.

The models are given in the Appendix. It is interesting to look closely at the last column on the right in which we plot the Hα and HI kinematical data with the different fits for the halo components of the three datasets using the Hα, HI and hybrid RCs. For 2/3 of the sample, the halo components are very similar while for the other 1/3, the Hα halo component is much less constrained than when using the HI or hybrid data.

4.7 Summary and conclusions

We have studied the mass distribution of a sample of 31 galaxies covering morphological types from Sa to Irr. We first constructed the mass models using the optical high resolution Hα rotation curves using W1-band surface brightness profiles. Secondly, the mass models were constructed using HI kinematics instead of Hα rotation curves, with W1-band surface brightness profiles and moreover we add the neutral gas component obtained from radio HI observations. Thirdly, we combine the Hα with HI rotation curves as well as the neutral gas component. We call this dataset the hybrid Hα / HI rotation curves, and also use the W1-band surface brightness profiles to build the mass models. To study the mass distribution, we used two models, the pseudo-isothermal sphere (ISO) and the Navarro-Frenk-White (NFW) with different techniques: a best fit model (BFM), a maximum disc model (MDM) and a fixed M/L calculated using the (W1 − W2) mid-IR colour.

Comparing the different datasets we find:

1. High resolution Hα data are needed to constrain the inner part of the RCs, in particular when a bar or bulge is present. In, those cases, mass models are better constrained with Hα or hybrid RCs than with HI RCs alone.

Table 4.3: Relation between the DM halo parameters for ISO and NFW models.

		a	δ a	b	δ b
Hα: ρ_0 vs r_0 (ISO)	BFM	-1.49	0.22	-0.45	0.11
	MDM	-1.48	0.23	-0.56	0.15
	fixed M/L	-1.07	0.17	-0.67	0.12
Hα/HI: ρ_0 vs r_0 (ISO)	BFM	-1.66	0.16	-0.51	0.08
	MDM	-1.71	0.19	-0.64	0.13
	fixed M/L	-1.87	0.15	-0.42	0.09
HI: ρ_0 vs r_0 (ISO)	BFM	-1.42	0.19	-0.66	0.11
	MDM	-1.09	0.27	-0.95	0.17
	fixed M/L	-1.66	0.16	-0.57	0.10
Hα: c vs V_{200} (NFW)	BFM	-1.21	0.16	+3.68	0.38
	fixed M/L	-0.99	0.16	+3.09	0.37
Hα/HI: c vs V_{200} (NFW)	BFM	-1.35	0.21	+3.87	0.46
	fixed M/L	-1.14	0.36	+3.38	0.75
HI: c vs V_{200} (NFW)	BFM	-1.12	0.21	+3.37	0.45
	fixed M/L	-0.96	0.25	+2.94	0.53

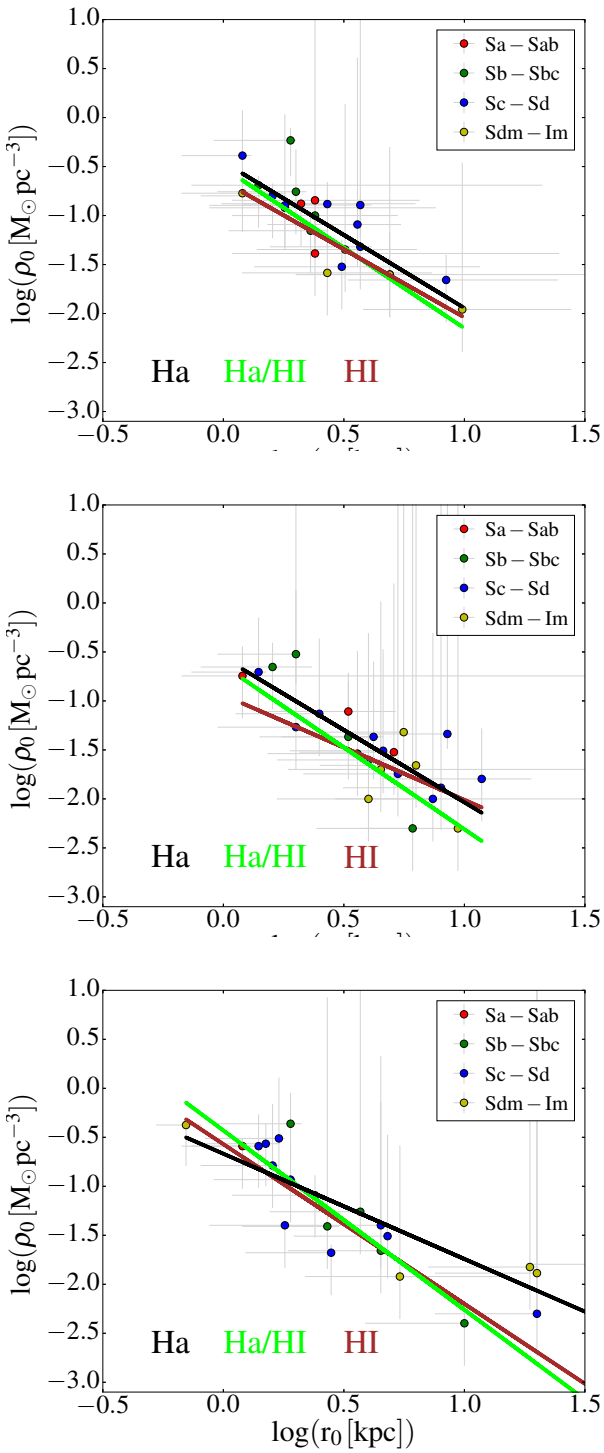

Figure 4.3: From top to bottom: Central halo density versus halo core radius for ISO BFM, MDM and Fixed M/L respectively. The points are obtained using Hα rotation curves. The black line represents the fits of the points. The lime and red lines represent the fit found using the hybrid and HI rotation curves respectively.

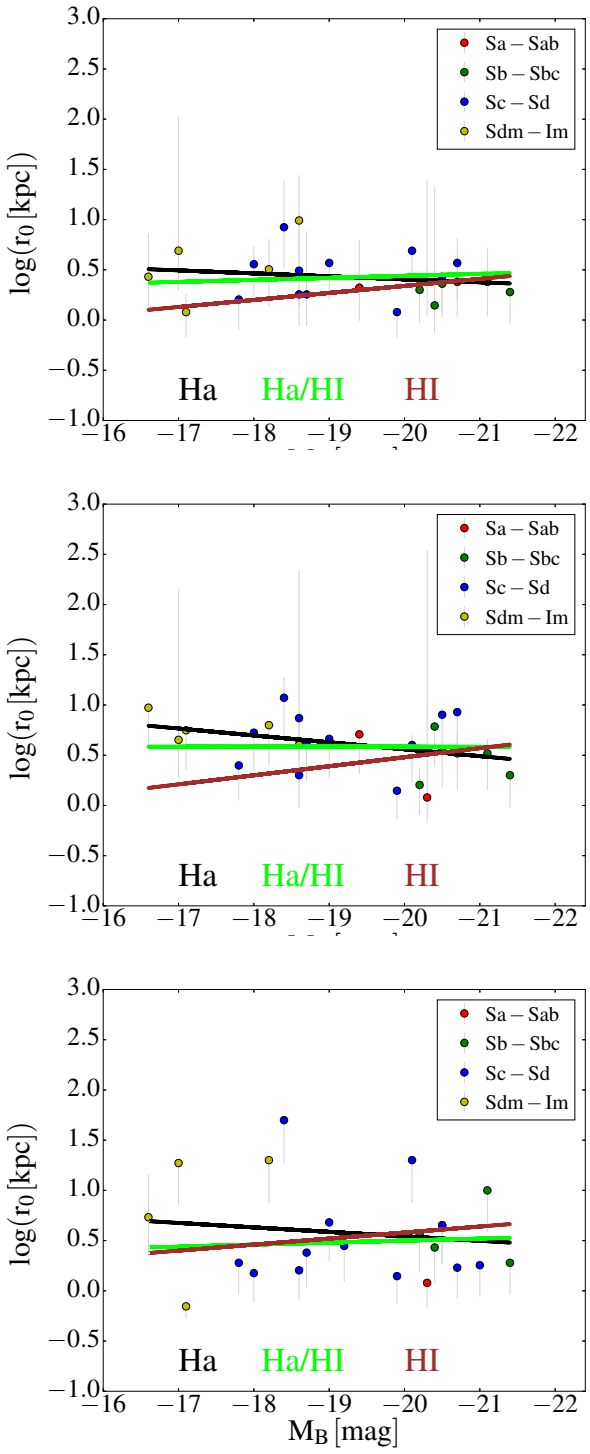

Figure 4.4: Plot of r_0 vs M_B for ISO models - from top to bottom: BFM, MDM and fixed M/L.

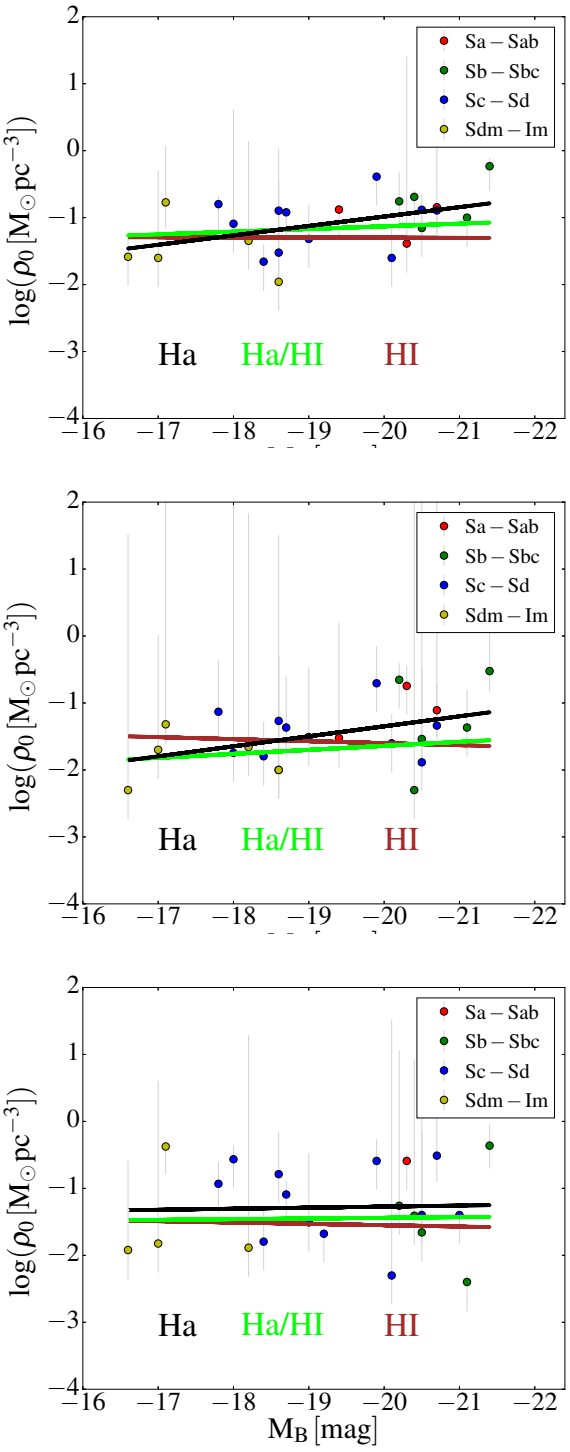

Figure 4.5: Plot of ρ_0 vs M_B for ISO models - from top to bottom: BFM, MDM and fixed M/L.

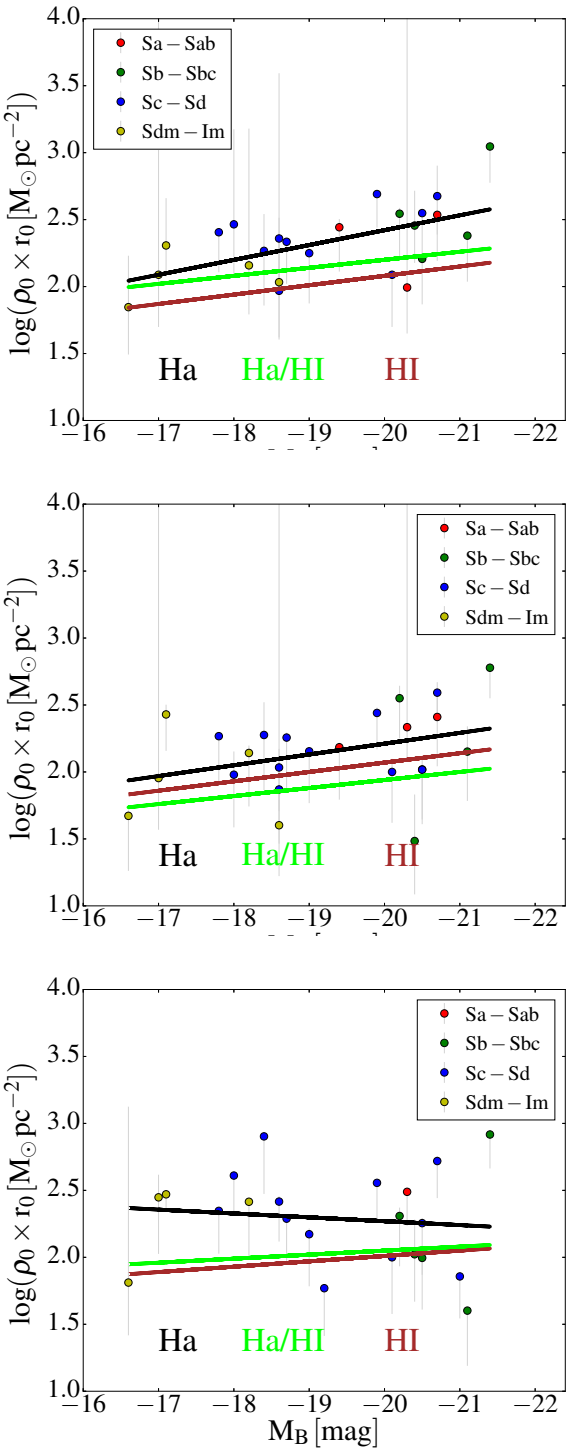

Figure 4.6: Plot of $\rho_0 \times r_0$ vs M_B for ISO models - from top to bottom: BFM, MDM and fixed M/L.

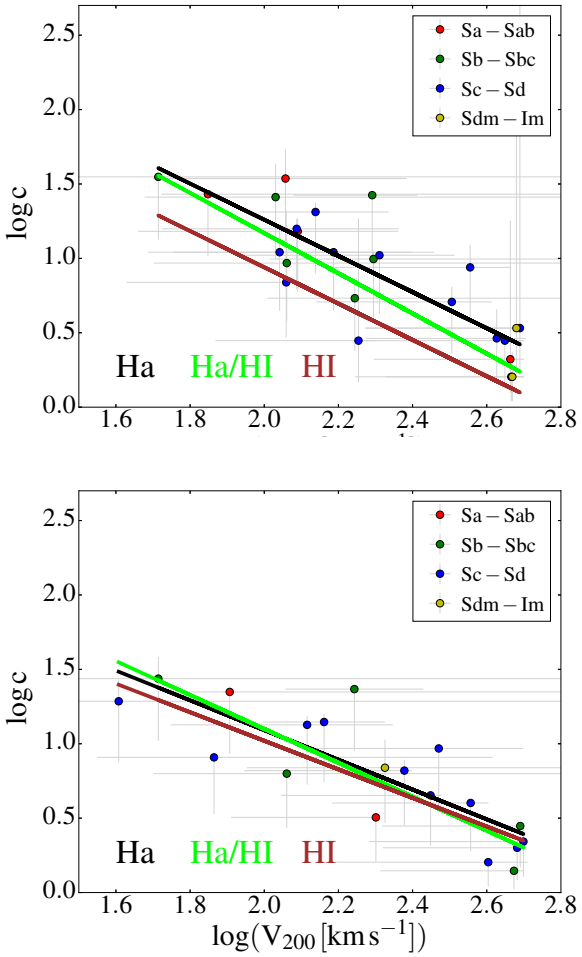

Figure 4.7: Plot of c vs V_{200} for the NFW models: top for the BFM and bottom for fixed M/L.

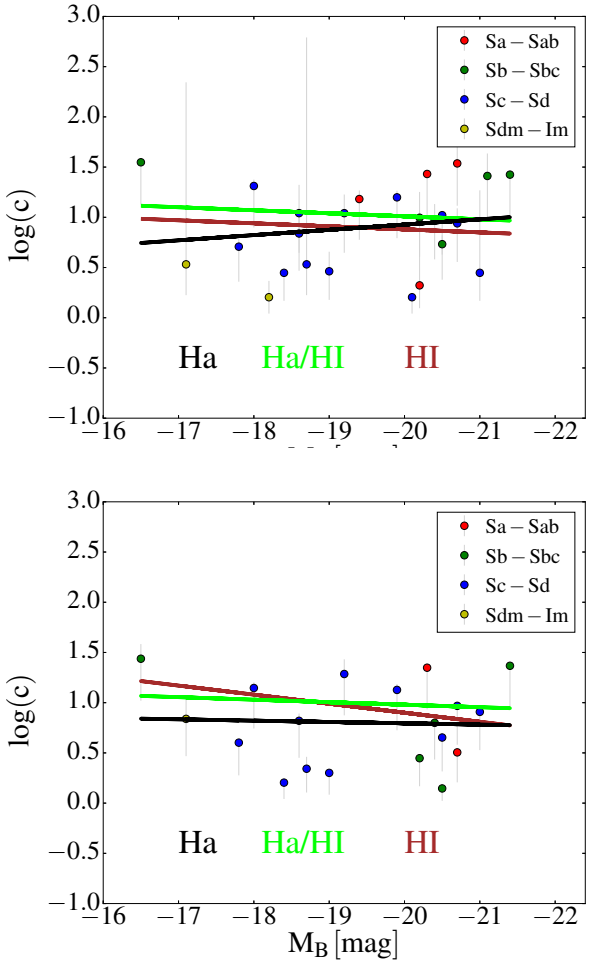

Figure 4.8: Plot of c vs M_B for the NFW models: top for the BFM and bottom for fixed M/L.

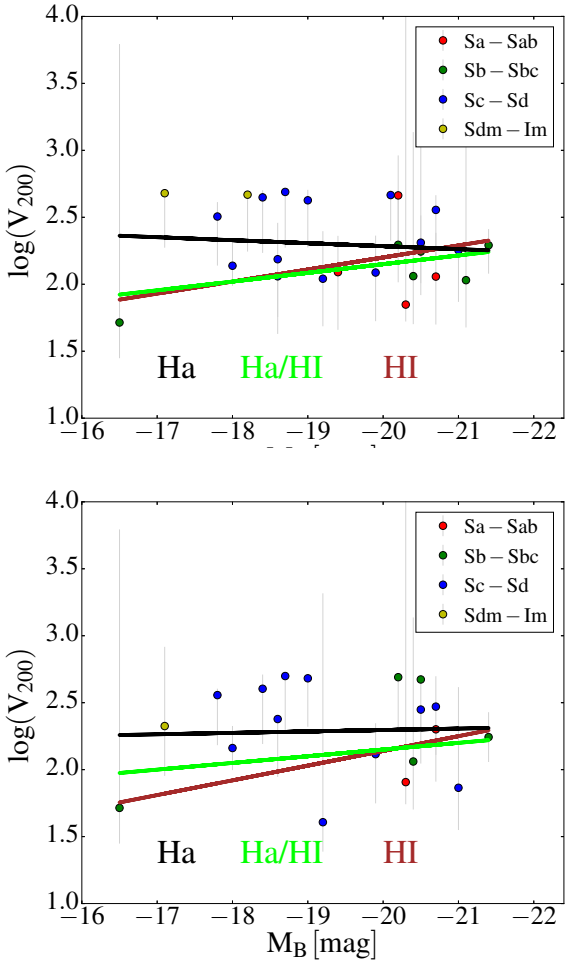

Figure 4.9: Plot of V_{200} vs M_B for the NFW models: top for the BFM and bottom for fixed M/L.

Table 4.4: Median, average and standard deviation values of the DM halo parameters for ISO and NFW models.

		Median (1)	Average (2)	δ (3)
Hα: r_0 (kpc) (ISO)	BFM	2.25	3.80	0.75
	MDM	3.85	4.87	0.60
	fixed M/L	2.95	4.55	0.72
Hα/HI: r_0 (kpc) (ISO)	BFM	2.50	3.85	0.76
	MDM	3.90	4.95	0.62
	fixed M/L	3.20	4.70	0.76
HI: r_0 (kpc) (ISO)	BFM	2.4	3.74	0.59
	MDM	3.90	4.30	0.51
	fixed M/L	3.20	5.22	0.81
Hα: ρ_0 ($\times 10^{-3}$ $M_\odot pc^{-3}$) (ISO)	BFM	110.00	125.25	26.08
	MDM	30.50	63.29	15.71
	fixed M/L	40.00	119.32	29.19
Hα/HI: ρ_0 ($\times 10^{-3}$ $M_\odot pc^{-3}$) (ISO)	BFM	66.50	111.17	22.90
	MDM	23.00	46.78	11.73
	fixed M/L	37.00	96.95	26.05
HI: ρ_0 ($\times 10^{-3}$ $M_\odot pc^{-3}$) (ISO)	BFM	46.00	112.24	29.96
	MDM	25.00	61.82	20.79
	fixed M/L	31.00	105.48	35.11
Hα: c (NFW)	BFM	9.30	11.96	2.05
	fixed M/L	6.60	9.40	1.83
Hα/HI: c (NFW)	BFM	12.2	13.81	1.64
	fixed M/L	10.50	12.11	1.64
HI: c (NFW)	BFM	10.25	14.08	1.99
	fixed M/L	9.6	12.49	2.14
Hα: V_{200} ($km\,s^{-1}$) (NFW)	BFM	179.50	243.18	30.19
	fixed M/L	211.60	249.62	35.58
Hα/HI: V_{200} ($km\,s^{-1}$) (NFW)	BFM	114.10	147.95	18.33
	fixed M/L	113.60	131.42	13.79
HI: V_{200} ($km\,s^{-1}$) (NFW)	BFM	118.20	165.51	22.51
	fixed M/L	121.95	150.61	24.15

2. The flat part of the RC and the optical radius are reached in Hα for two thirds of the sample but when the flat part is not reached with the Hα data only, additional HI data are mandatory to derive the halo's parameters.

3. The sample is divided into three subsamples with an almost equivalent size, having respectively rising, flat and decreasing HI RCs, but none of the Hα RC is decreasing. Hα and HI RCs match fairly well outside their rising part, up to the optical radius, when reached in Hα.

4. M/L values estimated from WISE colour indices make the stellar component velocity higher than the Hα and HI RCs in one third and half of the cases respectively.

The objective of this work is to study how the baryonic and DM halo's parameters distributions are recovered when including the HI gas component or using hybrid rotation curves instead of only Hα or HI rotation curves.

We find the following results about the baryonic component of ISO models:

1. For the mass models using Hα rotation curves with the W1-band surface brightness profiles, we find that ISO and NFW models describe well the rotation curves but ISO gives better fits. ISO with the MDM technique gives also good fits, but we find that $\sim$ 20% of galaxies do not need a DM halo to fit their rotation curves, these galaxies are well fitted with only a baryonic component (e.g., UGC 2080, UGC 9649). For the fixed M/L technique, the fit is acceptable for both ISO and NFW, however, we find non-physical fits for $\sim$ 20% of galaxies (e.g., UGC 3734, UGC 11670). We find median values of M/L equal to 0.16, 0.55 and 0.50 $M_\odot/L_\odot$ for ISO with BFM, MDM and fixed M/L respectively.

2. For the mass models constructed using Hα rotation curves, the W1-band surface brightness profiles and neutral gas component, we find median values of M/L for BFM and MDM equal to 0.15 and 0.53 $M_\odot/L_\odot$ respectively, which is close to what was found in (i).

3. For the mass models built using HI rotation curves, the W1-band surface brightness profiles and the neutral gas component, the M/L median values are 0.26and 0.49 $M_\odot/L_\odot$ for BFM and MDM respectively.

4. For the mass models built using the hybrid rotation curves, the W1-band surface brightness profiles and the neutral gas component, we find that only ~ 9% of galaxies do not need a DM halo to fit their rotation curves. In this case the median values of M/L for BFM and MDM are respectively 0.30 and 0.57 $M_\odot/L_\odot$ which are higher to those found in (i, ii & iii).

5. The M/L values are higher when using the hybrid rotation curves than only Hα or HI rotation curves.

The main results for the DM component are:

1. The dark matter halo is less concentrated when using the hybrid rotation curves than only Hα rotation curves.

2. The relation between the parameters of the ISO models varies from one dataset to the other (Hα RCs, hybrid RCs or HI RCs) depending of the fitting technique (BFM, MDM or fised M/L) used.

3. For the hybrid rotation curves, we find higher M/L values, lower central densities ρ_0 for ISO DM and higher concentration c for NFW DM halos than when using purely Hα kinematics. The same is true when comparing purely HI and purely Hα rotation curves.

4. The relation between the parameters of the NFW functional form (c & V_{200}) is less affected by either different dataset (Hα, HI or hybrid) or fitting technique (BFM or fixed M/L) than the one between the parameters of the ISO (ρ_0 & r_0) models. This means that Hα kinematics in the inner parts is sufficient to characterize a NFW halo.

5. The correlations between the dark matter halo parameters and the luminosity of the galaxy remain the same whatever the rotation curve used: optical rotation curve with and without gas component, optical rotation curve extended with HI rotation curve or HI rotation curve alone.

6. The differences between the fitting procedures are larger than between the different datasets.

This work is not intended to describe a representative sample of galaxies but rather a sample of galaxies of different morphological types, sizes and brightnesses. These results should be confirmed by studying a larger sample, representative of a complete universe volume.

Acknowledgements

Most of the research of MK was done while she was having a PhD Scholarship from the Science faculty of the University of Cape Town. CC's work is based upon research supported by the South African Research Chairs Initiative (SARChI) of the Department of Science and Technology (DST), the Square Kilometre Array South Africa (SKA SA) and the National Research Foundation (NRF). We acknowledge financial support from "Programme National de Cosmologie et Galaxies" (PNCG) funded by CNRS/INSU-IN2P3-INP (Centre national de la recherche scientifique/Institut national des sciences de l'Univers - Institut national de physique nucleaire et de physique des particules - Institut de physique), CEA (Commissariat à l'Energie atomique et aux Energies alternatives) and CNES (Centre national d'etudes spatiales) in France.

A Appendix: Mass models of galaxies

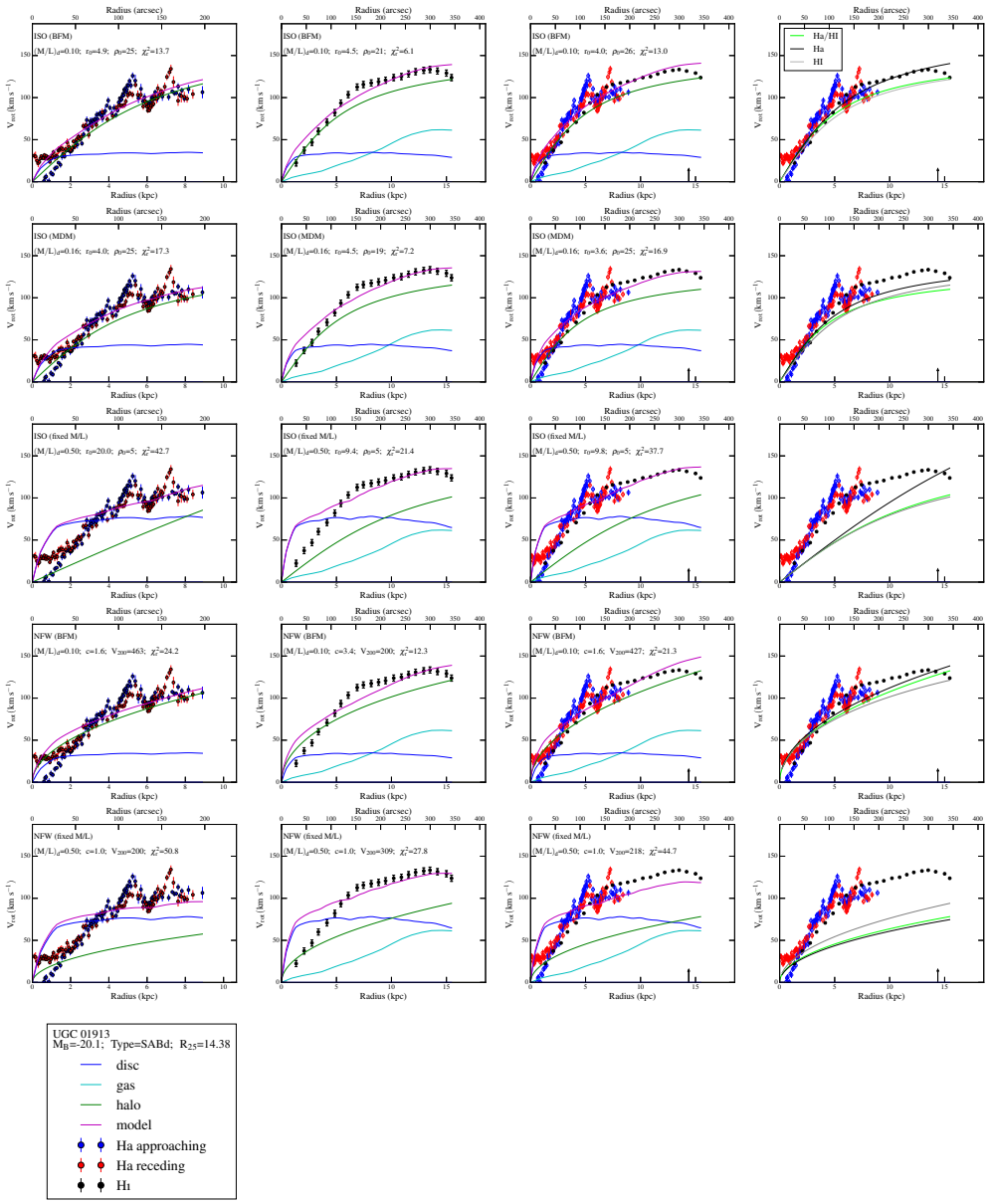

Figure 4.10: Mass models of galaxies. Lines 1-3: pseudo-isothermal sphere density profiles (ISO). Lines 4-5: Navarro, Frenk & White density profiles (NFW). First line: Best Fit Model (BFM). Second line: Maximum disc Model (MDM). Third line: Mass-to-Light ratio M/L fixed using W1 - W2 colour. Fourth line: Best Fit Model (BFM). Fifth line: Mass-to-Light ratio M/L fixed using W1 - W2 colour. The name of the galaxy, its B-band absolute magnitude, morphological type and optical radius in kpc have been indicated in the insert located at line 6. Row 1: Models using Hα rotation curves and no neutral gas distribution. Row 2: Models using HI rotation curves. Row 3: Models using the hybrid Hα/ HI rotation curves. Row 4: We show the halo derived from the different rotation curves. For each model, the fitted parameters and the reduced χ^2 have been indicated in each sub-panel. The legends are the same for the remaining figures.

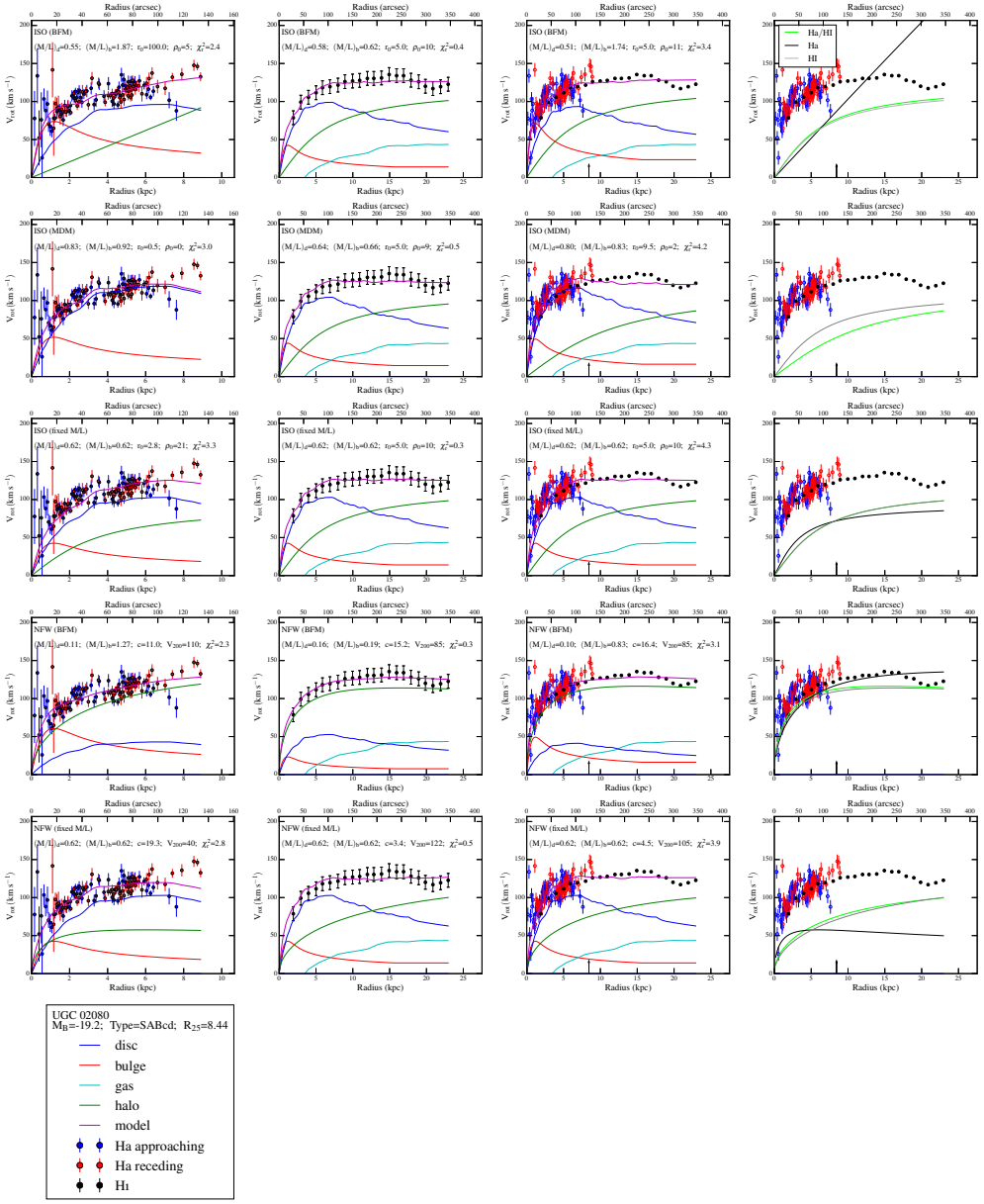
UGC 02080
M_B=-19.2; Type=SABcd; R_25=8.44
disc
bulge
gas
halo
model
Ha approaching
Ha receding
HI
Ha /HI
Radius (kpc)
Radius (arcsec)
V_rot (km s^-1)

Figure 4.11

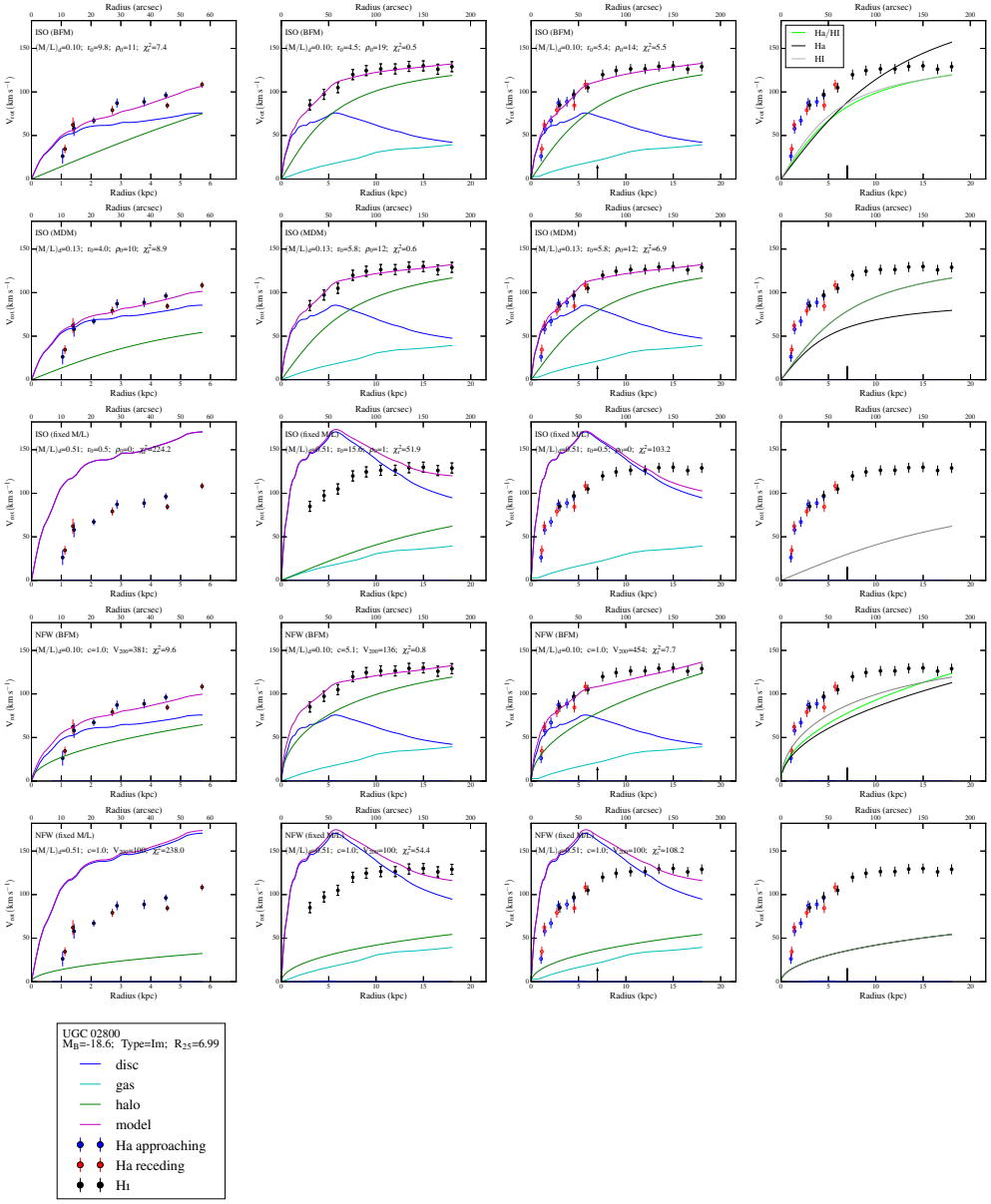
ISO (BFM)
ISO (MDM)
ISO (fixed M/L)
NFW (BFM)
NFW (fixed M/L)
Ha/HI
Ha
HI
Radius (arcsec)
Radius (kpc)
V_rot (km s^-1)
UGC 02800
M_B=-18.6; Type=Im; R_25=6.99
disc
gas
halo
model
Ha approaching
Ha receding
HI

Figure 4.12

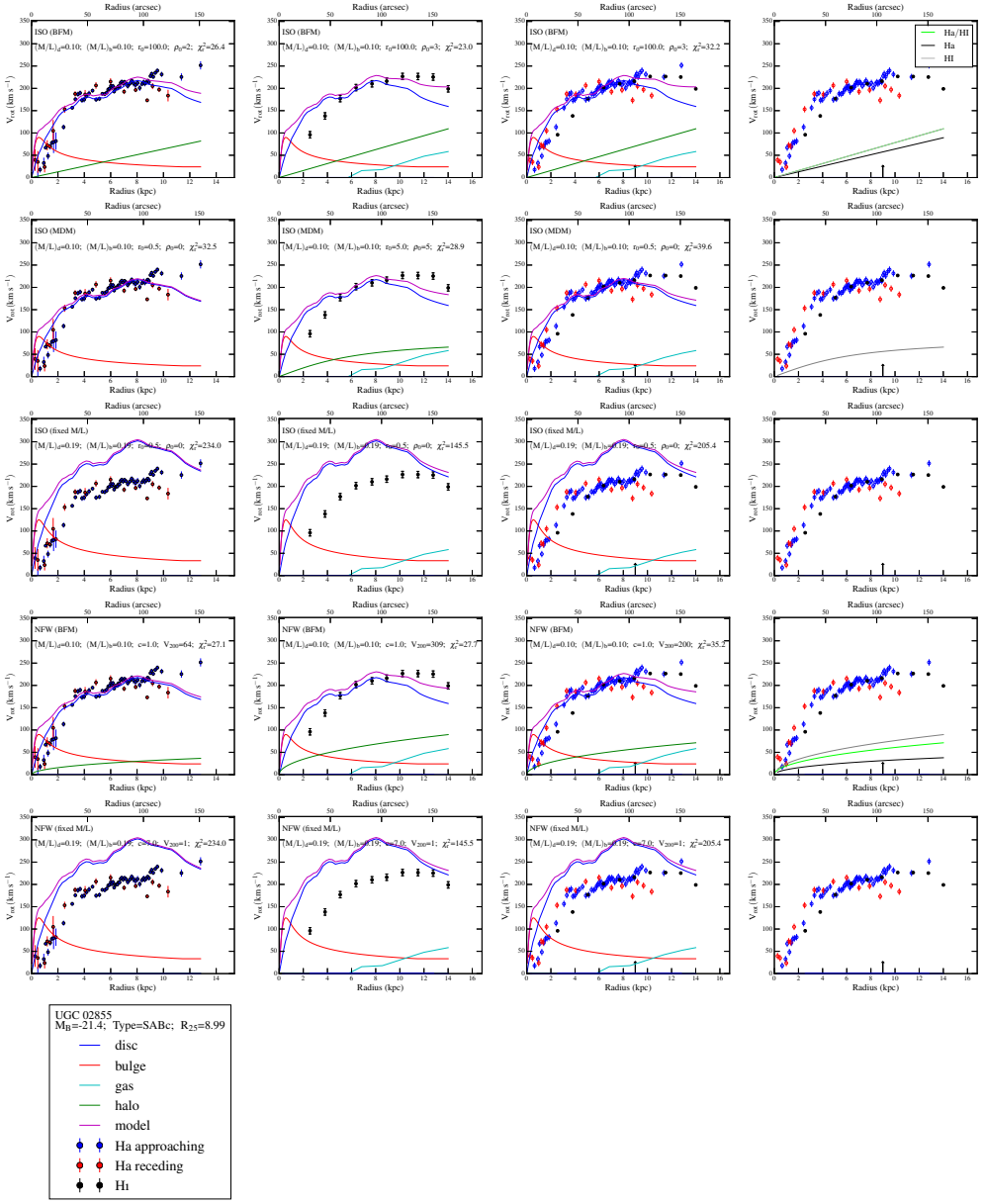
UGC 02855
M_B=-21.4; Type=SABc; R_{25}=8.99
disc
bulge
gas
halo
model
Ha approaching
Ha receding
HI
Ha/HI
Ha
HI
Radius (arcsec)
Radius (kpc)
V_{rot} (km s^{-1})

Figure 4.13

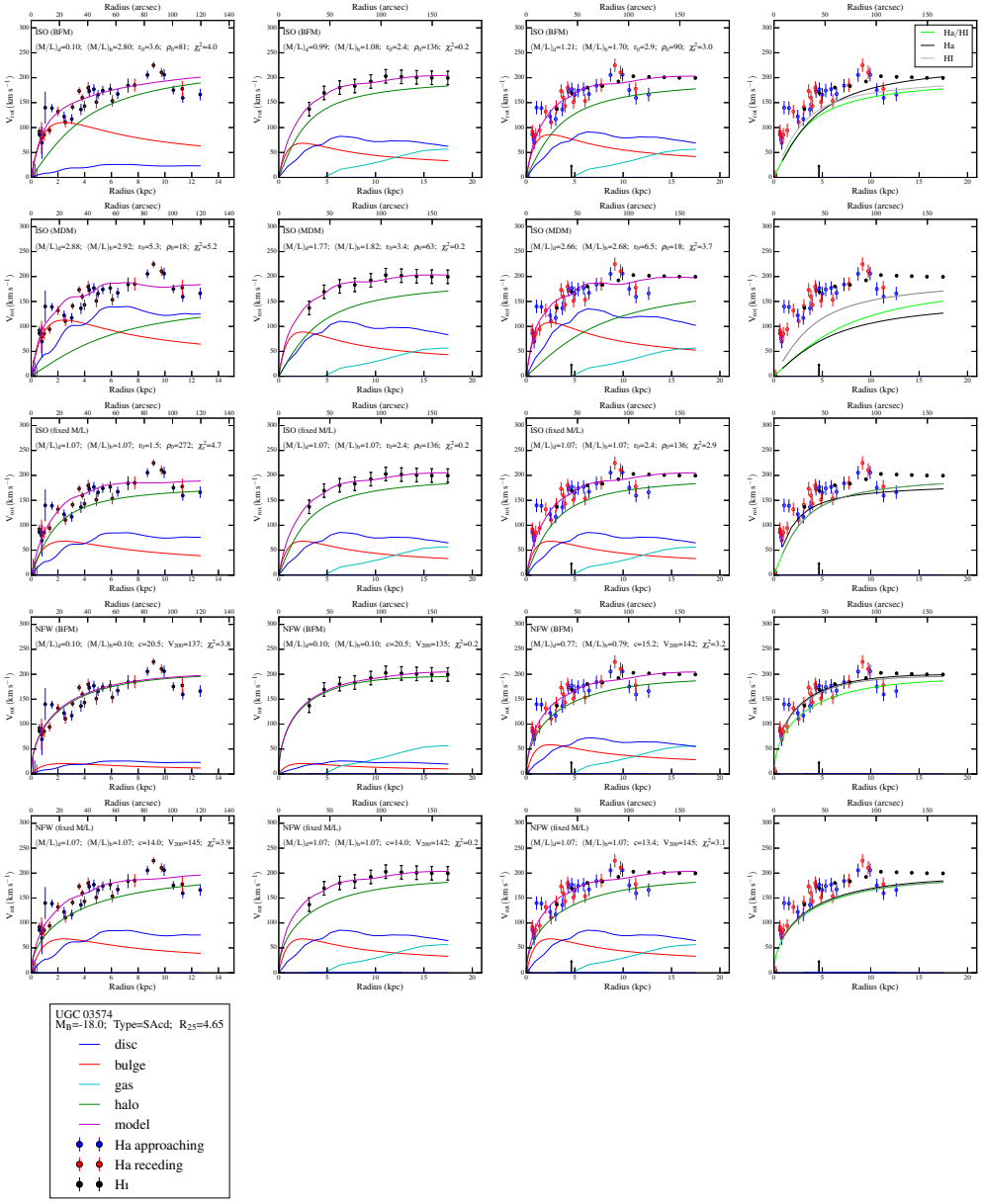
ISO (BFM)
ISO (MDM)
ISO (fixed M/L)
NFW (BFM)
NFW (fixed M/L)
Ha/HI
Ha
HI
Radius (arcsec)
Radius (kpc)
UGC 03574
M_B=-18.0; Type=SAcd; R_25=4.65
disc
bulge
gas
halo
model
Ha approaching
Ha receding
HI

Figure 4.14

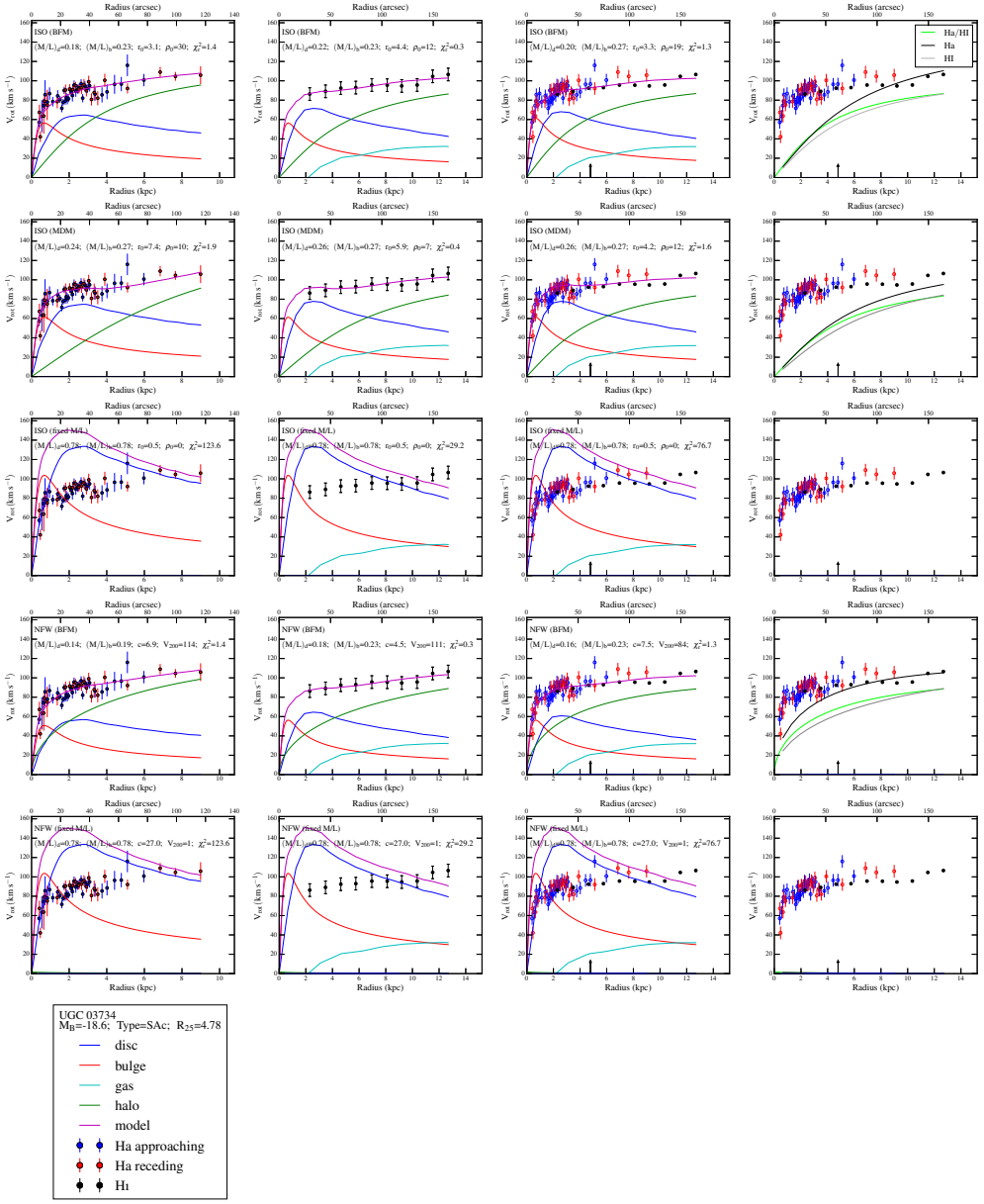
ISO (BFM)
ISO (MDM)
ISO (fixed M/L)
NFW (BFM)
NFW (fixed M/L)
Ha/HI
Ha
HI
Radius (arcsec)
Radius (kpc)
V_rot (km s^-1)
UGC 03734
M_B=-18.6; Type=SAc; R_25=4.78
disc
bulge
gas
halo
model
Ha approaching
Ha receding
HI

Figure 4.15

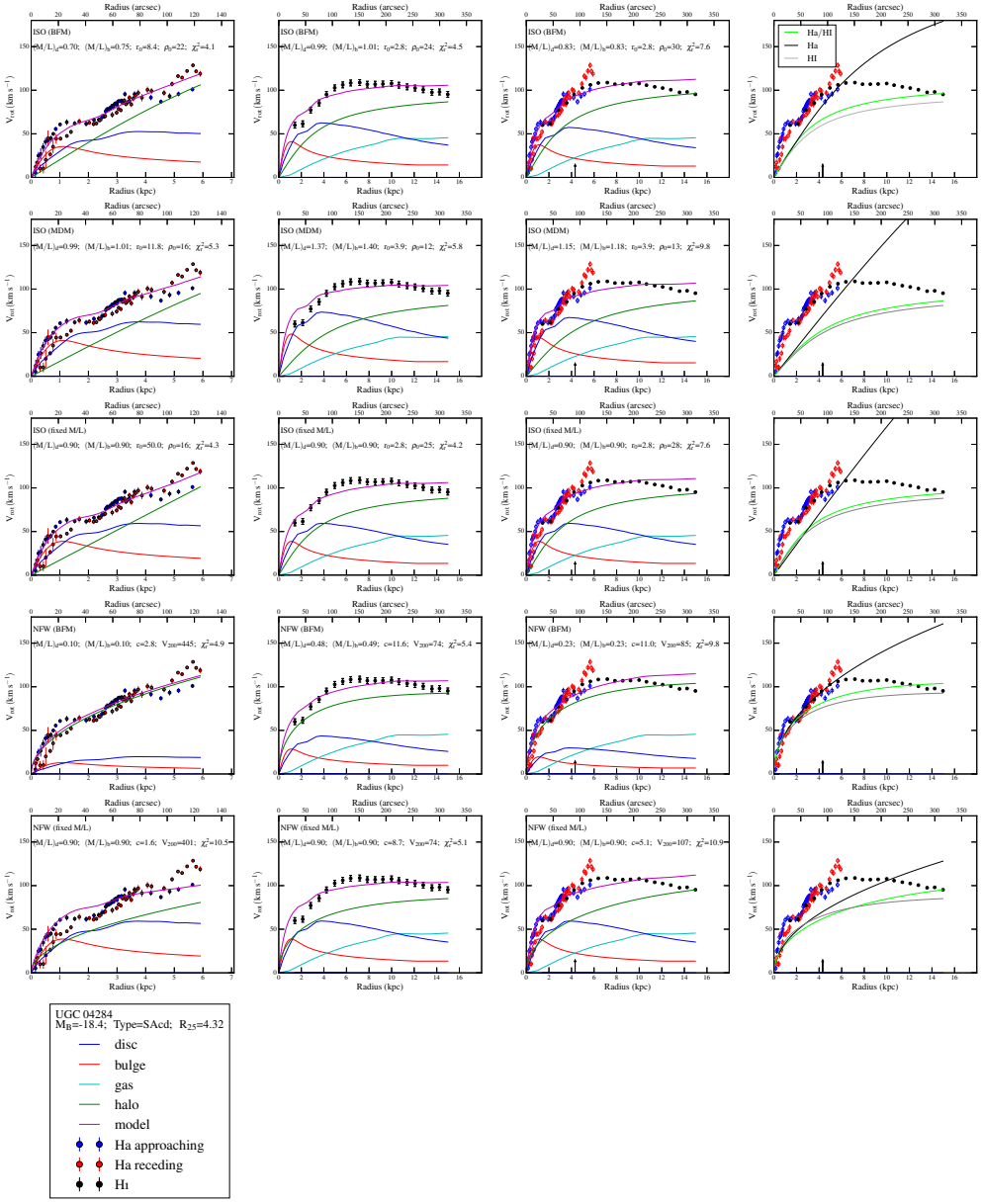
ISO (BFM)
ISO (MDM)
ISO (fixed M/L)
NFW (BFM)
NFW (fixed M/L)
Ha/HI
Ha
HI
Radius (arcsec)
Radius (kpc)
UGC 04284
M_B=-18.4; Type=SAcd; R_25=4.32
disc
bulge
gas
halo
model
Ha approaching
Ha receding
HI

Figure 4.16

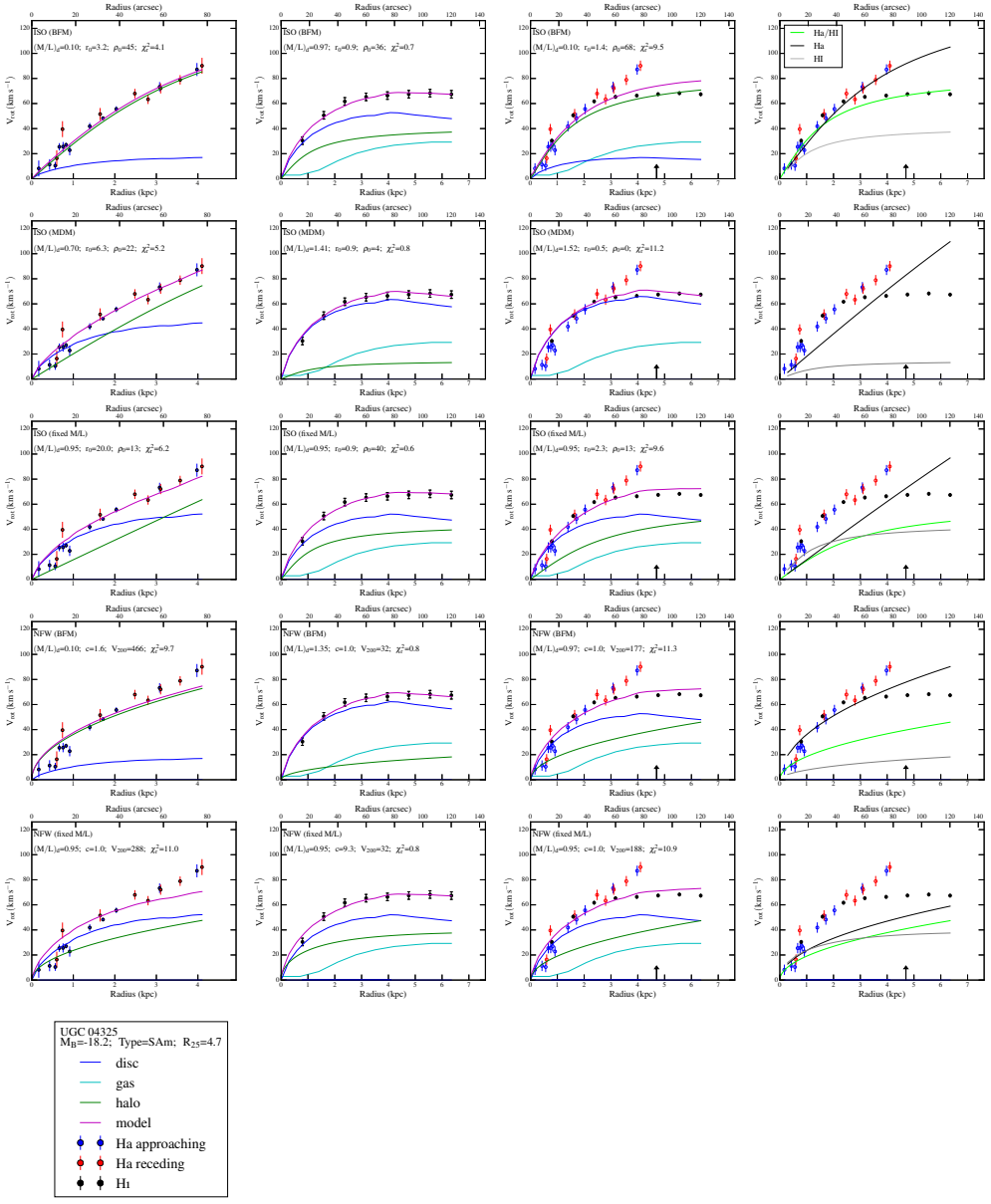
TSO (BFM)
TSO (MDM)
TSO (fixed M/L)
NFW (BFM)
NFW (fixed M/L)
Ha/HI
Ha
HI
Radius (arcsec)
Radius (kpc)
V_{rot} (km s^{-1})
UGC 04325
M_B=-18.2; Type=SAm; R_{25}=4.7
disc
gas
halo
model
Ha approaching
Ha receding
HI

Figure 4.17

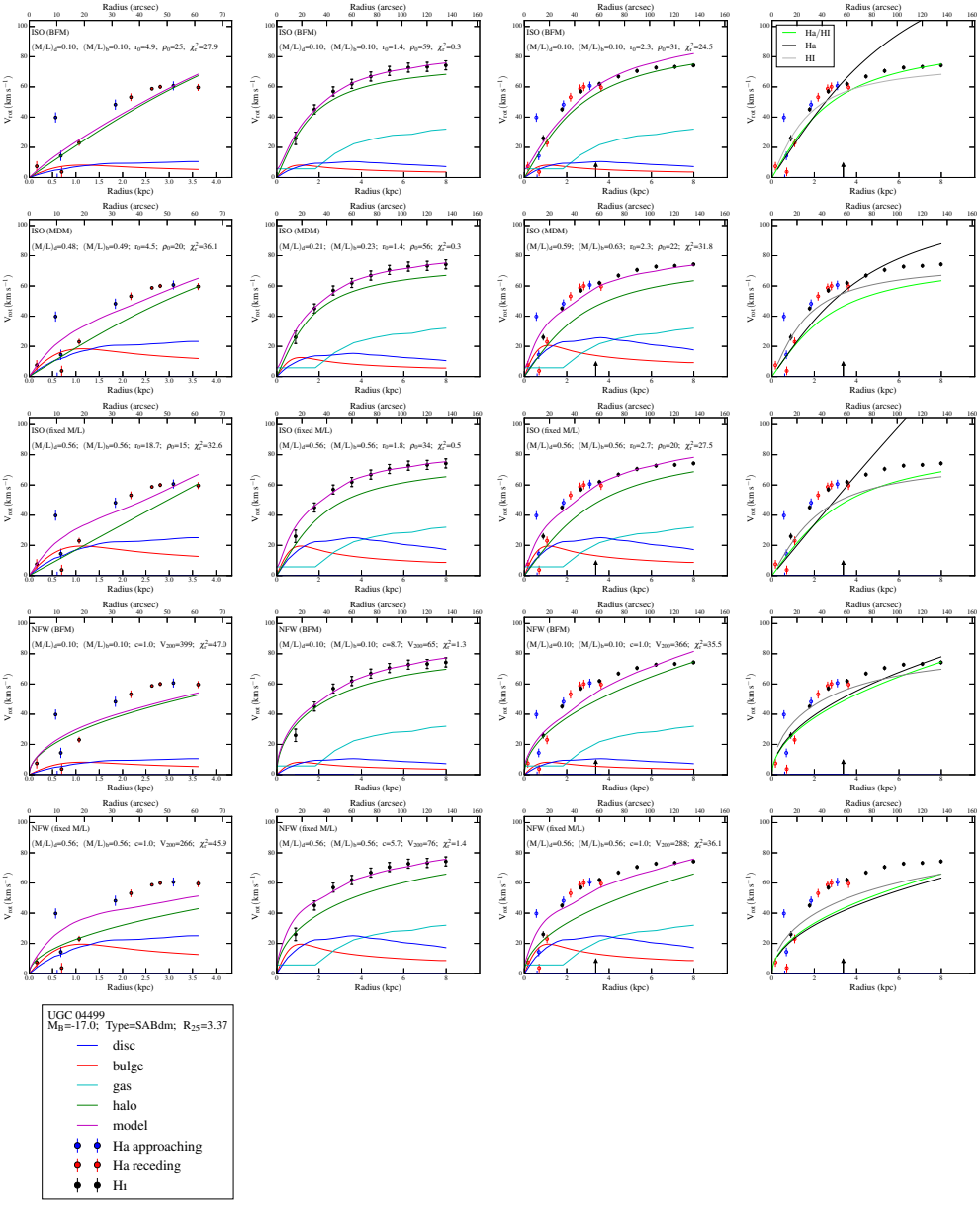
ISO (BFM)
(M/L)d=0.10; (M/L)b=0.10; rb=4.9; ρ0=25; χ2=27.9
ISO (BFM)
(M/L)d=0.10; (M/L)b=0.10; rb=1.4; ρ0=59; χ2=0.3
ISO (BFM)
(M/L)d=0.10; (M/L)b=0.10; rb=2.3; ρ0=31; χ2=24.5
Hα/HI
Hα
HI
ISO (MDM)
(M/L)d=0.48; (M/L)b=0.49; rb=4.5; ρ0=20; χ2=36.1
ISO (MDM)
(M/L)d=0.21; (M/L)b=0.23; rb=1.4; ρ0=56; χ2=0.3
ISO (MDM)
(M/L)d=0.59; (M/L)b=0.63; rb=2.3; ρ0=22; χ2=31.8
ISO (fixed M/L)
(M/L)d=0.56; (M/L)b=0.56; rb=18.7; ρ0=15; χ2=32.6
ISO (fixed M/L)
(M/L)d=0.56; (M/L)b=0.56; rb=1.8; ρ0=34; χ2=0.5
ISO (fixed M/L)
(M/L)d=0.56; (M/L)b=0.56; rb=2.7; ρ0=20; χ2=27.5
NFW (BFM)
(M/L)d=0.10; (M/L)b=0.10; c=1.0; V200=399; χ2=47.0
NFW (BFM)
(M/L)d=0.10; (M/L)b=0.10; c=8.7; V200=65; χ2=1.3
NFW (BFM)
(M/L)d=0.10; (M/L)b=0.10; c=1.0; V200=366; χ2=35.5
NFW (fixed M/L)
(M/L)d=0.56; (M/L)b=0.56; c=1.0; V200=266; χ2=45.9
NFW (fixed M/L)
(M/L)d=0.56; (M/L)b=0.56; c=5.7; V200=76; χ2=1.4
NFW (fixed M/L)
(M/L)d=0.56; (M/L)b=0.56; c=1.0; V200=288; χ2=36.1
Radius (arcsec)
Radius (kpc)
Vrot (km s−1)
UGC 04499
MB=-17.0; Type=SABdm; R25=3.37
disc
bulge
gas
halo
model
Ha approaching
Ha receding
HI

Figure 4.18

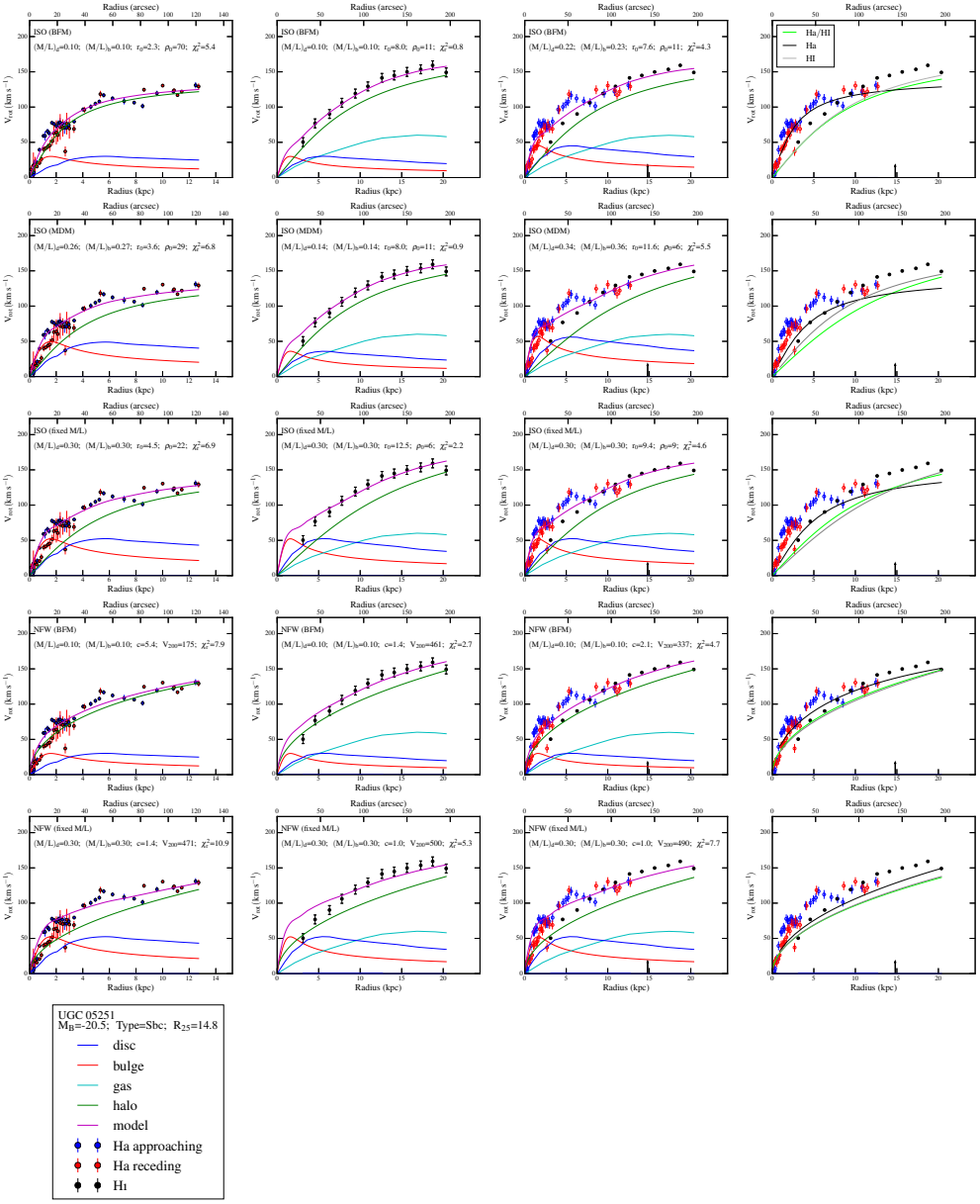
UGC 05251
MB=-20.5; Type=Sbc; R25=14.8
disc
bulge
gas
halo
model
Ha approaching
Ha receding
HI

Figure 4.19

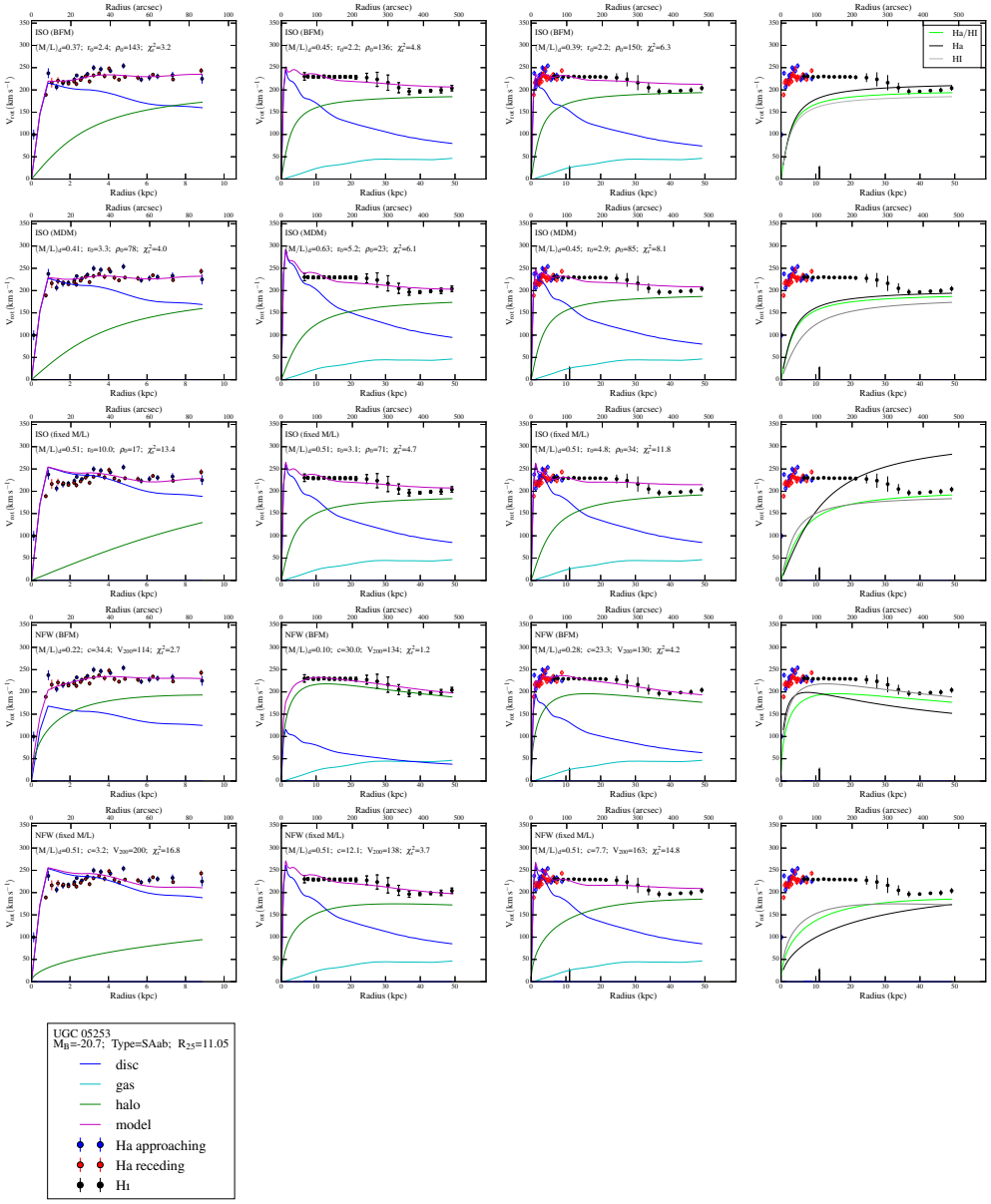
ISO (BFM)
ISO (MDM)
ISO (fixed M/L)
NFW (BFM)
NFW (fixed M/L)
Ha/HI
Ha
HI
Radius (arcsec)
Radius (kpc)
UGC 05253
MB=-20.7; Type=SAab; R25=11.05
disc
gas
halo
model
Ha approaching
Ha receding
HI

Figure 4.20

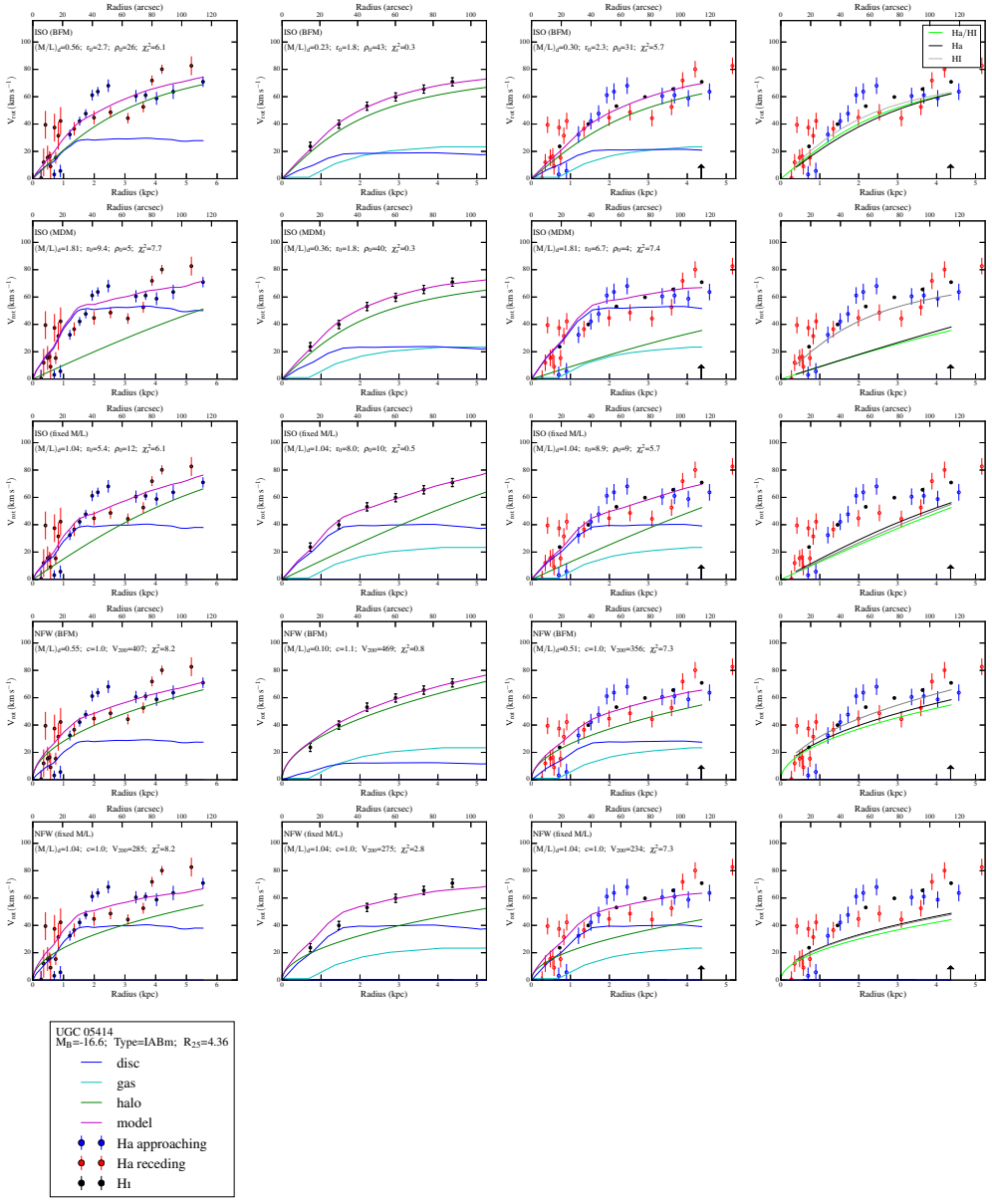
Radius (arcsec)
Radius (kpc)
V_{rot} (km s^{-1})
ISO (BFM)
ISO (MDM)
ISO (fixed M/L)
NFW (BFM)
NFW (fixed M/L)
Ha/HI
Ha
HI
UGC 05414
M_B=-16.6; Type=IABm; R_{25}=4.36
disc
gas
halo
model
Ha approaching
Ha receding
HI

Figure 4.21

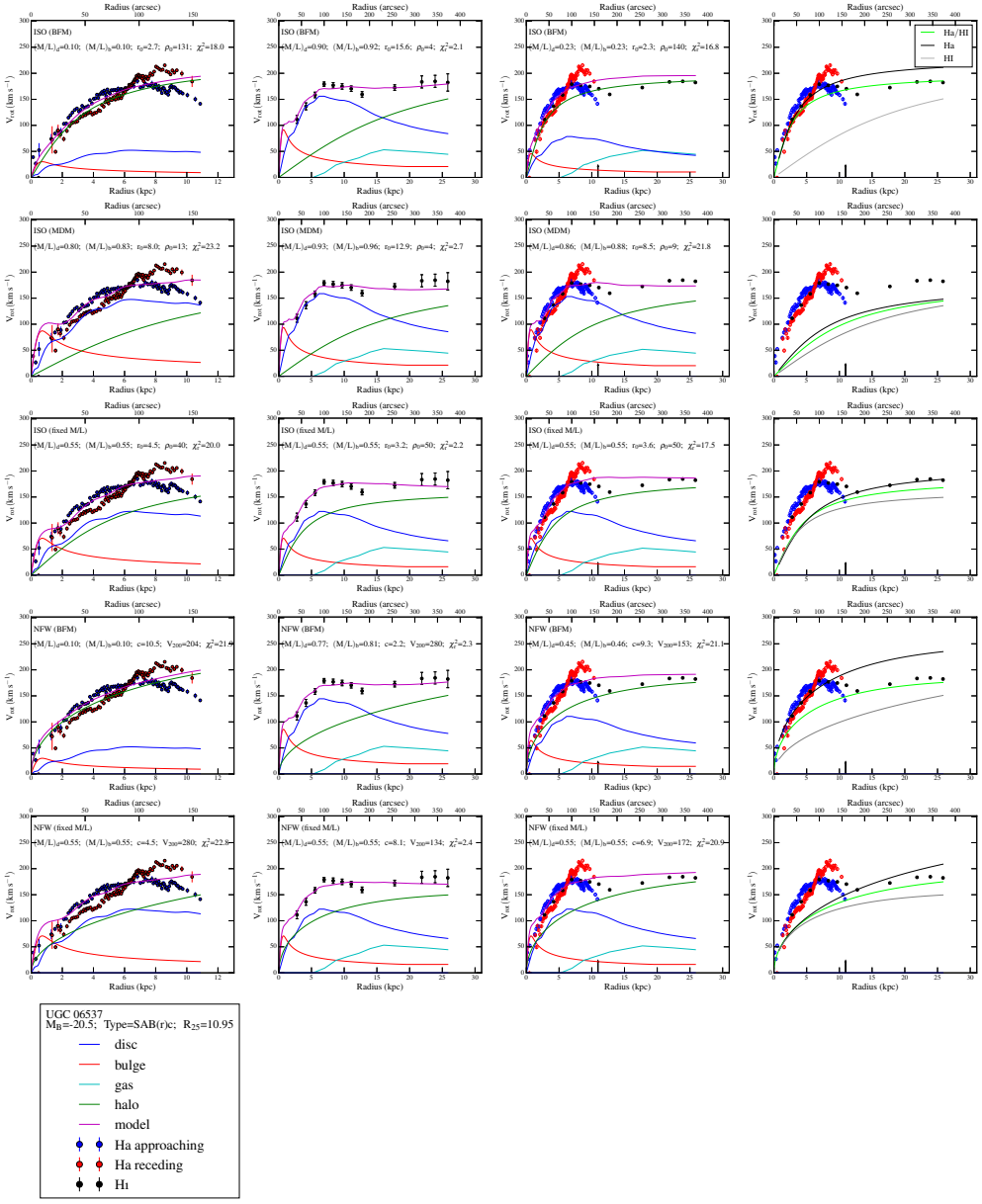
ISO (BFM)
ISO (MDM)
ISO (fixed M/L)
NFW (BFM)
NFW (fixed M/L)
Ha/HI
Ha
HI
Radius (arcsec)
Radius (kpc)
UGC 06537
M_B=-20.5; Type=SAB(r)c; R_25=10.95
disc
bulge
gas
halo
model
Ha approaching
Ha receding
HI

Figure 4.22

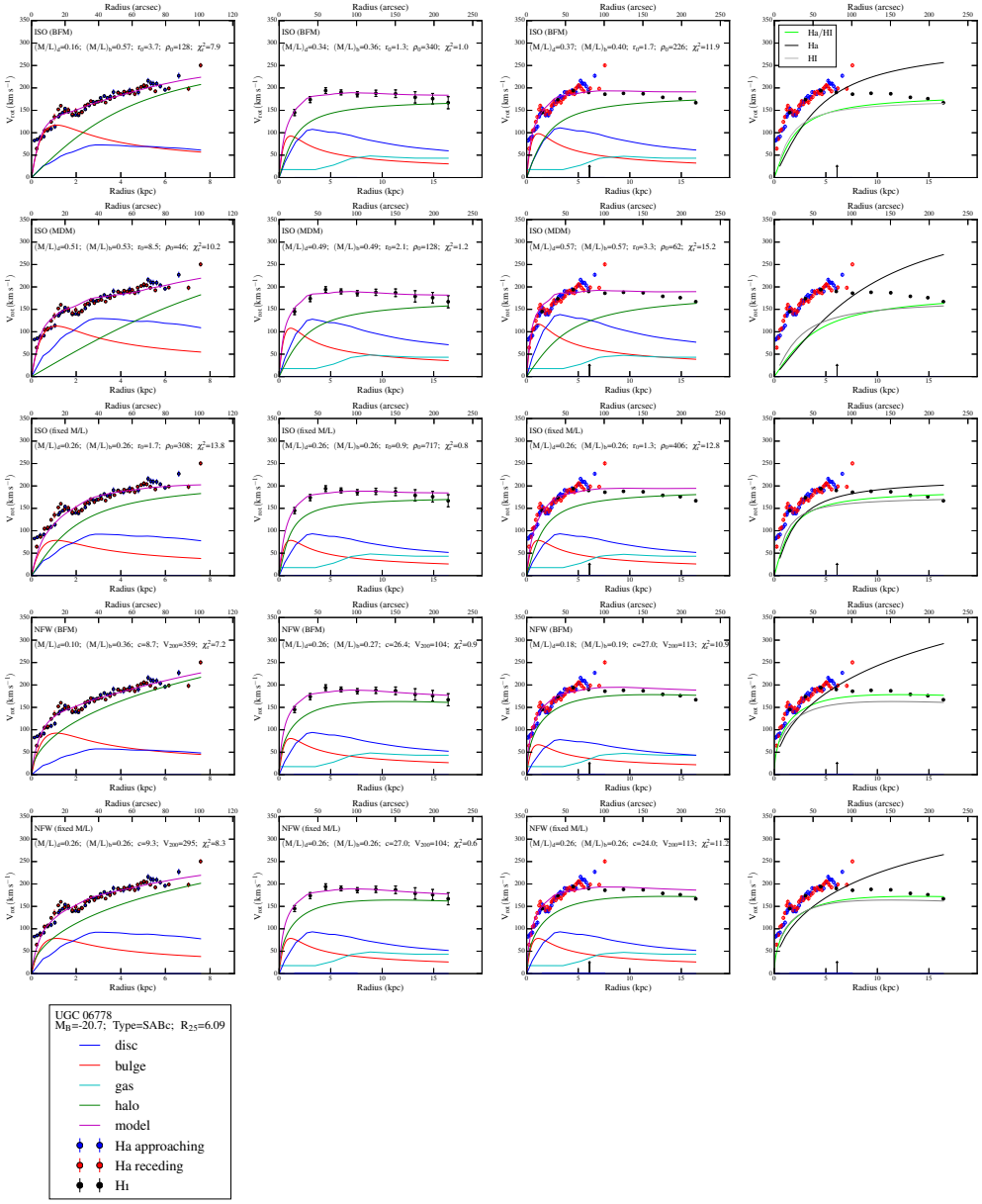
UGC 06778
M_B=-20.7; Type=SABc; R_{25}=6.09
disc
bulge
gas
halo
model
Ha approaching
Ha receding
HI

Figure 4.23

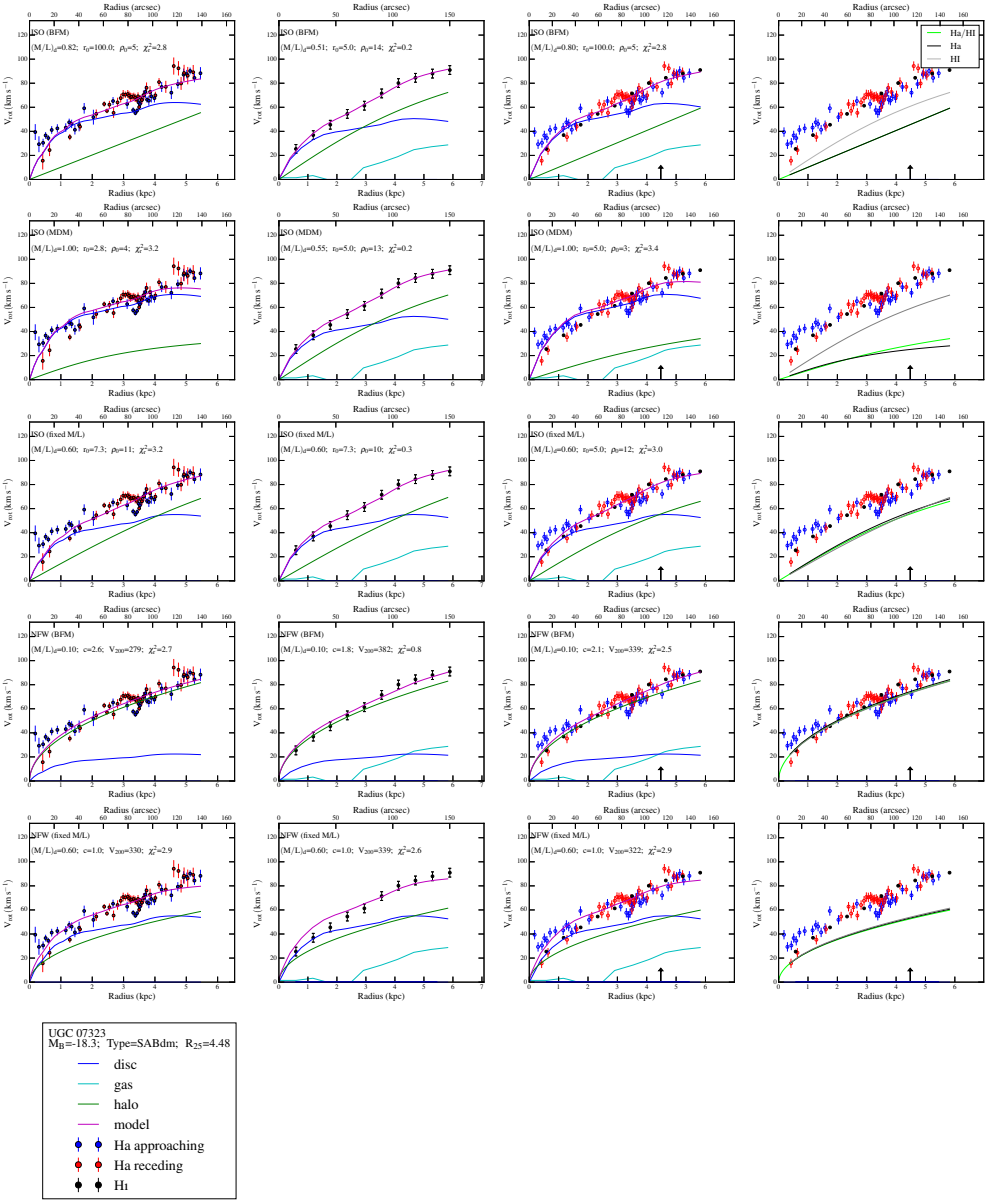
ISO (BFM)
(M/L)$_d$=0.82; r$_0$=100.0; ρ$_0$=5; χ^2=2.8
ISO (BFM)
(M/L)$_d$=0.51; r$_0$=5.0; ρ$_0$=14; χ^2=0.2
ISO (BFM)
(M/L)$_d$=0.80; r$_0$=100.0; ρ$_0$=5; χ^2=2.8
Ha/HI
Ha
HI
ISO (MDM)
(M/L)$_d$=1.00; r$_0$=2.8; ρ$_0$=4; χ^2=3.2
ISO (MDM)
(M/L)$_d$=0.55; r$_0$=5.0; ρ$_0$=13; χ^2=0.2
ISO (MDM)
(M/L)$_d$=1.00; r$_0$=5.0; ρ$_0$=3; χ^2=3.4
ISO (fixed M/L)
(M/L)$_d$=0.60; r$_0$=7.3; ρ$_0$=11; χ^2=3.2
ISO (fixed M/L)
(M/L)$_d$=0.60; r$_0$=7.3; ρ$_0$=10; χ^2=0.3
ISO (fixed M/L)
(M/L)$_d$=0.60; r$_0$=5.0; ρ$_0$=12; χ^2=3.0
NFW (BFM)
(M/L)$_d$=0.10; c=2.6; V$_{200}$=279; χ^2=2.7
NFW (BFM)
(M/L)$_d$=0.10; c=1.8; V$_{200}$=382; χ^2=0.8
NFW (BFM)
(M/L)$_d$=0.10; c=2.1; V$_{200}$=339; χ^2=2.5
NFW (fixed M/L)
(M/L)$_d$=0.60; c=1.0; V$_{200}$=330; χ^2=2.9
NFW (fixed M/L)
(M/L)$_d$=0.60; c=1.0; V$_{200}$=339; χ^2=2.6
NFW (fixed M/L)
(M/L)$_d$=0.60; c=1.0; V$_{200}$=322; χ^2=2.9
Radius (arcsec)
Radius (kpc)
V$_{rot}$ (km s^{-1})
UGC 07323
M$_B$=-18.3; Type=SABdm; R$_{25}$=4.48
disc
gas
halo
model
Ha approaching
Ha receding
HI

Figure 4.24

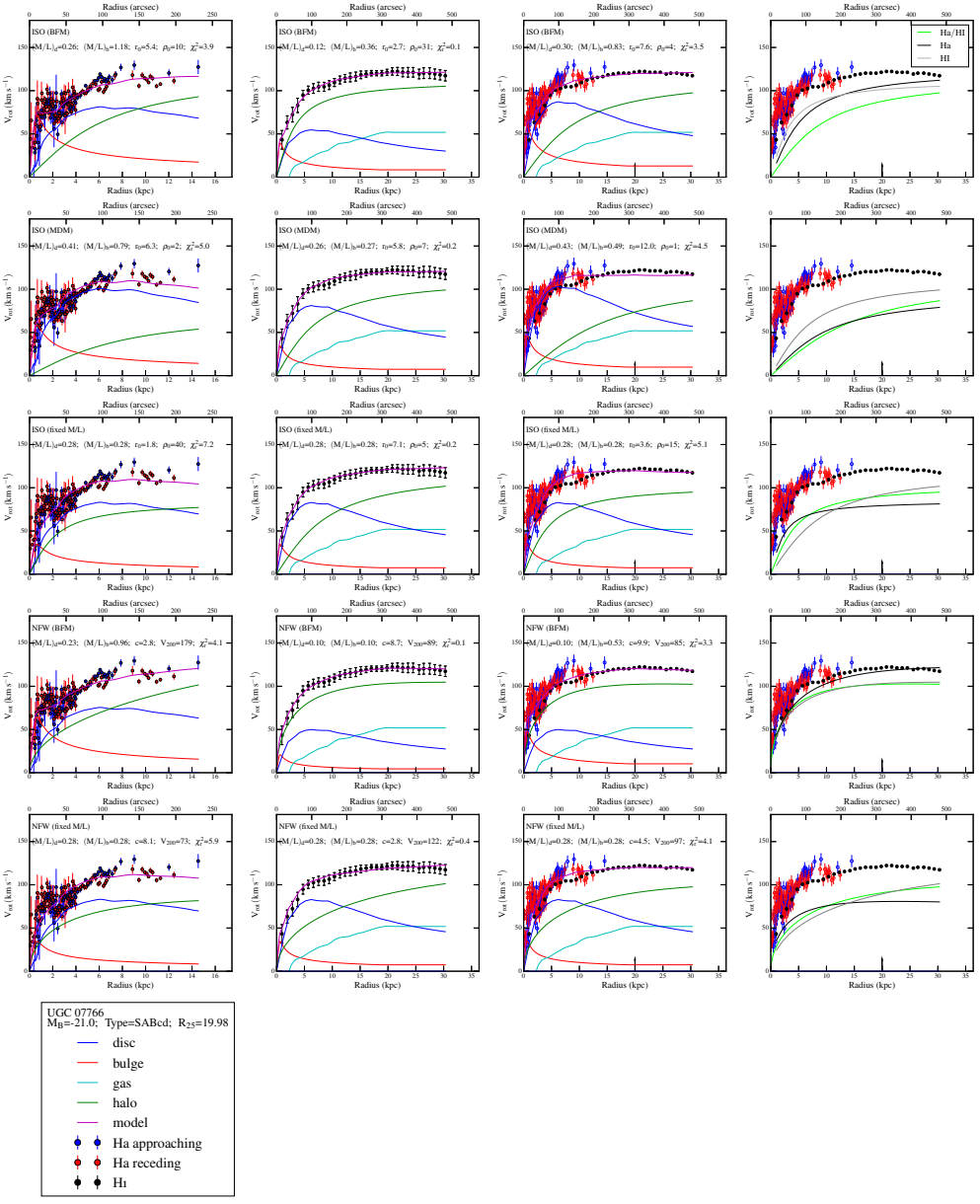
ISO (BFM)
ISO (MDM)
ISO (fixed M/L)
NFW (BFM)
NFW (fixed M/L)
Radius (arcsec)
Radius (kpc)
Ha/HI
Ha
HI
UGC 07766
M_B=-21.0; Type=SABcd; R_25=19.98
disc
bulge
gas
halo
model
Ha approaching
Ha receding
HI

Figure 4.25

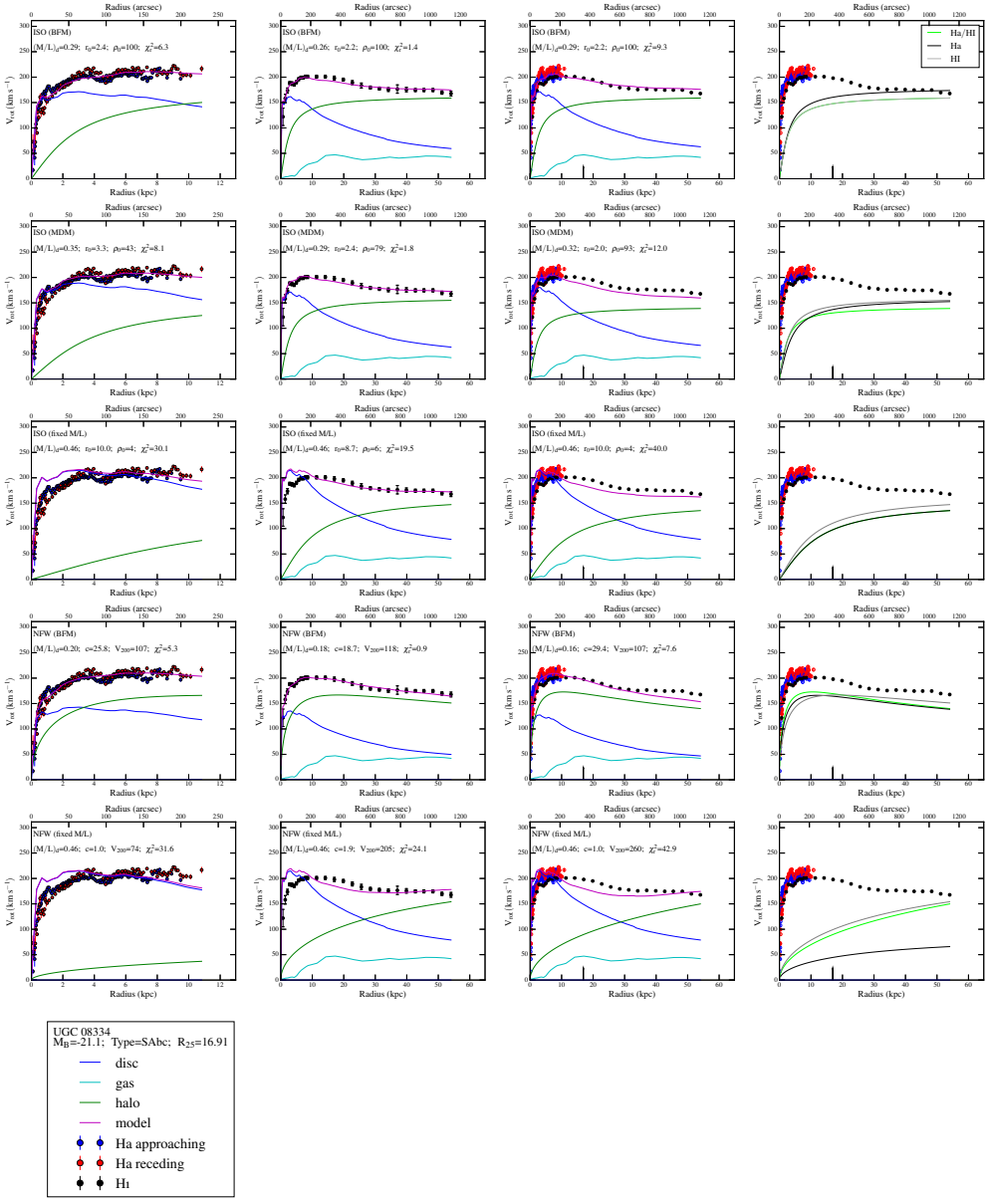
ISO (BFM)
ISO (MDM)
ISO (fixed M/L)
NFW (BFM)
NFW (fixed M/L)
Ha/HI
Ha
HI
Radius (arcsec)
Radius (kpc)
UGC 08334
MB=-21.1; Type=SAbc; R25=16.91
disc
gas
halo
model
Ha approaching
Ha receding
HI

Figure 4.26

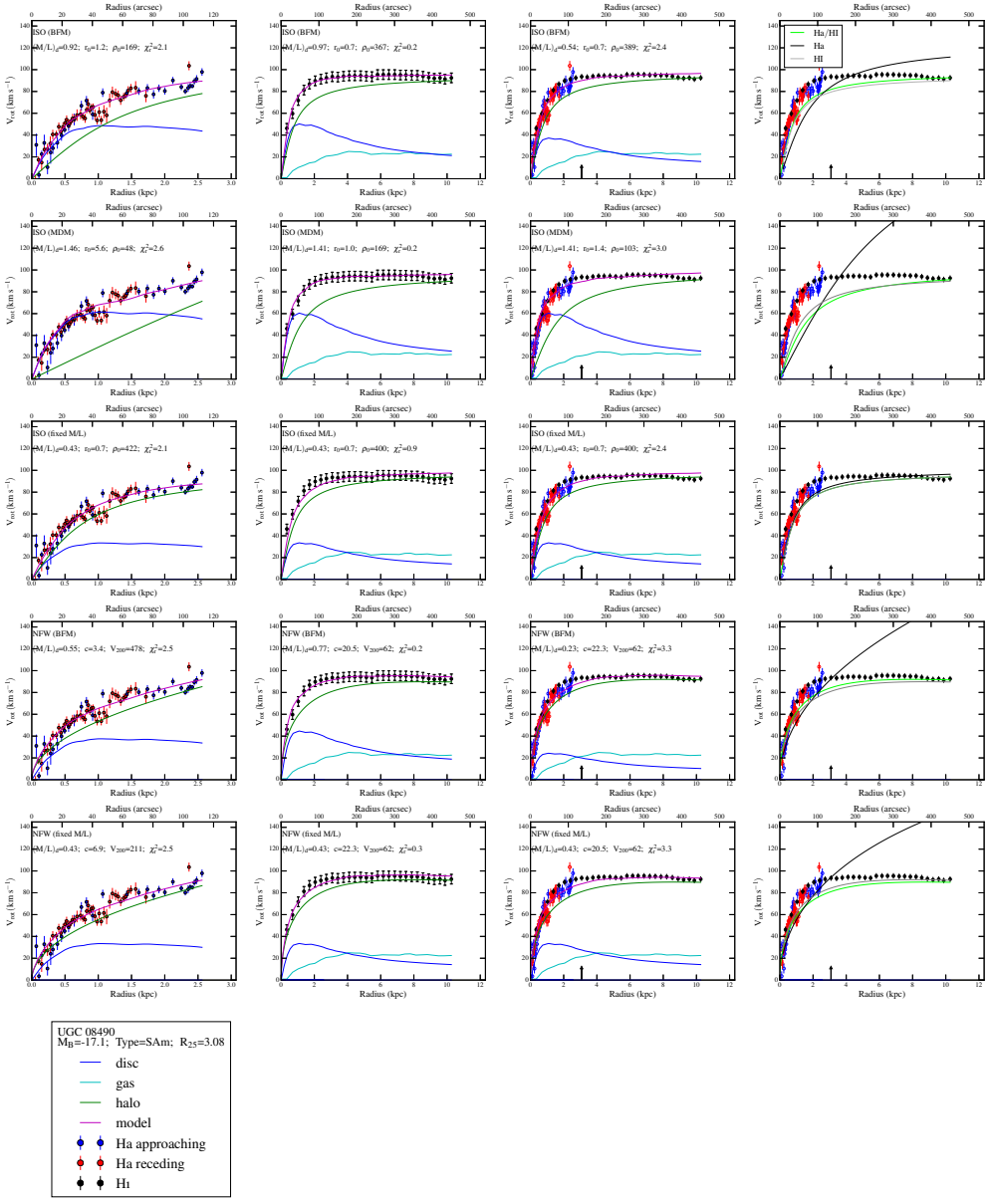
ISO (BFM)
ISO (MDM)
ISO (fixed M/L)
NFW (BFM)
NFW (fixed M/L)
Ha/HI
Ha
HI
Radius (arcsec)
Radius (kpc)
V_{rot} (km s^{-1})
UGC 08490
M_B=-17.1; Type=SAm; R_{25}=3.08
disc
gas
halo
model
Ha approaching
Ha receding
HI

Figure 4.27

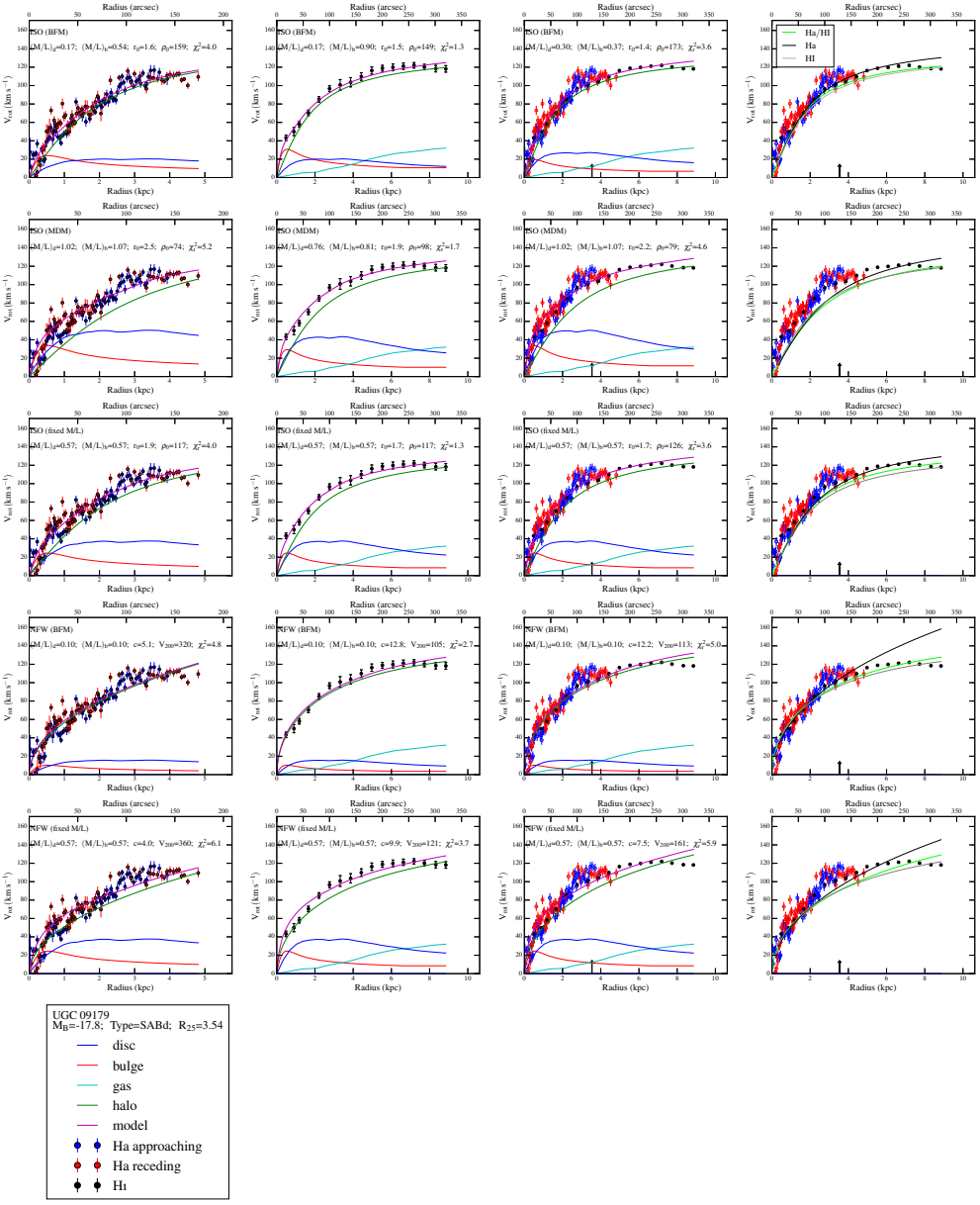
ISO (BFM)
ISO (MDM)
ISO (fixed M/L)
NFW (BFM)
NFW (fixed M/L)
Ha/HI
Ha
HI
Radius (arcsec)
Radius (kpc)
UGC 09179
M_B=-17.8; Type=SABd; R_25=3.54
disc
bulge
gas
halo
model
Ha approaching
Ha receding
HI

Figure 4.28

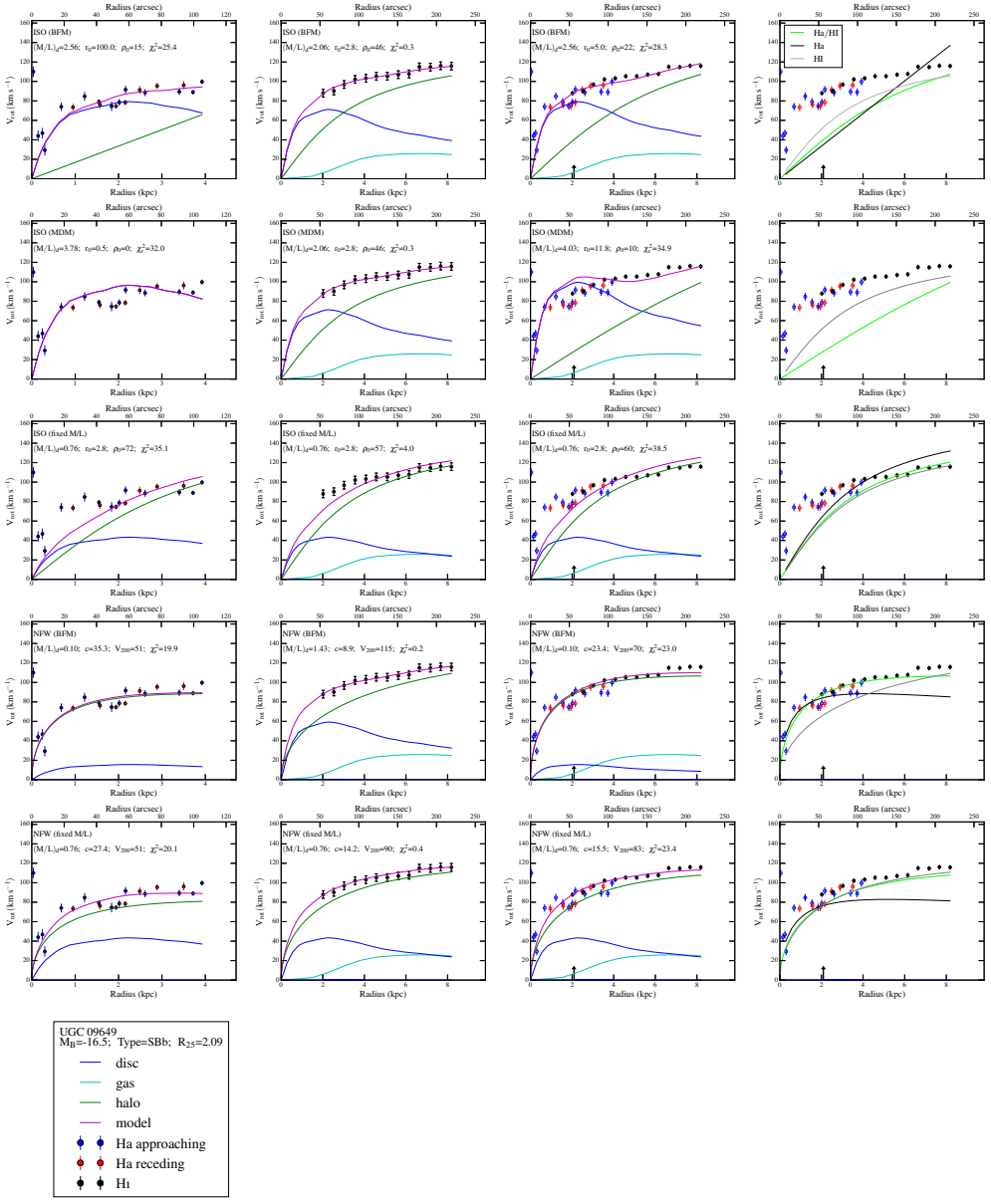
ISO (BFM)
ISO (MDM)
ISO (fixed M/L)
NFW (BFM)
NFW (fixed M/L)
Ha/HI
Ha
HI
Radius (arcsec)
Radius (kpc)
V_rot (km s^-1)
UGC 09649
M_B=-16.5; Type=SBb; R_25=2.09
disc
gas
halo
model
Ha approaching
Ha receding
HI

Figure 4.29

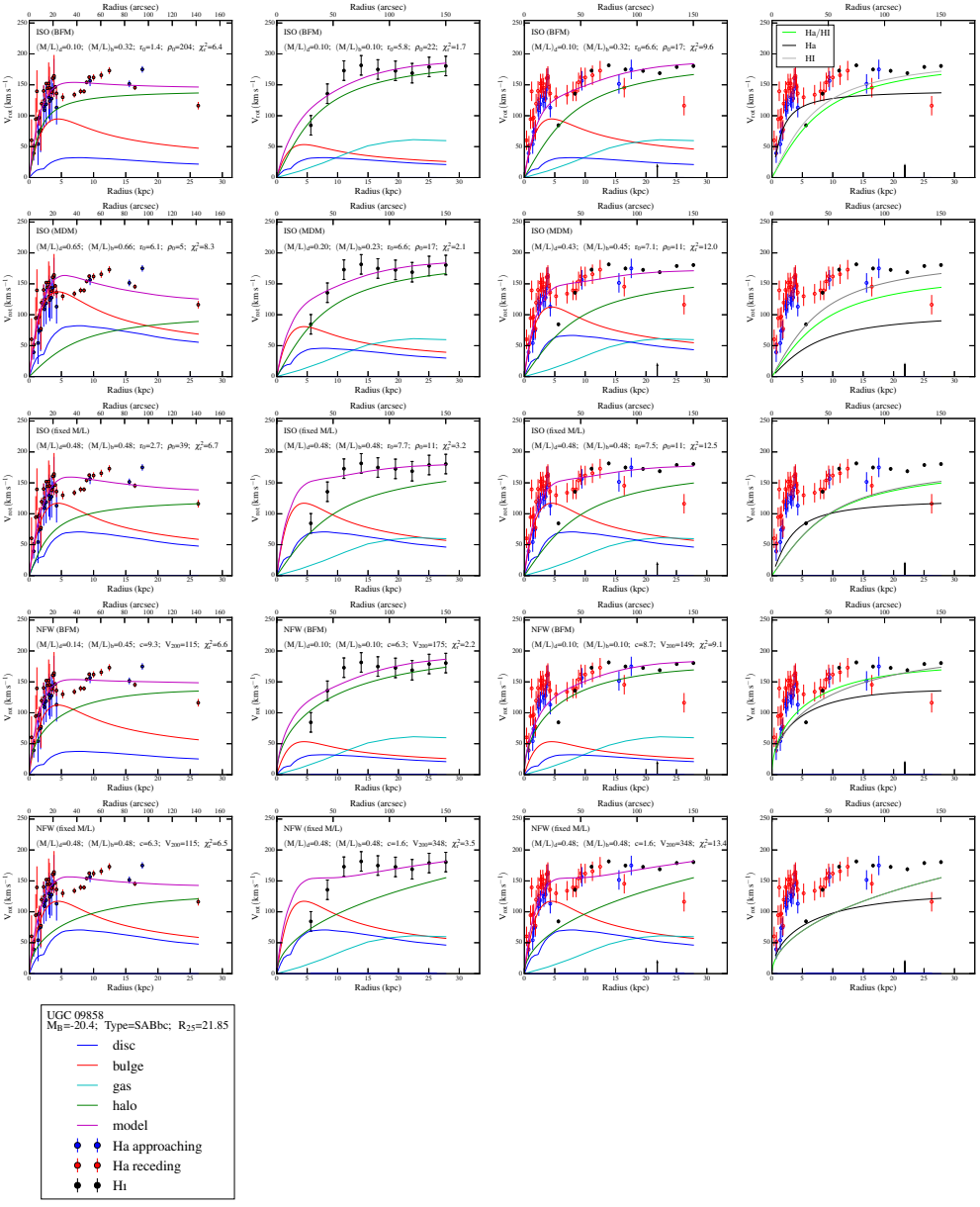
ISO (BFM)
ISO (MDM)
ISO (fixed M/L)
NFW (BFM)
NFW (fixed M/L)
Ha/HI
Ha
HI
Radius (arcsec)
Radius (kpc)
UGC 09858
M_B=-20.4; Type=SABbc; R_25=21.85
disc
bulge
gas
halo
model
Ha approaching
Ha receding
HI

Figure 4.30

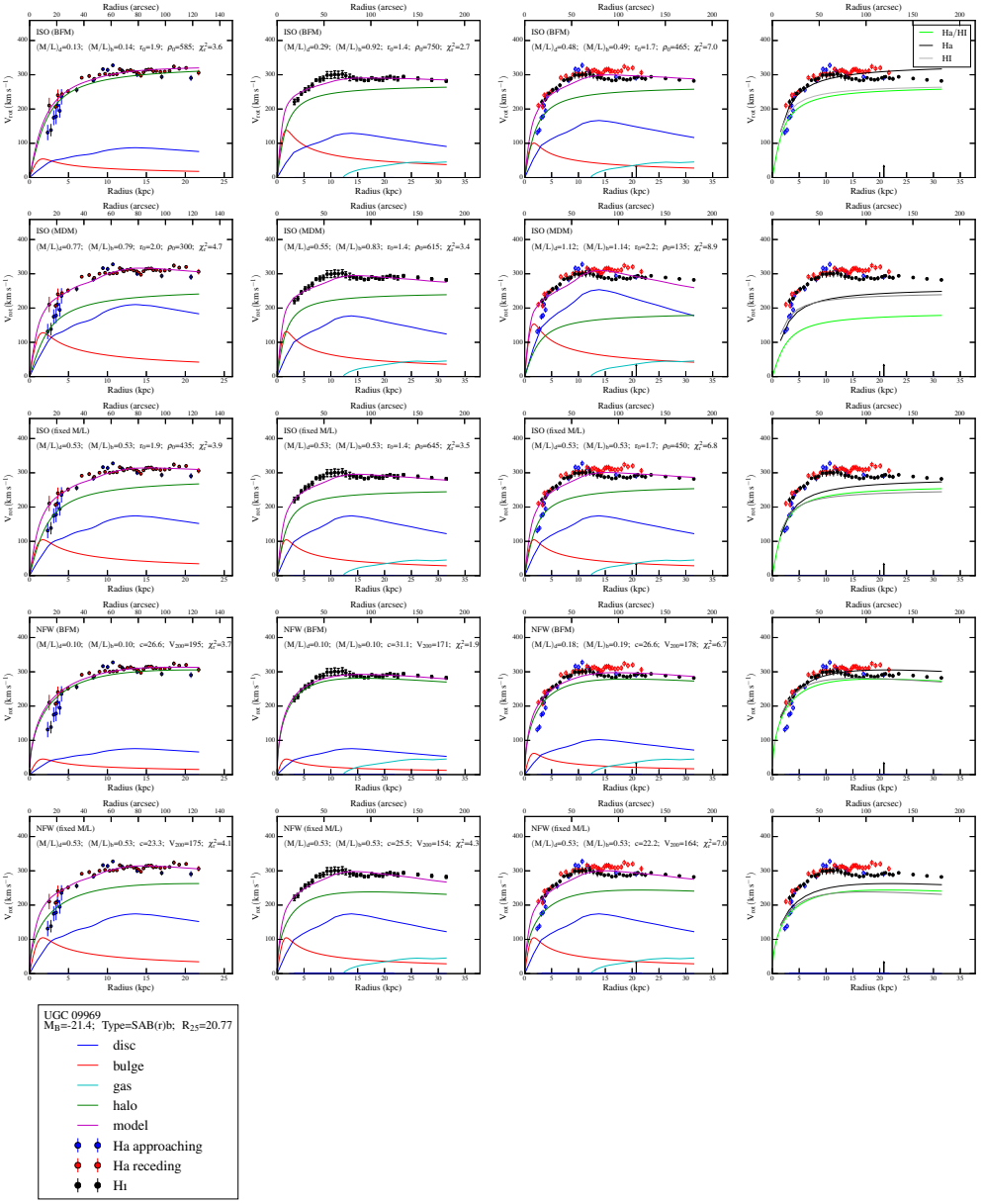
ISO (BFM)
ISO (MDM)
ISO (fixed M/L)
NFW (BFM)
NFW (fixed M/L)
Ha/HI
Ha
HI
Radius (arcsec)
Radius (kpc)
V_{rot} (km s^{-1})
UGC 09969
M_B=-21.4; Type=SAB(r)b; R_{25}=20.77
disc
bulge
gas
halo
model
Ha approaching
Ha receding
HI

Figure 4.31

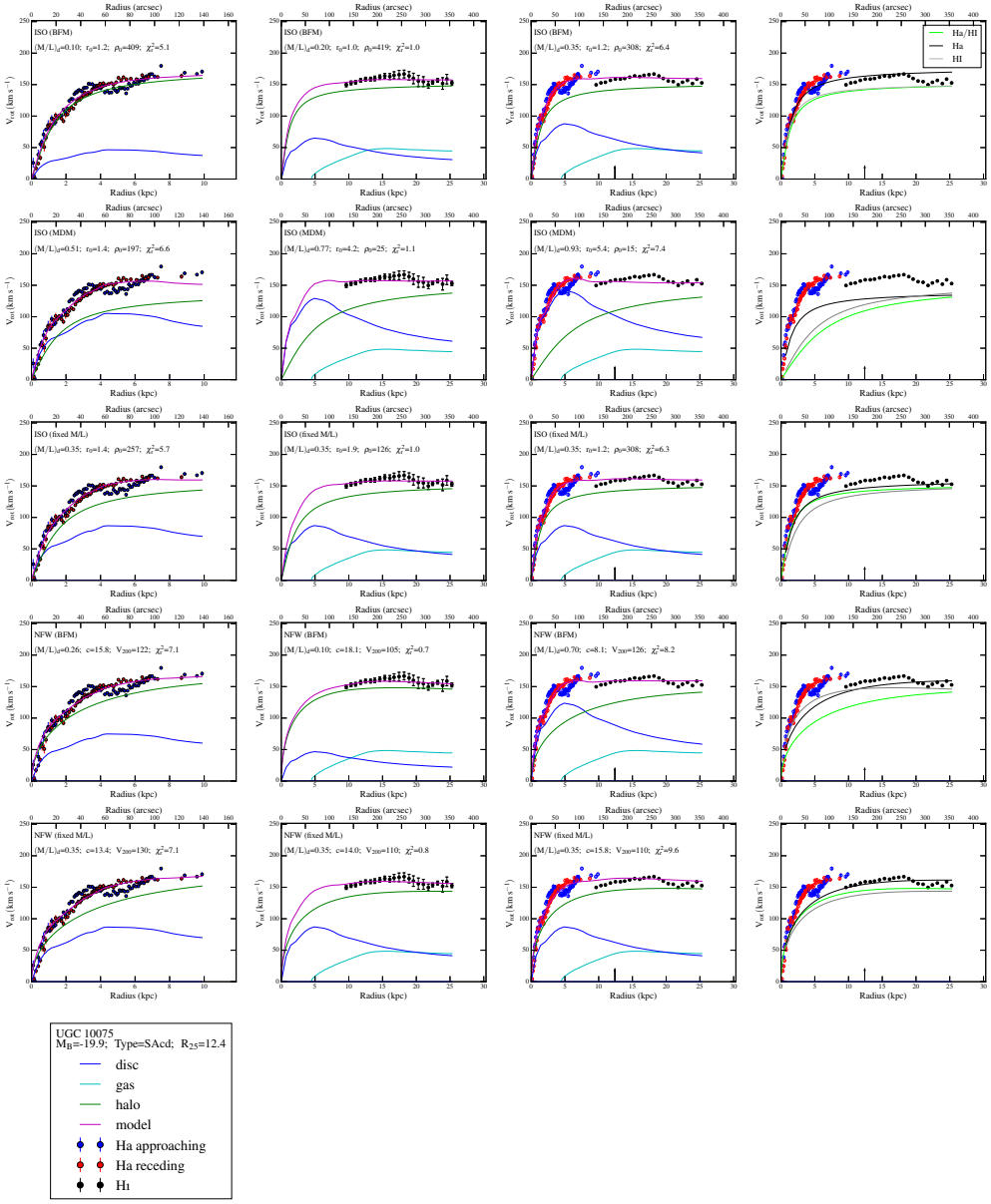
ISO (BFM)
ISO (MDM)
ISO (fixed M/L)
NFW (BFM)
NFW (fixed M/L)
Ha/HI
Ha
HI
Radius (arcsec)
Radius (kpc)
UGC 10075
M_B=-19.9; Type=SAcd; R_25=12.4
disc
gas
halo
model
Ha approaching
Ha receding
HI

Figure 4.32

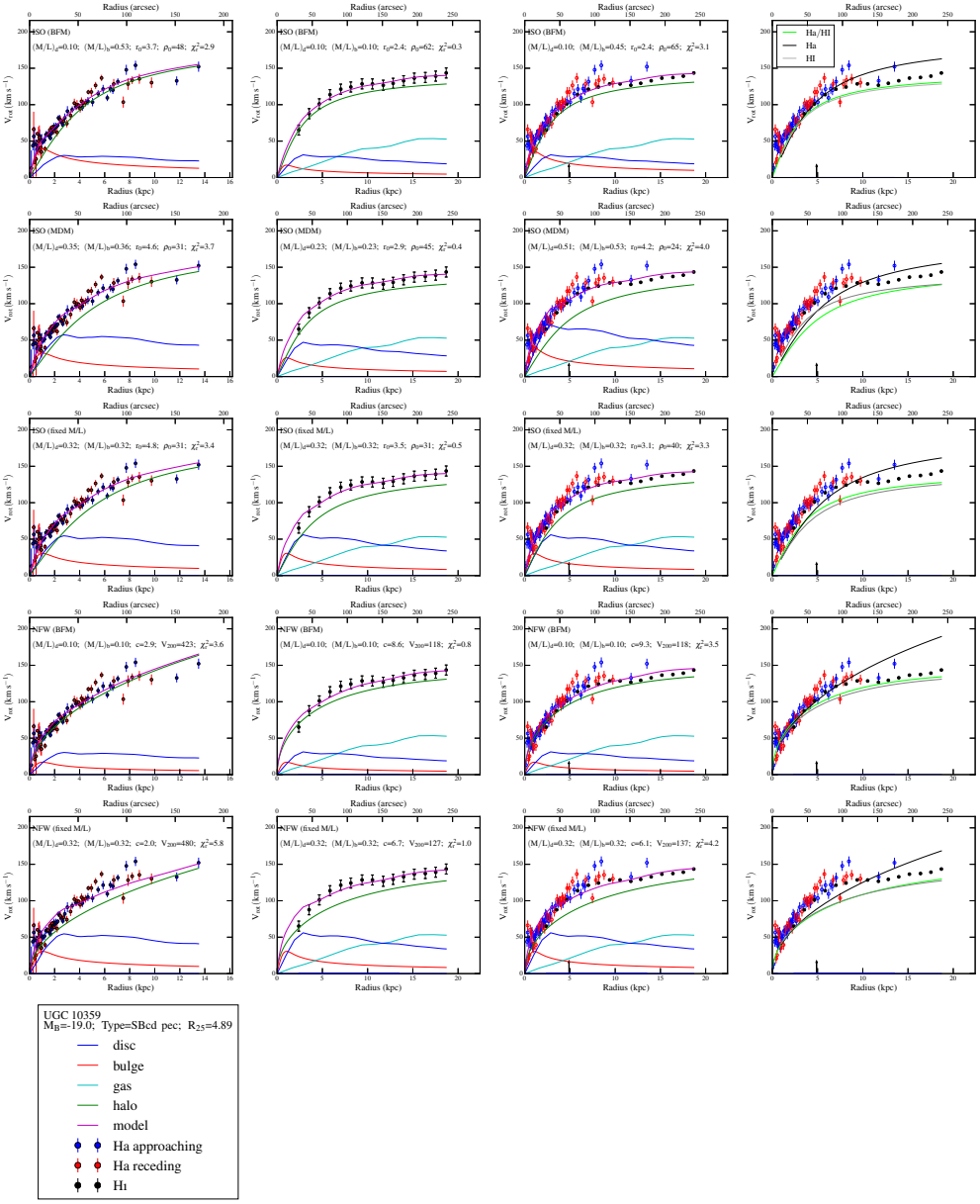
ISO (BFM)
ISO (MDM)
ISO (fixed M/L)
NFW (BFM)
NFW (fixed M/L)
Ha/HI
Ha
HI
Radius (arcsec)
Radius (kpc)
V_rot (km s^-1)
UGC 10359
M_B=-19.0; Type=SBcd pec; R_25=4.89
disc
bulge
gas
halo
model
Ha approaching
Ha receding
HI

Figure 4.33

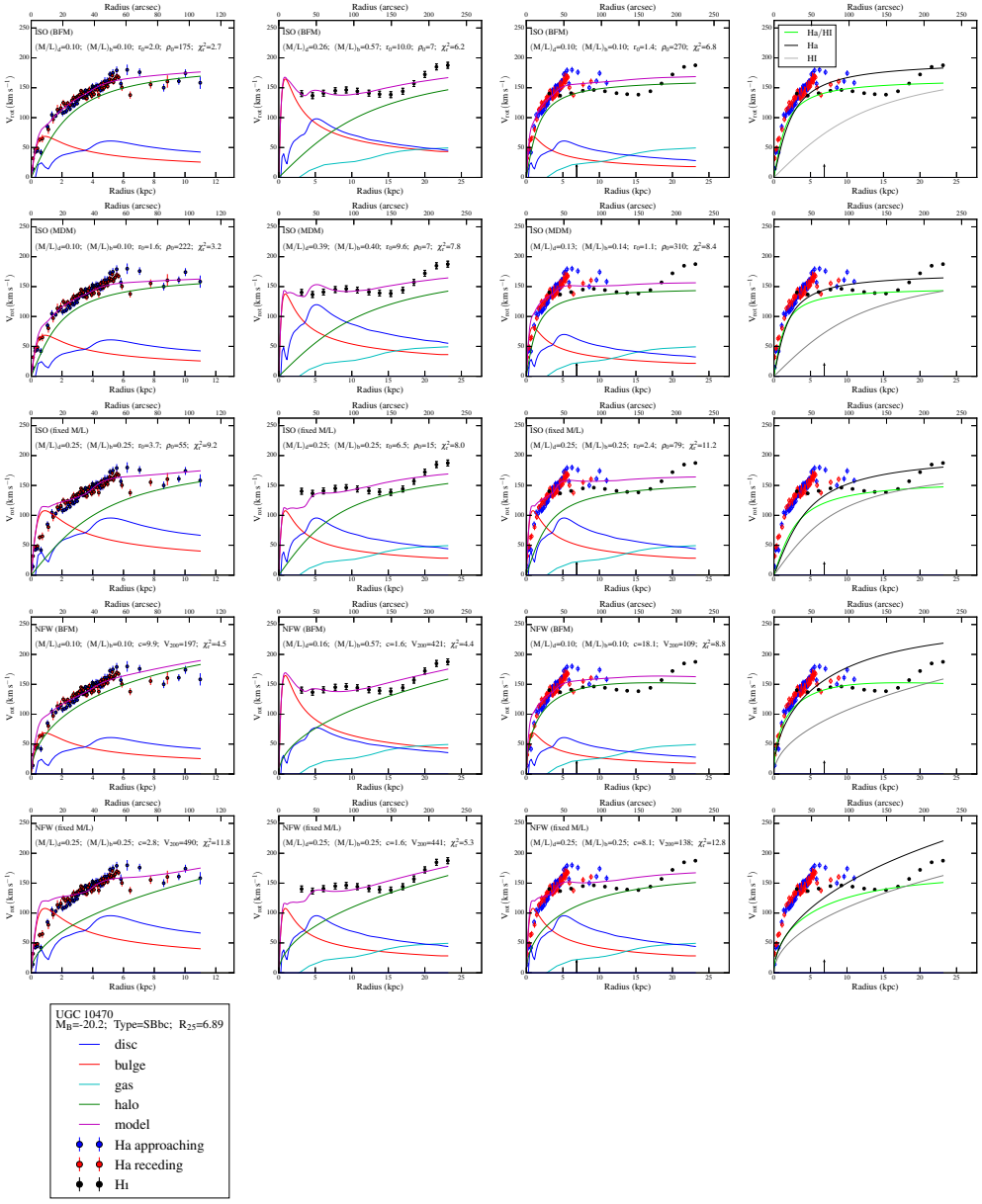
ISO (BFM)
ISO (MDM)
ISO (fixed M/L)
NFW (BFM)
NFW (fixed M/L)
Ha/HI
Ha
HI
Radius (arcsec)
Radius (kpc)
UGC 10470
M_B=-20.2; Type=SBbc; R_25=6.89
disc
bulge
gas
halo
model
Ha approaching
Ha receding
HI

Figure 4.34

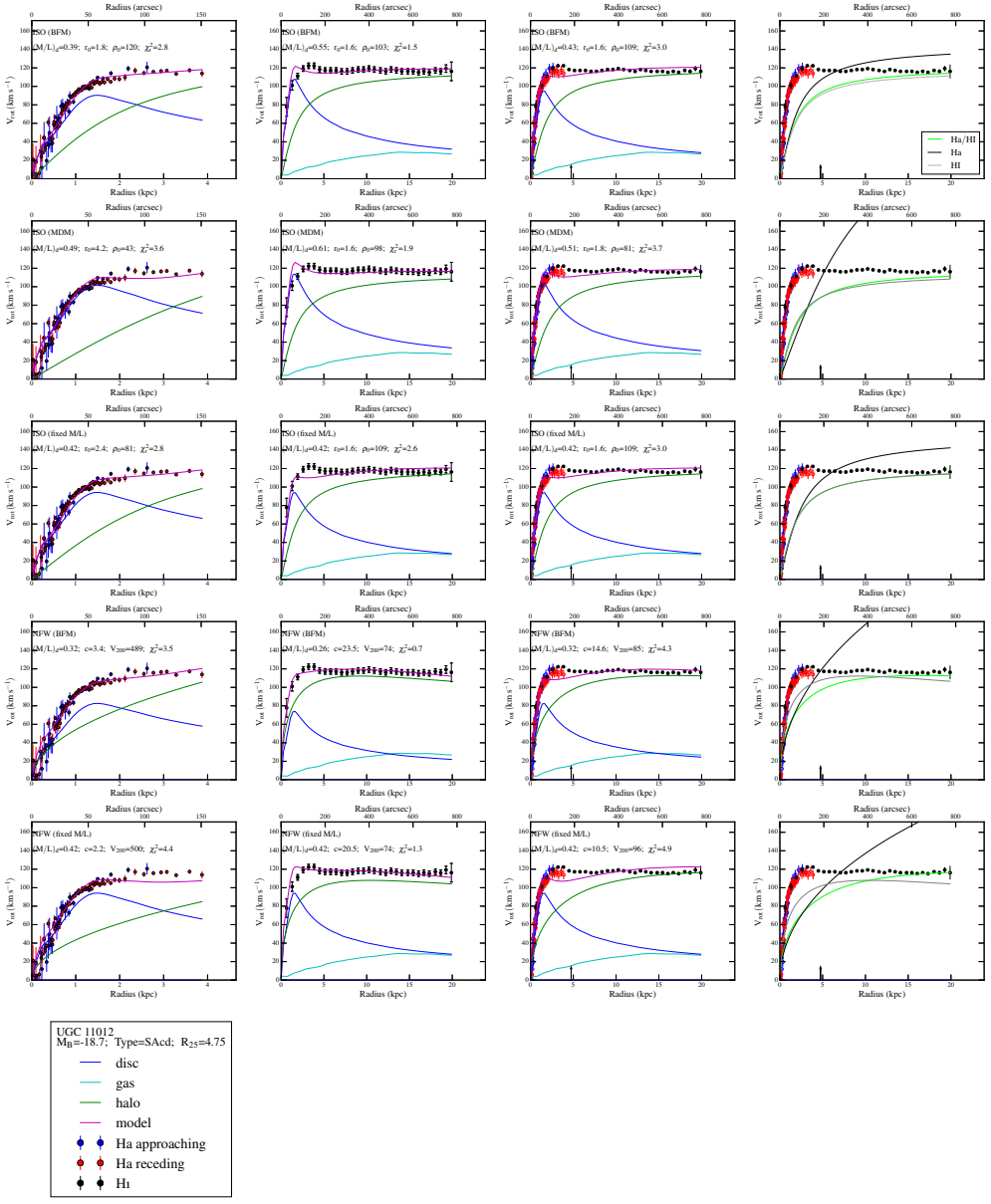
ISO (BFM)
ISO (MDM)
ISO (fixed M/L)
NFW (BFM)
NFW (fixed M/L)
Radius (arcsec)
Radius (kpc)
Ha/HI
Ha
HI
UGC 11012
M_B=-18.7; Type=SAcd; R_25=4.75
disc
gas
halo
model
Ha approaching
Ha receding
HI

Figure 4.35

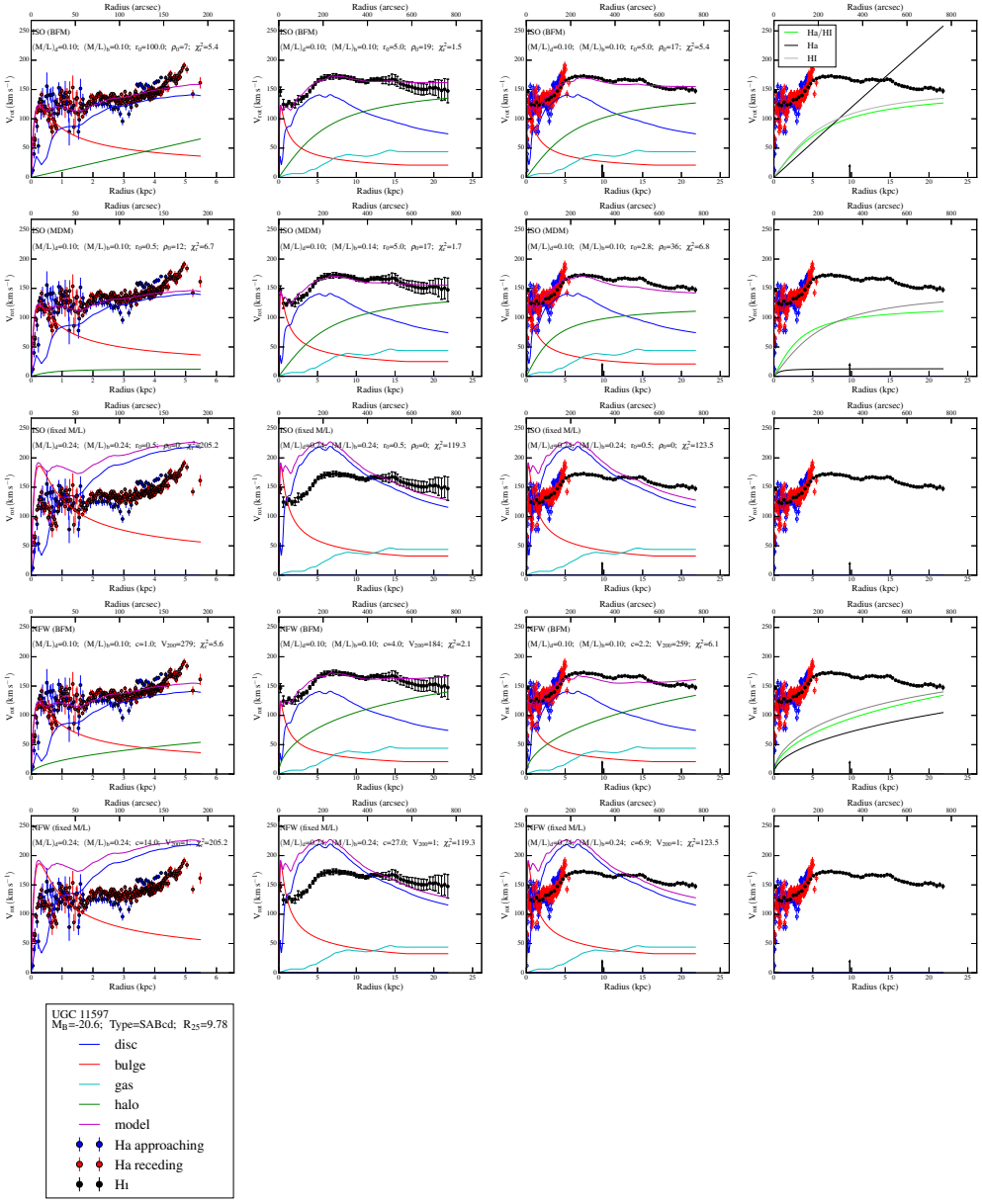
ISO (BFM)
ISO (MDM)
ISO (fixed M/L)
NFW (BFM)
NFW (fixed M/L)
Ha/HI
Ha
HI
Radius (arcsec)
Radius (kpc)
UGC 11597
M_B=-20.6; Type=SABcd; R_25=9.78
disc
bulge
gas
halo
model
Ha approaching
Ha receding
HI

Figure 4.36

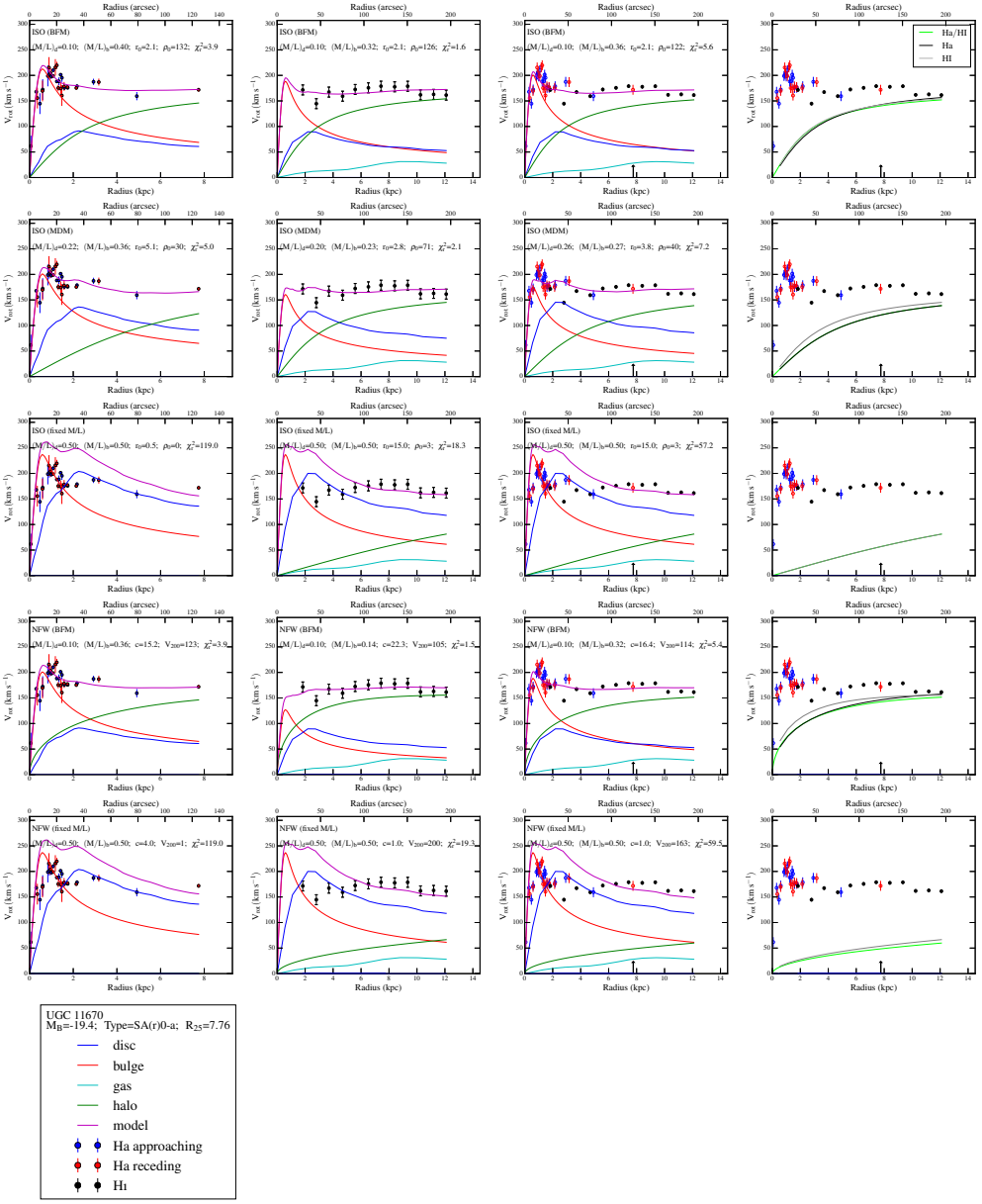
ISO (BFM)
ISO (MDM)
ISO (fixed M/L)
NFW (BFM)
NFW (fixed M/L)
Ha/HI
Ha
HI
Radius (arcsec)
Radius (kpc)
UGC 11670
M_B=-19.4; Type=SA(r)0-a; R_25=7.76
disc
bulge
gas
halo
model
Ha approaching
Ha receding
HI

Figure 4.37

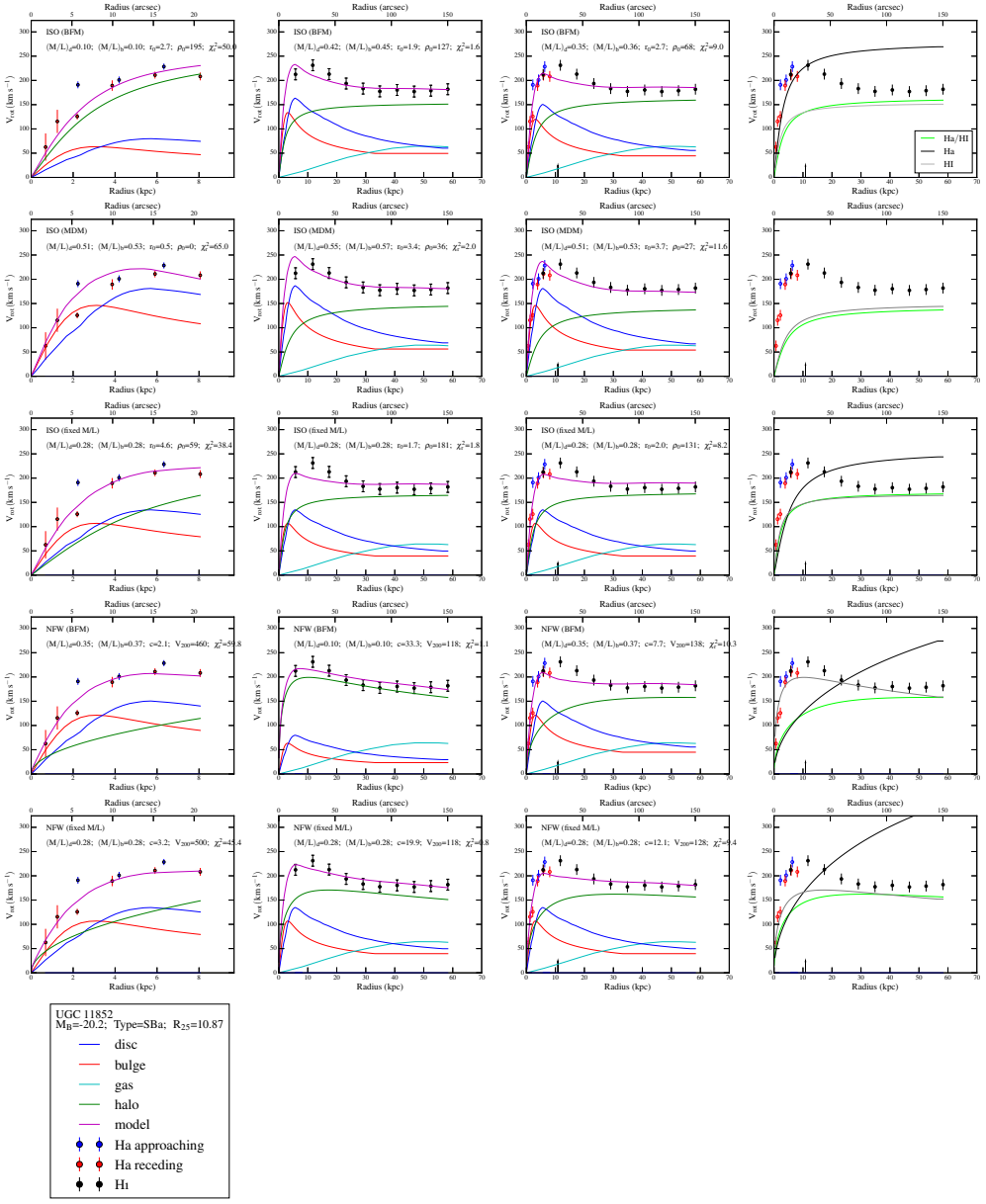
ISO (BFM)
ISO (MDM)
ISO (fixed M/L)
NFW (BFM)
NFW (fixed M/L)
Radius (arcsec)
Radius (kpc)
Ha/HI
Ha
HI
UGC 11852
M_B=-20.2; Type=SBa; R_25=10.87
disc
bulge
gas
halo
model
Ha approaching
Ha receding
HI

Figure 4.38

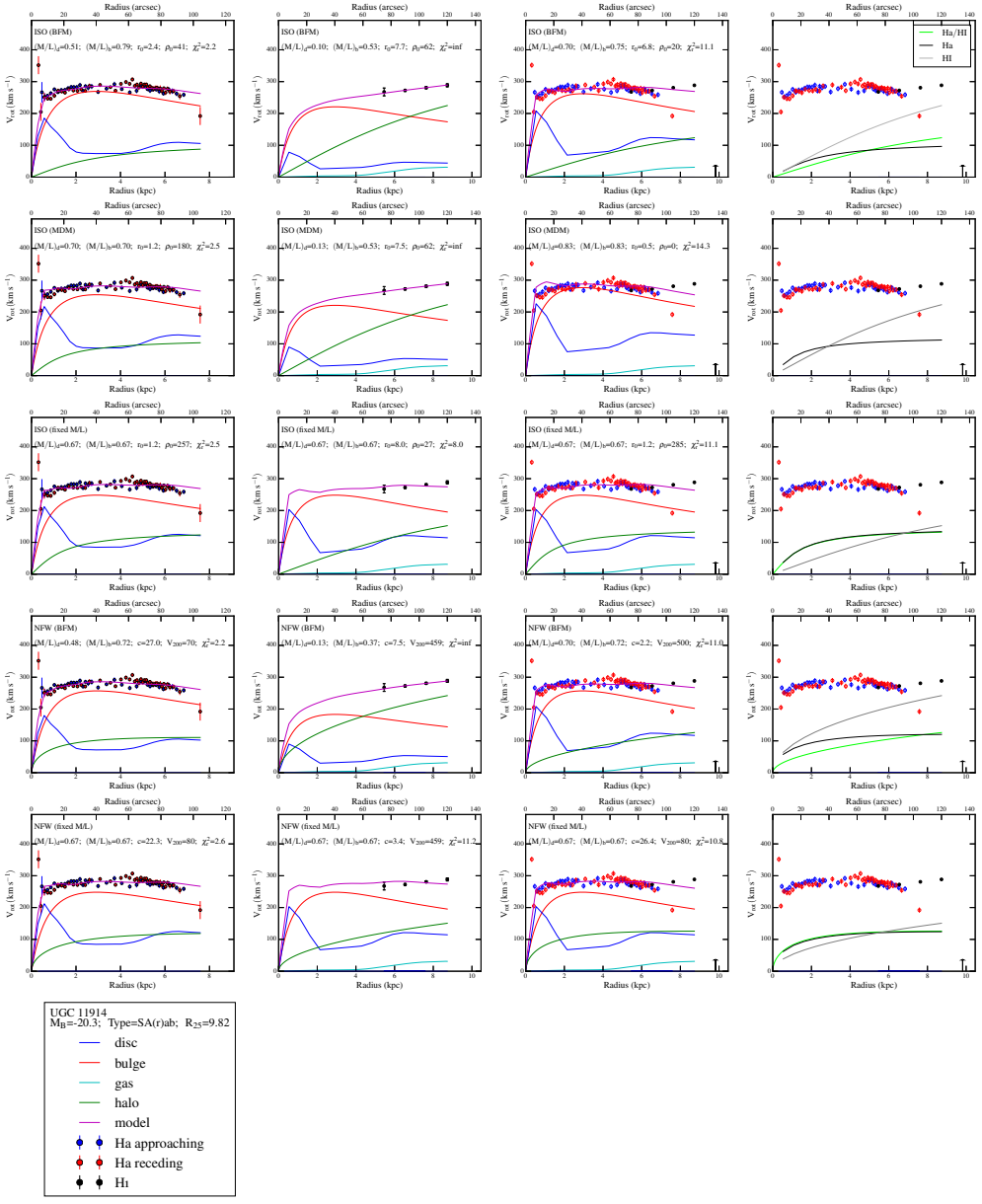
UGC 11914
M_B=-20.3; Type=SA(r)ab; R_{25}=9.82
disc
bulge
gas
halo
model
Ha approaching
Ha receding
HI
Ha/HI
Ha
HI
Radius (arcsec)
Radius (kpc)
V_{rot} (km s^{-1})

Figure 4.39

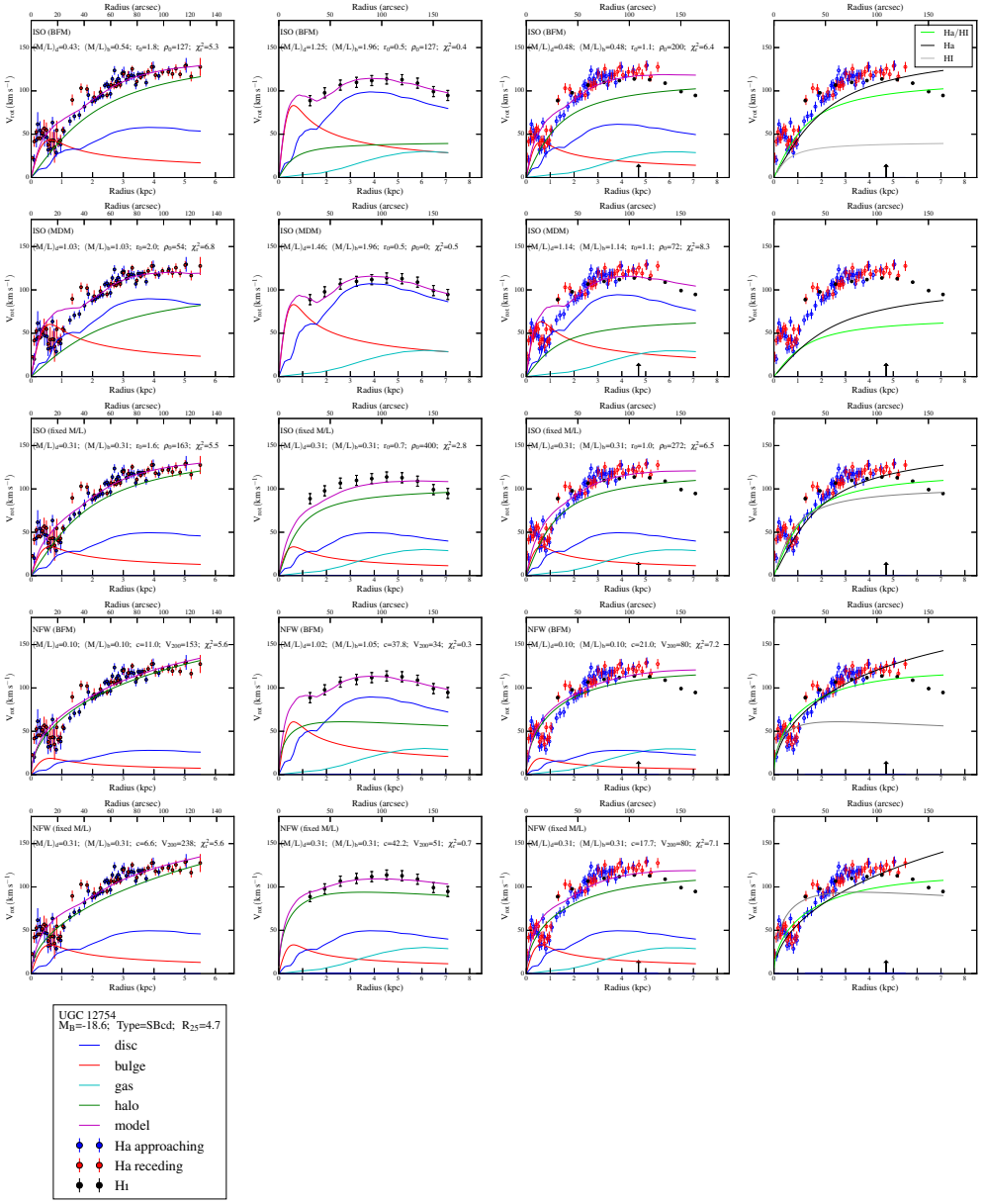
ISO (BFM)
ISO (MDM)
ISO (fixed M/L)
NFW (BFM)
NFW (fixed M/L)
Ha/HI
Ha
HI
Radius (arcsec)
Radius (kpc)
UGC 12754
M_B=-18.6; Type=SBcd; R_25=4.7
disc
bulge
gas
halo
model
Ha approaching
Ha receding
HI

Figure 4.40

Bibliography

Amram P., Le Coarer E., Marcelin M., Balkowski C., Sullivan III W. T., Cayatte V., 1992, A&AS, 94, 175

Barbieri C. V., Fraternali F., Oosterloo T., Bertin G., Boomsma R., Sancisi R., 2005, A&A, 439, 947

Battaglia G., Fraternali F., Oosterloo T., Sancisi R., 2006, A&A, 447, 49

Begeman K. G., 1987, PhD thesis, , Kapteyn Institute, (1987)

Begeman K. G., Broeils A. H., Sanders R. H., 1991, MNRAS, 249, 523

Bell E. F., de Jong R. S., 2001, ApJ, 550, 212

Blais-Ouellette S., Carignan C., Amram P., Côté S., 1999, AJ, 118, 2123

Blais-Ouellette S., Amram P., Carignan C., 2001, AJ, 121, 1952

Blais-Ouellette S., Amram P., Carignan C., Swaters R., 2004, A&A, 420, 147

Boomsma R., Oosterloo T. A., Fraternali F., van der Hulst J. M., Sancisi R., 2008, A&A, 490, 555

Bosma A., 1978, PhD thesis, PhD Thesis, Groningen Univ., (1978)

Broeils A. H., 1992, PhD thesis, PhD thesis, Univ. Groningen, (1992)

Bullock J. S., Kolatt T. S., Sigad Y., Somerville R. S., Kravtsov A. V., Klypin A. A., Primack J. R., Dekel A., 2001, MNRAS, 321, 559

Carignan C., Freeman K. C., 1985, ApJ, 294, 494

Cluver M. E., et al., 2014, ApJ, 782, 90

Cote S., Carignan C., Sancisi R., 1991, AJ, 102, 904

Di Teodoro E. M., Fraternali F., 2015, MNRAS, 451, 3021

Dicaire I., et al., 2008, MNRAS, 385, 553

Epinat B., Amram P., Marcelin M., 2008, MNRAS, 390, 466

Freeman K. C., 1970, ApJ, 160, 811

Garrido O., Marcelin M., Amram P., Boulesteix J., 2002, A&A, 387, 821

Jarrett T. H., et al., 2013, AJ, 145, 6

Kormendy J., Freeman K. C., 2004, in Ryder S., Pisano D., Walker M., Freeman K., eds, IAU Symposium Vol. 220, Dark Matter in Galaxies. p. 377

Korsaga M., Carignan C., Amram P., Epinat B., Jarrett T. H., 2018, MNRAS, 478, 50

Korsaga M., Amram P., Carignan C., Epinat B., 2019, MNRAS, 482, 154

Lelli F., McGaugh S. S., Schombert J. M., 2016, AJ, 152, 157

Martinsson T. P. K., Verheijen M. A. W., Westfall K. B., Bershady M. A., Andersen D. R., Swaters R. A., 2013, A&A, 557, A131

Navarro J. F., Frenk C. S., White S. D. M., 1996, ApJ, 462, 563

Navarro J. F., Frenk C. S., White S. D. M., 1997, ApJ, 490, 493

Noordermeer E., van der Hulst J. M., Sancisi R., Swaters R. A., van Albada T. S., 2005, A&A, 442, 137

Noordermeer E., van der Hulst J. M., Sancisi R., Swaters R. S., van Albada T. S., 2007, MNRAS, 376, 1513

Randriamampandry T. H., Carignan C., 2014, MNRAS, 439, 2132

Randriamampandry T. H., Combes F., Carignan C., Deg N., 2015, MNRAS, 454, 3743

Richards E. E., et al., 2018, MNRAS, 476, 5127

Sanders R. H., 1996, ApJ, 473, 117

Sanders R. H., Verheijen M. A. W., 1998, ApJ, 503, 97

Spano M., Marcelin M., Amram P., Carignan C., Epinat B., Hernandez O., 2008, MNRAS, 383, 297

Swaters R. A., van Albada T. S., van der Hulst J. M., Sancisi R., 2002, A&A, 390, 829

Swaters R. A., Sancisi R., van Albada T. S., van der Hulst J. M., 2009, A&A, 493, 871

Verdes-Montenegro L., Bosma A., Athanassoula E., 1997, A&A, 321, 754

Verheijen M. A. W., Sancisi R., 2001, A&A, 370, 765

de Blok W. J. G., Walter F., Brinks E., Trachternach C., Oh S.-H., Kennicutt Jr. R. C., 2008, AJ, 136, 2648

van Eymeren J., Jütte E., Jog C. J., Stein Y., Dettmar R.-J., 2011, A&A, 530, A29

Chapter 5

Conclusion and future prospects

1 Conclusion

In this thesis, we have presented the mass distribution of baryonic and dark matter (DM) in nearby galaxies by combining the kinematical data to the photometric data. For that, we first studied mass models within the optical disc using Hα rotation curves and mid-infrared 3.4μm of WISE photometry on a sample of 121 galaxies covering all morphological types (from early to late type spiral and irregular galaxies) (Korsaga et al. 2018). The surface brightness profiles have been decomposed if needed in a flat (disc, bar, spiral arm, etc.) and a spherical (bulge) components using the method developed by Barbosa et al. (2015). To describe the DM distribution, we used two main models: a pseudo-isothermal sphere (ISO) and a Navarro-Frenk-White (NFW) profile. Different fitting procedures are used: a best fit model (BFM) and M/L calculated using the (W1 - W2) colour. We also explore a pseudo-isothermal maximum disc model (MDM). We find that most of the galaxies are well described either by ISO or NFW models but ISO describes somewhat better the observed rotation curves. The M/L values derived from the ISO (MDM) are four times higher than the one for the ISO (BFM). However, we find similar median value for the M/L of ISO (MDM) and M/L determined by the (W1 - W2) colour which is equal to 0.4 suggesting that discs tend to be maximum. In order to understand how the DM is distributed, we studied the DM halo parameters as a function of the luminosity of galaxies (absolute B magnitude). We find no clear correlation between the core radius or the central density and the absolute B band magnitude for ISO (BFM, MDM, and fixed M/L).

However, previous authors (Kormendy & Freeman 2004, Randriamampandry & Carignan 2014), who studied mostly late type galaxies, find that less luminous galaxies tend to have smaller core radius and higher central density. To understand the difference between our results with those from the literature, we investigated different scenarios based on the quality of the rotation curves, the presence of bulge or not, and the presence of bar or not. We find that relations between the DM parameters and the luminous matter components do not depend on the quality of rotation curves, or on the fact that a galaxy has developed a bar or not, but depend on whether or not the galaxy has a bulge.

To investigate this, we divided our sample in two sub-samples (bulgeless galaxies composed mostly of late type galaxies, and bulgy galaxies which are mostly

composed of early type galaxies). We find that, for bulgeless galaxies, less luminous galaxies tend to have smaller core radius and higher central density, which is in agreement with the previous authors aforementioned. However, for bulge galaxies, less luminous galaxies tend to have smaller core radius and smaller central density. Another interesting relation is that, galaxies with a smaller core radius tends to have a smaller central density, this relation does not depend on the morphological type (same trend is found for the whole sample, that means for bulgeless, and bulgy galaxies).

For NFW model, we observe that low mass halos are more concentrated than high mass halos and the halo is more concentrated for early type than late type galaxies. In order to check if our results are not affected because we only used optical rotation curves, we therefore used the sample from Randriamampandry & Carignan (2014) by truncating their HI rotation curves to their optical radius and we found that mass models are in good agreement when the plateau is reached within this radius, which is usually the case for early types galaxies.

In the second part of the thesis, we study the mass distribution of the DM halo of 100 spiral and irregular galaxies using the Hα rotation curves and the optical R_c-band photometry (Korsaga et al. 2019). The sample covers morphological types (from early to late type spiral and irregular galaxies). We used the same method aforementioned to determine the baryonic and DM halo distribution of the galaxies such as the two models (a pseudo-isothermal sphere -ISO- with a core density profile and a cuspy dark halo density profile -NFW- with the different fitting procedures (BFM, MDM and Fixed M/L). However, for the Fixed M/L technique, we calculated the M/L using the (B - V) colour. This study gave us an opportunity to check if the derived DM halo parameters are different when using optical photometry compared to infrared for a similar sample of galaxies.

Similarly to what was found in the 3.4 μm band, we find that most of the observed rotation curves are better described by a central core profile than a cuspy one. The M/L values are smaller for the BFM (0.39 $M_\odot/L_\odot$), larger for the MDM (1.65 $M_\odot/L_\odot$) and intermediate values for the fixed M/L (1.07 $M_\odot/L_\odot$). We find that the dispersion of the M/L values are smaller in the infrared than in the optical, meaning that, 3.4 μm photometry should be preferred compared to R_c photometry when possible. We also find that, the relations between the DM halos parameters

(scaling radius and central density) and the absolute B-magnitude depend on the morphological types. Therefore, the results are comparable to the literature when we use bulge-poor galaxies (mostly composed of late type galaxies) because most of the previous results were mainly based on late type spirals. All the trend we found in this study for the whole sample, bulge-poor galaxies and bulge-rich (mostly composed of early type galaxies) galaxies are similar to those in Korsaga et al. (2018), suggesting that the results of the mass models are quite independent of the photometric band used.

We verified the impact of the band used in the relations found with the DM halo parameters and the luminosity of galaxies, for that, we used the magnitudes in the W1-band and we found similar trends to those found using the absolute B-band magnitude, meaning that these relations do not depend of the band used. In order to check if the disc and halo's parameters are not affected by irregular light distributions within the discs, we have modelled the observed disc with an exponential disc and we found the same trends between the DM halo parameters and the luminosity compared to the study using the true disc. This means that high-z galaxies, for which it is difficult to measure the detailed light distribution as a function of the distance, could be modelled using an exponential disc.

Studying the relation between the scaling radius and central density as a function of the disc scale length (h), we find that the scaling radius and central density seem quite independent of h for the whole sample and for bulge-rich galaxies but smaller h tend to have smaller scaling radius and higher central density for bulge-poor galaxies. For NFW model, we find that low mass halos are more concentrated than high mass halos. It is worthwhile to note that the halo is more concentrated when using the optical R_c-band photometry compared to the MIR W1-band for both ISO and NFW models.

In the last part of the thesis, we study the mass distribution of 31 galaxies using three different datasets. We first constructed the mass models using the Hα rotation curves from the GHASP survey, the mid-infrared 3.4 μm of WISE photometry with the contribution of the neutral gas component. Secondly, we used the hybrid (Hα and HI) extended rotation curves, mid-infrared photometry and the neutral gas component. Finally, we used the HI rotation curves from the literature, mid-infrared photometry and the neutral gas component. To determine the shape of the DM

halos, we used two models (the ISO core density profile and the NFW cuspy density profile) with different fitting procedures (BFM, MDM and fixed M/L obtained using W1-W2 colour). The aim is to understand how the luminous and DM parameters may vary when using the different kinematical data. In order to investigate if the neutral gas contribution may have influence on the distribution of the luminous and DM in galaxies, we compared the results obtained using Hα rotation curves and WISE photometry without the neutral gas component with those obtained when including the neutral gas component. We found that the relation between the DM parameters, and between the DM parameters and the luminosity of the galaxies remain very similar.

Using the three datasets, we found that M/L values are higher and the DM halo is less concentrated when using the hybrid rotation curves compared to Hα and HI rotation curves. The relation between the parameters of the ISO models varies from one dataset to the other depending of the fitting procedure (BFM, MDM or Fixed M/L). However, NFW models are less affected by either different datasets or fitting procedures, meaning that Hα rotation curves in the inner parts of galaxies is sufficient to characterize a NFW halo..

2 Future prospects

During this thesis, we have used high resolution optical rotation curves, MIR 3.4μm and R_c band photometry data to study mass distribution in the central part of spiral and irregular nearby galaxies. The HI rotation curves probe the mass distribution beyond the optical disk where the DM is expected to dominate. Therefore, the parameters of the DM distribution are very sensitive in the inner part of galaxies well studied using the emission line Hα observations. HI rotation curves are usually affected by beam smearing effects due to the poor angular resolution, which lead to uncertainties of the mass-to-light ratio (M/L). Because of the great sensitivity of the mass distribution parameters to the central part of the galaxies rotation curves, to observe the distribution of the luminous and DM halo in the inner part and also the outer region of galaxies, in near future work, we will combine the high resolution Hα rotation curves of the 121 galaxies with the HI rotation curves. The observed HI rotation curves will be obtained using deep, wide and high resolution HI observations with upgraded and new facilities such as ASKAP (Johnston et al.

2008, DeBoer et al. 2009), AperTIF (Oosterloo et al. 2010, Adams et al. 2018). It should also be interesting to combine integral field spectroscopic survey such as MaNGA (Bundy et al. 2015) or SAMI (Scott et al. 2018) with the aforementioned HI data to study the DM distribution in a large sample of galaxies. As for future work, it will be useful to study the mass distribution of a large sample of galaxies using high resolution HI rotation curves, the infrared photometry, and also taking into account the neutral gas component to construct the mass models of galaxies. This study will be possible with new telescopes such as MeerKAT (Camilo et al. 2018). The advent of this sensitive instrument will help advance this study by achieving direct detections of low column density HI. This instrument will provide high spatial resolution rotation curves similar to the optical resolution in the central and outer part of galaxies, this will allow to determine the distribution of the DM and luminous matter in the central and outer regions of galaxies with only HI rotation curves without the need of extended rotation curves (Hα extended to HI). We can therefore further our knowledge on the DM distribution inside the full region of galaxies. In that case, we do not need to deal with the difficulties to optimise the errors of the rotation curves in order get the same weight for optical and HI points when combining the two rotation curves to derive mass models.

Another interesting analysis will be the use of alternative MOND models (MOdified Newtonian Dynamics, Milgrom 1983) which describes the flatness of rotation curves without the need of DM by a modification of the gravitational laws. The modified dynamics involve a new constant with the dimension of an acceleration $a_0 \simeq 10^{-8}$ cm s^{-2}. The study with this theory will help answering to the challenge about the need or not of DM to construct the mass distribution in the outer region of galaxies using the MeerKAT data. The last point will be to derive the baryonic and DM halos distribution using a large sample of different redshift galaxies.

Bibliography

Adams, E., Adebahr, B., de Blok, W.J.G. et al. 2018, in American Astronomical Society Meeting Abstracts, Vol. 231, American Astronomical Society Meeting Abstracts #231, 354.04

Barbosa, C.E., Mendes de Oliveira, C., Amram, P. et al. 2015, MNRAS, 453, 2965

Bundy, K., Bershady, M.A., Law, D.R. et al. 2015, ApJ, 798, 7

Camilo, F., Scholz, P., Serylak, M. et al. 2018, ApJ, 856, 180

DeBoer, D.R., Gough, R.G., Bunton, J.D. et al. 2009, IEEE Proceedings, 97, 1507

Johnston, S., Taylor, R., Bailes, M. et al. 2008, Experimental Astronomy, 22, 151

Kormendy, J. and Freeman, K.C. 2004, in IAU Symposium, Vol. 220, Dark Matter in Galaxies, ed. S. Ryder, D. Pisano, M. Walker, & K. Freeman, 377

Korsaga, M., Amram, P., Carignan, C. et al. 2019, MNRAS, 482, 154

Korsaga, M., Carignan, C., Amram, P. et al. 2018, MNRAS, 478, 50

Milgrom, M. 1983, ApJ, 270, 371

Oosterloo, T., Verheijen, M. and van Cappellen, W. 2010, in ISKAF2010 Science Meeting, 43

Randriamampandry, T.H. and Carignan, C. 2014, MNRAS, 439, 2132

Scott, N., van de Sande, J., Croom, S.M. et al. 2018, MNRAS, 481, 2299

Appendices

Appendix A

1 Tables

We list here the global properties and mass models parameters of the 121 galaxies.

Table A.1: Global properties: (1) Name of the galaxy in the UGC catalogue. (2): Morphological type taken from the RC3 catalogue (except for galaxies UGC 3521, 3708, 3709, 3915, 4393, 10652, 11466 for which the morphological types are taken from Epinat et al. (2008a); (3) Absolute B-magnitude from Epinat et al. (2008a); (4): Central surface brightness from the observed data in mag arcsec^{-2}; (5): Isophotal radius at the limiting surface brightness of 25 mag arcsec^{-2} normalised by the disc scale length; (6): The last radius of the rotation curve normalised by the disc scale length; (7): Central surface brightness of the disc in mag arcsec^{-2}; (8): Disc scale length of the disc component in kpc; (9): Luminosity of the disc in unit of 10^8 L$\odot$ calculated at the isophotal radius; (10): Surface brightness of the bulge at the effective radius in mag arcsec^{-2}; (11): Effective radius of the bulge in kpc; (12): Sérsic index of the bulge; (13): Luminosity of the bulge in units of 10^8 L$\odot$, derived at the isophotal radius; (14): Classification flag of the rotation curves: 1 and 2 correspond respectively to very high and high quality rotation curves, while 3 represents poor quality rotation curves.

Galaxy						**Disc**			**Bulge**				**RC**
UGC	type	Mag	μ_{0obs}	R_{25}/h	R_{last}/h	μ_0	h	L_D	μ_e	r_e	n	L_B	**flag**
(1)	(2)	(3)	(4)	(5)	(6)	(7)	(8)	(9)	(10)	(11)	(12)	(13)	(14)
00089	SBa	−21.5	14.3	2.8	1.9	16.8	5.1	245.4	14.29	1.1	0.46	203.2	1
00094	SAab	−20.4	16.9	1.5	1.7	20.6	6.8	12.1	18.26	3.6	1.08	68.9	1
00508	SB(r)ab	−21.8	14.9	2.8	2.4	17.3	9.2	392.6	15.50	1.4	1.09	151.6	1
00528	SABb	−19.6	15.0	3.9	1.8	15.9	1.1	29.9	15.40	0.2	0.45	2.8	1
00763	SABm	−18.9	17.7	3.5	6.0	17.6	1.5	8.5	–	–	–	–	1
01256	SBcd	−18.9	17.6	4.6	5.3	17.5	1.6	10.1	–	–	–	–	3
01317	SAB(r)c	−21.5	15.5	5.4	5.6	15.3	4.3	447.4	–	–	–	–	1
01437	SABbc	−21.8	15.6	2.6	4.9	16.6	5.3	255.6	16.05	1.1	0.55	41.0	1
01655	Sa pec	−21.6	14.6	4.3	1.0	17.1	7.1	216.2	15.84	2.5	1.54	409.8	3

Continued . . .

Table A.1 – Continued from previous page

Galaxy						**Disc**			**Bulge**				**RC**
UGC	type	Mag	μ_{0obs}	R_{25}/h	R_{last}/h	μ_0	h	L_D	μ_e	r_e	n	L_B	**flag**
(1)	(2)	(3)	(4)	(5)	(6)	(7)	(8)	(9)	(10)	(11)	(12)	(13)	(14)
01736	SABc	−20.1	16.1	3.8	3.5	18.1	2.5	35.6	17.55	0.6	1.64	4.9	2
01886	SABbc	−20.8	15.8	0.8	4.8	17.4	6.6	70.5	16.03	1.2	0.59	49.5	2
01913	SABd	−20.1	17.2	4.9	3.0	17.2	3.0	32.9	–	–	–	–	2
02045	Sab	−20.5	14.2	6.7	2.9	14.4	1.8	195.2	14.87	0.4	0.02	6.5	1
02080	SABcd	−19.2	17.5	2.8	3.0	18.4	3.0	18.5	19.02	0.6	0.80	0.9	1
02141	S0 – a	−18.1	16.1	2.8	3.9	17.8	1.3	7.2	17.59	0.8	0.97	7.0	3
02183	Sa	−19.0	14.5	2.2	1.1	16.9	2.3	8.5	15.89	0.7	1.79	29.6	2
02193	SAc	−18.7	16.5	2.4	3.2	17.5	1.4	7.0	17.76	0.2	2.46	0.4	2
02503	SAB(r)b	−21.6	14.9	3.6	3.4	16.6	4.5	243.0	16.92	1.6	2.05	68.8	2
02800	Im	−18.6	17.8	3.8	3.2	17.8	1.8	14.7	–	–	–	–	1
02855	SABc	−21.4	14.6	3.9	5.6	15.8	2.3	191.0	14.77	0.3	0.32	11.7	1
03013	SBb	−21.3	15.2	1.5	3.6	17.9	6.6	60.5	16.54	1.8	1.28	96.3	1
03273	Sm	−18.3	17.9	4.0	6.6	17.8	1.1	7.8	–	–	–	–	3
03334	SABc	−22.8	14.9	3.3	2.9	17.1	10.9	584.3	16.91	3.0	2.01	268.0	1
03382	SBa	−20.4	15.8	3.6	4.1	17.6	3.3	83.5	15.36	0.7	0.46	31.5	2
03429	SBab pec	−21.3	13.0	4.2	3.6	15.6	3.3	195.3	13.75	0.7	0.70	150.5	1
03463	SABbc	−20.7	16.7	3.6	5.0	17.4	3.5	105.5	17.49	0.9	0.35	6.0	1

Continued . . .

Table A.1 – Continued from previous page

Galaxy						**Disc**			**Bulge**				**RC**
UGC	type	Mag	μ_{0obs}	R_{25}/h	R_{last}/h	μ_0	h	L_D	μ_e	r_e	n	L_B	**flag**
(1)	(2)	(3)	(4)	(5)	(6)	(7)	(8)	(9)	(10)	(11)	(12)	(13)	(14)
03521	Sc	−19.8	17.3	3.5	2.8	17.1	3.0	62.4	–	–	–	–	1
03528	SBab	−20.1	16.1	4.1	2.4	16.6	3.0	112.2	16.18	0.8	0.07	13.4	2
03574	SAcd	−18.0	18.0	1.2	3.3	19.8	3.8	4.0	19.67	1.5	1.19	3.3	1
03685	SBb	−19.7	16.3	2.0	3.6	18.2	3.6	30.5	16.72	0.5	0.78	5.8	2
03691	SAcd	−20.2	17.8	3.8	4.4	17.7	2.2	30.4	–	–	–	–	1
03708	Sbc pec	−20.7	15.3	3.0	1.1	14.8	2.9	170.8	–	–	–	–	2
03709	Sc	−21.5	15.6	3.8	4.3	16.4	3.2	182.6	14.58	0.5	0.08	26.3	1
03734	SAc	−18.6	15.8	2.6	5.0	17.3	1.8	11.6	16.29	0.3	1.22	2.6	1
03809	SAB(r)bc	−22.0	15.5	3.3	3.4	17.3	7.3	304.6	16.22	0.9	0.80	33.5	1
03826	SABd	−17.9	18.8	3.4	3.3	19.3	3.6	13.5	19.42	0.4	0.28	0.2	3
03876	SAd	−17.4	18.3	3.1	3.8	18.2	1.3	4.6	–	–	–	–	1
03915	SBc	−21.4	16.4	4.8	4.1	16.1	2.2	110.7	–	–	–	–	2
04026	Sab	−20.8	15.7	3.9	2.6	15.4	3.5	232.4	–	–	–	–	2
04165	SBd	−18.2	17.9	2.3	3.0	18.5	1.7	5.6	19.32	0.3	0.68	0.2	2
04256	SABc	−21.6	16.0	4.5	4.7	16.7	3.9	208.0	15.50	0.8	0.08	21.8	3
04273	SBb	−20.7	15.5	3.9	4.7	17.6	2.9	79.5	15.51	0.6	0.52	21.1	1
04274	SBm pec	−17.7	17.3	3.3	2.0	17.5	0.6	2.7	18.17	0.1	0.10	0.02	3

Continued . . .

Table A.1 – Continued from previous page

Galaxy						**Disc**			**Bulge**				**RC**
UGC	type	Mag	μ_{0obs}	R_{25}/h	R_{last}/h	μ_0	h	L_D	μ_e	r_e	n	L_B	**flag**
(1)	(2)	(3)	(4)	(5)	(6)	(7)	(8)	(9)	(10)	(11)	(12)	(13)	(14)
04284	SAcd	−18.4	18.1	2.4	3.3	18.8	1.8	4.5	19.45	0.6	0.55	0.5	1
04325	SAm	−18.2	18.9	3.1	2.7	18.9	1.5	3.3	–	–	–	–	1
04393	SBc	−19.3	17.3	2.9	4.3	18.7	2.3	8.6	18.48	1.1	0.99	5.1	3
04422	SABc	−21.1	16.0	2.4	3.7	18.6	5.9	96.5	16.02	1.1	0.48	38.5	1
04456	SAc	−20.8	18.0	2.8	4.2	17.8	3.9	50.2	–	–	–	–	2
04499	SABdm	−17.0	19.0	2.9	3.0	19.7	1.2	1.2	20.34	0.6	0.59	0.2	2
04555	SABbc	−20.9	17.4	4.1	3.8	17.2	3.1	84.9	–	–	–	–	1
04770	SBa	−21.3	16.1	4.0	3.2	17.7	5.6	236.1	15.76	1.2	0.22	48.9	3
04820	SA(r)ab	−20.3	14.2	2.7	1.6	16.0	3.8	120.0	15.00	0.4	1.02	25.8	2
04936	SABd	−20.6	17.6	2.7	4.1	19.1	4.7	24.1	18.98	1.2	1.10	4.2	1
05045	SAB(r)c	−21.2	16.8	4.0	3.8	17.3	4.4	168.3	16.03	0.8	0.13	14.3	2
05175	Sb	−20.6	16.1	7.0	4.5	15.9	1.9	98.3	–	–	–	–	1
05228	SBc	−19.9	17.0	4.3	4.6	16.9	1.9	40.2	–	–	–	–	1
05251	Sbc	−20.5	16.6	4.0	3.4	17.6	3.7	64.8	17.69	0.8	0.54	4.8	1
05253	SAab	−20.7	14.3	2.6	1.6	13.9	4.2	157.2	–	–	–	–	1
05316	SBd	−19.9	18.1	2.6	4.0	18.0	3.3	15.8	–	–	–	–	3
05319	SBc	−19.7	17.7	3.7	3.4	18.2	2.2	20.2	17.68	0.4	0.06	0.9	1

Continued . . .

Table A.1 – Continued from previous page

Galaxy						Disc			Bulge				RC
UGC	type	Mag	μ_{0obs}	R_{25}/h	R_{last}/h	μ_0	h	L_D	μ_e	r_e	n	L_B	**flag**
(1)	(2)	(3)	(4)	(5)	(6)	(7)	(8)	(9)	(10)	(11)	(12)	(13)	(14)
05373	IBm	−14.3	20.3	2.6	1.4	20.4	0.4	0.1	–	–	–	–	3
05414	IABm	−16.6	19.8	3.2	4.3	19.8	1.3	1.6	–	–	–	–	1
05510	SABbc	−19.3	16.3	4.1	5.3	17.4	1.4	17.9	16.57	0.3	0.65	1.9	1
05532	SAbc	−22.1	14.1	2.6	2.1	15.6	9.3	424.4	15.96	1.5	2.28	203.8	1
05721	SABd	−16.5	17.6	3.8	5.2	17.4	0.4	0.8	–	–	–	–	3
05786	SAB(r)bc pec	−19.6	14.7	1.8	3.0	18.7	2.1	6.5	15.99	0.7	1.16	20.8	3
05789	SBcd	−19.6	17.9	2.7	5.0	17.7	2.8	10.7	–	–	–	–	3
05829	Im	−16.2	20.8	4.2	4.7	20.9	1.4	0.6	–	–	–	–	3
05840	SAB(r)bc	−18.9	14.9	4.3	3.8	17.1	1.5	15.0	15.37	0.1	1.11	1.8	2
05842	SBcd	−18.8	17.5	3.6	3.7	18.2	1.6	13.6	17.76	0.3	0.10	0.3	1
05931	SABcd pec	−19.8	16.4	2.9	4.7	17.2	1.8	24.1	17.33	0.5	0.48	2.9	1
05982	SABc	−20.0	16.1	6.4	5.3	16.6	1.9	57.0	16.30	0.3	0.07	1.6	1
06118	SABab	−20.0	13.7	3.6	3.1	16.9	2.0	26.2	13.83	0.3	1.52	30.9	1
06277	SABc	−19.5	15.9	4.9	2.6	17.9	1.8	22.9	17.07	0.5	1.49	4.3	2
06419	SBm pec	−18.6	18.5	2.8	6.3	18.3	1.4	2.7	–	–	–	–	3
06521	SAbc pec	−21.2	17.0	5.0	4.8	16.9	3.8	176.1	–	–	–	–	1
06523	SAa	−21.0	15.8	3.6	1.4	17.2	3.5	103.4	16.17	1.6	0.54	72.1	3

Continued . . .

Table A.1 – Continued from previous page

Galaxy						**Disc**			**Bulge**				**RC**
UGC	type	Mag	μ_{0obs}	R_{25}/h	R_{last}/h	μ_0	h	L_D	μ_e	r_e	n	L_B	**flag**
(1)	(2)	(3)	(4)	(5)	(6)	(7)	(8)	(9)	(10)	(11)	(12)	(13)	(14)
06537	SAB(r)c	−20.5	16.1	4.3	4.2	17.7	2.6	58.7	16.52	0.3	0.59	2.5	1
06702	Sa	−20.6	16.1	2.7	3.2	18.1	4.3	57.7	15.57	1.3	0.12	61.2	1
06778	SABc	−20.7	15.2	2.2	2.7	16.4	2.8	52.1	16.56	0.6	1.11	10.9	1
07021	SAB(r)a	−19.7	14.7	3.2	1.9	17.0	3.2	59.2	14.76	0.4	0.66	26.8	1
07045	SAc	−19.2	16.2	4.7	4.7	17.0	1.5	39.0	16.89	0.5	0.00	1.2	1
07154	SABd	−20.0	17.0	3.5	5.3	18.4	3.1	31.5	18.32	0.6	1.07	2.0	2
07323	SABdm	−18.3	18.6	2.3	2.7	18.5	2.0	5.1	–	–	–	–	1
07766	SABcd	−21.0	16.5	5.9	4.3	17.2	3.4	98.1	17.12	0.3	0.04	1.0	1
07831	SBc pec	−18.5	16.2	4.3	2.6	16.2	1.0	9.8	–	–	–	–	1
07853	SBm	−18.9	17.1	3.5	5.4	17.7	1.3	9.2	18.68	0.3	0.92	0.3	3
07861	SABm pec	−17.3	16.8	2.9	3.0	18.6	0.7	2.3	17.88	0.3	0.90	0.8	2
07876	SABd	−17.9	18.2	2.7	2.5	18.0	1.5	5.1	–	–	–	–	1
07901	SAc	−20.6	15.1	4.4	5.1	16.2	2.6	105.7	15.50	0.4	0.56	8.6	1
07985	SABd	−18.7	17.1	3.2	4.8	17.5	1.1	8.8	18.95	0.4	0.84	0.5	2
08334	SAbc	−21.1	13.4	4.8	2.8	13.2	3.5	266.5	–	–	–	–	1
08403	SBcd	−19.2	17.7	3.6	5.1	17.6	2.3	18.0	–	–	–	–	1
08490	SAm	−17.1	18.0	4.3	3.7	17.9	0.7	1.5	–	–	–	–	1

Continued . . .

Table A.1 – Continued from previous page

Galaxy						Disc			Bulge				RC
UGC	type	Mag	μ_{0obs}	R_{25}/h	R_{last}/h	μ_0	h	L_D	μ_e	r_e	n	L_B	**flag**
(1)	(2)	(3)	(4)	(5)	(6)	(7)	(8)	(9)	(10)	(11)	(12)	(13)	(14)
08709	SABc	−21.4	16.0	3.9	4.7	16.9	4.9	223.6	16.78	0.8	0.60	11.7	1
08852	SAB(r)b	−20.0	15.9	6.4	3.6	16.6	1.8	74.0	16.01	0.5	0.07	5.0	1
08898	SBb pec	−20.5	14.9	2.8	0.4	19.1	6.6	35.9	15.07	0.8	0.87	71.4	3
08900	SAb pec	−21.7	15.7	3.4	2.4	17.2	5.2	353.3	16.88	1.6	0.99	49.2	2
08937	SBb	−21.1	14.7	4.9	4.3	16.5	3.4	154.0	14.80	0.8	0.75	71.4	1
09013	SAcd pec	−18.2	17.5	2.0	4.3	18.6	1.2	2.1	18.63	0.4	0.59	0.4	3
09179	SABd	−17.8	17.6	3.6	4.8	18.6	1.0	2.2	19.13	0.3	0.87	0.2	1
09248	Sb	−20.2	17.1	4.5	3.8	16.9	2.4	72.9	–	–	–	–	1
09358	SABb	−20.8	15.2	3.2	2.6	16.1	4.1	166.6	15.61	0.5	0.54	14.5	1
09363	SAd	−19.8	17.2	2.2	4.3	18.7	2.8	10.5	19.96	2.6	1.95	8.3	1
09366	SAbc	−21.7	15.1	4.6	3.7	15.8	4.3	435.7	16.08	0.9	0.74	29.3	1
09465	SABdm	−18.0	18.8	1.7	4.8	18.7	1.7	3.6	–	–	–	–	1
09576	SABd	−19.6	17.8	1.6	3.5	19.2	4.3	9.9	19.22	1.4	0.89	4.4	1
09649	SBb	−16.5	18.2	2.3	4.4	18.1	0.9	1.9	–	–	–	–	1
09736	SABc	−20.6	17.7	4.8	4.1	17.5	3.3	78.2	–	–	–	–	1
09753	SAbc	−19.1	15.1	5.0	4.6	16.1	1.4	27.1	16.41	0.4	0.90	5.7	1
09858	SABbc	−20.4	16.4	3.2	3.8	17.4	6.9	115.2	17.90	2.5	0.83	43.6	2

Continued . . .

Table A.1 – Continued from previous page

Galaxy						**Disc**			**Bulge**				**RC**
UGC	type	Mag	μ_{0obs}	R_{25}/h	R_{last}/h	μ_0	h	L_D	μ_e	r_e	n	L_B	**flag**
(1)	(2)	(3)	(4)	(5)	(6)	(7)	(8)	(9)	(10)	(11)	(12)	(13)	(14)
09866	SA(r)bc	−17.2	16.9	3.3	2.8	17.2	0.6	5.2	18.38	0.2	0.61	0.1	1
09943	SB(r)c	−20.7	15.7	5.7	5.8	15.4	1.9	101.3	–	–	–	–	1
09969	SAB(r)b	−21.4	16.0	4.2	4.4	17.1	4.9	301.8	16.45	0.7	0.40	13.1	1
10075	SAcd	−19.9	16.6	5.1	4.1	16.5	2.4	58.2	–	–	–	–	1
10359	SBcd pec	−19.0	17.5	1.9	5.2	18.6	2.6	8.2	18.43	0.5	0.53	1.0	1
10445	Scd	−17.6	18.5	3.1	4.4	19.0	1.5	3.1	19.43	0.4	0.27	0.2	3
10470	SBbc	−20.2	14.7	2.6	4.2	17.2	2.6	38.3	15.24	0.4	1.81	16.9	1
10502	SAc	−21.2	17.4	3.7	4.9	17.2	4.8	116.6	–	–	–	–	1
10521	SAc	−20.2	16.3	6.9	4.7	16.2	1.3	33.9	–	–	–	–	1
10564	SBd	−17.6	19.0	1.8	6.6	18.9	1.8	2.8	–	–	–	–	1
10652	S(r)bc	−17.7	17.4	3.9	4.0	17.2	0.7	4.3	–	–	–	–	1
10757	Scd	−17.7	18.5	3.5	3.4	18.3	1.0	3.0	–	–	–	–	1
10897	SAc	−19.5	16.9	3.6	3.2	17.7	1.8	19.0	17.06	0.3	0.33	1.0	1
11012	SAcd	−18.7	15.5	3.9	2.8	15.4	1.2	22.0	–	–	–	–	1
11124	SBcd	−18.6	18.5	4.4	4.5	18.3	1.8	8.3	–	–	–	–	1
11218	SAc	−20.8	15.6	4.2	3.7	16.1	2.6	141.0	15.54	0.3	0.10	3.0	1
11283	SBdm	−19.3	18.1	2.5	3.9	19.1	2.4	10.0	18.41	0.6	0.16	1.1	1

Continued . . .

Table A.1 – Continued from previous page

Galaxy						**Disc**			**Bulge**				**RC**
UGC	type	Mag	μ_{0obs}	R_{25}/h	R_{last}/h	μ_0	h	L_D	μ_e	r_e	n	L_B	**flag**
(1)	(2)	(3)	(4)	(5)	(6)	(7)	(8)	(9)	(10)	(11)	(12)	(13)	(14)
11300	Sd	−17.8	17.3	4.0	4.5	17.2	1.0	7.0	–	–	–	–	1
11407	SBbc	−20.8	15.3	3.2	3.1	17.8	4.1	68.5	16.14	0.8	1.82	31.7	1
11429	SBb	−21.8	15.9	3.4	3.6	16.8	5.8	400.4	16.11	0.7	0.05	27.6	2
11466	Sc	−18.5	15.3	3.0	5.1	17.2	1.0	7.1	16.46	0.5	1.13	7.2	1
11470	SAb	−21.3	14.4	1.4	0.4	16.3	12.9	147.3	16.17	2.9	1.67	408.2	3
11498	SBb	−20.5	15.1	4.4	4.7	16.4	4.2	351.8	15.09	0.8	0.09	37.9	2
11557	SABdm	−18.4	18.5	3.6	3.9	18.4	1.6	7.0	–	–	–	–	3
11597	SABcd	−20.6	13.3	4.5	2.5	15.3	2.2	67.1	14.51	0.1	2.29	9.7	1
11670	SA(r)0/a	−19.4	14.1	2.7	2.8	15.5	2.8	75.4	14.28	0.3	0.29	11.8	2
11707	SAdm	−16.6	18.9	1.2	6.0	19.8	2.1	1.1	20.12	0.8	0.56	0.5	1
11852	SBa	−20.2	16.1	3.1	2.3	17.1	3.5	96.0	16.24	1.1	0.42	33.1	2
11861	SABdm	−20.2	17.1	2.0	4.2	16.9	3.3	37.1	–	–	–	–	1
11872	SAB(r)b	−20.0	14.4	6.3	5.4	15.0	1.2	33.4	16.79	0.9	2.11	25.3	1
11914	SA(r)ab	−20.3	14.2	2.5	1.9	14.4	4.0	34.4	17.03	2.1	1.44	88.5	1
11951	SBa	−19.3	16.4	4.2	5.4	16.3	1.0	16.4	–	–	–	–	3
12060	IBm	−16.5	19.4	0.9	2.9	19.4	2.7	1.3	–	–	–	–	2
12276	SB(r)a	−20.7	16.5	3.1	3.6	17.6	4.1	96.2	16.44	1.1	0.36	23.6	3

Continued . . .

Table A.1 – Continued from previous page

Galaxy						**Disc**			**Bulge**				**RC**
UGC	type	Mag	$\mu_{0\,obs}$	R_{25}/h	R_{last}/h	μ_0	h	L_D	μ_e	r_e	n	L_B	**flag**
(1)	(2)	(3)	(4)	(5)	(6)	(7)	(8)	(9)	(10)	(11)	(12)	(13)	(14)
12343	SBc	−21.1	14.7	3.4	4.0	17.4	4.2	107.4	16.10	0.8	2.04	40.6	3
12754	SBcd	−18.6	17.2	2.8	3.2	18.8	1.7	6.4	17.92	0.3	0.56	0.6	2

Table A.2: Parameters of mass models using the Best Fit Model (BFM) and fixed M/L techniques with the pseudo-isothermal (ISO) model: (1) Name of the galaxy in the UGC catalogue, those marked with an asterisk (*) correspond to galaxies for which the presence of dark matter is not necessary. The columns (2) to (6) and (7) to (10) show respectively the BFM parameters, and the fixed M/L parameters for the ISO model. (2): M/L of the disc in $M_\odot/L_\odot$; (3): M/L of the bulge in $M_\odot/L_\odot$. (4) & (8): the core radius of the DM halo in kpc; (5) & (9): the Central density of the DM halo in 10^{-3} $M_\odot/pc^3$; (6) & (10): the reduced χ^2; (7): M/L derived using the W1-W2 colour in units of $M_\odot/L_\odot$.

Galaxy	**ISO (BFM)**					**ISO with fixed M/L**			
UGC	M/L Disc	M/L Bulge	r_0	ρ_0	χ^2	M/L	r_0	ρ_0	χ^2
(1)	(2)	(3)	(4)	(5)	(6)	(7)	(8)	(9)	(10)
00089	$0.10^{0.01}_{0.01}$	$0.30^{0.13}_{0.20}$	$36.2^{93.8}_{35.7}$	75^{24}_{35}	21.7	0.30	> 39.2	47^{252}_{47}	23.1
00094	$0.10^{0.08}_{0.01}$	$0.62^{0.26}_{0.52}$	$0.6^{0.2}_{0.1}$	750^{1}_{650}	7.1	0.45	$0.8^{0.1}_{0.3}$	750^{1}_{450}	7.6
00508	$0.64^{0.13}_{0.54}$	$0.66^{1.34}_{0.56}$	$4.9^{1.0}_{4.4}$	250^{49}_{20}	1.4	0.69	$5.1^{0.6}_{3.5}$	231^{168}_{31}	1.3
00528	$0.10^{0.01}_{0.01}$	$0.10^{0.01}_{0.01}$	$0.5^{9.5}_{0.1}$	0^{1}_{1}	4.2	0.24	$0.5^{9.5}_{0.1}$	0^{1}_{1}	53.9
00763	$0.16^{0.06}_{0.06}$	–	$1.9^{0.3}_{1.4}$	70^{29}_{20}	2.4	0.60	$17.5^{7.5}_{17.5}$	5^{44}_{5}	7.5
01317	$0.18^{0.01}_{0.08}$	–	$17.2^{0.8}_{16.7}$	5^{10}_{5}	6.5	0.33	$0.5^{17.5}_{0.1}$	0^{1}_{1}	117.2
01437	$0.14^{0.02}_{0.04}$	$0.36^{0.55}_{0.23}$	$0.8^{0.1}_{0.3}$	750^{1}_{550}	8.3	0.23	$0.7^{0.1}_{0.2}$	750^{1}_{750}	11.9
01736	$0.10^{0.01}_{0.01}$	$0.10^{1.90}_{0.01}$	$2.6^{0.6}_{2.1}$	138^{67}_{38}	5.4	0.51	$3.9^{0.1}_{3.4}$	48^{101}_{38}	9.6
01886	$0.30^{0.08}_{0.20}$	$0.32^{1.68}_{0.22}$	$1.9^{0.5}_{1.4}$	260^{145}_{60}	4.3	0.67	$39.0^{9.0}_{38.4}$	2^{53}_{2}	4.9
01913	$0.10^{0.01}_{0.01}$	–	$5.8^{0.2}_{5.3}$	20^{35}_{10}	15.4	0.50	> 35.6	1^{1}_{1}	65.8
02045	$0.10^{0.01}_{0.01}$	$0.10^{0.01}_{0.01}$	> 20.4	9^{1}_{9}	15.5	0.18	$0.5^{16.5}_{0.1}$	0^{1}_{1}	162.7
02080	$0.77^{0.06}_{0.67}$	$1.44^{0.56}_{1.34}$	> 35.6	4^{21}_{4}	2.6	0.62	$0.7^{0.2}_{0.2}$	229^{20}_{209}	2.6

Continued . . .

Table A.2 – Continued from previous page

Galaxy	ISO (BFM)					ISO with fixed M/L			
UGC	M/L Disc	M/L Bulge	r_0	ρ_0	χ^2	M/L	r_0	ρ_0	χ^2
(1)	(2)	(3)	(4)	(5)	(6)	(7)	(8)	(9)	(10)
02183	$0.10^{0.02}_{0.01}$	$0.23^{0.04}_{0.13}$	$2.4^{13.8}_{1.9}$	176^{73}_{176}	12.7	0.33	> 10.4	4^{11}_{4}	38.5
02193	$0.10^{0.38}_{0.01}$	$0.15^{2.35}_{0.05}$	$1.2^{0.9}_{0.7}$	600^{100}_{300}	2.1	0.48	$2.2^{1.4}_{1.7}$	230^{369}_{190}	2.0
02503*	$0.10^{0.01}_{0.01}$	$0.10^{1.90}_{0.01}$	$2.1^{0.2}_{1.6}$	362^{243}_{62}	16.2	0.72	$0.5^{12.5}_{0.1}$	0^{4}_{1}	45.5
02800	$0.10^{0.06}_{0.01}$	–	$2.4^{0.7}_{1.9}$	60^{45}_{60}	4.9	0.51	> 22.8	6^{26}_{6}	7.9
02855	$0.10^{0.01}_{0.01}$	$0.10^{0.26}_{0.01}$	$5.0^{0.1}_{4.5}$	65^{34}_{65}	18.1	0.19	$8.3^{0.1}_{6.7}$	24^{81}_{24}	30.9
03013	$0.10^{0.12}_{0.01}$	$0.23^{0.21}_{0.13}$	$2.9^{2.2}_{2.4}$	99^{6}_{89}	15.4	0.38	$7.3^{2.3}_{6.8}$	13^{86}_{13}	20.1
03334	$0.10^{0.04}_{0.01}$	$0.32^{0.52}_{0.22}$	$3.0^{0.1}_{2.5}$	300^{450}_{100}	10.1	0.41	$7.3^{0.1}_{6.8}$	47^{252}_{47}	9.9
03382*	$0.10^{0.51}_{0.01}$	$0.10^{1.90}_{0.01}$	$2.2^{3.1}_{1.7}$	543^{56}_{443}	1.7	0.68	$5.1^{0.9}_{3.5}$	109^{90}_{9}	1.9
03429	$0.10^{0.01}_{0.01}$	$0.10^{0.01}_{0.01}$	$22.2^{2.7}_{21.7}$	50^{365}_{1}	124.4	0.09	$9.5^{0.1}_{9.0}$	88^{611}_{78}	78.6
03463	$0.37^{0.01}_{0.27}$	$0.40^{1.60}_{0.30}$	$5.8^{0.9}_{5.3}$	10^{46}_{1}	2.3	0.42	$7.1^{0.4}_{5.5}$	5^{35}_{5}	2.5
03521*	$0.51^{0.06}_{0.41}$	–	$6.8^{1.2}_{6.3}$	6^{49}_{6}	0.3	0.39	$2.0^{0.5}_{1.5}$	63^{136}_{13}	0.3
03528	$0.77^{0.19}_{0.67}$	$0.79^{1.21}_{0.69}$	$0.5^{2.5}_{0.1}$	750^{1}_{725}	10.4	0.69	$0.7^{0.4}_{0.2}$	750^{1}_{730}	7.5
03574	$0.10^{1.15}_{0.01}$	$1.74^{0.76}_{1.64}$	$3.1^{0.9}_{2.6}$	110^{90}_{30}	3.9	1.07	$2.2^{0.4}_{0.6}$	161^{38}_{61}	4.2
03685	$0.10^{0.04}_{0.01}$	$0.10^{0.65}_{0.01}$	$4.6^{3.4}_{4.1}$	21^{84}_{21}	2.0	0.51	$0.5^{19.5}_{0.1}$	0^{2}_{1}	9.2
03691	$0.43^{0.02}_{0.33}$	–	> 38.8	6^{19}_{1}	4.4	0.39	$36.7^{63.3}_{36.2}$	7^{42}_{7}	4.5
03708*	$0.10^{0.08}_{0.01}$	–	$1.1^{0.5}_{0.6}$	750^{1}_{730}	3.0	0.12	$1.0^{0.5}_{0.5}$	750^{1}_{650}	2.7
03709	$0.20^{0.04}_{0.10}$	$0.23^{1.17}_{0.13}$	$3.4^{1.0}_{2.9}$	97^{8}_{87}	5.5	0.20	$2.9^{0.3}_{2.4}$	124^{125}_{104}	4.9

Continued . . .

Table A.2 – Continued from previous page

Galaxy	ISO (BFM)					ISO with fixed M/L			
UGC	M/L Disc	M/L Bulge	r_0	ρ_0	χ^2	M/L	r_0	ρ_0	χ^2
(1)	(2)	(3)	(4)	(5)	(6)	(7)	(8)	(9)	(10)
03734	$0.10^{0.08}_{0.01}$	$0.19^{0.56}_{0.09}$	$1.1^{0.6}_{0.6}$	186^{319}_{106}	1.5	0.78	$0.5^{3.5}_{0.1}$	0^{1}_{1}	61.3
03809*	$0.16^{0.10}_{0.06}$	$0.40^{1.60}_{0.30}$	$1.3^{0.5}_{0.8}$	597^{152}_{517}	6.0	0.47	$0.8^{0.1}_{0.3}$	703^{46}_{633}	6.6
03876	$0.58^{0.26}_{0.48}$	–	$2.2^{2.0}_{1.7}$	69^{36}_{69}	1.5	1.12	> 20.0	11^{4}_{11}	2.5
03915*	$0.29^{0.06}_{0.19}$	–	$0.7^{0.4}_{0.2}$	750^{1}_{740}	3.1	0.17	$1.0^{0.1}_{0.5}$	681^{68}_{681}	4.0
04026	$0.58^{0.01}_{0.48}$	–	> 36.0	5^{80}_{5}	15.3	0.60	> 36.0	1^{84}_{1}	14.9
04165*	$0.10^{0.19}_{0.01}$	$0.49^{1.51}_{0.39}$	$0.7^{0.2}_{0.2}$	251^{171}_{171}	2.4	0.32	$0.5^{0.1}_{0.1}$	252^{1}_{232}	2.5
04273	$0.20^{0.06}_{0.10}$	$0.27^{1.51}_{0.17}$	$4.9^{1.7}_{4.4}$	50^{55}_{50}	2.8	0.38	$15.0^{0.1}_{13.4}$	14^{55}_{14}	3.7
04284	$0.48^{0.03}_{0.38}$	$0.49^{1.51}_{0.39}$	$7.7^{2.4}_{7.2}$	23^{12}_{13}	4.1	0.90	> 23.6	11^{1}_{11}	9.4
04325	$0.10^{0.13}_{0.01}$	–	$3.4^{2.7}_{2.9}$	42^{24}_{42}	4.1	0.95	> 16.4	6^{7}_{6}	10.3
04422*	$0.10^{0.98}_{0.01}$	$1.90^{0.60}_{1.80}$	$3.4^{1.2}_{2.9}$	225^{80}_{215}	7.2	0.80	$1.7^{0.1}_{1.2}$	750^{1}_{740}	28.0
04456*	$0.10^{0.54}_{0.01}$	–	$1.8^{1.2}_{1.2}$	275^{230}_{175}	1.8	0.65	$2.9^{0.1}_{2.3}$	72^{177}_{52}	1.9
04499	$0.10^{0.01}_{0.01}$	$0.10^{0.69}_{0.01}$	$4.9^{0.1}_{4.4}$	24^{31}_{24}	29.7	0.56	$25.0^{0.1}_{23.4}$	11^{17}_{11}	43.1
04555*	$0.37^{0.20}_{0.27}$	–	$0.7^{0.7}_{0.2}$	734^{15}_{684}	0.8	0.55	$0.5^{0.2}_{0.1}$	702^{47}_{652}	0.8
04820*	$0.64^{0.19}_{0.54}$	$1.09^{0.91}_{0.99}$	$2.4^{0.6}_{1.9}$	243^{256}_{213}	1.8	0.73	$1.1^{0.3}_{0.6}$	702^{47}_{652}	1.9
04936	$0.10^{0.51}_{0.01}$	$0.45^{1.55}_{0.34}$	$4.1^{1.2}_{3.6}$	95^{10}_{65}	3.3	0.56	$4.9^{0.3}_{3.3}$	66^{39}_{36}	3.2
05045*	$0.84^{1.04}_{0.74}$	$3.13^{0.67}_{3.03}$	$1.9^{0.9}_{1.4}$	750^{1}_{733}	3.1	0.48	$2.4^{0.1}_{1.9}$	733^{16}_{718}	6.2
05175	$0.33^{0.01}_{0.23}$	–	$16.4^{1.6}_{15.9}$	13^{52}_{13}	1.2	0.32	$9.6^{1.6}_{9.1}$	16^{283}_{6}	1.2

Continued . . .

Table A.2 – Continued from previous page

Galaxy	ISO (BFM)					ISO with fixed M/L			
UGC	M/L Disc	M/L Bulge	r_0	ρ_0	χ^2	M/L	r_0	ρ_0	χ^2
(1)	(2)	(3)	(4)	(5)	(6)	(7)	(8)	(9)	(10)
05228	$0.26^{0.04}_{0.16}$	–	$2.0^{1.4}_{1.5}$	52^{3}_{52}	2.4	0.25	$1.9^{0.2}_{1.4}$	61^{138}_{51}	2.3
05251	$0.10^{0.01}_{0.01}$	$0.10^{0.17}_{0.01}$	$3.6^{0.5}_{3.1}$	30^{36}_{30}	5.8	0.30	> 50.8	2^{7}_{2}	28.3
05253	$0.28^{0.02}_{0.18}$	–	$1.5^{0.5}_{1.0}$	337^{112}_{337}	3.0	0.51	> 35.6	7^{1}_{7}	25.8
05319	$0.10^{0.03}_{0.01}$	$0.10^{1.90}_{0.01}$	$1.6^{0.3}_{1.1}$	303^{202}_{293}	8.3	0.62	$2.8^{0.1}_{2.3}$	104^{95}_{104}	9.2
05414*	$0.36^{0.30}_{0.26}$	–	$2.6^{2.4}_{2.1}$	28^{28}_{28}	6.1	1.04	$55.7^{144.3}_{54.1}$	6^{9}_{6}	6.6
05510	$0.10^{0.08}_{0.01}$	$0.36^{1.64}_{0.26}$	$1.0^{0.1}_{0.5}$	570^{180}_{540}	5.9	0.40	$1.5^{0.1}_{1.0}$	212^{293}_{202}	6.1
05532*	$0.57^{0.01}_{0.47}$	$0.57^{0.52}_{0.47}$	$2.8^{11.2}_{2.2}$	17^{8}_{16}	3.1	0.40	$1.1^{0.1}_{0.6}$	750^{1}_{740}	6.0
05840*	$1.68^{0.07}_{1.58}$	$1.72^{1.78}_{1.62}$	$1.0^{0.7}_{0.5}$	750^{1}_{680}	13.6	0.49	$1.6^{0.1}_{1.1}$	750^{1}_{720}	25.4
05842*	$0.10^{0.07}_{0.01}$	$0.10^{1.90}_{0.01}$	$1.5^{0.4}_{1.0}$	125^{80}_{115}	1.8	0.60	> 23.2	2^{56}_{2}	3.6
05931	$0.10^{0.01}_{0.01}$	$0.10^{0.22}_{0.01}$	$3.7^{1.0}_{3.2}$	58^{48}_{18}	4.1	0.28	> 33.6	11^{6}_{11}	17.0
05982	$0.10^{0.09}_{0.01}$	$1.70^{0.30}_{1.60}$	$1.5^{0.5}_{1.0}$	340^{409}_{310}	5.9	0.42	$0.7^{0.1}_{0.2}$	668^{81}_{638}	10.8
06118	$0.10^{0.01}_{0.01}$	$0.10^{0.09}_{0.01}$	$2.9^{0.1}_{2.4}$	95^{654}_{15}	5.5	0.13	$4.8^{0.1}_{4.3}$	56^{443}_{56}	7.1
06277	$0.10^{0.57}_{0.01}$	$0.48^{2.02}_{0.38}$	$3.3^{14.7}_{2.8}$	405^{50}_{395}	2.1	0.44	$3.5^{3.0}_{1.9}$	336^{354}_{236}	2.0
06521*	$0.51^{0.13}_{0.41}$	–	$0.8^{0.5}_{0.3}$	750^{1}_{740}	5.5	0.61	$0.8^{0.1}_{0.3}$	565^{185}_{555}	5.6
06537	$0.10^{0.01}_{0.01}$	$0.10^{1.90}_{0.01}$	$2.8^{0.1}_{2.2}$	125^{75}_{75}	18.3	0.55	$6.1^{0.1}_{4.5}$	20^{75}_{20}	22.6
06702	$0.10^{0.04}_{0.01}$	$0.23^{0.34}_{0.13}$	$0.8^{0.1}_{0.3}$	750^{1}_{740}	53.3	0.29	$0.7^{0.1}_{0.2}$	750^{1}_{710}	45.9
06778	$0.20^{0.04}_{0.10}$	$0.32^{0.56}_{0.22}$	$4.5^{1.2}_{4.0}$	98^{7}_{98}	9.1	0.26	$3.7^{0.1}_{3.2}$	100^{500}_{1}	9.8

Continued . . .

Table A.2 – Continued from previous page

Galaxy	ISO (BFM)					ISO with fixed M/L			
UGC	M/L Disc	M/L Bulge	r_0	ρ_0	χ^2	M/L	r_0	ρ_0	χ^2
(1)	(2)	(3)	(4)	(5)	(6)	(7)	(8)	(9)	(10)
07021	$0.10^{0.01}_{0.01}$	$0.10^{0.43}_{0.01}$	$1.3^{0.1}_{0.8}$	750^{1}_{740}	3.6	0.39	$16.3^{83.7}_{15.8}$	45^{354}_{45}	21.5
07045	$0.10^{0.01}_{0.01}$	$0.66^{1.34}_{0.56}$	$1.1^{0.1}_{0.6}$	408^{97}_{378}	3.4	0.44	$0.5^{0.1}_{0.1}$	298^{1}_{258}	7.2
07154	$0.34^{0.01}_{0.24}$	$0.36^{1.64}_{0.26}$	$7.6^{0.2}_{7.1}$	9^{27}_{9}	5.0	0.48	$10.0^{0.1}_{8.4}$	4^{31}_{4}	6.3
07323*	$0.61^{0.02}_{0.51}$	–	> 22.0	5^{17}_{5}	2.8	0.60	> 22.0	5^{30}_{5}	2.8
07766	$0.16^{0.01}_{0.06}$	$0.79^{1.17}_{0.69}$	$6.5^{1.5}_{6.0}$	6^{29}_{6}	4.5	0.28	$0.5^{7.5}_{0.1}$	0^{1}_{1}	10.3
07831	$0.14^{0.01}_{0.04}$	–	$7.8^{36.2}_{7.2}$	62^{43}_{52}	3.9	0.35	$0.5^{14.5}_{0.1}$	0^{1}_{1}	43.2
07861	$0.10^{0.01}_{0.01}$	$0.10^{0.01}_{0.01}$	> 8.4	14^{42}_{14}	2.4	0.44	$0.5^{6.5}_{0.1}$	0^{1}_{1}	41.9
07876	$0.24^{0.12}_{0.14}$	–	$1.6^{0.4}_{1.1}$	106^{1}_{76}	1.7	0.69	$7.3^{92.7}_{6.8}$	21^{84}_{21}	2.5
07901	$0.22^{0.02}_{0.12}$	$0.53^{1.47}_{0.43}$	$1.5^{0.3}_{1.0}$	306^{13}_{281}	3.9	0.48	$1.4^{0.1}_{0.9}$	80^{182}_{1}	30.8
07985	$0.39^{0.06}_{0.29}$	$0.66^{1.34}_{0.56}$	$4.1^{5.4}_{3.6}$	27^{18}_{27}	3.3	0.32	$1.1^{0.1}_{0.6}$	128^{310}_{98}	3.6
08334	$0.18^{0.01}_{0.08}$	–	$1.7^{0.5}_{1.2}$	183^{22}_{179}	5.6	0.46	$0.5^{4.5}_{0.1}$	0^{1}_{1}	296.8
08403	$0.10^{0.01}_{0.01}$	–	$7.8^{0.1}_{7.3}$	16^{129}_{16}	4.6	0.43	> 47.2	6^{23}_{6}	21.0
08490	$0.61^{0.12}_{0.51}$	–	$1.2^{0.5}_{0.7}$	167^{138}_{152}	2.1	0.43	$0.8^{0.1}_{0.3}$	286^{272}_{136}	2.1
08709	$0.22^{0.01}_{0.12}$	$0.23^{1.77}_{0.13}$	$4.8^{0.5}_{4.3}$	27^{8}_{27}	7.0	0.43	$0.5^{99.5}_{0.1}$	0^{1}_{1}	39.1
08852	$0.20^{0.02}_{0.10}$	$0.23^{1.77}_{0.13}$	$1.4^{0.3}_{0.9}$	293^{13}_{273}	5.8	0.58	$0.5^{14.5}_{0.1}$	0^{1}_{1}	49.7
08900	$0.14^{0.01}_{0.04}$	$0.14^{0.86}_{0.04}$	$9.2^{1.6}_{8.8}$	62^{43}_{62}	3.0	0.40	> 50.4	15^{84}_{15}	13.1
08937	$0.10^{0.08}_{0.01}$	$0.57^{0.78}_{0.47}$	$3.2^{0.7}_{2.7}$	195^{54}_{186}	11.2	0.24	$1.4^{0.1}_{0.9}$	750^{1}_{732}	17.1

Continued . . .

Table A.2 – Continued from previous page

Galaxy	ISO (BFM)					ISO with fixed M/L			
UGC	M/L Disc	M/L Bulge	r_0	ρ_0	χ^2	M/L	r_0	ρ_0	χ^2
(1)	(2)	(3)	(4)	(5)	(6)	(7)	(8)	(9)	(10)
09179	$0.10^{0.18}_{0.01}$	$0.32^{1.68}_{0.22}$	$1.5^{0.2}_{1.0}$	172^{33}_{112}	4.0	0.57	$2.5^{0.1}_{2.0}$	81^{68}_{81}	4.6
09248*	$0.12^{0.18}_{0.02}$	–	$1.0^{0.1}_{0.5}$	480^{269}_{470}	4.1	0.51	$0.8^{1.3}_{0.3}$	60^{60}_{60}	4.7
09358	$0.14^{0.01}_{0.04}$	$1.47^{0.03}_{1.37}$	$32.2^{107.8}_{31.7}$	22^{33}_{22}	7.4	0.28	$5.6^{0.2}_{5.1}$	31^{718}_{16}	37.8
09363	$0.10^{0.16}_{0.01}$	$0.23^{0.95}_{0.13}$	$3.1^{1.4}_{2.6}$	61^{44}_{31}	2.9	0.46	$11.5^{0.1}_{9.9}$	12^{67}_{12}	3.4
09366	$0.10^{0.01}_{0.01}$	$0.45^{0.86}_{0.34}$	$2.1^{0.1}_{1.6}$	177^{572}_{147}	5.3	0.27	$0.5^{0.1}_{0.1}$	40^{1}_{1}	11.4
09465	$0.10^{0.26}_{0.01}$	–	$1.5^{0.5}_{1.0}$	89^{16}_{49}	1.7	0.45	$2.2^{0.3}_{1.7}$	34^{45}_{34}	1.9
09576	$0.22^{0.04}_{0.12}$	$0.23^{1.04}_{0.13}$	$3.7^{1.4}_{3.2}$	17^{38}_{17}	6.7	0.62	$21.7^{78.3}_{20.1}$	1^{14}_{1}	14.8
09649*	$1.19^{0.05}_{1.09}$	–	> 15.6	15^{60}_{15}	25.4	0.76	$0.7^{0.2}_{0.2}$	231^{68}_{231}	25.6
09736*	$0.20^{0.18}_{0.10}$	–	$0.8^{0.2}_{0.3}$	665^{84}_{655}	9.8	0.65	$0.5^{0.1}_{0.1}$	701^{48}_{661}	11.8
09753	$0.20^{0.02}_{0.10}$	$0.23^{0.34}_{0.13}$	$1.2^{0.3}_{0.7}$	226^{73}_{176}	4.5	0.44	> 26.0	4^{1}_{4}	74.4
09858	$0.10^{0.04}_{0.01}$	$0.27^{0.26}_{0.17}$	$3.1^{2.7}_{2.6}$	40^{315}_{40}	6.4	0.48	$0.5^{2.5}_{0.1}$	0^{1}_{1}	38.9
09866*	$0.51^{0.06}_{0.41}$	$0.66^{1.34}_{0.56}$	> 6.8	64^{41}_{54}	1.6	0.51	$2.7^{0.3}_{2.2}$	79^{170}_{79}	1.6
09943	$0.37^{0.01}_{0.27}$	–	$6.6^{0.3}_{6.1}$	16^{133}_{6}	2.4	0.41	$100.0^{0.1}_{99.5}$	6^{83}_{6}	3.4
09969	$0.10^{0.06}_{0.01}$	$0.10^{1.90}_{0.01}$	$1.7^{0.2}_{1.2}$	675^{75}_{475}	3.7	0.53	$1.5^{0.1}_{0.5}$	427^{72}_{27}	5.1
10075	$0.10^{0.01}_{0.01}$	–	$1.3^{0.1}_{0.8}$	318^{181}_{318}	5.5	0.35	$2.1^{0.1}_{1.6}$	69^{130}_{49}	7.9
10359	$0.10^{0.02}_{0.01}$	$0.36^{1.64}_{0.26}$	$3.6^{0.3}_{3.1}$	50^{55}_{50}	2.7	0.32	$4.8^{0.2}_{3.2}$	31^{62}_{23}	3.3
10470	$0.10^{0.01}_{0.01}$	$0.10^{0.41}_{0.01}$	$2.1^{0.1}_{1.6}$	156^{49}_{106}	4.4	0.25	$4.2^{0.1}_{3.7}$	46^{159}_{46}	18.5

Continued . . .

Table A.2 – Continued from previous page

Galaxy	ISO (BFM)					ISO with fixed M/L			
UGC	M/L Disc	M/L Bulge	r_0	ρ_0	χ^2	M/L	r_0	ρ_0	χ^2
(1)	(2)	(3)	(4)	(5)	(6)	(7)	(8)	(9)	(10)
10502	$0.37^{0.04}_{0.27}$	–	$7.5^{0.5}_{7.0}$	7^{148}_{7}	1.0	0.63	$0.5^{7.5}_{0.1}$	0^{12}_{1}	4.2
10521	$0.14^{0.02}_{0.04}$	–	$2.5^{1.4}_{2.0}$	62^{3}_{52}	2.5	0.29	> 24.4	4^{1}_{4}	18.9
10564	$0.26^{0.06}_{0.16}$	–	$7.7^{3.6}_{7.2}$	7^{48}_{7}	3.2	0.58	$19.5^{29.1}_{17.9}$	3^{17}_{3}	7.0
10652	$0.10^{0.04}_{0.01}$	–	$1.3^{0.1}_{0.8}$	584^{165}_{564}	7.7	0.40	$1.5^{0.2}_{1.0}$	397^{102}_{347}	8.5
10757	$0.53^{0.10}_{0.43}$	–	> 13.6	24^{42}_{24}	2.0	0.48	> 13.6	27^{42}_{27}	1.9
10897	$0.10^{0.01}_{0.01}$	$0.10^{0.78}_{0.01}$	$2.0^{0.5}_{1.5}$	92^{414}_{92}	3.8	0.33	$3.5^{3.1}_{1.9}$	23^{31}_{23}	7.0
11012	$0.16^{0.01}_{0.06}$	–	$2.8^{0.1}_{2.3}$	74^{125}_{64}	2.9	0.42	$0.5^{17.5}_{0.1}$	0^{1}_{1}	119.1
11124	$0.10^{0.04}_{0.01}$	–	$4.9^{1.2}_{4.4}$	19^{57}_{19}	3.0	0.50	$30.7^{69.3}_{29.1}$	6^{23}_{6}	8.1
11218	$0.10^{0.01}_{0.01}$	$0.23^{1.77}_{0.13}$	$1.0^{0.1}_{0.5}$	528^{221}_{428}	3.7	0.25	$0.6^{0.1}_{0.1}$	431^{190}_{381}	4.9
11283*	$1.25^{0.49}_{1.15}$	$1.25^{2.46}_{1.15}$	$1.0^{0.2}_{0.5}$	336^{413}_{286}	9.6	0.38	$0.9^{0.1}_{0.4}$	643^{106}_{563}	9.3
11300	$0.33^{0.04}_{0.23}$	–	$3.1^{1.0}_{2.6}$	52^{253}_{32}	4.4	0.60	> 18.0	9^{3}_{9}	10.3
11407	$0.10^{0.01}_{0.01}$	$0.10^{0.17}_{0.01}$	$20.5^{7.5}_{20.0}$	8^{17}_{8}	15.6	0.29	> 50.8	1^{1}_{1}	55.5
11429	$0.10^{0.01}_{0.01}$	$0.10^{0.13}_{0.01}$	$10.2^{4.3}_{9.7}$	14^{42}_{14}	8.8	0.54	$0.5^{11.5}_{0.1}$	0^{1}_{1}	86.2
11466	$0.10^{0.04}_{0.01}$	$0.14^{0.13}_{0.04}$	$3.1^{1.3}_{2.6}$	86^{19}_{76}	7.3	0.19	$23.1^{76.9}_{22.6}$	41^{108}_{31}	11.6
11498	$0.10^{0.01}_{0.01}$	$0.10^{1.21}_{0.01}$	$4.1^{0.3}_{3.6}$	104^{95}_{54}	46.1	0.63	$0.5^{99.5}_{0.1}$	0^{2}_{1}	202.7
11597	$0.20^{0.06}_{0.10}$	$0.23^{0.95}_{0.13}$	$0.8^{0.3}_{0.3}$	406^{1}_{396}	5.8	0.24	$0.6^{0.1}_{0.1}$	669^{80}_{629}	5.7
11670	$0.22^{0.01}_{0.12}$	$0.57^{0.30}_{0.47}$	$12.7^{167.3}_{12.2}$	18^{48}_{18}	6.0	0.50	$0.5^{2.5}_{0.1}$	0^{1}_{1}	67.9

Continued . . .

Table A.2 – Continued from previous page

Galaxy	ISO (BFM)					ISO with fixed M/L			
UGC	M/L Disc	M/L Bulge	r_0	ρ_0	χ^2	M/L	r_0	ρ_0	χ^2
(1)	(2)	(3)	(4)	(5)	(6)	(7)	(8)	(9)	(10)
11707	$0.20^{0.33}_{0.10}$	$0.23^{1.77}_{0.13}$	$3.4^{1.4}_{2.9}$	24^{81}_{24}	2.6	0.37	$4.1^{0.5}_{2.5}$	18^{31}_{8}	2.4
11852	$0.10^{0.04}_{0.01}$	$0.10^{0.56}_{0.01}$	$2.9^{0.8}_{2.4}$	178^{21}_{168}	50.8	0.28	$7.0^{1.0}_{6.5}$	40^{259}_{40}	42.6
11861	$0.10^{0.01}_{0.01}$	–	$4.8^{0.3}_{4.3}$	38^{67}_{38}	3.4	0.31	$7.3^{0.7}_{5.7}$	16^{33}_{6}	6.0
11872	$0.10^{0.01}_{0.01}$	$0.14^{0.47}_{0.04}$	$1.0^{0.2}_{0.5}$	664^{85}_{664}	2.0	0.65	$0.5^{9.5}_{0.1}$	0^{1}_{1}	139.0
11914	$0.55^{0.02}_{0.45}$	$0.57^{0.26}_{0.47}$	$2.0^{0.7}_{1.5}$	207^{98}_{67}	2.4	0.67	$6.4^{2.0}_{5.9}$	40^{159}_{40}	4.1
12060*	$1.18^{0.31}_{1.08}$	–	$2.0^{1.0}_{1.5}$	43^{62}_{43}	12.9	0.94	$1.6^{0.4}_{0.7}$	66^{9}_{26}	12.5
12754	$0.10^{0.33}_{0.01}$	$0.43^{2.07}_{0.33}$	$1.7^{0.2}_{1.2}$	176^{73}_{176}	5.0	0.31	$1.6^{0.1}_{0.1}$	159^{6}_{59}	5.0

Table A.3: Parameters of mass models using the maximum disc model (MDM) technique with the pseudo-isothermal (ISO) model: (1) Name of the galaxy in the UGC catalogue; (2) M/L of the disc in $M_\odot/L_\odot$; (3) M/L of the bulge in $M_\odot/L_\odot$; (4) Core radius of the DM halo in kpc; (5) Central density of the DM halo in 10^{-3} $M_\odot/pc^3$; (6) The reduced χ^2.

Galaxy	**Maximum Disc Model**				
UGC	M/L Disc	M/L Bulge	r_0	ρ_0	χ^2
(1)	(2)	(3)	(4)	(5)	(6)
00089	$0.29^{0.01}_{0.19}$	$0.32^{0.13}_{0.22}$	$8.4^{41.6}_{7.9}$	50^{50}_{50}	27.9
00094	$0.61^{0.01}_{0.51}$	$0.65^{0.25}_{0.45}$	$0.5^{0.3}_{0.1}$	733^{16}_{713}	9.0
00508	$0.93^{0.01}_{0.83}$	$0.94^{1.06}_{0.74}$	$5.8^{0.8}_{4.8}$	166^{233}_{146}	1.8
00528	$0.10^{0.01}_{0.01}$	$0.10^{0.01}_{0.01}$	$0.5^{9.5}_{0.1}$	0^{13}_{1}	5.1
00763	$0.37^{0.01}_{0.27}$	–	$2.8^{0.1}_{2.3}$	30^{39}_{30}	3.1
01317	$0.18^{0.01}_{0.08}$	–	$7.9^{10.1}_{6.3}$	9^{6}_{9}	7.8
01437	$0.27^{0.01}_{0.17}$	$0.46^{0.51}_{0.26}$	$0.5^{4.7}_{0.1}$	321^{428}_{321}	12.0
01736	$0.61^{0.01}_{0.21}$	$0.62^{0.99}_{0.22}$	$10.0^{0.1}_{9.5}$	19^{81}_{18}	11.3
01886	$0.61^{0.01}_{0.51}$	$0.62^{1.38}_{0.52}$	$10.5^{2.5}_{9.9}$	8^{41}_{7}	5.6
01913	$0.14^{0.01}_{0.04}$	–	$3.8^{2.2}_{2.2}$	25^{30}_{25}	19.7
02045	$0.10^{0.01}_{0.01}$	$0.10^{0.01}_{0.01}$	$0.5^{7.5}_{0.1}$	0^{11}_{1}	20.4
02080	$1.05^{0.01}_{0.95}$	$1.06^{0.94}_{0.86}$	$0.5^{4.5}_{0.1}$	0^{30}_{1}	3.5
02183	$0.23^{0.01}_{0.13}$	$0.23^{0.04}_{0.13}$	$0.7^{7.3}_{0.2}$	384^{365}_{334}	15.2
02193	$1.12^{0.01}_{1.02}$	$1.14^{0.86}_{1.04}$	$4.8^{3.2}_{4.3}$	62^{43}_{57}	2.8
02503	$0.65^{0.01}_{0.55}$	$0.66^{1.34}_{0.56}$	$0.5^{2.5}_{0.1}$	0^{70}_{1}	42.7
02800	$0.30^{0.01}_{0.20}$	–	$3.2^{0.1}_{1.6}$	28^{72}_{28}	6.3
02855	$0.12^{0.01}_{0.02}$	$0.14^{0.01}_{0.04}$	$3.8^{0.1}_{2.2}$	80^{119}_{30}	20.4
03013	$0.32^{0.01}_{0.22}$	$0.32^{0.12}_{0.12}$	$2.0^{1.0}_{1.5}$	115^{510}_{65}	18.4
03334	$0.49^{0.01}_{0.39}$	$0.49^{0.39}_{0.39}$	$2.7^{0.3}_{2.2}$	155^{450}_{115}	12.9
03382	$0.61^{0.03}_{0.51}$	$0.62^{1.38}_{0.52}$	$4.3^{1.7}_{3.7}$	141^{158}_{131}	2.4
03429	$0.10^{0.01}_{0.01}$	$0.10^{0.01}_{0.01}$	$2.5^{5.5}_{2.0}$	63^{6}_{63}	126.4
03463	$0.42^{0.01}_{0.32}$	$0.45^{1.55}_{0.24}$	$4.4^{0.6}_{3.9}$	8^{47}_{8}	2.8
03521	$0.51^{0.06}_{0.41}$	–	$3.0^{2.0}_{2.5}$	12^{43}_{12}	0.3
03528	$1.03^{0.01}_{0.93}$	$1.05^{0.95}_{0.95}$	$0.5^{99.5}_{0.1}$	0^{750}_{1}	13.3
03574	$2.00^{0.01}_{1.90}$	$2.00^{0.01}_{1.80}$	$2.5^{1.7}_{2.0}$	82^{24}_{72}	5.0

Continued . . .

Table A.3 – Continued from previous page

Galaxy	Maximum Disc Model				
UGC	M/L Disc	M/L Bulge	r_0	ρ_0	χ^2
(1)	(2)	(3)	(4)	(5)	(6)
03685	$0.23^{0.01}_{0.13}$	$0.23^{0.52}_{0.13}$	$6.1^{1.9}_{5.6}$	7^{98}_{7}	2.5
03691	$0.51^{0.01}_{0.41}$	–	$24.8^{35.2}_{24.3}$	4^{21}_{4}	5.6
03708	$0.23^{0.01}_{0.13}$	–	$0.5^{99.5}_{0.1}$	0^{750}_{1}	4.3
03709	$0.26^{0.01}_{0.16}$	$0.28^{1.06}_{0.08}$	$3.1^{1.5}_{2.6}$	89^{16}_{39}	7.1
03734	$0.26^{0.01}_{0.16}$	$0.28^{0.61}_{0.08}$	$2.2^{0.1}_{1.8}$	40^{65}_{40}	2.0
03809	$0.67^{0.01}_{0.57}$	$0.88^{1.12}_{0.78}$	$0.5^{1.3}_{0.1}$	275^{474}_{245}	7.4
03876	$0.99^{0.01}_{0.89}$	–	$6.0^{0.1}_{5.5}$	19^{86}_{19}	1.9
03915	$0.40^{0.01}_{0.30}$	–	$0.5^{7.1}_{0.1}$	535^{214}_{535}	3.6
04026	$0.64^{0.01}_{0.54}$	–	$0.5^{7.5}_{0.1}$	0^{16}_{1}	17.8
04165	$0.67^{0.01}_{0.57}$	$0.69^{1.31}_{0.49}$	$0.5^{0.7}_{0.1}$	0^{106}_{1}	3.3
04273	$0.32^{0.01}_{0.22}$	$0.32^{1.47}_{0.12}$	$5.6^{1.0}_{5.1}$	31^{24}_{26}	3.7
04284	$0.67^{0.01}_{0.57}$	$0.69^{1.31}_{0.49}$	$12.8^{0.1}_{12.3}$	16^{19}_{16}	5.2
04325	$0.45^{0.01}_{0.35}$	–	$5.3^{0.7}_{4.8}$	22^{43}_{22}	5.1
04422	$1.80^{0.01}_{1.70}$	$1.91^{0.09}_{1.81}$	$0.8^{3.7}_{0.3}$	474^{31}_{424}	8.9
04456	$0.96^{0.01}_{0.86}$	–	$1.1^{1.2}_{0.6}$	220^{285}_{20}	2.3
04499	$0.30^{0.01}_{0.20}$	$0.32^{0.47}_{0.22}$	$4.3^{0.7}_{3.8}$	20^{35}_{20}	38.0
04555	$0.60^{0.01}_{0.50}$	–	$0.5^{7.1}_{0.1}$	428^{321}_{428}	1.0
04820	$0.93^{0.01}_{0.83}$	$0.94^{1.06}_{0.74}$	$1.9^{1.1}_{1.4}$	79^{670}_{49}	2.2
04936	$1.12^{0.01}_{1.02}$	$1.14^{0.86}_{1.04}$	$6.8^{0.1}_{6.3}$	38^{67}_{35}	4.2
05045	$2.64^{0.01}_{2.54}$	$3.91^{0.09}_{3.81}$	$0.5^{2.3}_{0.1}$	10^{740}_{1}	4.0
05175	$0.32^{0.01}_{0.22}$	–	$5.3^{12.7}_{4.8}$	22^{43}_{22}	1.5
05228	$0.35^{0.01}_{0.26}$	–	$5.3^{0.1}_{4.8}$	8^{47}_{8}	3.1
05251	$0.14^{0.01}_{0.04}$	$0.19^{0.09}_{0.09}$	$6.1^{0.3}_{5.6}$	12^{3}_{12}	8.9
05253	$0.34^{0.01}_{0.24}$	–	$2.0^{0.2}_{1.5}$	163^{243}_{153}	3.9
05319	$0.88^{0.01}_{0.78}$	$0.88^{1.12}_{0.78}$	$1.8^{0.1}_{1.3}$	136^{369}_{36}	10.8
05414	$1.34^{0.01}_{1.24}$	–	$41.2^{0.1}_{40.7}$	4^{11}_{4}	8.1
05510	$0.74^{0.01}_{0.64}$	$0.75^{1.25}_{0.65}$	$5.8^{0.1}_{5.3}$	27^{172}_{27}	8.1
05532	$0.58^{0.01}_{0.48}$	$0.62^{0.48}_{0.52}$	$0.5^{2.5}_{0.1}$	0^{26}_{1}	3.1
05840	$2.00^{0.01}_{1.90}$	$2.00^{0.01}_{1.90}$	$0.5^{3.5}_{0.1}$	0^{16}_{1}	26.4

Continued . . .

Table A.3 – Continued from previous page

Galaxy	Maximum Disc Model				
UGC	M/L Disc	M/L Bulge	r_0	ρ_0	χ^2
(1)	(2)	(3)	(4)	(5)	(6)
05842	$0.35^{0.01}_{0.26}$	$0.39^{1.81}_{0.29}$	$2.0^{0.1}_{1.5}$	45^{54}_{45}	2.7
05931	$0.14^{0.01}_{0.04}$	$0.14^{0.17}_{0.04}$	$3.6^{1.2}_{3.1}$	46^{60}_{6}	5.2
05982	$0.57^{0.01}_{0.47}$	$1.12^{1.78}_{1.02}$	$31.1^{0.1}_{30.1}$	9^{196}_{4}	7.0
06118	$0.10^{0.01}_{0.01}$	$0.10^{0.13}_{0.01}$	$1.9^{1.4}_{1.4}$	133^{16}_{128}	7.1
06277	$0.99^{0.01}_{0.89}$	$1.01^{0.99}_{0.91}$	$7.7^{0.3}_{6.8}$	146^{209}_{46}	2.7
06521	$0.90^{0.01}_{0.80}$	–	$0.5^{7.1}_{0.1}$	0^{750}_{1}	7.5
06537	$0.57^{0.01}_{0.47}$	$0.57^{1.43}_{0.47}$	$4.0^{0.1}_{3.5}$	27^{78}_{7}	24.2
06702	$0.42^{0.01}_{0.32}$	$0.45^{0.13}_{0.34}$	$0.5^{11.3}_{0.1}$	187^{562}_{187}	77.0
06778	$0.30^{0.01}_{0.20}$	$0.32^{0.56}_{0.22}$	$3.9^{2.2}_{3.4}$	74^{31}_{44}	11.8
07021	$0.18^{0.01}_{0.08}$	$0.19^{0.35}_{0.09}$	$1.7^{0.6}_{1.2}$	350^{1}_{334}	7.9
07045	$0.34^{0.01}_{0.24}$	$0.96^{1.04}_{0.86}$	$2.7^{0.1}_{2.2}$	48^{257}_{48}	4.6
07154	$0.48^{0.01}_{0.38}$	$0.49^{1.51}_{0.29}$	$8.9^{0.1}_{6.8}$	5^{30}_{4}	6.4
07323	$0.80^{0.01}_{0.70}$	–	$6.8^{8.2}_{6.3}$	1^{4}_{1}	2.9
07766	$0.20^{0.01}_{0.10}$	$0.62^{1.34}_{0.52}$	$1.9^{6.0}_{1.4}$	13^{22}_{13}	5.8
07831	$0.16^{0.01}_{0.06}$	–	$2.8^{1.2}_{1.2}$	57^{28}_{37}	4.8
07861	$0.10^{0.01}_{0.01}$	$0.10^{0.01}_{0.01}$	$1.1^{26.9}_{0.6}$	12^{3}_{12}	2.4
07876	$0.61^{0.01}_{0.51}$	–	$2.7^{0.2}_{2.2}$	38^{38}_{38}	2.3
07901	$0.35^{0.01}_{0.26}$	$0.45^{1.55}_{0.34}$	$3.0^{0.1}_{2.5}$	70^{85}_{65}	5.6
07985	$0.51^{0.01}_{0.41}$	$0.53^{1.47}_{0.43}$	$5.0^{0.1}_{4.5}$	12^{33}_{12}	4.2
08334	$0.22^{0.01}_{0.12}$	–	$2.8^{0.1}_{2.3}$	60^{145}_{60}	7.1
08403	$0.15^{0.01}_{0.05}$	–	$8.5^{0.1}_{8.0}$	14^{31}_{14}	5.9
08490	$0.99^{0.01}_{0.89}$	–	$3.7^{0.1}_{3.2}$	53^{52}_{15}	2.8
08709	$0.28^{0.01}_{0.18}$	$0.32^{1.68}_{0.22}$	$5.8^{0.1}_{5.3}$	13^{22}_{13}	9.1
08852	$0.35^{0.01}_{0.26}$	$0.36^{1.64}_{0.16}$	$1.7^{0.1}_{1.2}$	83^{222}_{83}	7.4
08900	$0.23^{0.01}_{0.13}$	$0.24^{0.78}_{0.04}$	$13.2^{2.4}_{12.7}$	41^{64}_{37}	4.2
08937	$0.61^{0.01}_{0.51}$	$0.62^{0.73}_{0.52}$	$7.8^{0.1}_{7.3}$	21^{84}_{21}	14.7
09179	$0.67^{0.01}_{0.57}$	$0.69^{1.31}_{0.49}$	$2.5^{0.1}_{2.0}$	74^{131}_{24}	5.2
09248	$0.57^{0.01}_{0.47}$	–	$0.5^{4.7}_{0.1}$	0^{750}_{1}	6.2
09358	$0.20^{0.01}_{0.10}$	$1.22^{0.78}_{1.12}$	$18.5^{21.5}_{18.0}$	20^{35}_{20}	9.3

Continued . . .

Table A.3 – Continued from previous page

Galaxy	Maximum Disc Model				
UGC	M/L Disc	M/L Bulge	r_0	ρ_0	χ^2
(1)	(2)	(3)	(4)	(5)	(6)
09363	$0.48^{0.01}_{0.38}$	$0.49^{0.74}_{0.29}$	$7.8^{0.1}_{7.3}$	14^{141}_{14}	3.7
09366	$0.23^{0.01}_{0.13}$	$0.46^{0.86}_{0.26}$	$0.5^{4.7}_{0.1}$	35^{714}_{35}	8.6
09465	$0.59^{0.01}_{0.49}$	–	$3.1^{0.1}_{2.6}$	17^{88}_{13}	2.2
09576	$0.39^{0.01}_{0.29}$	$0.40^{0.86}_{0.30}$	$4.6^{0.5}_{4.1}$	10^{45}_{10}	8.4
09649	$1.80^{0.01}_{1.70}$	–	$0.5^{9.5}_{0.1}$	0^{100}_{1}	31.7
09736	$0.77^{0.01}_{0.67}$	–	$0.5^{2.3}_{0.1}$	426^{323}_{426}	11.9
09753	$0.22^{0.01}_{0.12}$	$0.24^{0.37}_{0.04}$	$1.7^{0.8}_{1.2}$	103^{2}_{93}	6.8
09858	$0.26^{0.01}_{0.16}$	$0.27^{0.22}_{0.17}$	$2.4^{3.1}_{1.9}$	25^{330}_{15}	8.0
09866	$0.64^{0.01}_{0.54}$	$0.66^{1.34}_{0.56}$	$0.5^{17.5}_{0.1}$	0^{16}_{1}	2.4
09943	$0.39^{0.01}_{0.29}$	–	$6.1^{1.9}_{5.6}$	14^{91}_{4}	3.1
09969	$0.86^{0.01}_{0.76}$	$0.88^{1.12}_{0.78}$	$1.5^{3.4}_{1.0}$	89^{16}_{89}	8.7
10075	$0.28^{0.01}_{0.18}$	–	$1.5^{0.1}_{1.0}$	148^{151}_{138}	7.1
10359	$0.32^{0.01}_{0.22}$	$0.36^{1.64}_{0.26}$	$4.6^{0.1}_{4.1}$	31^{24}_{31}	3.5
10470	$0.12^{0.01}_{0.02}$	$0.12^{0.40}_{0.02}$	$2.1^{0.2}_{1.6}$	152^{147}_{132}	5.7
10502	$0.44^{0.01}_{0.34}$	–	$7.5^{0.5}_{7.0}$	4^{51}_{3}	1.3
10521	$0.18^{0.01}_{0.08}$	–	$3.6^{0.5}_{3.1}$	34^{31}_{34}	3.2
10564	$0.42^{0.01}_{0.32}$	–	$12.4^{0.1}_{11.9}$	5^{50}_{5}	4.1
10652	$0.70^{0.01}_{0.60}$	–	$2.1^{0.1}_{1.6}$	225^{180}_{125}	10.9
10757	$0.67^{0.01}_{0.57}$	–	$8.4^{41.6}_{7.9}$	16^{49}_{16}	2.4
10897	$0.18^{0.01}_{0.08}$	$0.18^{0.69}_{0.08}$	$1.7^{0.8}_{1.2}$	85^{20}_{85}	5.0
11012	$0.18^{0.01}_{0.08}$	–	$3.3^{0.1}_{2.8}$	47^{52}_{47}	3.6
11124	$0.23^{0.01}_{0.13}$	–	$5.9^{0.5}_{5.4}$	14^{61}_{14}	3.6
11218	$0.30^{0.01}_{0.20}$	$0.36^{1.64}_{0.16}$	$0.5^{1.4}_{0.1}$	165^{40}_{155}	6.2
11283	$3.11^{0.01}_{3.01}$	$3.11^{0.89}_{3.01}$	$0.5^{6.3}_{0.1}$	0^{40}_{1}	13.2
11300	$0.47^{0.01}_{0.37}$	–	$4.6^{3.4}_{4.1}$	25^{20}_{25}	5.7
11407	$0.12^{0.01}_{0.02}$	$0.13^{0.15}_{0.03}$	$9.8^{13.7}_{9.3}$	9^{46}_{9}	19.7
11429	$0.14^{0.01}_{0.04}$	$0.14^{0.09}_{0.04}$	$4.9^{3.1}_{4.4}$	22^{13}_{22}	11.1
11466	$0.14^{0.01}_{0.04}$	$0.14^{0.13}_{0.04}$	$1.9^{2.9}_{1.4}$	103^{2}_{103}	9.3
11498	$0.28^{0.01}_{0.18}$	$0.28^{1.05}_{0.18}$	$7.4^{1.7}_{6.9}$	26^{9}_{26}	74.4

Continued . . .

Table A.3 – Continued from previous page

Galaxy	**Maximum Disc Model**				
UGC	M/L Disc	M/L Bulge	r_0	ρ_0	χ^2
(1)	(2)	(3)	(4)	(5)	(6)
11597	$0.34^{0.01}_{0.24}$	$0.36^{0.70}_{0.16}$	$0.5^{0.7}_{0.1}$	232^{173}_{132}	7.2
11670	$0.26^{0.01}_{0.16}$	$0.53^{0.35}_{0.43}$	$4.5^{13.5}_{4.0}$	22^{43}_{22}	7.6
11707	$0.78^{0.01}_{0.68}$	$0.81^{1.19}_{0.61}$	$5.8^{0.1}_{5.3}$	10^{45}_{10}	3.4
11852	$0.39^{0.01}_{0.29}$	$0.40^{0.26}_{0.30}$	$3.1^{4.9}_{2.6}$	33^{22}_{33}	66.5
11861	$0.18^{0.01}_{0.08}$	–	$4.8^{0.3}_{4.3}$	33^{72}_{33}	4.4
11872	$0.20^{0.01}_{0.10}$	$0.23^{0.41}_{0.13}$	$2.3^{0.4}_{1.8}$	150^{1}_{150}	5.1
11914	$0.61^{0.01}_{0.51}$	$0.62^{0.22}_{0.52}$	$1.9^{0.7}_{1.4}$	181^{124}_{31}	3.0
12060	$2.80^{0.01}_{2.70}$	–	$0.5^{2.6}_{0.1}$	0^{106}_{1}	16.3
12754	$0.80^{0.01}_{0.70}$	$0.81^{1.19}_{0.61}$	$2.0^{0.1}_{1.5}$	68^{681}_{68}	6.4

Table A.4: Parameters of mass models using the Best Fit Model (BFM) and fixed M/L techniques with the Navarro-Frenk-White model (NFW): (1) Name of the galaxy in the UGC catalogue; the columns (2) to (6) and (7) to (10) show respectively the BFM parameters, and the fixed M/L parameters for the ISO model. (2): M/L of the disc in $M_\odot/L_\odot$; (3): M/L of the bulge in $M_\odot/L_\odot$. (4) & (8): the central halo concentration index; (5) & (9): the halo velocity in km s^{-1}; (6) & (10): the reduced χ^2; (7): M/L derived using the W1-W2 colour in units of $M_\odot/L_\odot$.

Galaxy	**NFW (BFM)**					**NFW with fixed M/L**			
UGC	M/L Disc	M/L Bulge	c	V_{200}	χ^2	M/L	c	V_{200}	χ^2
(1)	(2)	(3)	(4)	(5)	(6)	(7)	(8)	(9)	(10)
00089	$0.10^{0.01}_{0.01}$	$0.10^{0.34}_{0.01}$	$79.5^{0.1}_{78.5}$	$128.3^{371.7}_{118.3}$	22.3	0.30	$6.4^{0.1}_{5.4}$	$409.3^{90.7}_{408.3}$	27.6
00094	$0.10^{0.10}_{0.01}$	$0.13^{0.71}_{0.03}$	$48.4^{1.9}_{44.4}$	$99.3^{0.7}_{19.3}$	4.2	0.45	$54.5^{2.5}_{19.5}$	$70.5^{10.2}_{20.5}$	5.3
00508	$0.41^{0.25}_{0.31}$	$0.45^{1.55}_{0.34}$	$20.6^{4.4}_{19.6}$	$377.3^{122.7}_{27.3}$	1.3	0.69	$15.0^{2.5}_{10.0}$	$427.3^{72.7}_{127.3}$	1.4
00528	$0.10^{0.01}_{0.01}$	$0.10^{0.01}_{0.01}$	$100.0^{0.1}_{99.9}$	$5.5^{44.5}_{4.5}$	4.1	0.24	$1.0^{6.0}_{0.1}$	$1.0^{1.1}_{0.1}$	53.9
00763	$0.10^{0.01}_{0.01}$	–	$10.5^{0.6}_{9.5}$	$93.6^{106.4}_{73.6}$	3.0	0.60	$1.0^{0.1}_{0.1}$	$248.6^{8.4}_{218.6}$	11.8
01317	$0.10^{0.01}_{0.01}$	–	$15.2^{0.6}_{14.2}$	$126.4^{73.6}_{106.4}$	5.5	0.33	$100.0^{0.1}_{99.0}$	$1.0^{0.1}_{0.1}$	117.2
01437	$0.10^{0.01}_{0.01}$	$0.10^{0.82}_{0.01}$	$53.2^{0.1}_{51.1}$	$95.0^{105.0}_{35.0}$	3.4	0.23	$70.8^{4.5}_{69.8}$	$63.5^{86.5}_{54.5}$	5.6
01736	$0.10^{0.01}_{0.01}$	$0.10^{0.90}_{0.01}$	$4.5^{3.0}_{3.5}$	$500.0^{0.1}_{300.0}$	6.5	0.51	$2.6^{0.8}_{1.6}$	$500.0^{0.1}_{400.0}$	10.4
01886	$0.10^{0.43}_{0.01}$	$0.10^{1.90}_{0.01}$	$30.3^{5.1}_{29.2}$	$152.3^{147.7}_{102.3}$	4.2	0.67	$1.0^{0.5}_{0.1}$	$480.0^{20.0}_{420.0}$	6.8
01913	$0.10^{0.01}_{0.01}$	–	$1.6^{0.1}_{0.6}$	$436.4^{63.6}_{336.4}$	26.3	0.50	$1.0^{4.0}_{0.1}$	$1.0^{0.1}_{0.1}$	67.4
02045	$0.10^{0.01}_{0.01}$	$0.10^{0.01}_{0.01}$	$1.0^{3.5}_{0.1}$	$61.2^{67.5}_{56.2}$	16.7	0.18	$100.0^{0.1}_{99.0}$	$1.0^{0.1}_{0.1}$	162.7
02080	$0.10^{0.08}_{0.01}$	$0.49^{1.51}_{0.39}$	$18.1^{2.4}_{17.1}$	$85.5^{114.5}_{65.5}$	2.3	0.62	$13.5^{4.1}_{12.4}$	$60.9^{139.1}_{40.9}$	2.7
02183	$0.10^{0.01}_{0.01}$	$0.10^{0.17}_{0.01}$	$77.5^{4.5}_{76.5}$	$58.2^{241.8}_{38.2}$	6.5	0.33	$1.0^{49.0}_{0.1}$	$1.0^{36.0}_{0.1}$	38.5

Continued . . .

Table A.4 – Continued from previous page

Galaxy	NFW (BFM)					NFW with fixed M/L			
UGC	M/L Disc	M/L Bulge	c	V_{200}	χ^2	M/L	c	V_{200}	χ^2
(1)	(2)	(3)	(4)	(5)	(6)	(7)	(8)	(9)	(10)
02193	$0.10^{0.25}_{0.01}$	$0.10^{3.90}_{0.01}$	$7.5^{4.1}_{6.5}$	$486.4^{13.6}_{186.4}$	2.1	0.48	$6.6^{3.5}_{1.5}$	$395.5^{4.5}_{195.5}$	2.2
02503	$0.10^{0.01}_{0.01}$	$0.10^{0.90}_{0.01}$	$20.5^{2.4}_{19.4}$	$190.9^{109.1}_{90.9}$	20.9	0.72	$12.2^{87.8}_{11.2}$	$1.0^{6.8}_{0.1}$	45.5
02800	$0.10^{0.05}_{0.01}$	–	$3.4^{1.8}_{2.4}$	$286.4^{13.6}_{186.4}$	7.0	0.51	$1.0^{0.1}_{0.1}$	$250.0^{45.5}_{0.1}$	9.8
02855	$0.10^{0.01}_{0.01}$	$0.10^{0.26}_{0.01}$	$4.4^{0.3}_{3.4}$	$500.0^{0.1}_{490.0}$	22.8	0.19	$2.5^{0.1}_{1.5}$	$490.9^{9.1}_{390.9}$	35.5
03013	$0.10^{0.01}_{0.01}$	$0.10^{0.35}_{0.01}$	$27.1^{2.5}_{25.0}$	$121.6^{78.4}_{71.6}$	7.4	0.38	$4.0^{0.6}_{3.0}$	$200.0^{0.1}_{180.0}$	21.0
03334	$0.10^{0.03}_{0.01}$	$0.28^{0.62}_{0.18}$	$16.4^{1.2}_{15.4}$	$277.3^{122.7}_{177.3}$	9.7	0.41	$5.1^{0.6}_{4.1}$	$459.1^{40.9}_{259.1}$	9.8
03382	$0.10^{0.41}_{0.01}$	$0.10^{3.37}_{0.01}$	$22.9^{4.1}_{21.9}$	$236.4^{163.6}_{36.4}$	1.9	0.68	$8.6^{4.0}_{3.5}$	$386.4^{13.6}_{186.4}$	2.3
03429	$0.10^{0.01}_{0.01}$	$0.10^{0.01}_{0.01}$	$3.4^{0.1}_{2.4}$	$500.0^{0.1}_{440.0}$	162.4	0.09	$4.6^{0.1}_{3.5}$	$500.0^{0.1}_{300.0}$	112.0
03463	$0.30^{0.06}_{0.20}$	$0.32^{1.68}_{0.22}$	$6.0^{1.0}_{5.0}$	$126.4^{73.6}_{106.4}$	2.4	0.42	$1.4^{0.4}_{0.4}$	$187.7^{12.3}_{167.7}$	2.8
03521	$0.47^{0.10}_{0.37}$	–	$1.6^{16.0}_{0.6}$	$287.3^{12.7}_{267.3}$	0.3	0.39	$5.8^{5.3}_{4.7}$	$140.9^{159.1}_{120.9}$	0.3
03528	$0.26^{0.24}_{0.16}$	$0.27^{1.73}_{0.17}$	$51.9^{5.1}_{50.9}$	$115.5^{184.5}_{95.5}$	9.2	0.69	$78.4^{21.6}_{73.3}$	$56.4^{43.6}_{36.4}$	6.7
03574	$0.10^{0.40}_{0.01}$	$0.10^{1.90}_{0.01}$	$20.5^{2.4}_{19.5}$	$137.5^{62.5}_{47.5}$	3.8	1.07	$11.1^{1.8}_{10.0}$	$175.5^{24.5}_{155.5}$	3.8
03685	$0.10^{0.01}_{0.01}$	$0.10^{0.56}_{0.01}$	$1.4^{3.6}_{0.4}$	$479.5^{20.5}_{429.5}$	2.0	0.51	$3.3^{3.7}_{2.3}$	$1.0^{4.5}_{0.1}$	9.2
03691	$0.12^{0.05}_{0.02}$	–	$2.4^{2.0}_{1.4}$	$469.3^{30.7}_{419.3}$	4.1	0.39	$1.9^{0.1}_{0.8}$	$300.0^{0.1}_{100.0}$	6.3
03708	$0.10^{0.03}_{0.01}$	–	$12.2^{14.8}_{11.2}$	$303.6^{196.4}_{283.6}$	1.9	0.12	$13.6^{3.0}_{8.5}$	$231.8^{168.2}_{31.8}$	1.8
03709	$0.10^{0.01}_{0.01}$	$0.10^{1.24}_{0.01}$	$18.1^{2.4}_{17.1}$	$170.0^{50.0}_{150.0}$	5.6	0.20	$9.6^{2.0}_{4.5}$	$222.7^{77.3}_{122.7}$	5.3
03734	$0.14^{0.04}_{0.04}$	$0.14^{0.73}_{0.04}$	$12.8^{6.5}_{11.8}$	$81.4^{38.6}_{61.4}$	1.5	0.78	$12.2^{14.8}_{11.2}$	$1.0^{1.5}_{0.1}$	61.3

Continued . . .

Table A.4 – Continued from previous page

Galaxy	NFW (BFM)					NFW with fixed M/L			
UGC	M/L Disc	M/L Bulge	c	V_{200}	χ^2	M/L	c	V_{200}	χ^2
(1)	(2)	(3)	(4)	(5)	(6)	(7)	(8)	(9)	(10)
03809	$0.11^{0.06}_{0.01}$	$0.49^{1.51}_{0.39}$	$20.5^{3.0}_{19.5}$	$159.1^{40.9}_{139.1}$	6.1	0.47	$31.0^{1.2}_{26.0}$	$93.6^{106.4}_{73.6}$	6.5
03876	$0.26^{0.19}_{0.16}$	–	$6.3^{5.9}_{5.3}$	$210.9^{9.1}_{190.9}$	1.7	1.12	$1.0^{1.2}_{0.1}$	$325.0^{34.1}_{225.0}$	4.0
03915	$0.10^{0.10}_{0.01}$	–	$40.0^{1.5}_{39.0}$	$102.3^{47.7}_{52.3}$	2.2	0.17	$36.0^{4.2}_{30.9}$	$95.5^{54.5}_{45.5}$	2.2
04026	$0.10^{0.02}_{0.01}$	–	$54.3^{3.1}_{53.3}$	$130.5^{69.5}_{110.5}$	12.5	0.60	$100.0^{0.1}_{99.0}$	$21.2^{78.8}_{20.2}$	14.9
04165	$0.11^{0.15}_{0.01}$	$0.19^{1.81}_{0.09}$	$18.7^{3.5}_{17.7}$	$50.9^{49.1}_{30.9}$	2.5	0.32	$19.9^{2.4}_{18.8}$	$36.4^{63.6}_{16.4}$	2.5
04273	$0.16^{0.01}_{0.06}$	$0.19^{1.33}_{0.09}$	$7.5^{3.0}_{6.5}$	$250.0^{150.0}_{50.0}$	2.8	0.38	$2.1^{0.4}_{0.7}$	$500.0^{109.1}_{490.9}$	5.6
04284	$0.10^{0.01}_{0.01}$	$0.10^{1.90}_{0.01}$	$4.0^{0.1}_{3.0}$	$293.2^{6.8}_{93.2}$	5.2	0.90	$1.0^{0.1}_{0.1}$	$336.4^{9.1}_{236.4}$	16.3
04325	$0.10^{0.05}_{0.01}$	–	$1.6^{0.6}_{0.6}$	$448.9^{51.1}_{398.9}$	9.8	0.95	$1.0^{1.1}_{0.1}$	$50.5^{36.0}_{49.5}$	12.4
04422	$0.74^{0.22}_{0.64}$	$0.81^{2.30}_{0.71}$	$60.6^{6.3}_{59.6}$	$145.5^{104.5}_{125.5}$	3.2	0.80	$59.7^{4.4}_{54.6}$	$145.5^{154.5}_{45.5}$	3.0
04456	$0.10^{0.82}_{0.01}$	–	$15.2^{10.6}_{14.2}$	$155.0^{45.0}_{135.0}$	1.8	0.65	$4.0^{7.7}_{2.9}$	$304.5^{295.5}_{204.5}$	1.8
04499	$0.10^{0.01}_{0.01}$	$0.10^{0.01}_{0.01}$	$1.0^{0.6}_{0.1}$	$379.5^{20.5}_{279.5}$	48.3	0.56	$1.0^{0.1}_{0.1}$	$165.9^{31.8}_{15.9}$	53.0
04555	$0.51^{0.16}_{0.41}$	–	$36.6^{20.4}_{35.6}$	$57.5^{142.5}_{47.5}$	0.6	0.55	$40.5^{16.5}_{39.4}$	$52.7^{147.3}_{32.7}$	0.6
04820	$0.70^{0.16}_{0.60}$	$0.99^{3.01}_{0.89}$	$8.1^{18.9}_{7.1}$	$374.1^{25.9}_{354.1}$	1.8	0.73	$24.3^{5.9}_{19.2}$	$131.8^{168.2}_{31.8}$	1.8
04936	$0.10^{0.01}_{0.01}$	$0.10^{3.90}_{0.01}$	$8.7^{1.2}_{7.7}$	$277.3^{122.7}_{77.3}$	3.5	0.56	$5.6^{0.5}_{0.5}$	$374.1^{25.9}_{354.1}$	4.0
05045	$0.13^{0.89}_{0.03}$	$0.17^{2.83}_{0.07}$	$51.9^{5.1}_{50.9}$	$213.9^{186.1}_{203.9}$	2.1	0.48	$49.9^{4.7}_{44.8}$	$202.3^{197.7}_{102.3}$	1.9
05175	$0.23^{0.03}_{0.13}$	–	$7.5^{4.1}_{6.5}$	$200.0^{200.0}_{0.1}$	1.0	0.32	$2.2^{0.6}_{1.2}$	$391.4^{8.6}_{371.4}$	2.1
05228	$0.28^{0.02}_{0.18}$	–	$1.3^{11.8}_{0.3}$	$421.1^{78.9}_{417.1}$	3.4	0.25	$2.5^{1.4}_{1.4}$	$288.6^{11.4}_{238.6}$	3.6

Continued . . .

Table A.4 – Continued from previous page

Galaxy	NFW (BFM)					NFW with fixed M/L			
UGC	M/L Disc	M/L Bulge	c	V_{200}	χ^2	M/L	c	V_{200}	χ^2
(1)	(2)	(3)	(4)	(5)	(6)	(7)	(8)	(9)	(10)
05251	$0.10^{0.01}_{0.01}$	$0.10^{0.17}_{0.01}$	$1.4^{0.7}_{0.4}$	$466.6^{33.4}_{456.6}$	7.9	0.30	$1.0^{0.1}_{0.1}$	$114.1^{12.3}_{94.1}$	33.6
05253	$0.20^{0.04}_{0.10}$	–	$34.1^{22.9}_{33.1}$	$114.1^{85.9}_{94.1}$	2.7	0.51	$1.0^{0.6}_{0.1}$	$75.9^{72.5}_{65.9}$	27.8
05319	$0.96^{0.25}_{0.86}$	$0.96^{1.04}_{0.86}$	$3.4^{7.7}_{2.4}$	$400.0^{0.1}_{380.0}$	13.4	0.62	$3.9^{1.9}_{2.9}$	$500.0^{0.1}_{300.0}$	12.4
05414	$0.39^{0.22}_{0.29}$	–	$1.0^{1.8}_{0.1}$	$412.7^{87.3}_{392.7}$	8.2	1.04	$1.0^{0.7}_{0.1}$	$193.2^{20.5}_{143.2}$	8.7
05510	$0.10^{0.16}_{0.01}$	$0.10^{1.90}_{0.01}$	$25.0^{1.0}_{24.0}$	$107.3^{92.7}_{27.3}$	6.1	0.40	$11.3^{0.1}_{10.2}$	$155.7^{44.3}_{105.7}$	6.1
05532	$0.48^{0.06}_{0.38}$	$0.53^{0.56}_{0.43}$	$23.5^{3.5}_{22.5}$	$93.6^{106.4}_{73.6}$	3.0	0.40	$80.0^{2.2}_{78.0}$	$96.4^{403.6}_{76.4}$	3.0
05840	$0.10^{0.01}_{0.01}$	$0.10^{2.90}_{0.01}$	$66.2^{0.1}_{65.2}$	$114.1^{85.9}_{94.1}$	13.3	0.49	$58.6^{0.1}_{28.6}$	$110.9^{66.8}_{50.9}$	13.3
05842	$0.10^{0.08}_{0.01}$	$0.10^{1.90}_{0.01}$	$3.4^{3.0}_{2.4}$	$356.8^{43.2}_{336.8}$	2.7	0.60	$1.0^{2.4}_{0.1}$	$89.3^{40.8}_{88.3}$	3.8
05931	$0.10^{0.01}_{0.01}$	$0.10^{0.22}_{0.01}$	$3.4^{0.6}_{2.4}$	$348.2^{51.8}_{328.2}$	6.7	0.28	$1.0^{0.1}_{0.1}$	$146.0^{50.8}_{145.0}$	22.2
05982	$0.10^{0.16}_{0.01}$	$1.25^{2.75}_{1.15}$	$18.7^{3.0}_{17.7}$	$140.9^{159.1}_{120.9}$	5.2	0.42	$11.1^{1.1}_{1.1}$	$138.6^{13.6}_{88.6}$	9.1
06118	$0.10^{0.01}_{0.01}$	$0.10^{0.13}_{0.01}$	$4.5^{1.2}_{3.5}$	$391.4^{8.6}_{371.4}$	6.2	0.13	$3.2^{0.1}_{2.2}$	$489.1^{10.9}_{469.1}$	9.8
06277	$0.80^{0.10}_{0.70}$	$0.81^{2.04}_{0.71}$	$7.0^{0.1}_{6.0}$	$500.0^{0.1}_{440.0}$	3.2	0.44	$10.0^{4.0}_{7.9}$	$500.0^{0.1}_{420.0}$	2.4
06521	$0.70^{0.03}_{0.64}$	–	$98.0^{0.1}_{96.0}$	$54.0^{50.9}_{29.1}$	3.2	0.61	$59.1^{10.2}_{49.1}$	$70.5^{68.2}_{20.5}$	3.2
06537	$0.10^{0.01}_{0.01}$	$0.10^{3.90}_{0.01}$	$8.7^{0.1}_{7.7}$	$236.4^{63.6}_{216.4}$	21.9	0.55	$2.1^{0.1}_{1.1}$	$393.2^{6.8}_{293.2}$	25.0
06702	$0.10^{0.01}_{0.01}$	$0.10^{0.47}_{0.01}$	$75.5^{5.7}_{74.4}$	$78.5^{121.5}_{76.5}$	18.3	0.29	$100.0^{0.1}_{67.0}$	$54.0^{14.5}_{30.9}$	27.6
06778	$0.10^{0.01}_{0.01}$	$0.19^{0.69}_{0.09}$	$11.6^{0.1}_{10.6}$	$255.0^{245.0}_{245.0}$	7.8	0.26	$4.5^{0.1}_{3.5}$	$500.0^{0.1}_{400.0}$	11.0
07021	$0.10^{0.01}_{0.01}$	$0.10^{0.43}_{0.01}$	$20.7^{4.5}_{19.7}$	$188.2^{311.8}_{178.2}$	7.7	0.39	$2.8^{1.2}_{1.8}$	$500.0^{0.1}_{430.0}$	26.1

Continued . . .

Table A.4 – Continued from previous page

Galaxy	NFW (BFM)					NFW with fixed M/L			
UGC	M/L Disc	M/L Bulge	c	V_{200}	χ^2	M/L	c	V_{200}	χ^2
(1)	(2)	(3)	(4)	(5)	(6)	(7)	(8)	(9)	(10)
07045	$0.10^{0.01}_{0.01}$	$0.36^{3.64}_{0.18}$	$21.2^{0.1}_{20.2}$	$104.5^{95.5}_{54.5}$	3.0	0.44	$5.1^{0.1}_{0.1}$	$100.0^{0.1}_{80.0}$	6.9
07154	$0.23^{0.01}_{0.13}$	$0.23^{1.77}_{0.13}$	$2.8^{2.4}_{1.8}$	$240.7^{59.3}_{230.7}$	5.3	0.48	$1.0^{0.1}_{0.1}$	$300.0^{0.1}_{290.0}$	8.7
07323	$0.11^{0.13}_{0.01}$	–	$2.2^{3.0}_{1.2}$	$313.6^{86.4}_{293.6}$	2.7	0.60	$1.0^{0.6}_{0.1}$	$201.4^{8.6}_{181.4}$	3.3
07766	$0.10^{0.04}_{0.01}$	$0.66^{1.25}_{0.56}$	$5.7^{0.6}_{4.7}$	$110.0^{90.0}_{90.0}$	4.4	0.28	$100.0^{0.1}_{99.0}$	$2.8^{1.8}_{1.8}$	10.3
07831	$0.10^{0.01}_{0.01}$	–	$3.4^{0.1}_{2.4}$	$381.8^{18.2}_{181.8}$	5.4	0.35	$1.0^{6.5}_{0.1}$	$1.0^{0.1}_{0.1}$	43.2
07861	$0.10^{0.01}_{0.01}$	$0.10^{0.01}_{0.01}$	$1.6^{5.3}_{0.6}$	$100.0^{0.1}_{99.0}$	3.0	0.44	$1.0^{69.0}_{0.1}$	$1.0^{2.6}_{0.1}$	42.0
07876	$0.10^{0.06}_{0.01}$	–	$2.8^{1.8}_{1.8}$	$500.0^{0.1}_{450.0}$	3.0	0.69	$1.0^{1.4}_{0.1}$	$459.1^{30.7}_{409.1}$	4.5
07901	$0.10^{0.01}_{0.01}$	$0.19^{2.75}_{0.09}$	$41.5^{0.1}_{40.5}$	$108.9^{141.1}_{88.9}$	3.1	0.48	$1.0^{0.1}_{0.1}$	$500.0^{0.1}_{490.0}$	24.1
07985	$0.14^{0.10}_{0.04}$	$0.14^{1.86}_{0.04}$	$16.4^{2.4}_{15.4}$	$81.4^{118.6}_{61.4}$	3.0	0.32	$6.3^{1.8}_{5.3}$	$140.0^{360.0}_{120.0}$	3.1
08334	$0.14^{0.01}_{0.04}$	–	$24.0^{3.0}_{23.0}$	$108.0^{92.0}_{58.0}$	5.3	0.46	$28.0^{72.0}_{27.0}$	$1.0^{0.1}_{0.1}$	296.8
08403	$0.10^{0.01}_{0.01}$	–	$1.6^{0.1}_{0.6}$	$477.7^{22.3}_{467.7}$	15.9	0.43	$1.0^{0.1}_{0.1}$	$377.3^{0.1}_{177.3}$	36.9
08490	$0.39^{0.06}_{0.29}$	–	$3.4^{11.8}_{2.4}$	$467.3^{32.7}_{447.3}$	2.5	0.43	$7.0^{0.6}_{5.9}$	$188.6^{11.4}_{88.6}$	2.5
08709	$0.22^{0.01}_{0.12}$	$0.23^{1.77}_{0.13}$	$6.3^{10.6}_{5.3}$	$163.2^{36.8}_{143.2}$	9.0	0.43	$1.0^{0.1}_{0.1}$	$50.0^{0.1}_{0.1}$	39.2
08852	$0.10^{0.01}_{0.01}$	$0.10^{1.90}_{0.01}$	$24.3^{0.1}_{14.3}$	$115.5^{140.0}_{95.5}$	6.5	0.58	$100.0^{0.1}_{99.0}$	$1.0^{0.1}_{0.1}$	49.7
08900	$0.10^{0.01}_{0.01}$	$0.10^{0.89}_{0.01}$	$6.9^{0.1}_{5.9}$	$500.0^{0.1}_{480.0}$	9.6	0.40	$2.8^{0.1}_{1.8}$	$468.6^{31.4}_{428.6}$	22.0
08937	$0.10^{0.02}_{0.01}$	$0.45^{0.91}_{0.34}$	$21.7^{1.8}_{20.7}$	$192.5^{7.5}_{102.5}$	10.7	0.24	$41.5^{6.8}_{40.5}$	$135.2^{64.8}_{85.2}$	12.6
09179	$0.10^{0.01}_{0.01}$	$0.10^{1.90}_{0.01}$	$4.5^{1.2}_{3.5}$	$365.5^{34.5}_{345.5}$	4.9	0.57	$4.0^{0.1}_{3.0}$	$320.0^{30.0}_{300.0}$	7.6

Continued . . .

Table A.4 – Continued from previous page

Galaxy	NFW (BFM)					NFW with fixed M/L			
UGC	M/L Disc	M/L Bulge	c	V_{200}	χ^2	M/L	c	V_{200}	χ^2
(1)	(2)	(3)	(4)	(5)	(6)	(7)	(8)	(9)	(10)
09248	$0.34^{0.16}_{0.24}$	–	$17.0^{8.9}_{16.0}$	$74.8^{125.2}_{64.8}$	4.9	0.51	$15.8^{11.2}_{14.8}$	$29.9^{170.1}_{26.9}$	4.7
09358	$0.10^{0.01}_{0.01}$	$1.22^{0.78}_{1.12}$	$4.5^{0.1}_{3.5}$	$481.8^{18.2}_{381.8}$	8.6	0.28	$100.0^{0.1}_{99.0}$	$52.8^{47.2}_{51.8}$	34.9
09363	$0.10^{0.08}_{0.01}$	$0.10^{1.08}_{0.01}$	$5.5^{2.2}_{4.5}$	$244.3^{255.7}_{194.3}$	3.1	0.46	$1.6^{0.1}_{0.6}$	$440.6^{9.4}_{405.6}$	5.2
09366	$0.10^{0.01}_{0.01}$	$0.32^{0.99}_{0.22}$	$21.1^{1.2}_{20.1}$	$126.4^{73.6}_{106.4}$	5.1	0.27	$100.0^{0.1}_{98.9}$	$15.4^{0.1}_{13.4}$	10.8
09465	$0.47^{0.12}_{0.37}$	–	$2.8^{5.9}_{1.8}$	$178.4^{21.6}_{168.4}$	3.0	0.45	$2.9^{1.2}_{1.8}$	$179.5^{20.5}_{159.5}$	2.8
09576	$0.10^{0.04}_{0.01}$	$0.10^{1.08}_{0.01}$	$5.7^{0.6}_{4.7}$	$114.1^{85.9}_{94.1}$	7.5	0.62	$1.0^{0.1}_{0.1}$	$128.2^{12.7}_{108.2}$	17.9
09649	$0.10^{0.04}_{0.01}$	–	$35.3^{4.0}_{34.3}$	$50.9^{49.1}_{30.9}$	20.1	0.76	$19.5^{10.5}_{18.4}$	$50.9^{49.1}_{30.9}$	22.0
09736	$0.10^{0.06}_{0.01}$	–	$22.3^{2.4}_{21.3}$	$110.9^{109.1}_{90.9}$	9.7	0.65	$51.9^{5.1}_{50.8}$	$48.4^{251.6}_{18.4}$	10.1
09753	$0.16^{0.01}_{0.06}$	$0.19^{0.44}_{0.09}$	$19.9^{7.1}_{18.9}$	$86.5^{113.5}_{71.5}$	6.2	0.44	$1.0^{26.0}_{0.1}$	$1.0^{0.1}_{0.1}$	75.9
09858	$0.10^{0.06}_{0.01}$	$0.23^{0.26}_{0.13}$	$9.3^{3.5}_{8.3}$	$114.1^{85.9}_{94.1}$	6.5	0.48	$100.0^{0.1}_{99.0}$	$1.0^{2.2}_{0.1}$	38.9
09866	$0.48^{0.13}_{0.38}$	$0.49^{1.51}_{0.39}$	$2.2^{7.1}_{1.2}$	$446.6^{53.4}_{416.6}$	1.9	0.51	$1.6^{4.7}_{0.6}$	$472.7^{27.3}_{372.7}$	1.8
09943	$0.33^{0.01}_{0.23}$	–	$5.1^{21.9}_{4.1}$	$197.7^{2.3}_{97.7}$	2.4	0.41	$2.6^{0.1}_{1.6}$	$186.4^{13.6}_{185.4}$	6.5
09969	$0.10^{0.04}_{0.01}$	$0.10^{1.90}_{0.01}$	$26.6^{0.1}_{25.6}$	$190.0^{60.0}_{180.0}$	3.7	0.53	$23.5^{1.7}_{13.5}$	$137.5^{78.4}_{37.5}$	5.2
10075	$0.16^{0.01}_{0.06}$	–	$14.0^{2.4}_{13.0}$	$123.6^{276.4}_{103.6}$	7.4	0.35	$4.5^{0.6}_{3.5}$	$200.0^{0.1}_{150.0}$	7.7
10359	$0.10^{0.01}_{0.01}$	$0.10^{1.90}_{0.01}$	$2.5^{0.1}_{1.5}$	$488.9^{11.1}_{478.9}$	3.6	0.32	$2.9^{0.1}_{1.8}$	$300.0^{0.1}_{150.0}$	7.0
10470	$0.10^{0.01}_{0.01}$	$0.10^{0.43}_{0.01}$	$9.9^{0.6}_{8.9}$	$195.9^{4.1}_{175.9}$	7.1	0.25	$2.8^{0.1}_{1.8}$	$455.5^{44.5}_{445.5}$	21.4
10502	$0.30^{0.10}_{0.20}$	–	$4.0^{7.7}_{3.0}$	$150.9^{49.1}_{130.9}$	1.0	0.63	$100.0^{0.1}_{99.0}$	$1.0^{18.0}_{0.1}$	4.2

Continued . . .

Table A.4 – Continued from previous page

Galaxy	NFW (BFM)					NFW with fixed M/L			
UGC	M/L Disc	M/L Bulge	c	V_{200}	χ^2	M/L	c	V_{200}	χ^2
(1)	(2)	(3)	(4)	(5)	(6)	(7)	(8)	(9)	(10)
10521	$0.10^{0.01}_{0.01}$	–	$3.5^{1.3}_{2.5}$	$381.8^{118.2}_{281.8}$	3.4	0.29	$1.0^{26.0}_{0.1}$	$1.0^{45.0}_{0.1}$	21.1
10564	$0.10^{0.02}_{0.01}$	–	$1.0^{0.8}_{0.1}$	$366.4^{11.1}_{356.4}$	4.5	0.58	$1.0^{0.1}_{0.1}$	$178.4^{17.7}_{168.4}$	13.2
10652	$0.10^{0.05}_{0.01}$	–	$8.7^{1.8}_{7.7}$	$400.0^{0.1}_{300.0}$	14.0	0.40	$7.6^{1.0}_{2.5}$	$377.3^{22.7}_{77.3}$	14.5
10757	$0.10^{0.15}_{0.01}$	–	$2.8^{5.9}_{1.8}$	$422.0^{78.0}_{412.0}$	1.8	0.48	$1.6^{3.0}_{0.6}$	$372.7^{127.3}_{272.7}$	2.7
10897	$0.10^{0.01}_{0.01}$	$0.10^{0.73}_{0.01}$	$3.4^{1.8}_{2.4}$	$356.8^{43.2}_{336.8}$	5.7	0.33	$1.0^{1.2}_{0.1}$	$428.4^{51.1}_{378.4}$	8.1
11012	$0.13^{0.01}_{0.03}$	–	$3.4^{6.5}_{2.4}$	$434.5^{65.5}_{414.5}$	3.6	0.42	$1.0^{6.0}_{0.1}$	$1.0^{0.1}_{0.1}$	119.2
11124	$0.10^{0.01}_{0.01}$	–	$1.1^{0.7}_{0.1}$	$478.6^{21.4}_{448.6}$	6.6	0.50	$1.7^{0.1}_{0.6}$	$165.9^{34.1}_{115.9}$	12.8
11218	$0.10^{0.01}_{0.01}$	$0.10^{1.90}_{0.01}$	$23.9^{0.1}_{22.9}$	$105.0^{95.0}_{95.0}$	3.7	0.25	$18.2^{0.1}_{17.2}$	$63.6^{136.4}_{13.6}$	5.0
11283	$2.39^{0.11}_{2.29}$	$2.40^{1.60}_{2.30}$	$9.9^{17.1}_{8.9}$	$41.8^{58.2}_{21.8}$	10.7	0.38	$24.2^{1.5}_{19.2}$	$101.1^{98.9}_{51.1}$	12.6
11300	$0.10^{0.06}_{0.01}$	–	$6.3^{1.8}_{5.3}$	$216.4^{283.6}_{196.4}$	4.6	0.60	$1.0^{0.6}_{0.1}$	$72.1^{27.1}_{71.1}$	12.2
11407	$0.10^{0.01}_{0.01}$	$0.10^{0.17}_{0.01}$	$1.4^{0.4}_{0.4}$	$477.7^{22.3}_{467.7}$	21.0	0.29	$1.0^{0.1}_{0.1}$	$43.0^{13.2}_{33.0}$	56.8
11429	$0.10^{0.01}_{0.01}$	$0.10^{0.13}_{0.01}$	$2.2^{1.2}_{1.2}$	$455.5^{44.5}_{445.5}$	10.3	0.54	$100.0^{0.1}_{99.0}$	$1.0^{4.4}_{0.1}$	86.2
11466	$0.10^{0.01}_{0.01}$	$0.10^{0.17}_{0.01}$	$4.0^{0.6}_{3.0}$	$425.2^{74.8}_{395.2}$	7.4	0.19	$2.8^{0.1}_{1.8}$	$370.9^{49.1}_{310.9}$	20.3
11498	$0.10^{0.01}_{0.01}$	$0.10^{1.24}_{0.01}$	$8.7^{1.8}_{7.7}$	$288.4^{211.6}_{278.4}$	59.5	0.63	$4.7^{2.3}_{3.7}$	$1.0^{4.5}_{0.1}$	202.7
11597	$0.10^{0.01}_{0.01}$	$0.19^{0.97}_{0.09}$	$24.0^{0.1}_{23.0}$	$93.2^{156.8}_{73.2}$	5.6	0.24	$16.5^{3.1}_{15.5}$	$83.6^{16.4}_{63.6}$	5.6
11670	$0.10^{0.04}_{0.01}$	$0.57^{0.30}_{0.47}$	$25.8^{1.2}_{24.8}$	$93.6^{106.4}_{73.6}$	5.6	0.50	$100.0^{0.1}_{99.0}$	$1.0^{3.4}_{0.1}$	67.9
11707	$0.10^{0.17}_{0.01}$	$0.10^{1.90}_{0.01}$	$4.5^{2.4}_{3.5}$	$142.7^{57.3}_{122.7}$	3.6	0.37	$3.5^{1.2}_{2.4}$	$161.4^{38.6}_{61.4}$	3.6

Continued . . .

Table A.4 – Continued from previous page

Galaxy	NFW (BFM)					NFW with fixed M/L			
UGC	M/L Disc	M/L Bulge	c	V_{200}	χ^2	M/L	c	V_{200}	χ^2
(1)	(2)	(3)	(4)	(5)	(6)	(7)	(8)	(9)	(10)
11852	$0.16^{0.10}_{0.06}$	$0.19^{0.44}_{0.09}$	$4.7^{3.5}_{3.7}$	$500.0^{0.1}_{460.0}$	67.0	0.28	$3.4^{1.2}_{2.4}$	$400.0^{0.1}_{370.0}$	50.7
11861	$0.10^{0.01}_{0.01}$	–	$3.4^{0.1}_{2.4}$	$382.7^{17.3}_{362.7}$	5.7	0.31	$2.3^{0.1}_{1.2}$	$370.5^{29.5}_{70.5}$	8.3
11872	$0.10^{0.01}_{0.01}$	$0.10^{0.53}_{0.01}$	$27.7^{1.3}_{26.7}$	$114.1^{135.9}_{94.1}$	2.4	0.65	$10.0^{90.0}_{9.0}$	$1.0^{0.1}_{0.1}$	139.0
11914	$0.51^{0.01}_{0.41}$	$0.54^{0.27}_{0.44}$	$17.0^{10.0}_{16.0}$	$155.2^{64.8}_{85.2}$	2.4	0.67	$4.1^{0.1}_{3.1}$	$354.7^{45.3}_{353.7}$	5.2
12060	$0.50^{0.01}_{0.40}$	–	$6.9^{4.1}_{5.9}$	$118.2^{81.8}_{98.2}$	15.2	0.94	$4.5^{1.2}_{3.5}$	$143.6^{356.4}_{133.6}$	14.3
12754	$1.31^{0.01}_{1.21}$	$1.31^{0.69}_{1.21}$	$6.3^{0.7}_{5.3}$	$20.0^{0.1}_{19.0}$	11.9	0.31	$6.9^{1.2}_{5.9}$	$223.2^{276.8}_{143.2}$	5.5

2 Surface brightness profile and mass models

We present the photometry, the luminosity profiles and the mass models of the sample.

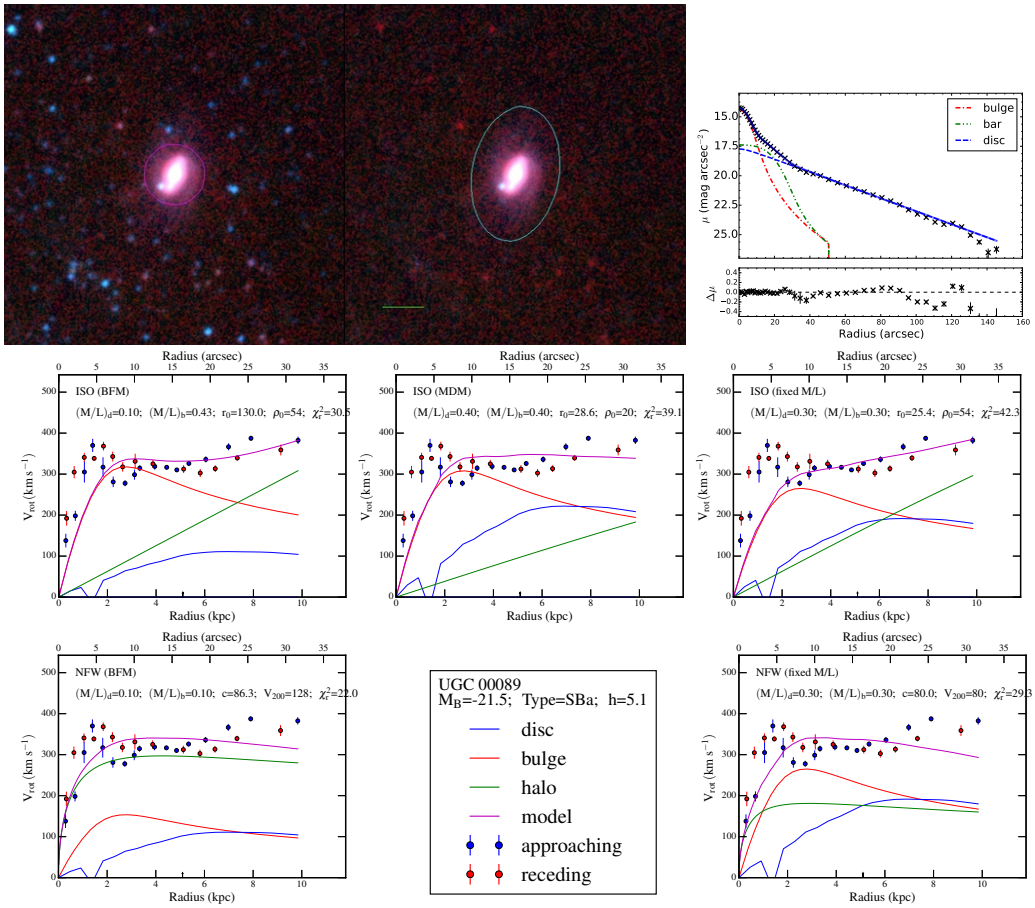

Figure A.1: Surface brightness profile decomposition and mass models. First line - (Left panel) WISE surface brightness image at 3.4 μm. Left side: image showing the field and galaxy. Right side: image after stars removed; the circle represents the 1σ isophotal ellipse, used for integrated photometry and the green line shows 1 arcmin in length. (Right panel) Luminosity profile decomposition corresponding to the left image. Lines 2 and 3 - Mass models. Second line: pseudo-isothermal sphere density profiles (ISO). Third line: Navarro, Frenk & White density profiles (NFW). First column: Best Fit Model (BFM). Second column: Maximum disc Model (MDM) for line 2 (ISO model). Third column: Mass-to-Light ratio M/L fixed using WISE W_1-W_2 color. The name of the galaxy, its B-band absolute magnitude, morphological type and disc scale length have been indicated in the insert located line 3-column 2. For each model, the fitted parameters and the reduced χ^2 have been indicated in each sub-panel. The legends are the same for Figs. B.2 – A.121. The surface brightness profiles decomposition for the 27 galaxies from SDSS are shown in this work while we do not present the remaining 73 galaxies from OHP because they have already been published in Barbosa et al. (2015). Note that 4 of the 27 SDSS galaxies have not been decomposed, for these galaxies, we just show the observed surface brightness profiles.

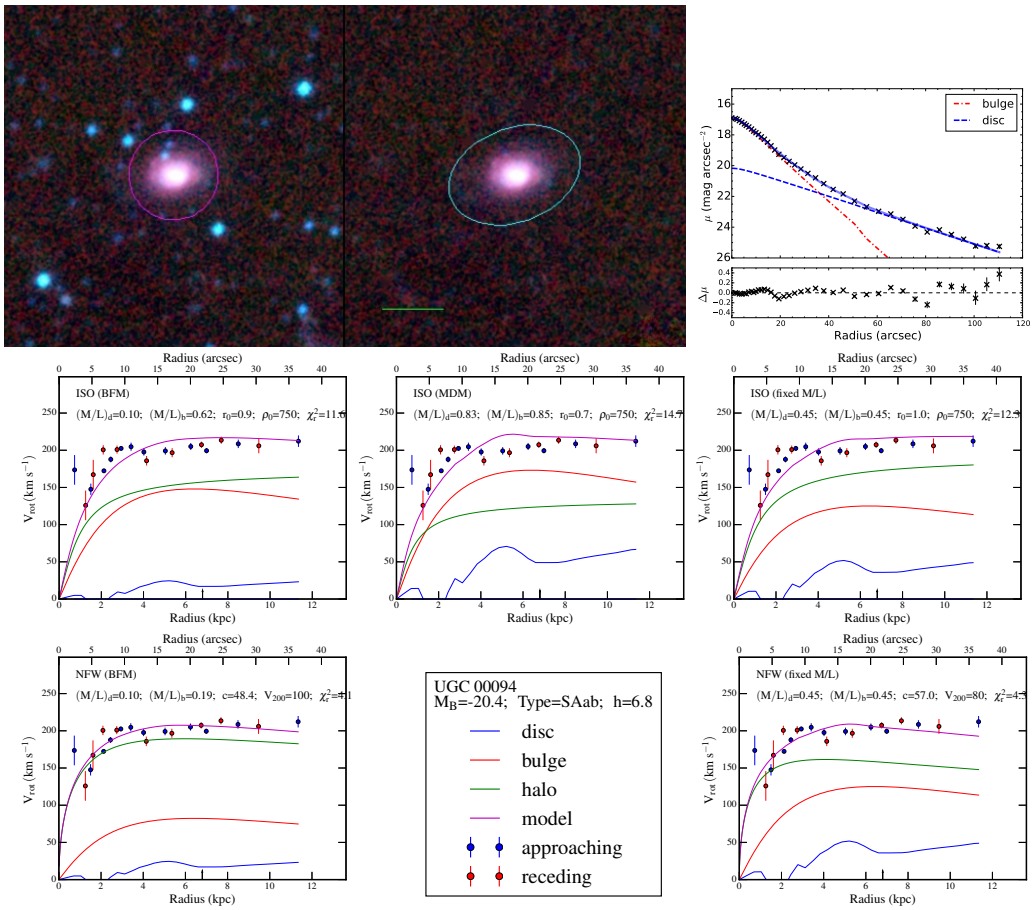
bulge
disc
μ (mag arcsec⁻²)
Δμ
Radius (arcsec)
ISO (BFM)
(M/L)d=0.10; (M/L)b=0.62; r0=0.9; ρ0=750;
ISO (MDM)
(M/L)d=0.83; (M/L)b=0.85; r0=0.7; ρ0=750;
ISO (fixed M/L)
(M/L)d=0.45; (M/L)b=0.45; r0=1.0; ρ0=750;
NFW (BFM)
(M/L)d=0.10; (M/L)b=0.19; c=48.4; V200=100;
NFW (fixed M/L)
(M/L)d=0.45; (M/L)b=0.45; c=57.0; V200=80;
Vrot (km s⁻¹)
Radius (kpc)
UGC 00094
MB=-20.4; Type=SAab; h=6.8
disc
bulge
halo
model
approaching
receding

Figure A.2

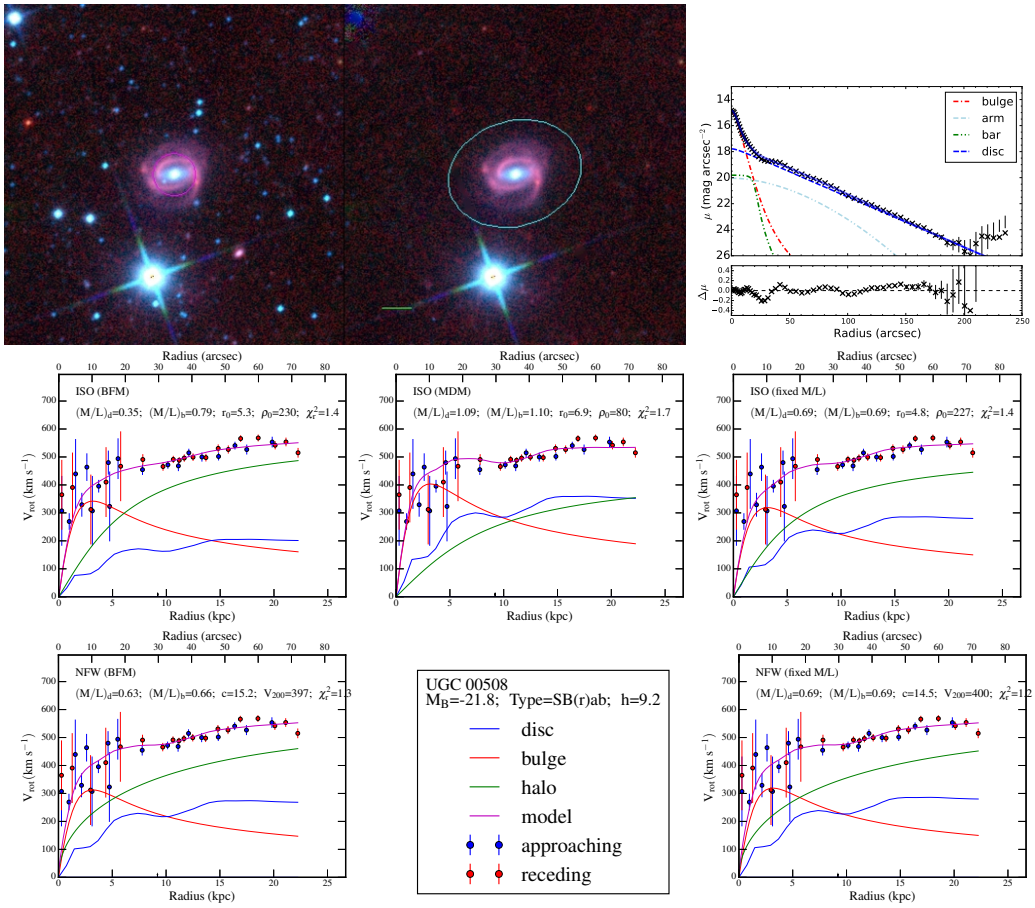
bulge
arm
bar
disc
μ (mag arcsec⁻²)
Δμ
Radius (arcsec)
ISO (BFM)
(M/L)d=0.35; (M/L)b=0.79; r0=5.3; ρ0=230; χ²r=1.4
ISO (MDM)
(M/L)d=1.09; (M/L)b=1.10; r0=6.9; ρ0=80; χ²r=1.7
ISO (fixed M/L)
(M/L)d=0.69; (M/L)b=0.69; r0=4.8; ρ0=227; χ²r=1.4
NFW (BFM)
(M/L)d=0.63; (M/L)b=0.66; c=15.2; V200=397; χ²r=1.3
NFW (fixed M/L)
(M/L)d=0.69; (M/L)b=0.69; c=14.5; V200=400; χ²r=1.2
Vrot (km s⁻¹)
Radius (kpc)
UGC 00508
MB=-21.8; Type=SB(r)ab; h=9.2
disc
bulge
halo
model
approaching
receding

Figure A.3

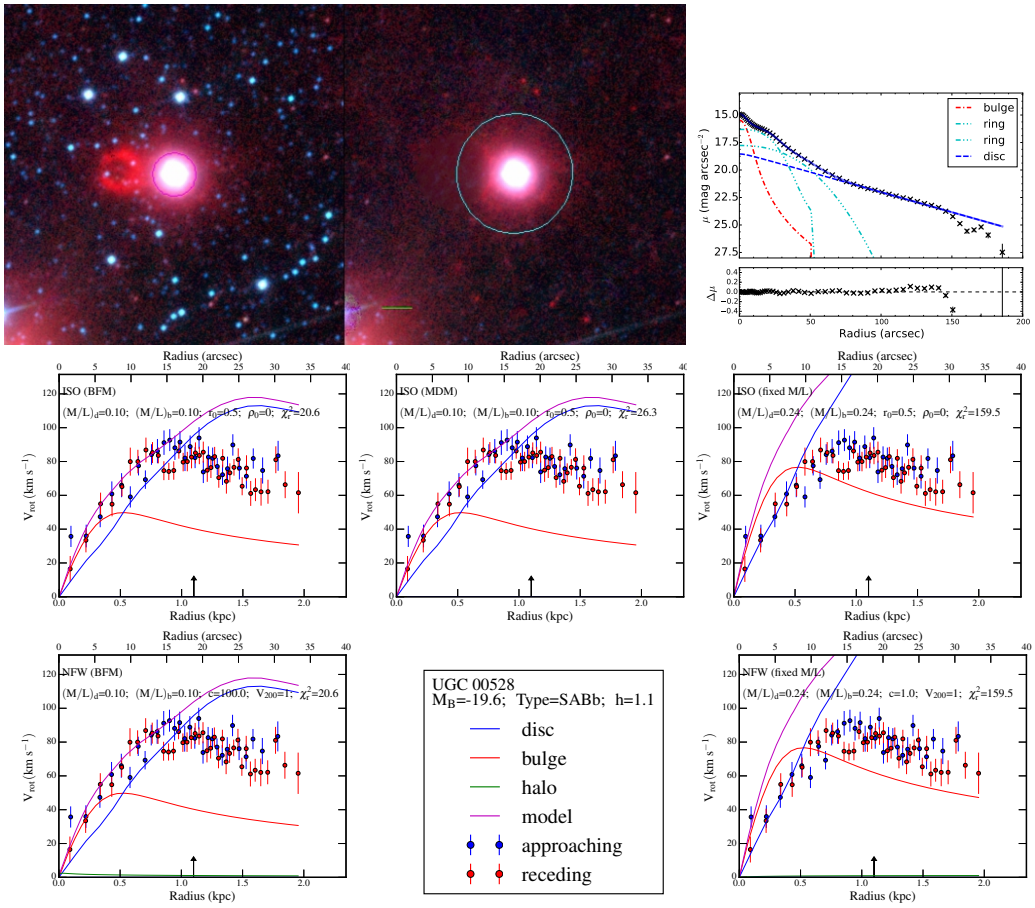
bulge
ring
ring
disc
μ (mag arcsec⁻²)
Δμ
Radius (arcsec)
ISO (BFM)
(M/L)d=0.10; (M/L)b=0.10; r0=0.5; ρ0=0; χ²r=20.6
ISO (MDM)
(M/L)d=0.10; (M/L)b=0.10; r0=0.5; ρ0=0; χ²r=26.3
ISO (fixed M/L)
(M/L)d=0.24; (M/L)b=0.24; r0=0.5; ρ0=0; χ²r=159.5
NFW (BFM)
(M/L)d=0.10; (M/L)b=0.10; c=100.0; V200=1; χ²r=20.6
NFW (fixed M/L)
(M/L)d=0.24; (M/L)b=0.24; c=1.0; V200=1; χ²r=159.5
Vrot (km s⁻¹)
Radius (kpc)
UGC 00528
MB=-19.6; Type=SABb; h=1.1
disc
bulge
halo
model
approaching
receding

Figure A.4

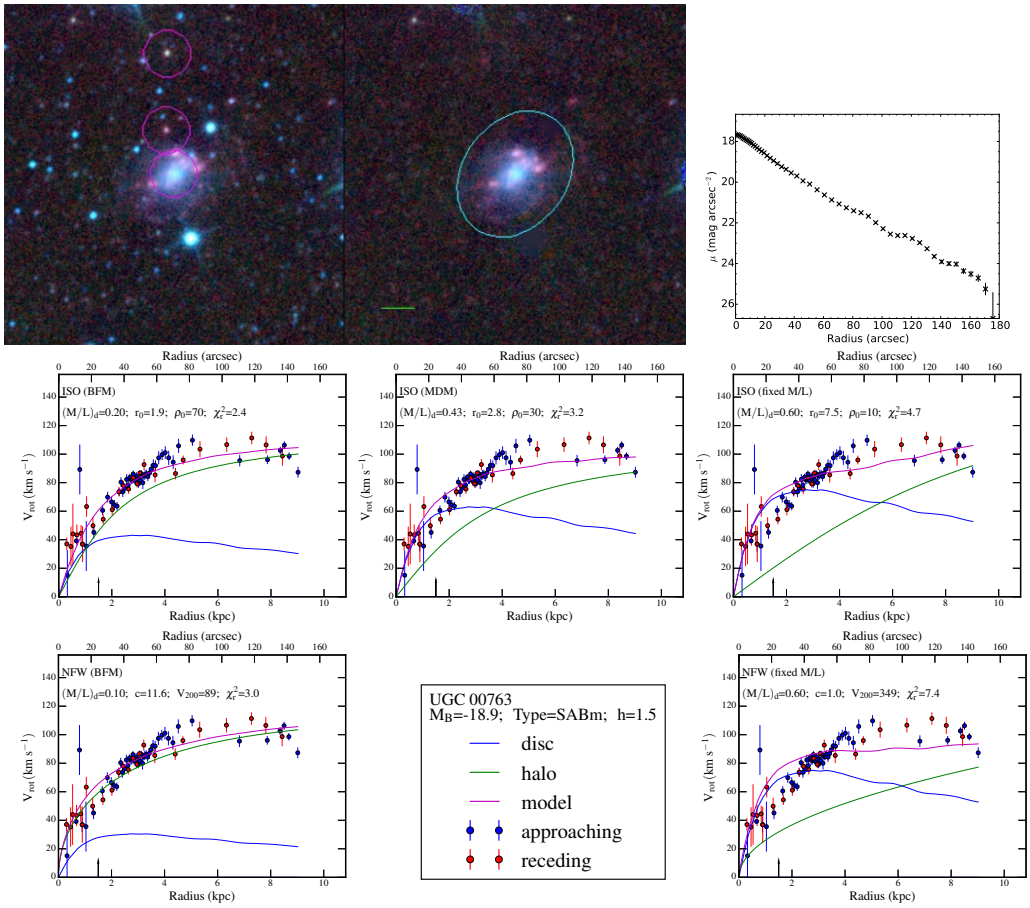
Radius (arcsec)
μ (mag arcsec⁻²)
ISO (BFM)
(M/L)d=0.20; r0=1.9; ρ0=70; χr²=2.4
ISO (MDM)
(M/L)d=0.43; r0=2.8; ρ0=30; χr²=3.2
ISO (fixed M/L)
(M/L)d=0.60; r0=7.5; ρ0=10; χr²=4.7
NFW (BFM)
(M/L)d=0.10; c=11.6; V200=89; χr²=3.0
NFW (fixed M/L)
(M/L)d=0.60; c=1.0; V200=349; χr²=7.4
Vrot (km s⁻¹)
Radius (kpc)
UGC 00763
MB=-18.9; Type=SABm; h=1.5
disc
halo
model
approaching
receding

Figure A.5

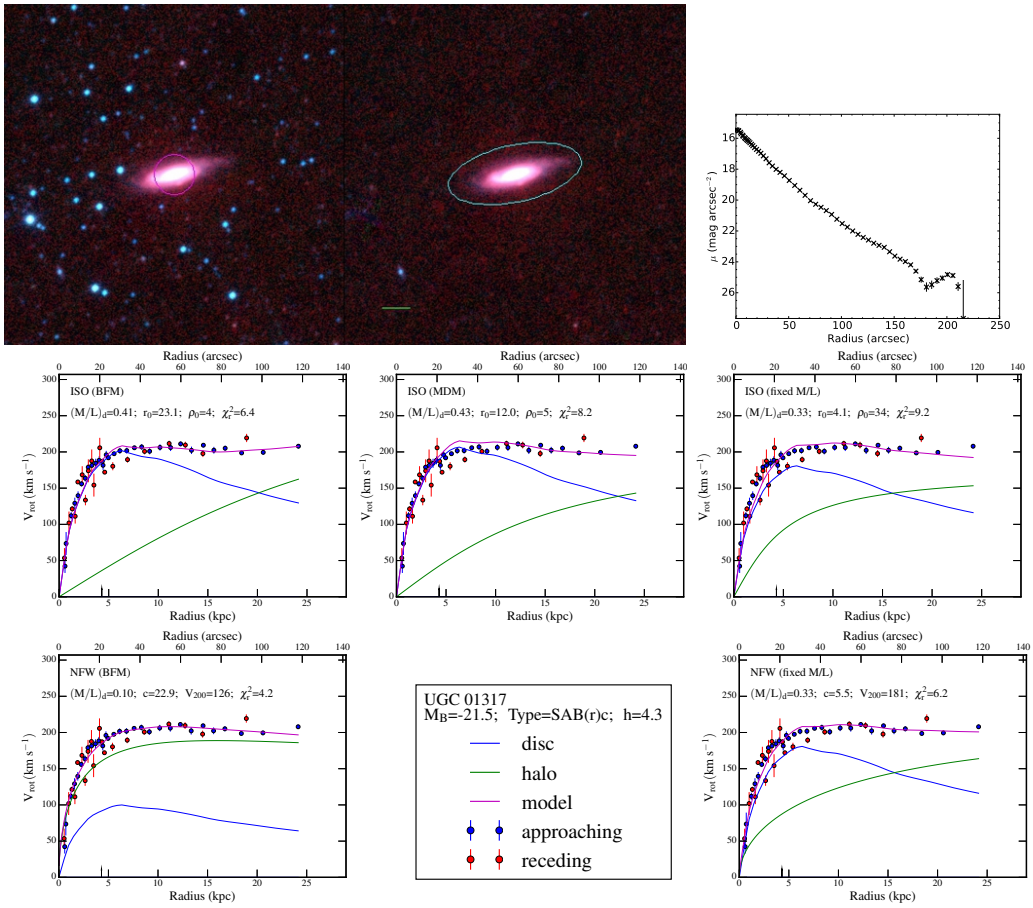
μ (mag arcsec⁻²)
Radius (arcsec)
ISO (BFM)
(M/L)d=0.41; r0=23.1; ρ0=4; χ²r=6.4
ISO (MDM)
(M/L)d=0.43; r0=12.0; ρ0=5; χ²r=8.2
ISO (fixed M/L)
(M/L)d=0.33; r0=4.1; ρ0=34; χ²r=9.2
NFW (BFM)
(M/L)d=0.10; c=22.9; V200=126; χ²r=4.2
NFW (fixed M/L)
(M/L)d=0.33; c=5.5; V200=181; χ²r=6.2
Vrot (km s⁻¹)
Radius (kpc)
UGC 01317
MB=-21.5; Type=SAB(r)c; h=4.3
disc
halo
model
approaching
receding

Figure A.6

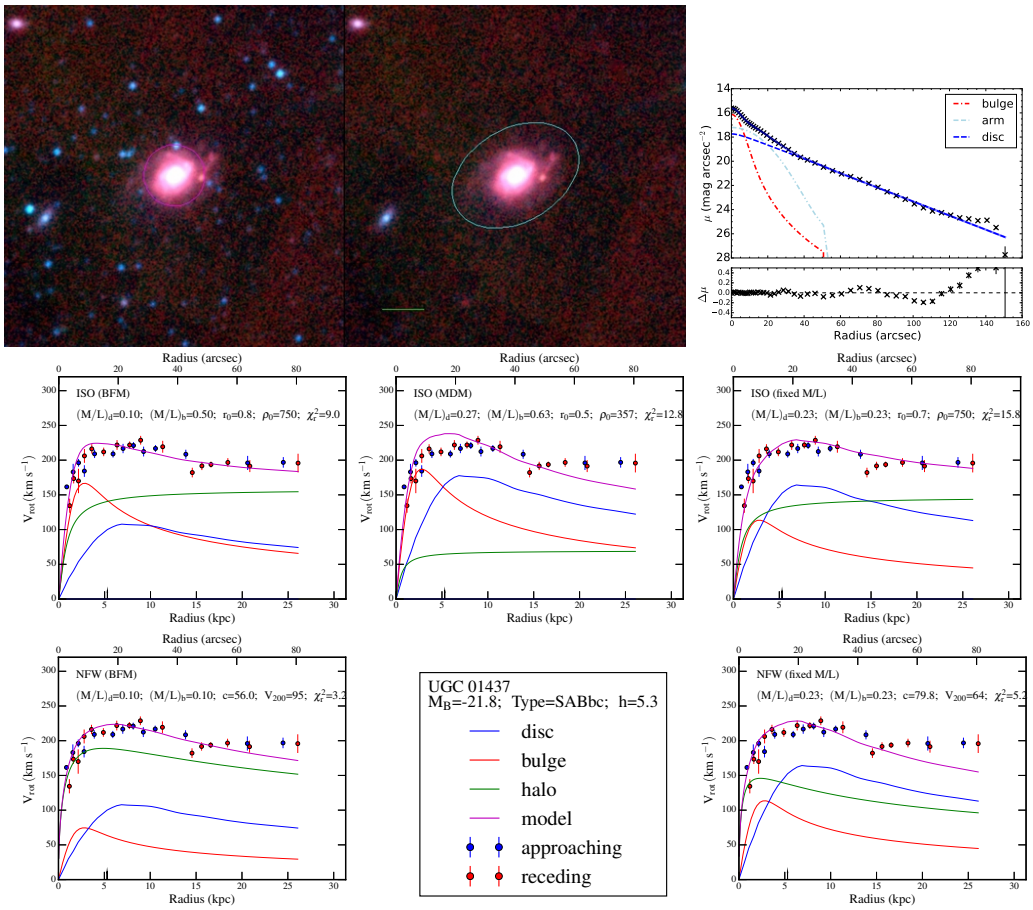
bulge
arm
disc
μ (mag arcsec⁻²)
Δμ
Radius (arcsec)
ISO (BFM)
(M/L)d=0.10; (M/L)b=0.50; r0=0.8; ρ0=750; χ²r=9.0
ISO (MDM)
(M/L)d=0.27; (M/L)b=0.63; r0=0.5; ρ0=357; χ²r=12.8
ISO (fixed M/L)
(M/L)d=0.23; (M/L)b=0.23; r0=0.7; ρ0=750; χ²r=15.8
NFW (BFM)
(M/L)d=0.10; (M/L)b=0.10; c=56.0; V200=95; χ²r=3.2
NFW (fixed M/L)
(M/L)d=0.23; (M/L)b=0.23; c=79.8; V200=64; χ²r=5.2
Vrot (km s⁻¹)
Radius (kpc)
UGC 01437
MB=-21.8; Type=SABbc; h=5.3
disc
bulge
halo
model
approaching
receding

Figure A.7

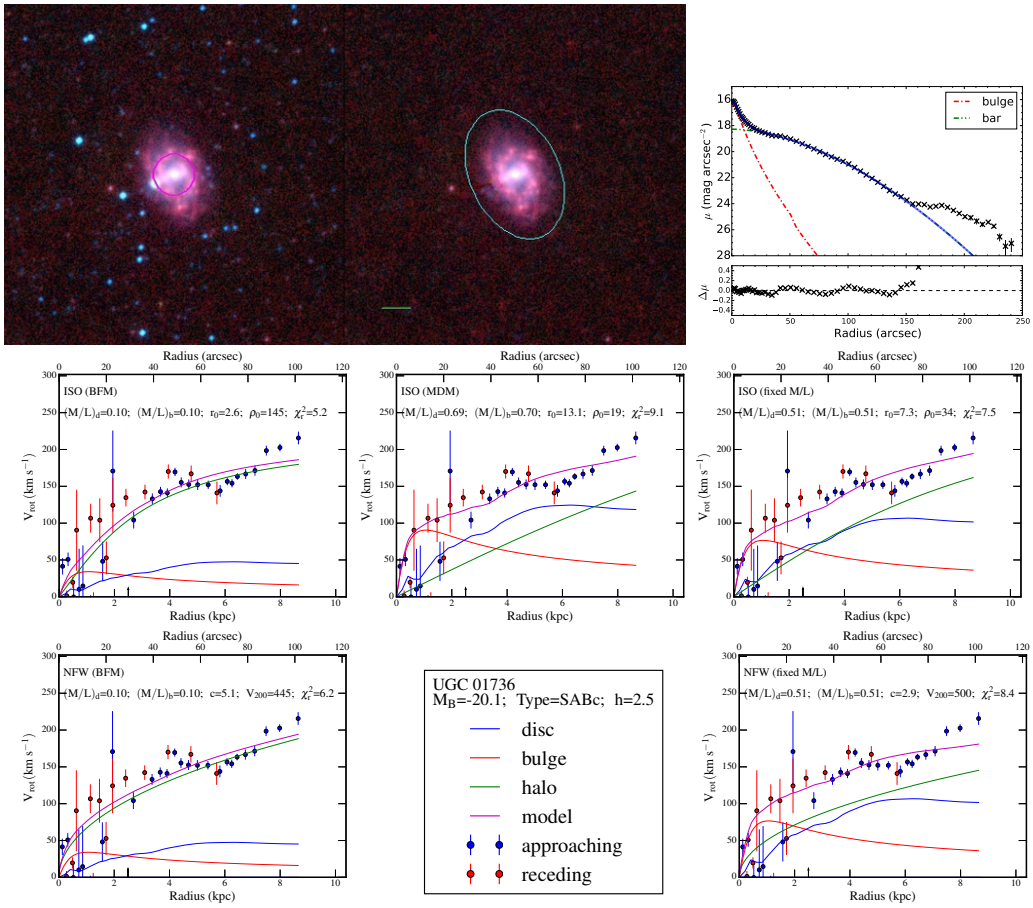
bulge
bar
μ (mag arcsec⁻²)
Δμ
Radius (arcsec)
ISO (BFM)
(M/L)d=0.10; (M/L)b=0.10; r0=2.6; ρ0=145; χ²r=5.2
ISO (MDM)
(M/L)d=0.69; (M/L)b=0.70; r0=13.1; ρ0=19; χ²r=9.1
ISO (fixed M/L)
(M/L)d=0.51; (M/L)b=0.51; r0=7.3; ρ0=34; χ²r=7.5
NFW (BFM)
(M/L)d=0.10; (M/L)b=0.10; c=5.1; V200=445; χ²r=6.2
NFW (fixed M/L)
(M/L)d=0.51; (M/L)b=0.51; c=2.9; V200=500; χ²r=8.4
Vrot (km s⁻¹)
Radius (kpc)
UGC 01736
MB=-20.1; Type=SABc; h=2.5
disc
bulge
halo
model
approaching
receding

Figure A.8

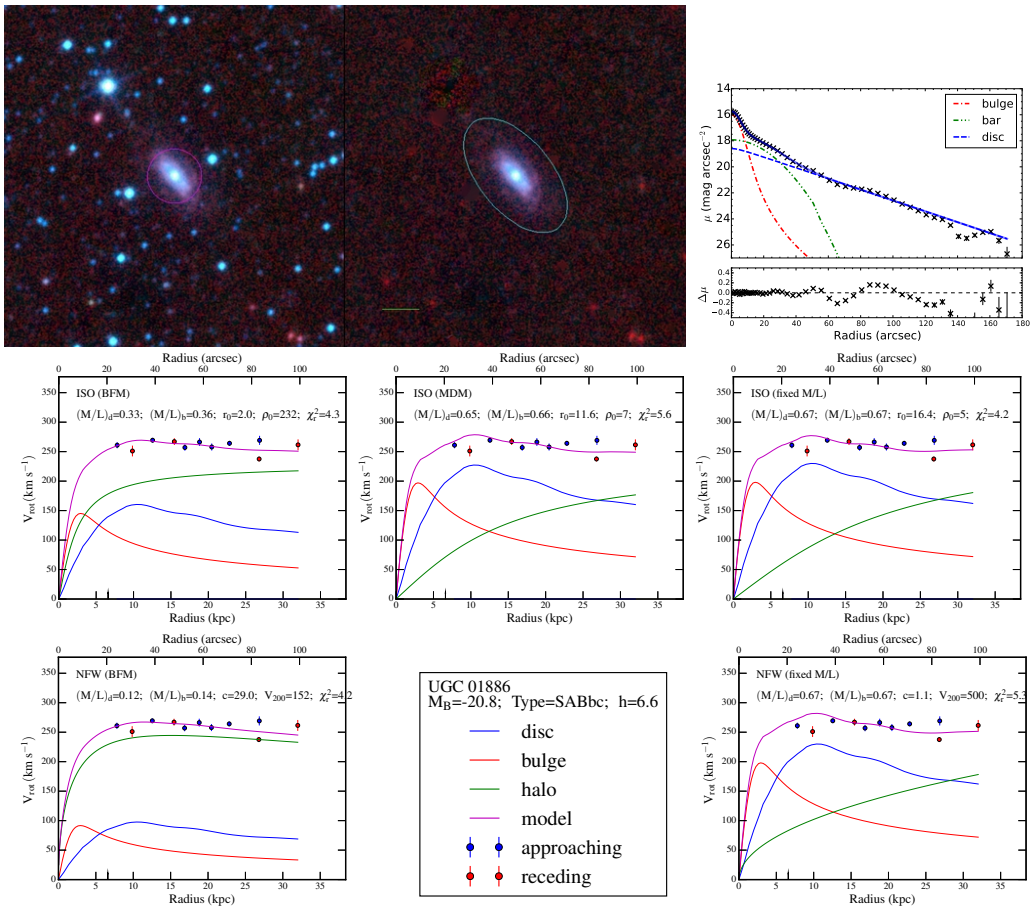
bulge
bar
disc
μ (mag arcsec⁻²)
Δμ
Radius (arcsec)
ISO (BFM)
(M/L)d=0.33; (M/L)b=0.36; r0=2.0; ρ0=232; χ²r=4.3
ISO (MDM)
(M/L)d=0.65; (M/L)b=0.66; r0=11.6; ρ0=7; χ²r=5.6
ISO (fixed M/L)
(M/L)d=0.67; (M/L)b=0.67; r0=16.4; ρ0=5; χ²r=4.2
NFW (BFM)
(M/L)d=0.12; (M/L)b=0.14; c=29.0; V200=152; χ²r=4.2
NFW (fixed M/L)
(M/L)d=0.67; (M/L)b=0.67; c=1.1; V200=500; χ²r=5.3
Vrot (km s⁻¹)
Radius (kpc)
UGC 01886
MB=-20.8; Type=SABbc; h=6.6
disc
bulge
halo
model
approaching
receding

Figure A.9

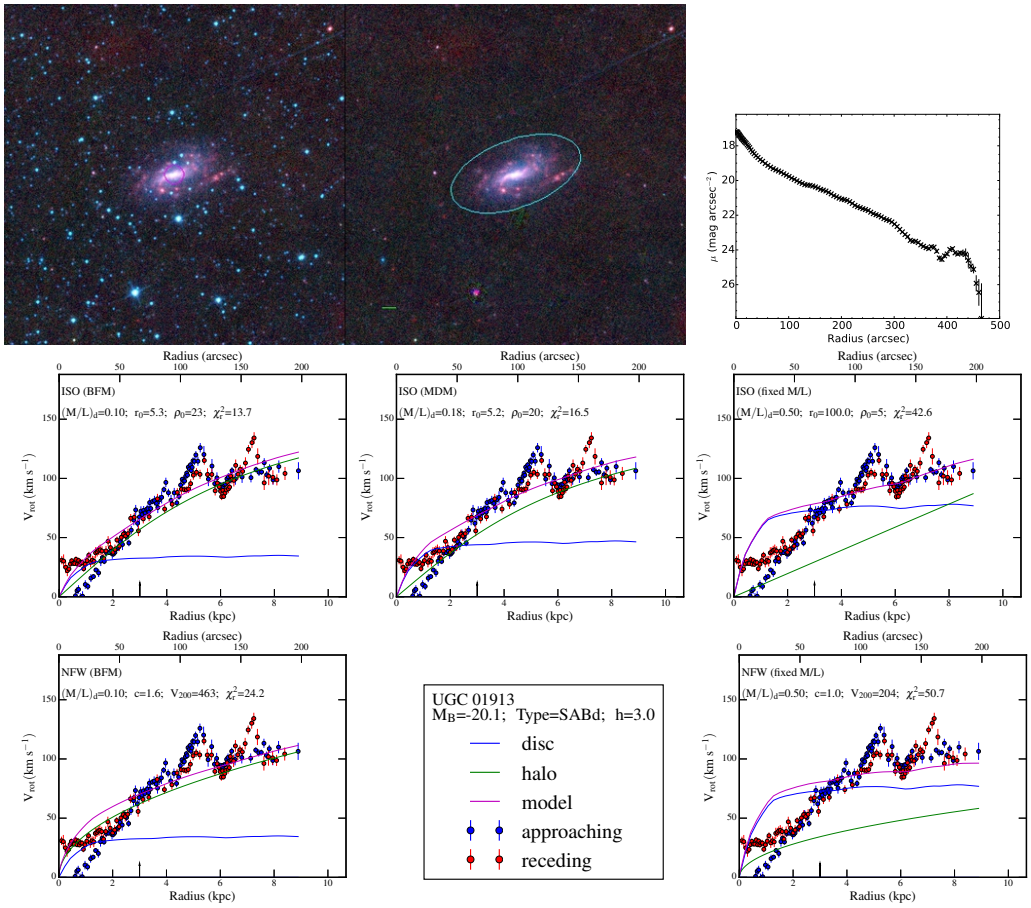
μ (mag arcsec⁻²)
Radius (arcsec)
ISO (BFM)
(M/L)d=0.10; r0=5.3; ρ0=23; χ²r=13.7
ISO (MDM)
(M/L)d=0.18; r0=5.2; ρ0=20; χ²r=16.5
ISO (fixed M/L)
(M/L)d=0.50; r0=100.0; ρ0=5; χ²r=42.6
NFW (BFM)
(M/L)d=0.10; c=1.6; V200=463; χ²r=24.2
NFW (fixed M/L)
(M/L)d=0.50; c=1.0; V200=204; χ²r=50.7
Vrot (km s⁻¹)
Radius (kpc)
UGC 01913
MB=-20.1; Type=SABd; h=3.0
disc
halo
model
approaching
receding

Figure A.10

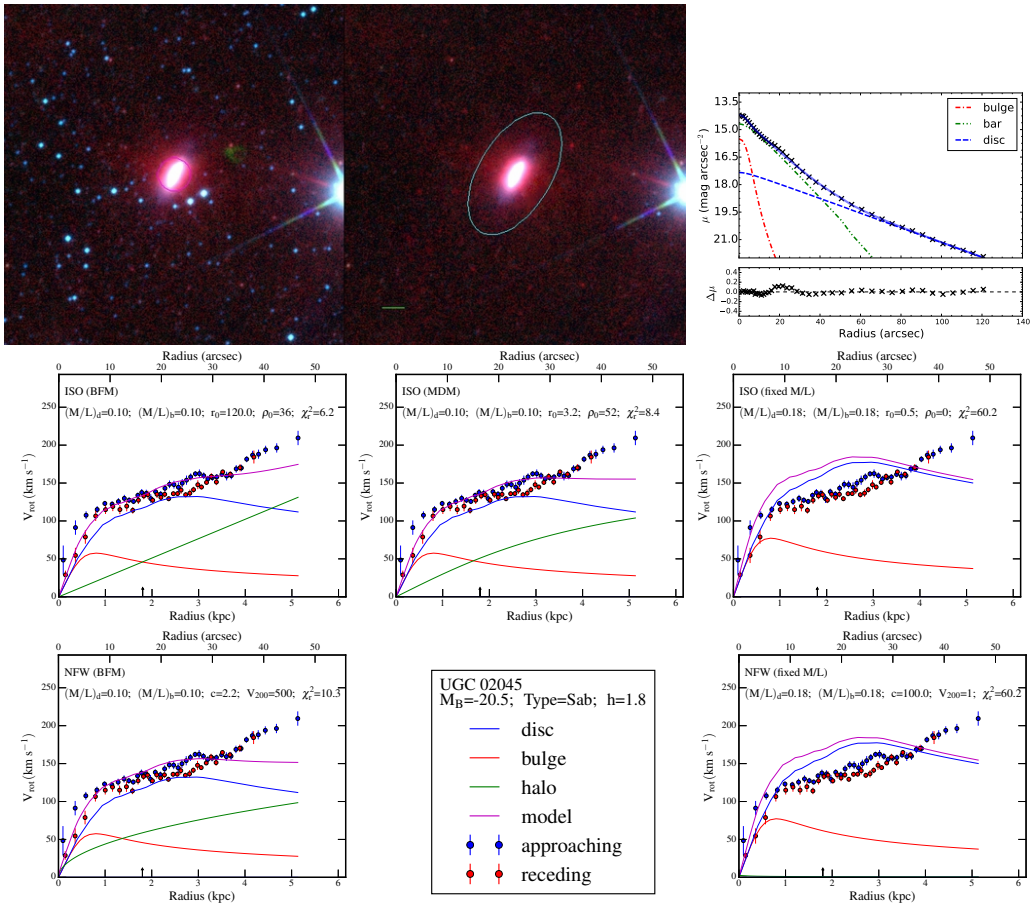
bulge
bar
disc
μ (mag arcsec⁻²)
Δμ
Radius (arcsec)
ISO (BFM)
(M/L)d=0.10; (M/L)b=0.10; r0=120.0; ρ0=36; χ²r=6.2
ISO (MDM)
(M/L)d=0.10; (M/L)b=0.10; r0=3.2; ρ0=52; χ²r=8.4
ISO (fixed M/L)
(M/L)d=0.18; (M/L)b=0.18; r0=0.5; ρ0=0; χ²r=60.2
NFW (BFM)
(M/L)d=0.10; (M/L)b=0.10; c=2.2; V200=500; χ²r=10.3
NFW (fixed M/L)
(M/L)d=0.18; (M/L)b=0.18; c=100.0; V200=1; χ²r=60.2
Vrot (km s⁻¹)
Radius (kpc)
UGC 02045
MB=-20.5; Type=Sab; h=1.8
disc
bulge
halo
model
approaching
receding

Figure A.11

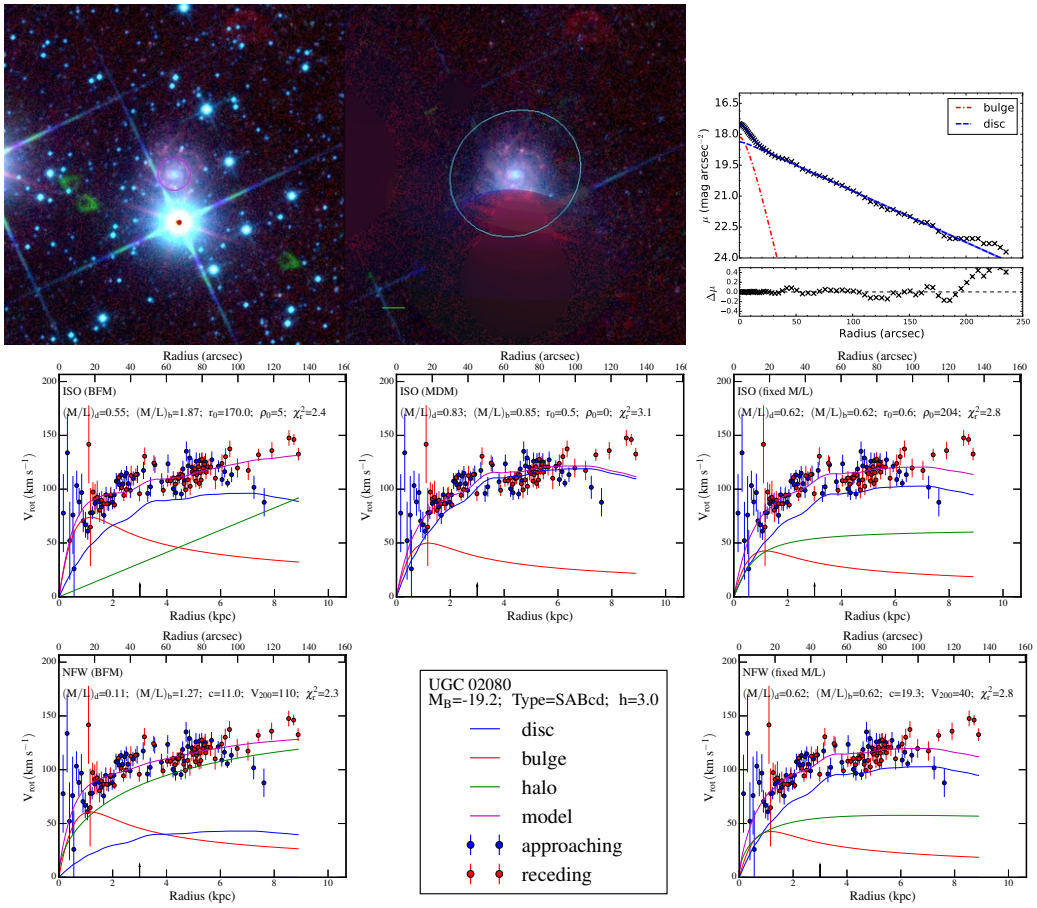
bulge
disc
μ (mag arcsec⁻²)
Δμ
Radius (arcsec)
ISO (BFM)
(M/L)d=0.55; (M/L)b=1.87; r0=170.0; ρ0=5; χ²r=2.4
ISO (MDM)
(M/L)d=0.83; (M/L)b=0.85; r0=0.5; ρ0=0; χ²r=3.1
ISO (fixed M/L)
(M/L)d=0.62; (M/L)b=0.62; r0=0.6; ρ0=204; χ²r=2.8
NFW (BFM)
(M/L)d=0.11; (M/L)b=1.27; c=11.0; V200=110; χ²r=2.3
NFW (fixed M/L)
(M/L)d=0.62; (M/L)b=0.62; c=19.3; V200=40; χ²r=2.8
Vrot (km s⁻¹)
Radius (kpc)
UGC 02080
MB=-19.2; Type=SABcd; h=3.0
disc
bulge
halo
model
approaching
receding

Figure A.12

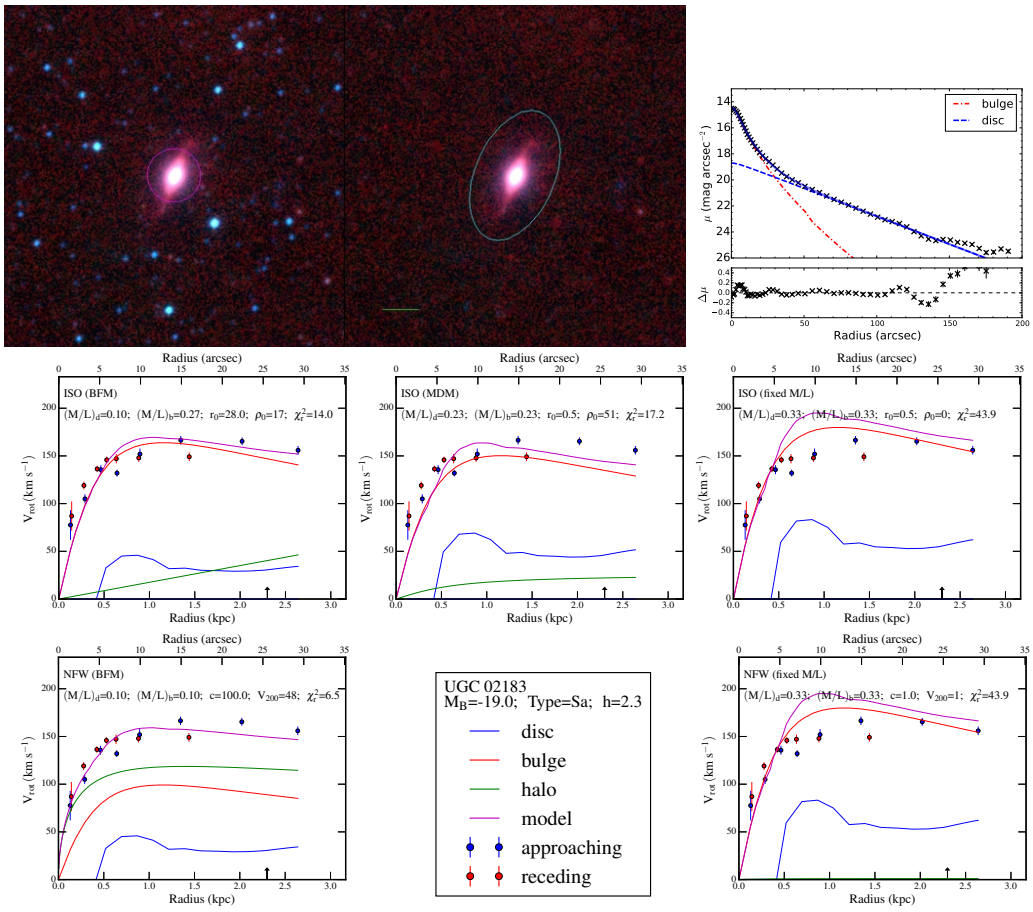
bulge
disc
μ (mag arcsec⁻²)
Δμ
Radius (arcsec)
ISO (BFM)
(M/L)d=0.10; (M/L)b=0.27; r0=28.0; ρ0=17; χr²=14.0
ISO (MDM)
(M/L)d=0.23; (M/L)b=0.23; r0=0.5; ρ0=51; χr²=17.2
ISO (fixed M/L)
(M/L)d=0.33; (M/L)b=0.33; r0=0.5; ρ0=0; χr²=43.9
NFW (BFM)
(M/L)d=0.10; (M/L)b=0.10; c=100.0; V200=48; χr²=6.5
NFW (fixed M/L)
(M/L)d=0.33; (M/L)b=0.33; c=1.0; V200=1; χr²=43.9
Vrot (km s⁻¹)
Radius (kpc)
UGC 02183
MB=-19.0; Type=Sa; h=2.3
disc
bulge
halo
model
approaching
receding

Figure A.13

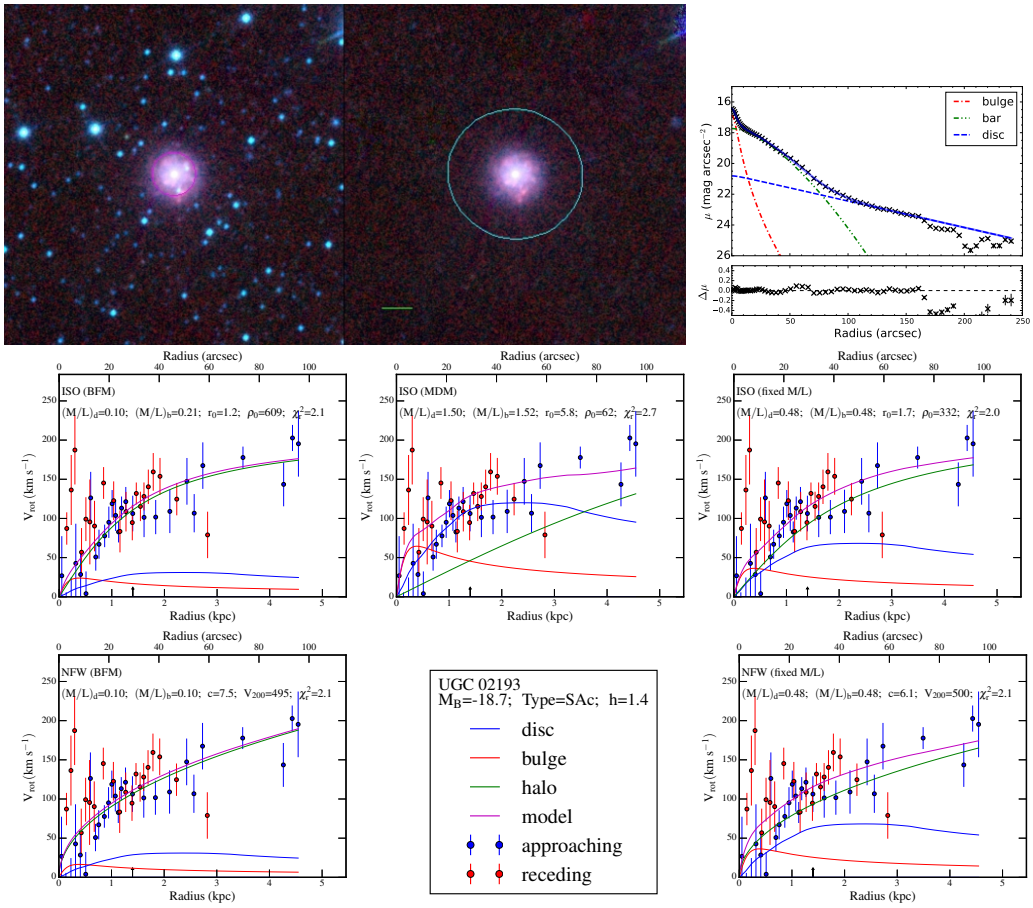
bulge
bar
disc
μ (mag arcsec⁻²)
Δμ
Radius (arcsec)
ISO (BFM)
(M/L)d=0.10; (M/L)b=0.21; r0=1.2; ρ0=609; χ²G=2.1
ISO (MDM)
(M/L)d=1.50; (M/L)b=1.52; r0=5.8; ρ0=62; χ²G=2.7
ISO (fixed M/L)
(M/L)d=0.48; (M/L)b=0.48; r0=1.7; ρ0=332; χ²G=2.0
NFW (BFM)
(M/L)d=0.10; (M/L)b=0.10; c=7.5; V200=495; χ²G=2.1
NFW (fixed M/L)
(M/L)d=0.48; (M/L)b=0.48; c=6.1; V200=500; χ²G=2.1
Vrot (km s⁻¹)
Radius (kpc)
UGC 02193
MB=-18.7; Type=SAc; h=1.4
disc
bulge
halo
model
approaching
receding

Figure A.14

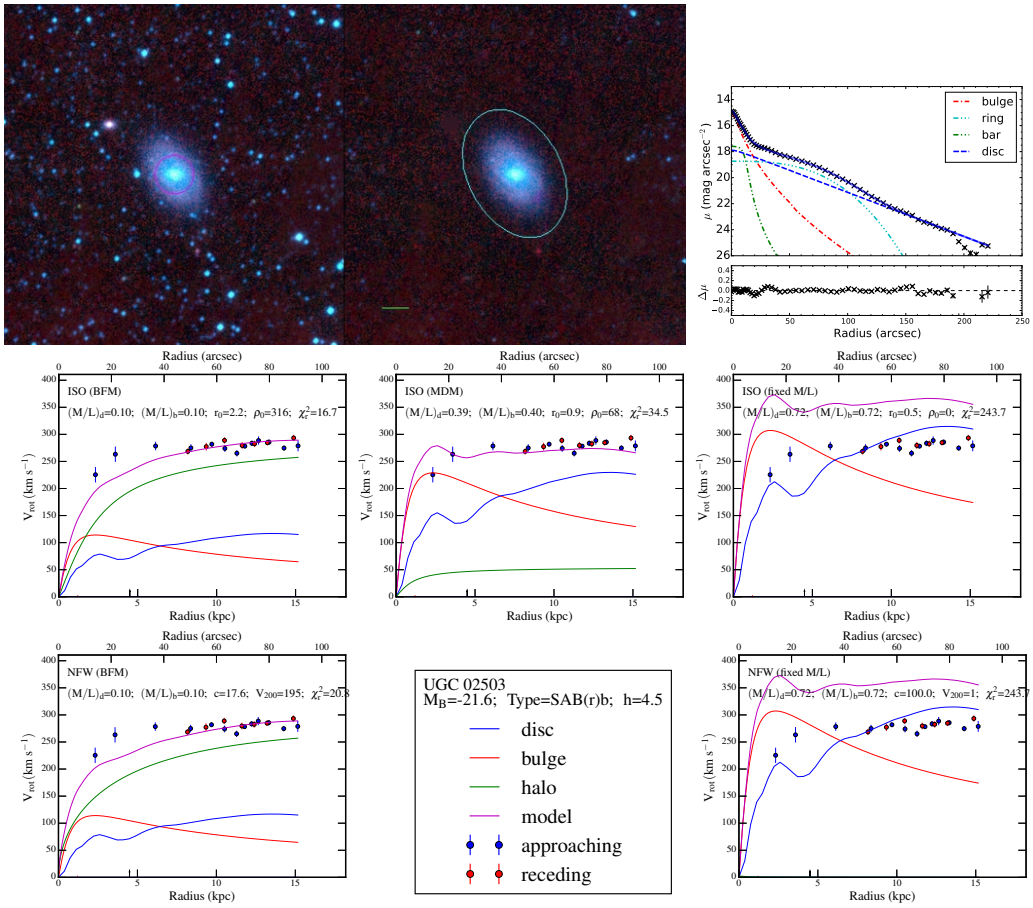
bulge
ring
bar
disc
μ (mag arcsec⁻²)
Δμ
Radius (arcsec)
ISO (BFM)
(M/L)d=0.10; (M/L)h=0.10; r0=2.2; ρ0=316; χ²r=16.7
ISO (MDM)
(M/L)d=0.39; (M/L)h=0.40; r0=0.9; ρ0=68; χ²r=34.5
ISO (fixed M/L)
(M/L)d=0.72; (M/L)h=0.72; r0=0.5; ρ0=0; χ²r=243.7
NFW (BFM)
(M/L)d=0.10; (M/L)h=0.10; c=17.6; V200=195; χ²r=20
NFW (fixed M/L)
(M/L)d=0.72; (M/L)h=0.72; c=100.0; V200=1; χ²r=243.7
Vrot (km s⁻¹)
Radius (kpc)
UGC 02503
MB=-21.6; Type=SAB(r)b; h=4.5
disc
bulge
halo
model
approaching
receding

Figure A.15

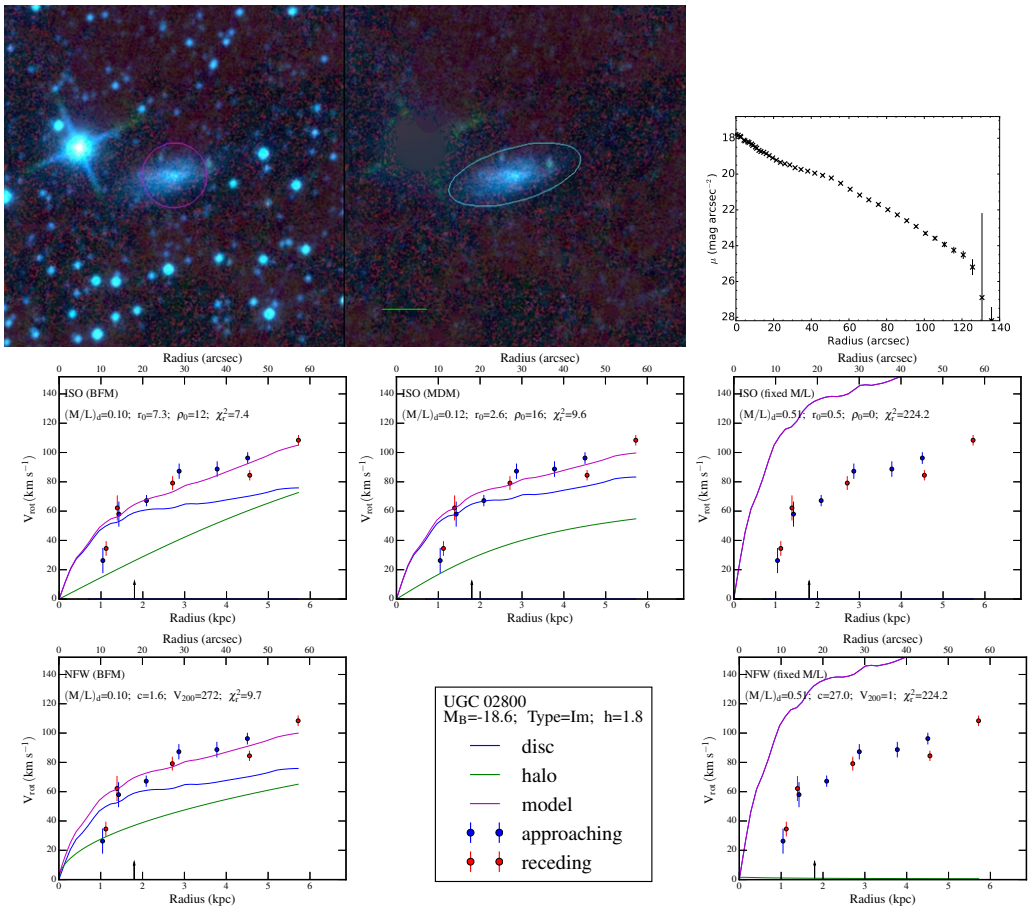
μ (mag arcsec⁻²)
Radius (arcsec)
ISO (BFM)
(M/L)d=0.10; r0=7.3; ρ0=12; χ²r=7.4
ISO (MDM)
(M/L)d=0.12; r0=2.6; ρ0=16; χ²r=9.6
ISO (fixed M/L)
(M/L)d=0.5; r0=0.5; ρ0=0; χ²r=224.2
NFW (BFM)
(M/L)d=0.10; c=1.6; V200=272; χ²r=9.7
NFW (fixed M/L)
(M/L)d=0.5; c=27.0; V200=1; χ²r=224.2
Vrot (km s⁻¹)
Radius (kpc)
UGC 02800
MB=-18.6; Type=Im; h=1.8
disc
halo
model
approaching
receding

Figure A.16

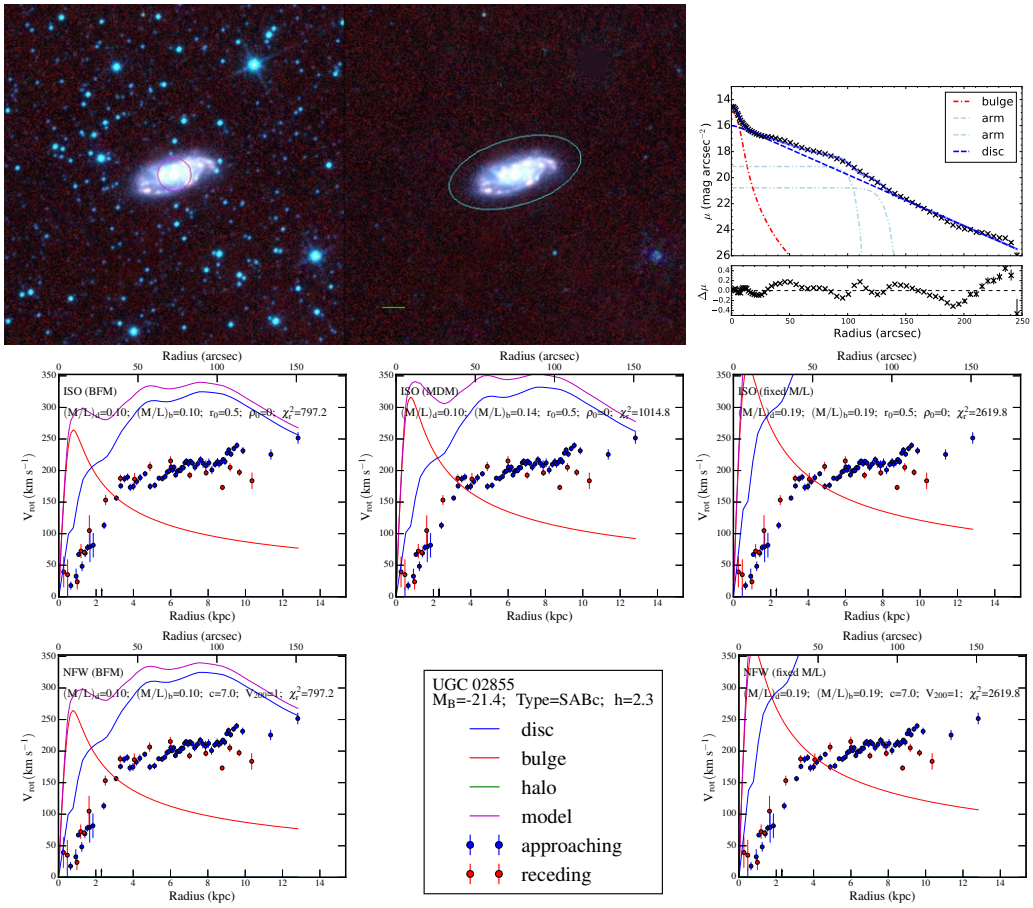
bulge
arm
arm
disc
μ (mag arcsec⁻²)
Δμ
Radius (arcsec)
ISO (BFM)
(M/L)d=0.10; (M/L)b=0.10; r0=0.5; ρ0=0; χ²c=797.2
ISO (MDM)
(M/L)d=0.10; (M/L)b=0.14; r0=0.5; ρ0=0; χ²c=1014.8
ISO (fixed M/L)
(M/L)d=0.19; (M/L)b=0.19; r0=0.5; ρ0=0; χ²c=2619.8
NFW (BFM)
(M/L)d=0.10; (M/L)b=0.10; c=7.0; V200=1; χ²c=797.2
NFW (fixed M/L)
(M/L)d=0.19; (M/L)b=0.19; c=7.0; V200=1; χ²c=2619.8
Vrot (km s⁻¹)
Radius (kpc)
UGC 02855
MB=-21.4; Type=SABc; h=2.3
disc
bulge
halo
model
approaching
receding

Figure A.17

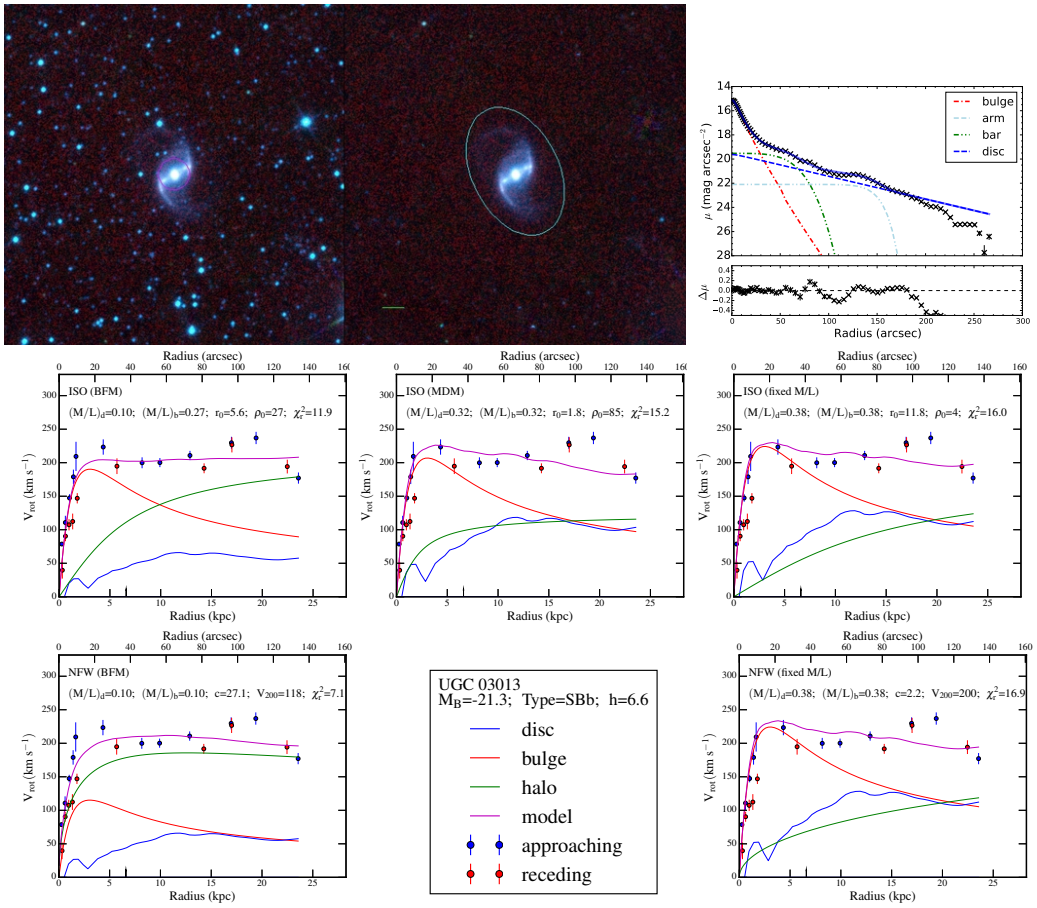
bulge
arm
bar
disc
μ (mag arcsec⁻²)
Δμ
Radius (arcsec)
ISO (BFM)
(M/L)d=0.10; (M/L)b=0.27; r0=5.6; ρ0=27; χ²r=11.9
ISO (MDM)
(M/L)d=0.32; (M/L)b=0.32; r0=1.8; ρ0=85; χ²r=15.2
ISO (fixed M/L)
(M/L)d=0.38; (M/L)b=0.38; r0=11.8; ρ0=4; χ²r=16.0
NFW (BFM)
(M/L)d=0.10; (M/L)b=0.10; c=27.1; V200=118; χ²r=7.1
NFW (fixed M/L)
(M/L)d=0.38; (M/L)b=0.38; c=2.2; V200=200; χ²r=16.9
Vrot (km s⁻¹)
Radius (kpc)
UGC 03013
MB=-21.3; Type=SBb; h=6.6
disc
bulge
halo
model
approaching
receding

Figure A.18

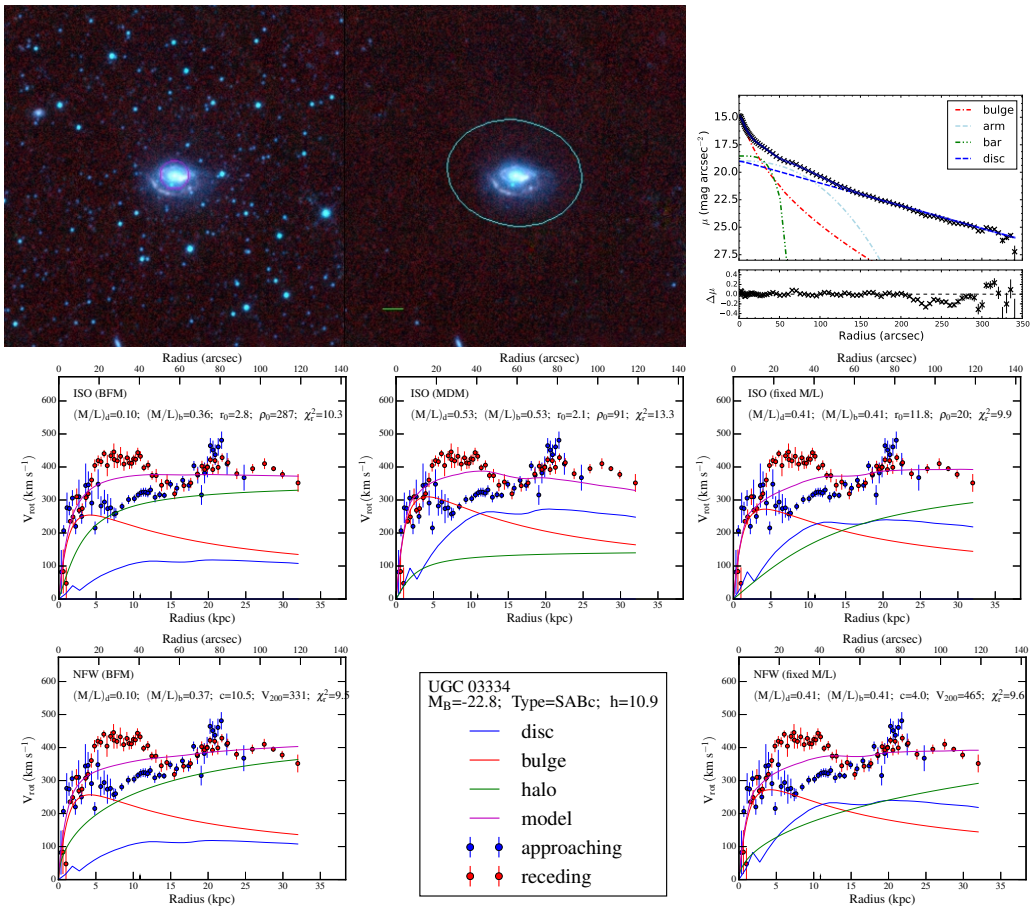
bulge
arm
bar
disc
μ (mag arcsec⁻²)
Δμ
Radius (arcsec)
ISO (BFM)
(M/L)d=0.10; (M/L)b=0.36; r0=2.8; ρ0=287; χ²r=10.3
ISO (MDM)
(M/L)d=0.53; (M/L)b=0.53; r0=2.1; ρ0=91; χ²r=13.3
ISO (fixed M/L)
(M/L)d=0.41; (M/L)b=0.41; r0=11.8; ρ0=20; χ²r=9.9
NFW (BFM)
(M/L)d=0.10; (M/L)b=0.37; c=10.5; V200=331; χ²r=9.5
NFW (fixed M/L)
(M/L)d=0.41; (M/L)b=0.41; c=4.0; V200=465; χ²r=9.6
Vrot (km s⁻¹)
Radius (kpc)
UGC 03334
MB=-22.8; Type=SABc; h=10.9
disc
bulge
halo
model
approaching
receding

Figure A.19

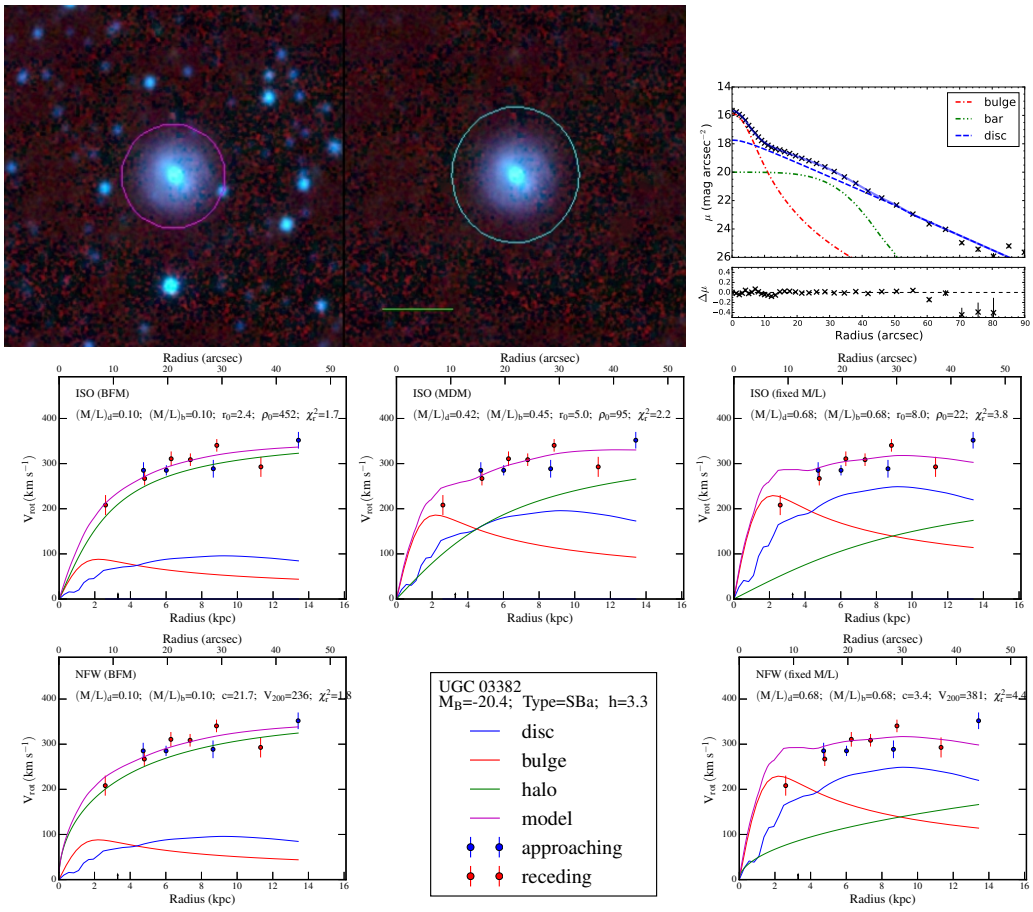
bulge
bar
disc
μ (mag arcsec⁻²)
Δμ
Radius (arcsec)
ISO (BFM)
(M/L)d=0.10; (M/L)b=0.10; r0=2.4; ρ0=452; χr²=1.7
ISO (MDM)
(M/L)d=0.42; (M/L)b=0.45; r0=5.0; ρ0=95; χr²=2.2
ISO (fixed M/L)
(M/L)d=0.68; (M/L)b=0.68; r0=8.0; ρ0=22; χr²=3.8
NFW (BFM)
(M/L)d=0.10; (M/L)b=0.10; c=21.7; V200=236; χr²=1.8
NFW (fixed M/L)
(M/L)d=0.68; (M/L)b=0.68; c=3.4; V200=381; χr²=4.4
Vrot (km s⁻¹)
Radius (kpc)
UGC 03382
MB=-20.4; Type=SBa; h=3.3
disc
bulge
halo
model
approaching
receding

Figure A.20

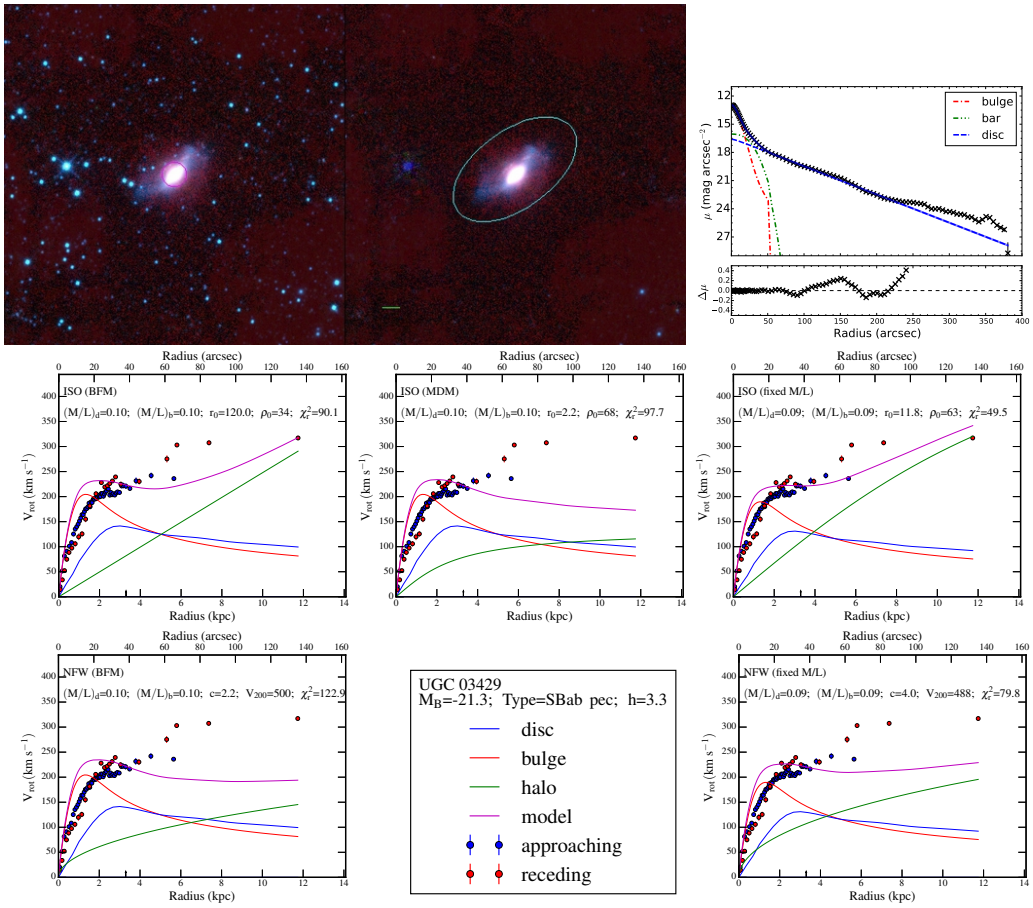
bulge
bar
disc
μ (mag arcsec⁻²)
Δμ
Radius (arcsec)
ISO (BFM)
(M/L)d=0.10; (M/L)b=0.10; r0=120.0; ρ0=34; χ²r=90.1
ISO (MDM)
(M/L)d=0.10; (M/L)b=0.10; r0=2.2; ρ0=68; χ²r=97.7
ISO (fixed M/L)
(M/L)d=0.09; (M/L)b=0.09; r0=11.8; ρ0=63; χ²r=49.5
NFW (BFM)
(M/L)d=0.10; (M/L)b=0.10; c=2.2; V200=500; χ²r=122.9
NFW (fixed M/L)
(M/L)d=0.09; (M/L)b=0.09; c=4.0; V200=488; χ²r=79.8
Vrot (km s⁻¹)
Radius (kpc)
UGC 03429
MB=-21.3; Type=SBab pec; h=3.3
disc
bulge
halo
model
approaching
receding

Figure A.21

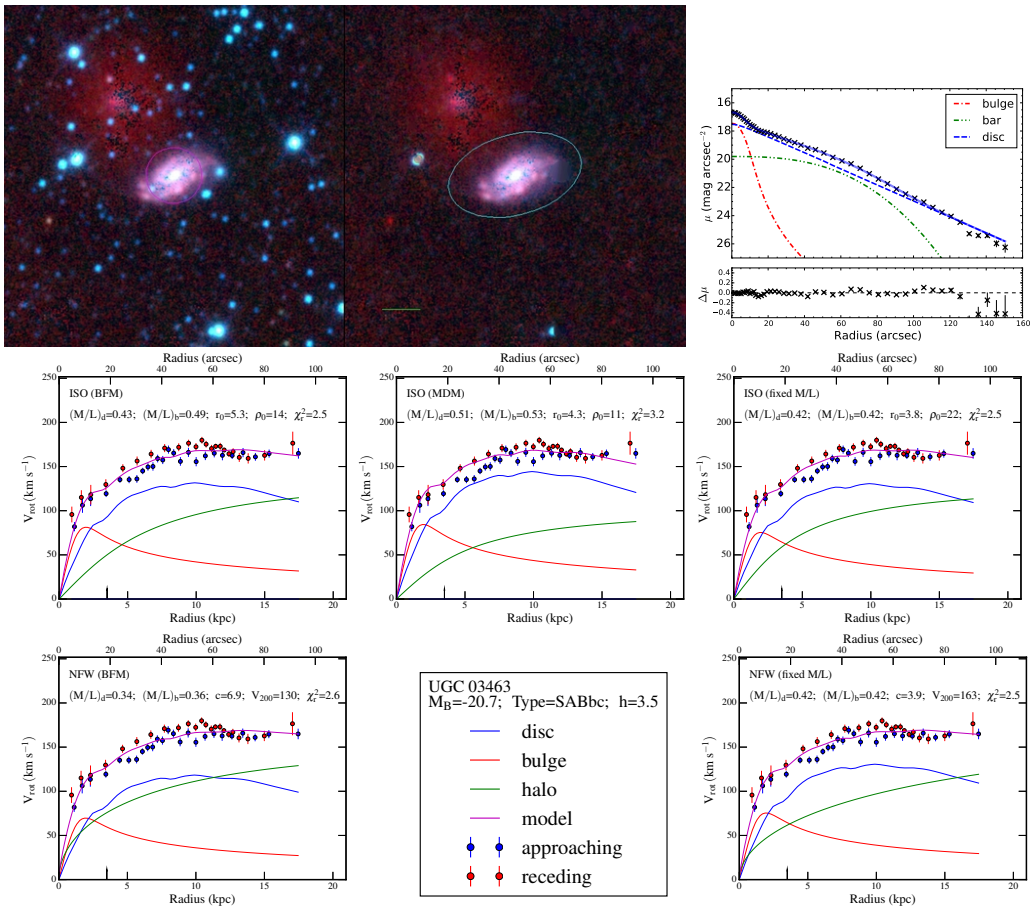
bulge
bar
disc
μ (mag arcsec⁻²)
Δμ
Radius (arcsec)
ISO (BFM)
(M/L)d=0.43; (M/L)b=0.49; r0=5.3; ρ0=14; χ²r=2.5
ISO (MDM)
(M/L)d=0.51; (M/L)b=0.53; r0=4.3; ρ0=11; χ²r=3.2
ISO (fixed M/L)
(M/L)d=0.42; (M/L)b=0.42; r0=3.8; ρ0=22; χ²r=2.5
NFW (BFM)
(M/L)d=0.34; (M/L)b=0.36; c=6.9; V200=130; χ²r=2.6
NFW (fixed M/L)
(M/L)d=0.42; (M/L)b=0.42; c=3.9; V200=163; χ²r=2.5
Vrot (km s⁻¹)
Radius (kpc)
UGC 03463
MB=-20.7; Type=SABbc; h=3.5
disc
bulge
halo
model
approaching
receding

Figure A.22

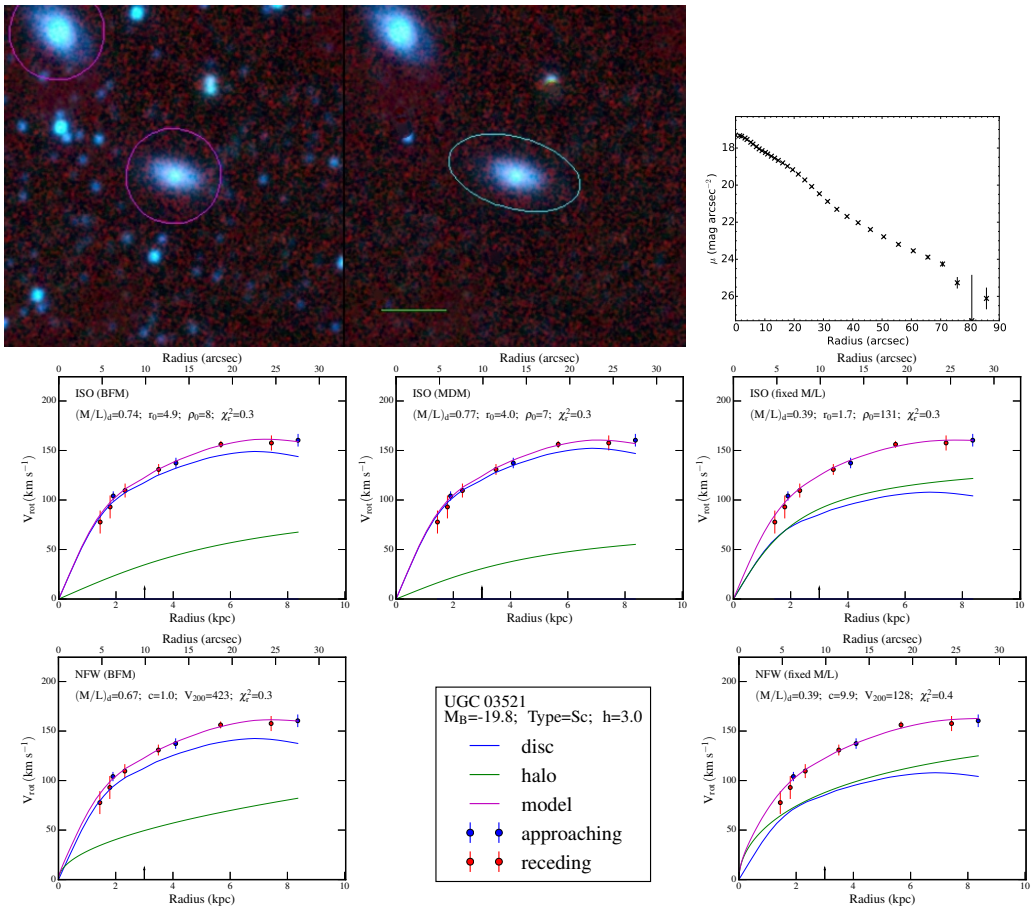
Radius (arcsec)
μ (mag arcsec⁻²)
ISO (BFM)
(M/L)d=0.74; r0=4.9; ρ0=8; χ²r=0.3
ISO (MDM)
(M/L)d=0.77; r0=4.0; ρ0=7; χ²r=0.3
ISO (fixed M/L)
(M/L)d=0.39; r0=1.7; ρ0=131; χ²r=0.3
NFW (BFM)
(M/L)d=0.67; c=1.0; V200=423; χ²r=0.3
NFW (fixed M/L)
(M/L)d=0.39; c=9.9; V200=128; χ²r=0.4
Vrot (km s⁻¹)
Radius (kpc)
UGC 03521
MB=-19.8; Type=Sc; h=3.0
disc
halo
model
approaching
receding

Figure A.23

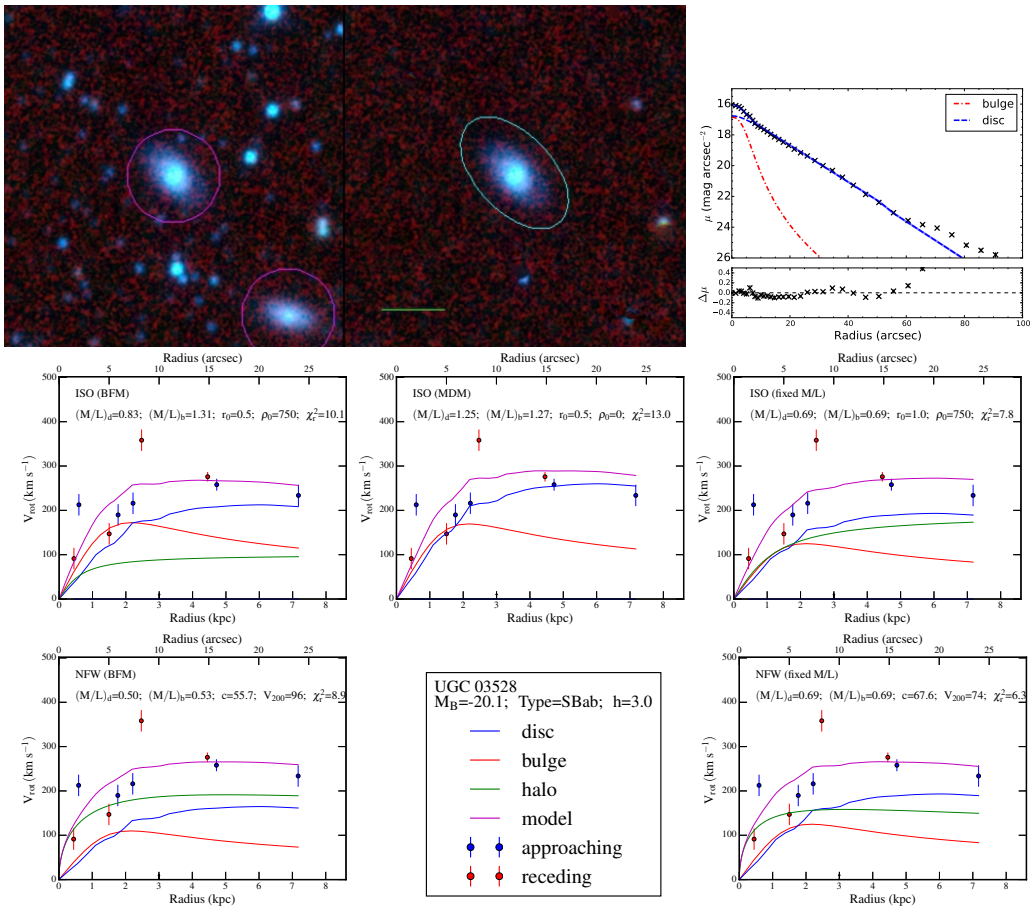
bulge
disc
μ (mag arcsec⁻²)
Δμ
Radius (arcsec)
ISO (BFM)
(M/L)d=0.83; (M/L)b=1.31; r0=0.5; ρ0=750; χ²r=10.1
ISO (MDM)
(M/L)d=1.25; (M/L)b=1.27; r0=0.5; ρ0=0; χ²r=13.0
ISO (fixed M/L)
(M/L)d=0.69; (M/L)b=0.69; r0=1.0; ρ0=750; χ²r=7.8
NFW (BFM)
(M/L)d=0.50; (M/L)b=0.53; c=55.7; V200=96; χ²r=8.9
NFW (fixed M/L)
(M/L)d=0.69; (M/L)b=0.69; c=67.6; V200=74; χ²r=6.3
Vrot (km s⁻¹)
Radius (kpc)
UGC 03528
MB=-20.1; Type=SBab; h=3.0
disc
bulge
halo
model
approaching
receding

Figure A.24

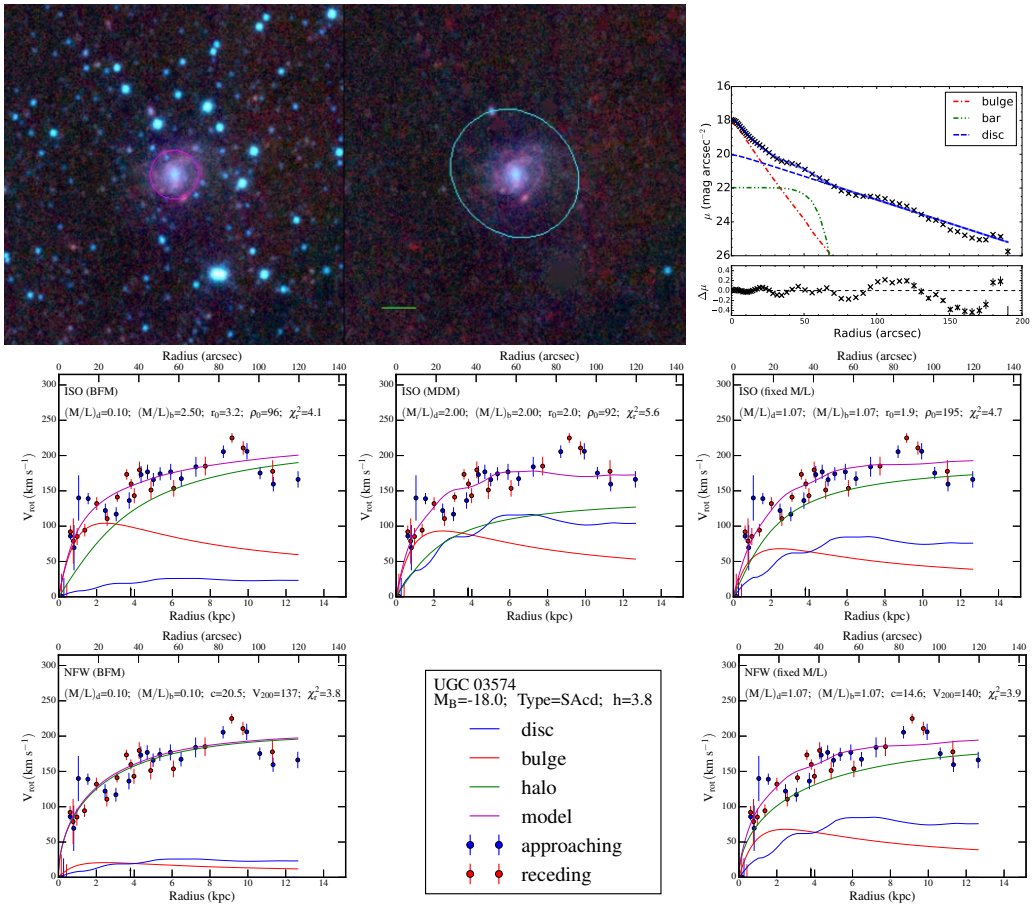
bulge
bar
disc
μ (mag arcsec⁻²)
Δμ
Radius (arcsec)
ISO (BFM)
(M/L)d=0.10; (M/L)b=2.50; r0=3.2; ρ0=96; χ²r=4.1
ISO (MDM)
(M/L)d=2.00; (M/L)b=2.00; r0=2.0; ρ0=92; χ²r=5.6
ISO (fixed M/L)
(M/L)d=1.07; (M/L)b=1.07; r0=1.9; ρ0=195; χ²r=4.7
NFW (BFM)
(M/L)d=0.10; (M/L)b=0.10; c=20.5; V200=137; χ²r=3.8
NFW (fixed M/L)
(M/L)d=1.07; (M/L)b=1.07; c=14.6; V200=140; χ²r=3.9
Vrot (km s⁻¹)
Radius (kpc)
UGC 03574
MB=-18.0; Type=SAcd; h=3.8
disc
bulge
halo
model
approaching
receding

Figure A.25

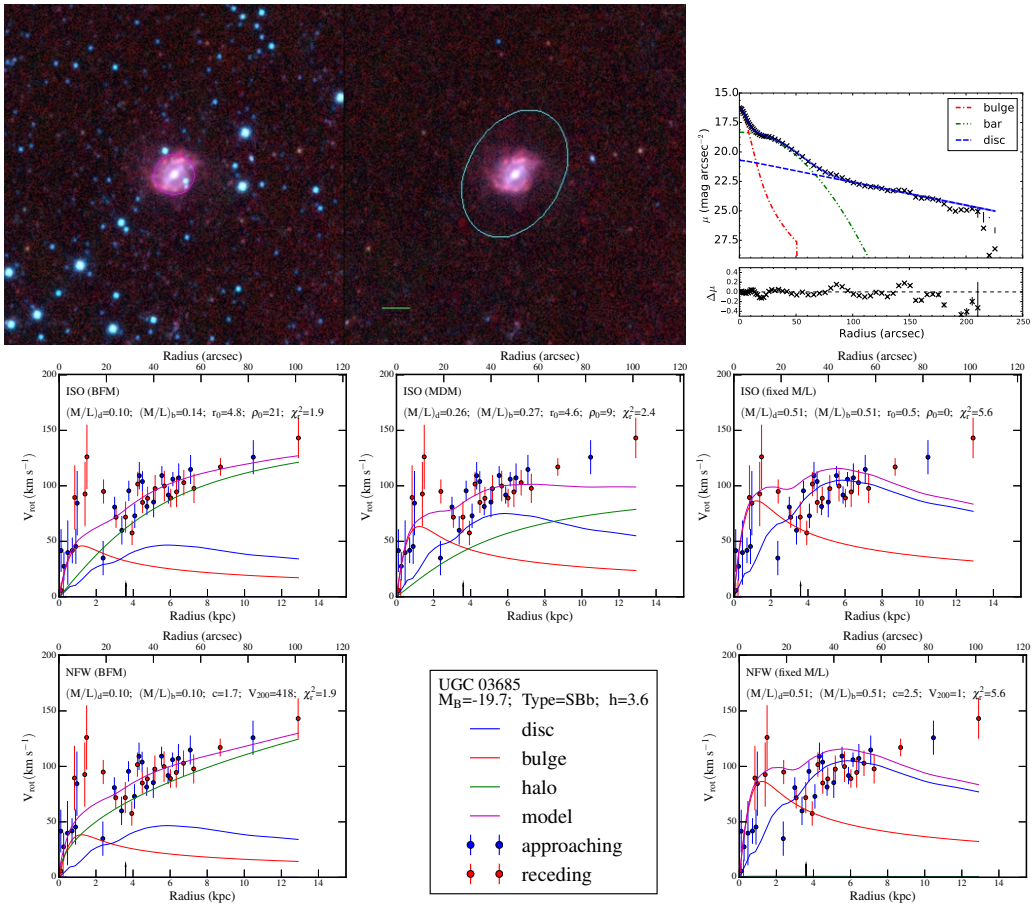
bulge
bar
disc
μ (mag arcsec⁻²)
Δμ
Radius (arcsec)
ISO (BFM)
(M/L)d=0.10; (M/L)b=0.14; r0=4.8; ρ0=21; χ²z=1.9
ISO (MDM)
(M/L)d=0.26; (M/L)b=0.27; r0=4.6; ρ0=9; χ²z=2.4
ISO (fixed M/L)
(M/L)d=0.51; (M/L)b=0.51; r0=0.5; ρ0=0; χ²z=5.6
NFW (BFM)
(M/L)d=0.10; (M/L)b=0.10; c=1.7; V200=418; χ²z=1.9
NFW (fixed M/L)
(M/L)d=0.51; (M/L)b=0.51; c=2.5; V200=1; χ²z=5.6
Vrot (km s⁻¹)
Radius (kpc)
UGC 03685
MB=-19.7; Type=SBb; h=3.6
disc
bulge
halo
model
approaching
receding

Figure A.26

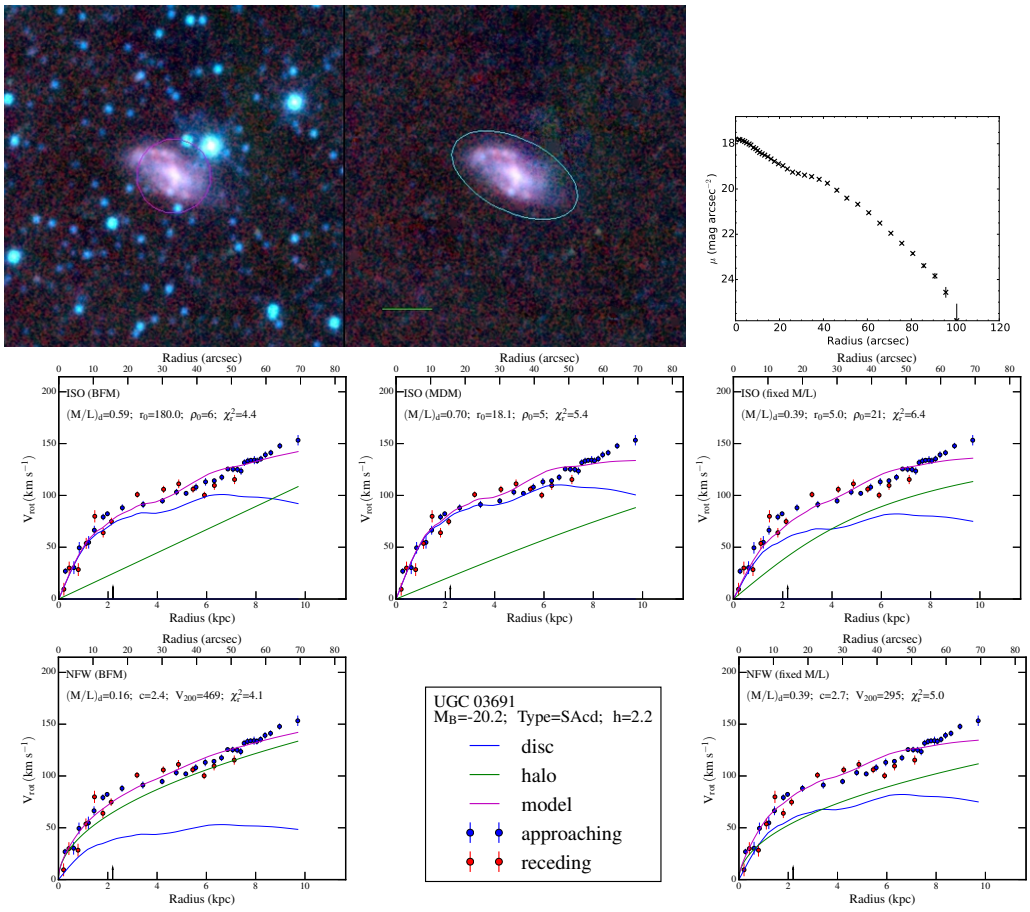
Radius (arcsec)
μ (mag arcsec⁻²)
ISO (BFM)
(M/L)d=0.59; r0=180.0; ρ0=6; χ²r=4.4
ISO (MDM)
(M/L)d=0.70; r0=18.1; ρ0=5; χ²r=5.4
ISO (fixed M/L)
(M/L)d=0.39; r0=5.0; ρ0=21; χ²r=6.4
NFW (BFM)
(M/L)d=0.16; c=2.4; V200=469; χ²r=4.1
NFW (fixed M/L)
(M/L)d=0.39; c=2.7; V200=295; χ²r=5.0
Vrot (km s⁻¹)
Radius (kpc)
UGC 03691
MB=-20.2; Type=SAcd; h=2.2
disc
halo
model
approaching
receding

Figure A.27

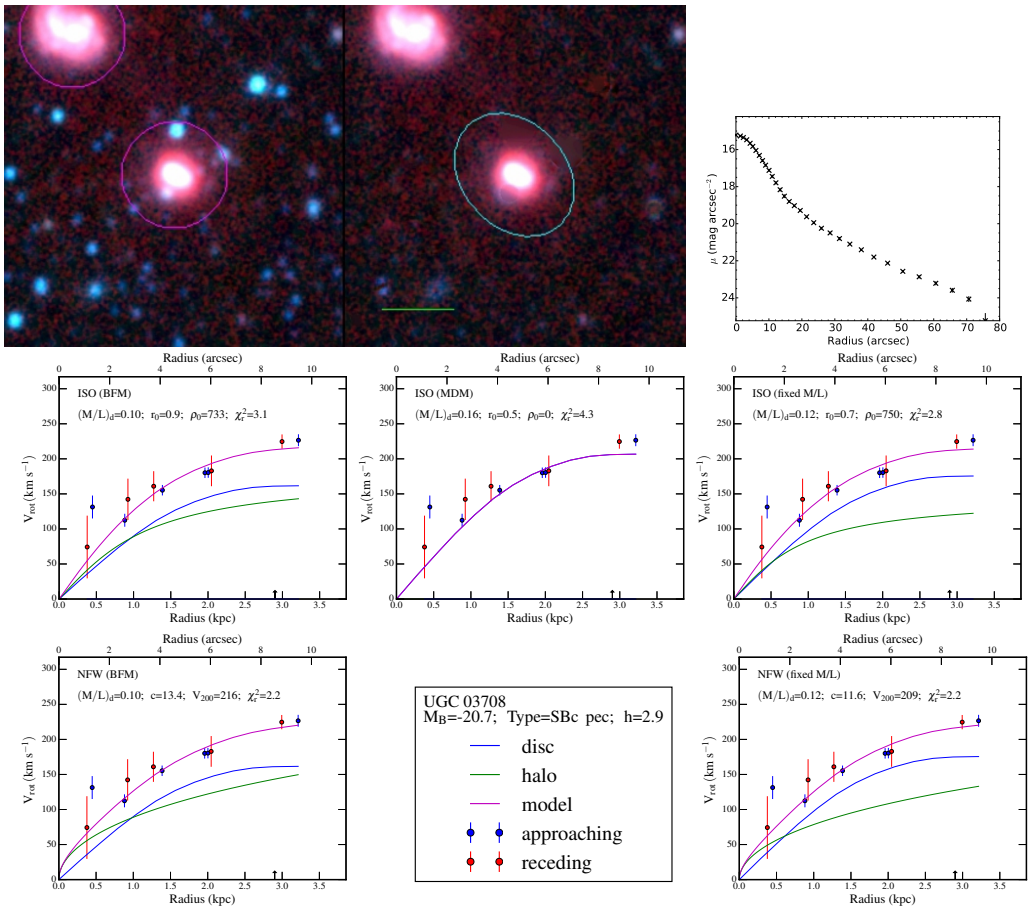
μ (mag arcsec⁻²)
Radius (arcsec)
ISO (BFM)
(M/L)d=0.10; r0=0.9; ρ0=733; χr²=3.1
ISO (MDM)
(M/L)d=0.16; r0=0.5; ρ0=0; χr²=4.3
ISO (fixed M/L)
(M/L)d=0.12; r0=0.7; ρ0=750; χr²=2.8
NFW (BFM)
(M/L)d=0.10; c=13.4; V200=216; χr²=2.2
NFW (fixed M/L)
(M/L)d=0.12; c=11.6; V200=209; χr²=2.2
Vrot (km s⁻¹)
Radius (kpc)
UGC 03708
MB=-20.7; Type=SBc pec; h=2.9
disc
halo
model
approaching
receding

Figure A.28

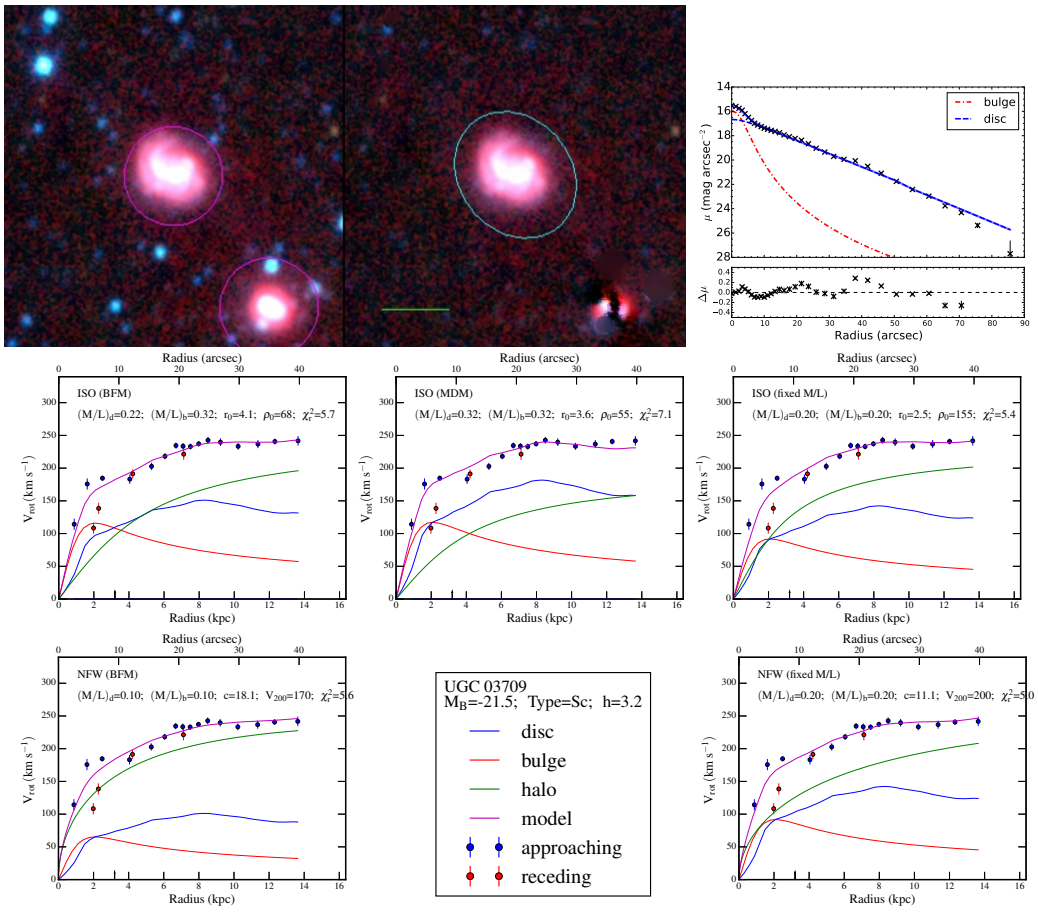
bulge
disc
μ (mag arcsec⁻²)
Δμ
Radius (arcsec)
ISO (BFM)
(M/L)d=0.22; (M/L)b=0.32; r0=4.1; ρ0=68; χ²r=5.7
ISO (MDM)
(M/L)d=0.32; (M/L)b=0.32; r0=3.6; ρ0=55; χ²r=7.1
ISO (fixed M/L)
(M/L)d=0.20; (M/L)b=0.20; r0=2.5; ρ0=155; χ²r=5.4
NFW (BFM)
(M/L)d=0.10; (M/L)b=0.10; c=18.1; V200=170; χ²r=5.6
NFW (fixed M/L)
(M/L)d=0.20; (M/L)b=0.20; c=11.1; V200=200; χ²r=5.0
Vrot (km s⁻¹)
Radius (kpc)
UGC 03709
MB=-21.5; Type=Sc; h=3.2
disc
bulge
halo
model
approaching
receding

Figure A.29

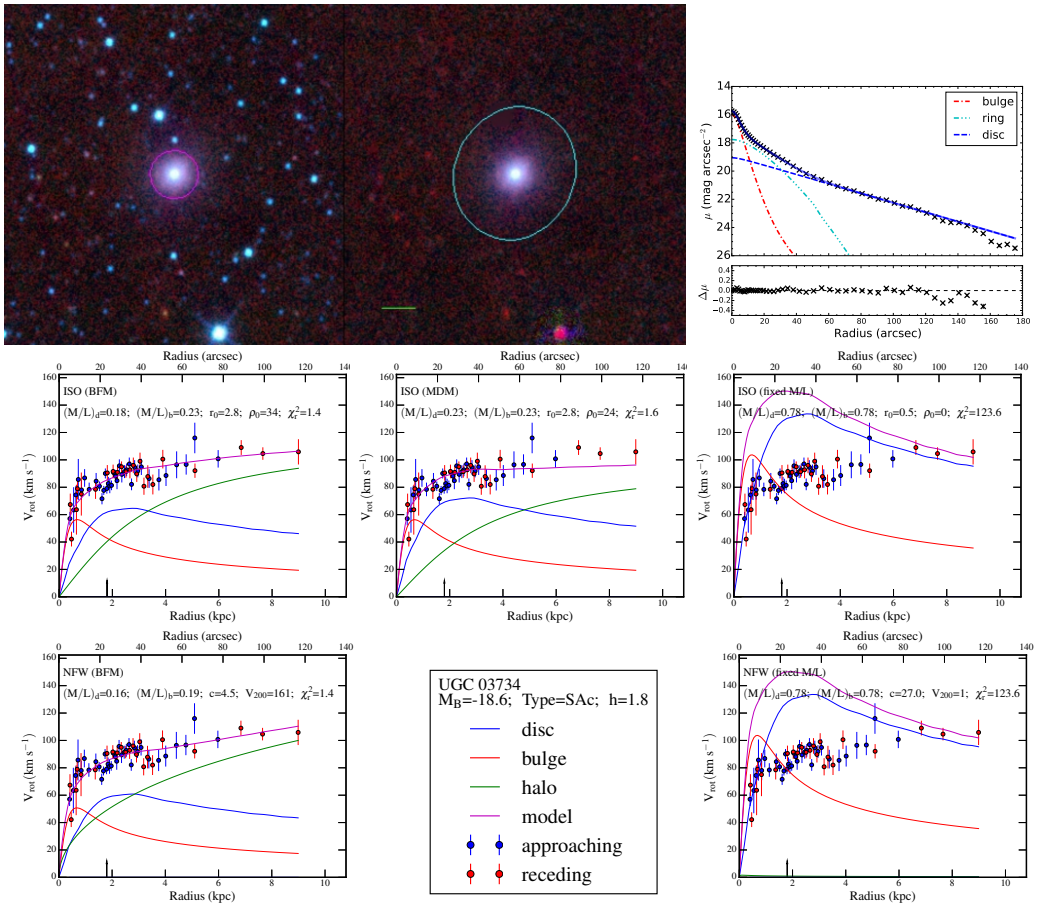
bulge
ring
disc
μ (mag arcsec⁻²)
Δμ
Radius (arcsec)
ISO (BFM)
(M/L)d=0.18; (M/L)b=0.23; r0=2.8; ρ0=34; χ²r=1.4
ISO (MDM)
(M/L)d=0.23; (M/L)b=0.23; r0=2.8; ρ0=24; χ²r=1.6
ISO (fixed M/L)
(M/L)d=0.78; (M/L)b=0.78; r0=0.5; ρ0=0; χ²r=123.6
NFW (BFM)
(M/L)d=0.16; (M/L)b=0.19; c=4.5; V200=161; χ²r=1.4
NFW (fixed M/L)
(M/L)d=0.78; (M/L)b=0.78; c=27.0; V200=1; χ²r=123.6
V_rot (km s⁻¹)
Radius (kpc)
UGC 03734
MB=-18.6; Type=SAc; h=1.8
disc
bulge
halo
model
approaching
receding

Figure A.30

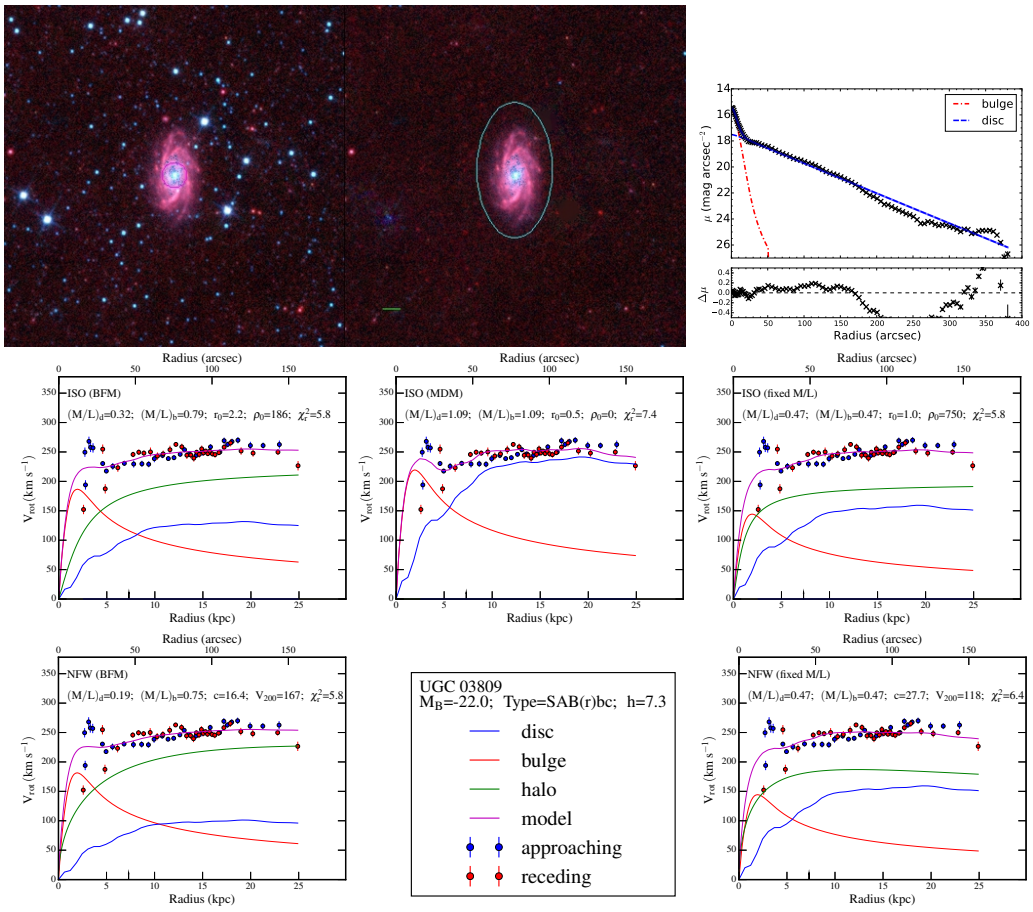
bulge
disc
μ (mag arcsec⁻²)
Δμ
Radius (arcsec)
ISO (BFM)
(M/L)d=0.32; (M/L)b=0.79; r0=2.2; ρ0=186; χr²=5.8
ISO (MDM)
(M/L)d=1.09; (M/L)b=1.09; r0=0.5; ρ0=0; χr²=7.4
ISO (fixed M/L)
(M/L)d=0.47; (M/L)b=0.47; r0=1.0; ρ0=750; χr²=5.8
NFW (BFM)
(M/L)d=0.19; (M/L)b=0.75; c=16.4; V200=167; χr²=5.8
NFW (fixed M/L)
(M/L)d=0.47; (M/L)b=0.47; c=27.7; V200=118; χr²=6.4
Vrot (km s⁻¹)
Radius (kpc)
UGC 03809
MB=-22.0; Type=SAB(r)bc; h=7.3
disc
bulge
halo
model
approaching
receding

Figure A.31

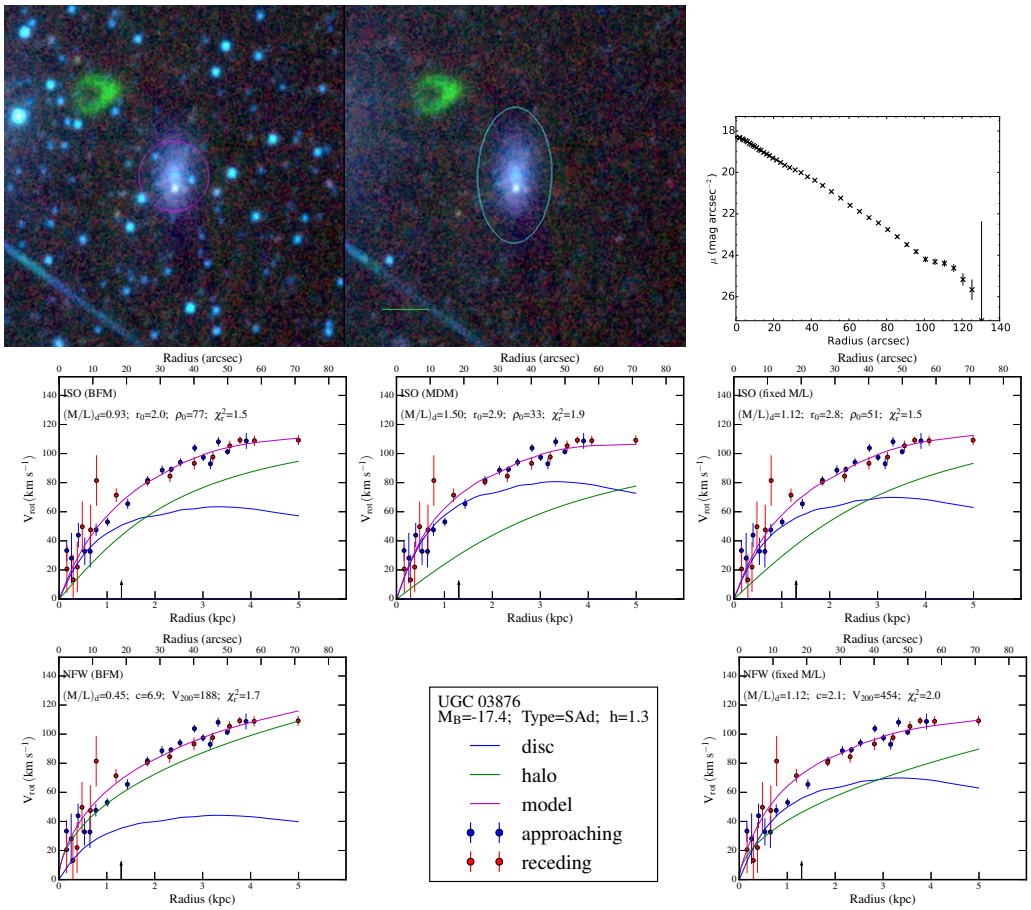
μ (mag arcsec⁻²)
Radius (arcsec)
ISO (BFM)
(M/L)d=0.93; r0=2.0; ρ0=77; χ²ν=1.5
ISO (MDM)
(M/L)d=1.50; r0=2.9; ρ0=33; χ²ν=1.9
ISO (fixed M/L)
(M/L)d=1.12; r0=2.8; ρ0=51; χ²ν=1.5
NFW (BFM)
(M/L)d=0.45; c=6.9; V200=188; χ²ν=1.7
NFW (fixed M/L)
(M/L)d=1.12; c=2.1; V200=454; χ²ν=2.0
Vrot (km s⁻¹)
Radius (kpc)
UGC 03876
MB=-17.4; Type=SAd; h=1.3
disc
halo
model
approaching
receding

Figure A.32

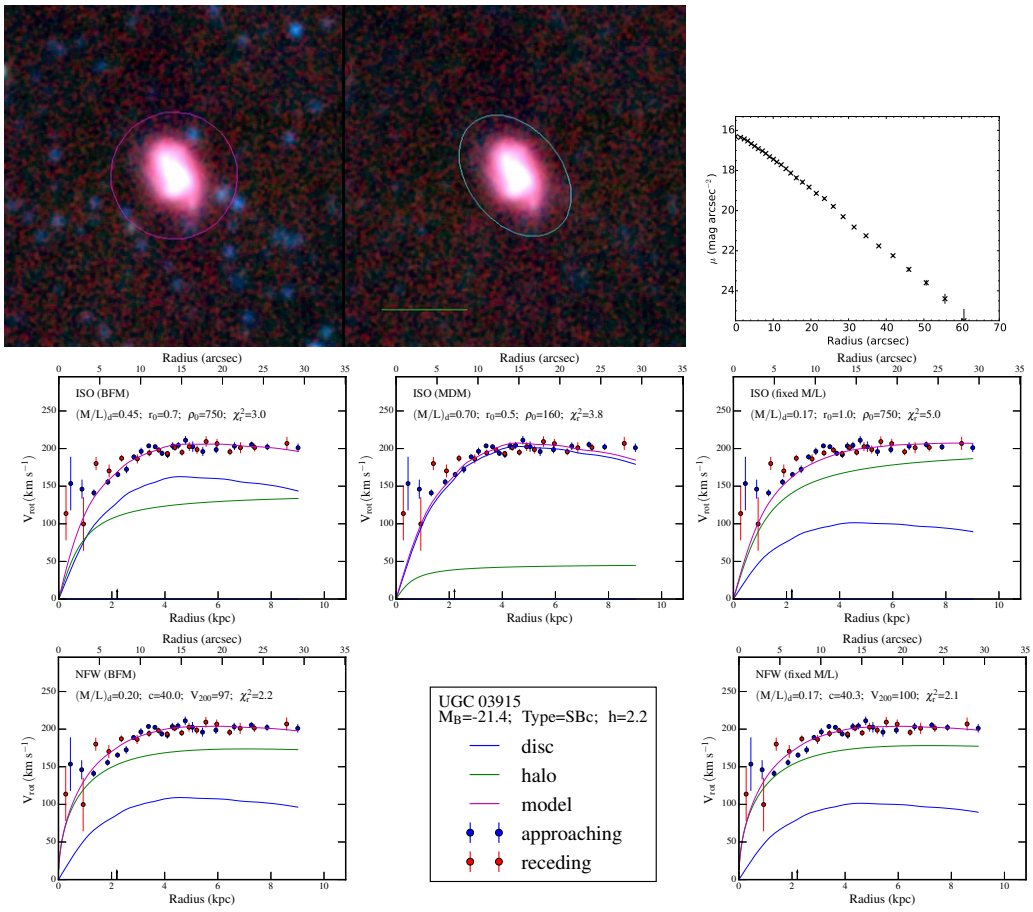
Radius (arcsec)
μ (mag arcsec⁻²)
ISO (BFM)
(M/L)d=0.45; r0=0.7; ρ0=750; χ²r=3.0
ISO (MDM)
(M/L)d=0.70; r0=0.5; ρ0=160; χ²r=3.8
ISO (fixed M/L)
(M/L)d=0.17; r0=1.0; ρ0=750; χ²r=5.0
NFW (BFM)
(M/L)d=0.20; c=40.0; V200=97; χ²r=2.2
NFW (fixed M/L)
(M/L)d=0.17; c=40.3; V200=100; χ²r=2.1
Vrot (km s⁻¹)
Radius (kpc)
UGC 03915
MB=-21.4; Type=SBc; h=2.2
disc
halo
model
approaching
receding

Figure A.33

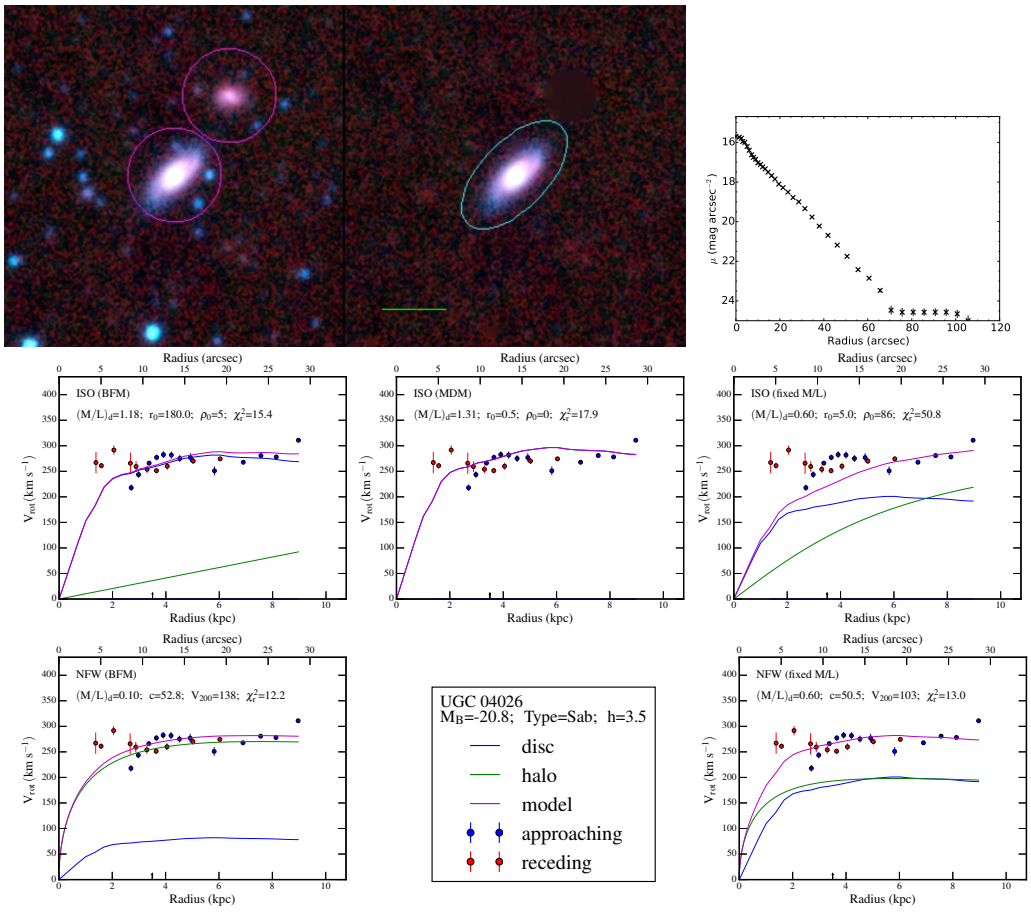
μ (mag arcsec⁻²)
Radius (arcsec)
ISO (BFM)
(M/L)d=1.18; r0=180.0; ρ0=5; χ²r=15.4
ISO (MDM)
(M/L)d=1.31; r0=0.5; ρ0=0; χ²r=17.9
ISO (fixed M/L)
(M/L)d=0.60; r0=5.0; ρ0=86; χ²r=50.8
NFW (BFM)
(M/L)d=0.10; c=52.8; V200=138; χ²r=12.2
NFW (fixed M/L)
(M/L)d=0.60; c=50.5; V200=103; χ²r=13.0
Vrot (km s⁻¹)
Radius (kpc)
UGC 04026
MB=-20.8; Type=Sab; h=3.5
disc
halo
model
approaching
receding

Figure A.34

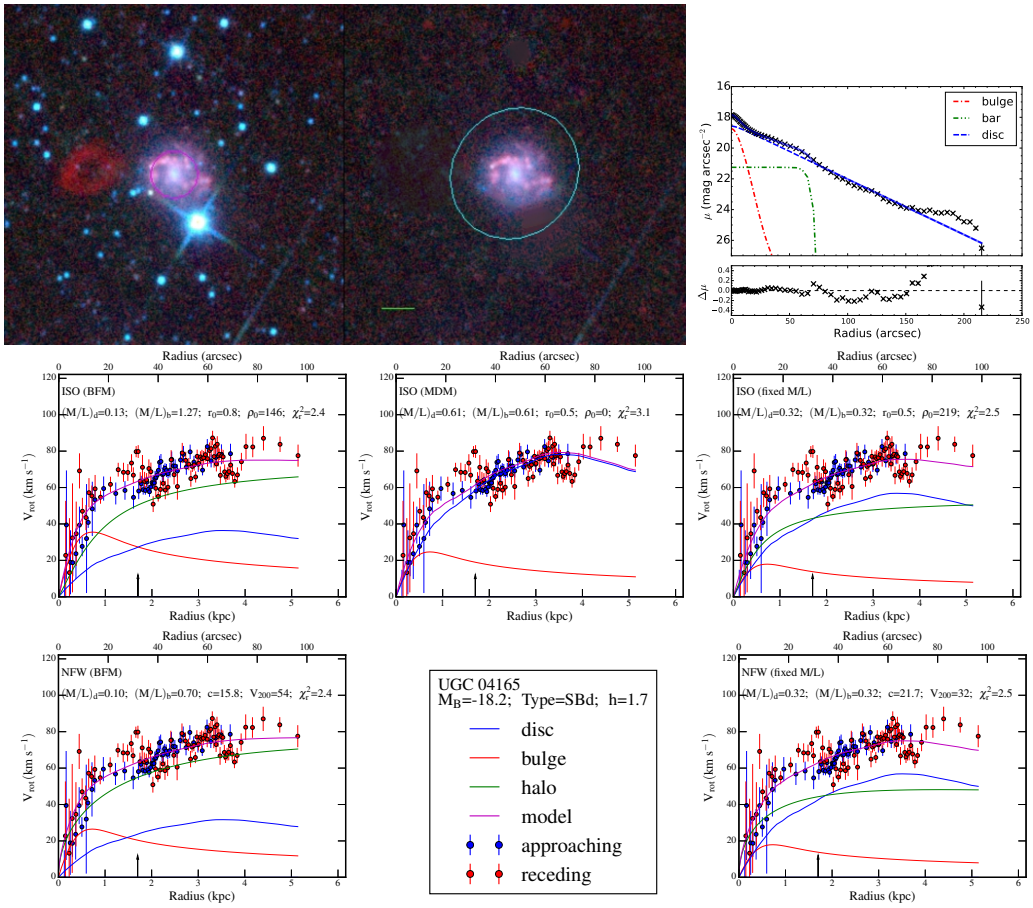
bulge
bar
disc
μ (mag arcsec⁻²)
Δμ
Radius (arcsec)
ISO (BFM)
(M/L)d=0.13; (M/L)b=1.27; r0=0.8; ρ0=146; χ²r=2.4
ISO (MDM)
(M/L)d=0.61; (M/L)b=0.61; r0=0.5; ρ0=0; χ²r=3.1
ISO (fixed M/L)
(M/L)d=0.32; (M/L)b=0.32; r0=0.5; ρ0=219; χ²r=2.5
NFW (BFM)
(M/L)d=0.10; (M/L)b=0.70; c=15.8; V200=54; χ²r=2.4
NFW (fixed M/L)
(M/L)d=0.32; (M/L)b=0.32; c=21.7; V200=32; χ²r=2.5
Vrot (km s⁻¹)
Radius (kpc)
UGC 04165
MB=-18.2; Type=SBd; h=1.7
disc
bulge
halo
model
approaching
receding

Figure A.35

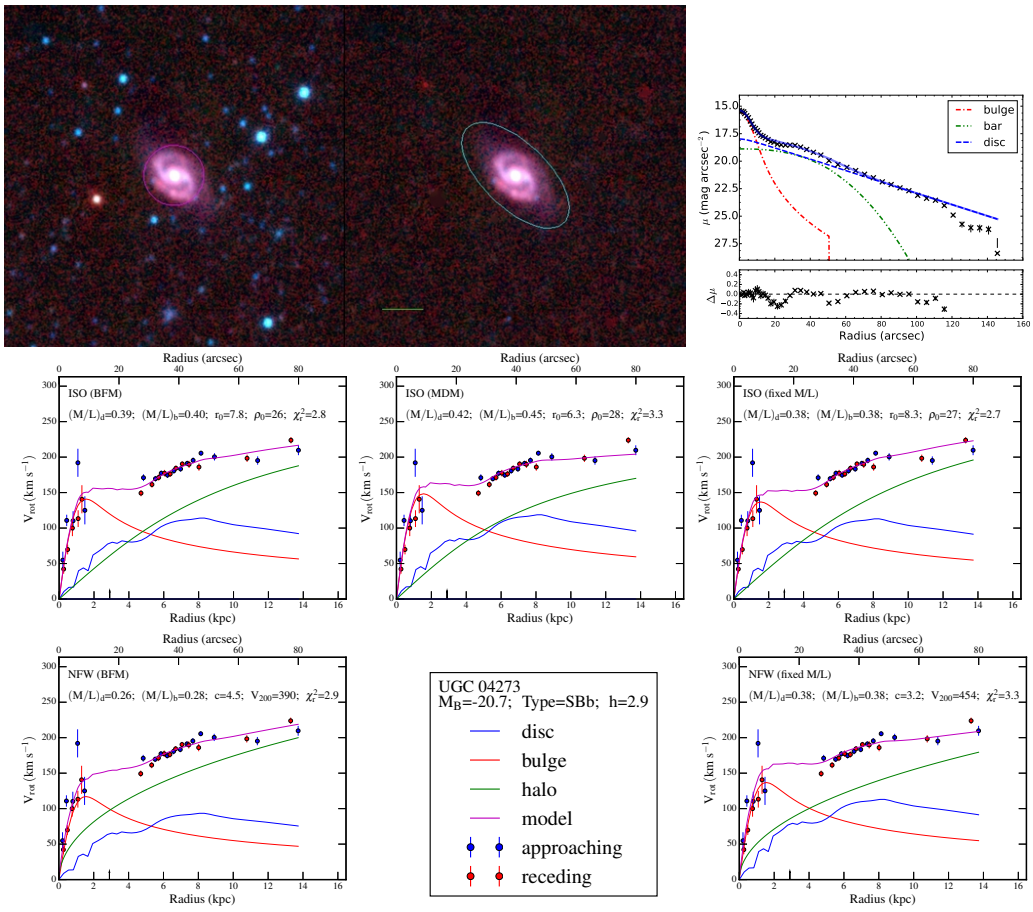
bulge
bar
disc
Radius (arcsec)
ISO (BFM)
(M/L)d=0.39; (M/L)h=0.40; r0=7.8; ρ0=26; χ2r=2.8
ISO (MDM)
(M/L)d=0.42; (M/L)h=0.45; r0=6.3; ρ0=28; χ2r=3.3
ISO (fixed M/L)
(M/L)d=0.38; (M/L)h=0.38; r0=8.3; ρ0=27; χ2r=2.7
NFW (BFM)
(M/L)d=0.26; (M/L)h=0.28; c=4.5; V200=390; χ2r=2.9
NFW (fixed M/L)
(M/L)d=0.38; (M/L)h=0.38; c=3.2; V200=454; χ2r=3.3
Vrot (km s−1)
Radius (kpc)
UGC 04273
MB=-20.7; Type=SBb; h=2.9
disc
bulge
halo
model
approaching
receding

Figure A.36

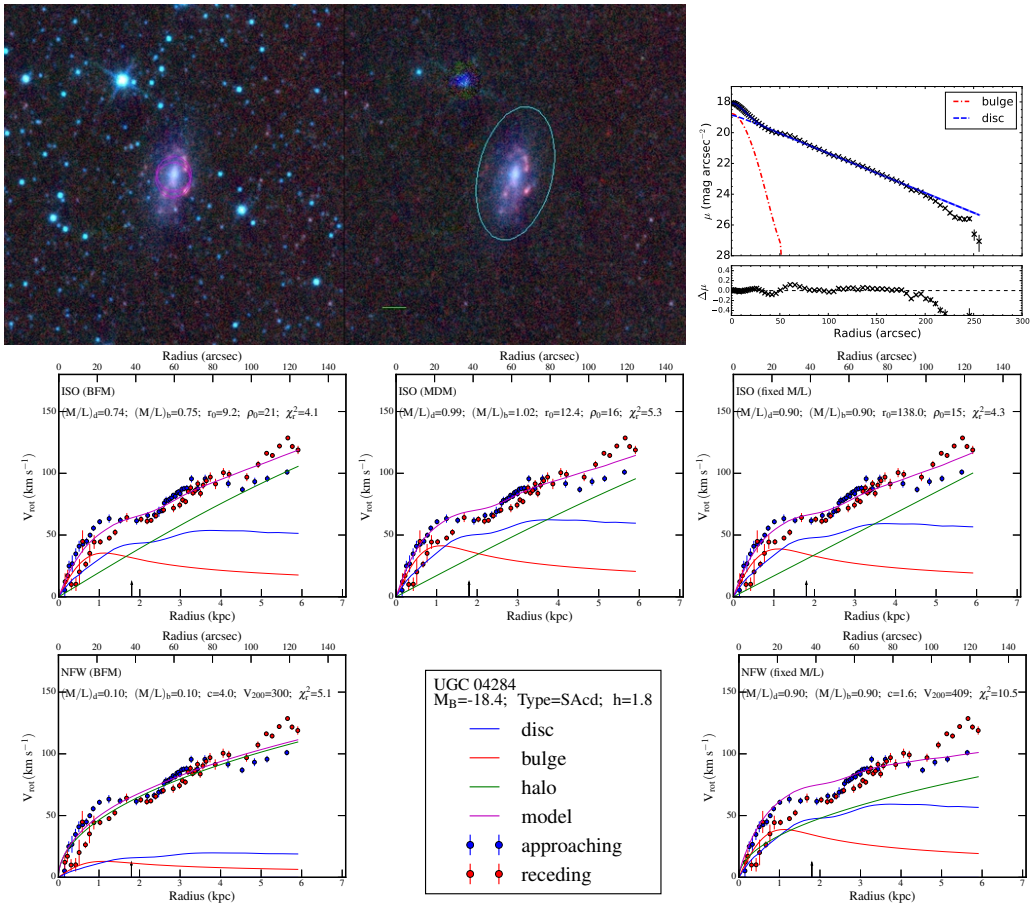
bulge
disc
μ (mag arcsec⁻²)
Δμ
Radius (arcsec)
ISO (BFM)
(M/L)d=0.74; (M/L)b=0.75; r0=9.2; ρ0=21; χ²r=4.1
ISO (MDM)
(M/L)d=0.99; (M/L)b=1.02; r0=12.4; ρ0=16; χ²r=5.3
ISO (fixed M/L)
(M/L)d=0.90; (M/L)b=0.90; r0=138.0; ρ0=15; χ²r=4.3
NFW (BFM)
(M/L)d=0.10; (M/L)b=0.10; c=4.0; V200=300; χ²r=5.1
NFW (fixed M/L)
(M/L)d=0.90; (M/L)b=0.90; c=1.6; V200=409; χ²r=10.5
Vrot (km s⁻¹)
Radius (kpc)
UGC 04284
MB=-18.4; Type=SAcd; h=1.8
disc
bulge
halo
model
approaching
receding

Figure A.37

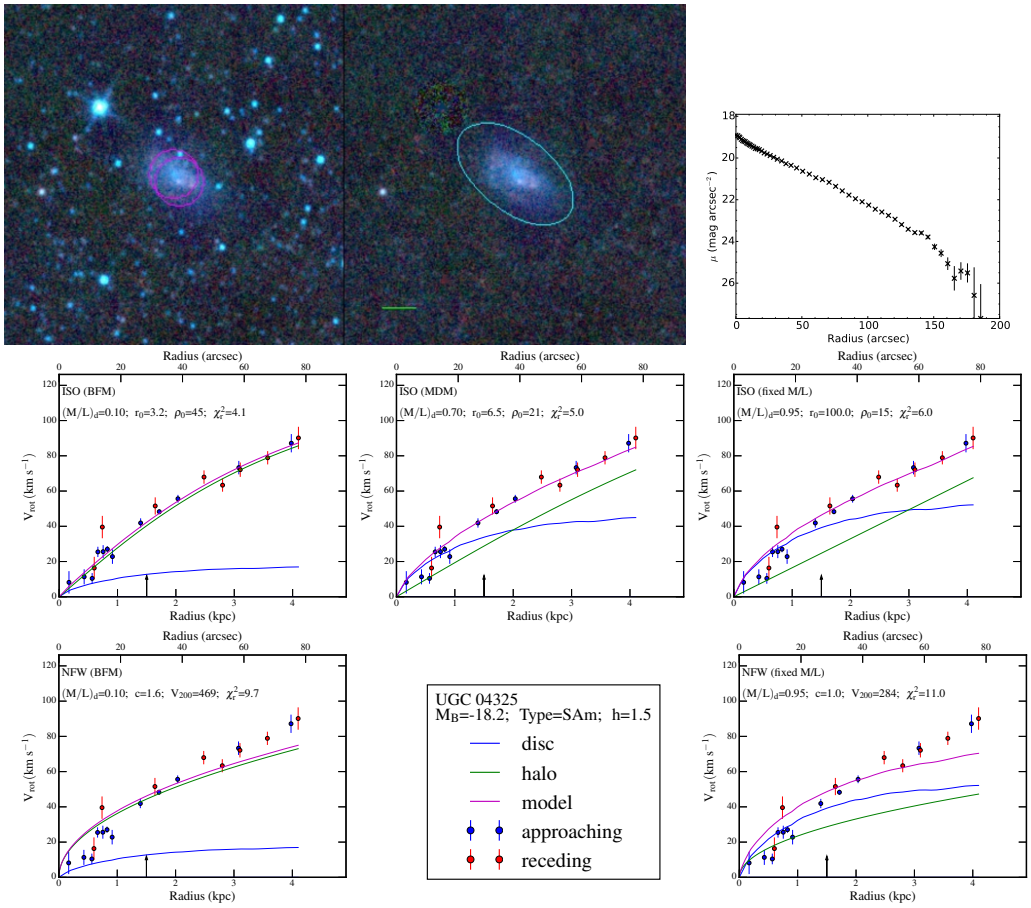
μ (mag arcsec⁻²)
Radius (arcsec)
ISO (BFM)
(M/L)d=0.10; r0=3.2; ρ0=45; χ²ν=4.1
ISO (MDM)
(M/L)d=0.70; r0=6.5; ρ0=21; χ²ν=5.0
ISO (fixed M/L)
(M/L)d=0.95; r0=100.0; ρ0=15; χ²ν=6.0
NFW (BFM)
(M/L)d=0.10; c=1.6; V200=469; χ²ν=9.7
NFW (fixed M/L)
(M/L)d=0.95; c=1.0; V200=284; χ²ν=11.0
Vrot (km s⁻¹)
Radius (kpc)
UGC 04325
MB=-18.2; Type=SAm; h=1.5
disc
halo
model
approaching
receding

Figure A.38

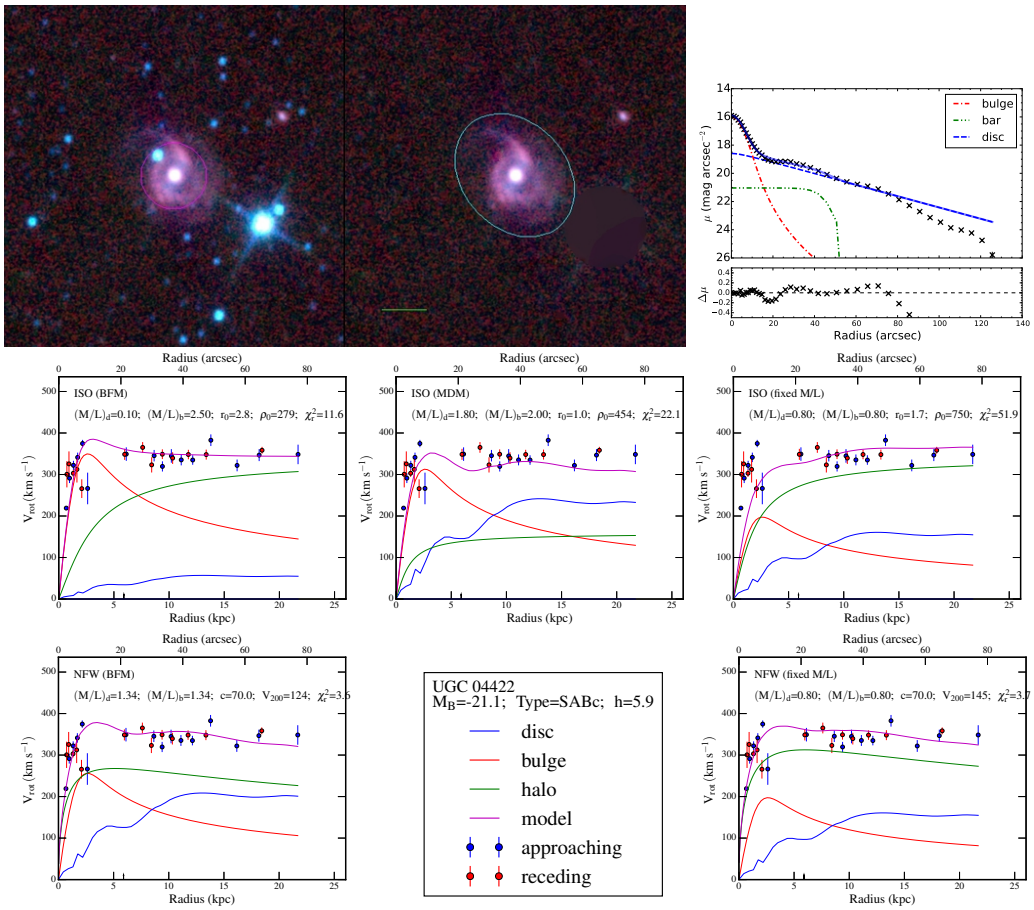
bulge
bar
disc
μ (mag arcsec⁻²)
Δμ
Radius (arcsec)
ISO (BFM)
(M/L)d=0.10; (M/L)b=2.50; r0=2.8; ρ0=279; χ²r=11.6
ISO (MDM)
(M/L)d=1.80; (M/L)b=2.00; r0=1.0; ρ0=454; χ²r=22.1
ISO (fixed M/L)
(M/L)d=0.80; (M/L)b=0.80; r0=1.7; ρ0=750; χ²r=51.9
NFW (BFM)
(M/L)d=1.34; (M/L)b=1.34; c=70.0; V200=124; χ²r=3.6
NFW (fixed M/L)
(M/L)d=0.80; (M/L)b=0.80; c=70.0; V200=145; χ²r=3.7
Vrot (km s⁻¹)
Radius (kpc)
UGC 04422
MB=-21.1; Type=SABc; h=5.9
disc
bulge
halo
model
approaching
receding

Figure A.39

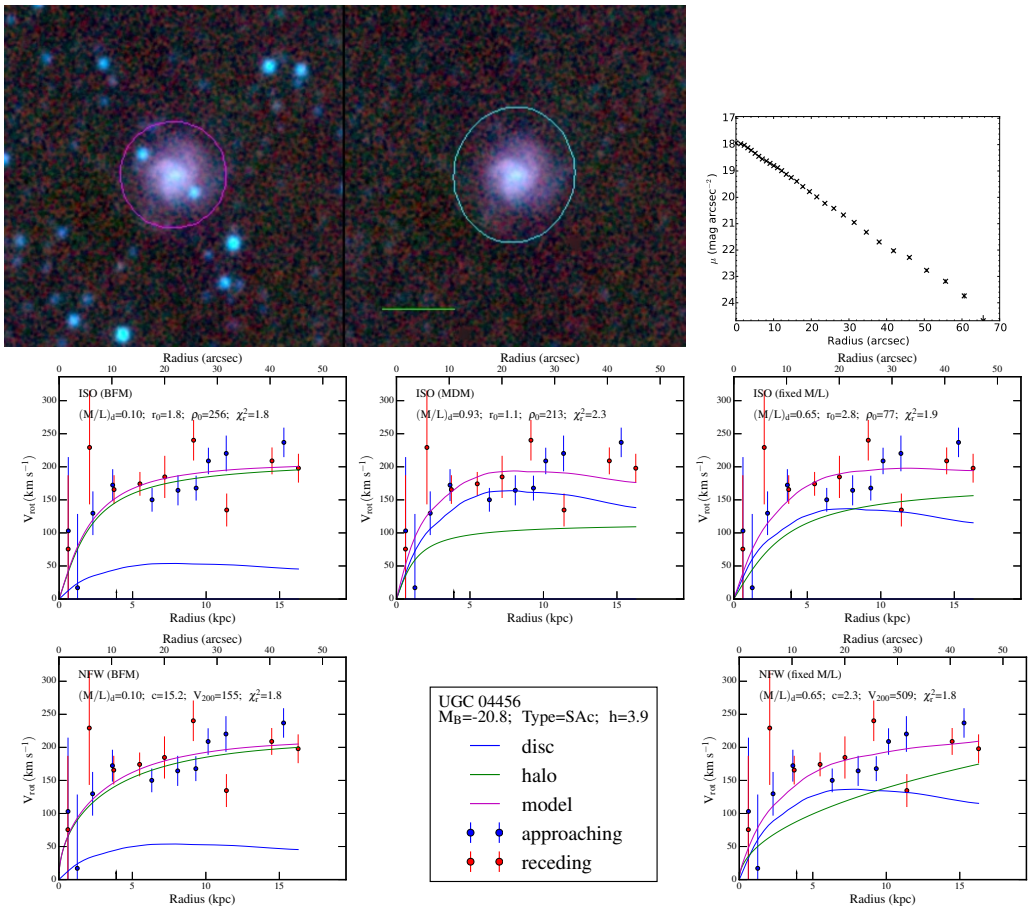
μ (mag arcsec⁻²)
Radius (arcsec)
ISO (BFM)
(M/L)d=0.10; r0=1.8; ρ0=256; χ²r=1.8
ISO (MDM)
(M/L)d=0.93; r0=1.1; ρ0=213; χ²r=2.3
ISO (fixed M/L)
(M/L)d=0.65; r0=2.8; ρ0=77; χ²r=1.9
NFW (BFM)
(M/L)d=0.10; c=15.2; V200=155; χ²r=1.8
NFW (fixed M/L)
(M/L)d=0.65; c=2.3; V200=509; χ²r=1.8
Vrot (km s⁻¹)
Radius (kpc)
UGC 04456
MB=-20.8; Type=SAc; h=3.9
disc
halo
model
approaching
receding

Figure A.40

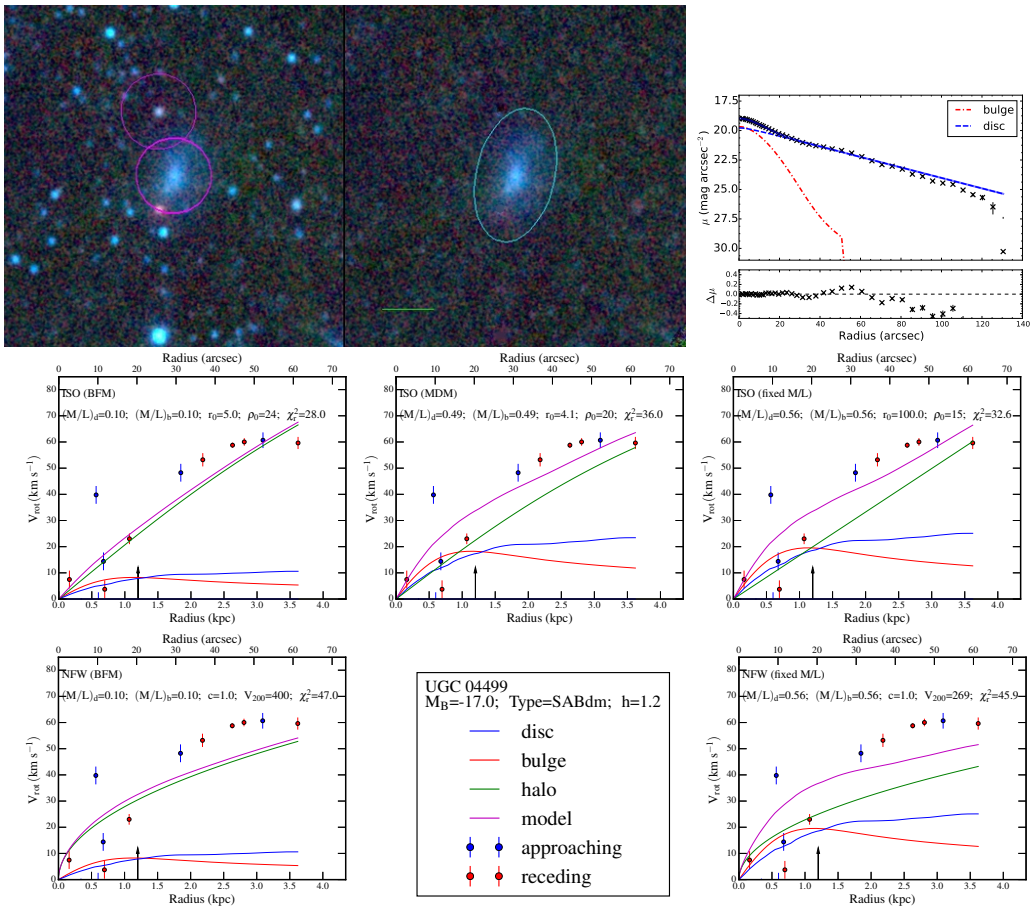
bulge
disc
μ (mag arcsec⁻²)
Δμ
Radius (arcsec)
TSO (BFM)
(M/L)d=0.10; (M/L)b=0.10; r0=5.0; ρ0=24; χ²r=28.0
TSO (MDM)
(M/L)d=0.49; (M/L)b=0.49; r0=4.1; ρ0=20; χ²r=36.0
TSO (fixed M/L)
(M/L)d=0.56; (M/L)b=0.56; r0=100.0; ρ0=15; χ²r=32.6
NFW (BFM)
(M/L)d=0.10; (M/L)b=0.10; c=1.0; V200=400; χ²r=47.0
NFW (fixed M/L)
(M/L)d=0.56; (M/L)b=0.56; c=1.0; V200=269; χ²r=45.9
Vrot (km s⁻¹)
Radius (kpc)
UGC 04499
MB=-17.0; Type=SABdm; h=1.2
disc
bulge
halo
model
approaching
receding

Figure A.41

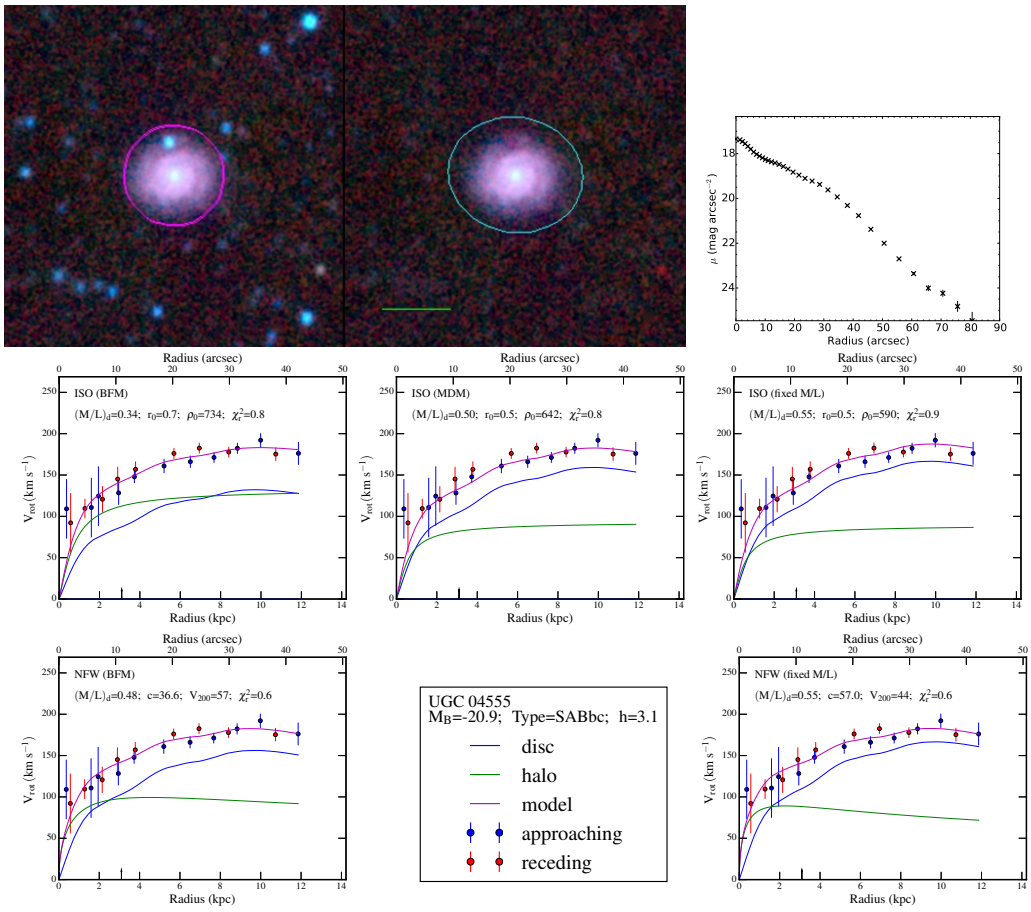
μ (mag arcsec⁻²)
Radius (arcsec)
ISO (BFM)
(M/L)d=0.34; r0=0.7; ρ0=734; χ²r=0.8
ISO (MDM)
(M/L)d=0.50; r0=0.5; ρ0=642; χ²r=0.8
ISO (fixed M/L)
(M/L)d=0.55; r0=0.5; ρ0=590; χ²r=0.9
NFW (BFM)
(M/L)d=0.48; c=36.6; V200=57; χ²r=0.6
NFW (fixed M/L)
(M/L)d=0.55; c=57.0; V200=44; χ²r=0.6
Vrot (km s⁻¹)
Radius (kpc)
UGC 04555
MB=-20.9; Type=SABbc; h=3.1
disc
halo
model
approaching
receding

Figure A.42

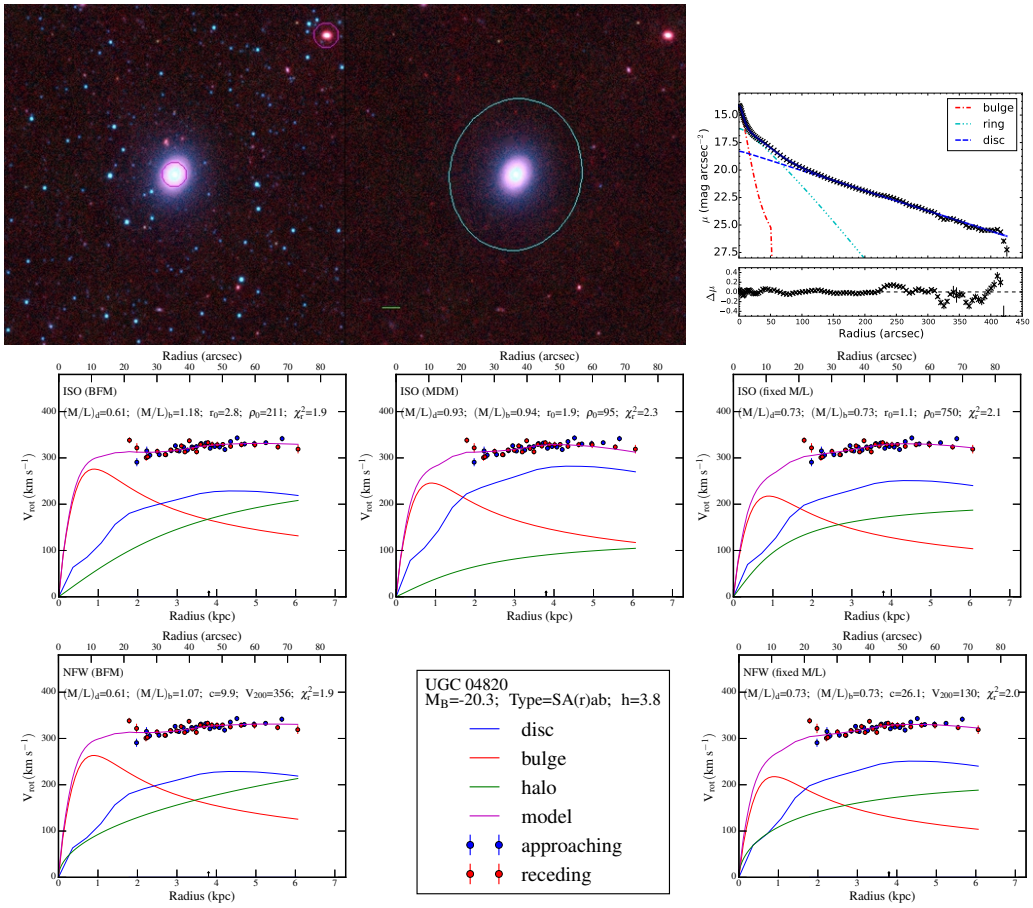
bulge
ring
disc
μ (mag arcsec⁻²)
Δμ
Radius (arcsec)
ISO (BFM)
(M/L)d=0.61; (M/L)b=1.18; r0=2.8; ρ0=211; χ²r=1.9
ISO (MDM)
(M/L)d=0.93; (M/L)b=0.94; r0=1.9; ρ0=95; χ²r=2.3
ISO (fixed M/L)
(M/L)d=0.73; (M/L)b=0.73; r0=1.1; ρ0=750; χ²r=2.1
NFW (BFM)
(M/L)d=0.61; (M/L)b=1.07; c=9.9; V200=356; χ²r=1.9
NFW (fixed M/L)
(M/L)d=0.73; (M/L)b=0.73; c=26.1; V200=130; χ²r=2.0
Vrot (km s⁻¹)
Radius (kpc)
UGC 04820
MB=-20.3; Type=SA(r)ab; h=3.8
disc
bulge
halo
model
approaching
receding

Figure A.43

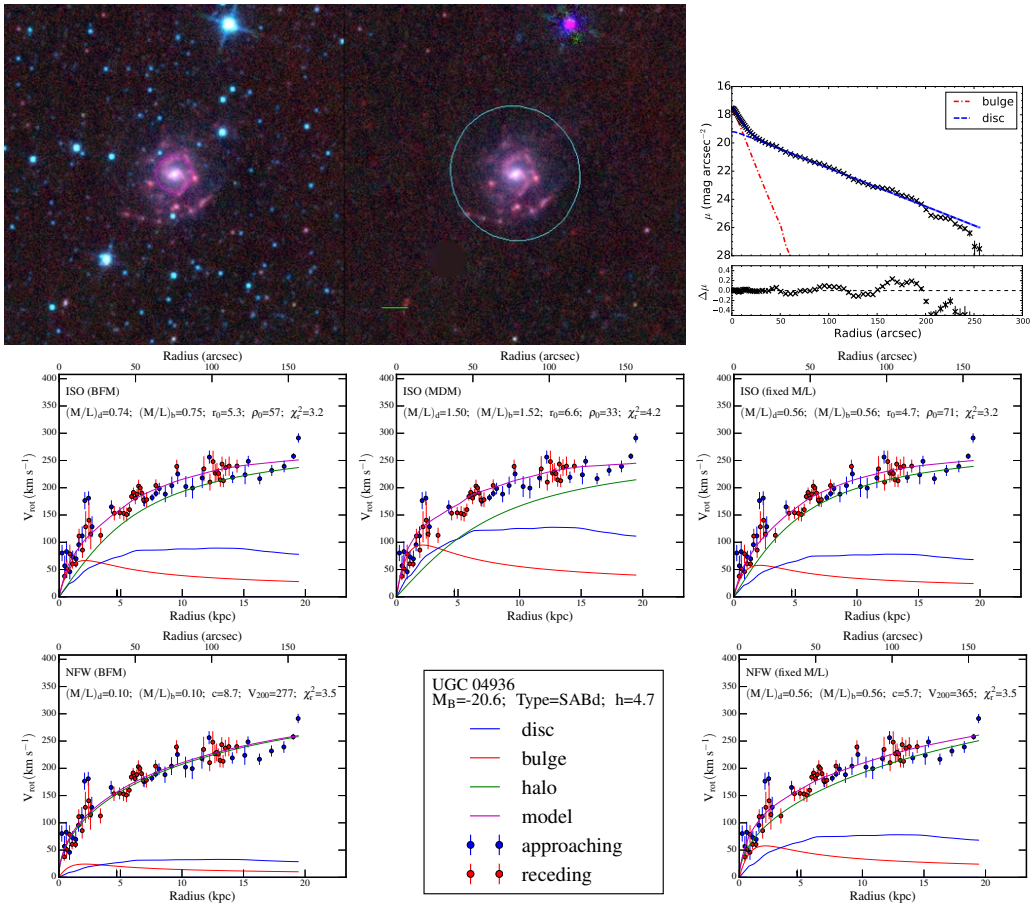
bulge
disc
μ (mag arcsec⁻²)
Δμ
Radius (arcsec)
ISO (BFM)
(M/L)d=0.74; (M/L)b=0.75; r0=5.3; ρ0=57; χ²r=3.2
ISO (MDM)
(M/L)d=1.50; (M/L)b=1.52; r0=6.6; ρ0=33; χ²r=4.2
ISO (fixed M/L)
(M/L)d=0.56; (M/L)b=0.56; r0=4.7; ρ0=71; χ²r=3.2
NFW (BFM)
(M/L)d=0.10; (M/L)b=0.10; c=8.7; V200=277; χ²r=3.5
NFW (fixed M/L)
(M/L)d=0.56; (M/L)b=0.56; c=5.7; V200=365; χ²r=3.5
Vrot (km s⁻¹)
Radius (kpc)
UGC 04936
MB=-20.6; Type=SABd; h=4.7
disc
bulge
halo
model
approaching
receding

Figure A.44

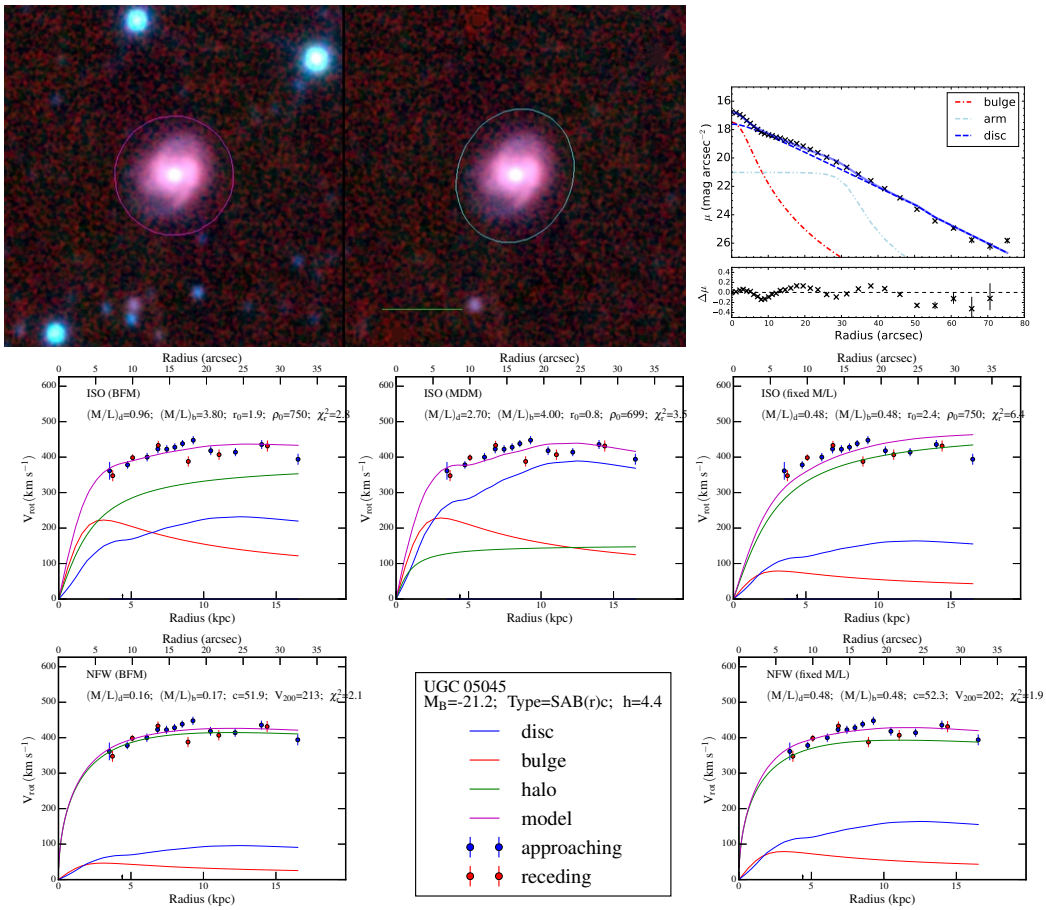
bulge
arm
disc
μ (mag arcsec⁻²)
Δμ
Radius (arcsec)
ISO (BFM)
(M/L)d=0.96; (M/L)b=3.80; r0=1.9; ρ0=750; χ²r=2.8
ISO (MDM)
(M/L)d=2.70; (M/L)b=4.00; r0=0.8; ρ0=699; χ²r=3.5
ISO (fixed M/L)
(M/L)d=0.48; (M/L)b=0.48; r0=2.4; ρ0=750; χ²r=6.4
NFW (BFM)
(M/L)d=0.16; (M/L)b=0.17; c=51.9; V200=213; χ²r=2.1
NFW (fixed M/L)
(M/L)d=0.48; (M/L)b=0.48; c=52.3; V200=202; χ²r=1.9
Vrot (km s⁻¹)
Radius (kpc)
UGC 05045
MB=-21.2; Type=SAB(r)c; h=4.4
disc
bulge
halo
model
approaching
receding

Figure A.45

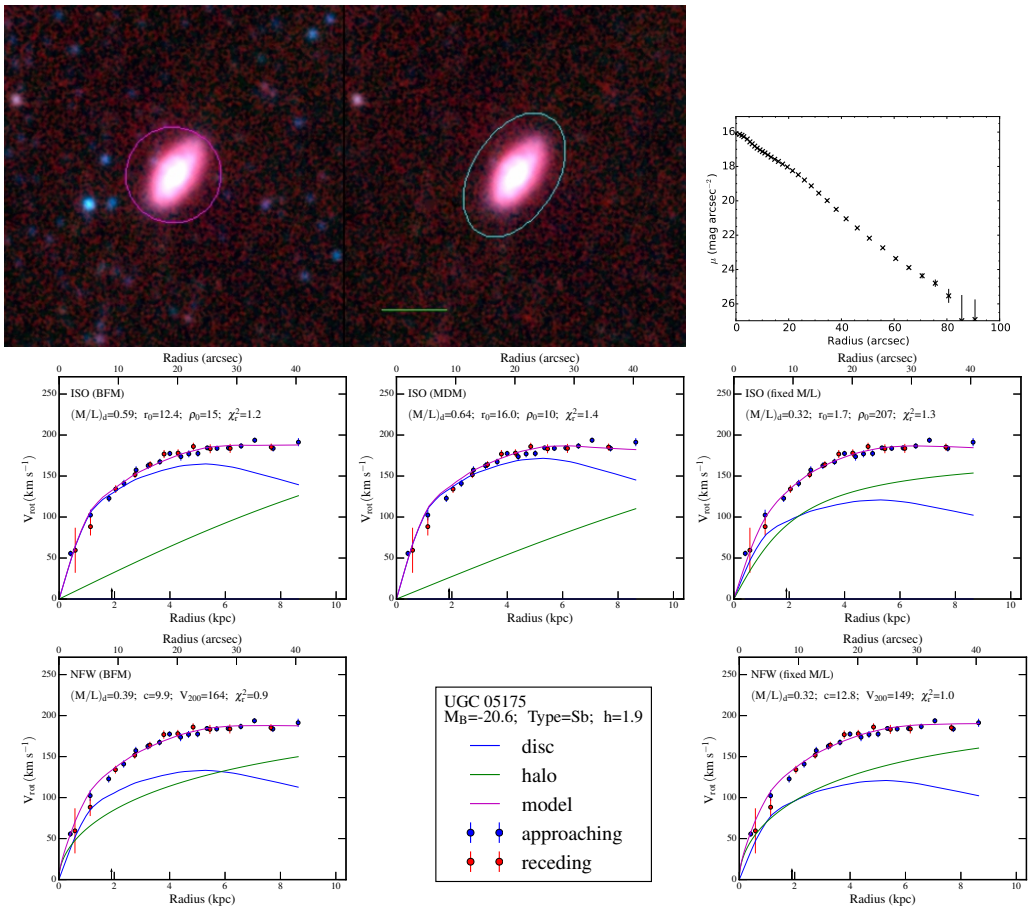
μ (mag arcsec⁻²)
Radius (arcsec)
ISO (BFM)
(M/L)d=0.59; r0=12.4; ρ0=15; χ²r=1.2
ISO (MDM)
(M/L)d=0.64; r0=16.0; ρ0=10; χ²r=1.4
ISO (fixed M/L)
(M/L)d=0.32; r0=1.7; ρ0=207; χ²r=1.3
NFW (BFM)
(M/L)d=0.39; c=9.9; V200=164; χ²r=0.9
NFW (fixed M/L)
(M/L)d=0.32; c=12.8; V200=149; χ²r=1.0
Vrot (km s⁻¹)
Radius (kpc)
UGC 05175
MB=-20.6; Type=Sb; h=1.9
disc
halo
model
approaching
receding

Figure A.46

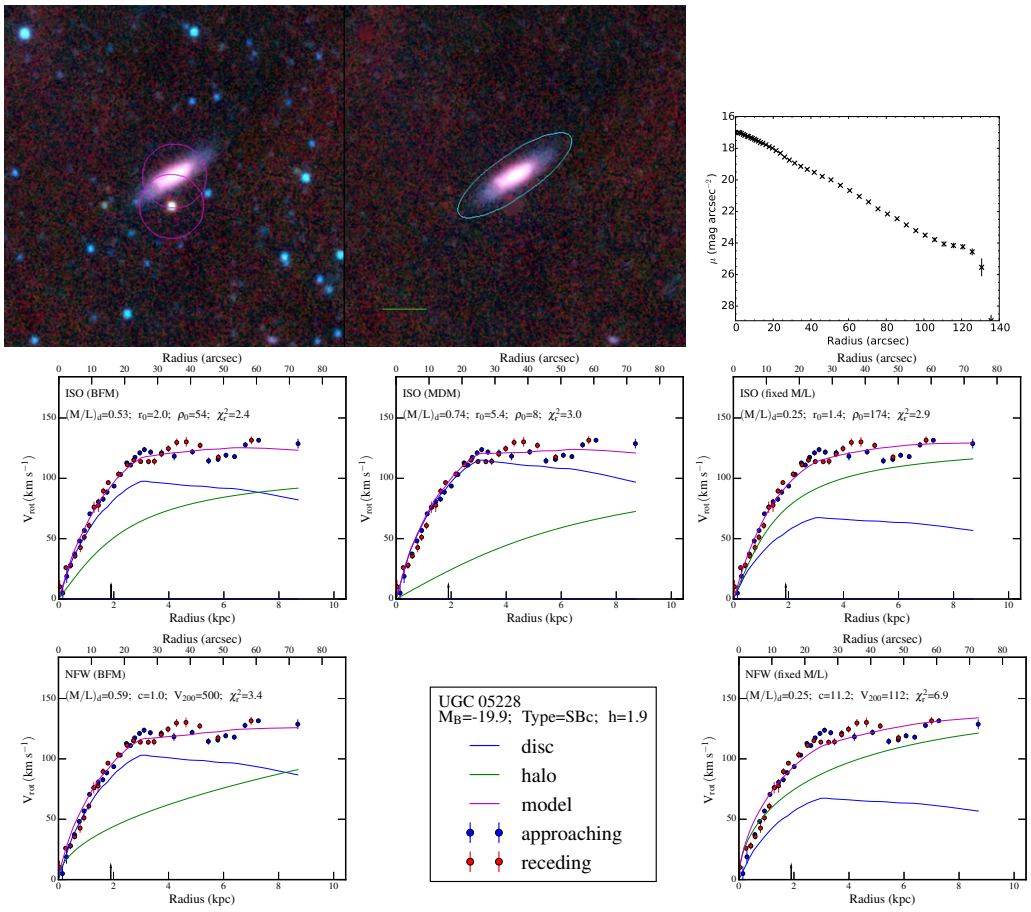
Radius (arcsec)
μ (mag arcsec⁻²)
ISO (BFM)
(M/L)d=0.53; r0=2.0; ρ0=54; χν²=2.4
ISO (MDM)
(M/L)d=0.74; r0=5.4; ρ0=8; χν²=3.0
ISO (fixed M/L)
(M/L)d=0.25; r0=1.4; ρ0=174; χν²=2.9
NFW (BFM)
(M/L)d=0.59; c=1.0; V200=500; χν²=3.4
NFW (fixed M/L)
(M/L)d=0.25; c=11.2; V200=112; χν²=6.9
Vrot (km s⁻¹)
Radius (kpc)
UGC 05228
MB=-19.9; Type=SBc; h=1.9
disc
halo
model
approaching
receding

Figure A.47

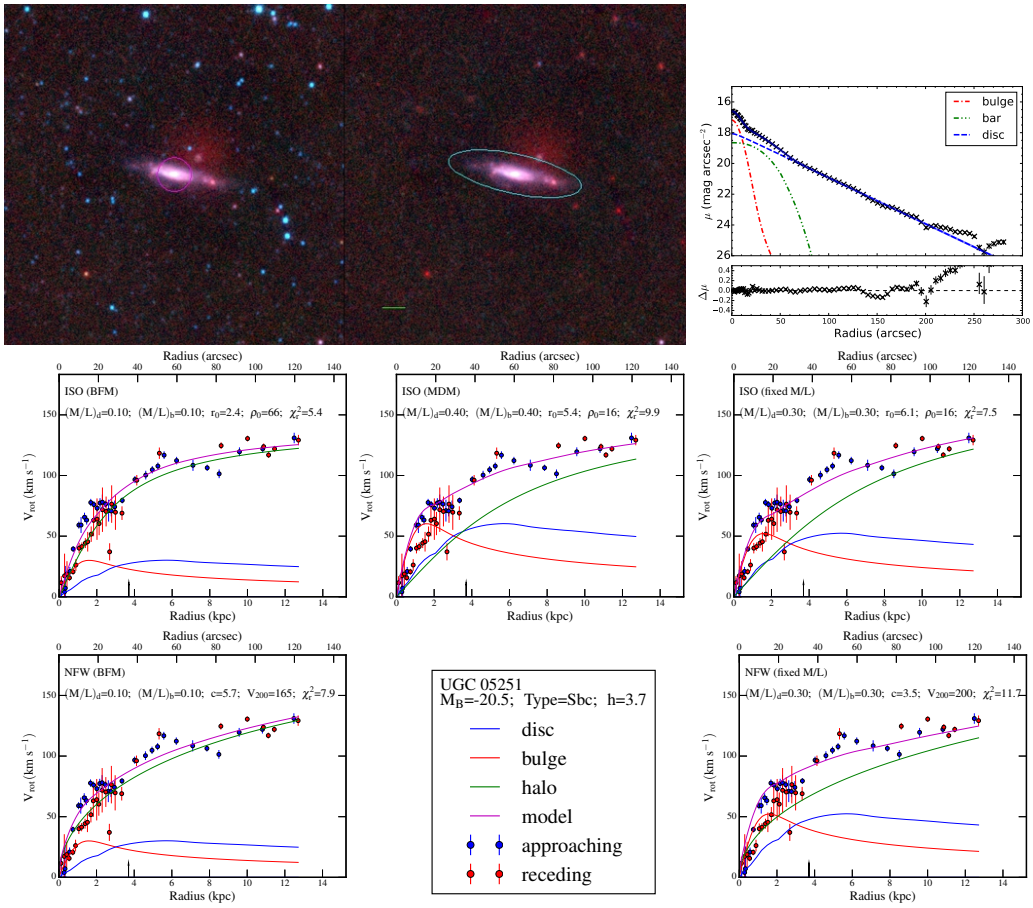
bulge
bar
disc
μ (mag arcsec⁻²)
Δμ
Radius (arcsec)
ISO (BFM)
(M/L)d=0.10; (M/L)b=0.10; r0=2.4; ρ0=66; χ²r=5.4
ISO (MDM)
(M/L)d=0.40; (M/L)b=0.40; r0=5.4; ρ0=16; χ²r=9.9
ISO (fixed M/L)
(M/L)d=0.30; (M/L)b=0.30; r0=6.1; ρ0=16; χ²r=7.5
NFW (BFM)
(M/L)d=0.10; (M/L)b=0.10; c=5.7; V200=165; χ²r=7.9
NFW (fixed M/L)
(M/L)d=0.30; (M/L)b=0.30; c=3.5; V200=200; χ²r=11.7
Vrot (km s⁻¹)
Radius (kpc)
UGC 05251
MB=-20.5; Type=Sbc; h=3.7
disc
bulge
halo
model
approaching
receding

Figure A.48

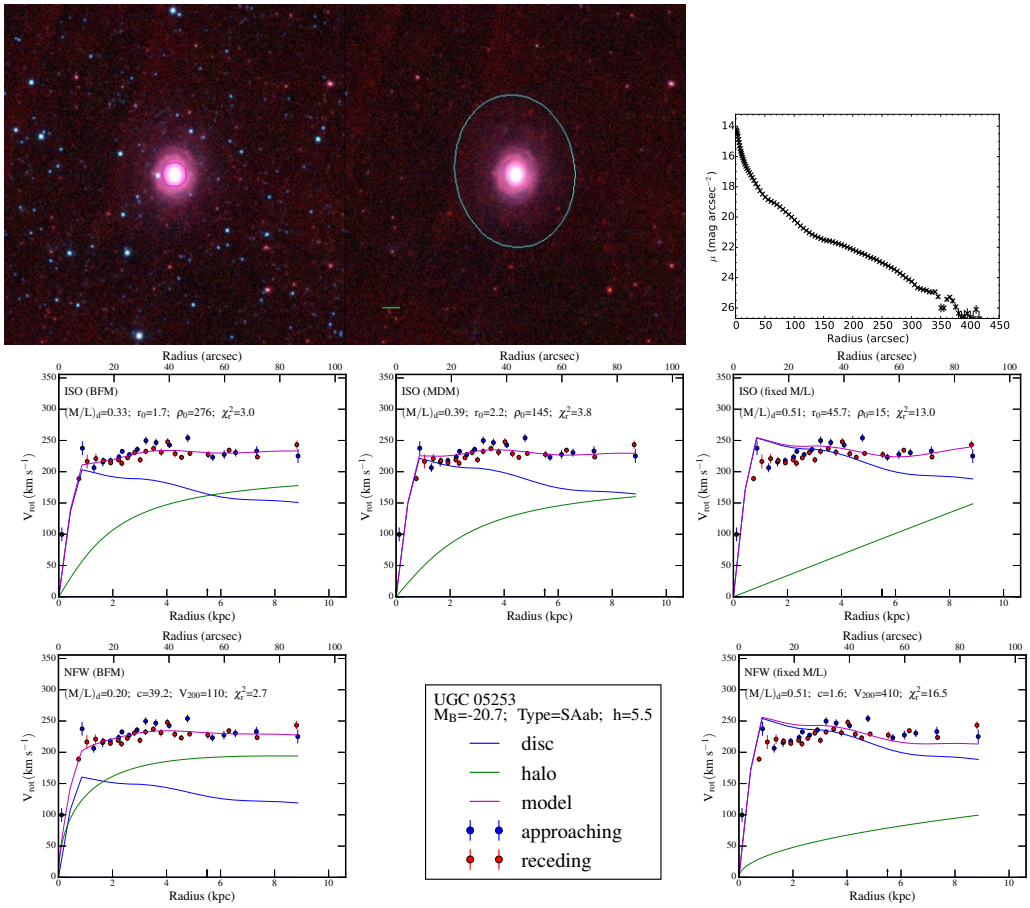
μ (mag arcsec⁻²)
Radius (arcsec)
ISO (BFM)
[M/L]d=0.33; r0=1.7; ρ0=276; χ²r=3.0
ISO (MDM)
[M/L]d=0.39; r0=2.2; ρ0=145; χ²r=3.8
ISO (fixed M/L)
[M/L]d=0.51; r0=45.7; ρ0=15; χ²r=13.0
NFW (BFM)
[M/L]d=0.20; c=39.2; V200=110; χ²r=2.7
NFW (fixed M/L)
[M/L]d=0.51; c=1.6; V200=410; χ²r=16.5
Vrot (km s⁻¹)
Radius (kpc)
UGC 05253
MB=-20.7; Type=SAab; h=5.5
disc
halo
model
approaching
receding

Figure A.49

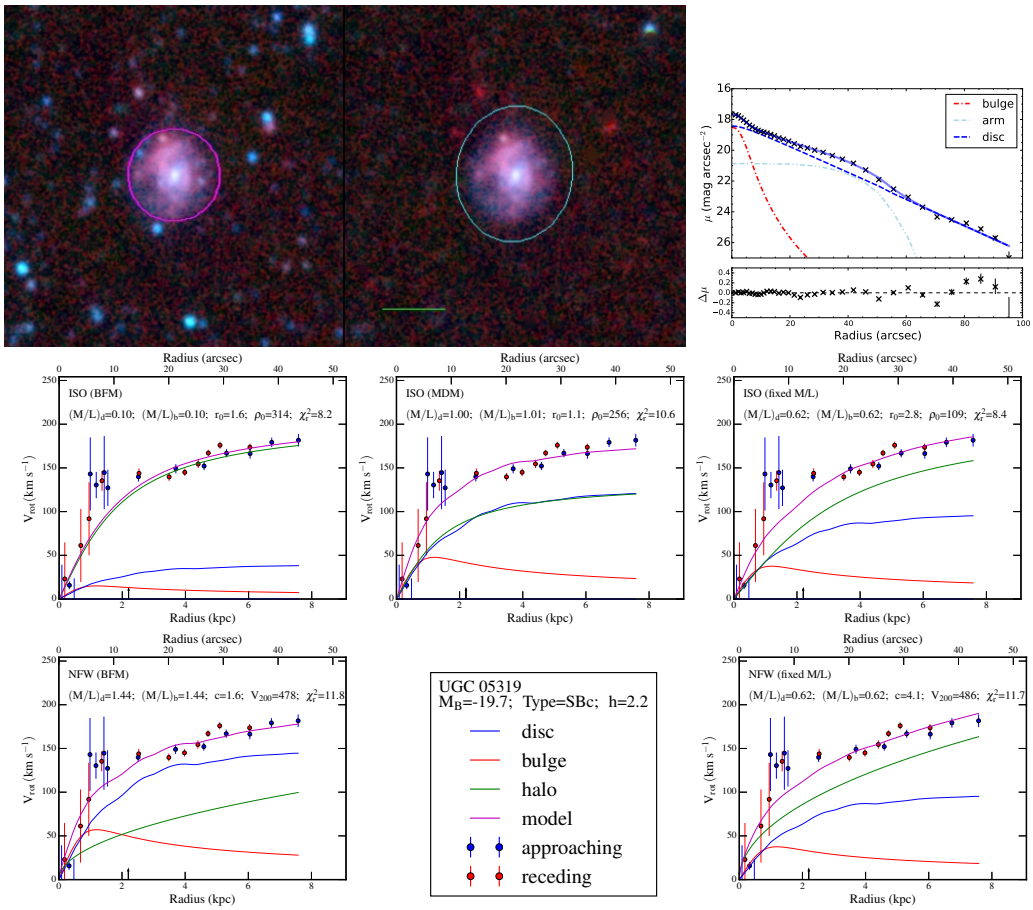
bulge
arm
disc
μ (mag arcsec⁻²)
Δμ
Radius (arcsec)
ISO (BFM)
(M/L)d=0.10; (M/L)h=0.10; r0=1.6; ρ0=314; χ²r=8.2
ISO (MDM)
(M/L)d=1.00; (M/L)h=1.01; r0=1.1; ρ0=256; χ²r=10.6
ISO (fixed M/L)
(M/L)d=0.62; (M/L)h=0.62; r0=2.8; ρ0=109; χ²r=8.4
NFW (BFM)
(M/L)d=1.44; (M/L)h=1.44; c=1.6; V200=478; χ²r=11.8
NFW (fixed M/L)
(M/L)d=0.62; (M/L)h=0.62; c=4.1; V200=486; χ²r=11.7
Vrot (km s⁻¹)
Radius (kpc)
UGC 05319
MB=-19.7; Type=SBc; h=2.2
disc
bulge
halo
model
approaching
receding

Figure A.50

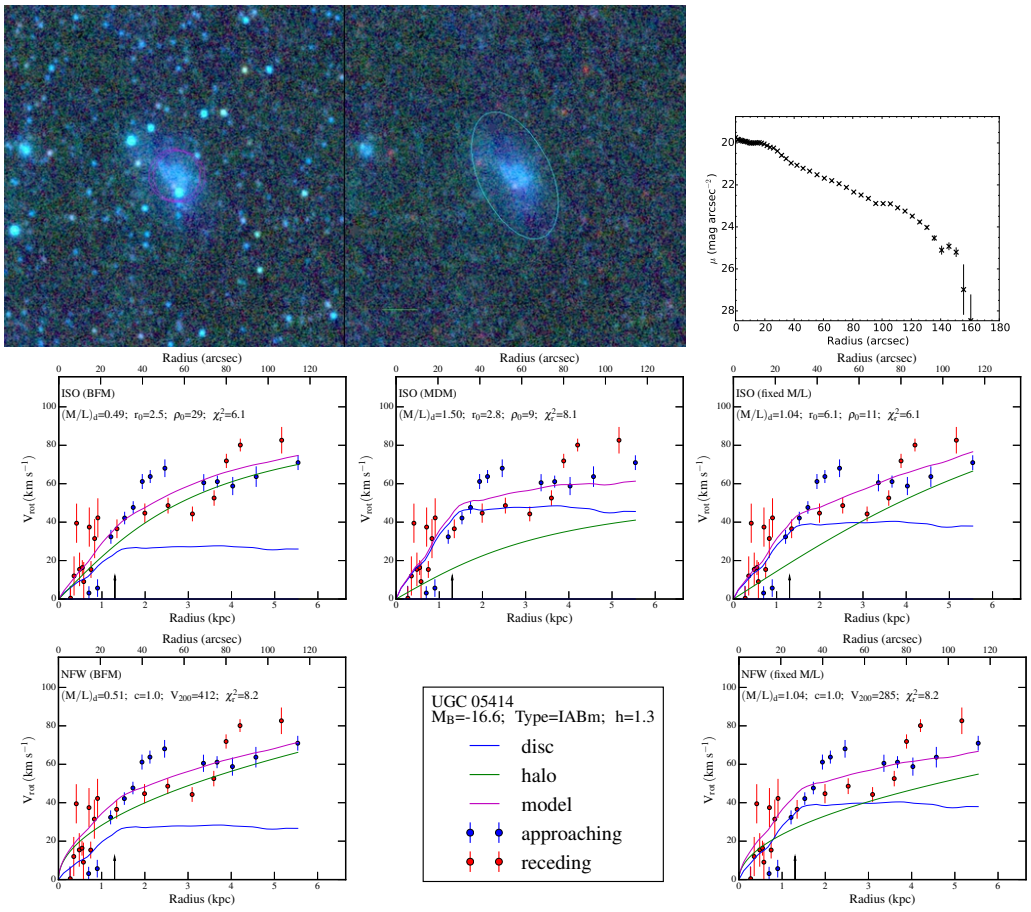
μ (mag arcsec⁻²)
Radius (arcsec)
ISO (BFM)
(M/L)d=0.49; r0=2.5; ρ0=29; χ²r=6.1
ISO (MDM)
(M/L)d=1.50; r0=2.8; ρ0=9; χ²r=8.1
ISO (fixed M/L)
(M/L)d=1.04; r0=6.1; ρ0=11; χ²r=6.1
NFW (BFM)
(M/L)d=0.51; c=1.0; V200=412; χ²r=8.2
NFW (fixed M/L)
(M/L)d=1.04; c=1.0; V200=285; χ²r=8.2
Vrot (km s⁻¹)
Radius (kpc)
UGC 05414
MB=-16.6; Type=IABm; h=1.3
disc
halo
model
approaching
receding

Figure A.51

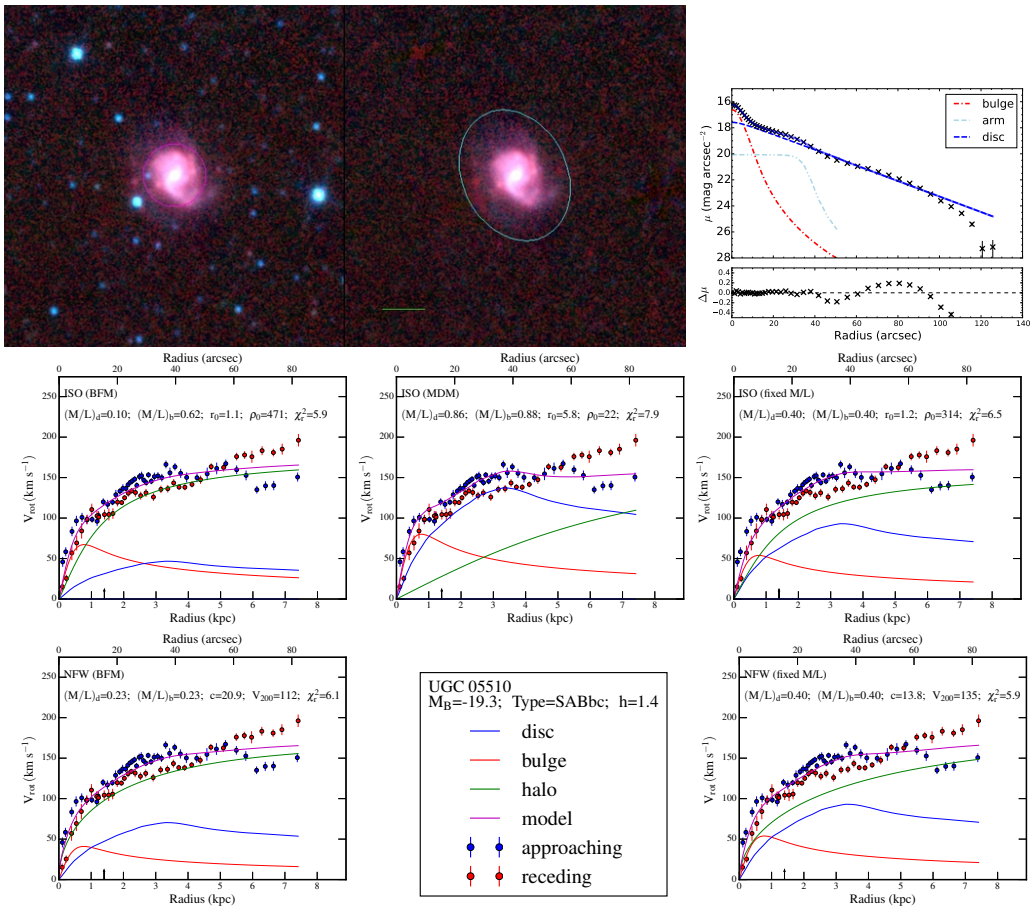
bulge
arm
disc
μ (mag arcsec⁻²)
Δμ
Radius (arcsec)
ISO (BFM)
(M/L)d=0.10; (M/L)b=0.62; r0=1.1; ρ0=471; χr²=5.9
ISO (MDM)
(M/L)d=0.86; (M/L)b=0.88; r0=5.8; ρ0=22; χr²=7.9
ISO (fixed M/L)
(M/L)d=0.40; (M/L)b=0.40; r0=1.2; ρ0=314; χr²=6.5
NFW (BFM)
(M/L)d=0.23; (M/L)b=0.23; c=20.9; V200=112; χr²=6.1
NFW (fixed M/L)
(M/L)d=0.40; (M/L)b=0.40; c=13.8; V200=135; χr²=5.9
Vrot (km s⁻¹)
Radius (kpc)
UGC 05510
MB=-19.3; Type=SABbc; h=1.4
disc
bulge
halo
model
approaching
receding

Figure A.52

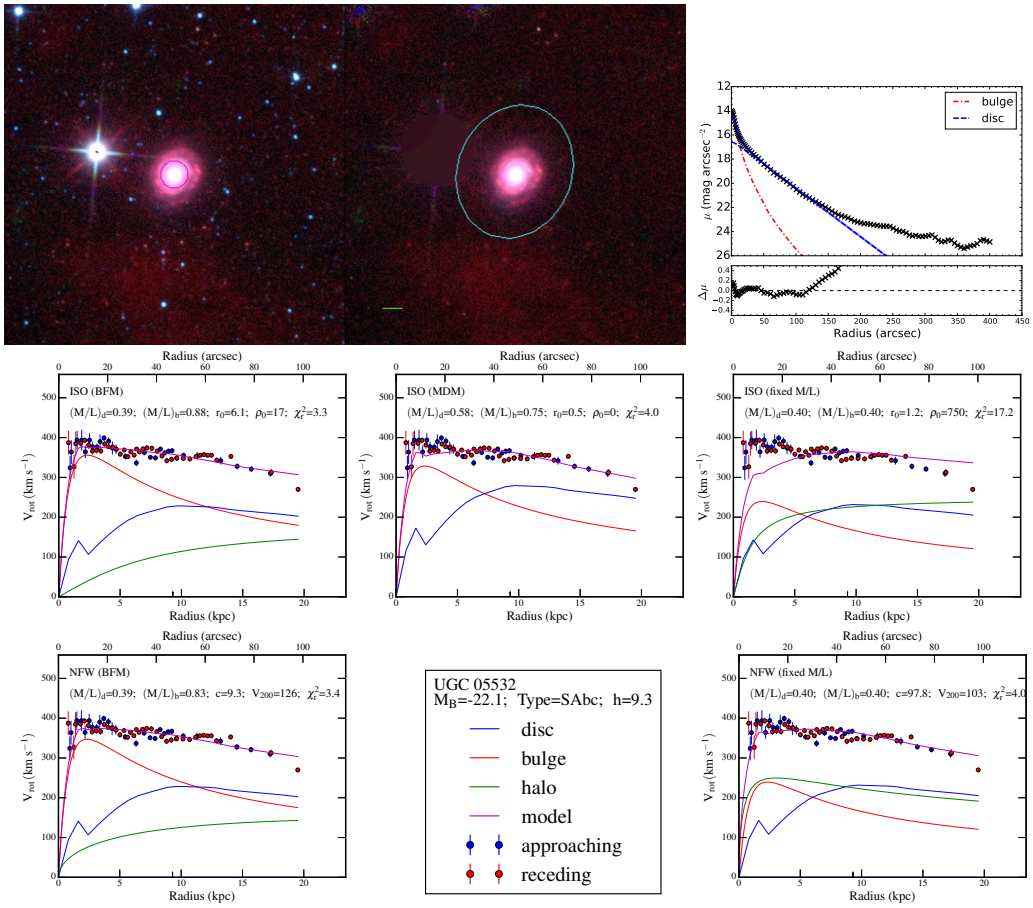
bulge
disc
μ (mag arcsec⁻²)
Δμ
Radius (arcsec)
ISO (BFM)
(M/L)d=0.39; (M/L)b=0.88; r0=6.1; ρ0=17; χ²r=3.3
ISO (MDM)
(M/L)d=0.58; (M/L)b=0.75; r0=0.5; ρ0=0; χ²r=4.0
ISO (fixed M/L)
(M/L)d=0.40; (M/L)b=0.40; r0=1.2; ρ0=750; χ²r=17.2
NFW (BFM)
(M/L)d=0.39; (M/L)b=0.83; c=9.3; V200=126; χ²r=3.4
NFW (fixed M/L)
(M/L)d=0.40; (M/L)b=0.40; c=97.8; V200=103; χ²r=4.0
Vrot (km s⁻¹)
Radius (kpc)
UGC 05532
MB=-22.1; Type=SAbc; h=9.3
disc
bulge
halo
model
approaching
receding

Figure A.53

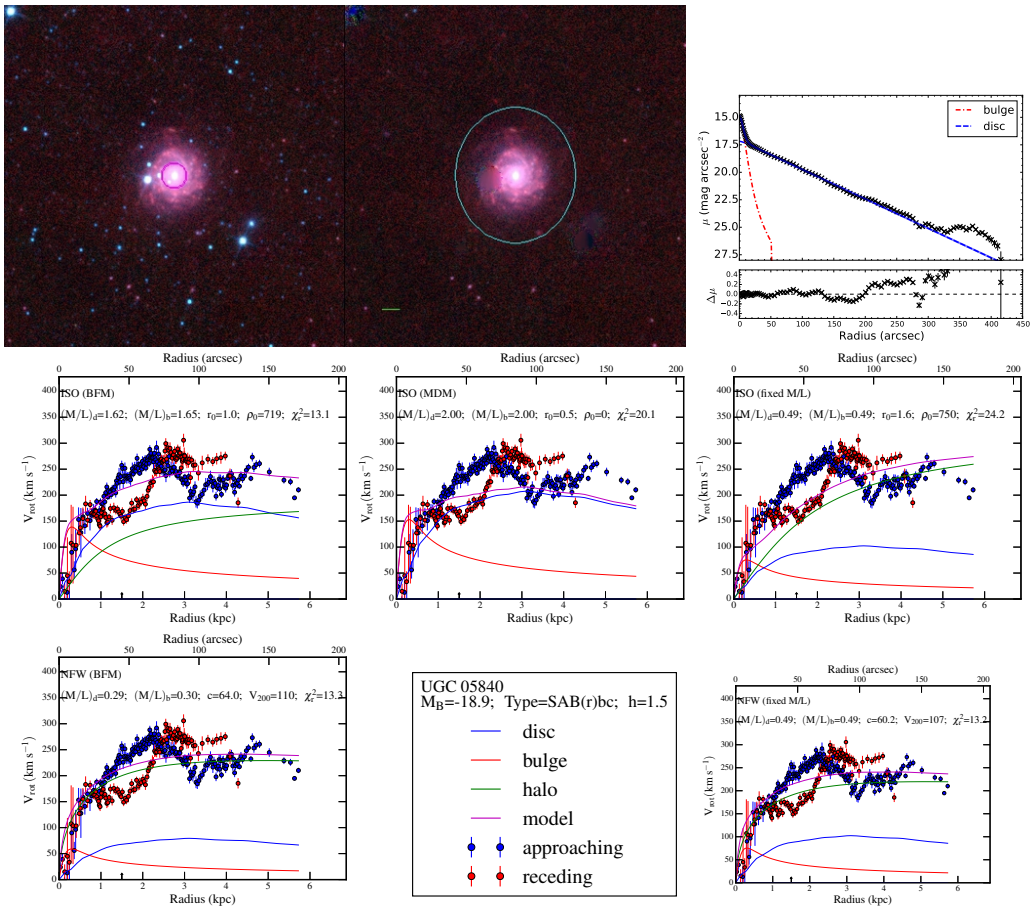
bulge
disc
μ (mag arcsec⁻²)
Δμ
Radius (arcsec)
ISO (BFM)
(M/L)d=1.62; (M/L)h=1.65; r0=1.0; ρ0=719; χ²r=13.1
ISO (MDM)
(M/L)d=2.00; (M/L)h=2.00; r0=0.5; ρ0=0; χ²r=20.1
ISO (fixed M/L)
(M/L)d=0.49; (M/L)h=0.49; r0=1.6; ρ0=750; χ²r=24.2
NFW (BFM)
(M/L)d=0.29; (M/L)h=0.30; c=64.0; V200=110; χ²r=13.3
NFW (fixed M/L)
(M/L)d=0.49; (M/L)h=0.49; c=60.2; V200=107; χ²r=13.2
Vrot (km s⁻¹)
Radius (kpc)
UGC 05840
MB=-18.9; Type=SAB(r)bc; h=1.5
disc
bulge
halo
model
approaching
receding

Figure A.54

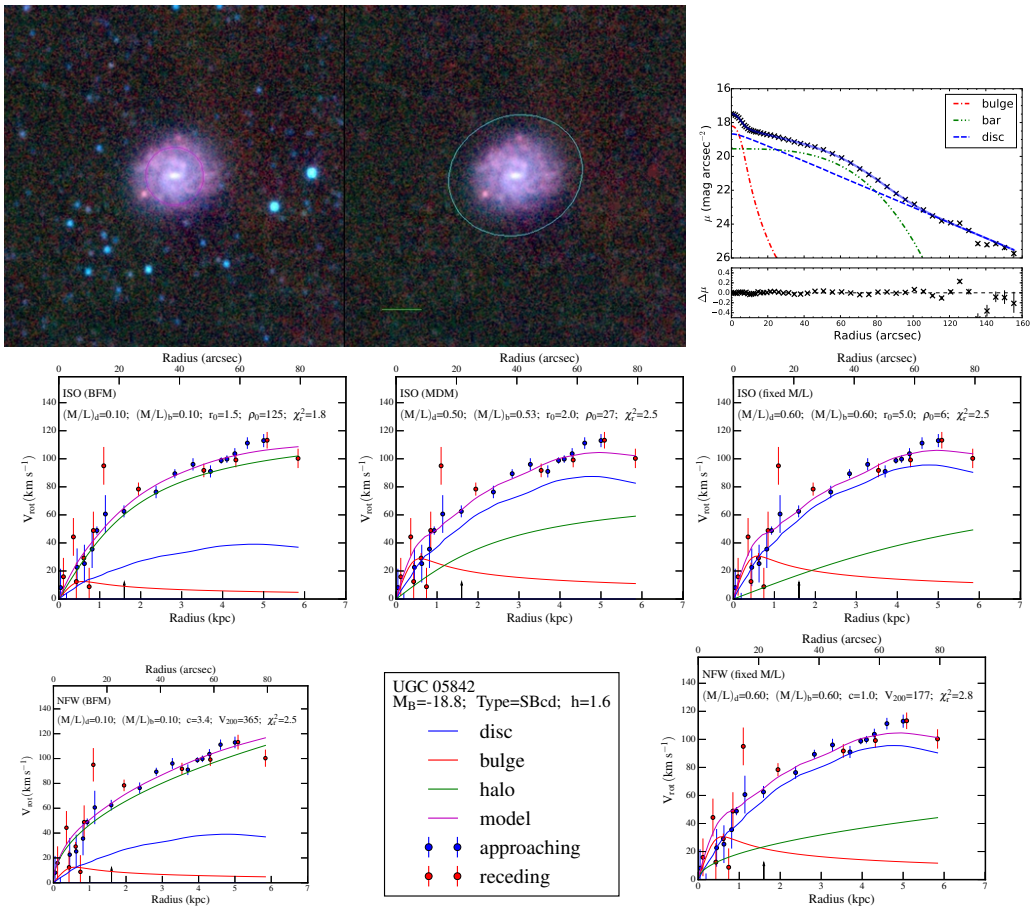
bulge
bar
disc
μ (mag arcsec⁻²)
Δμ
Radius (arcsec)
ISO (BFM)
(M/L)d=0.10; (M/L)b=0.10; r0=1.5; ρ0=125; χ²r=1.8
ISO (MDM)
(M/L)d=0.50; (M/L)b=0.53; r0=2.0; ρ0=27; χ²r=2.5
ISO (fixed M/L)
(M/L)d=0.60; (M/L)b=0.60; r0=5.0; ρ0=6; χ²r=2.5
NFW (BFM)
(M/L)d=0.10; (M/L)b=0.10; c=3.4; V200=365; χ²r=2.5
NFW (fixed M/L)
(M/L)d=0.60; (M/L)b=0.60; c=1.0; V200=177; χ²r=2.8
Vrot (km s⁻¹)
Radius (kpc)
UGC 05842
MB=-18.8; Type=SBcd; h=1.6
disc
bulge
halo
model
approaching
receding

Figure A.55

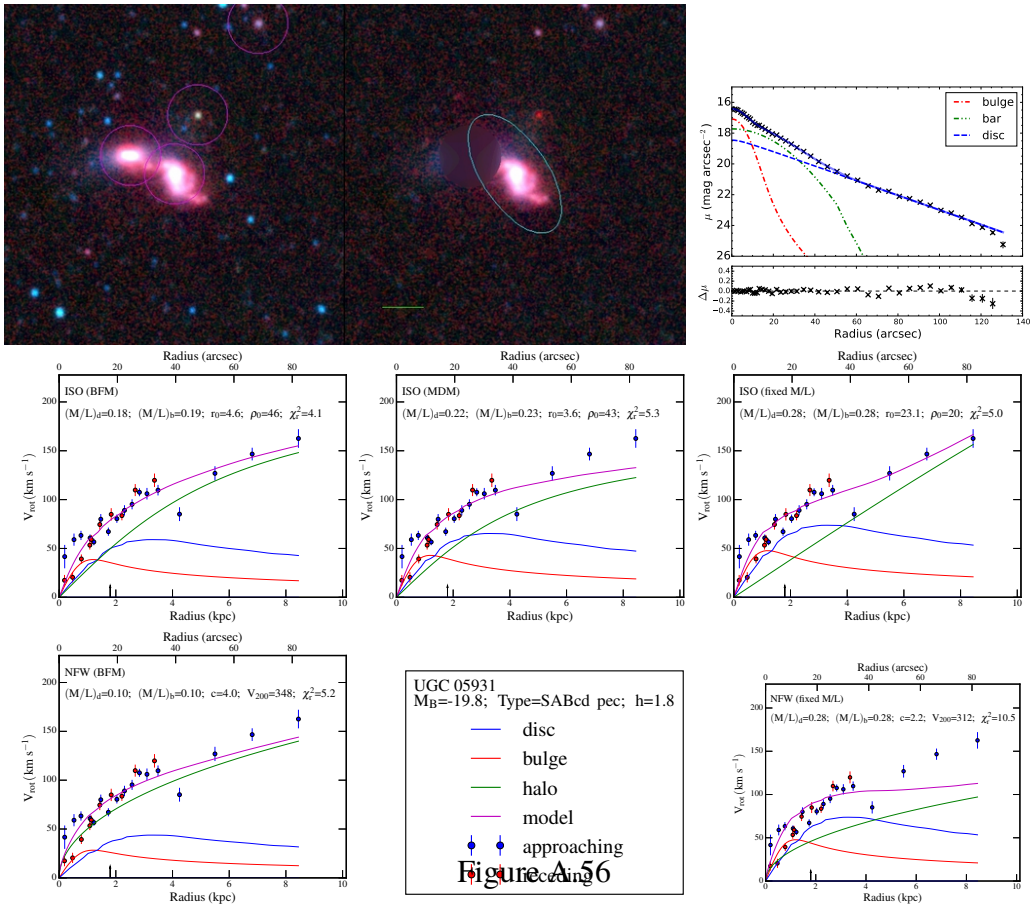
bulge
bar
disc
μ (mag arcsec⁻²)
Δμ
Radius (arcsec)
ISO (BFM)
(M/L)d=0.18; (M/L)b=0.19; r0=4.6; ρ0=46; χ²r=4.1
ISO (MDM)
(M/L)d=0.22; (M/L)b=0.23; r0=3.6; ρ0=43; χ²r=5.3
ISO (fixed M/L)
(M/L)d=0.28; (M/L)b=0.28; r0=23.1; ρ0=20; χ²r=5.0
NFW (BFM)
(M/L)d=0.10; (M/L)b=0.10; c=4.0; V200=348; χ²r=5.2
NFW (fixed M/L)
(M/L)d=0.28; (M/L)h=0.28; c=2.2; V200=312; χ²r=10.5
Vrot (km s⁻¹)
Radius (kpc)
UGC 05931
MB=-19.8; Type=SABcd pec; h=1.8
disc
bulge
halo
model
approaching
receding

Figure A.56

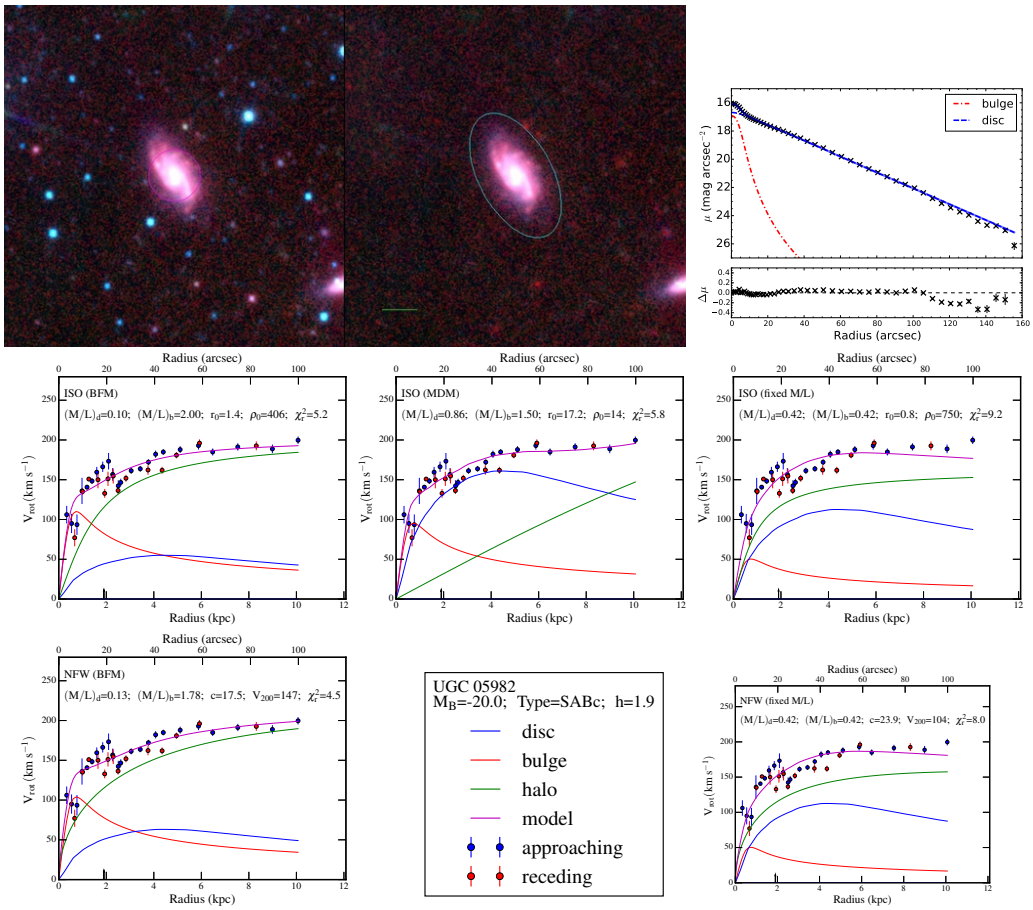
bulge
disc
μ (mag arcsec⁻²)
Δμ
Radius (arcsec)
ISO (BFM)
(M/L)d=0.10; (M/L)h=2.00; r0=1.4; ρ0=406; χ²r=5.2
ISO (MDM)
(M/L)d=0.86; (M/L)h=1.50; r0=17.2; ρ0=14; χ²r=5.8
ISO (fixed M/L)
(M/L)d=0.42; (M/L)h=0.42; r0=0.8; ρ0=750; χ²r=9.2
NFW (BFM)
(M/L)d=0.13; (M/L)h=1.78; c=17.5; V200=147; χ²r=4.5
NFW (fixed M/L)
(M/L)d=0.42; (M/L)h=0.42; c=23.9; V200=104; χ²r=8.0
Vrot (km s⁻¹)
Radius (kpc)
UGC 05982
MB=-20.0; Type=SABc; h=1.9
disc
bulge
halo
model
approaching
receding

Figure A.57

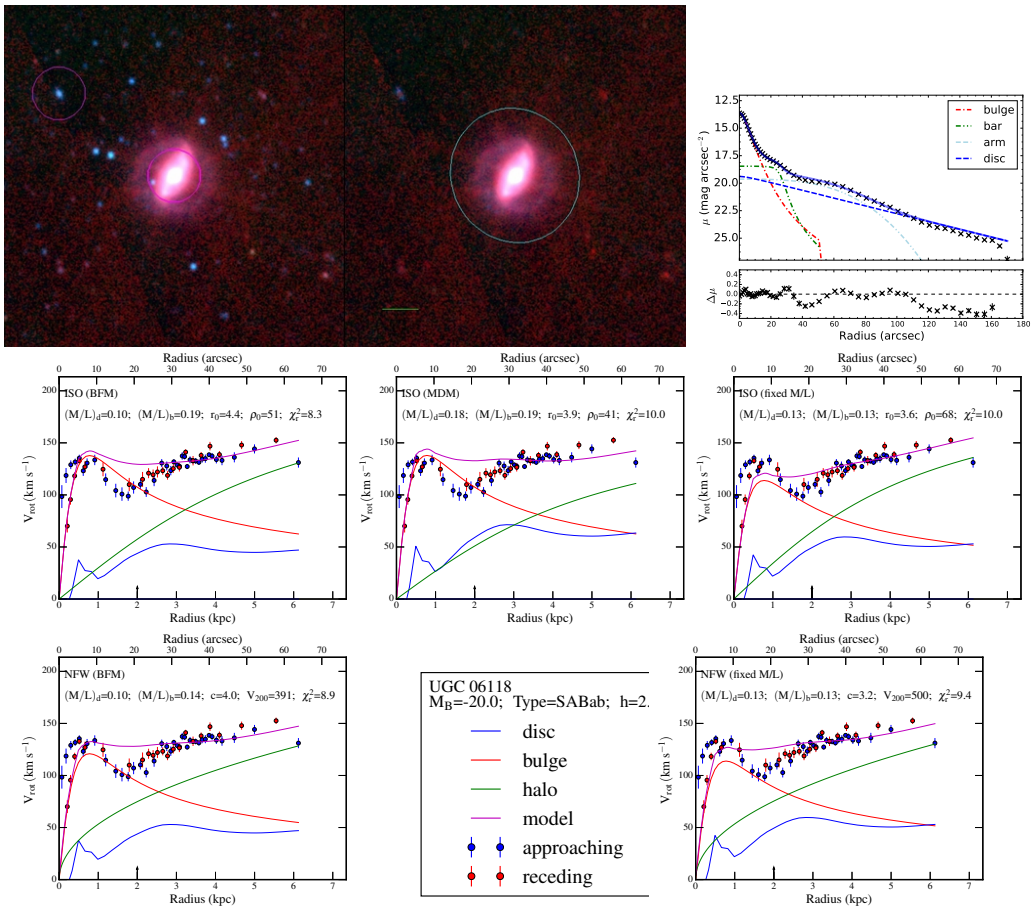
bulge
bar
arm
disc
μ (mag arcsec⁻²)
Δμ
Radius (arcsec)
ISO (BFM)
(M/L)d=0.10; (M/L)b=0.19; r0=4.4; ρ0=51; χ²r=8.3
ISO (MDM)
(M/L)d=0.18; (M/L)b=0.19; r0=3.9; ρ0=41; χ²r=10.0
ISO (fixed M/L)
(M/L)d=0.13; (M/L)b=0.13; r0=3.6; ρ0=68; χ²r=10.0
NFW (BFM)
(M/L)d=0.10; (M/L)b=0.14; c=4.0; V200=391; χ²r=8.9
NFW (fixed M/L)
(M/L)d=0.13; (M/L)b=0.13; c=3.2; V200=500; χ²r=9.4
Vrot (km s⁻¹)
Radius (kpc)
UGC 06118
MB=-20.0; Type=SABab; h=2.
disc
bulge
halo
model
approaching
receding

Figure A.58

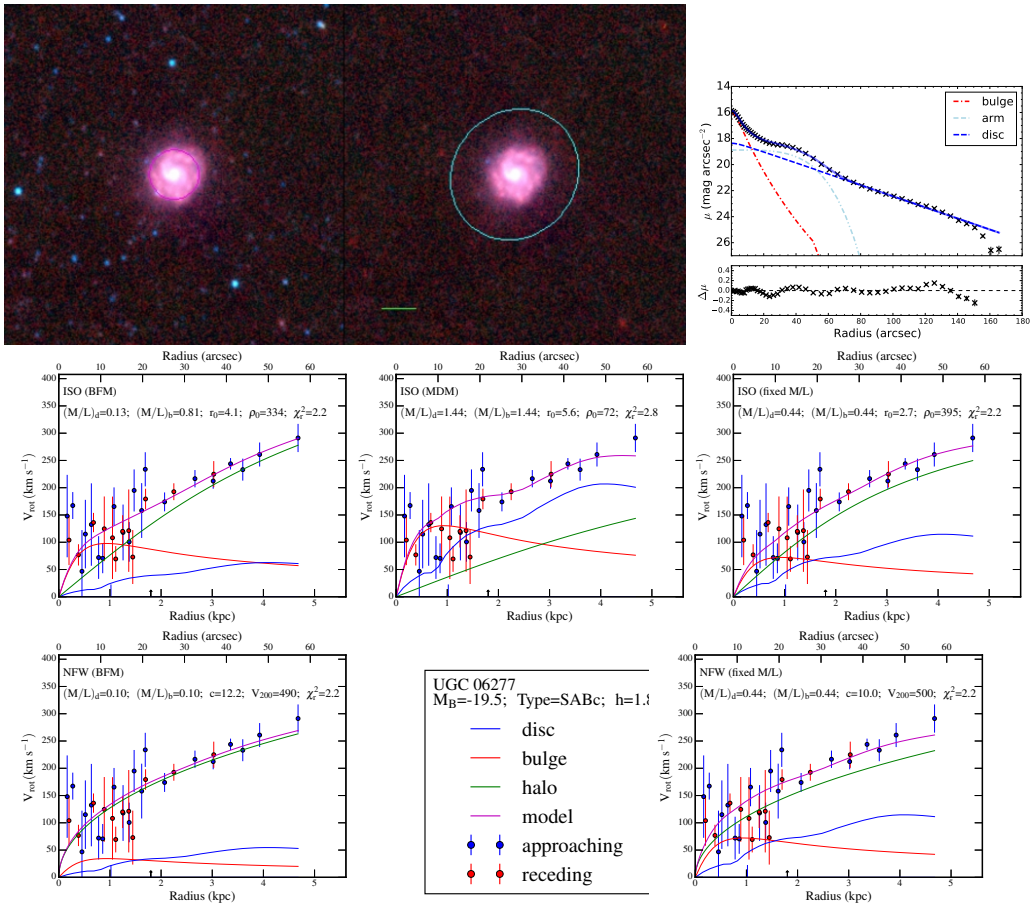
bulge
arm
disc
μ (mag arcsec⁻²)
Δμ
Radius (arcsec)
ISO (BFM)
(M/L)d=0.13; (M/L)b=0.81; r0=4.1; ρ0=334; χ²r=2.2
ISO (MDM)
(M/L)d=1.44; (M/L)b=1.44; r0=5.6; ρ0=72; χ²r=2.8
ISO (fixed M/L)
(M/L)d=0.44; (M/L)b=0.44; r0=2.7; ρ0=395; χ²r=2.2
NFW (BFM)
(M/L)d=0.10; (M/L)b=0.10; c=12.2; V200=490; χ²r=2.2
NFW (fixed M/L)
(M/L)d=0.44; (M/L)b=0.44; c=10.0; V200=500; χ²r=2.2
Vrot (km s⁻¹)
Radius (kpc)
UGC 06277
MB=-19.5; Type=SABc; h=1.
disc
bulge
halo
model
approaching
receding

Figure A.59

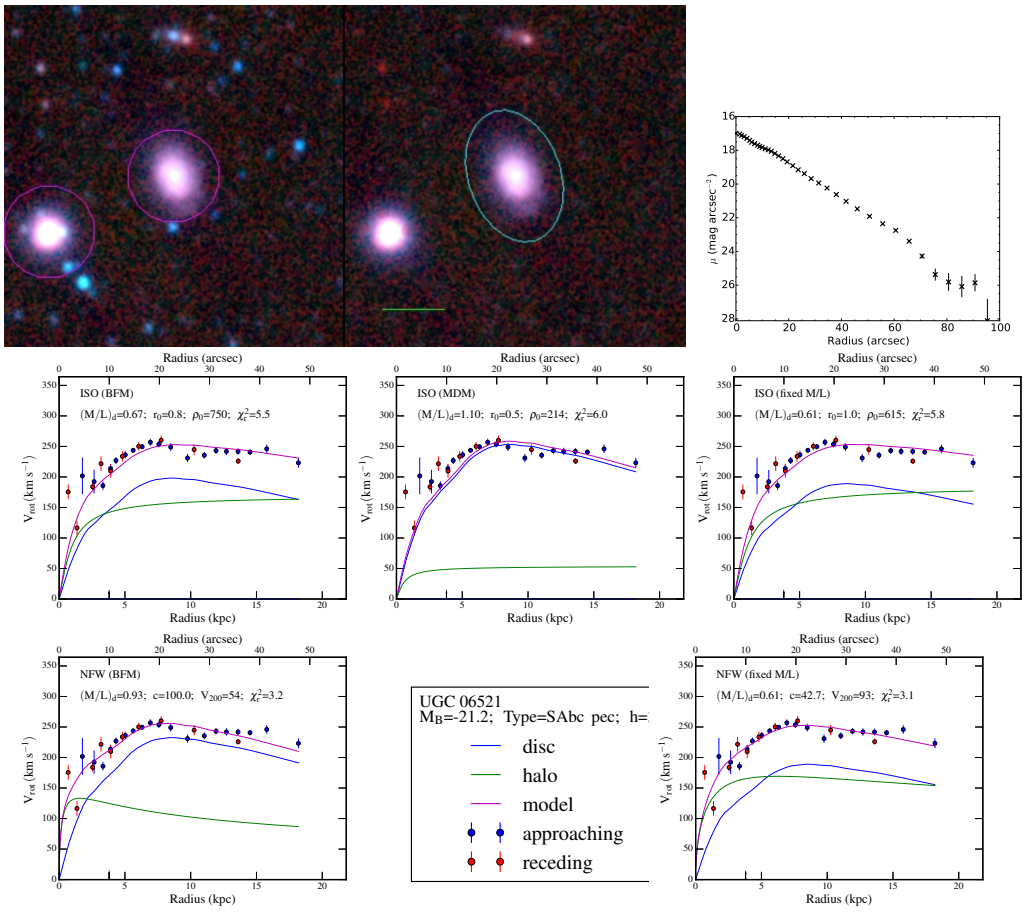
μ (mag arcsec⁻²)
Radius (arcsec)
ISO (BFM)
(M/L)d=0.67; r0=0.8; ρ0=750; χ²r=5.5
ISO (MDM)
(M/L)d=1.10; r0=0.5; ρ0=214; χ²r=6.0
ISO (fixed M/L)
(M/L)d=0.61; r0=1.0; ρ0=615; χ²r=5.8
NFW (BFM)
(M/L)d=0.93; c=100.0; V200=54; χ²r=3.2
NFW (fixed M/L)
(M/L)d=0.61; c=42.7; V200=93; χ²r=3.1
Vrot (km s⁻¹)
Radius (kpc)
UGC 06521
MB=-21.2; Type=SAbc pec; h=
disc
halo
model
approaching
receding

Figure A.60

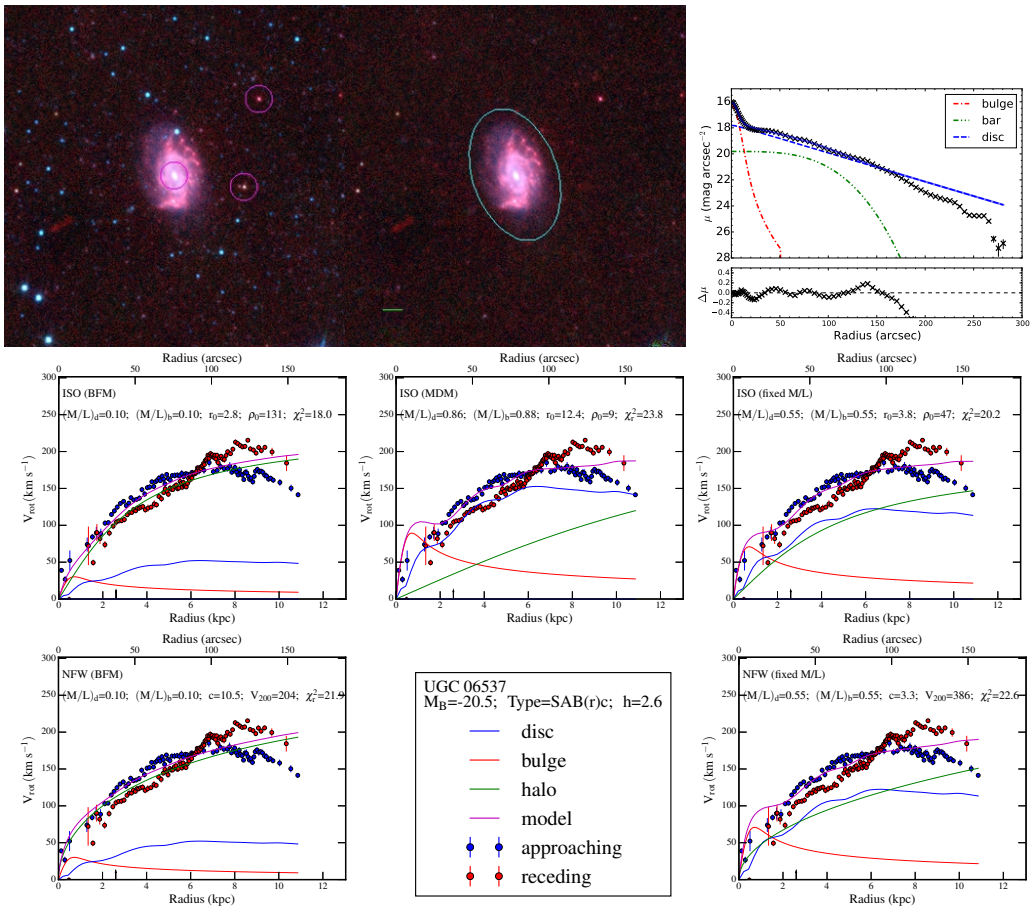
bulge
bar
disc
μ (mag arcsec⁻²)
Δμ
Radius (arcsec)
ISO (BFM)
(M/L)d=0.10; (M/L)b=0.10; r0=2.8; ρ0=131; χ²r=18.0
ISO (MDM)
(M/L)d=0.86; (M/L)b=0.88; r0=12.4; ρ0=9; χ²r=23.8
ISO (fixed M/L)
(M/L)d=0.55; (M/L)b=0.55; r0=3.8; ρ0=47; χ²r=20.2
NFW (BFM)
(M/L)d=0.10; (M/L)b=0.10; c=10.5; V200=204; χ²r=21.9
NFW (fixed M/L)
(M/L)d=0.55; (M/L)b=0.55; c=3.3; V200=386; χ²r=22.6
Vrot (km s⁻¹)
Radius (kpc)
UGC 06537
MB=-20.5; Type=SAB(r)c; h=2.6
disc
bulge
halo
model
approaching
receding

Figure A.61

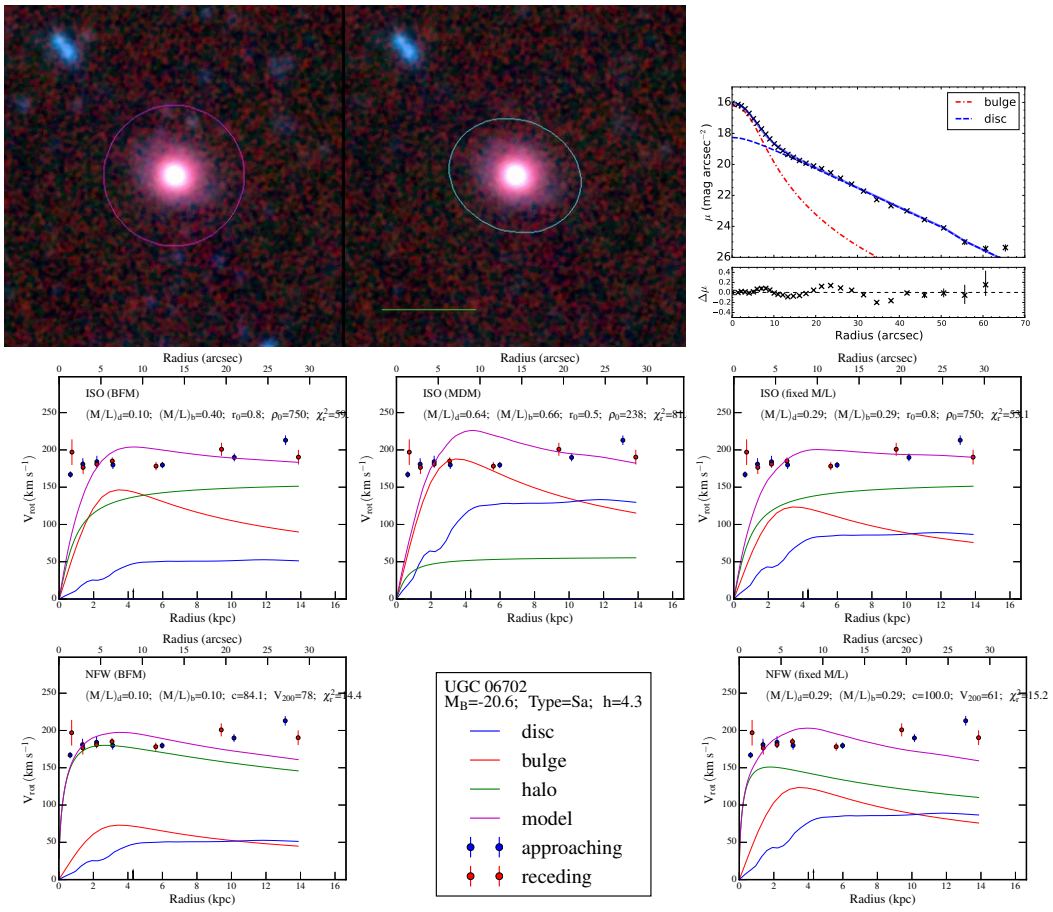
bulge
disc
μ (mag arcsec⁻²)
Δμ
Radius (arcsec)
ISO (BFM)
(M/L)d=0.10; (M/L)b=0.40; r0=0.8; ρ0=750; χ²r=59
ISO (MDM)
(M/L)d=0.64; (M/L)b=0.66; r0=0.5; ρ0=238; χ²r=81
ISO (fixed M/L)
(M/L)d=0.29; (M/L)b=0.29; r0=0.8; ρ0=750; χ²r=55.1
NFW (BFM)
(M/L)d=0.10; (M/L)b=0.10; c=84.1; V200=78; χ²r=14.4
NFW (fixed M/L)
(M/L)d=0.29; (M/L)b=0.29; c=100.0; V200=61; χ²r=15.2
Vrot (km s⁻¹)
Radius (kpc)
UGC 06702
MB=-20.6; Type=Sa; h=4.3
disc
bulge
halo
model
approaching
receding

Figure A.62

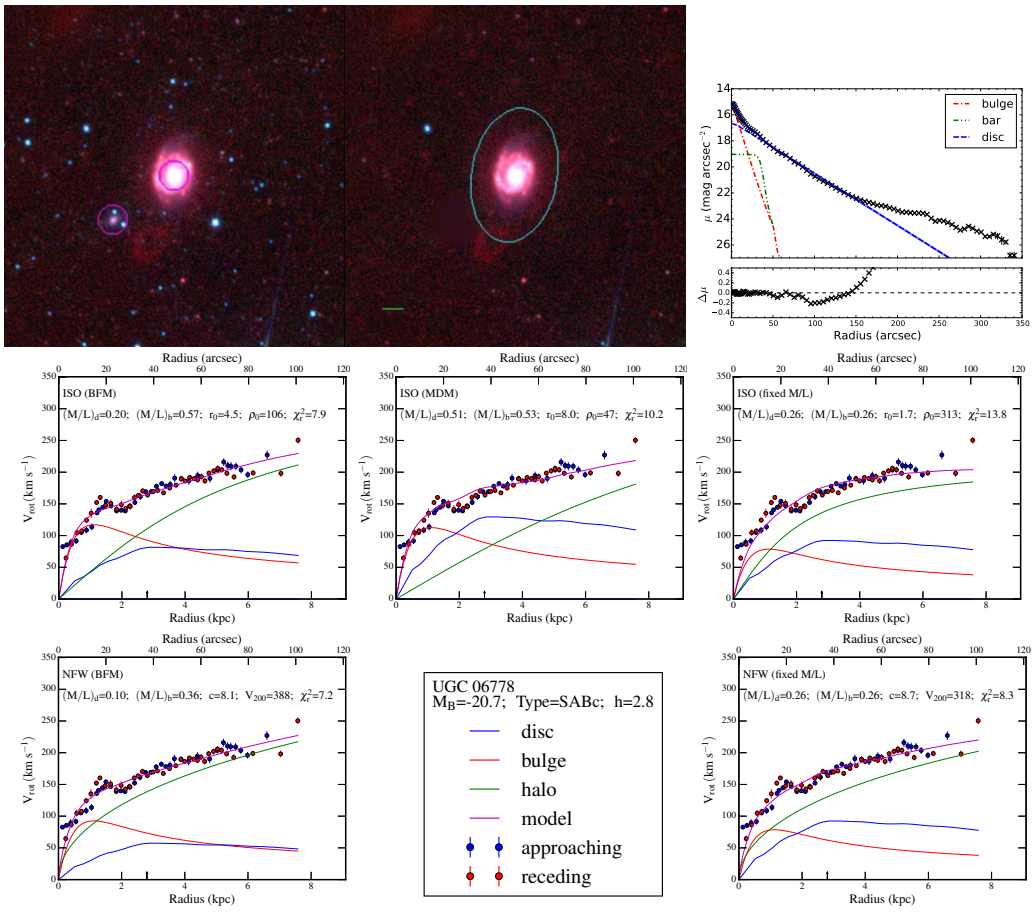
bulge
bar
disc
μ (mag arcsec⁻²)
Δμ
Radius (arcsec)
ISO (BFM)
(M/L)d=0.20; (M/L)b=0.57; r0=4.5; ρ0=106; χ²r=7.9
ISO (MDM)
(M/L)d=0.51; (M/L)b=0.53; r0=8.0; ρ0=47; χ²r=10.2
ISO (fixed M/L)
(M/L)d=0.26; (M/L)b=0.26; r0=1.7; ρ0=313; χ²r=13.8
NFW (BFM)
(M/L)d=0.10; (M/L)b=0.36; c=8.1; V200=388; χ²r=7.2
NFW (fixed M/L)
(M/L)d=0.26; (M/L)b=0.26; c=8.7; V200=318; χ²r=8.3
Vrot (km s⁻¹)
Radius (kpc)
UGC 06778
MB=-20.7; Type=SABc; h=2.8
disc
bulge
halo
model
approaching
receding

Figure A.63

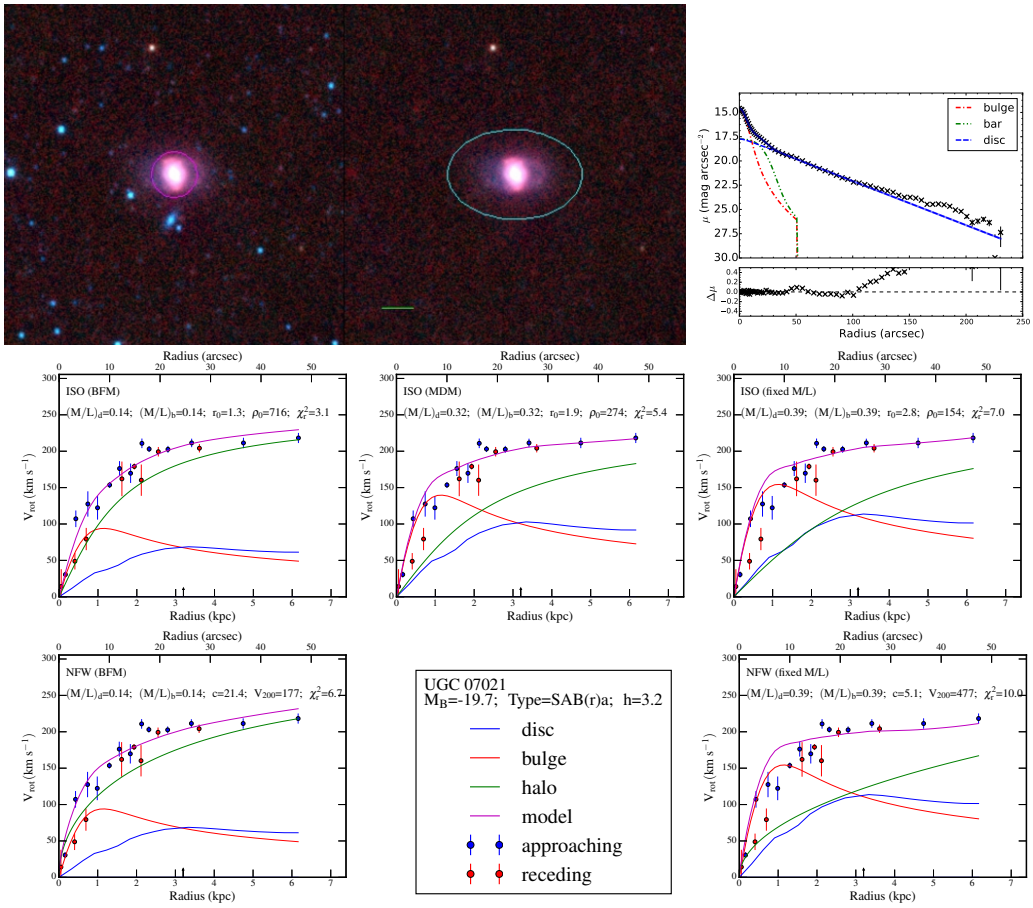
bulge
bar
disc
Radius (arcsec)
ISO (BFM)
(M/L)d=0.14; (M/L)b=0.14; r0=1.3; ρ0=716; χ2r=3.1
ISO (MDM)
(M/L)d=0.32; (M/L)b=0.32; r0=1.9; ρ0=274; χ2r=5.4
ISO (fixed M/L)
(M/L)d=0.39; (M/L)b=0.39; r0=2.8; ρ0=154; χ2r=7.0
NFW (BFM)
(M/L)d=0.14; (M/L)b=0.14; c=21.4; V200=177; χ2r=6.7
NFW (fixed M/L)
(M/L)d=0.39; (M/L)b=0.39; c=5.1; V200=477; χ2r=10.0
Vrot (km s−1)
Radius (kpc)
UGC 07021
MB=-19.7; Type=SAB(r)a; h=3.2
disc
bulge
halo
model
approaching
receding

Figure A.64

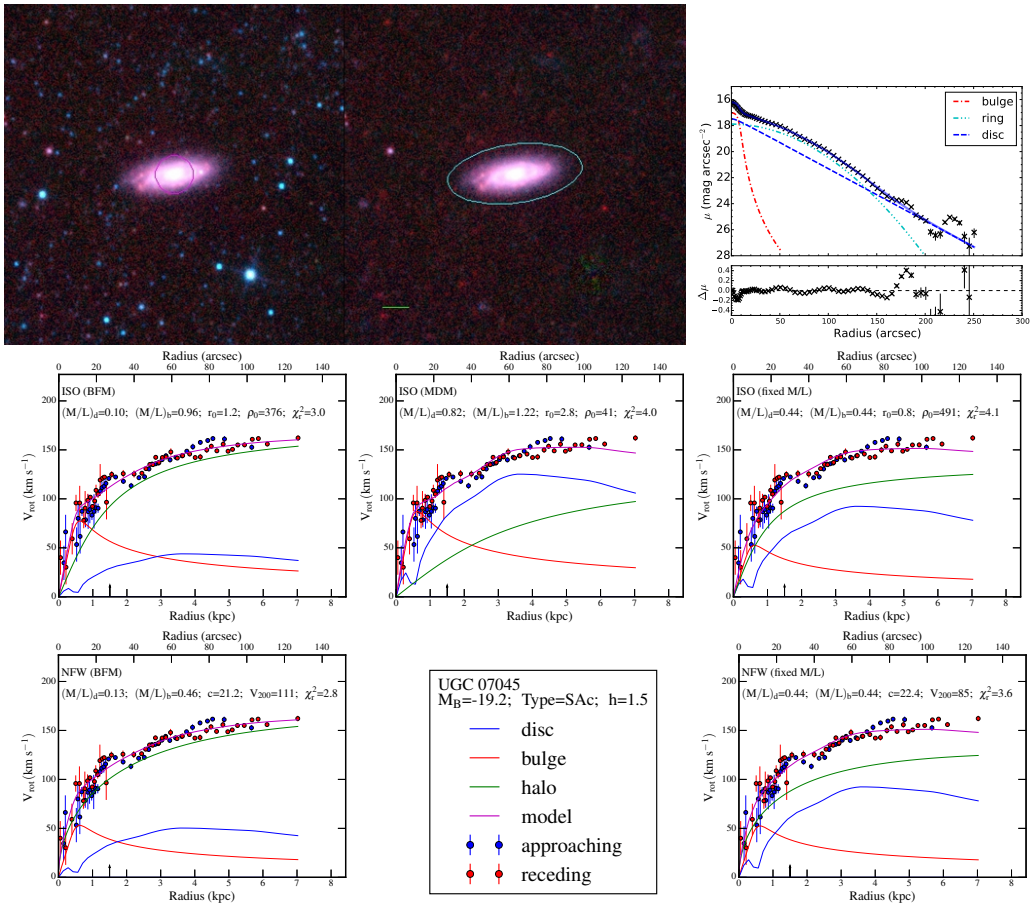
bulge
ring
disc
μ (mag arcsec⁻²)
Δμ
Radius (arcsec)
ISO (BFM)
(M/L)d=0.10; (M/L)b=0.96; r0=1.2; ρ0=376; χr²=3.0
ISO (MDM)
(M/L)d=0.82; (M/L)b=1.22; r0=2.8; ρ0=41; χr²=4.0
ISO (fixed M/L)
(M/L)d=0.44; (M/L)b=0.44; r0=0.8; ρ0=491; χr²=4.1
NFW (BFM)
(M/L)d=0.13; (M/L)b=0.46; c=21.2; V200=111; χr²=2.8
NFW (fixed M/L)
(M/L)d=0.44; (M/L)b=0.44; c=22.4; V200=85; χr²=3.6
Vrot (km s⁻¹)
Radius (kpc)
UGC 07045
MB=-19.2; Type=SAc; h=1.5
disc
bulge
halo
model
approaching
receding

Figure A.65

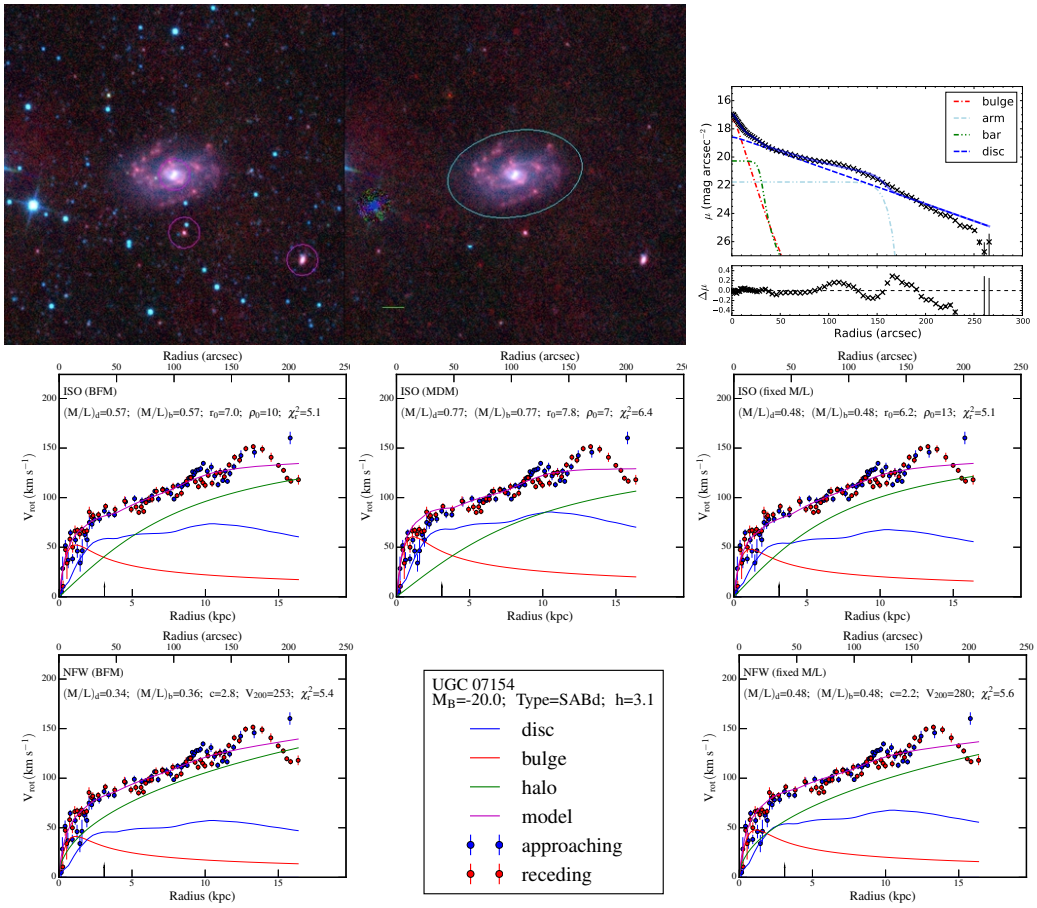
bulge
arm
bar
disc
μ (mag arcsec⁻²)
Δμ
Radius (arcsec)
ISO (BFM)
(M/L)d=0.57; (M/L)b=0.57; r0=7.0; ρ0=10; χ²r=5.1
ISO (MDM)
(M/L)d=0.77; (M/L)b=0.77; r0=7.8; ρ0=7; χ²r=6.4
ISO (fixed M/L)
(M/L)d=0.48; (M/L)b=0.48; r0=6.2; ρ0=13; χ²r=5.1
NFW (BFM)
(M/L)d=0.34; (M/L)b=0.36; c=2.8; V200=253; χ²r=5.4
NFW (fixed M/L)
(M/L)d=0.48; (M/L)b=0.48; c=2.2; V200=280; χ²r=5.6
Vrot (km s⁻¹)
Radius (kpc)
UGC 07154
MB=-20.0; Type=SABd; h=3.1
disc
bulge
halo
model
approaching
receding

Figure A.66

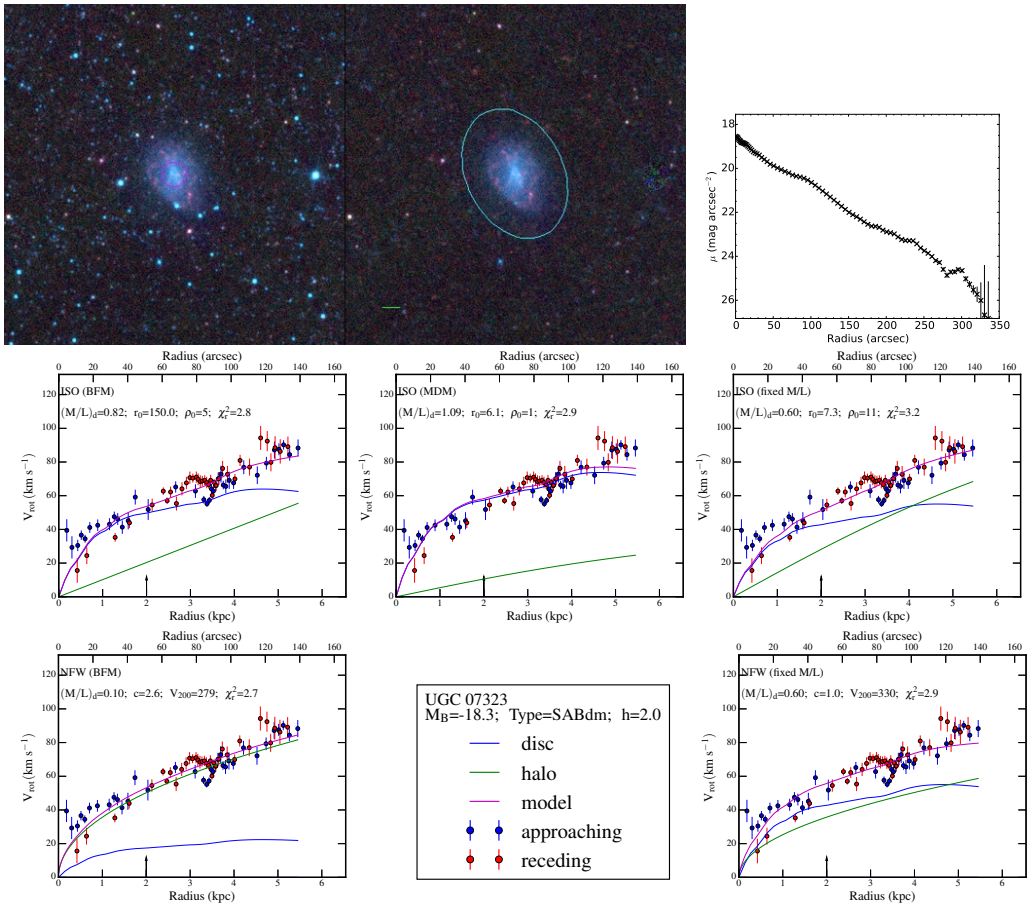
μ (mag arcsec⁻²)
Radius (arcsec)
ISO (BFM)
(M/L)d=0.82; r0=150.0; ρ0=5; χ²r=2.8
ISO (MDM)
(M/L)d=1.09; r0=6.1; ρ0=1; χ²r=2.9
ISO (fixed M/L)
(M/L)d=0.60; r0=7.3; ρ0=11; χ²r=3.2
NFW (BFM)
(M/L)d=0.10; c=2.6; V200=279; χ²r=2.7
NFW (fixed M/L)
(M/L)d=0.60; c=1.0; V200=330; χ²r=2.9
Vrot (km s⁻¹)
Radius (kpc)
UGC 07323
MB=-18.3; Type=SABdm; h=2.0
disc
halo
model
approaching
receding

Figure A.67

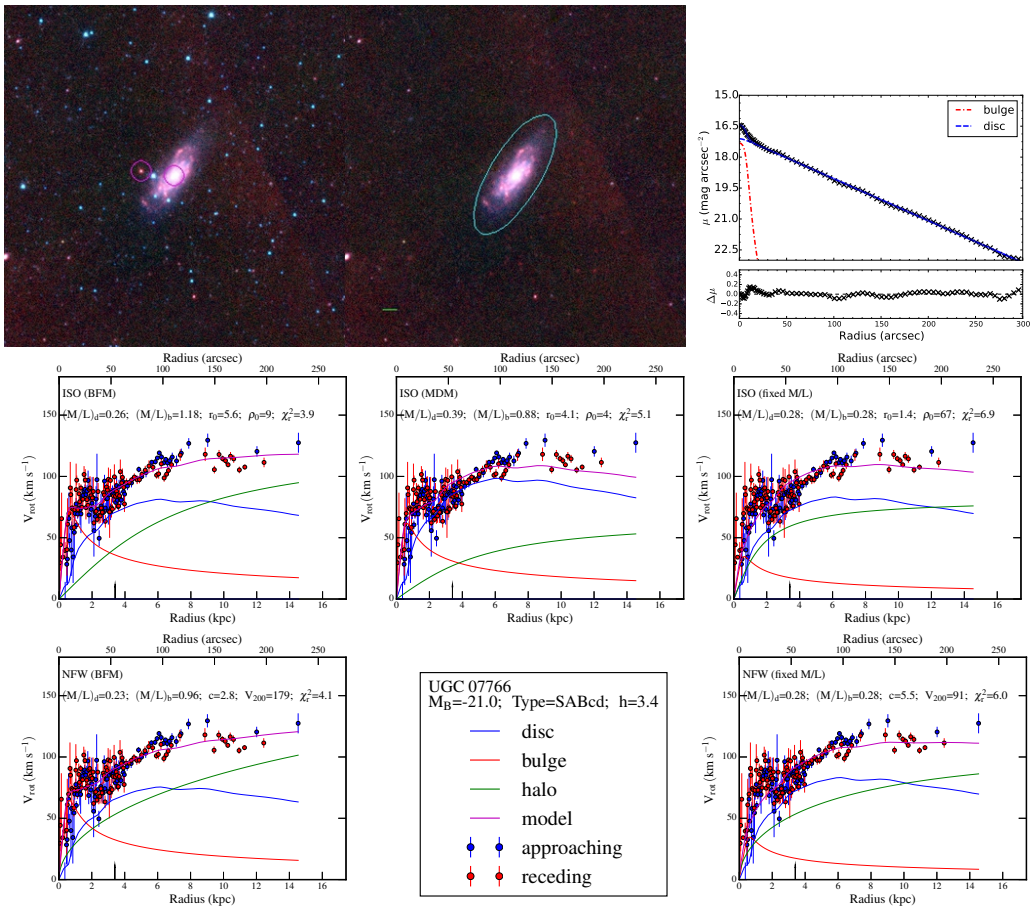
bulge
disc
μ (mag arcsec⁻²)
Δμ
Radius (arcsec)
ISO (BFM)
(M/L)d=0.26; (M/L)b=1.18; r0=5.6; ρ0=9; χr²=3.9
ISO (MDM)
(M/L)d=0.39; (M/L)b=0.88; r0=4.1; ρ0=4; χr²=5.1
ISO (fixed M/L)
(M/L)d=0.28; (M/L)b=0.28; r0=1.4; ρ0=67; χr²=6.9
NFW (BFM)
(M/L)d=0.23; (M/L)b=0.96; c=2.8; V200=179; χr²=4.1
NFW (fixed M/L)
(M/L)d=0.28; (M/L)b=0.28; c=5.5; V200=91; χr²=6.0
Vrot (km s⁻¹)
Radius (kpc)
UGC 07766
MB=-21.0; Type=SABcd; h=3.4
disc
bulge
halo
model
approaching
receding

Figure A.68

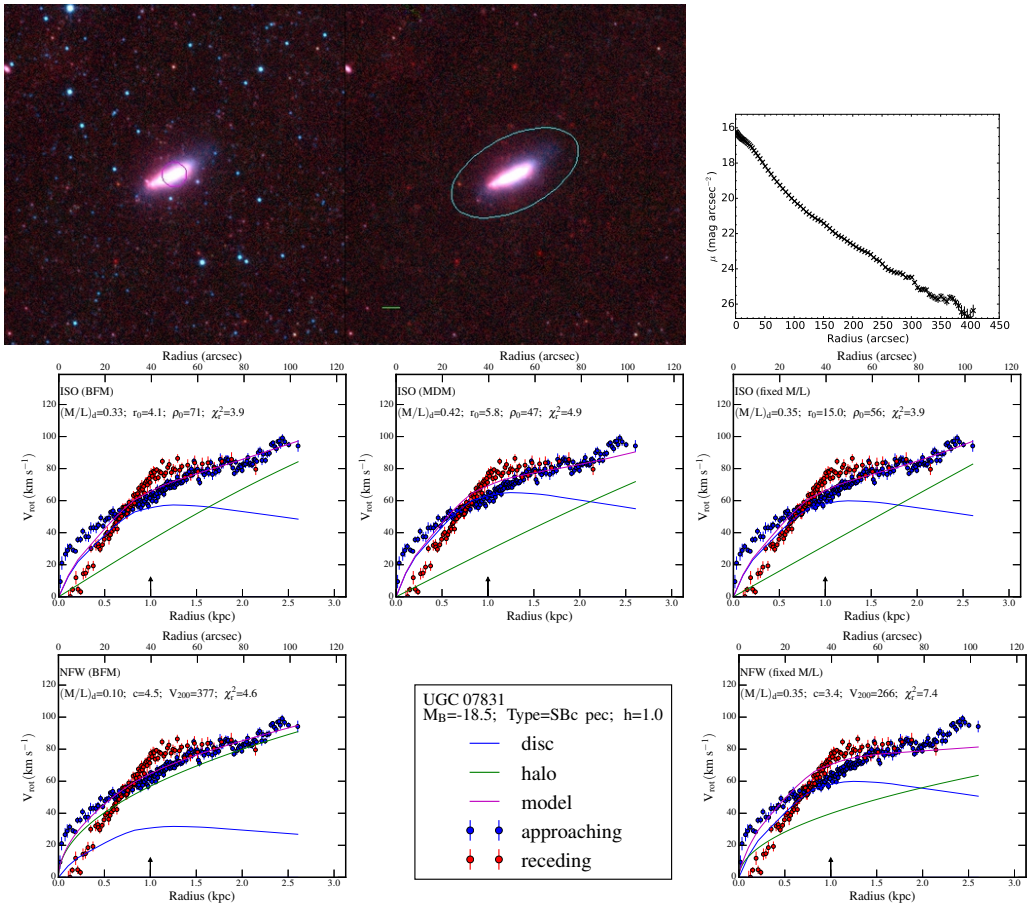
μ (mag arcsec⁻²)
Radius (arcsec)
ISO (BFM)
(M/L)d=0.33; r0=4.1; ρ0=71; χr²=3.9
ISO (MDM)
(M/L)d=0.42; r0=5.8; ρ0=47; χr²=4.9
ISO (fixed M/L)
(M/L)d=0.35; r0=15.0; ρ0=56; χr²=3.9
NFW (BFM)
(M/L)d=0.10; c=4.5; V200=377; χr²=4.6
NFW (fixed M/L)
(M/L)d=0.35; c=3.4; V200=266; χr²=7.4
Vrot (km s⁻¹)
Radius (kpc)
UGC 07831
MB=-18.5; Type=SBc pec; h=1.0
disc
halo
model
approaching
receding

Figure A.69

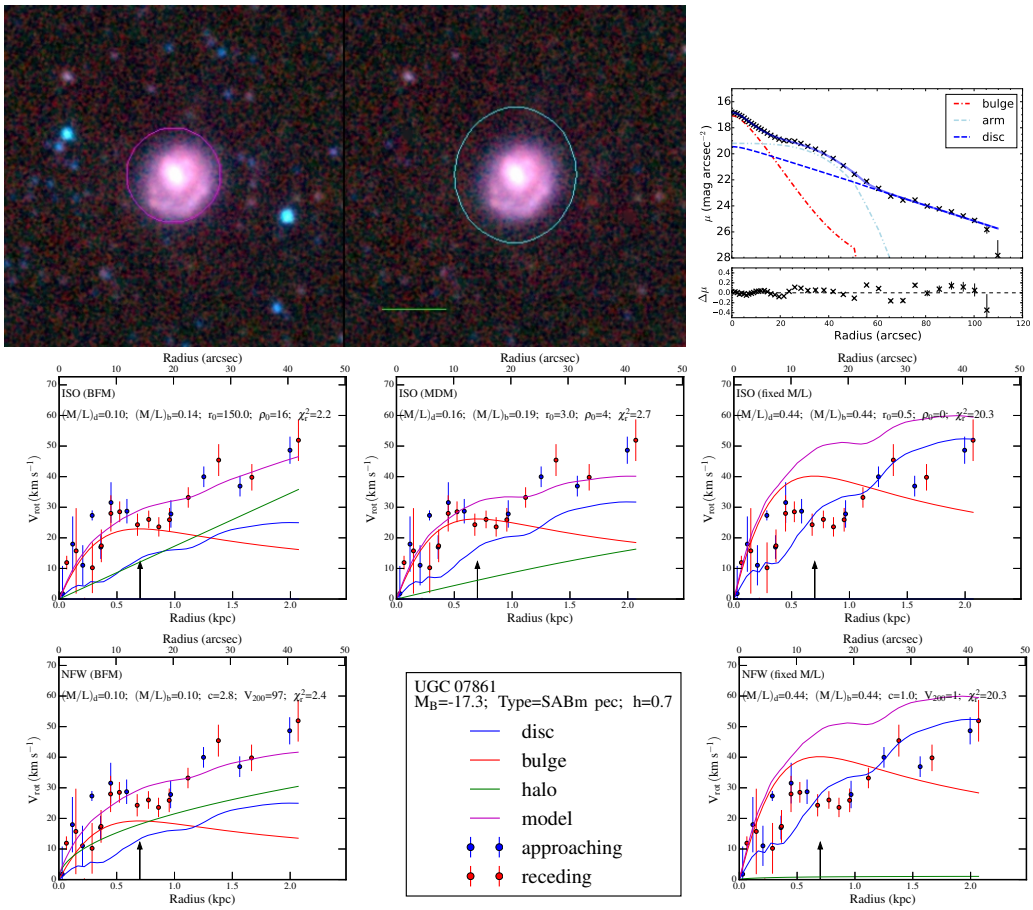
bulge
arm
disc
μ (mag arcsec⁻²)
Δμ
Radius (arcsec)
ISO (BFM)
(M/L)d=0.10; (M/L)b=0.14; r0=150.0; ρ0=16; χ²r=2.2
ISO (MDM)
(M/L)d=0.16; (M/L)b=0.19; r0=3.0; ρ0=4; χ²r=2.7
ISO (fixed M/L)
(M/L)d=0.44; (M/L)b=0.44; r0=0.5; ρ0=0; χ²r=20.3
NFW (BFM)
(M/L)d=0.10; (M/L)b=0.10; c=2.8; V200=97; χ²r=2.4
NFW (fixed M/L)
(M/L)d=0.44; (M/L)b=0.44; c=1.0; V200=1; χ²r=20.3
Vrot (km s⁻¹)
Radius (kpc)
UGC 07861
MB=-17.3; Type=SABm pec; h=0.7
disc
bulge
halo
model
approaching
receding

Figure A.70

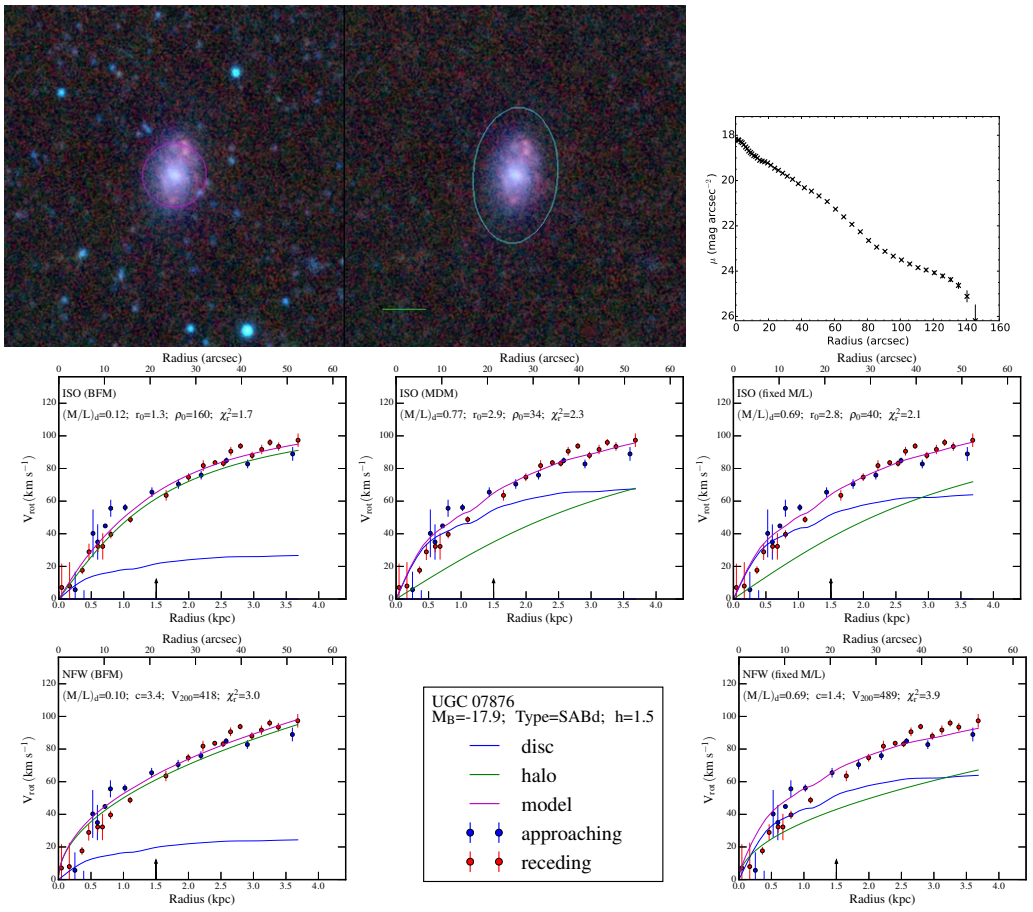
Radius (arcsec)
μ (mag arcsec⁻²)
ISO (BFM)
(M/L)d=0.12; r0=1.3; ρ0=160; χ²r=1.7
ISO (MDM)
(M/L)d=0.77; r0=2.9; ρ0=34; χ²r=2.3
ISO (fixed M/L)
(M/L)d=0.69; r0=2.8; ρ0=40; χ²r=2.1
NFW (BFM)
(M/L)d=0.10; c=3.4; V200=418; χ²r=3.0
NFW (fixed M/L)
(M/L)d=0.69; c=1.4; V200=489; χ²r=3.9
Vrot (km s⁻¹)
Radius (kpc)
UGC 07876
MB=-17.9; Type=SABd; h=1.5
disc
halo
model
approaching
receding

Figure A.71

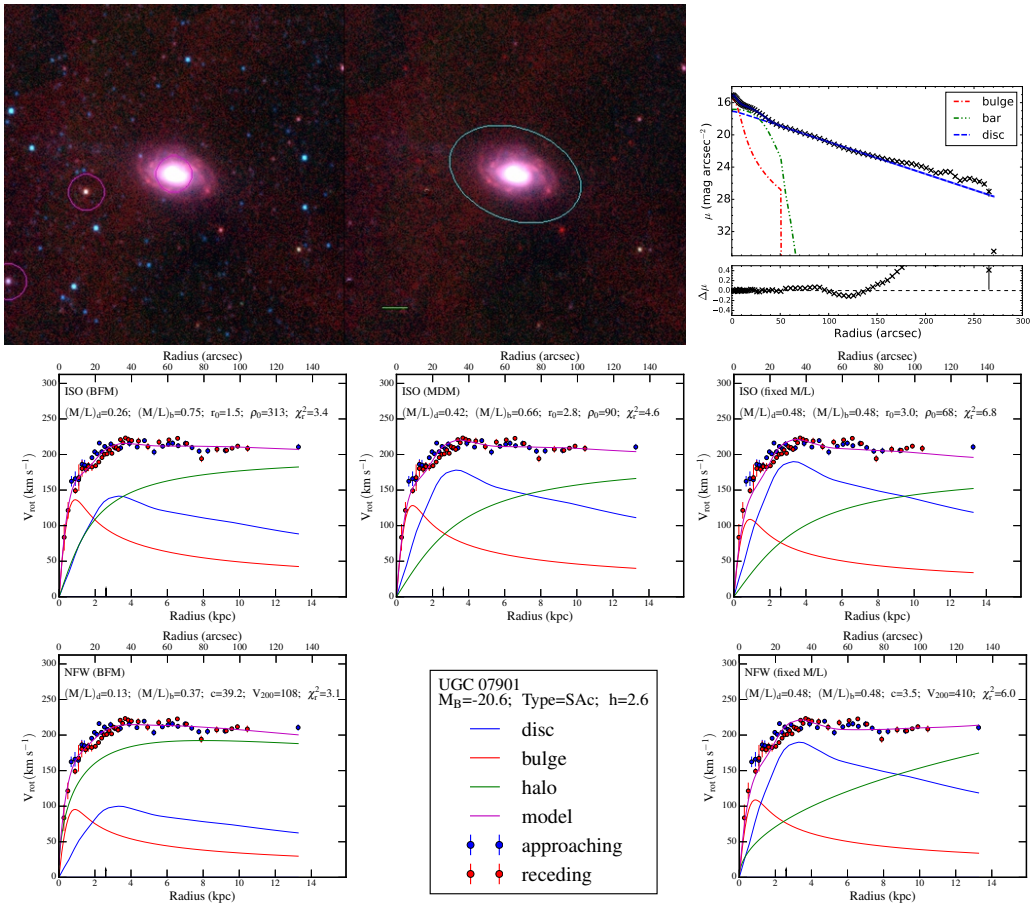
bulge
bar
disc
μ (mag arcsec⁻²)
Δμ
Radius (arcsec)
ISO (BFM)
(M/L)d=0.26; (M/L)b=0.75; r0=1.5; ρ0=313; χ²r=3.4
ISO (MDM)
(M/L)d=0.42; (M/L)b=0.66; r0=2.8; ρ0=90; χ²r=4.6
ISO (fixed M/L)
(M/L)d=0.48; (M/L)b=0.48; r0=3.0; ρ0=68; χ²r=6.8
NFW (BFM)
(M/L)d=0.13; (M/L)b=0.37; c=39.2; V200=108; χ²r=3.1
NFW (fixed M/L)
(M/L)d=0.48; (M/L)b=0.48; c=3.5; V200=410; χ²r=6.0
Vrot (km s⁻¹)
Radius (kpc)
UGC 07901
MB=-20.6; Type=SAc; h=2.6
disc
bulge
halo
model
approaching
receding

Figure A.72

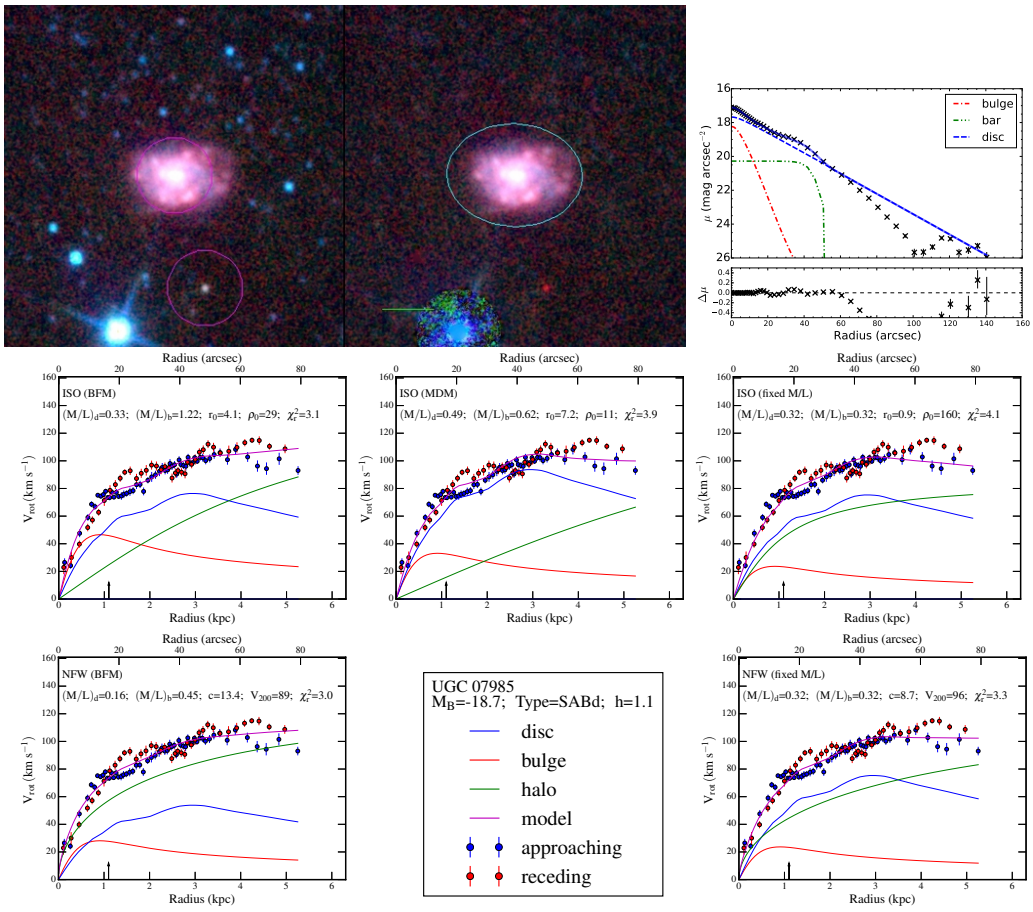
bulge
bar
disc
μ (mag arcsec⁻²)
Δμ
Radius (arcsec)
ISO (BFM)
(M/L)d=0.33; (M/L)b=1.22; r0=4.1; ρ0=29; χ²r=3.1
ISO (MDM)
(M/L)d=0.49; (M/L)b=0.62; r0=7.2; ρ0=11; χ²r=3.9
ISO (fixed M/L)
(M/L)d=0.32; (M/L)b=0.32; r0=0.9; ρ0=160; χ²r=4.1
NFW (BFM)
(M/L)d=0.16; (M/L)b=0.45; c=13.4; V200=89; χ²r=3.0
NFW (fixed M/L)
(M/L)d=0.32; (M/L)b=0.32; c=8.7; V200=96; χ²r=3.3
Vrot (km s⁻¹)
Radius (kpc)
UGC 07985
MB=-18.7; Type=SABd; h=1.1
disc
bulge
halo
model
approaching
receding

Figure A.73

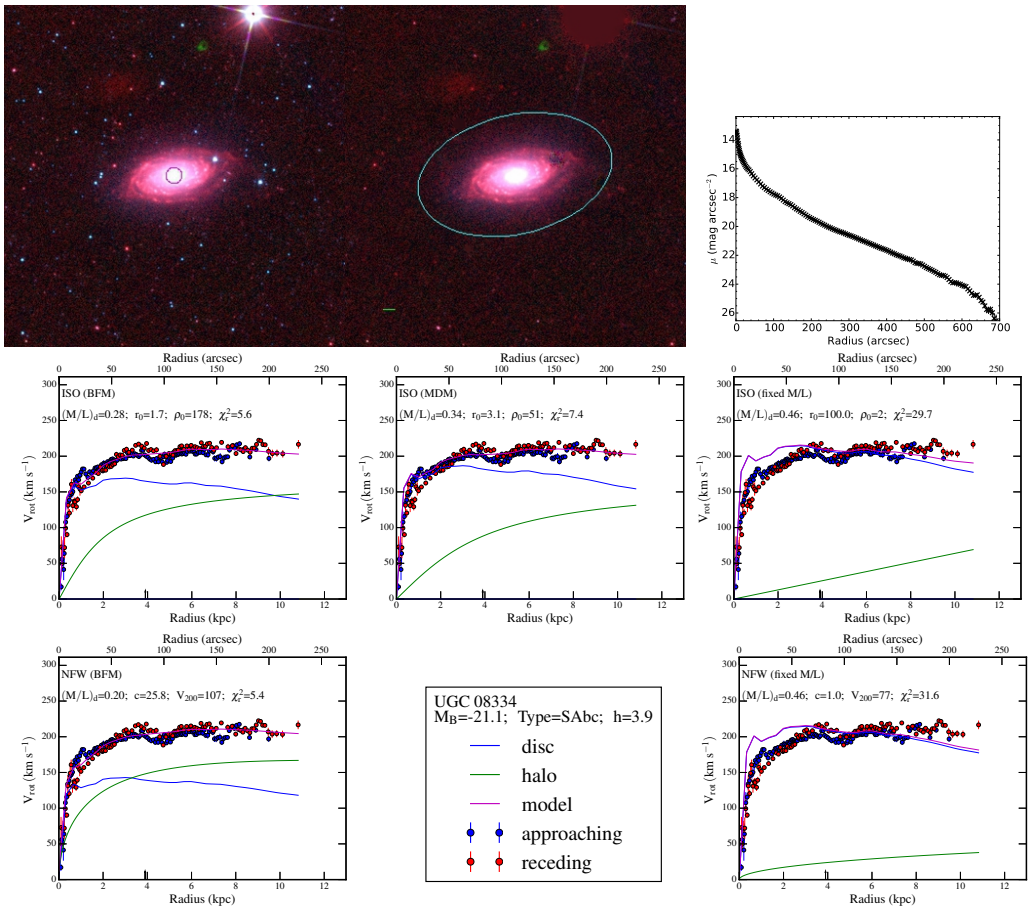
μ (mag arcsec⁻²)
Radius (arcsec)
ISO (BFM)
(M/L)d=0.28; r0=1.7; ρ0=178; χ²r=5.6
ISO (MDM)
(M/L)d=0.34; r0=3.1; ρ0=51; χ²r=7.4
ISO (fixed M/L)
(M/L)d=0.46; r0=100.0; ρ0=2; χ²r=29.7
NFW (BFM)
(M/L)d=0.20; c=25.8; V200=107; χ²r=5.4
NFW (fixed M/L)
(M/L)d=0.46; c=1.0; V200=77; χ²r=31.6
Vrot (km s⁻¹)
Radius (kpc)
UGC 08334
MB=-21.1; Type=SAbc; h=3.9
disc
halo
model
approaching
receding

Figure A.74

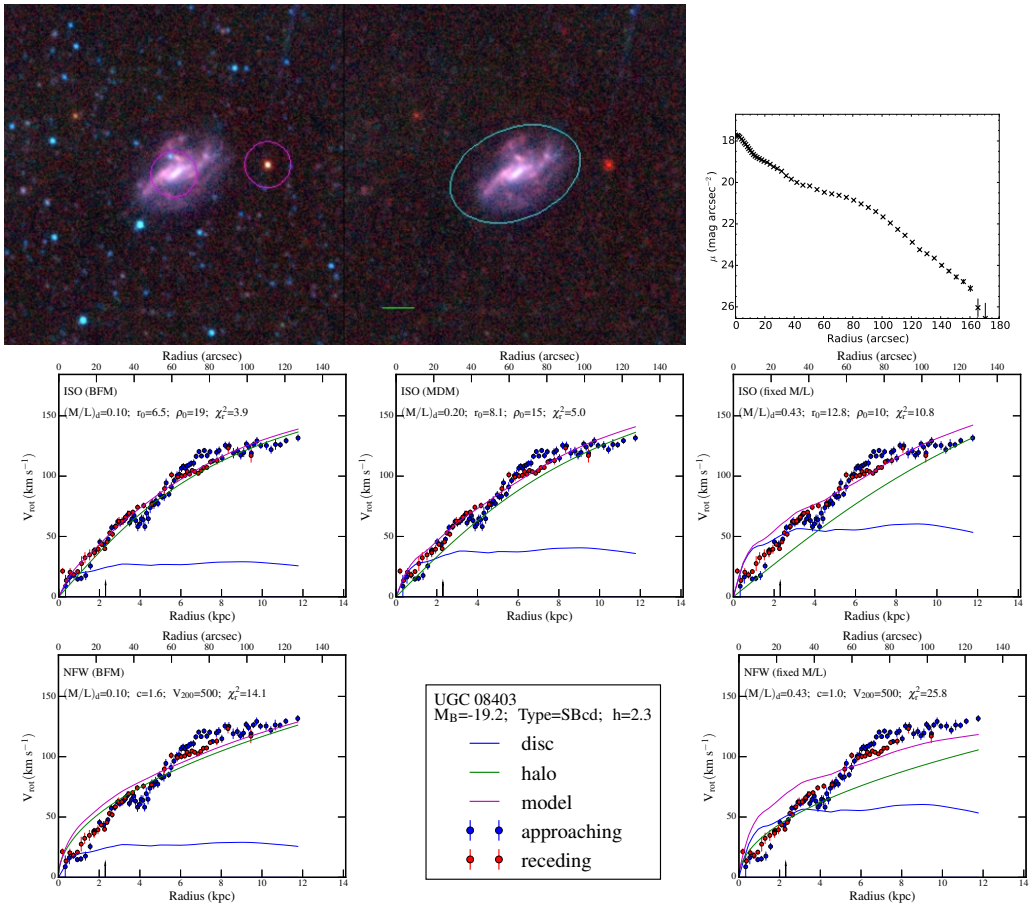
μ (mag arcsec⁻²)
Radius (arcsec)
ISO (BFM)
(M/L)d=0.10; r0=6.5; ρ0=19; χr²=3.9
ISO (MDM)
(M/L)d=0.20; r0=8.1; ρ0=15; χr²=5.0
ISO (fixed M/L)
(M/L)d=0.43; r0=12.8; ρ0=10; χr²=10.8
NFW (BFM)
(M/L)d=0.10; c=1.6; V200=500; χr²=14.1
NFW (fixed M/L)
(M/L)d=0.43; c=1.0; V200=500; χr²=25.8
Vrot (km s⁻¹)
Radius (kpc)
UGC 08403
MB=-19.2; Type=SBcd; h=2.3
disc
halo
model
approaching
receding

Figure A.75

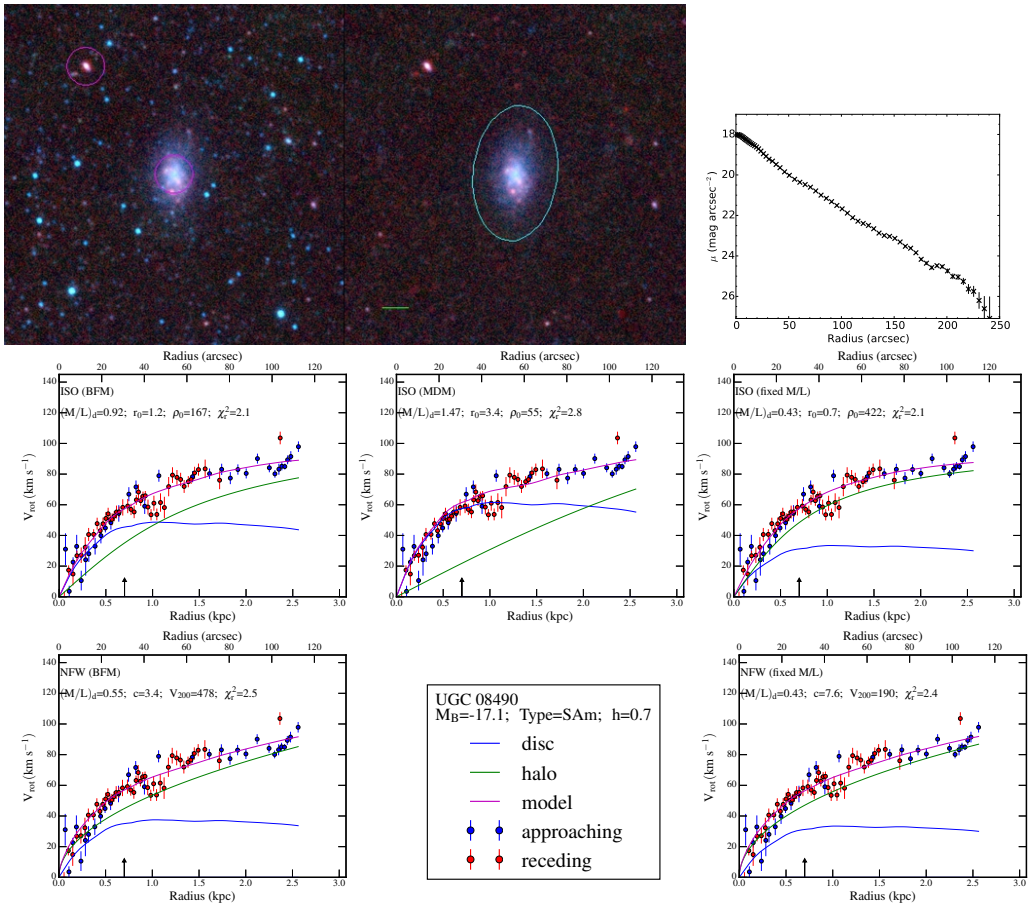
μ (mag arcsec⁻²)
Radius (arcsec)
ISO (BFM)
(M/L)d=0.92; r0=1.2; ρ0=167; χ²r=2.1
ISO (MDM)
(M/L)d=1.47; r0=3.4; ρ0=55; χ²r=2.8
ISO (fixed M/L)
(M/L)d=0.43; r0=0.7; ρ0=422; χ²r=2.1
NFW (BFM)
(M/L)d=0.55; c=3.4; V200=478; χ²r=2.5
NFW (fixed M/L)
(M/L)d=0.43; c=7.6; V200=190; χ²r=2.4
Vrot (km s⁻¹)
Radius (kpc)
UGC 08490
MB=-17.1; Type=SAm; h=0.7
disc
halo
model
approaching
receding

Figure A.76

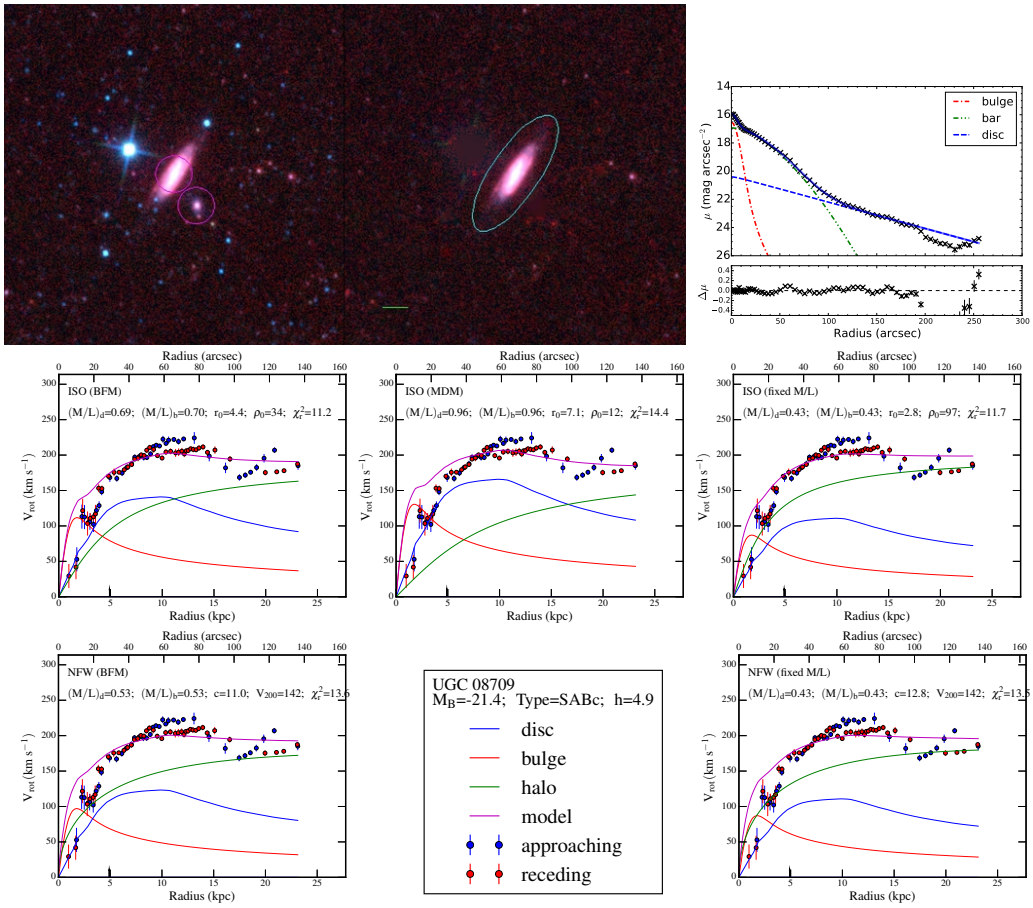
bulge
bar
disc
μ (mag arcsec⁻²)
Δμ
Radius (arcsec)
ISO (BFM)
(M/L)d=0.69; (M/L)b=0.70; r0=4.4; ρ0=34; χ²r=11.2
ISO (MDM)
(M/L)d=0.96; (M/L)b=0.96; r0=7.1; ρ0=12; χ²r=14.4
ISO (fixed M/L)
(M/L)d=0.43; (M/L)b=0.43; r0=2.8; ρ0=97; χ²r=11.7
NFW (BFM)
(M/L)d=0.53; (M/L)b=0.53; c=11.0; V200=142; χ²r=13.6
NFW (fixed M/L)
(M/L)d=0.43; (M/L)b=0.43; c=12.8; V200=142; χ²r=13.5
Vrot (km s⁻¹)
Radius (kpc)
UGC 08709
MB=-21.4; Type=SABc; h=4.9
disc
bulge
halo
model
approaching
receding

Figure A.77

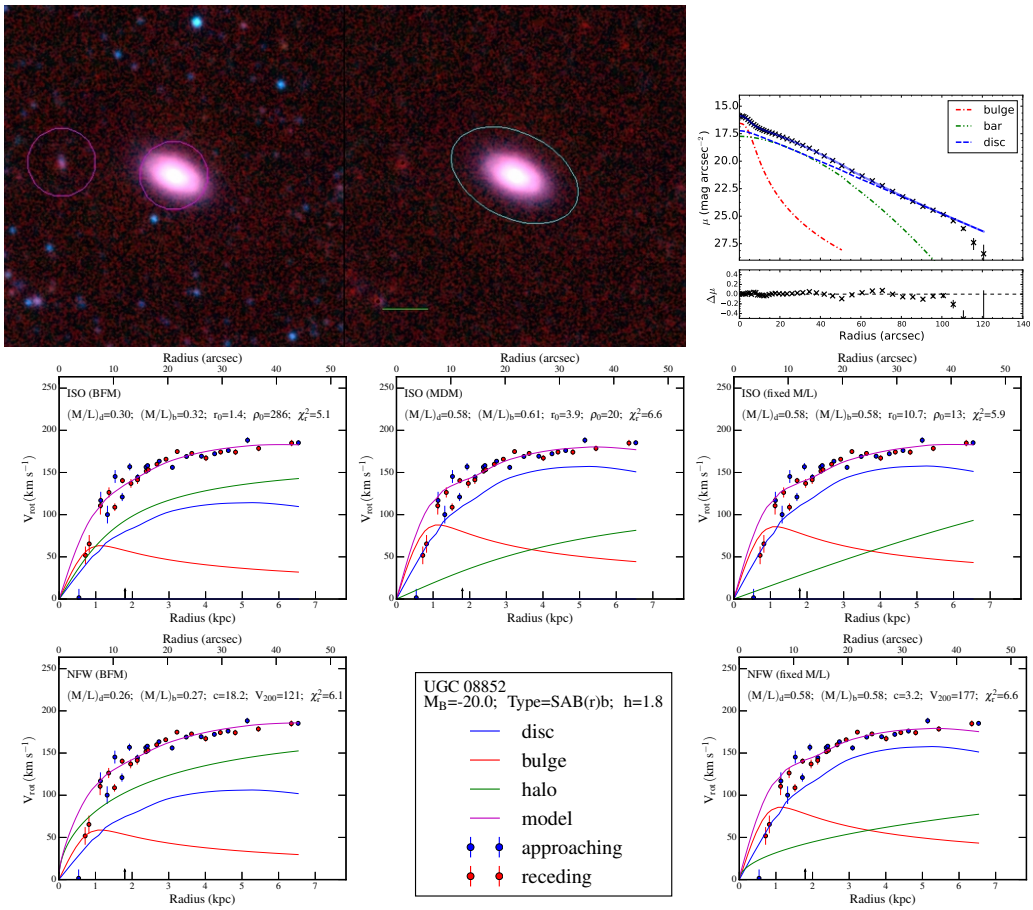
bulge
bar
disc
μ (mag arcsec⁻²)
Δμ
Radius (arcsec)
ISO (BFM)
(M/L)d=0.30; (M/L)b=0.32; r0=1.4; ρ0=286; χ²r=5.1
ISO (MDM)
(M/L)d=0.58; (M/L)b=0.61; r0=3.9; ρ0=20; χ²r=6.6
ISO (fixed M/L)
(M/L)d=0.58; (M/L)b=0.58; r0=10.7; ρ0=13; χ²r=5.9
NFW (BFM)
(M/L)d=0.26; (M/L)b=0.27; c=18.2; V200=121; χ²r=6.1
NFW (fixed M/L)
(M/L)d=0.58; (M/L)b=0.58; c=3.2; V200=177; χ²r=6.6
Vrot (km s⁻¹)
Radius (kpc)
UGC 08852
MB=-20.0; Type=SAB(r)b; h=1.8
disc
bulge
halo
model
approaching
receding

Figure A.78

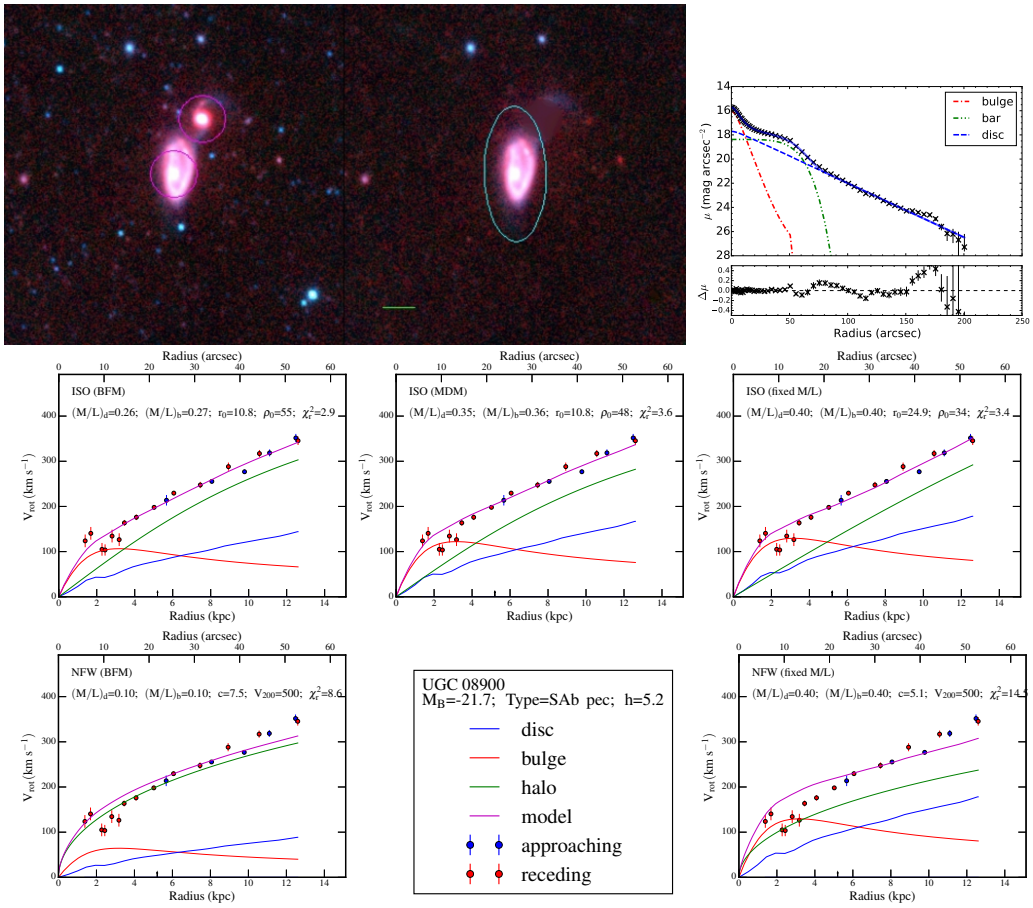
bulge
bar
disc
μ (mag arcsec⁻²)
Δμ
Radius (arcsec)
ISO (BFM)
(M/L)d=0.26; (M/L)b=0.27; r0=10.8; ρ0=55; χ²r=2.9
ISO (MDM)
(M/L)d=0.35; (M/L)b=0.36; r0=10.8; ρ0=48; χ²r=3.6
ISO (fixed M/L)
(M/L)d=0.40; (M/L)b=0.40; r0=24.9; ρ0=34; χ²r=3.4
NFW (BFM)
(M/L)d=0.10; (M/L)b=0.10; c=7.5; V200=500; χ²r=8.6
NFW (fixed M/L)
(M/L)d=0.40; (M/L)b=0.40; c=5.1; V200=500; χ²r=14.5
Vrot (km s⁻¹)
Radius (kpc)
UGC 08900
MB=-21.7; Type=SAb pec; h=5.2
disc
bulge
halo
model
approaching
receding

Figure A.79

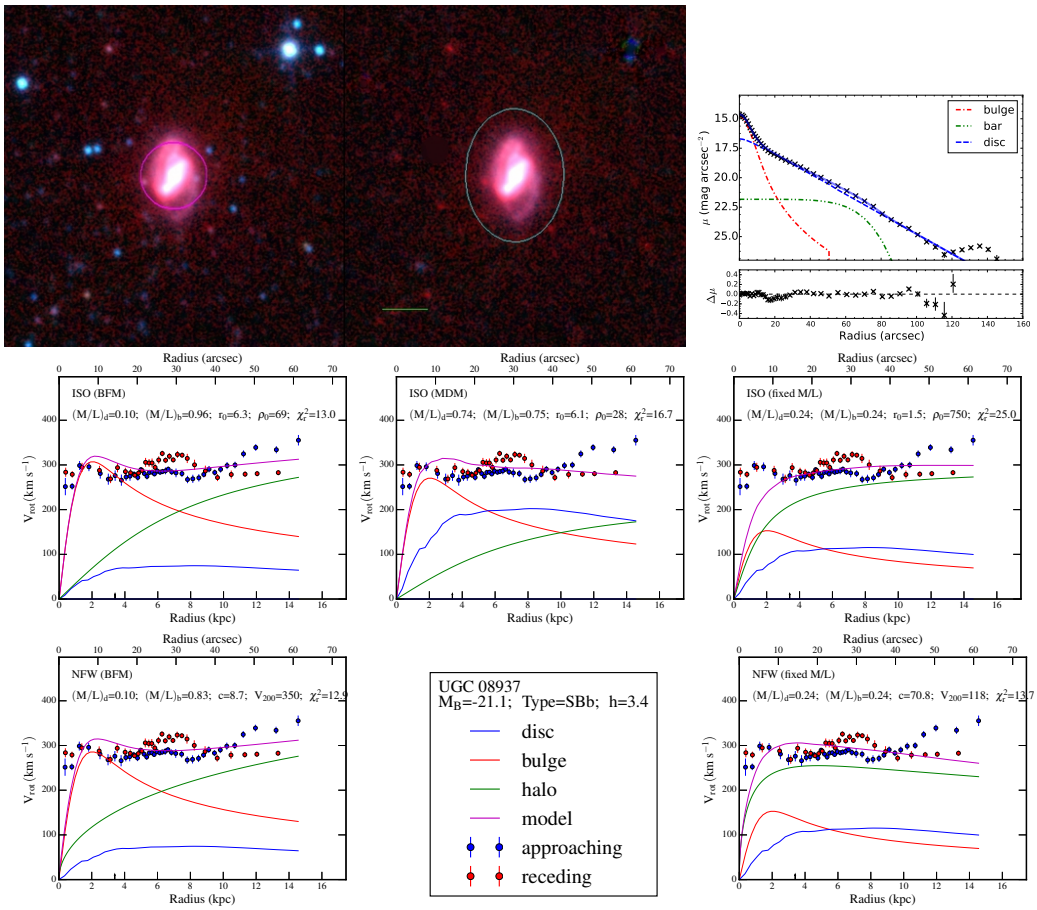
bulge
bar
disc
Radius (arcsec)
ISO (BFM)
ISO (MDM)
ISO (fixed M/L)
NFW (BFM)
NFW (fixed M/L)
Radius (kpc)
UGC 08937
M_B=-21.1; Type=SBb; h=3.4
disc
bulge
halo
model
approaching
receding

Figure A.80

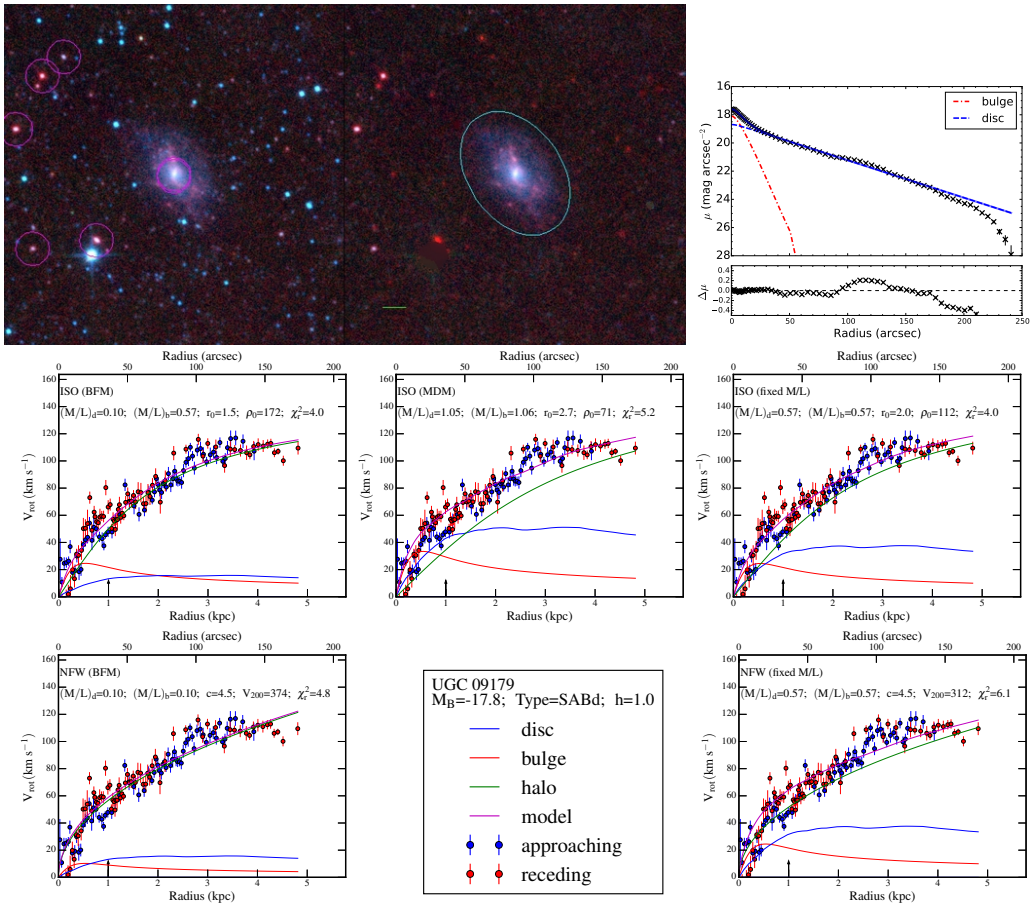
bulge
disc
μ (mag arcsec⁻²)
Δμ
Radius (arcsec)
ISO (BFM)
(M/L)d=0.10; (M/L)b=0.57; r0=1.5; ρ0=172; χr²=4.0
ISO (MDM)
(M/L)d=1.05; (M/L)b=1.06; r0=2.7; ρ0=71; χr²=5.2
ISO (fixed M/L)
(M/L)d=0.57; (M/L)b=0.57; r0=2.0; ρ0=112; χr²=4.0
NFW (BFM)
(M/L)d=0.10; (M/L)b=0.10; c=4.5; V200=374; χr²=4.8
NFW (fixed M/L)
(M/L)d=0.57; (M/L)b=0.57; c=4.5; V200=312; χr²=6.1
Vrot (km s⁻¹)
Radius (kpc)
UGC 09179
MB=-17.8; Type=SABd; h=1.0
disc
bulge
halo
model
approaching
receding

Figure A.81

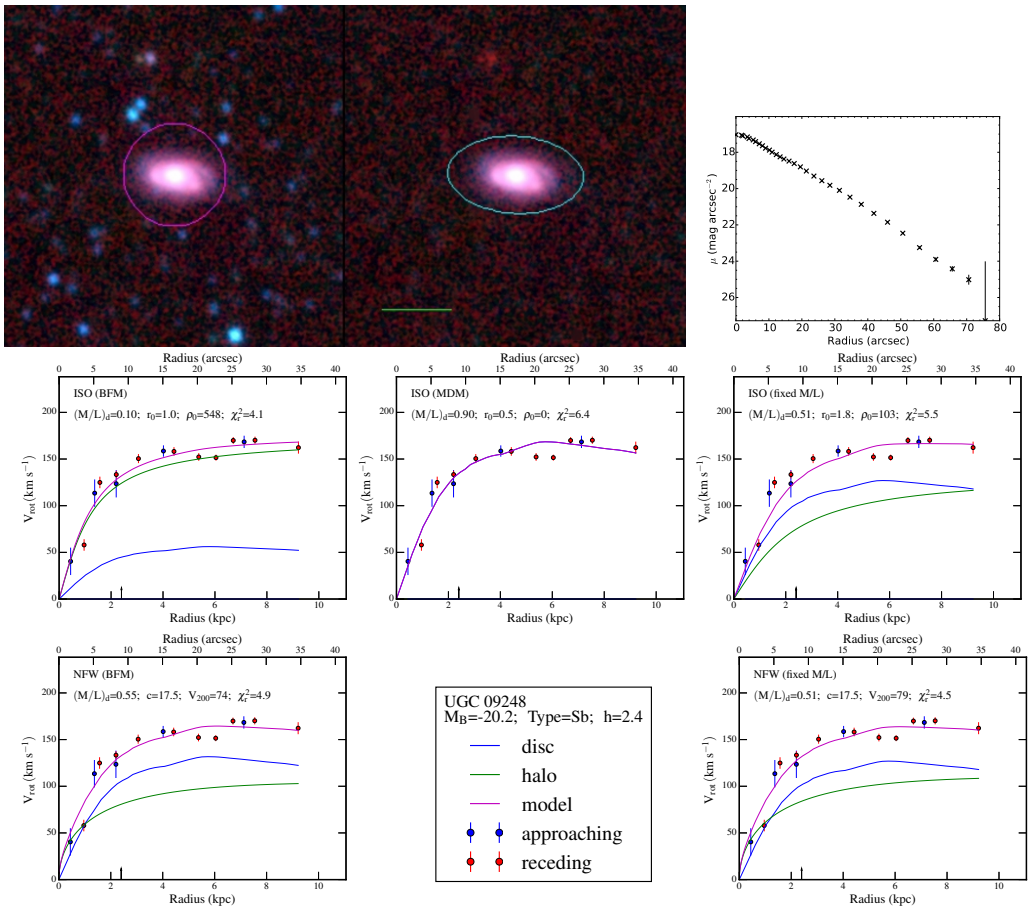
μ (mag arcsec⁻²)
Radius (arcsec)
ISO (BFM)
(M/L)d=0.10; r0=1.0; ρ0=548; χ²ν=4.1
ISO (MDM)
(M/L)d=0.90; r0=0.5; ρ0=0; χ²ν=6.4
ISO (fixed M/L)
(M/L)d=0.51; r0=1.8; ρ0=103; χ²ν=5.5
NFW (BFM)
(M/L)d=0.55; c=17.5; V200=74; χ²ν=4.9
NFW (fixed M/L)
(M/L)d=0.51; c=17.5; V200=79; χ²ν=4.5
Vrot (km s⁻¹)
Radius (kpc)
UGC 09248
MB=-20.2; Type=Sb; h=2.4
disc
halo
model
approaching
receding

Figure A.82

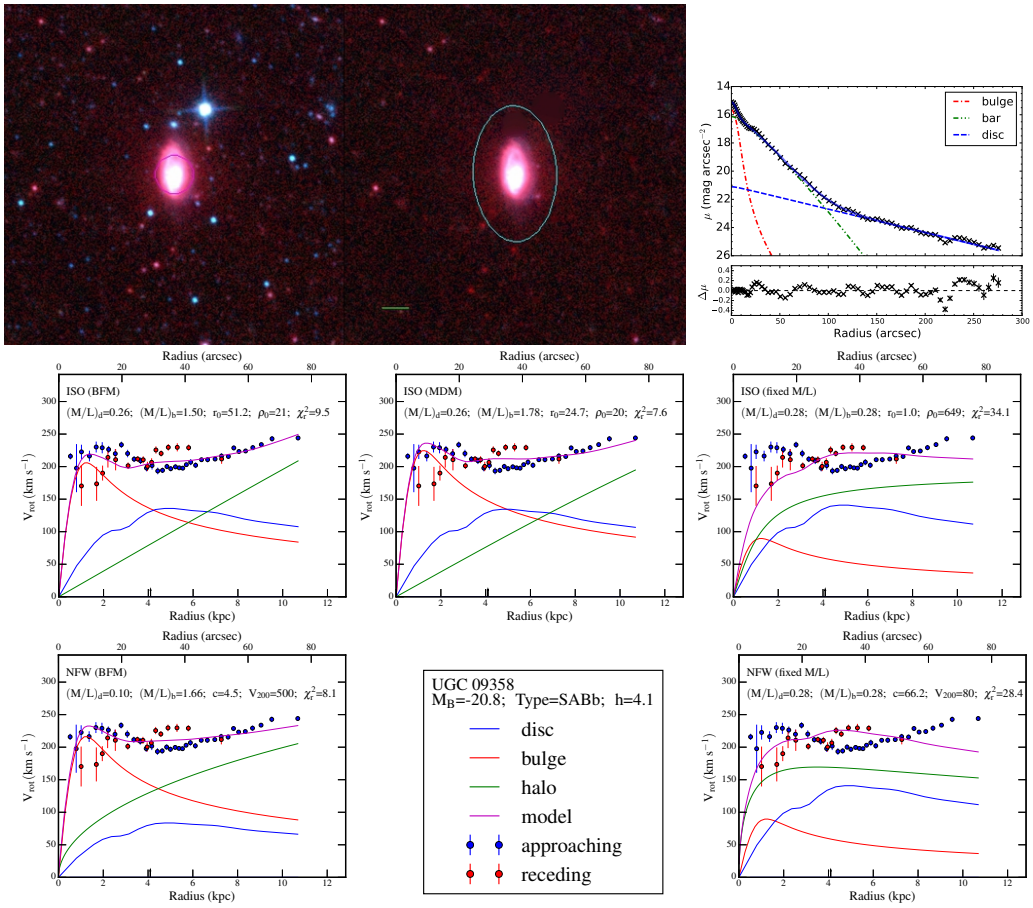
bulge
bar
disc
μ (mag arcsec⁻²)
Δμ
Radius (arcsec)
ISO (BFM)
(M/L)d=0.26; (M/L)b=1.50; r0=51.2; ρ0=21; χ²r=9.5
ISO (MDM)
(M/L)d=0.26; (M/L)b=1.78; r0=24.7; ρ0=20; χ²r=7.6
ISO (fixed M/L)
(M/L)d=0.28; (M/L)b=0.28; r0=1.0; ρ0=649; χ²r=34.1
NFW (BFM)
(M/L)d=0.10; (M/L)b=1.66; c=4.5; V200=500; χ²r=8.1
NFW (fixed M/L)
(M/L)d=0.28; (M/L)b=0.28; c=66.2; V200=80; χ²r=28.4
Vrot (km s⁻¹)
Radius (kpc)
UGC 09358
MB=-20.8; Type=SABb; h=4.1
disc
bulge
halo
model
approaching
receding

Figure A.83

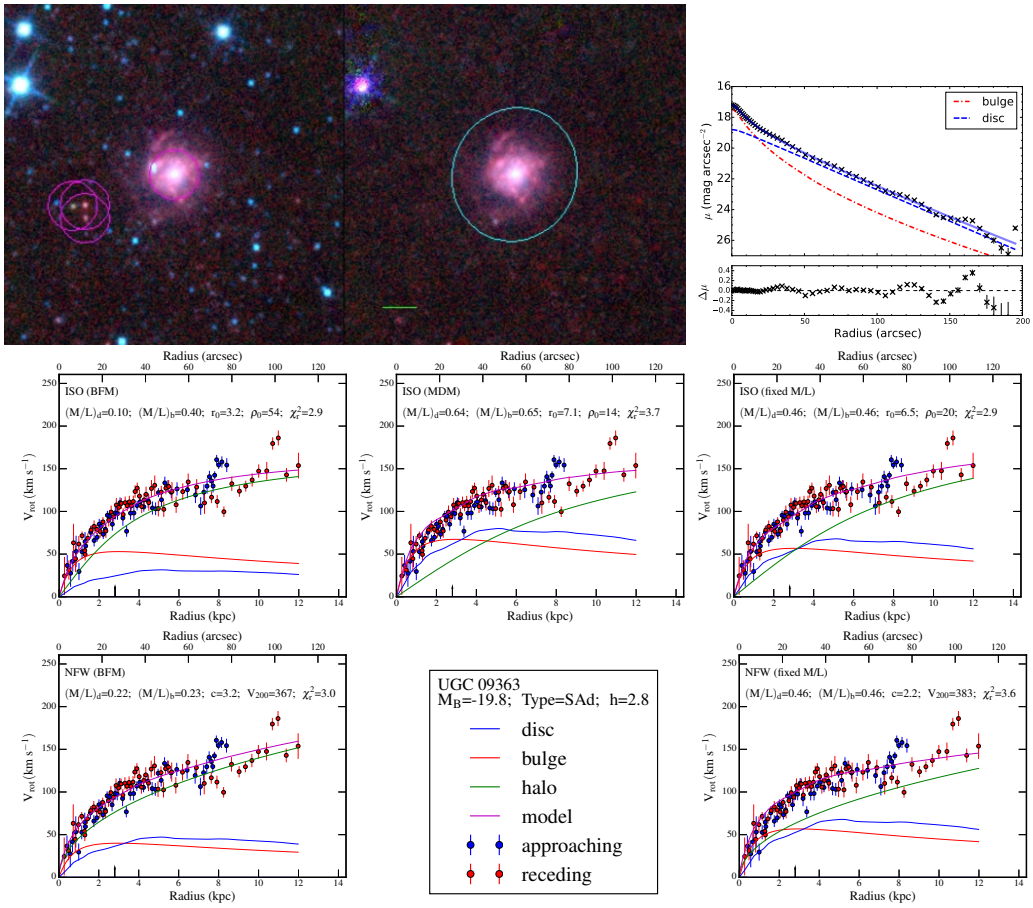
bulge
disc
μ (mag arcsec⁻²)
Δμ
Radius (arcsec)
ISO (BFM)
(M/L)d=0.10; (M/L)b=0.40; r0=3.2; ρ0=54; χ²r=2.9
ISO (MDM)
(M/L)d=0.64; (M/L)b=0.65; r0=7.1; ρ0=14; χ²r=3.7
ISO (fixed M/L)
(M/L)d=0.46; (M/L)b=0.46; r0=6.5; ρ0=20; χ²r=2.9
NFW (BFM)
(M/L)d=0.22; (M/L)b=0.23; c=3.2; V200=367; χ²r=3.0
NFW (fixed M/L)
(M/L)d=0.46; (M/L)b=0.46; c=2.2; V200=383; χ²r=3.6
Vrot (km s⁻¹)
Radius (kpc)
UGC 09363
MB=-19.8; Type=SAd; h=2.8
disc
bulge
halo
model
approaching
receding

Figure A.84

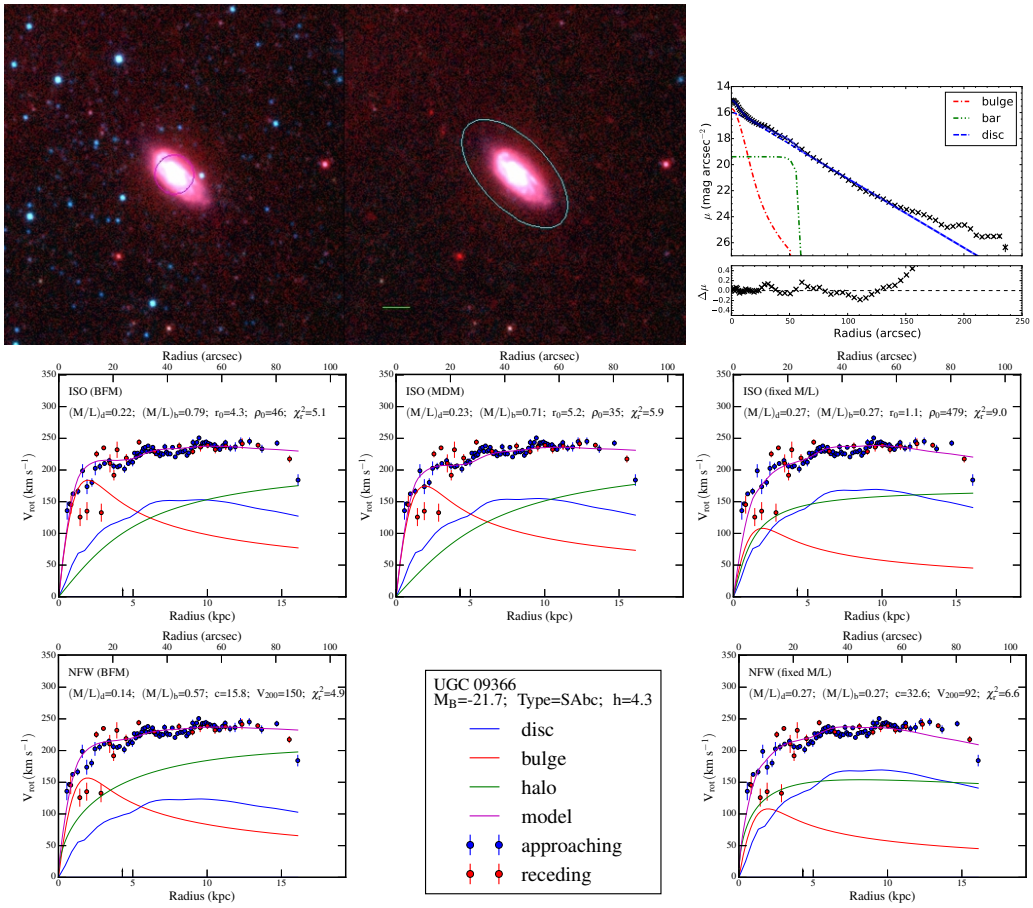
bulge
bar
disc
μ (mag arcsec⁻²)
Δμ
Radius (arcsec)
ISO (BFM)
(M/L)d=0.22; (M/L)b=0.79; r0=4.3; ρ0=46; χr²=5.1
ISO (MDM)
(M/L)d=0.23; (M/L)b=0.71; r0=5.2; ρ0=35; χr²=5.9
ISO (fixed M/L)
(M/L)d=0.27; (M/L)b=0.27; r0=1.1; ρ0=479; χr²=9.0
NFW (BFM)
(M/L)d=0.14; (M/L)b=0.57; c=15.8; V200=150; χr²=4.9
NFW (fixed M/L)
(M/L)d=0.27; (M/L)b=0.27; c=32.6; V200=92; χr²=6.6
Vrot (km s⁻¹)
Radius (kpc)
UGC 09366
MB=-21.7; Type=SAbc; h=4.3
disc
bulge
halo
model
approaching
receding

Figure A.85

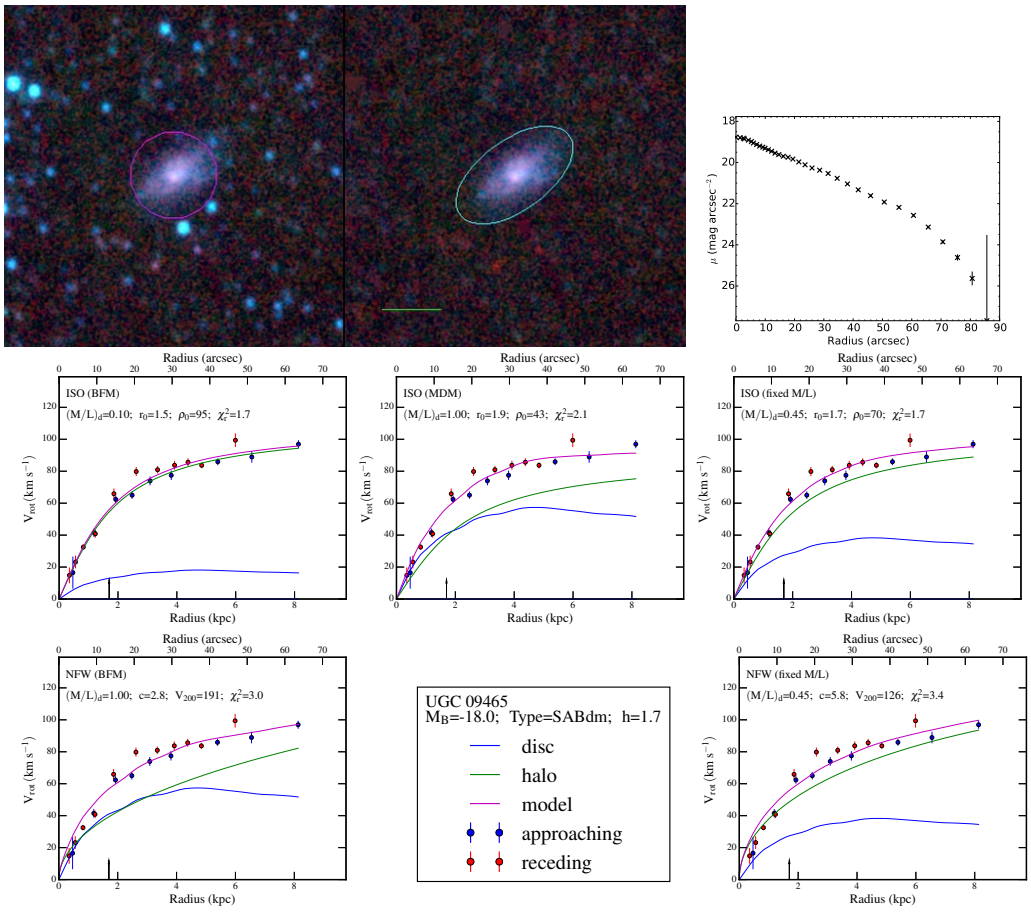
μ (mag arcsec⁻²)
Radius (arcsec)
ISO (BFM)
(M/L)d=0.10; r0=1.5; ρ0=95; χ²r=1.7
ISO (MDM)
(M/L)d=1.00; r0=1.9; ρ0=43; χ²r=2.1
ISO (fixed M/L)
(M/L)d=0.45; r0=1.7; ρ0=70; χ²r=1.7
NFW (BFM)
(M/L)d=1.00; c=2.8; V200=191; χ²r=3.0
NFW (fixed M/L)
(M/L)d=0.45; c=5.8; V200=126; χ²r=3.4
Vrot (km s⁻¹)
Radius (kpc)
UGC 09465
MB=-18.0; Type=SABdm; h=1.7
disc
halo
model
approaching
receding

Figure A.86

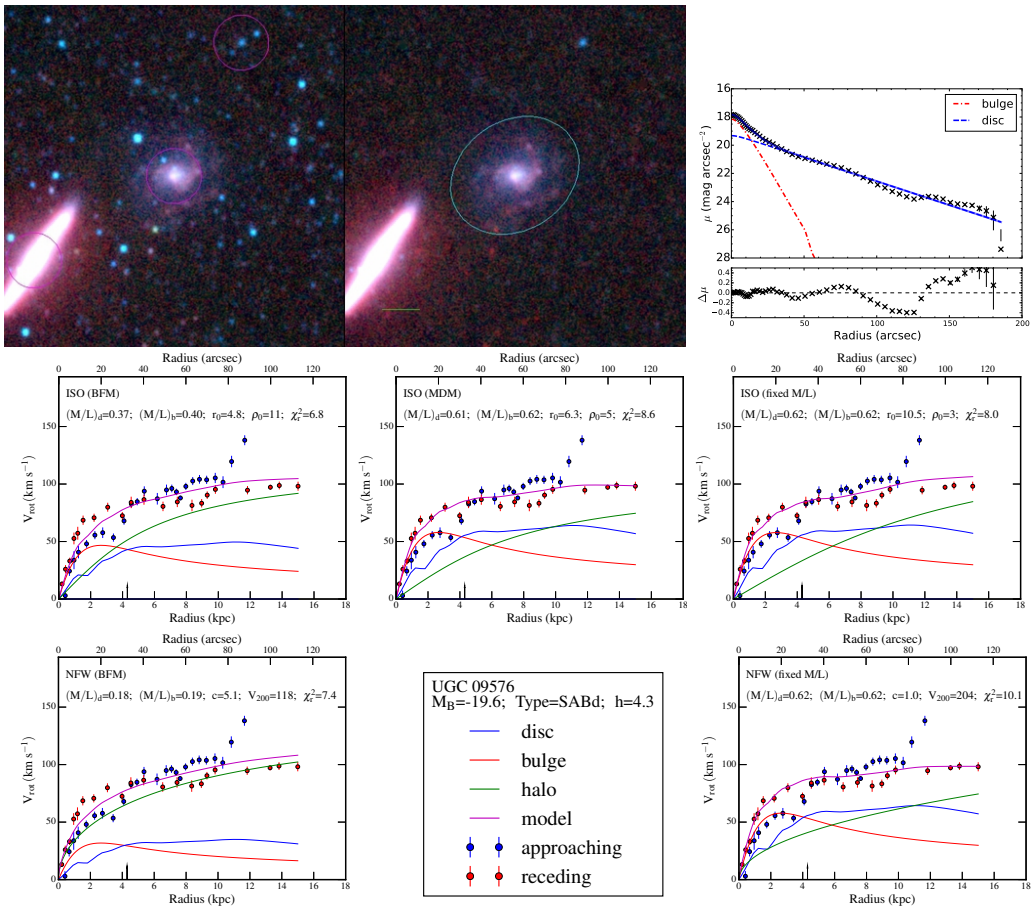
bulge
disc
μ (mag arcsec⁻²)
Δμ
Radius (arcsec)
ISO (BFM)
(M/L)d=0.37; (M/L)h=0.40; r0=4.8; ρ0=11; χ²r=6.8
ISO (MDM)
(M/L)d=0.61; (M/L)h=0.62; r0=6.3; ρ0=5; χ²r=8.6
ISO (fixed M/L)
(M/L)d=0.62; (M/L)h=0.62; r0=10.5; ρ0=3; χ²r=8.0
NFW (BFM)
(M/L)d=0.18; (M/L)h=0.19; c=5.1; V200=118; χ²r=7.4
NFW (fixed M/L)
(M/L)d=0.62; (M/L)h=0.62; c=1.0; V200=204; χ²r=10.1
Vrot (km s⁻¹)
Radius (kpc)
UGC 09576
MB=-19.6; Type=SABd; h=4.3
disc
bulge
halo
model
approaching
receding

Figure A.87

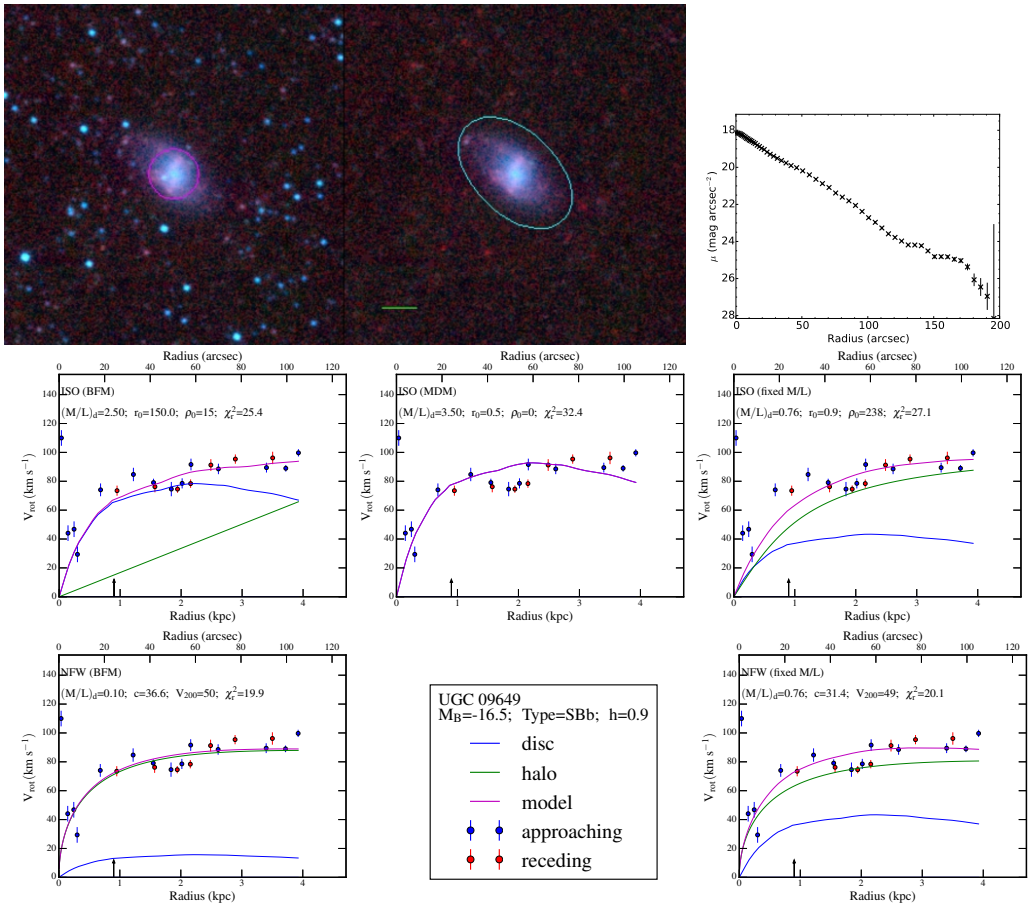
μ (mag arcsec⁻²)
Radius (arcsec)
ISO (BFM)
(M/L)d=2.50; r0=150.0; ρ0=15; χ²r=25.4
ISO (MDM)
(M/L)d=3.50; r0=0.5; ρ0=0; χ²r=32.4
ISO (fixed M/L)
(M/L)d=0.76; r0=0.9; ρ0=238; χ²r=27.1
NFW (BFM)
(M/L)d=0.10; c=36.6; V200=50; χ²r=19.9
NFW (fixed M/L)
(M/L)d=0.76; c=31.4; V200=49; χ²r=20.1
Vrot (km s⁻¹)
Radius (kpc)
UGC 09649
MB=-16.5; Type=SBb; h=0.9
disc
halo
model
approaching
receding

Figure A.88

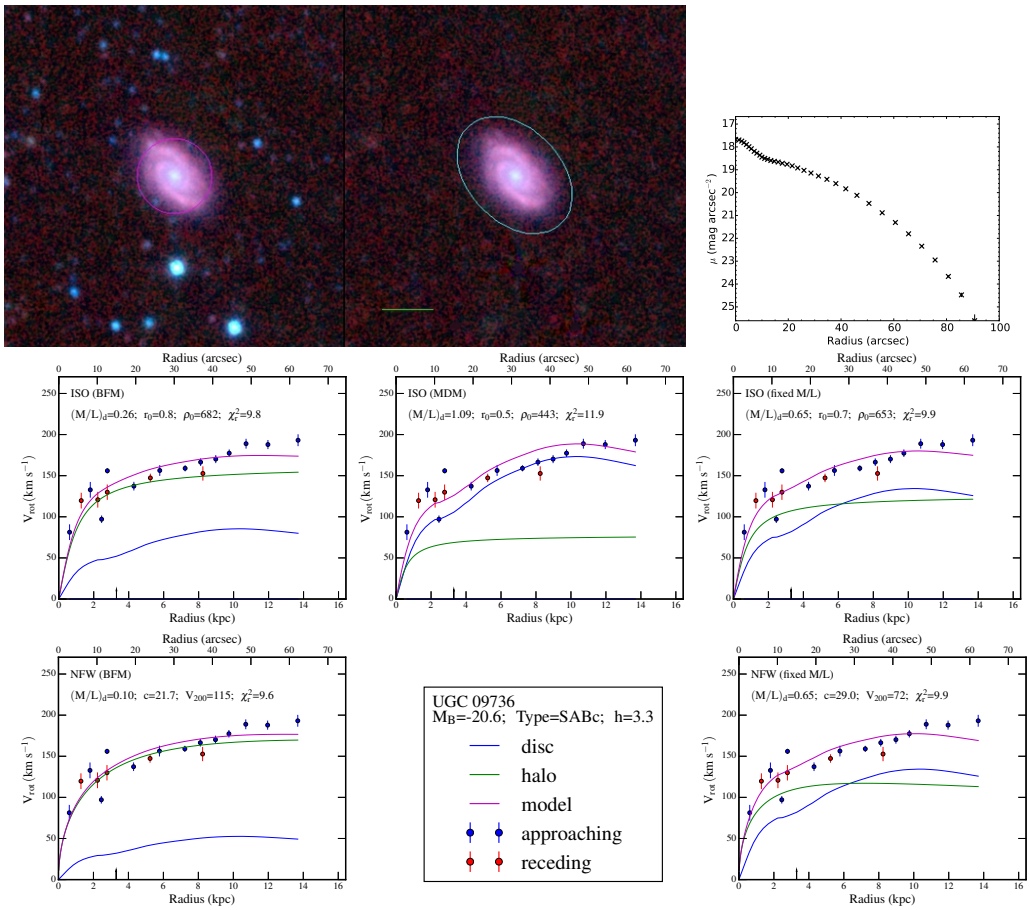
Radius (arcsec)
μ (mag arcsec⁻²)
ISO (BFM)
(M/L)d=0.26; r0=0.8; ρ0=682; χ²r=9.8
ISO (MDM)
(M/L)d=1.09; r0=0.5; ρ0=443; χ²r=11.9
ISO (fixed M/L)
(M/L)d=0.65; r0=0.7; ρ0=653; χ²r=9.9
NFW (BFM)
(M/L)d=0.10; c=21.7; V200=115; χ²r=9.6
NFW (fixed M/L)
(M/L)d=0.65; c=29.0; V200=72; χ²r=9.9
Vrot (km s⁻¹)
Radius (kpc)
UGC 09736
MB=-20.6; Type=SABc; h=3.3
disc
halo
model
approaching
receding

Figure A.89

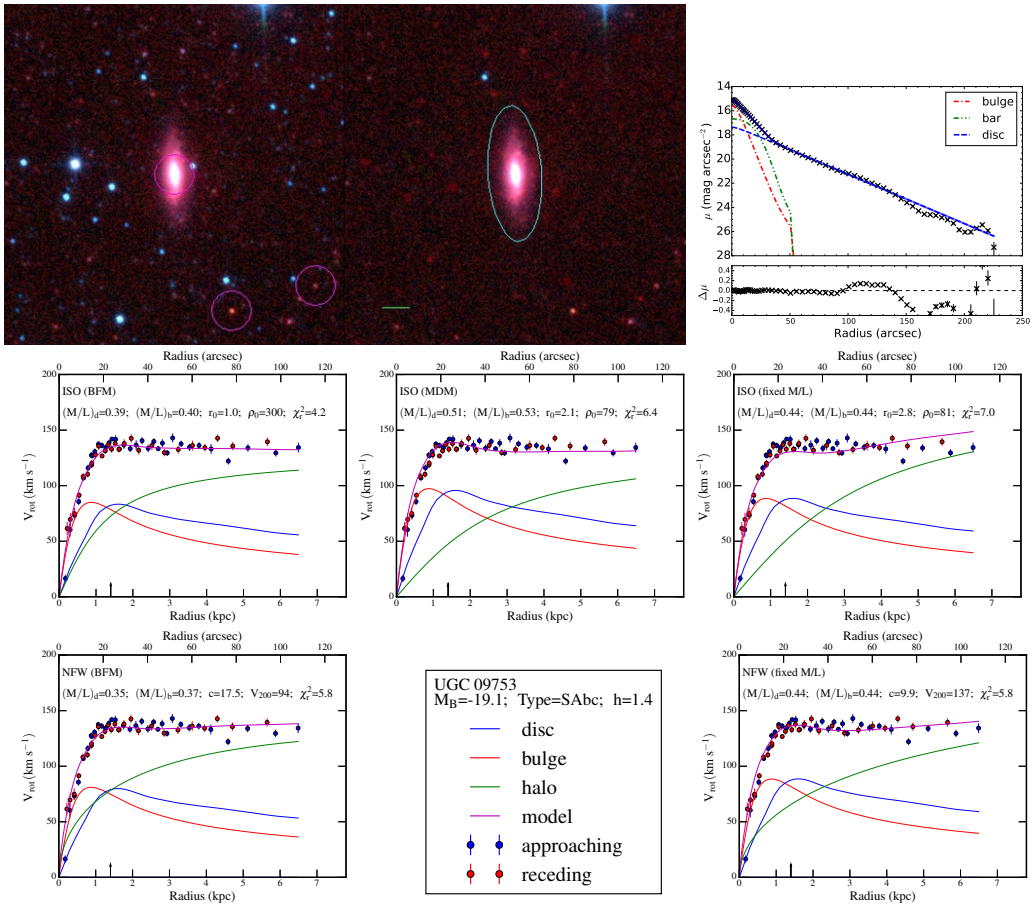
bulge
bar
disc
μ (mag arcsec⁻²)
Δμ
Radius (arcsec)
ISO (BFM)
(M/L)d=0.39; (M/L)b=0.40; r0=1.0; ρ0=300; χr²=4.2
ISO (MDM)
(M/L)d=0.51; (M/L)b=0.53; r0=2.1; ρ0=79; χr²=6.4
ISO (fixed M/L)
(M/L)d=0.44; (M/L)b=0.44; r0=2.8; ρ0=81; χr²=7.0
NFW (BFM)
(M/L)d=0.35; (M/L)b=0.37; c=17.5; V200=94; χr²=5.8
NFW (fixed M/L)
(M/L)d=0.44; (M/L)b=0.44; c=9.9; V200=137; χr²=5.8
Vrot (km s⁻¹)
Radius (kpc)
UGC 09753
MB=-19.1; Type=SAbc; h=1.4
disc
bulge
halo
model
approaching
receding

Figure A.90

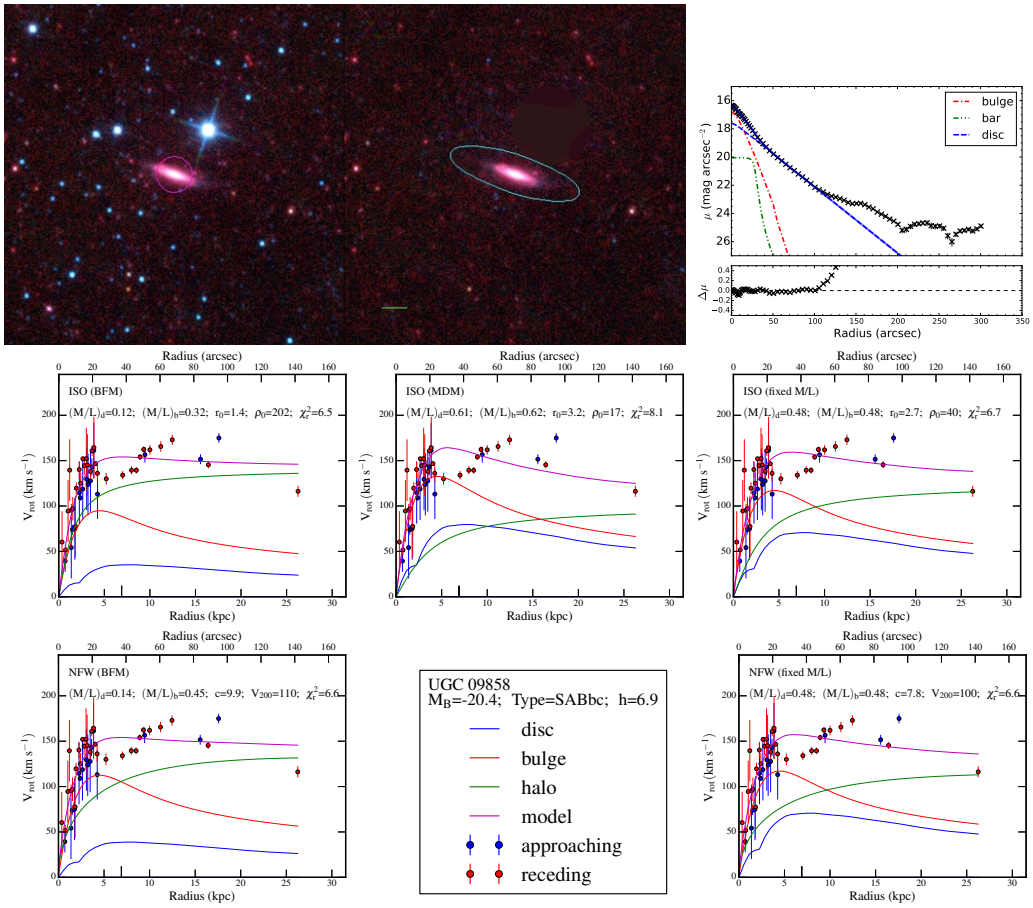
bulge
bar
disc
μ (mag arcsec⁻²)
Δμ
Radius (arcsec)
ISO (BFM)
(M/L)d=0.12; (M/L)b=0.32; r0=1.4; ρ0=202; χ²r=6.5
ISO (MDM)
(M/L)d=0.61; (M/L)b=0.62; r0=3.2; ρ0=17; χ²r=8.1
ISO (fixed M/L)
(M/L)d=0.48; (M/L)b=0.48; r0=2.7; ρ0=40; χ²r=6.7
NFW (BFM)
(M/L)d=0.14; (M/L)b=0.45; c=9.9; V200=110; χ²r=6.6
NFW (fixed M/L)
(M/L)d=0.48; (M/L)b=0.48; c=7.8; V200=100; χ²r=6.6
Vrot (km s⁻¹)
Radius (kpc)
UGC 09858
MB=-20.4; Type=SABbc; h=6.9
disc
bulge
halo
model
approaching
receding

Figure A.91

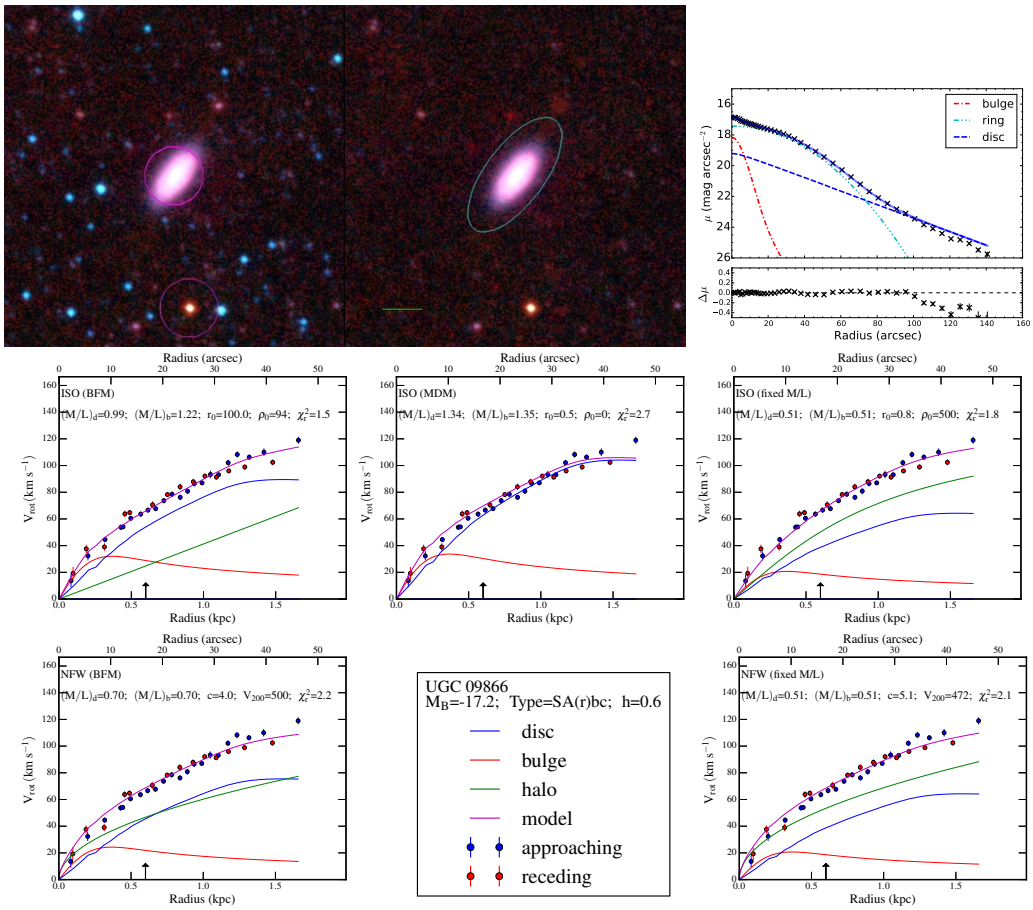
bulge
ring
disc
μ (mag arcsec⁻²)
Δμ
Radius (arcsec)
ISO (BFM)
(M/L)d=0.99; (M/L)h=1.22; r0=100.0; ρ0=94; χ²r=1.5
ISO (MDM)
(M/L)d=1.34; (M/L)h=1.35; r0=0.5; ρ0=0; χ²r=2.7
ISO (fixed M/L)
(M/L)d=0.51; (M/L)h=0.51; r0=0.8; ρ0=500; χ²r=1.8
NFW (BFM)
(M/L)d=0.70; (M/L)h=0.70; c=4.0; V200=500; χ²r=2.2
NFW (fixed M/L)
(M/L)d=0.51; (M/L)h=0.51; c=5.1; V200=472; χ²r=2.1
Vrot (km s⁻¹)
Radius (kpc)
UGC 09866
MB=-17.2; Type=SA(r)bc; h=0.6
disc
bulge
halo
model
approaching
receding

Figure A.92

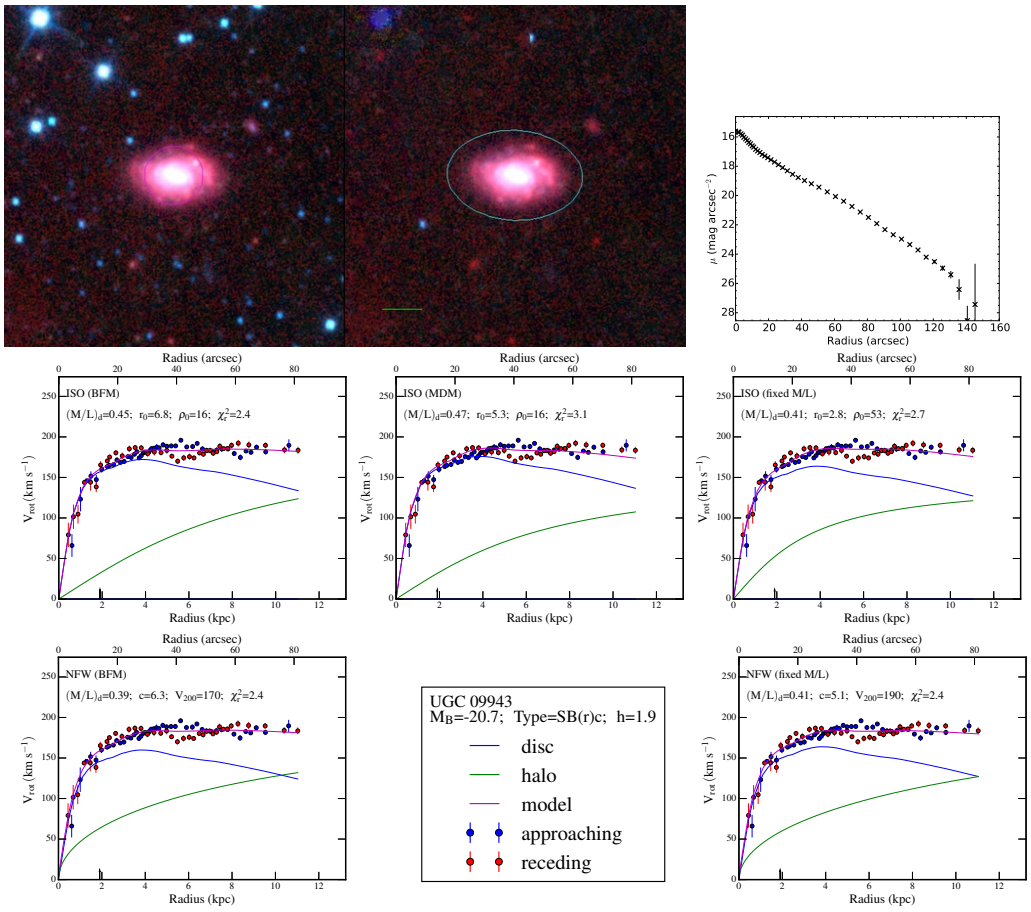
Radius (arcsec)
μ (mag arcsec⁻²)
ISO (BFM)
(M/L)d=0.45; r0=6.8; ρ0=16; χ²r=2.4
ISO (MDM)
(M/L)d=0.47; r0=5.3; ρ0=16; χ²r=3.1
ISO (fixed M/L)
(M/L)d=0.41; r0=2.8; ρ0=53; χ²r=2.7
NFW (BFM)
(M/L)d=0.39; c=6.3; V200=170; χ²r=2.4
NFW (fixed M/L)
(M/L)d=0.41; c=5.1; V200=190; χ²r=2.4
Vrot (km s⁻¹)
Radius (kpc)
UGC 09943
MB=-20.7; Type=SB(r)c; h=1.9
disc
halo
model
approaching
receding

Figure A.93

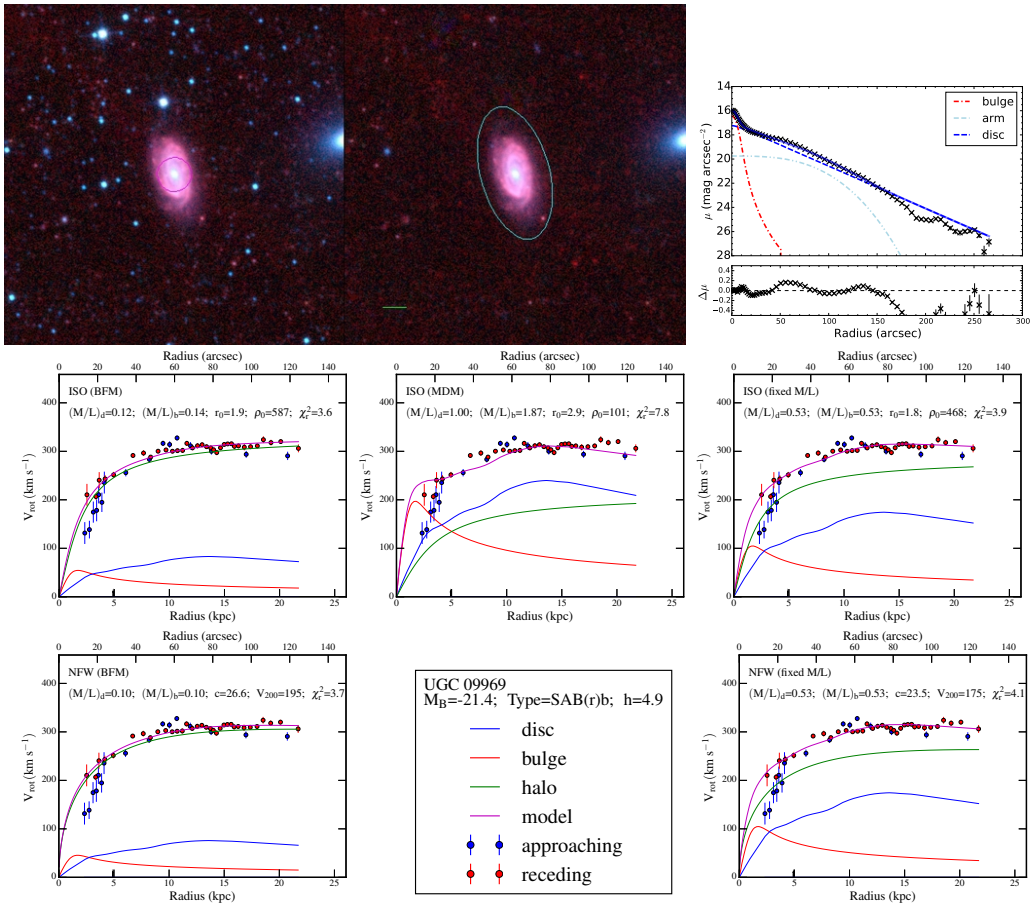
bulge
arm
disc
μ (mag arcsec⁻²)
Δμ
Radius (arcsec)
ISO (BFM)
(M/L)d=0.12; (M/L)h=0.14; r0=1.9; ρ0=587; χ²r=3.6
ISO (MDM)
(M/L)d=1.00; (M/L)h=1.87; r0=2.9; ρ0=101; χ²r=7.8
ISO (fixed M/L)
(M/L)d=0.53; (M/L)h=0.53; r0=1.8; ρ0=468; χ²r=3.9
NFW (BFM)
(M/L)d=0.10; (M/L)h=0.10; c=26.6; V200=195; χ²r=3.7
NFW (fixed M/L)
(M/L)d=0.53; (M/L)h=0.53; c=23.5; V200=175; χ²r=4.1
Vrot (km s⁻¹)
Radius (kpc)
UGC 09969
MB=-21.4; Type=SAB(r)b; h=4.9
disc
bulge
halo
model
approaching
receding

Figure A.94

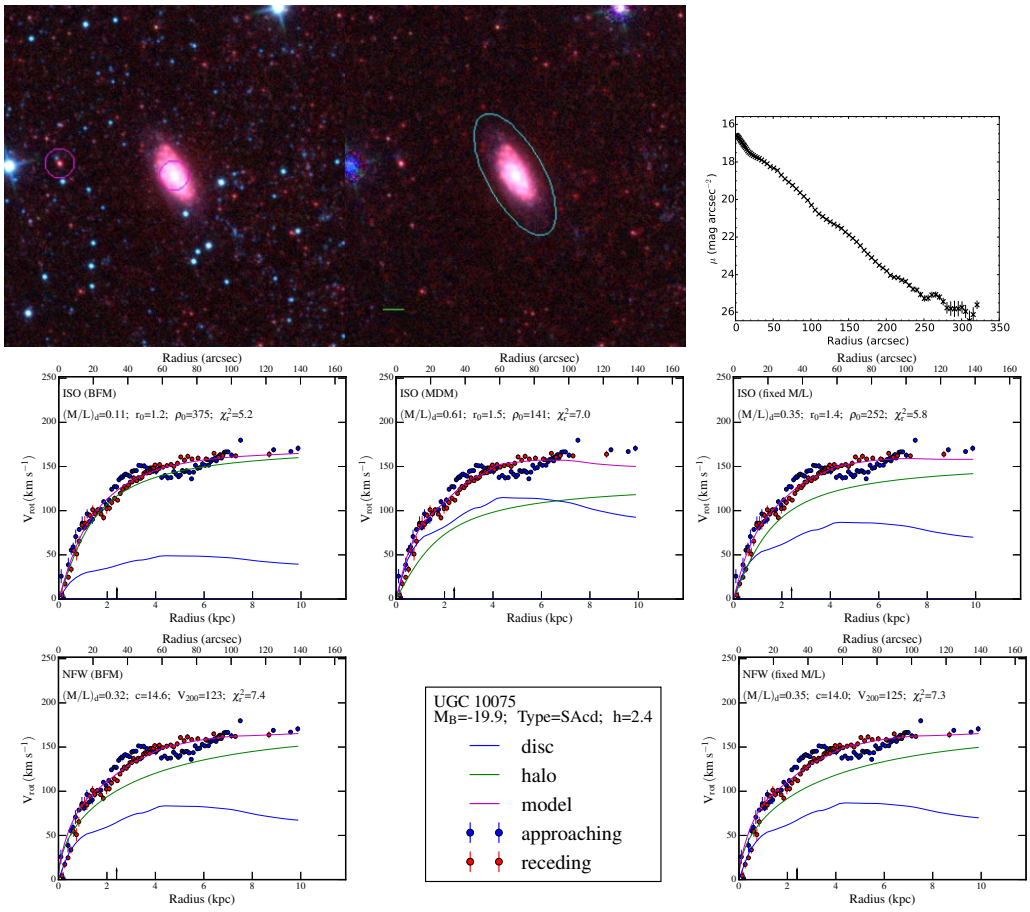
μ (mag arcsec⁻²)
Radius (arcsec)
ISO (BFM)
(M/L)d=0.11; r0=1.2; ρ0=375; χ²r=5.2
ISO (MDM)
(M/L)d=0.61; r0=1.5; ρ0=141; χ²r=7.0
ISO (fixed M/L)
(M/L)d=0.35; r0=1.4; ρ0=252; χ²r=5.8
NFW (BFM)
(M/L)d=0.32; c=14.6; V200=123; χ²r=7.4
NFW (fixed M/L)
(M/L)d=0.35; c=14.0; V200=125; χ²r=7.3
Vrot (km s⁻¹)
Radius (kpc)
UGC 10075
MB=-19.9; Type=SAcd; h=2.4
disc
halo
model
approaching
receding

Figure A.95

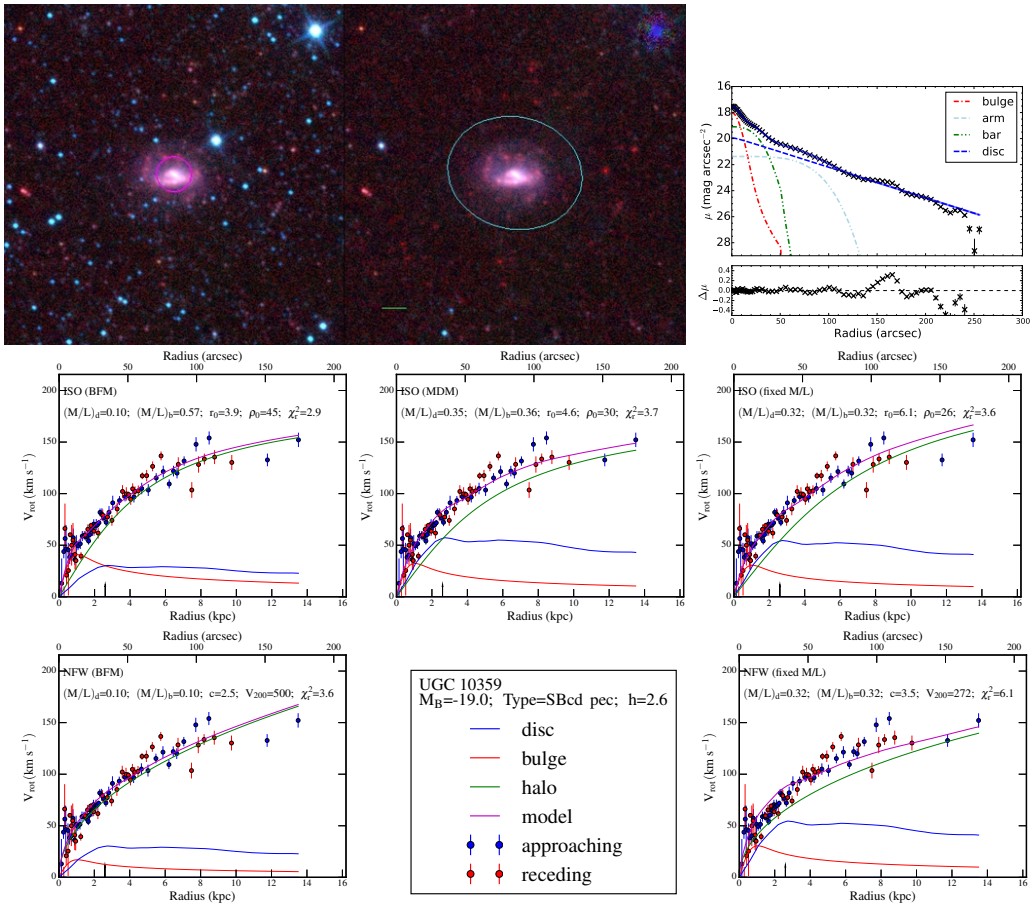
bulge
arm
bar
disc
μ (mag arcsec⁻²)
Δμ
Radius (arcsec)
ISO (BFM)
(M/L)d=0.10; (M/L)b=0.57; r0=3.9; ρ0=45; χ²r=2.9
ISO (MDM)
(M/L)d=0.35; (M/L)b=0.36; r0=4.6; ρ0=30; χ²r=3.7
ISO (fixed M/L)
(M/L)d=0.32; (M/L)b=0.32; r0=6.1; ρ0=26; χ²r=3.6
NFW (BFM)
(M/L)d=0.10; (M/L)b=0.10; c=2.5; V200=500; χ²r=3.6
NFW (fixed M/L)
(M/L)d=0.32; (M/L)b=0.32; c=3.5; V200=272; χ²r=6.1
Vrot (km s⁻¹)
Radius (kpc)
UGC 10359
MB=-19.0; Type=SBcd pec; h=2.6
disc
bulge
halo
model
approaching
receding

Figure A.96

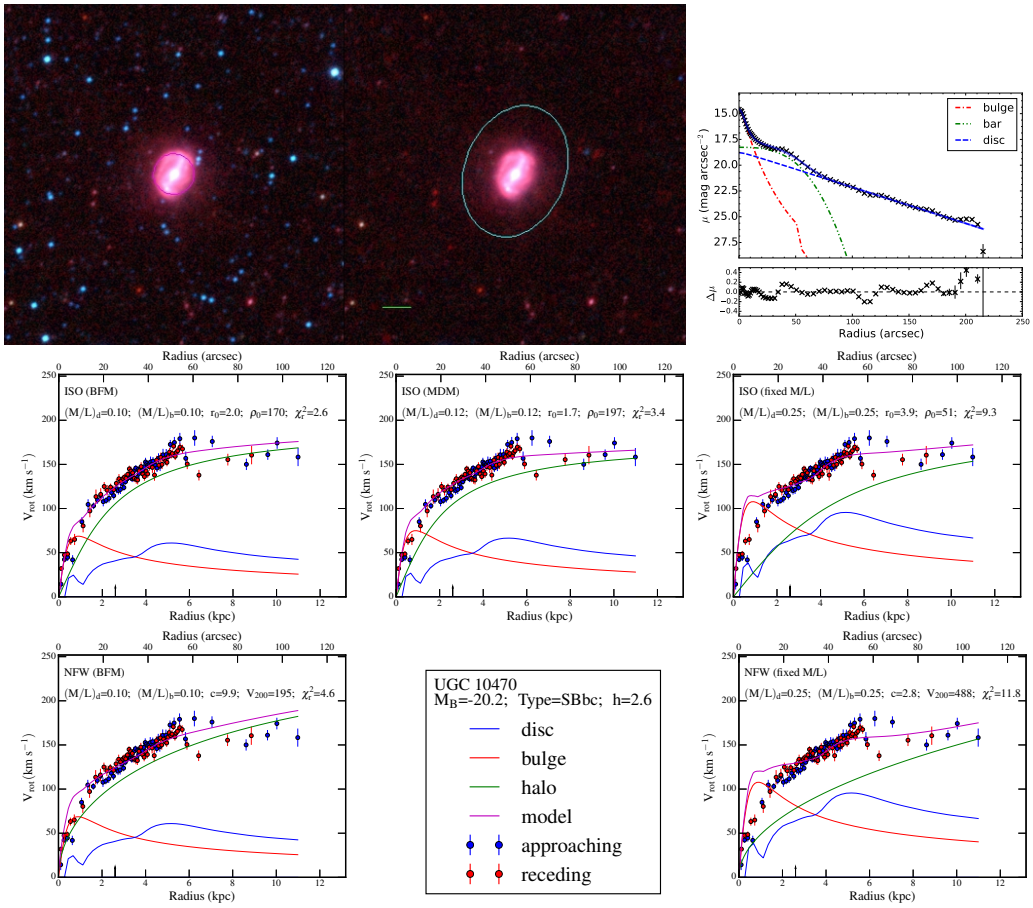
bulge
bar
disc
μ (mag arcsec⁻²)
Δμ
Radius (arcsec)
ISO (BFM)
(M/L)d=0.10; (M/L)b=0.10; r0=2.0; ρ0=170; χr²=2.6
ISO (MDM)
(M/L)d=0.12; (M/L)b=0.12; r0=1.7; ρ0=197; χr²=3.4
ISO (fixed M/L)
(M/L)d=0.25; (M/L)b=0.25; r0=3.9; ρ0=51; χr²=9.3
NFW (BFM)
(M/L)d=0.10; (M/L)b=0.10; c=9.9; V200=195; χr²=4.6
NFW (fixed M/L)
(M/L)d=0.25; (M/L)b=0.25; c=2.8; V200=488; χr²=11.8
Vrot (km s⁻¹)
Radius (kpc)
UGC 10470
MB=-20.2; Type=SBbc; h=2.6
disc
bulge
halo
model
approaching
receding

Figure A.97

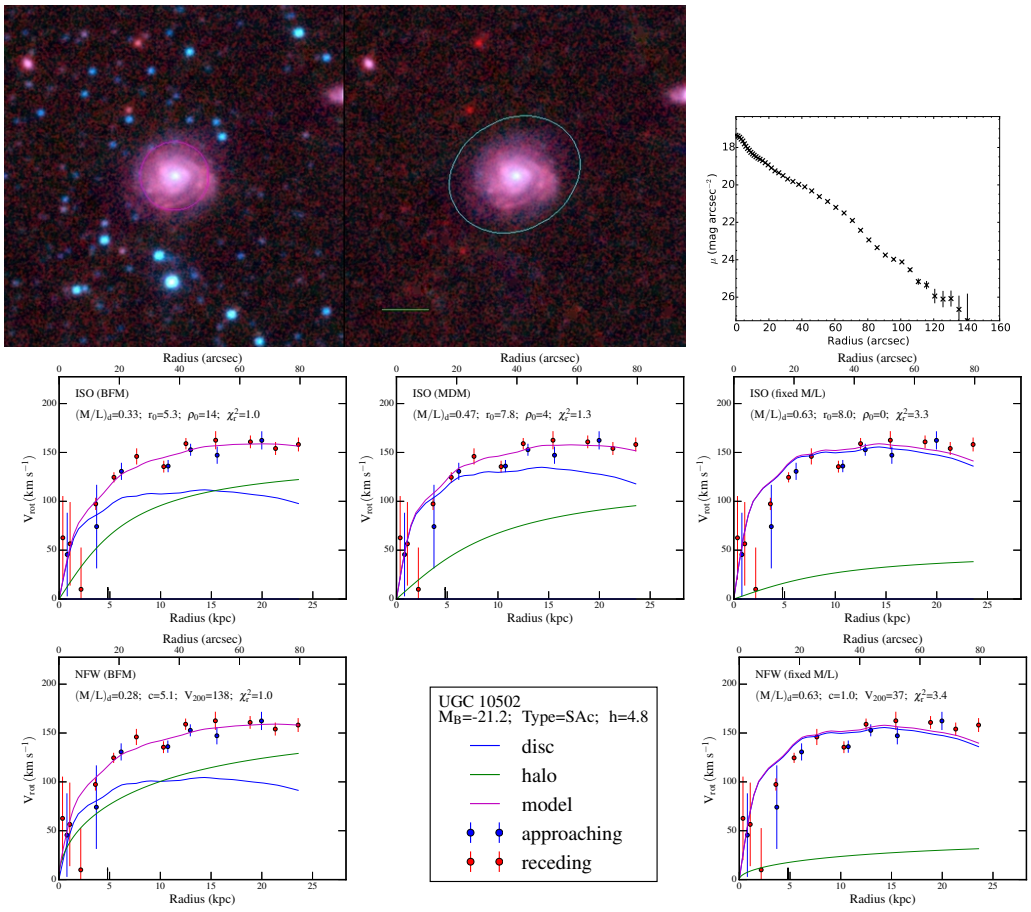
μ (mag arcsec⁻²)
Radius (arcsec)
ISO (BFM)
(M/L)d=0.33; r0=5.3; ρ0=14; χ²r=1.0
ISO (MDM)
(M/L)d=0.47; r0=7.8; ρ0=4; χ²r=1.3
ISO (fixed M/L)
(M/L)d=0.63; r0=8.0; ρ0=0; χ²r=3.3
NFW (BFM)
(M/L)d=0.28; c=5.1; V200=138; χ²r=1.0
NFW (fixed M/L)
(M/L)d=0.63; c=1.0; V200=37; χ²r=3.4
Vrot (km s⁻¹)
Radius (kpc)
UGC 10502
MB=-21.2; Type=SAc; h=4.8
disc
halo
model
approaching
receding

Figure A.98

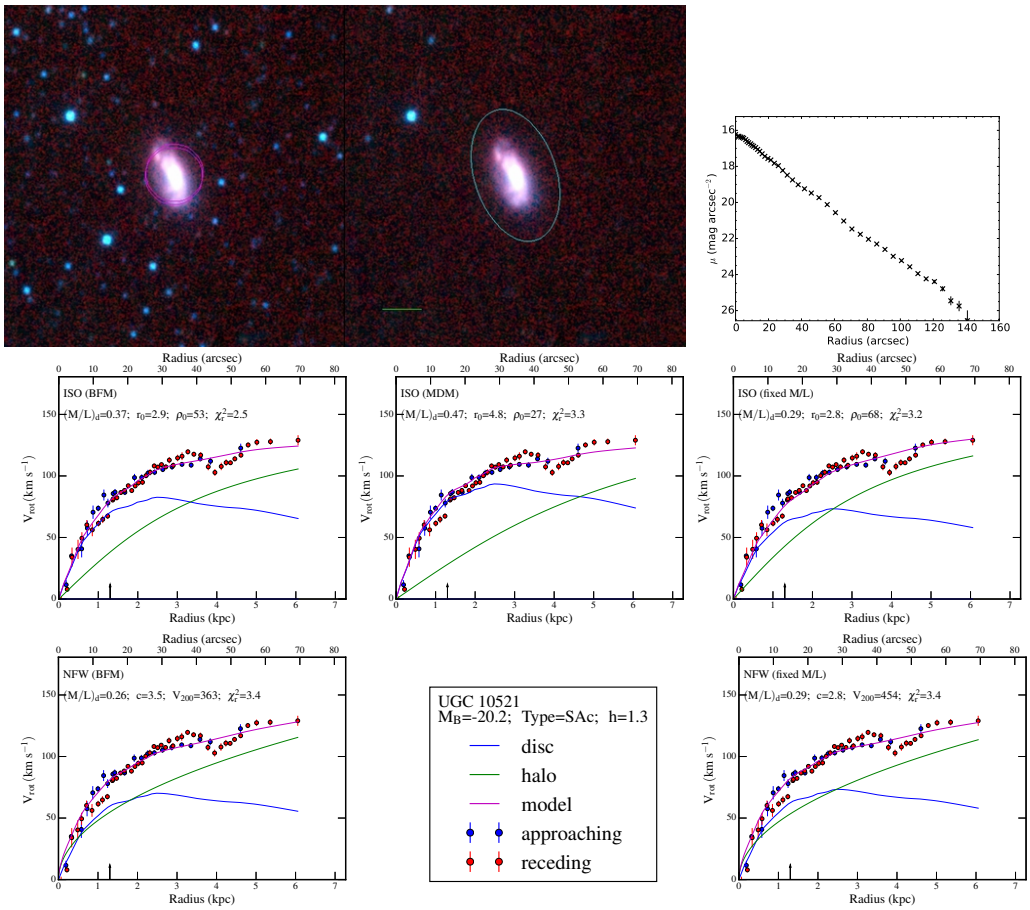
Radius (arcsec)
μ (mag arcsec⁻²)
ISO (BFM)
(M/L)d=0.37; r0=2.9; ρ0=53; χr²=2.5
ISO (MDM)
(M/L)d=0.47; r0=4.8; ρ0=27; χr²=3.3
ISO (fixed M/L)
(M/L)d=0.29; r0=2.8; ρ0=68; χr²=3.2
NFW (BFM)
(M/L)d=0.26; c=3.5; V200=363; χr²=3.4
NFW (fixed M/L)
(M/L)d=0.29; c=2.8; V200=454; χr²=3.4
Vrot (km s⁻¹)
Radius (kpc)
UGC 10521
MB=-20.2; Type=SAc; h=1.3
disc
halo
model
approaching
receding

Figure A.99

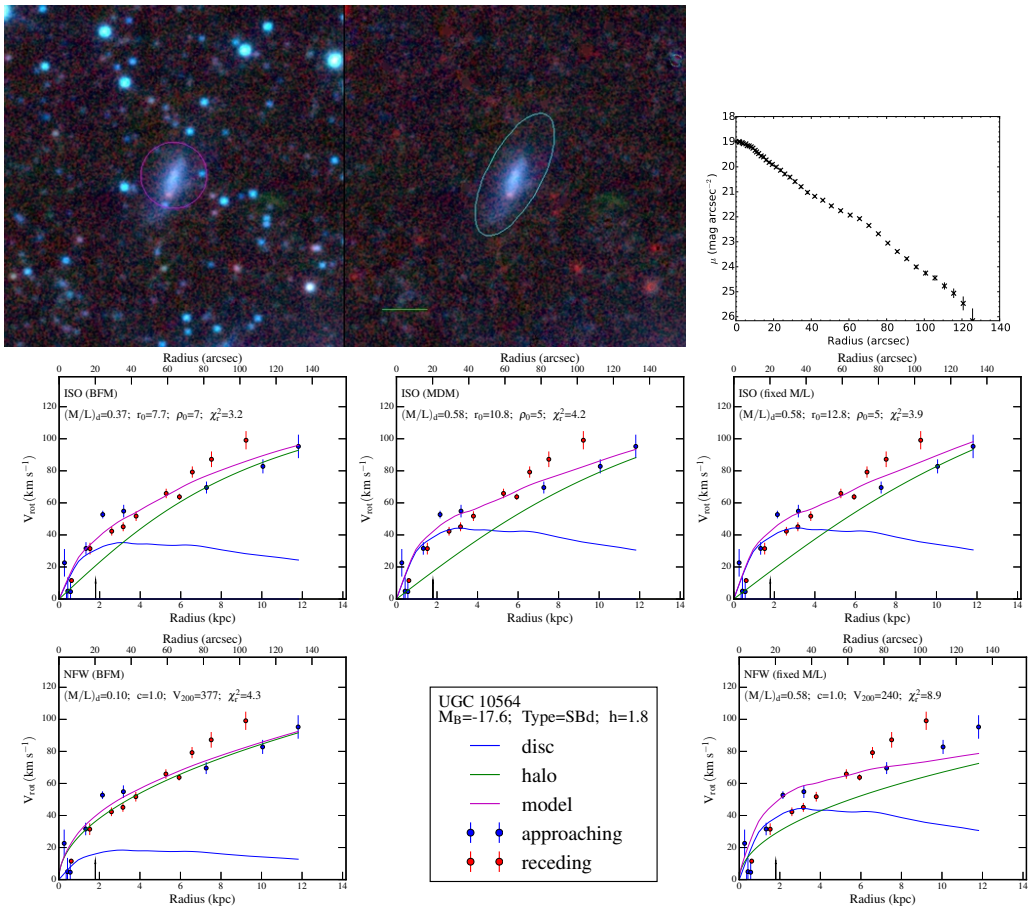
μ (mag arcsec⁻²)
Radius (arcsec)
ISO (BFM)
(M/L)d=0.37; r0=7.7; ρ0=7; χ²r=3.2
ISO (MDM)
(M/L)d=0.58; r0=10.8; ρ0=5; χ²r=4.2
ISO (fixed M/L)
(M/L)d=0.58; r0=12.8; ρ0=5; χ²r=3.9
NFW (BFM)
(M/L)d=0.10; c=1.0; V200=377; χ²r=4.3
NFW (fixed M/L)
(M/L)d=0.58; c=1.0; V200=240; χ²r=8.9
Vrot (km s⁻¹)
Radius (kpc)
UGC 10564
MB=-17.6; Type=SBd; h=1.8
disc
halo
model
approaching
receding

Figure A.100

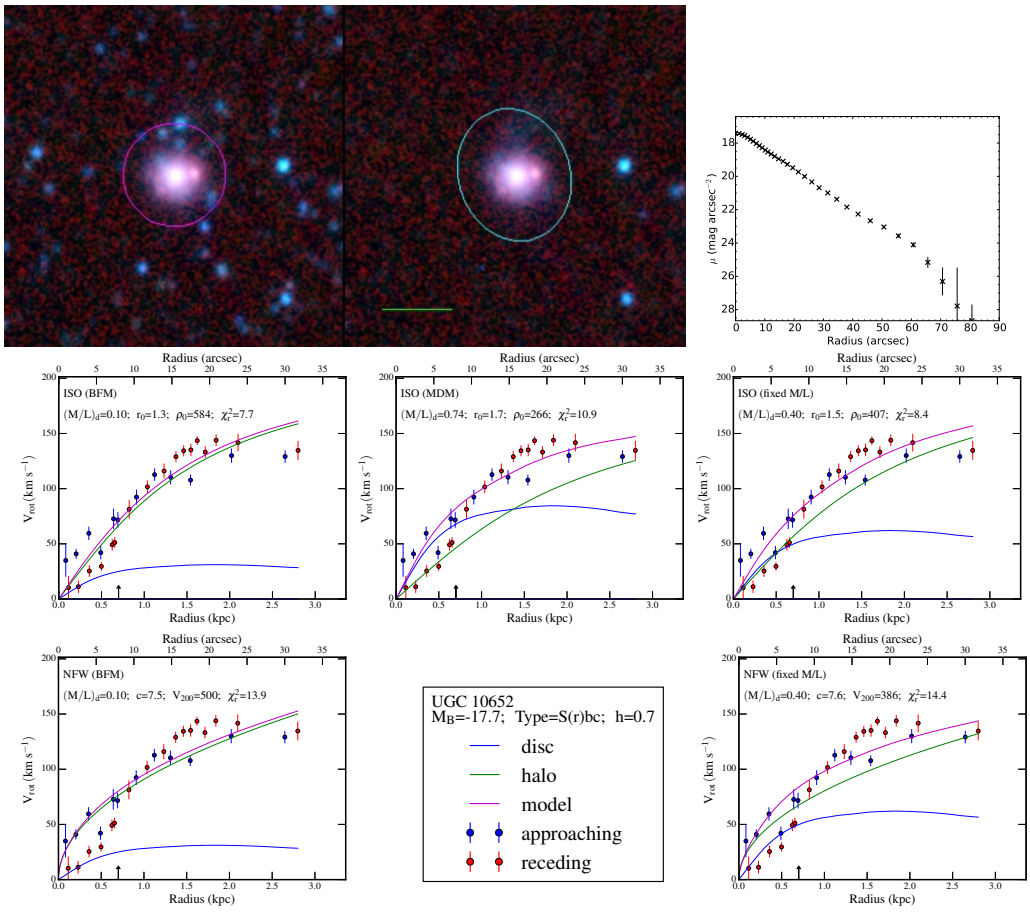
Radius (arcsec)
μ (mag arcsec⁻²)
ISO (BFM)
(M/L)d=0.10; r0=1.3; ρ0=584; χ²r=7.7
ISO (MDM)
(M/L)d=0.74; r0=1.7; ρ0=266; χ²r=10.9
ISO (fixed M/L)
(M/L)d=0.40; r0=1.5; ρ0=407; χ²r=8.4
NFW (BFM)
(M/L)d=0.10; c=7.5; V200=500; χ²r=13.9
NFW (fixed M/L)
(M/L)d=0.40; c=7.6; V200=386; χ²r=14.4
Vrot (km s⁻¹)
Radius (kpc)
UGC 10652
MB=-17.7; Type=S(r)bc; h=0.7
disc
halo
model
approaching
receding

Figure A.101

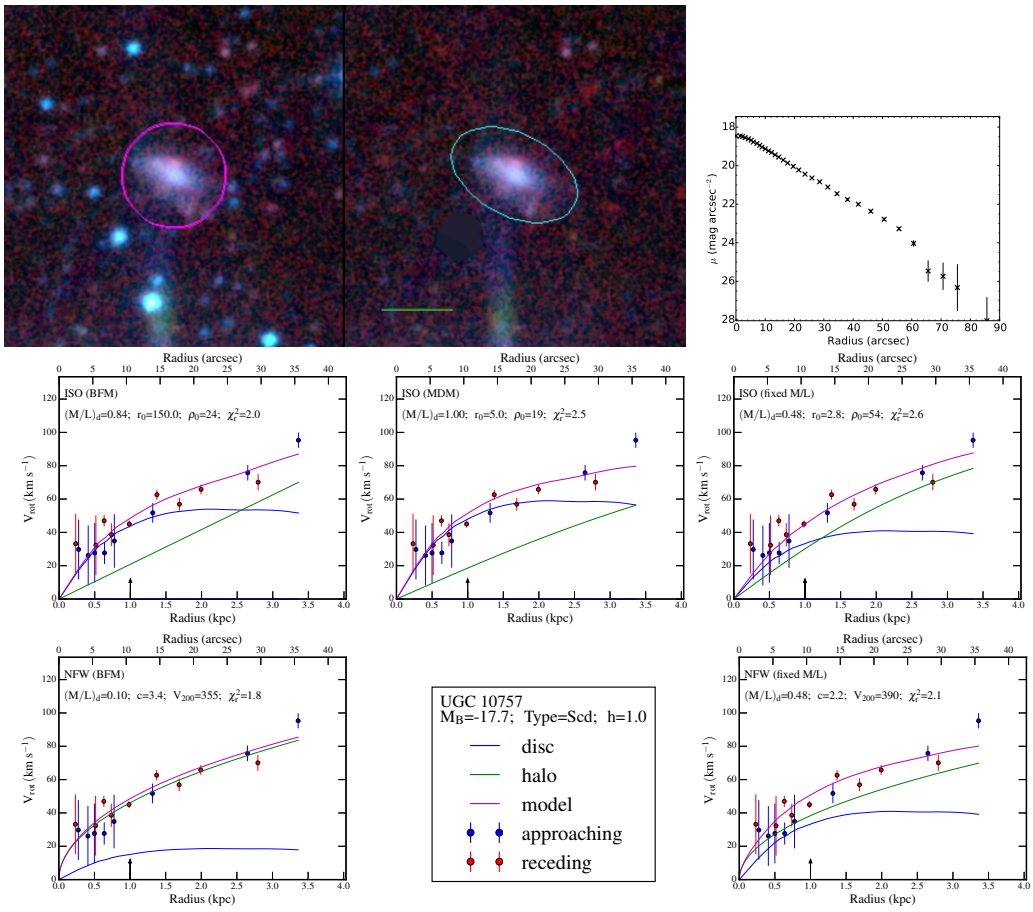
μ (mag arcsec⁻²)
Radius (arcsec)
ISO (BFM)
(M/L)d=0.84; r0=150.0; ρ0=24; χ²r=2.0
ISO (MDM)
(M/L)d=1.00; r0=5.0; ρ0=19; χ²r=2.5
ISO (fixed M/L)
(M/L)d=0.48; r0=2.8; ρ0=54; χ²r=2.6
NFW (BFM)
(M/L)d=0.10; c=3.4; V200=355; χ²r=1.8
NFW (fixed M/L)
(M/L)d=0.48; c=2.2; V200=390; χ²r=2.1
Vrot (km s⁻¹)
Radius (kpc)
UGC 10757
MB=-17.7; Type=Scd; h=1.0
disc
halo
model
approaching
receding

Figure A.102

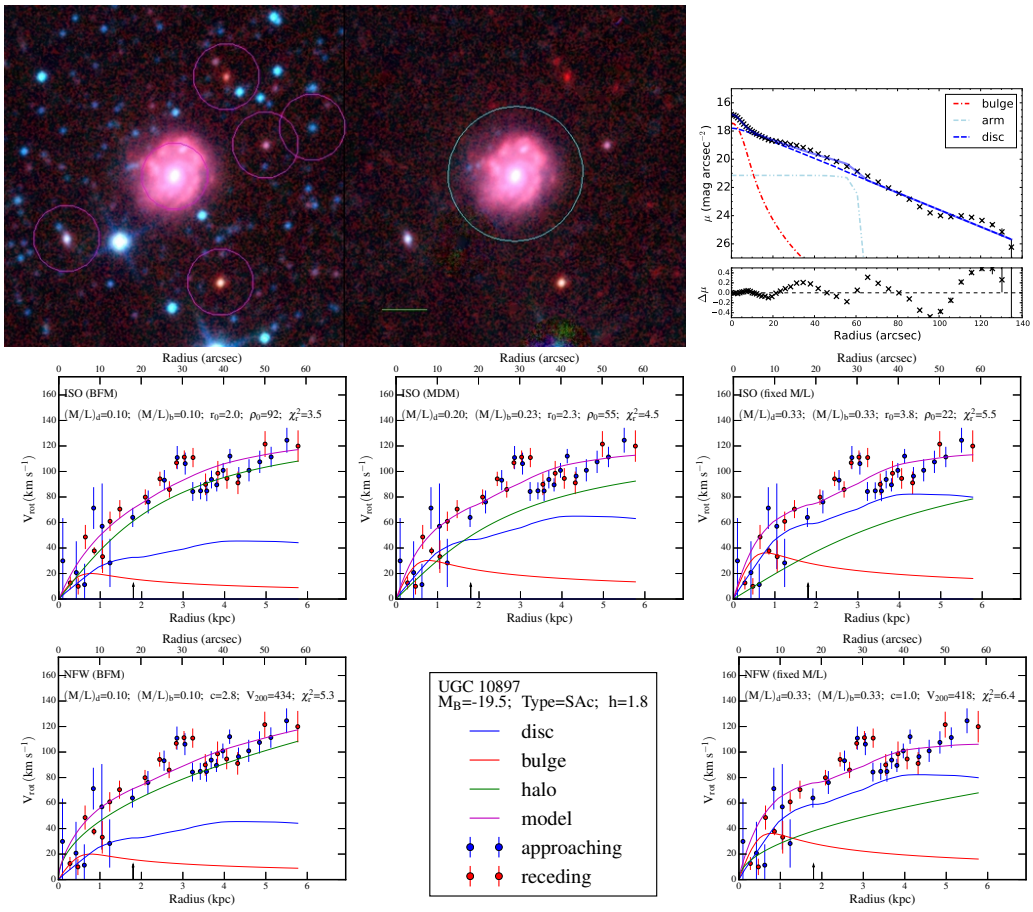
bulge
arm
disc
μ (mag arcsec⁻²)
Δμ
Radius (arcsec)
ISO (BFM)
(M/L)d=0.10; (M/L)b=0.10; r0=2.0; ρ0=92; χ²r=3.5
ISO (MDM)
(M/L)d=0.20; (M/L)b=0.23; r0=2.3; ρ0=55; χ²r=4.5
ISO (fixed M/L)
(M/L)d=0.33; (M/L)b=0.33; r0=3.8; ρ0=22; χ²r=5.5
NFW (BFM)
(M/L)d=0.10; (M/L)b=0.10; c=2.8; V200=434; χ²r=5.3
NFW (fixed M/L)
(M/L)d=0.33; (M/L)b=0.33; c=1.0; V200=418; χ²r=6.4
Vrot (km s⁻¹)
Radius (kpc)
UGC 10897
MB=-19.5; Type=SAc; h=1.8
disc
bulge
halo
model
approaching
receding

Figure A.103

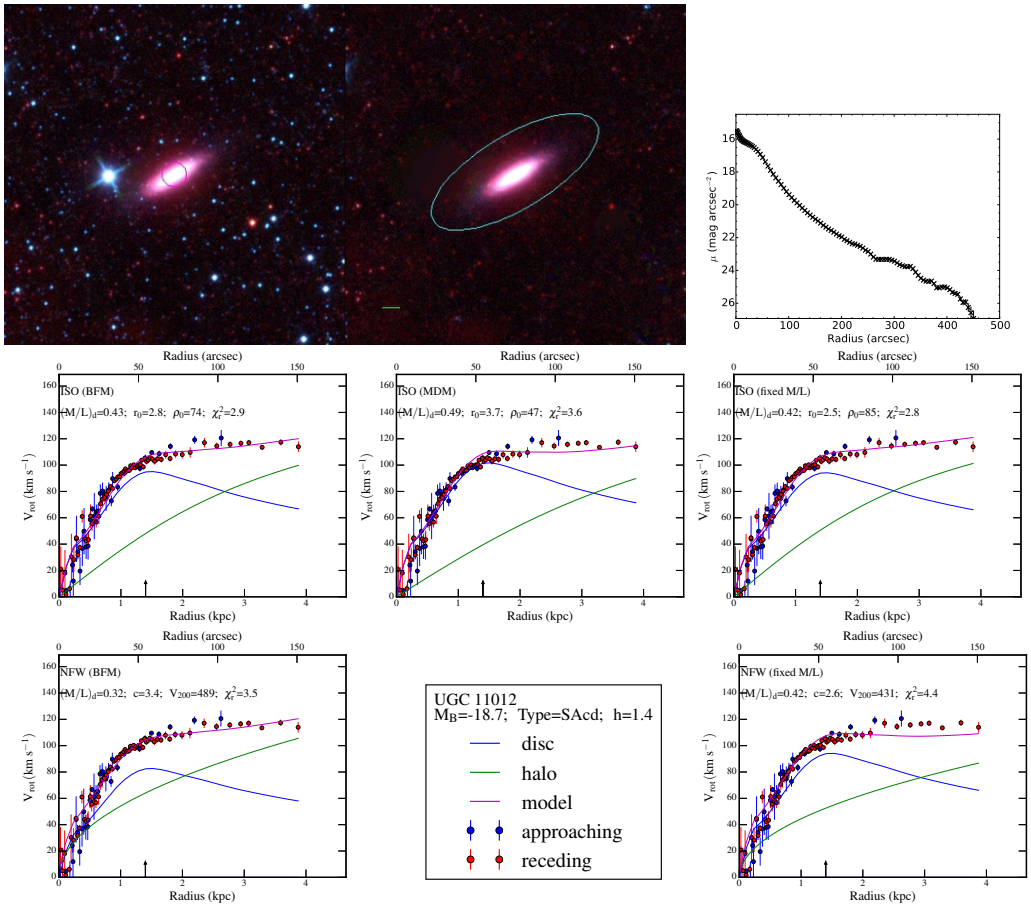
μ (mag arcsec⁻²)
Radius (arcsec)
ISO (BFM)
(M/L)d=0.43; r0=2.8; ρ0=74; χ²r=2.9
ISO (MDM)
(M/L)d=0.49; r0=3.7; ρ0=47; χ²r=3.6
ISO (fixed M/L)
(M/L)d=0.42; r0=2.5; ρ0=85; χ²r=2.8
NFW (BFM)
(M/L)d=0.32; c=3.4; V200=489; χ²r=3.5
NFW (fixed M/L)
(M/L)d=0.42; c=2.6; V200=431; χ²r=4.4
Vrot (km s⁻¹)
Radius (kpc)
UGC 11012
MB=-18.7; Type=SAcd; h=1.4
disc
halo
model
approaching
receding

Figure A.104

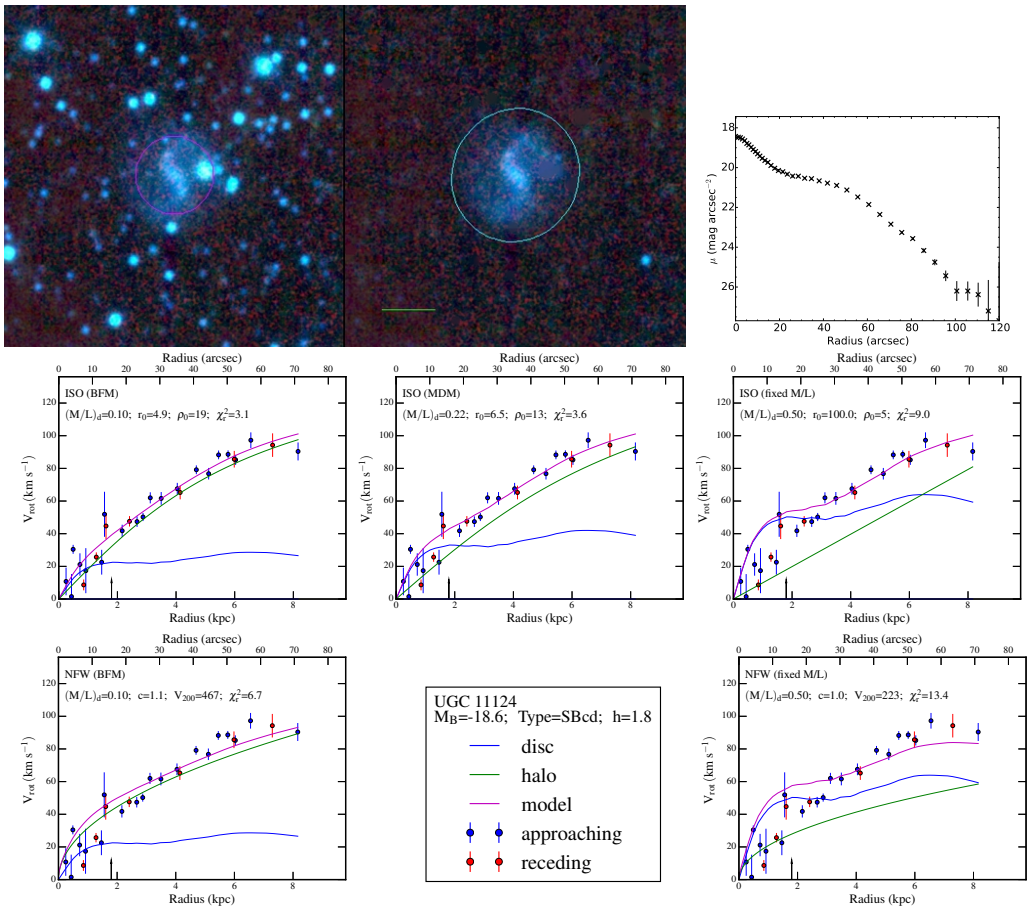
μ (mag arcsec⁻²)
Radius (arcsec)
ISO (BFM)
(M/L)d=0.10; r0=4.9; ρ0=19; χ²r=3.1
ISO (MDM)
(M/L)d=0.22; r0=6.5; ρ0=13; χ²r=3.6
ISO (fixed M/L)
(M/L)d=0.50; r0=100.0; ρ0=5; χ²r=9.0
NFW (BFM)
(M/L)d=0.10; c=1.1; V200=467; χ²r=6.7
NFW (fixed M/L)
(M/L)d=0.50; c=1.0; V200=223; χ²r=13.4
Vrot (km s⁻¹)
Radius (kpc)
UGC 11124
MB=-18.6; Type=SBcd; h=1.8
disc
halo
model
approaching
receding

Figure A.105

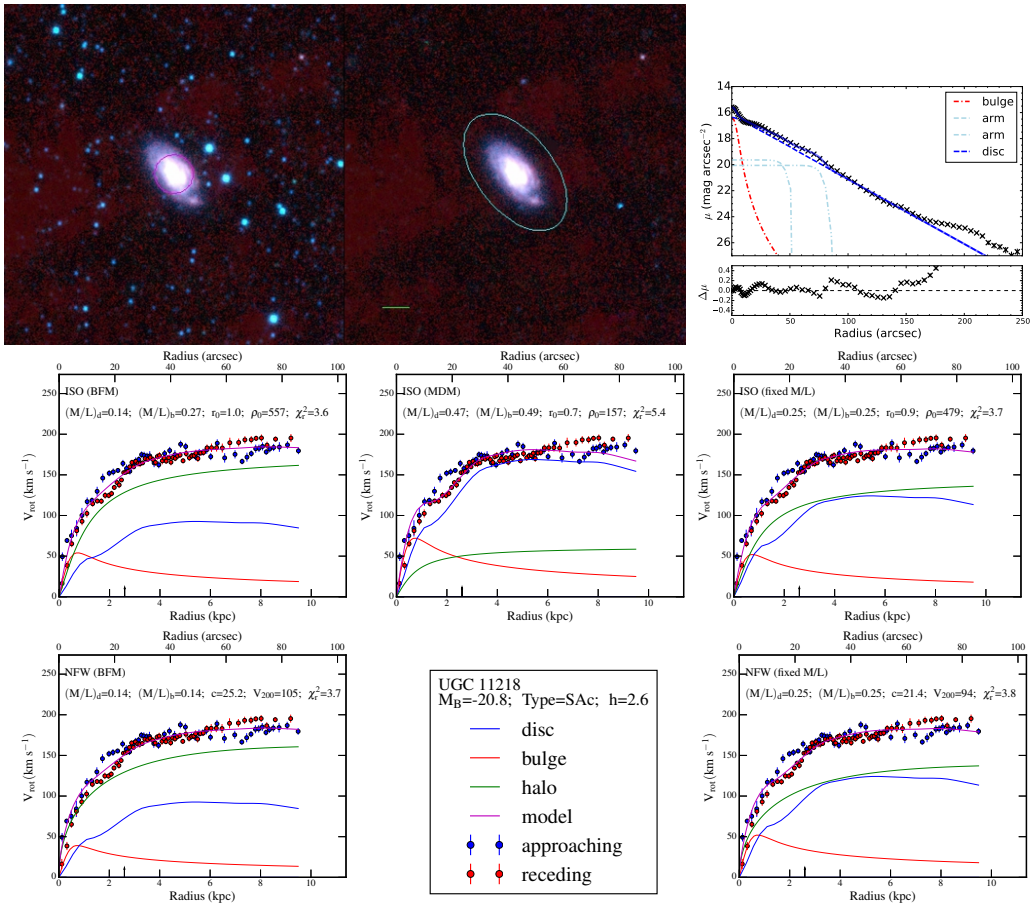
bulge
arm
arm
disc
μ (mag arcsec⁻²)
Δμ
Radius (arcsec)
ISO (BFM)
(M/L)d=0.14; (M/L)b=0.27; r0=1.0; ρ0=557; χ²r=3.6
ISO (MDM)
(M/L)d=0.47; (M/L)b=0.49; r0=0.7; ρ0=157; χ²r=5.4
ISO (fixed M/L)
(M/L)d=0.25; (M/L)b=0.25; r0=0.9; ρ0=479; χ²r=3.7
NFW (BFM)
(M/L)d=0.14; (M/L)b=0.14; c=25.2; V200=105; χ²r=3.7
NFW (fixed M/L)
(M/L)d=0.25; (M/L)b=0.25; c=21.4; V200=94; χ²r=3.8
Vrot (km s⁻¹)
Radius (kpc)
UGC 11218
MB=-20.8; Type=SAc; h=2.6
disc
bulge
halo
model
approaching
receding

Figure A.106

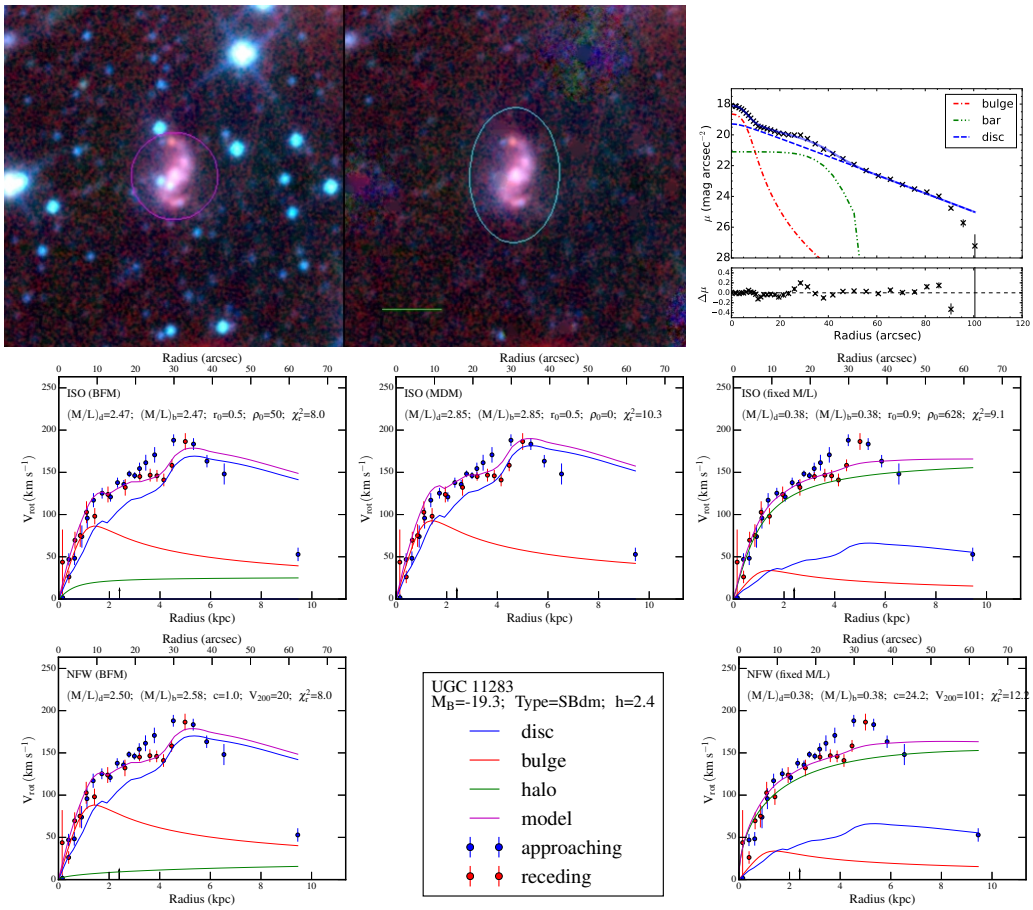
bulge
bar
disc
μ (mag arcsec⁻²)
Δμ
Radius (arcsec)
ISO (BFM)
(M/L)d=2.47; (M/L)h=2.47; r0=0.5; ρ0=50; χ²r=8.0
ISO (MDM)
(M/L)d=2.85; (M/L)h=2.85; r0=0.5; ρ0=0; χ²r=10.3
ISO (fixed M/L)
(M/L)d=0.38; (M/L)h=0.38; r0=0.9; ρ0=628; χ²r=9.1
NFW (BFM)
(M/L)d=2.50; (M/L)h=2.58; c=1.0; V200=20; χ²r=8.0
NFW (fixed M/L)
(M/L)d=0.38; (M/L)h=0.38; c=24.2; V200=101; χ²r=12.2
Vrot (km s⁻¹)
Radius (kpc)
UGC 11283
MB=-19.3; Type=SBdm; h=2.4
disc
bulge
halo
model
approaching
receding

Figure A.107

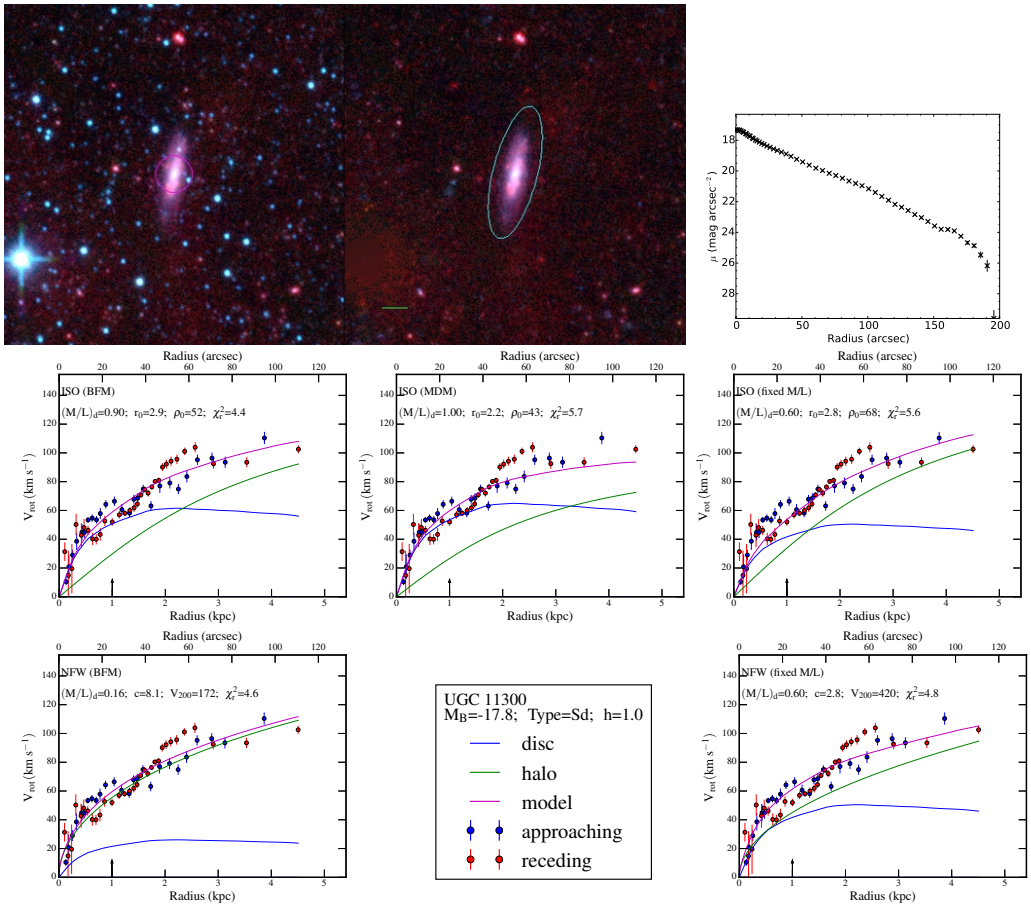
μ (mag arcsec⁻²)
Radius (arcsec)
ISO (BFM)
(M/L)d=0.90; r0=2.9; ρ0=52; χ²r=4.4
ISO (MDM)
(M/L)d=1.00; r0=2.2; ρ0=43; χ²r=5.7
ISO (fixed M/L)
(M/L)d=0.60; r0=2.8; ρ0=68; χ²r=5.6
NFW (BFM)
(M/L)d=0.16; c=8.1; V200=172; χ²r=4.6
NFW (fixed M/L)
(M/L)d=0.60; c=2.8; V200=420; χ²r=4.8
Vrot (km s⁻¹)
Radius (kpc)
UGC 11300
MB=-17.8; Type=Sd; h=1.0
disc
halo
model
approaching
receding

Figure A.108

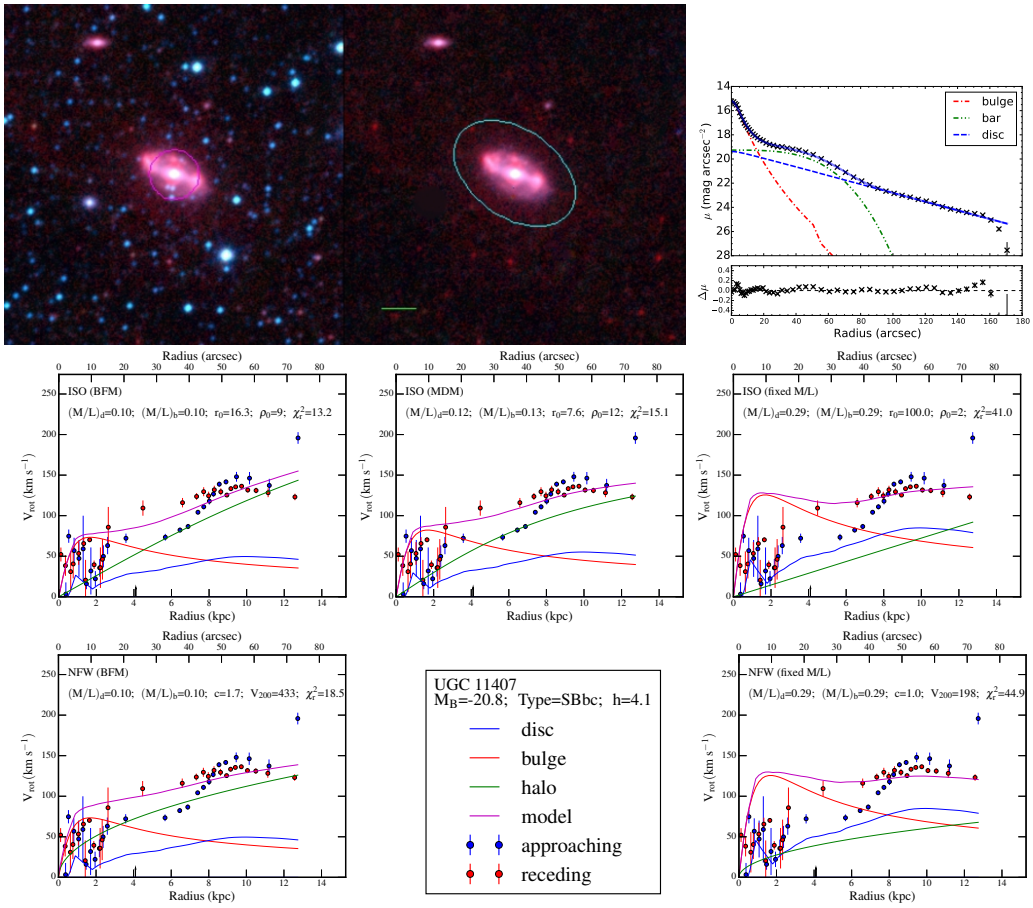
bulge
bar
disc
μ (mag arcsec⁻²)
Δμ
Radius (arcsec)
ISO (BFM)
(M/L)d=0.10; (M/L)b=0.10; r0=16.3; ρ0=9; χ²r=13.2
ISO (MDM)
(M/L)d=0.12; (M/L)b=0.13; r0=7.6; ρ0=12; χ²r=15.1
ISO (fixed M/L)
(M/L)d=0.29; (M/L)b=0.29; r0=100.0; ρ0=2; χ²r=41.0
NFW (BFM)
(M/L)d=0.10; (M/L)b=0.10; c=1.7; V200=433; χ²r=18.5
NFW (fixed M/L)
(M/L)d=0.29; (M/L)b=0.29; c=1.0; V200=198; χ²r=44.9
Vrot (km s⁻¹)
Radius (kpc)
UGC 11407
MB=-20.8; Type=SBbc; h=4.1
disc
bulge
halo
model
approaching
receding

Figure A.109

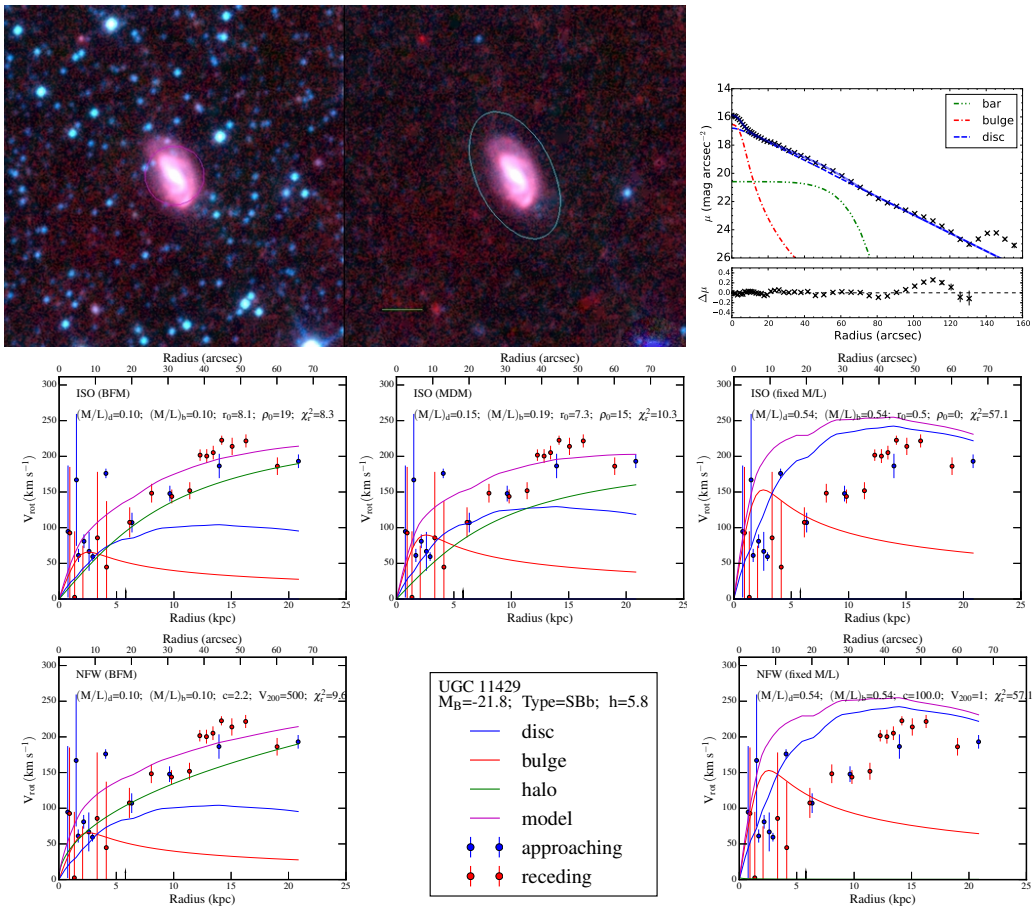
bar
bulge
disc
μ (mag arcsec⁻²)
Δμ
Radius (arcsec)
ISO (BFM)
(M/L)d=0.10; (M/L)h=0.10; r0=8.1; ρ0=19; χ²r=8.3
ISO (MDM)
(M/L)d=0.15; (M/L)h=0.19; r0=7.3; ρ0=15; χ²r=10.3
ISO (fixed M/L)
(M/L)d=0.54; (M/L)h=0.54; r0=0.5; ρ0=0; χ²r=57.1
NFW (BFM)
(M/L)d=0.10; (M/L)h=0.10; c=2.2; V200=500; χ²r=9.6
NFW (fixed M/L)
(M/L)d=0.54; (M/L)h=0.54; c=100.0; V200=1; χ²r=57.1
Vrot (km s⁻¹)
Radius (kpc)
UGC 11429
MB=-21.8; Type=SBb; h=5.8
disc
bulge
halo
model
approaching
receding

Figure A.110

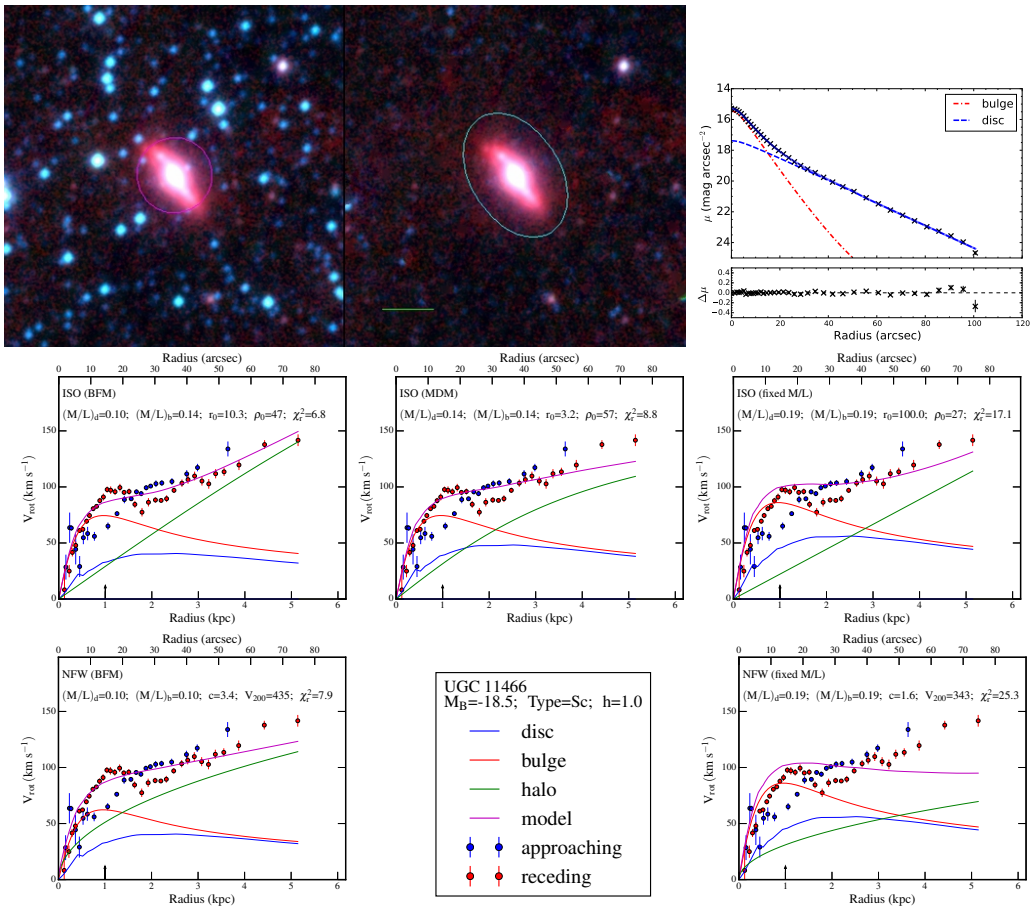
bulge
disc
μ (mag arcsec⁻²)
Δμ
Radius (arcsec)
ISO (BFM)
(M/L)d=0.10; (M/L)b=0.14; r0=10.3; ρ0=47; χ²r=6.8
ISO (MDM)
(M/L)d=0.14; (M/L)b=0.14; r0=3.2; ρ0=57; χ²r=8.8
ISO (fixed M/L)
(M/L)d=0.19; (M/L)b=0.19; r0=100.0; ρ0=27; χ²r=17.1
NFW (BFM)
(M/L)d=0.10; (M/L)b=0.10; c=3.4; V200=435; χ²r=7.9
NFW (fixed M/L)
(M/L)d=0.19; (M/L)b=0.19; c=1.6; V200=343; χ²r=25.3
Vrot (km s⁻¹)
Radius (kpc)
UGC 11466
MB=-18.5; Type=Sc; h=1.0
disc
bulge
halo
model
approaching
receding

Figure A.111

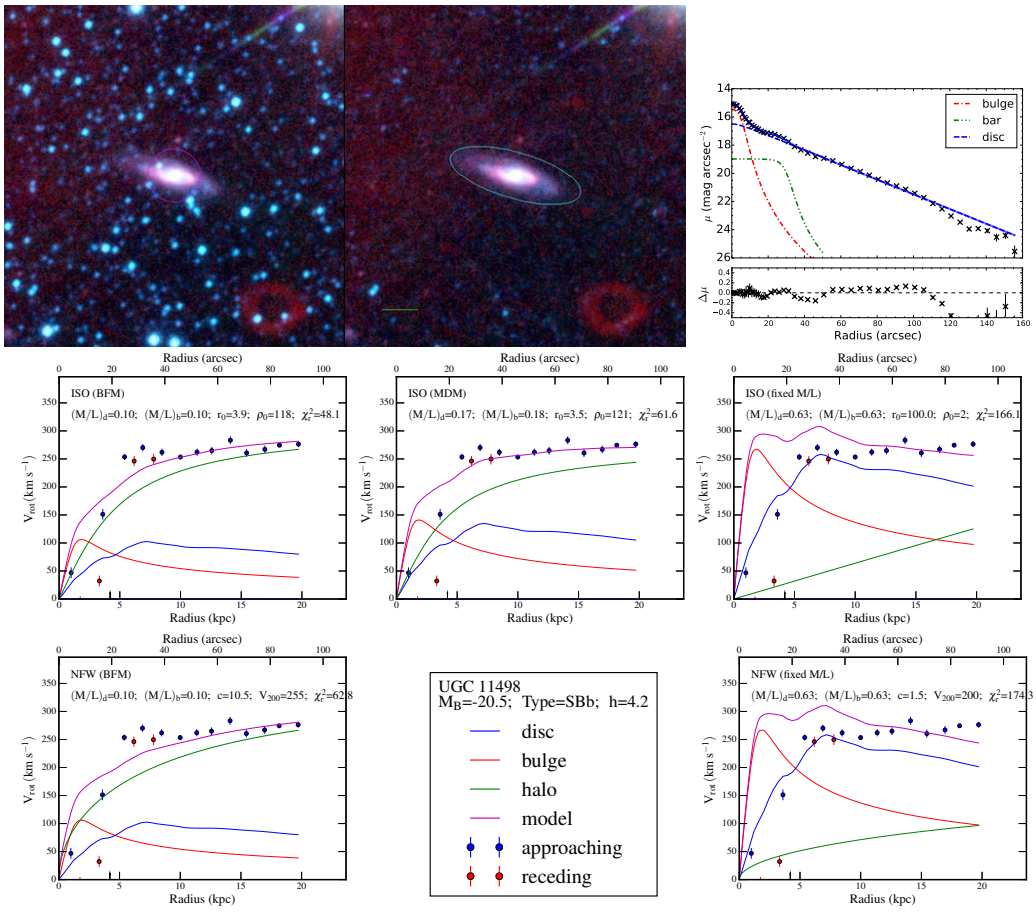
bulge
bar
disc
μ (mag arcsec⁻²)
Δμ
Radius (arcsec)
ISO (BFM)
(M/L)d=0.10; (M/L)b=0.10; r0=3.9; ρ0=118; χr²=48.1
ISO (MDM)
(M/L)d=0.17; (M/L)b=0.18; r0=3.5; ρ0=121; χr²=61.6
ISO (fixed M/L)
(M/L)d=0.63; (M/L)b=0.63; r0=100.0; ρ0=2; χr²=166.1
NFW (BFM)
(M/L)d=0.10; (M/L)b=0.10; c=10.5; V200=255; χr²=62.8
NFW (fixed M/L)
(M/L)d=0.63; (M/L)b=0.63; c=1.5; V200=200; χr²=174.3
Vrot (km s⁻¹)
Radius (kpc)
UGC 11498
MB=-20.5; Type=SBb; h=4.2
disc
bulge
halo
model
approaching
receding

Figure A.112

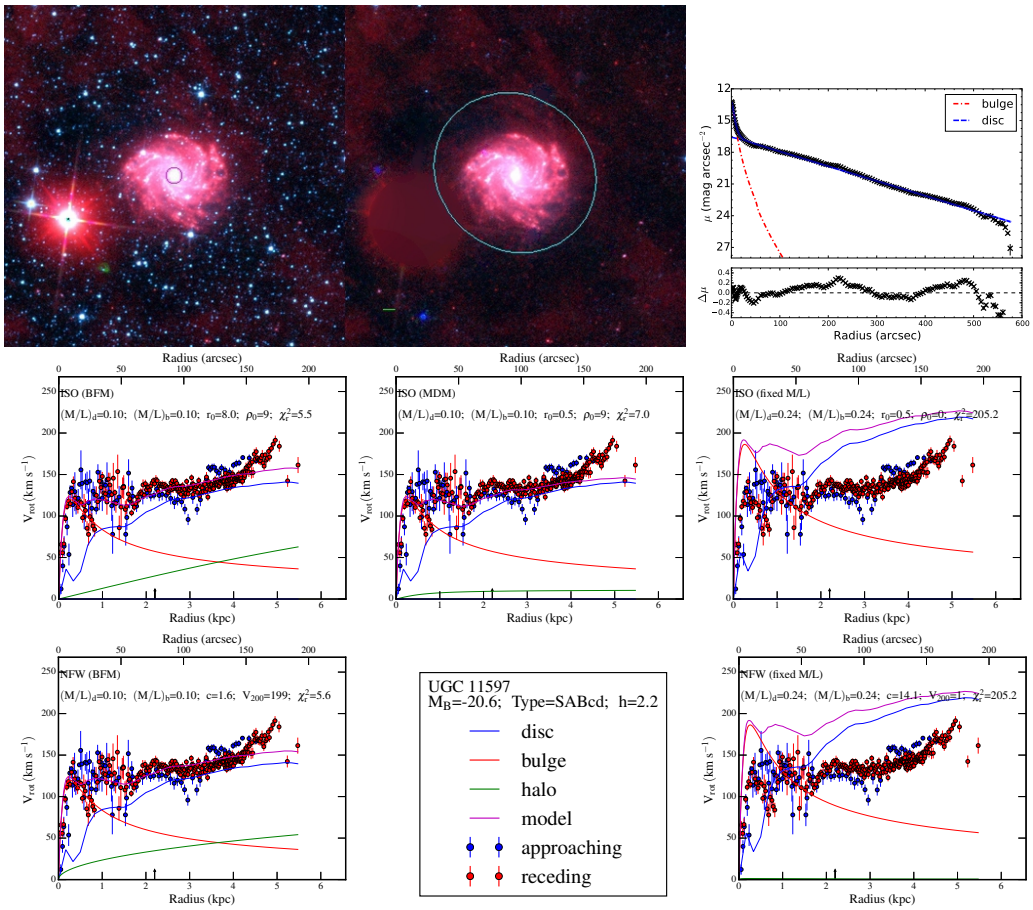
bulge
disc
μ (mag arcsec⁻²)
Δμ
Radius (arcsec)
ISO (BFM)
(M/L)d=0.10; (M/L)b=0.10; r0=8.0; ρ0=9; χ²r=5.5
ISO (MDM)
(M/L)d=0.10; (M/L)b=0.10; r0=0.5; ρ0=9; χ²r=7.0
ISO (fixed M/L)
(M/L)d=0.24; (M/L)b=0.24; r0=0.5; ρ0=0; χ²r=205.2
NFW (BFM)
(M/L)d=0.10; (M/L)b=0.10; c=1.6; V200=199; χ²r=5.6
NFW (fixed M/L)
(M/L)d=0.24; (M/L)b=0.24; c=14.1; V200=1; χ²r=205.2
Vrot (km s⁻¹)
Radius (kpc)
UGC 11597
MB=-20.6; Type=SABcd; h=2.2
disc
bulge
halo
model
approaching
receding

Figure A.113

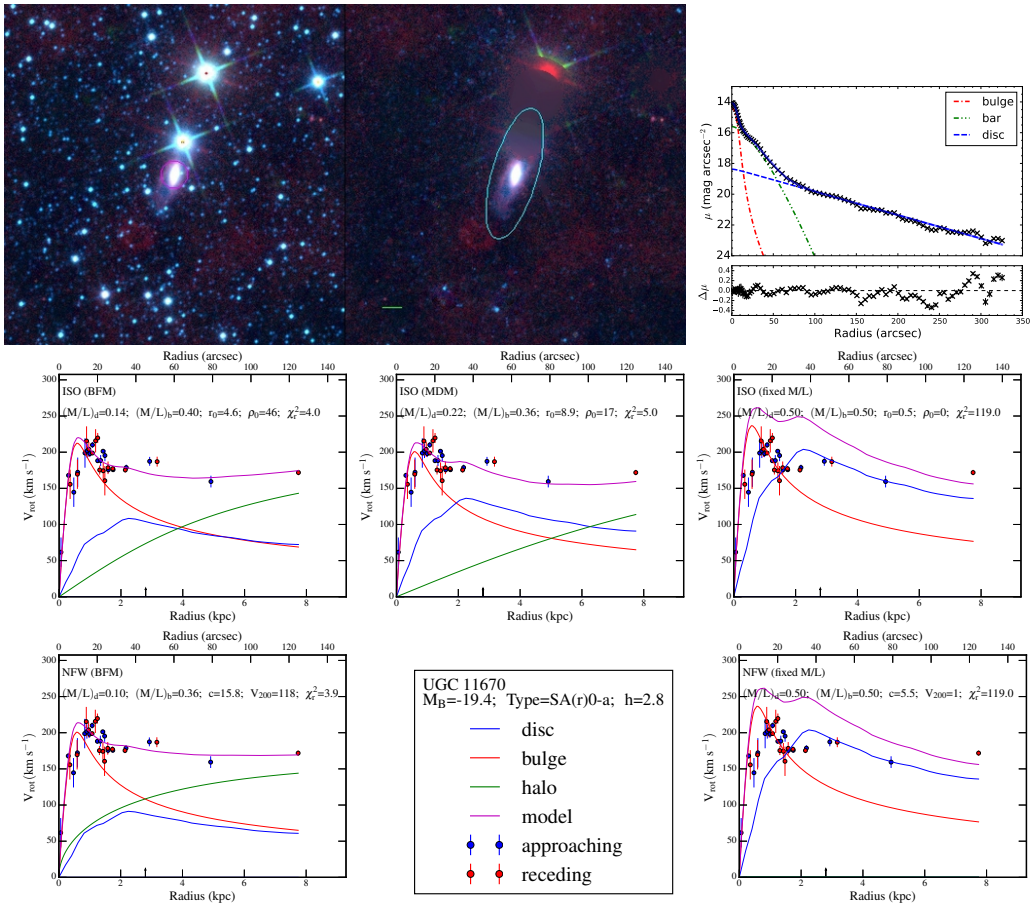
bulge
bar
disc
μ (mag arcsec⁻²)
Δμ
Radius (arcsec)
ISO (BFM)
(M/L)d=0.14; (M/L)b=0.40; r0=4.6; ρ0=46; χ²r=4.0
ISO (MDM)
(M/L)d=0.22; (M/L)b=0.36; r0=8.9; ρ0=17; χ²r=5.0
ISO (fixed M/L)
(M/L)d=0.50; (M/L)b=0.50; r0=0.5; ρ0=0; χ²r=119.0
NFW (BFM)
(M/L)d=0.10; (M/L)b=0.36; c=15.8; V200=118; χ²r=3.9
NFW (fixed M/L)
(M/L)d=0.50; (M/L)b=0.50; c=5.5; V200=1; χ²r=119.0
Vrot (km s⁻¹)
Radius (kpc)
UGC 11670
MB=-19.4; Type=SA(r)0-a; h=2.8
disc
bulge
halo
model
approaching
receding

Figure A.114

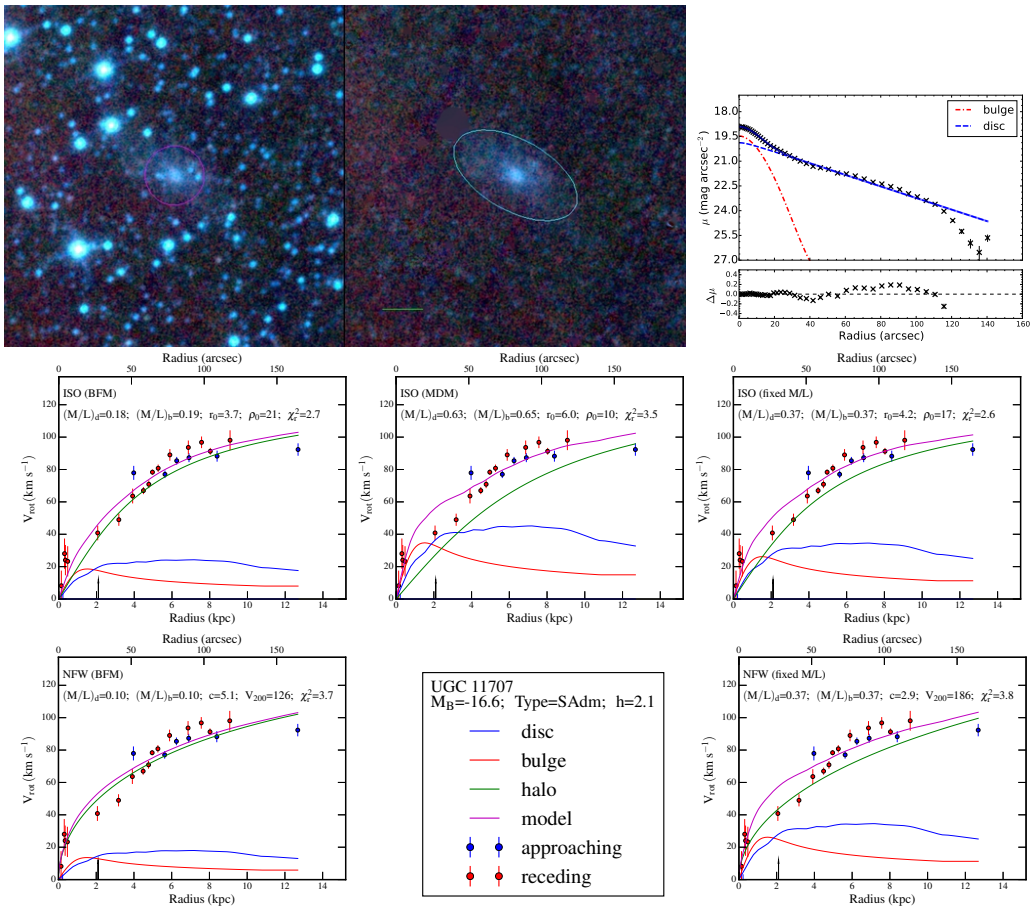
bulge
disc
Radius (arcsec)
ISO (BFM)
(M/L)d=0.18; (M/L)b=0.19; r0=3.7; ρ0=21; χ2r=2.7
ISO (MDM)
(M/L)d=0.63; (M/L)b=0.65; r0=6.0; ρ0=10; χ2r=3.5
ISO (fixed M/L)
(M/L)d=0.37; (M/L)b=0.37; r0=4.2; ρ0=17; χ2r=2.6
NFW (BFM)
(M/L)d=0.10; (M/L)b=0.10; c=5.1; V200=126; χ2r=3.7
NFW (fixed M/L)
(M/L)d=0.37; (M/L)b=0.37; c=2.9; V200=186; χ2r=3.8
Vrot (km s−1)
Radius (kpc)
UGC 11707
MB=-16.6; Type=SAdm; h=2.1
disc
bulge
halo
model
approaching
receding

Figure A.115

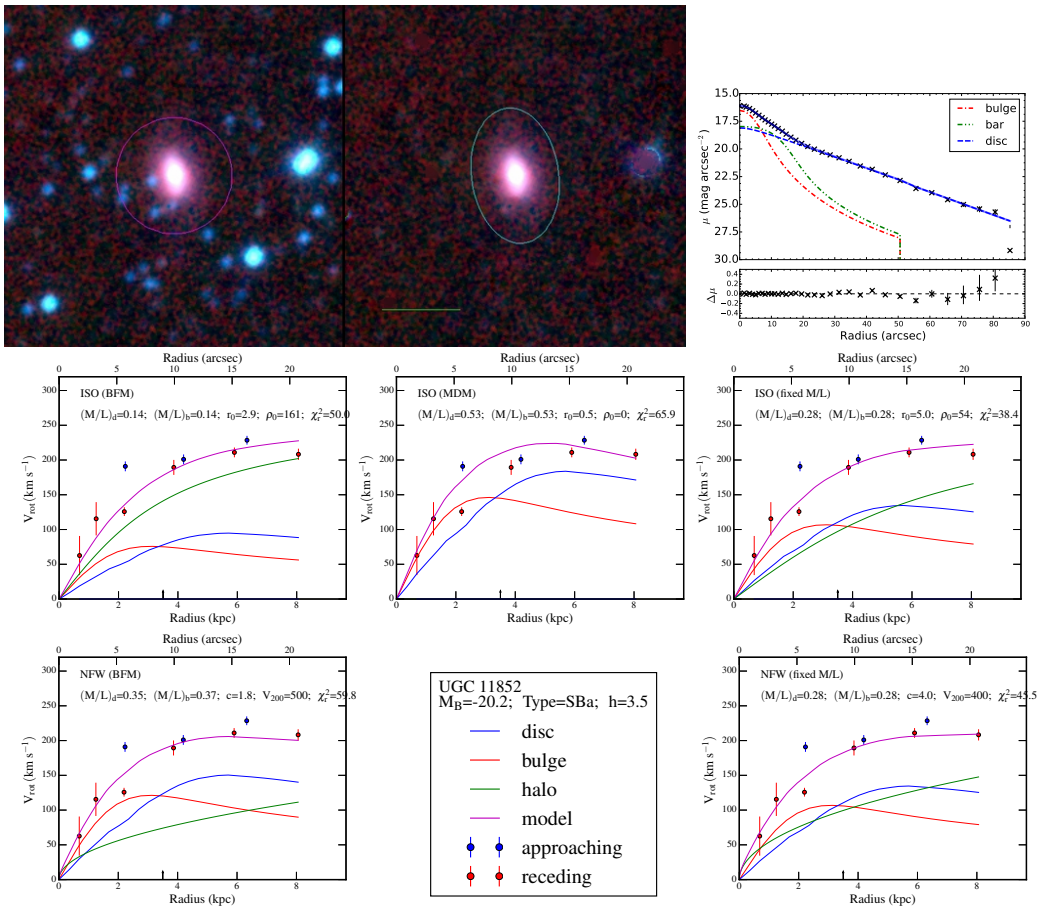
bulge
bar
disc
μ (mag arcsec⁻²)
Δμ
Radius (arcsec)
ISO (BFM)
(M/L)d=0.14; (M/L)b=0.14; r0=2.9; ρ0=161; χr²=50.0
ISO (MDM)
(M/L)d=0.53; (M/L)b=0.53; r0=0.5; ρ0=0; χr²=65.9
ISO (fixed M/L)
(M/L)d=0.28; (M/L)b=0.28; r0=5.0; ρ0=54; χr²=38.4
NFW (BFM)
(M/L)d=0.35; (M/L)b=0.37; c=1.8; V200=500; χr²=59.8
NFW (fixed M/L)
(M/L)d=0.28; (M/L)b=0.28; c=4.0; V200=400; χr²=45.5
Vrot (km s⁻¹)
Radius (kpc)
UGC 11852
MB=-20.2; Type=SBa; h=3.5
disc
bulge
halo
model
approaching
receding

Figure A.116

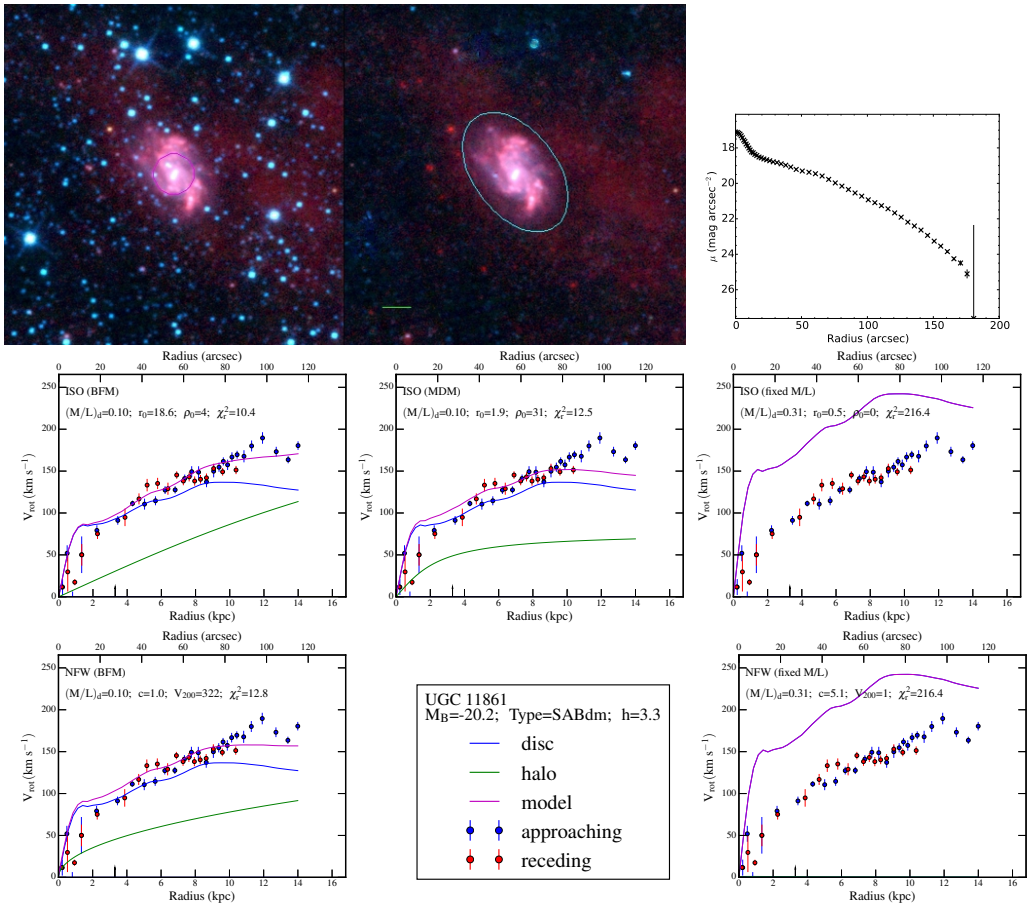
Radius (arcsec)
μ (mag arcsec⁻²)
Radius (arcsec)
ISO (BFM)
(M/L)d=0.10; r0=18.6; ρ0=4; χ²r=10.4
ISO (MDM)
(M/L)d=0.10; r0=1.9; ρ0=31; χ²r=12.5
ISO (fixed M/L)
(M/L)d=0.31; r0=0.5; ρ0=0; χ²r=216.4
Vrot (km s⁻¹)
Radius (kpc)
NFW (BFM)
(M/L)d=0.10; c=1.0; V200=322; χ²r=12.8
UGC 11861
MB=-20.2; Type=SABdm; h=3.3
disc
halo
model
approaching
receding
NFW (fixed M/L)
(M/L)d=0.31; c=5.1; V200=1; χ²r=216.4

Figure A.117

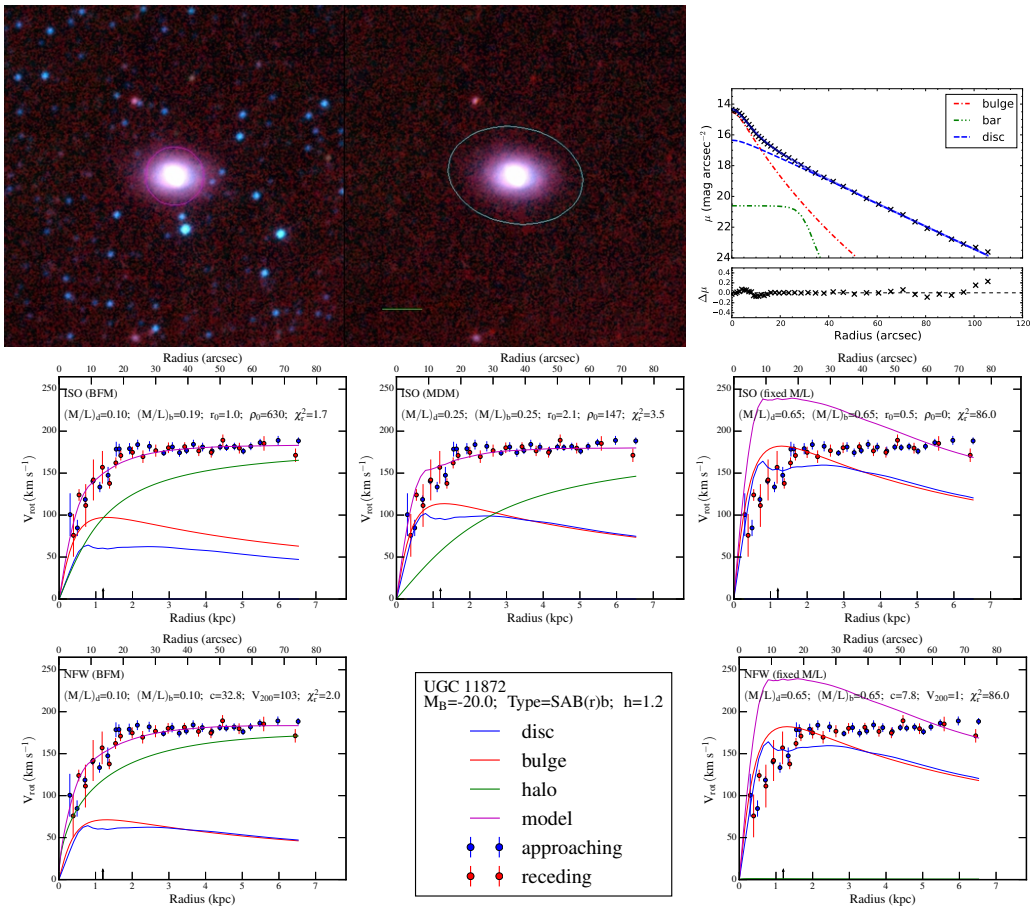
bulge
bar
disc
μ (mag arcsec⁻²)
Δμ
Radius (arcsec)
ISO (BFM)
(M/L)d=0.10; (M/L)b=0.19; r0=1.0; ρ0=630; χ²r=1.7
ISO (MDM)
(M/L)d=0.25; (M/L)b=0.25; r0=2.1; ρ0=147; χ²r=3.5
ISO (fixed M/L)
(M/L)d=0.65; (M/L)b=0.65; r0=0.5; ρ0=0; χ²r=86.0
NFW (BFM)
(M/L)d=0.10; (M/L)b=0.10; c=32.8; V200=103; χ²r=2.0
NFW (fixed M/L)
(M/L)d=0.65; (M/L)b=0.65; c=7.8; V200=1; χ²r=86.0
Vrot (km s⁻¹)
Radius (kpc)
UGC 11872
MB=-20.0; Type=SAB(r)b; h=1.2
disc
bulge
halo
model
approaching
receding

Figure A.118

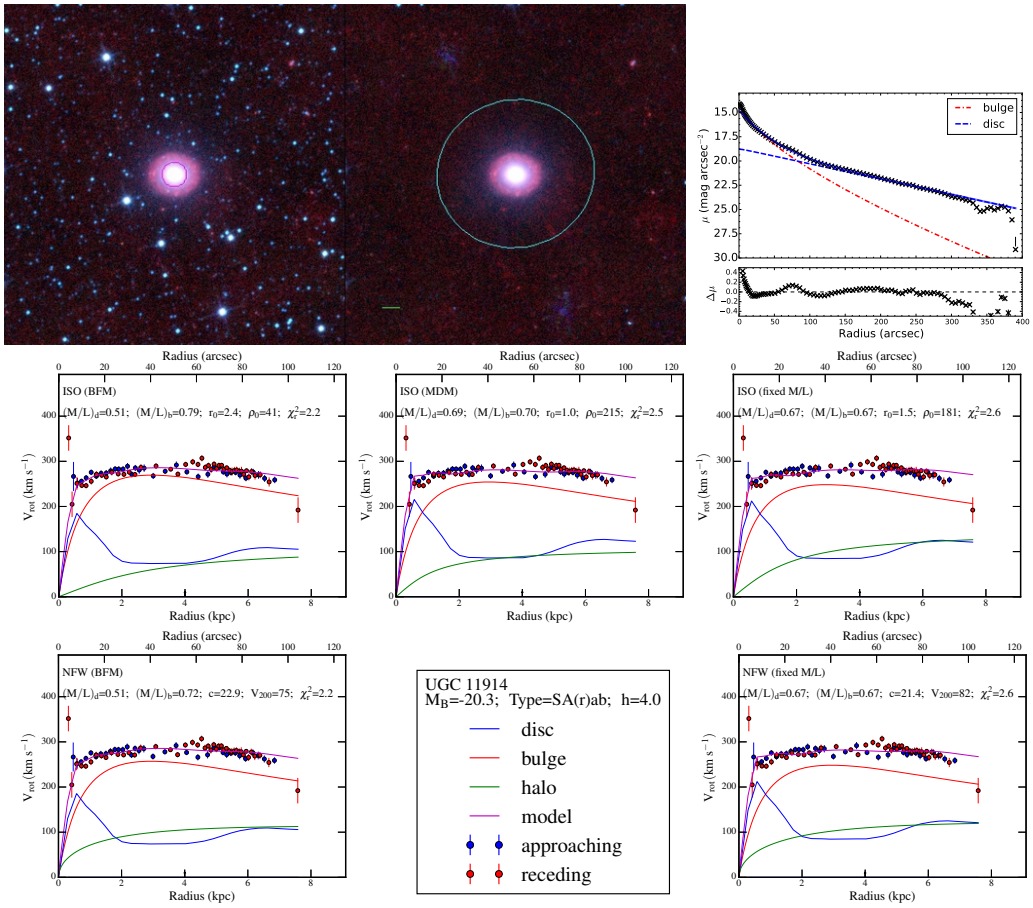
bulge
disc
μ (mag arcsec⁻²)
Δμ
Radius (arcsec)
ISO (BFM)
(M/L)d=0.51; (M/L)b=0.79; r0=2.4; ρ0=41; χr²=2.2
ISO (MDM)
(M/L)d=0.69; (M/L)b=0.70; r0=1.0; ρ0=215; χr²=2.5
ISO (fixed M/L)
(M/L)d=0.67; (M/L)b=0.67; r0=1.5; ρ0=181; χr²=2.6
NFW (BFM)
(M/L)d=0.51; (M/L)b=0.72; c=22.9; V200=75; χr²=2.2
NFW (fixed M/L)
(M/L)d=0.67; (M/L)b=0.67; c=21.4; V200=82; χr²=2.6
Vrot (km s⁻¹)
Radius (kpc)
UGC 11914
MB=-20.3; Type=SA(r)ab; h=4.0
disc
bulge
halo
model
approaching
receding

Figure A.119

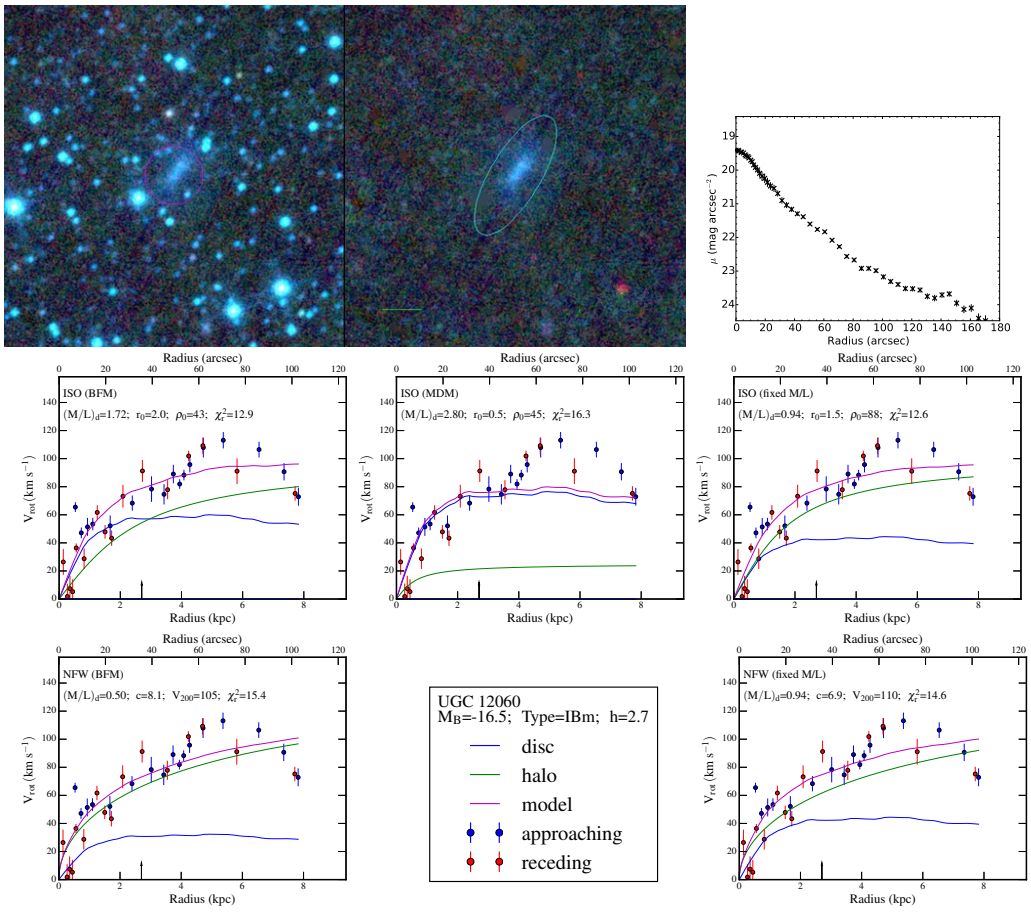
μ (mag arcsec⁻²)
Radius (arcsec)
ISO (BFM)
(M/L)d=1.72; r0=2.0; ρ0=43; χ²r=12.9
ISO (MDM)
(M/L)d=2.80; r0=0.5; ρ0=45; χ²r=16.3
ISO (fixed M/L)
(M/L)d=0.94; r0=1.5; ρ0=88; χ²r=12.6
NFW (BFM)
(M/L)d=0.50; c=8.1; V200=105; χ²r=15.4
NFW (fixed M/L)
(M/L)d=0.94; c=6.9; V200=110; χ²r=14.6
Vrot (km s⁻¹)
Radius (kpc)
UGC 12060
MB=-16.5; Type=IBm; h=2.7
disc
halo
model
approaching
receding

Figure A.120

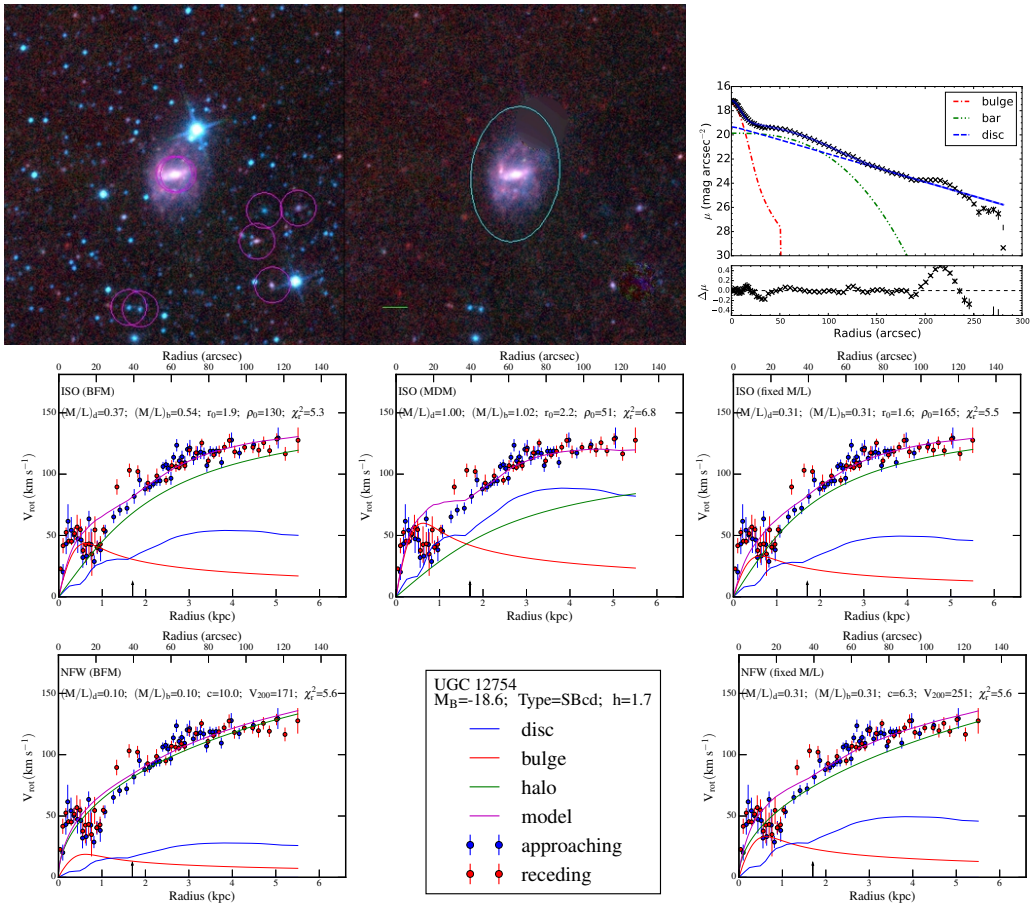
bulge
bar
disc
μ (mag arcsec⁻²)
Δμ
Radius (arcsec)
ISO (BFM)
(M/L)d=0.37; (M/L)b=0.54; r0=1.9; ρ0=130; χ²r=5.3
ISO (MDM)
(M/L)d=1.00; (M/L)b=1.02; r0=2.2; ρ0=51; χ²r=6.8
ISO (fixed M/L)
(M/L)d=0.31; (M/L)b=0.31; r0=1.6; ρ0=165; χ²r=5.5
NFW (BFM)
(M/L)d=0.10; (M/L)b=0.10; c=10.0; V200=171; χ²r=5.6
NFW (fixed M/L)
(M/L)d=0.31; (M/L)b=0.31; c=6.3; V200=251; χ²r=5.6
Vrot (km s⁻¹)
Radius (kpc)
UGC 12754
MB=-18.6; Type=SBcd; h=1.7
disc
bulge
halo
model
approaching
receding

Figure A.121

3 Mass models derived from HI and optical radii-limited rotation curves taken from Randriamampandry et al. 2014

This appendix contains the comparison between the mass models derived from HI and optical rotation curves limited to the solid body rising parts for the 15 galaxies.

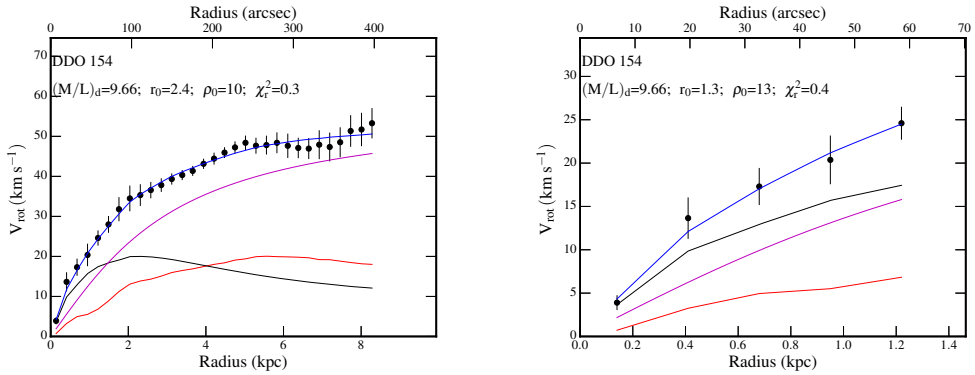

Figure A.122: Mass models using the ISO (BFM): left panel when using the HI rotation curve and right panel the rotation within the optical radius $D_{25}/2$ kpc. The blue, magenta, black, green, red lines represent the model, the halo, the disc, the bulge and the gas component respectively.

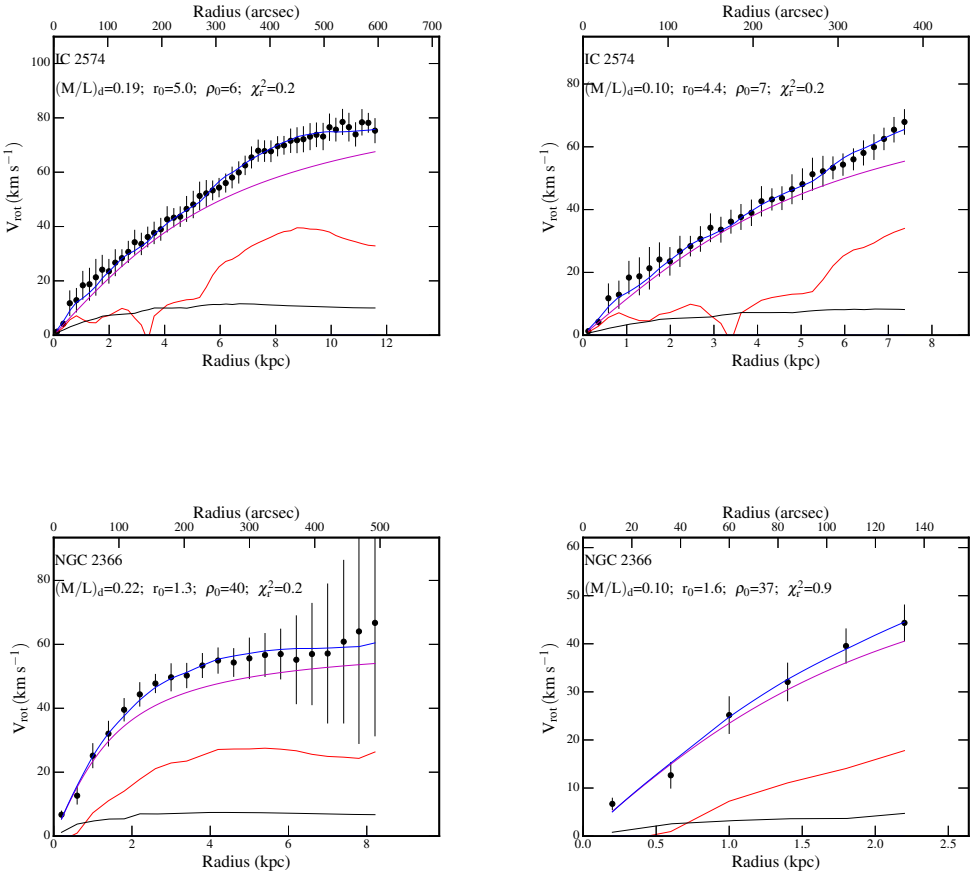

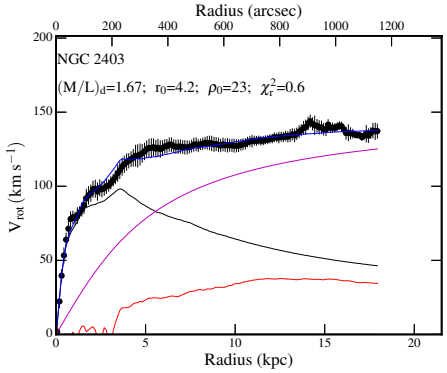
Radius (arcsec)
NGC 2403
(M/L)d=1.67; r0=4.2; ρ0=23; χr2=0.6
Vrot (km s−1)
Radius (kpc)

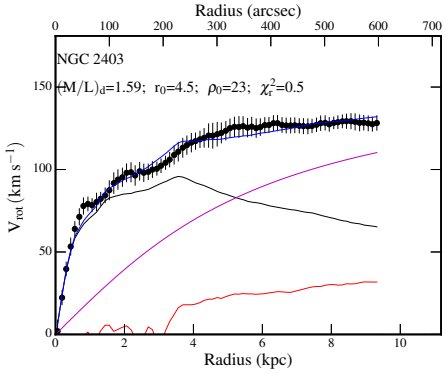
Radius (arcsec)
NGC 2403
(M/L)d=1.59; r0=4.5; ρ0=23; χr2=0.5
Vrot (km s−1)
Radius (kpc)

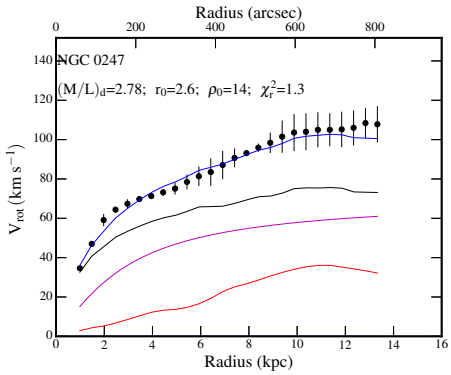
Radius (arcsec)
NGC 0247
(M/L)d=2.78; r0=2.6; ρ0=14; χr2=1.3
Vrot (km s−1)
Radius (kpc)

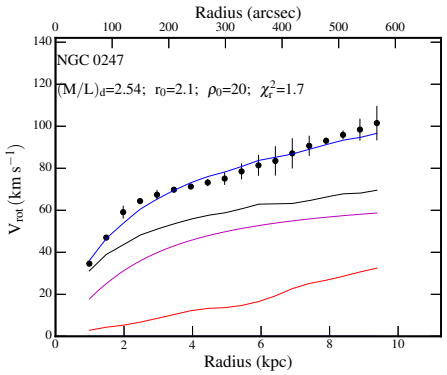
Radius (arcsec)
NGC 0247
(M/L)d=2.54; r0=2.1; ρ0=20; χr2=1.7
Vrot (km s−1)
Radius (kpc)

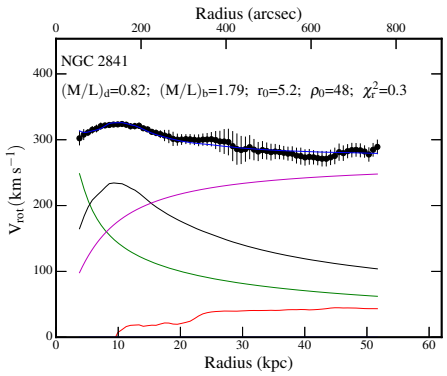
Radius (arcsec)
NGC 2841
(M/L)d=0.82; (M/L)b=1.79; r0=5.2; ρ0=48; χr2=0.3
Vrot (km s−1)
Radius (kpc)

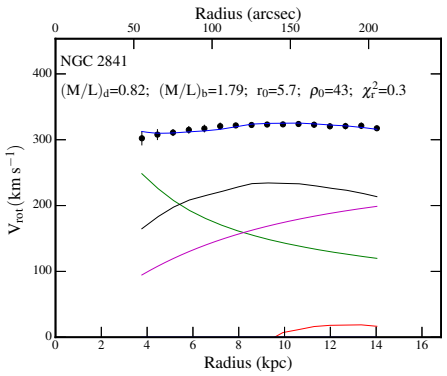
Radius (arcsec)
NGC 2841
(M/L)d=0.82; (M/L)b=1.79; r0=5.7; ρ0=43; χr2=0.3
Vrot (km s−1)
Radius (kpc)

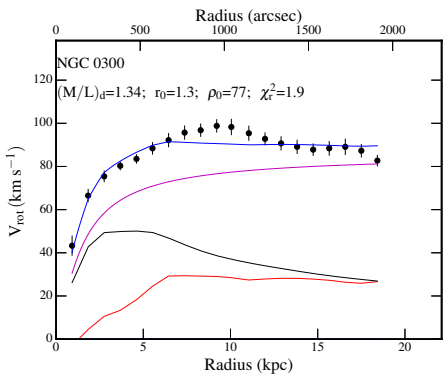
Radius (arcsec)
NGC 0300
(M/L)d=1.34; r0=1.3; ρ0=77; χr2=1.9
Vrot (km s−1)
Radius (kpc)

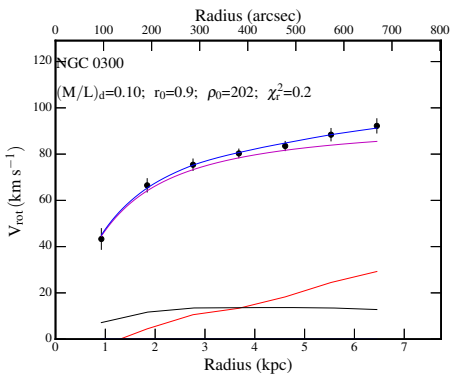
Radius (arcsec)
NGC 0300
(M/L)d=0.10; r0=0.9; ρ0=202; χr2=0.2
Vrot (km s−1)
Radius (kpc)

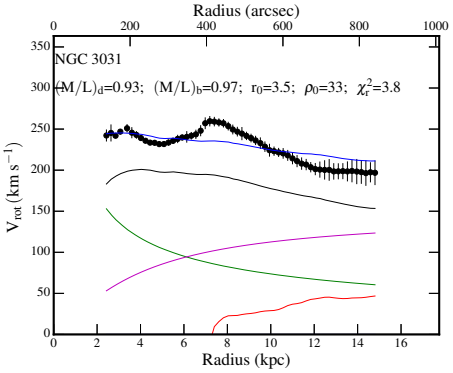
Radius (arcsec)
NGC 3031
(M/L)d=0.93; (M/L)b=0.97; r0=3.5; ρ0=33; χr2=3.8
Vrot (km s−1)
Radius (kpc)

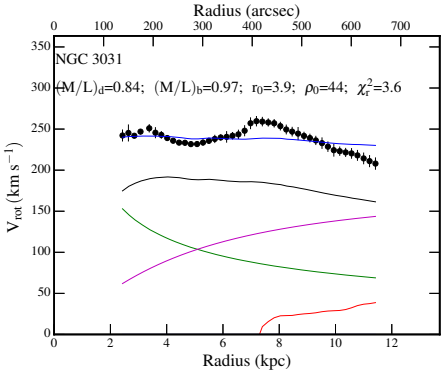
Radius (arcsec)
NGC 3031
(M/L)d=0.84; (M/L)b=0.97; r0=3.9; ρ0=44; χr2=3.6
Vrot (km s−1)
Radius (kpc)

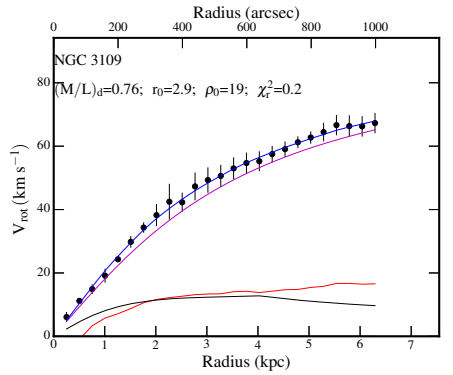
Radius (arcsec)
NGC 3109
(M/L)d=0.76; r0=2.9; ρ0=19; χr2=0.2
Vrot (km s−1)
Radius (kpc)

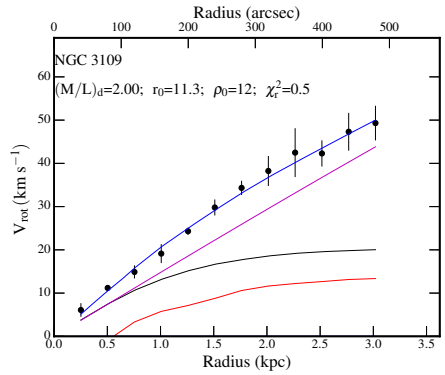
Radius (arcsec)
NGC 3109
(M/L)d=2.00; r0=11.3; ρ0=12; χr2=0.5
Vrot (km s−1)
Radius (kpc)

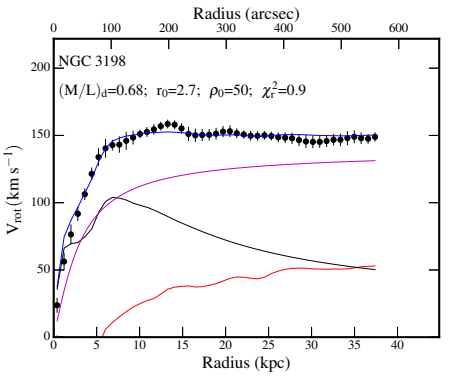
Radius (arcsec)
NGC 3198
(M/L)d=0.68; r0=2.7; ρ0=50; χr2=0.9
Vrot (km s−1)
Radius (kpc)

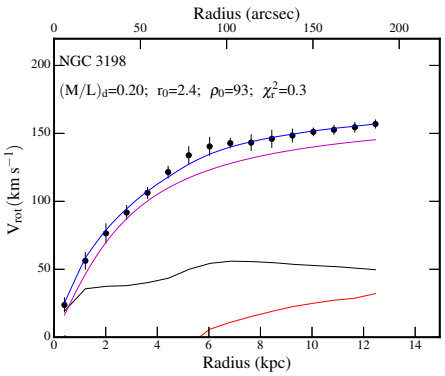
Radius (arcsec)
NGC 3198
(M/L)d=0.20; r0=2.4; ρ0=93; χr2=0.3
Vrot (km s−1)
Radius (kpc)

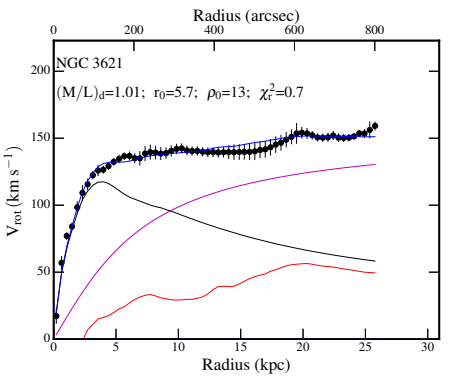
Radius (arcsec)
NGC 3621
(M/L)d=1.01; r0=5.7; ρ0=13; χr2=0.7
Vrot (km s−1)
Radius (kpc)

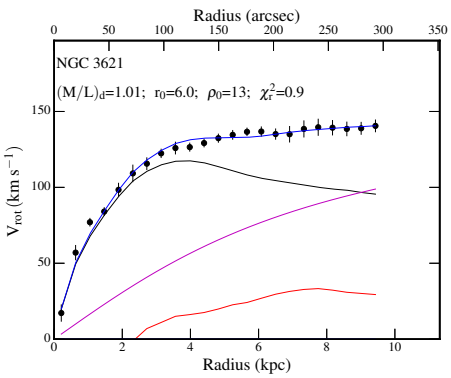
Radius (arcsec)
NGC 3621
(M/L)d=1.01; r0=6.0; ρ0=13; χr2=0.9
Vrot (km s−1)
Radius (kpc)

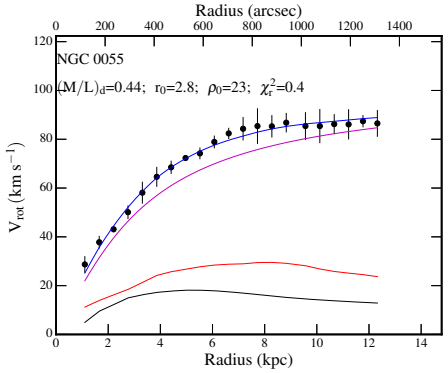
Radius (arcsec)
NGC 0055
(M/L)d=0.44; r0=2.8; ρ0=23; χr2=0.4
Vrot (km s−1)
Radius (kpc)

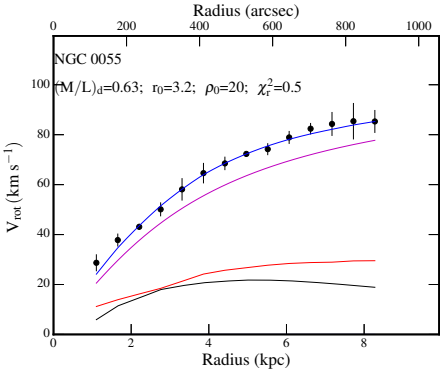
Radius (arcsec)
NGC 0055
(M/L)d=0.63; r0=3.2; ρ0=20; χr2=0.5
Vrot (km s−1)
Radius (kpc)

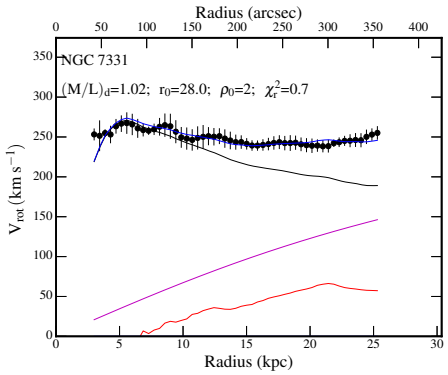
Radius (arcsec)
NGC 7331
(M/L)d=1.02; r0=28.0; ρ0=2; χr2=0.7
Vrot (km s−1)
Radius (kpc)

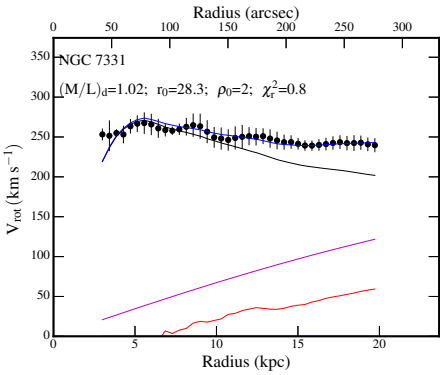
Radius (arcsec)
NGC 7331
(M/L)d=1.02; r0=28.3; ρ0=2; χr2=0.8
Vrot (km s−1)
Radius (kpc)

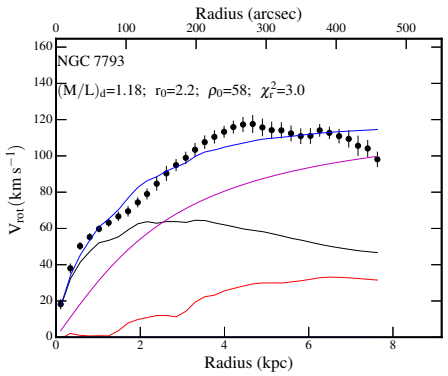
Radius (arcsec)
NGC 7793
(M/L)d=1.18; r0=2.2; ρ0=58; χr2=3.0
Vrot (km s−1)
Radius (kpc)

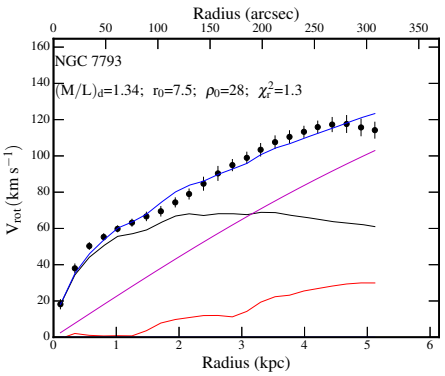
Radius (arcsec)
NGC 7793
(M/L)d=1.34; r0=7.5; ρ0=28; χr2=1.3
Vrot (km s−1)
Radius (kpc)

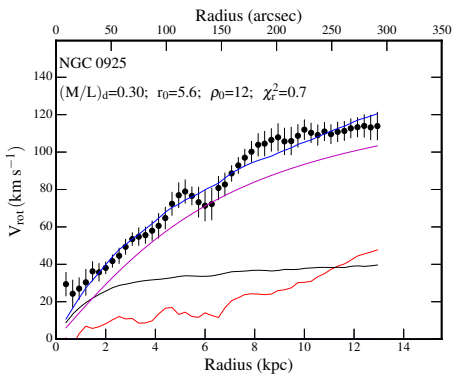
Radius (arcsec)
NGC 0925
(M/L)d=0.30; r0=5.6; ρ0=12; χr2=0.7
Vrot (km s−1)
Radius (kpc)

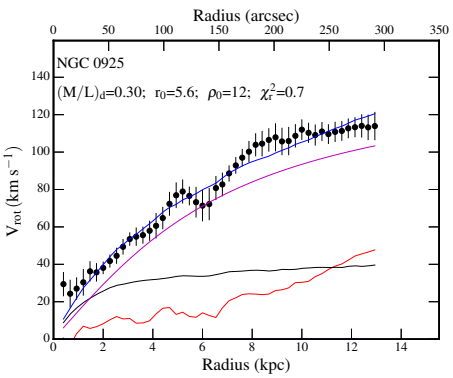
Radius (arcsec)
NGC 0925
(M/L)d=0.30; r0=5.6; ρ0=12; χr2=0.7
Vrot (km s−1)
Radius (kpc)

Appendix B

1 Tables

We list here the global properties and mass models parameters of the sample of 100 galaxies.

Table B.1: Global properties

Table B.1: Global properties: (1) Name of the galaxy in the UGC catalogue. (2): Morphological type taken from the RC3 catalogue (except for galaxies UGC 3521, 3708, 3915, 4393, 10652 for which the morphological types are taken from Epinat et al. (2008a); (3): Absolute B-magnitude from Epinat et al. (2008a); (4): (B-V) colors corrected for galactic and internal extinction from RC3 catalogue when available. For galaxies with no (B-V) color available in the RC3 catalogue, the value has been computed as explained in Section 3.3, those galaxies are marked with an asterisk (*). (5): Central surface brightness from the observed data in mag arcsec^{-2}; (6): Isophotal radius at the limiting surface brightness of 25 mag arcsec^{-2} normalised by the disc scale length; (7): The last radius of the rotation curve normalised by the disc scale length; (8): Central surface brightness of the disc in mag arcsec^{-2}; (9): disc scale length of the disc component in kpc; (10): Luminosity of the disc in unit of 10^7 L$\odot$ calculated at the isophotal radius; (11): Surface brightness of the bulge at the effective radius in mag arcsec^{-2}; (12): Effective radius of the bulge in kpc; (13): Sérsic index of the bulge; (14): Luminosity of the bulge in units of 10^7 L$\odot$, derived at the isophotal radius; (15): Classification flag of the rotation curves: 1 and 2 correspond respectively to very high and high quality rotation curves, while 3 represents poor quality rotation curves.

Galaxy							**Disc**			**Bulge**				**RC**
UGC	type	Mag	(B − V)	μ_{0obs}	R_{25}/h	R_{last}/h	μ_0	h	L_D	μ_e	r_e	n	L_B	**flag**
(1)	(2)	(3)	(4)	(5)	(6)	(7)	(8)	(9)	(10)	(11)	(12)	(13)	(14)	(15)
00089	SBa	−21.5	0.69	16.4	2.4	1.6	19.6	6.0	547.3	16.73	0.71	1.0	331.8	1
00094*	SAab	−20.4	0.64	18.7	2.6	2.8	19.7	4.0	232.7	18.69	0.26	1.57	10.2	1
00508	SB(r)ab	−21.8	0.82	16.6	3.5	3.0	19.4	7.5	1378.5	17.75	0.6	2.16	235.13	1
00528	SABb	−19.6	0.45	16.2	4.2	2.0	18.0	1.0	90.3	20.13	0.71	3.22	12.88	1
00763	SABm	−18.9	0.43	19.6	3.4	6.0	19.9	1.5	33.4	24.62	0.77	3.79	3.55	1
01256	SBcd	−18.9	0.45	19.4	5.3	6.1	19.4	1.4	4.9	–	–	–	–	3

Continued . . .

Table B.1 – Continued from previous page

Galaxy							**Disc**			**Bulge**				**RC**
UGC	type	Mag	(B − V)	μ_{0obs}	R_{25}/h	R_{last}/h	μ_0	h	L_D	μ_e	r_e	n	L_B	**flag**
(1)	(2)	(3)	(4)	(5)	(6)	(7)	(8)	(9)	(10)	(11)	(12)	(13)	(14)	(15)
01317	SAB(r)c	−21.5	0.59	18.1	4.3	4.5	18.1	5.4	1023.7	–	–	–	–	1
01437	SABbc	−21.8	0.54	17.6	2.7	5.0	19.3	5.2	578.7	20.59	1.79	3.24	100.34	1
01655	Sa pec	−21.6	0.79	16.2	5.1	1.2	17.4	6.0	6181.2	18.44	3.05	1.53	221.4	3
01736	SABc	−20.1	0.48	17.9	3.9	3.5	19.5	2.5	131.2	25.38	0.69	5.82	2.42	2
01886*	SABbc	−20.8	0.58	17.4	0.7	4.1	19.9	7.9	136.0	19.73	1.38	0.2	81.22	2
01913	SABd	−20.1	0.50	19.1	4.9	3.0	19.9	3.0	142.9	21.23	0.42	0.86	1.98	2
02045	Sab	−20.5	0.64	17.3	5.4	2.2	18.1	2.3	450.4	16.81	0.14	0.06	7.39	1
02080	SABcd	−19.2	0.63	19.5	2.8	3.0	20.2	3.0	92.9	22.94	0.42	2.33	0.51	1
02141*	S0 – a	−18.1	0.70	18.7	3.1	4.2	19.3	1.2	34.4	20.32	0.58	0.61	6.21	3
02183*	Sa	−19.0	0.67	17.1	2.2	1.1	20.7	2.3	26.7	19.05	0.64	2.35	44.83	2
02193	SAc	−18.7	0.55	17.7	2.8	3.5	19.8	1.3	23.9	20.99	0.24	0.05	0.9	2
02503	SAB(r)b	−21.6	0.64	17.0	3.8	3.5	19.1	4.3	568.0	18.14	1.39	0.68	90.86	2
02800*	Im	−18.6	0.39	19.8	2.7	2.2	20.1	2.6	7.1	–	–	–	–	1
02855*	SABc	−21.4	0.54	17.2	3.6	5.1	17.9	2.5	572.6	18.44	0.25	1.07	9.35	1
03013	SBb	−21.3	0.55	17.6	1.2	3.1	20.1	7.7	298.4	21.5	4.78	3.11	216.89	1
03273*	Sm	−18.3	0.42	19.6	2.7	4.3	19.9	1.7	37.3	20.87	0.13	0.06	0.14	3
03334	SABc	−22.8	0.57	17.5	4.1	3.7	19.2	8.7	2275.6	21.24	4.82	0.35	98.31	1

Continued . . .

Table B.1 – Continued from previous page

Galaxy							Disc			Bulge				RC
UGC	type	Mag	(B − V)	μ_{0obs}	R_{25}/h	R_{last}/h	μ_0	h	L_D	μ_e	r_e	n	L_B	**flag**
(1)	(2)	(3)	(4)	(5)	(6)	(7)	(8)	(9)	(10)	(11)	(12)	(13)	(14)	(15)
03382*	SBa	−20.4	0.67	17.2	3.5	4.1	19.3	3.3	292.2	18.34	0.52	2.34	56.19	2
03463*	SABbc	−20.7	0.58	18.7	2.8	3.9	19.9	4.5	276.7	19.71	0.32	1.0	11.73	1
03521*	Sc	−19.8	0.55	19.0	2.7	2.1	20.1	4.0	154.4	20.84	0.69	1.04	6.77	1
03528*	SBab	−20.1	0.64	17.2	4.3	2.5	19.1	2.9	277.5	18.83	0.56	1.10	29.72	2
03708*	Sbc pec	−20.7	0.56	17.5	3.6	1.4	17.6	2.3	360.3	–	–	–	–	2
03740	SABc	−19.8	0.45	18.6	2.8	4.6	19.6	2.0	69.8	19.08	0.25	0.69	3.89	3
03809	SAB(r)bc	−22.0	0.49	17.0	4.2	4.4	18.9	5.6	1225.3	19.87	1.11	1.32	24.0	1
03876*	SAd	−17.4	0.48	20.3	2.1	2.6	20.8	1.9	16.6	22.44	0.58	1.06	0.74	1
03915*	SBc	−21.4	0.56	18.3	3.9	3.3	19.2	2.7	225.3	17.01	0.1	1.17	7.16	2
04026*	Sab	−20.8	0.64	17.4	4.1	2.7	18.7	3.3	523.1	19.71	1.31	2.62	31.74	2
04165	SBd	−18.2	0.54	19.6	2.6	3.4	20.0	1.5	25.1	20.35	0.09	0.06	0.11	2
04256	SABc	−21.6	0.51	18.4	3.3	3.5	19.9	5.3	412.1	30.0	0.35	8.42	32.0	3
04273*	SBb	−20.7	0.61	16.9	3.9	4.9	19.3	2.8	225.9	17.85	0.22	0.66	10.9	1
04274	SBm pec	−17.7	0.59	19.5	3.4	2.0	19.4	0.6	0.9	–	–	–	–	3
04284	SAcd	−18.4	0.37	19.7	2.4	3.3	20.6	1.8	19.6	27.49	2.26	4.04	4.37	1
04325	SAm	−18.2	0.39	21.0	2.2	1.9	21.1	2.2	16.3	–	–	–	0.1	1
04393*	SBc	−19.3	0.56	18.7	3.6	5.6	19.2	1.8	100.4	18.68	0.1	0.37	0.94	3

Continued . . .

Table B.1 – Continued from previous page

Galaxy							**Disc**			**Bulge**				**RC**
UGC	type	Mag	(B − V)	μ_{0obs}	R_{25}/h	R_{last}/h	μ_0	h	L_D	μ_e	r_e	n	L_B	**flag**
(1)	(2)	(3)	(4)	(5)	(6)	(7)	(8)	(9)	(10)	(11)	(12)	(13)	(14)	(15)
04456	SAc	−20.8	0.53	19.6	2.4	3.5	20.4	4.7	157.9	20.52	0.35	2.28	4.67	2
04499*	SABdm	−17.0	0.45	20.4	3.3	3.6	20.5	1.0	0.8	–	–	–	–	2
04555*	SABbc	−20.9	0.58	19.5	2.7	2.6	20.3	4.6	183.3	18.84	0.46	0.08	8.35	1
04820	SA(r)ab	−20.3	0.83	15.3	3.8	2.2	19.0	2.7	270.4	19.23	0.87	2.53	80.6	2
04936	SABd	−20.6	0.44	19.2	2.8	4.3	20.7	4.5	126.5	21.52	0.98	0.96	3.32	1
05045*	SAB(r)c	−21.2	0.54	17.3	2.3	2.2	20.5	7.6	389.2	21.29	2.17	2.78	74.31	2
05228*	SBc	−19.9	0.54	19.8	2.8	2.9	19.6	3.0	15.4	–	–	–	–	1
05251	Sbc	−20.5	0.21	18.8	3.4	3.0	20.3	4.3	189.9	20.71	1.02	0.2	10.96	1
05253	SAab	−20.7	0.68	16.4	1.9	1.5	20.8	5.9	142.1	19.72	1.83	1.89	201.86	1
05316	SBd	−19.9	0.40	19.9	2.0	3.2	21.4	4.2	45.9	21.37	1.21	0.68	10.76	3
05414*	IABm	−16.6	0.42	21.5	3.0	3.7	21.1	1.5	1.0	–	–	–	–	1
05510	SABbc	−19.3	0.52	16.8	3.2	4.1	19.6	1.8	60.0	18.84	0.16	1.63	3.46	1
05721	SABd	−16.5	0.36	19.2	1.5	2.1	21.9	1.0	1.2	22.39	0.15	2.02	2.55	3
05786	SAB(r)bc pec	−19.6	0.31	16.3	3.1	5.2	18.3	1.2	86.4	20.35	1.29	0.87	38.02	3
05789	SBcd	−19.6	0.37	19.3	2.9	5.4	19.9	2.6	90.1	–	–	–	0.16	3
05829	Im	−16.2	0.20	22.3	3.5	3.9	22.1	1.7	0.5	–	–	–	–	3
05840	SAB(r)bc	−18.9	0.57	15.3	8.2	7.2	17.8	0.8	81.1	27.48	0.39	6.56	1.71	2

Continued . . .

Table B.1 – Continued from previous page

Galaxy							Disc			Bulge				RC
UGC	type	Mag	(B − V)	μ_{0obs}	R_{25}/h	R_{last}/h	μ_0	h	L_D	μ_e	r_e	n	L_B	**flag**
(1)	(2)	(3)	(4)	(5)	(6)	(7)	(8)	(9)	(10)	(11)	(12)	(13)	(14)	(15)
05842*	SBcd	−18.8	0.51	19.8	2.9	2.9	20.4	2.0	35.5	21.44	0.28	1.07	0.65	1
05931	SABcd pec	−19.8	0.28	18.4	3.6	5.6	19.0	1.5	77.7	18.43	0.11	0.36	1.19	1
05982	SABc	−20.0	0.57	18.5	5.0	4.2	19.6	2.4	127.3	19.51	0.17	2.97	6.32	1
06118	SABab	−20.0	0.64	15.8	4.8	4.1	18.1	1.5	188.3	16.77	0.21	0.64	24.97	1
06277*	SABc	−19.5	0.54	16.5	5.4	2.9	19.2	1.6	74.3	18.51	0.13	1.62	3.32	2
06419	SBm pec	−18.6	0.35	20.4	2.0	4.2	20.2	2.1	3.1	–	–	–	–	3
06521	SAbc pec	−21.2	0.50	18.1	3.3	3.1	20.0	5.8	401.8	19.83	0.66	1.15	17.55	1
06523	SAa	−21.0	0.68	18.2	4.4	1.8	19.0	2.8	301.1	20.2	2.13	0.05	41.23	3
06537	SAB(r)c	−20.5	0.44	17.4	3.1	3.0	20.0	3.6	163.0	19.04	0.13	2.71	10.16	1
06702	Sa	−20.6	0.60	18.0	2.2	2.6	20.9	5.3	121.5	17.98	0.64	1.4	137.77	1
06778*	SABc	−20.7	0.54	17.1	3.0	3.8	19.0	2.0	131.7	21.49	1.15	3.74	18.68	1
07021	SAB(r)a	−19.7	0.74	16.4	3.5	2.2	19.7	2.8	150.2	18.55	0.39	1.43	22.9	1
07045	SAc	−19.2	0.66	18.4	3.1	3.2	19.6	2.2	88.5	22.94	1.53	3.31	6.43	1
07154	SABd	−20.0	0.50	18.2	2.5	3.7	20.9	4.4	91.6	21.06	0.6	0.27	11.08	2
07323	SABdm	−18.3	0.54	20.9	2.3	2.7	20.9	2.0	20.7	–	–	–	–	1
07766	SABcd	−21.0	0.37	17.9	4.8	3.5	19.5	4.1	367.7	20.69	0.39	1.62	4.63	1
07831	SBc pec	−18.5	0.45	19.0	5.1	2.9	18.5	0.9	4.5	–	–	–	–	1

Continued . . .

Table B.1 – Continued from previous page

Galaxy							**Disc**			**Bulge**				**RC**
UGC	type	Mag	(B − V)	μ_{0obs}	R_{25}/h	R_{last}/h	μ_0	h	L_D	μ_e	r_e	n	L_B	**flag**
(1)	(2)	(3)	(4)	(5)	(6)	(7)	(8)	(9)	(10)	(11)	(12)	(13)	(14)	(15)
07853	SBm	−18.9	0.44	19.4	3.5	5.4	19.3	1.3	4.4	–	–	–	–	3
07861	SABm pec	−17.3	0.57	18.6	2.1	2.1	20.7	1.0	4.7	20.64	0.4	0.41	3.5	2
07876*	SABd	−17.9	0.48	20.0	2.3	2.0	21.2	1.8	11.1	22.88	0.87	1.7	3.37	1
07901	SAc	−20.6	0.51	17.0	3.8	4.4	19.2	3.0	270.3	20.27	2.1	0.19	47.01	1
07985	SABd	−18.7	0.47	18.4	2.0	3.1	20.1	1.7	25.7	21.76	0.65	1.97	3.39	2
08334	SAbc	−21.1	0.64	16.2	5.2	3.3	18.6	3.3	605.6	19.08	0.5	0.33	28.05	1
08403	SBcd	−19.2	0.43	19.8	3.7	5.1	19.7	2.3	9.2	–	–	–	–	1
08490	SAm	−17.1	0.41	19.9	4.2	3.7	20.0	0.7	7.5	21.42	0.08	0.06	0.03	1
08709	SABc	−21.4	0.43	17.9	3.1	3.8	20.0	6.1	468.6	22.85	6.57	3.42	104.69	1
08852*	SAB(r)b	−20.0	0.61	17.8	5.0	2.8	19.0	2.3	178.3	18.90	0.46	0.50	13.81	1
08900	SAb pec	−21.7	0.61	18.0	2.5	1.7	19.9	7.2	630.0	21.7	3.23	3.55	111.92	2
08937*	SBb	−21.1	0.61	17.0	4.5	4.0	19.0	3.6	481.4	17.1	0.37	0.56	54.26	1
09013	SAcdpec	−18.2	0.48	19.4	1.5	3.1	21.0	1.7	7.8	21.0	0.54	0.89	2.25	3
09179	SABd	−17.8	0.46	19.1	2.2	3.0	21.0	1.6	10.0	21.62	0.41	1.38	1.29	1
09248*	Sb	−20.2	0.61	18.8	2.8	2.4	20.0	3.9	177.1	21.15	1.11	1.30	14.59	1
09358*	SABb	−20.8	0.61	17.1	4.4	3.6	18.9	3.0	372.0	19.98	0.74	1.78	22.99	1
09363	SAd	−19.8	0.65	19.0	1.8	3.6	21.0	3.3	39.7	22.3	3.3	2.11	28.56	1

Continued . . .

Table B.1 – Continued from previous page

Galaxy							Disc			Bulge				RC
UGC	type	Mag	(B − V)	μ_{0obs}	R_{25}/h	R_{last}/h	μ_0	h	L_D	μ_e	r_e	n	L_B	**flag**
(1)	(2)	(3)	(4)	(5)	(6)	(7)	(8)	(9)	(10)	(11)	(12)	(13)	(14)	(15)
09366	SAbc	−21.7	0.55	17.1	4.1	3.4	19.2	4.8	711.9	19.7	0.96	1.6	124.7	1
09465*	SABdm	−18.0	0.45	20.3	1.5	4.1	20.4	2.0	1.8	–	–	–	–	1
09576	SABd	−19.6	0.56	19.8	1.9	4.1	20.8	3.7	58.0	21.17	1.04	0.55	8.64	1
09649*	SBb	−16.5	0.61	19.6	2.2	3.9	19.7	1.0	6.9	–	–	–	–	1
09736	SABc	−20.6	0.60	19.4	2.4	2.1	20.7	6.6	214.0	20.93	0.72	0.80	6.14	1
09753	SAbc	−19.1	0.47	17.1	5.5	5.0	18.4	1.3	101.3	19.38	0.81	0.48	5.5	1
09858*	SABbc	−20.4	0.58	18.6	4.7	5.7	19.4	4.6	548.7	18.65	0.23	0.25	4.53	2
09866*	SA(r)bc	−17.2	0.58	18.6	3.2	2.8	19.2	0.6	9.9	23.45	0.05	4.13	0.07	1
09943	SB(r)c	−20.7	0.64	17.3	5.4	5.3	18.3	2.1	315.1	19.39	0.33	1.06	6.37	1
09969	SAB(r)b	−21.4	0.65	17.7	2.6	2.7	20.4	8.1	533.4	20.89	2.07	2.12	100.18	1
10075	SAcd	−19.9	0.50	18.7	4.5	3.5	18.7	2.8	105.8	–	–	–	–	1
10359	SBcd pec	−19.0	0.48	19.4	2.3	6.4	19.6	2.1	68.7	–	–	–	–	1
10445*	Scd	−17.6	0.51	20.2	2.9	4.1	21.0	1.6	12.8	21.94	0.6	1.1	0.99	3
10521	SAc	−20.2	0.42	18.6	5.5	3.6	18.9	1.7	111.5	20.50	0.19	0.42	0.53	1
10652*	S(r)bc	−17.7	0.58	19.1	3.3	3.1	19.7	0.9	13.0	21.05	0.36	0.81	1.61	1
10757*	Scd	−17.7	0.51	20.2	2.4	2.4	21.1	1.4	8.1	22.45	0.47	1.08	3.34	1
10897	SAc	−19.5	0.46	18.8	3.4	3.0	19.7	1.9	63.9	20.7	0.69	0.24	1.58	1

Continued . . .

Table B.1 – Continued from previous page

Galaxy							**Disc**			**Bulge**				**RC**
UGC	type	Mag	(B − V)	μ_{0obs}	R_{25}/h	R_{last}/h	μ_0	h	L_D	μ_e	r_e	n	L_B	**flag**
(1)	(2)	(3)	(4)	(5)	(6)	(7)	(8)	(9)	(10)	(11)	(12)	(13)	(14)	(15)
11283	SBdm	−19.3	0.50	21.3	2.1	3.3	21.0	2.9	33.5	20.71	0.5	0.65	3.39	1
11300	Sd	−17.8	0.59	19.5	3.0	3.2	20.0	1.4	23.5	21.82	0.34	1.22	0.72	1
11470	SAb	−21.3	0.54	16.4	3.5	1.1	19.1	5.0	787.3	18.47	1.3	1.76	384.52	3
11557*	SABdm	−18.4	0.45	20.4	3.4	3.9	20.3	1.6	2.2	–	–	–	–	3
11597	SABcd	−20.6	0.40	16.5	3.4	2.0	19.1	2.8	227.4	20.18	0.37	0.37	7.3	1
11670	SA(r)0/a	−19.4	0.71	15.8	3.8	3.7	18.8	2.1	173.2	18.05	0.35	1.91	32.52	2
11707*	SAdm	−16.6	0.45	20.6	0.4	2.2	22.1	5.7	4.3	21.87	0.77	0.65	2.72	1
11852*	SBa	−20.2	0.67	17.9	2.9	2.1	19.6	3.8	254.3	18.36	0.45	1.58	37.35	2
11861*	SABdm	−20.2	0.45	18.7	1.0	2.2	18.7	6.5	121.6	–	–	–	–	1
11914	SA(r)ab	−20.3	0.77	15.2	4.3	3.3	17.8	2.3	595.0	17.28	0.59	1.49	314.29	1
11951*	SBa	−19.3	0.67	18.2	3.6	4.5	18.8	1.2	55.7	19.59	0.61	0.36	7.55	3
12060*	IBm	−16.5	0.42	21.0	1.2	3.9	20.9	2.0	1.0	–	–	–	–	2
12101	SAd	−18.5	0.51	19.4	3.5	2.0	20.3	1.6	27.0	21.16	0.42	0.54	1.13	3
12276	SB(r)a	−20.7	0.73	20.6	8.9	10.6	20.8	1.4	15.8	18.2	0.0	2.77	0.72	3
12343	SBc	−21.1	0.66	17.5	3.7	4.4	19.0	3.8	511.1	21.92	0.01	4.04	49.32	3
12754	SBcd	−18.6	0.46	19.1	3.9	4.6	19.1	1.2	38.3	–	–	–	–	2

mass models using the Best Fit Model (BFM) and fixed M/L techniques with the pseudo-isothermal
f the galaxy in the UGC catalogue, those marked with an asterisk (*) correspond to galaxies for which
er is not necessary. The columns (2) to (6) and (7) to (10) show respectively the BFM parameters, and
for the ISO model. (2): M/L of the disc in $M_\odot/L_\odot$; (3): M/L of the bulge in $M_\odot/L_\odot$. (4) & (8): the core
kpc; (5) & (9): the Central density of the DM halo in 10^{-3} $M_\odot/pc^3$; (6) & (10): the reduced χ^2; (7):
V colour in units of $M_\odot/L_\odot$.

Galaxies marked with an asterisk (*) correspond to those for which the presence of DM is not necessary.

Galaxy	**ISO (BFM)**					**ISO with fixed M/L**			
UGC	M/L Disc	M/L Bulge	r_0	ρ_0	χ^2	M/L	r_0	ρ_0	χ^2
(1)	(2)	(3)	(4)	(5)	(6)	(7)	(8)	(9)	(10)
00089*	$1.84^{0.01}_{1.74}$	$1.87^{0.97}_{1.77}$	> 39.2	27^{372}_{17}	7.0	1.52	$2.8^{2.3}_{2.3}$	196^{203}_{186}	9.3
00094	$0.81^{0.60}_{0.71}$	$5.13^{2.87}_{5.03}$	$1.0^{0.7}_{0.5}$	702^{47}_{652}	3.7	1.41	$1.0^{0.1}_{0.5}$	686^{63}_{636}	7.5
00508	$2.81^{0.69}_{2.71}$	$3.02^{0.98}_{2.92}$	$7.3^{6.0}_{6.8}$	102^{397}_{102}	1.4	2.20	$4.9^{0.4}_{4.4}$	215^{284}_{215}	1.5
00528*	$0.10^{0.05}_{0.01}$	$0.28^{0.18}_{0.18}$	$0.5^{7.5}_{0.1}$	203^{36}_{203}	2.5	0.78	$0.5^{7.5}_{0.1}$	0^{1}_{1}	177.7
00763	$0.32^{0.22}_{0.22}$	$2.94^{1.06}_{2.84}$	$2.0^{0.5}_{1.5}$	62^{43}_{52}	2.2	0.73	$2.7^{0.2}_{2.2}$	38^{67}_{28}	2.4
01317*	$0.43^{0.05}_{0.33}$	–	$1.0^{0.2}_{0.5}$	750^{1}_{730}	4.2	1.15	$0.8^{0.1}_{0.3}$	750^{1}_{730}	4.4
01437	$1.08^{0.27}_{0.98}$	$2.14^{1.86}_{2.04}$	$3.4^{3.1}_{2.9}$	26^{723}_{16}	2.4	1.00	$0.7^{0.1}_{0.2}$	750^{1}_{740}	6.2
01736	$0.10^{0.05}_{0.01}$	$0.10^{3.90}_{0.01}$	$2.5^{0.3}_{2.0}$	155^{145}_{145}	4.9	0.84	$3.6^{0.5}_{3.1}$	82^{217}_{72}	6.4
01886	$0.95^{0.93}_{0.85}$	$4.41^{3.59}_{4.31}$	$1.7^{5.8}_{1.2}$	329^{70}_{319}	4.4	1.18	$1.5^{0.2}_{1.0}$	391^{8}_{381}	3.6
01913	$0.10^{0.01}_{0.01}$	$0.10^{3.90}_{0.01}$	$5.9^{0.1}_{5.4}$	24^{81}_{24}	12.6	0.89	$33.1^{86.9}_{32.6}$	7^{98}_{7}	28.5
02045	$0.37^{0.01}_{0.27}$	$2.14^{1.86}_{2.04}$	> 20.4	67^{38}_{67}	3.3	1.32	$0.5^{99.5}_{0.1}$	0^{1}_{1}	63.0
02080*	$1.03^{0.62}_{0.93}$	$8.00^{0.01}_{7.90}$	$1.0^{0.2}_{0.5}$	188^{561}_{88}	2.2	1.29	$0.7^{0.2}_{0.2}$	336^{221}_{236}	2.2

Continued . . .

Table B.2 – Continued from previous page

Galaxy	ISO (BFM)					ISO with fixed M/L			
UGC	M/L Disc	M/L Bulge	r_0	ρ_0	χ^2	M/L	r_0	ρ_0	χ^2
(1)	(2)	(3)	(4)	(5)	(6)	(7)	(8)	(9)	(10)
02183	$0.10^{0.38}_{0.01}$	$1.25^{0.18}_{1.15}$	$2.8^{97.2}_{2.3}$	129^{170}_{129}	6.3	1.55	$0.5^{99.5}_{0.1}$	0^{6}_{1}	18.1
02193	$0.10^{0.66}_{0.01}$	$4.00^{0.01}_{3.90}$	$1.2^{0.3}_{0.7}$	617^{132}_{517}	2.0	1.03	$1.4^{0.3}_{0.9}$	469^{280}_{369}	2.1
02503	$0.10^{0.01}_{0.01}$	$0.10^{3.90}_{0.01}$	$2.0^{0.2}_{1.5}$	444^{55}_{434}	14.2	1.32	$2.7^{0.5}_{2.2}$	87^{412}_{77}	33.7
02800	$0.10^{0.01}_{0.01}$	–	$2.5^{1.0}_{2.0}$	45^{60}_{45}	5.3	0.69	$0.5^{7.5}_{0.1}$	0^{1}_{1}	82.7
02855*	$0.10^{0.01}_{0.01}$	$0.10^{0.01}_{0.01}$	$3.1^{1.3}_{2.6}$	6^{1}_{6}	26.9	1.08	$0.5^{57.5}_{0.1}$	0^{1}_{1}	6891.3
03013*	$0.21^{0.49}_{0.11}$	$1.16^{0.89}_{1.06}$	$2.9^{5.1}_{2.4}$	72^{327}_{72}	7.7	1.03	$0.7^{0.7}_{0.2}$	345^{54}_{345}	7.9
03334*	$1.18^{0.62}_{1.08}$	$1.96^{2.04}_{1.86}$	$1.9^{0.3}_{1.4}$	534^{215}_{34}	9.6	1.09	$1.7^{0.1}_{1.2}$	721^{28}_{221}	10.2
03382	$0.30^{1.20}_{0.20}$	$0.37^{3.63}_{0.27}$	$2.5^{10.7}_{2.0}$	422^{77}_{412}	1.7	1.55	$16.4^{1.6}_{15.9}$	32^{467}_{22}	1.9
03463	$1.46^{0.38}_{1.36}$	$1.52^{2.48}_{1.42}$	$2.0^{0.7}_{1.5}$	67^{38}_{67}	2.4	1.18	$1.9^{0.2}_{1.4}$	101^{4}_{101}	2.4
03521	$0.59^{1.91}_{0.49}$	$0.63^{3.37}_{0.53}$	$1.5^{1.7}_{1.0}$	227^{72}_{217}	0.6	1.10	$1.5^{0.3}_{1.0}$	174^{125}_{164}	0.5
03528*	$1.80^{1.30}_{1.70}$	$1.90^{6.11}_{1.79}$	$1.3^{2.8}_{0.8}$	699^{50}_{689}	9.1	1.41	$1.3^{0.4}_{0.8}$	750^{1}_{740}	6.8
03708	$0.70^{0.11}_{0.60}$	–	$16.3^{83.7}_{15.8}$	90^{409}_{90}	1.6	1.13	$0.5^{99.5}_{0.1}$	0^{22}_{1}	7.8
03809	$2.26^{0.15}_{2.16}$	$8.00^{0.01}_{7.90}$	$1.0^{0.3}_{0.5}$	738^{11}_{488}	6.4	0.87	$1.4^{0.1}_{0.9}$	636^{113}_{386}	7.7
03876	$0.90^{2.10}_{0.80}$	$2.66^{2.34}_{2.56}$	$1.5^{0.7}_{1.0}$	143^{56}_{133}	1.5	0.90	$1.4^{0.1}_{0.9}$	174^{25}_{164}	1.5
03915*	$0.10^{0.01}_{0.01}$	$4.00^{0.01}_{3.90}$	$1.2^{0.1}_{0.7}$	712^{37}_{512}	3.8	1.12	$1.0^{0.1}_{0.5}$	675^{75}_{475}	9.5
04026	$4.59^{0.18}_{4.49}$	$4.77^{3.23}_{4.67}$	$11.4^{108.6}_{10.9}$	17^{732}_{17}	5.2	1.41	$3.2^{0.1}_{2.7}$	255^{494}_{255}	40.4
04165*	$0.15^{0.27}_{0.05}$	$0.43^{4.57}_{0.33}$	$0.5^{0.1}_{0.1}$	436^{27}_{436}	2.5	1.00	$0.5^{0.1}_{0.1}$	109^{1}_{109}	2.7

Continued . . .

Table B.2 – Continued from previous page

Galaxy	ISO (BFM)					ISO with fixed M/L			
UGC	M/L Disc	M/L Bulge	r_0	ρ_0	χ^2	M/L	r_0	ρ_0	χ^2
(1)	(2)	(3)	(4)	(5)	(6)	(7)	(8)	(9)	(10)
04273	$0.70^{0.11}_{0.60}$	$0.72^{3.28}_{0.62}$	$3.6^{0.3}_{3.1}$	92^{13}_{82}	4.5	1.29	$4.6^{0.7}_{4.1}$	55^{50}_{45}	6.1
04284	$2.01^{0.27}_{1.91}$	$2.14^{1.86}_{2.04}$	$7.3^{2.3}_{6.8}$	23^{82}_{13}	4.3	0.62	$2.8^{0.1}_{2.3}$	60^{45}_{50}	6.0
04325	$0.10^{0.82}_{0.01}$	–	$2.9^{2.0}_{2.4}$	49^{56}_{39}	4.1	0.66	$3.7^{1.5}_{3.2}$	36^{69}_{26}	3.9
04456*	$0.10^{2.32}_{0.01}$	$0.10^{3.90}_{0.01}$	$1.7^{1.7}_{1.2}$	300^{200}_{200}	1.9	0.97	$1.9^{1.2}_{1.4}$	200^{300}_{100}	1.8
04499	$0.10^{0.01}_{0.01}$	–	$5.0^{4.5}_{4.5}$	25^{80}_{15}	25.5	0.82	$7.3^{92.7}_{6.8}$	18^{87}_{8}	32.3
04555	$0.70^{1.00}_{0.60}$	$0.99^{4.01}_{0.89}$	$0.8^{2.0}_{0.3}$	686^{63}_{636}	0.8	1.18	$0.7^{0.2}_{0.2}$	750^{1}_{700}	0.9
04820	$1.12^{1.45}_{1.02}$	$4.95^{3.05}_{4.85}$	$2.1^{0.8}_{1.6}$	479^{270}_{429}	2.0	2.26	$1.7^{0.1}_{1.2}$	734^{15}_{684}	6.1
04936	$1.60^{0.60}_{1.50}$	$1.66^{3.34}_{1.56}$	$4.6^{0.9}_{4.1}$	70^{129}_{20}	3.3	0.75	$3.6^{0.3}_{3.1}$	111^{88}_{61}	3.3
05045*	$4.98^{2.85}_{4.88}$	$13.12^{4.88}_{13.02}$	$1.7^{4.4}_{1.2}$	632^{117}_{622}	1.8	1.08	$2.5^{0.1}_{2.0}$	750^{1}_{740}	7.1
05228	$0.89^{0.13}_{0.79}$	–	$1.0^{0.2}_{0.5}$	245^{504}_{235}	2.7	1.08	$1.0^{0.1}_{0.5}$	228^{420}_{218}	2.9
05251	$0.15^{0.27}_{0.05}$	$1.07^{2.92}_{0.97}$	$2.9^{0.3}_{2.4}$	49^{56}_{39}	4.8	0.40	$2.2^{0.1}_{1.7}$	73^{32}_{63}	5.1
05253	$0.76^{0.38}_{0.66}$	$2.14^{1.24}_{2.04}$	$1.7^{2.0}_{1.2}$	240^{509}_{190}	2.8	1.48	$1.0^{0.1}_{0.5}$	670^{79}_{620}	3.4
05414*	$1.19^{0.60}_{1.09}$	–	$3.2^{3.6}_{2.7}$	20^{85}_{10}	6.0	0.75	$2.5^{0.3}_{2.0}$	29^{76}_{19}	5.8
05510	$0.41^{0.08}_{0.31}$	$0.46^{3.54}_{0.35}$	$0.8^{0.2}_{0.3}$	750^{1}_{550}	6.4	0.95	$1.0^{0.1}_{0.5}$	462^{287}_{262}	7.2
05840*	$5.38^{0.12}_{5.28}$	$5.49^{2.51}_{5.39}$	$1.0^{0.5}_{0.5}$	750^{1}_{650}	16.9	1.09	$1.7^{0.1}_{1.2}$	750^{1}_{650}	31.4
05842	$0.21^{0.76}_{0.11}$	$0.28^{3.72}_{0.18}$	$1.5^{0.7}_{1.0}$	134^{372}_{124}	1.7	0.99	$1.9^{0.3}_{1.4}$	66^{372}_{56}	1.8
05931	$0.48^{0.11}_{0.38}$	$0.54^{3.46}_{0.44}$	$3.1^{1.4}_{2.6}$	73^{32}_{63}	4.0	0.48	$3.1^{0.3}_{2.6}$	73^{32}_{63}	3.7

Continued . . .

Table B.2 – Continued from previous page

Galaxy	ISO (BFM)					ISO with fixed M/L			
UGC	M/L Disc	M/L Bulge	r_0	ρ_0	χ^2	M/L	r_0	ρ_0	χ^2
(1)	(2)	(3)	(4)	(5)	(6)	(7)	(8)	(9)	(10)
05982	$0.10^{0.74}_{0.01}$	$8.00^{0.01}_{7.90}$	$1.5^{0.2}_{1.0}$	357^{392}_{357}	5.0	1.09	$1.0^{0.1}_{0.5}$	681^{68}_{681}	13.2
06118	$0.32^{0.05}_{0.22}$	$0.72^{1.24}_{0.62}$	$2.2^{0.7}_{1.7}$	101^{4}_{101}	4.3	1.32	$0.5^{7.5}_{0.1}$	0^{1}_{1}	113.4
06277	$0.10^{1.90}_{0.01}$	$3.69^{4.31}_{3.59}$	$2.9^{10.3}_{2.4}$	469^{280}_{369}	1.7	1.08	$2.9^{1.6}_{2.4}$	395^{354}_{295}	1.9
06521*	$3.20^{0.70}_{3.10}$	$5.31^{2.69}_{5.21}$	$0.7^{0.7}_{0.2}$	705^{44}_{605}	3.5	0.89	$1.2^{0.1}_{0.7}$	750^{1}_{650}	7.2
06537	$0.10^{0.01}_{0.01}$	$0.10^{3.90}_{0.01}$	$2.5^{0.1}_{2.0}$	156^{149}_{136}	18.0	0.75	$2.9^{0.1}_{2.4}$	104^{201}_{84}	19.4
06702	$0.10^{0.27}_{0.01}$	$2.67^{0.62}_{2.57}$	$20.1^{13.6}_{19.6}$	11^{494}_{11}	22.9	1.18	$1.4^{0.1}_{0.9}$	322^{184}_{322}	37.1
06778	$2.06^{0.05}_{1.96}$	$2.14^{1.86}_{2.04}$	$5.5^{0.6}_{5.0}$	68^{631}_{63}	5.6	1.08	$1.8^{0.1}_{1.2}$	320^{379}_{315}	9.8
07021	$0.49^{0.08}_{0.39}$	$0.54^{3.46}_{0.44}$	$1.4^{0.2}_{0.9}$	750^{1}_{650}	7.3	1.76	$1.7^{0.2}_{1.2}$	365^{384}_{265}	18.5
07045	$0.60^{0.50}_{0.50}$	$5.13^{2.87}_{5.03}$	$1.4^{0.3}_{0.9}$	279^{470}_{269}	2.8	1.40	$0.7^{0.1}_{0.2}$	750^{1}_{740}	3.5
07154	$1.03^{0.27}_{0.93}$	$1.78^{2.22}_{1.68}$	$5.1^{0.7}_{4.6}$	16^{89}_{16}	5.4	0.89	$3.4^{0.1}_{2.9}$	31^{74}_{31}	6.5
07323	$1.57^{0.27}_{1.47}$	–	> 22.0	7^{98}_{7}	3.5	1.00	$2.9^{0.1}_{2.4}$	21^{84}_{21}	4.3
07766*	$0.92^{0.11}_{0.82}$	$3.11^{0.89}_{3.01}$	$3.2^{0.2}_{2.7}$	17^{732}_{17}	4.7	0.62	$0.5^{0.1}_{0.1}$	528^{1}_{528}	5.5
07831*	$0.10^{0.01}_{0.01}$	–	$0.7^{0.1}_{0.2}$	480^{218}_{470}	4.0	0.78	$0.5^{0.1}_{0.1}$	380^{16}_{370}	4.3
07861	$0.32^{0.01}_{0.22}$	$0.37^{0.35}_{0.27}$	> 8.4	16^{89}_{16}	2.0	1.09	$0.5^{119.5}_{0.1}$	0^{1}_{1}	14.3
07876	$0.10^{0.62}_{0.01}$	$0.28^{3.72}_{0.18}$	$1.4^{0.2}_{0.9}$	164^{141}_{154}	1.7	0.90	$1.5^{0.2}_{1.0}$	117^{188}_{107}	1.8
07901	$0.54^{0.16}_{0.44}$	$2.94^{1.06}_{2.84}$	$1.2^{0.3}_{0.7}$	535^{214}_{235}	3.3	0.92	$1.0^{0.1}_{0.5}$	750^{1}_{450}	10.6
07985	$0.10^{0.11}_{0.01}$	$0.37^{3.63}_{0.27}$	$0.7^{0.2}_{0.2}$	548^{201}_{538}	3.0	0.82	$0.7^{0.1}_{0.2}$	312^{168}_{302}	3.8

Continued . . .

Table B.2 – Continued from previous page

Galaxy	ISO (BFM)					ISO with fixed M/L			
UGC	M/L Disc	M/L Bulge	r_0	ρ_0	χ^2	M/L	r_0	ρ_0	χ^2
(1)	(2)	(3)	(4)	(5)	(6)	(7)	(8)	(9)	(10)
08334	$0.48^{0.01}_{0.38}$	$3.65^{0.35}_{3.54}$	$1.0^{0.2}_{0.5}$	733^{16}_{723}	4.9	1.32	$0.8^{0.1}_{0.3}$	615^{134}_{605}	13.0
08403	$0.10^{0.01}_{0.01}$	–	$5.5^{0.1}_{5.0}$	24^{81}_{24}	3.9	0.73	$15.4^{0.1}_{14.9}$	9^{96}_{9}	10.6
08490	$1.96^{0.54}_{1.85}$	$1.96^{2.04}_{1.86}$	$1.0^{0.9}_{0.5}$	195^{555}_{185}	2.1	0.69	$0.7^{0.1}_{0.2}$	447^{218}_{437}	2.2
08709	$3.11^{0.15}_{3.01}$	$3.11^{0.89}_{3.01}$	$3.7^{0.1}_{3.2}$	34^{465}_{34}	11.1	0.73	$1.7^{0.1}_{1.2}$	272^{227}_{272}	15.6
08852	$0.96^{0.17}_{0.86}$	$1.21^{2.79}_{1.11}$	$1.6^{0.5}_{1.1}$	263^{42}_{253}	7.4	1.29	$1.6^{0.1}_{1.1}$	221^{84}_{211}	7.4
08900	$0.10^{0.66}_{0.01}$	$1.34^{2.66}_{1.24}$	$8.6^{3.1}_{8.1}$	77^{28}_{67}	3.0	1.22	$8.0^{0.6}_{7.5}$	71^{34}_{61}	3.2
08937	$2.11^{0.08}_{2.01}$	$5.31^{2.69}_{5.21}$	$7.0^{0.5}_{6.5}$	43^{706}_{33}	6.1	1.29	$1.4^{0.1}_{0.9}$	750^{1}_{740}	20.1
09179	$0.10^{0.66}_{0.01}$	$0.90^{3.10}_{0.80}$	$1.5^{0.1}_{1.0}$	178^{127}_{168}	4.1	0.80	$1.5^{0.2}_{1.0}$	164^{141}_{154}	4.1
09248	$0.10^{0.27}_{0.01}$	$0.10^{3.90}_{0.01}$	$1.0^{0.2}_{0.5}$	598^{151}_{588}	4.6	1.29	$1.0^{0.2}_{0.5}$	380^{370}_{370}	5.6
09358	$1.41^{0.16}_{1.31}$	$8.00^{0.01}_{7.90}$	$10.7^{2.4}_{9.7}$	26^{723}_{16}	6.5	1.29	$1.0^{0.1}_{0.1}$	733^{1}_{723}	27.3
09363	$0.10^{0.44}_{0.01}$	$0.99^{3.01}_{0.89}$	$3.2^{0.1}_{2.7}$	58^{48}_{48}	3.0	1.36	$8.6^{0.1}_{8.1}$	14^{91}_{4}	3.2
09366	$0.97^{0.16}_{0.87}$	$2.32^{1.68}_{2.22}$	$1.0^{1.2}_{0.5}$	598^{151}_{588}	4.4	1.03	$1.0^{0.1}_{0.5}$	750^{1}_{740}	7.5
09465	$0.15^{0.49}_{0.05}$	–	$1.5^{0.2}_{1.0}$	97^{8}_{87}	1.7	0.82	$1.7^{0.1}_{1.2}$	73^{32}_{63}	1.9
09576	$0.10^{0.60}_{0.01}$	$0.81^{3.19}_{0.71}$	$2.8^{1.1}_{2.2}$	33^{72}_{33}	6.9	1.06	$5.0^{0.1}_{4.5}$	9^{96}_{9}	7.3
09649*	$6.40^{0.38}_{6.30}$	$18.00^{0.01}_{17.90}$	$7.8^{100.2}_{7.3}$	17^{732}_{17}	17.7	1.29	$0.5^{0.1}_{0.1}$	664^{17}_{664}	23.0
09736	$1.49^{0.85}_{1.39}$	$4.59^{3.41}_{4.49}$	$1.2^{2.0}_{0.7}$	288^{461}_{238}	9.0	1.18	$0.8^{0.1}_{0.3}$	638^{111}_{588}	8.1
09753	$1.41^{0.01}_{1.31}$	$1.43^{2.57}_{1.33}$	$0.7^{0.2}_{0.2}$	732^{17}_{732}	8.4	0.82	$0.8^{0.1}_{0.3}$	681^{68}_{681}	18.5

Continued . . .

Table B.2 – Continued from previous page

Galaxy	ISO (BFM)					ISO with fixed M/L			
UGC	M/L Disc	M/L Bulge	r_0	ρ_0	χ^2	M/L	r_0	ρ_0	χ^2
(1)	(2)	(3)	(4)	(5)	(6)	(7)	(8)	(9)	(10)
09858*	$1.52^{0.98}_{1.42}$	$1.54^{6.46}_{1.44}$	$1.0^{0.3}_{0.5}$	392^{357}_{392}	7.3	1.18	$1.0^{0.1}_{0.5}$	409^{340}_{409}	7.0
09866*	$3.11^{0.78}_{3.01}$	$3.11^{1.89}_{3.01}$	$1.1^{1.9}_{0.6}$	233^{173}_{173}	2.1	1.18	$1.8^{0.1}_{1.2}$	398^{7}_{338}	5.8
09943	$1.14^{0.06}_{1.04}$	$1.61^{2.39}_{1.51}$	$2.8^{2.3}_{2.3}$	72^{33}_{72}	3.1	1.32	$2.8^{0.1}_{2.3}$	57^{48}_{57}	3.9
09969	$0.10^{0.49}_{0.01}$	$0.28^{7.72}_{0.18}$	$1.9^{0.2}_{1.4}$	619^{130}_{589}	3.6	1.36	$1.7^{0.1}_{1.2}$	602^{147}_{572}	3.8
10075*	$0.21^{0.11}_{0.11}$	–	$1.2^{0.1}_{0.7}$	427^{78}_{417}	5.1	0.89	$1.2^{0.1}_{0.7}$	370^{135}_{360}	5.2
10359	$0.33^{0.08}_{0.23}$	$8.00^{0.01}_{7.90}$	$3.6^{0.1}_{3.1}$	48^{57}_{48}	3.2	0.84	$6.8^{0.1}_{6.2}$	21^{84}_{21}	5.4
10521*	$0.10^{0.11}_{0.01}$	$0.10^{3.90}_{0.01}$	$1.0^{0.1}_{0.5}$	359^{146}_{349}	2.9	0.71	$1.0^{0.1}_{0.5}$	246^{259}_{236}	3.5
10652	$0.10^{0.08}_{0.01}$	$0.10^{5.90}_{0.01}$	$1.1^{0.1}_{0.6}$	682^{67}_{672}	7.9	1.18	$1.8^{0.1}_{1.2}$	346^{403}_{336}	9.6
10757	$0.10^{1.23}_{0.01}$	$2.97^{3.05}_{2.87}$	> 13.6	31^{74}_{21}	1.7	0.99	$3.0^{0.1}_{2.5}$	51^{54}_{41}	2.8
10897	$0.10^{0.01}_{0.01}$	$0.10^{3.90}_{0.01}$	$1.7^{0.4}_{1.2}$	127^{78}_{112}	3.2	0.80	$2.9^{0.4}_{2.4}$	36^{169}_{21}	6.3
11283*	$1.79^{0.71}_{1.69}$	$1.79^{0.71}_{1.69}$	$0.8^{0.2}_{0.3}$	555^{194}_{255}	9.7	0.89	$0.8^{0.1}_{0.3}$	698^{51}_{398}	9.2
11300	$0.37^{1.42}_{0.27}$	$2.94^{1.06}_{2.84}$	$1.7^{0.5}_{1.2}$	134^{71}_{124}	4.2	1.15	$1.4^{0.2}_{0.9}$	152^{53}_{142}	4.7
11597*	$0.26^{0.01}_{0.15}$	$0.88^{2.45}_{0.78}$	$0.5^{0.9}_{0.1}$	490^{109}_{490}	6.0	0.67	$0.5^{7.5}_{0.1}$	0^{1}_{1}	82.5
11670	$0.10^{0.08}_{0.01}$	$1.20^{0.50}_{1.10}$	$0.8^{0.1}_{0.3}$	715^{34}_{715}	6.3	1.61	$0.5^{7.5}_{0.1}$	0^{1}_{1}	43.8
11707	$0.10^{0.49}_{0.01}$	$0.19^{3.81}_{0.09}$	$3.2^{0.7}_{2.7}$	27^{78}_{17}	2.7	0.82	$3.6^{0.5}_{3.1}$	18^{87}_{8}	2.8
11852	$0.10^{0.01}_{0.01}$	$0.10^{3.81}_{0.01}$	$2.5^{0.1}_{2.0}$	266^{233}_{256}	53.4	1.55	$9.6^{3.6}_{9.1}$	32^{467}_{22}	73.4
11861	$0.10^{0.01}_{0.01}$	–	$7.3^{0.1}_{6.8}$	19^{86}_{19}	5.3	0.82	$0.5^{99.5}_{0.1}$	0^{1}_{1}	302.5

Continued . . .

Table B.2 – Continued from previous page

Galaxy	ISO (BFM)					ISO with fixed M/L			
UGC	M/L Disc	M/L Bulge	r_0	ρ_0	χ^2	M/L	r_0	ρ_0	χ^2
(1)	(2)	(3)	(4)	(5)	(6)	(7)	(8)	(9)	(10)
11914*	$0.26^{0.27}_{0.16}$	$0.99^{0.62}_{0.89}$	$1.9^{0.5}_{1.4}$	293^{6}_{293}	2.3	1.91	$0.5^{7.5}_{0.1}$	0^{1}_{1}	419.3
12060*	$3.54^{0.49}_{3.44}$	–	$4.1^{3.9}_{3.6}$	9^{190}_{9}	11.8	0.75	$1.2^{0.1}_{0.7}$	136^{63}_{136}	12.3
12754	$0.76^{0.01}_{0.66}$	–	$1.8^{0.1}_{1.2}$	136^{613}_{136}	6.3	0.80	$1.8^{0.1}_{1.2}$	136^{613}_{136}	6.3

Table B.3: Parameters of mass models using the maximum disc model (MDM) technique with the pseudo-isothermal (ISO) model: (1) Name of the galaxy in the UGC catalogue; (2) M/L of the disc in $M_\odot/L_\odot$; (3) M/L of the bulge in $M_\odot/L_\odot$; (4) Core radius of the DM halo in kpc; (5) Central density of the DM halo in 10^{-3} $M_\odot/pc^3$; (6) The reduced χ^2.

Galaxy	**Maximum Disc Model**				
UGC	M/L Disc	M/L Bulge	r_0	ρ_0	χ^2
(1)	(2)	(3)	(4)	(5)	(6)
00089	$2.01^{0.01}_{1.91}$	$2.05^{0.80}_{1.95}$	$3.6^{4.4}_{3.1}$	36^{363}_{36}	9.4
00094	$2.20^{0.01}_{2.10}$	$7.82^{0.18}_{7.72}$	$2.4^{0.1}_{1.9}$	81^{668}_{31}	4.8
00508	$4.10^{0.01}_{4.00}$	$4.11^{0.89}_{4.01}$	$18.6^{0.1}_{18.1}$	23^{483}_{23}	1.9
00528	$0.18^{0.01}_{0.08}$	$0.19^{0.27}_{0.09}$	$0.5^{0.1}_{0.1}$	0^{239}_{1}	3.2
00763	$0.97^{0.01}_{0.87}$	$0.99^{3.01}_{0.89}$	$3.4^{0.1}_{2.9}$	23^{82}_{13}	2.8
01317	$3.10^{0.01}_{3.00}$	–	$0.5^{2.9}_{0.1}$	0^{106}_{1}	16.0
01437	$1.57^{0.01}_{1.47}$	$1.96^{2.04}_{1.86}$	$5.8^{2.2}_{5.3}$	2^{103}_{2}	3.0
01736	$0.70^{0.01}_{0.60}$	$0.72^{3.28}_{0.62}$	$2.7^{0.3}_{2.2}$	115^{35}_{105}	6.4
01886	$2.50^{0.01}_{2.40}$	$2.61^{5.39}_{2.51}$	$14.1^{2.3}_{13.6}$	4^{101}_{4}	5.9
01913	$0.32^{0.01}_{0.22}$	$0.37^{3.63}_{0.27}$	$4.6^{0.1}_{4.1}$	23^{82}_{13}	15.0
02045	$0.48^{0.01}_{0.38}$	$1.70^{2.30}_{1.59}$	$5.6^{2.4}_{5.1}$	67^{38}_{67}	4.4
02080	$2.73^{0.01}_{2.63}$	$2.79^{5.21}_{2.69}$	$0.5^{1.5}_{0.1}$	0^{106}_{1}	2.9
02183	$1.25^{0.01}_{1.15}$	$1.25^{0.18}_{1.15}$	$1.2^{6.8}_{0.7}$	81^{218}_{81}	8.0
02193	$3.65^{0.01}_{3.54}$	$3.65^{0.35}_{3.54}$	$7.1^{0.1}_{6.6}$	77^{428}_{67}	2.7
02503	$0.26^{0.01}_{0.16}$	$0.28^{3.72}_{0.18}$	$1.5^{0.7}_{1.0}$	661^{88}_{561}	18.5
02800	$0.21^{0.01}_{0.11}$	–	$2.4^{1.0}_{1.9}$	25^{80}_{15}	6.8
02855	$0.10^{0.01}_{0.01}$	$0.10^{0.01}_{0.01}$	$0.5^{7.0}_{0.1}$	0^{9}_{1}	29.5
03013	$1.30^{0.01}_{1.20}$	$1.34^{0.71}_{1.24}$	$0.5^{7.5}_{0.1}$	0^{106}_{1}	9.9
03334	$3.17^{0.01}_{3.07}$	$3.33^{4.67}_{3.23}$	$0.5^{7.5}_{0.1}$	0^{106}_{1}	12.4
03382	$1.50^{0.10}_{1.40}$	$1.55^{3.45}_{1.45}$	$8.5^{9.5}_{8.0}$	49^{50}_{19}	2.5
03463	$2.34^{0.01}_{2.24}$	$2.40^{1.60}_{2.30}$	$1.9^{0.9}_{1.4}$	7^{98}_{7}	3.2
03521	$1.52^{0.98}_{1.42}$	$1.52^{2.48}_{1.42}$	$1.5^{1.7}_{1.0}$	135^{164}_{125}	0.7
03528	$4.00^{0.01}_{3.90}$	$4.05^{3.95}_{3.95}$	$0.5^{6.0}_{0.1}$	0^{200}_{1}	12.2
03708	$0.76^{0.01}_{0.66}$	–	$2.2^{35.8}_{1.7}$	90^{109}_{10}	2.0
03809	$4.59^{0.01}_{4.49}$	$7.64^{0.36}_{7.54}$	$0.7^{0.7}_{0.2}$	484^{265}_{384}	8.0

Continued . . .

Table B.3 – Continued from previous page

Galaxy	Maximum Disc Model				
UGC	M/L Disc	M/L Bulge	r_0	ρ_0	χ^2
(1)	(2)	(3)	(4)	(5)	(6)
03876	$4.00^{0.01}_{3.90}$	$4.11^{0.89}_{4.01}$	$3.4^{0.1}_{2.9}$	26^{73}_{16}	1.9
03915	$2.60^{0.01}_{2.50}$	$8.00^{0.01}_{7.90}$	$0.5^{4.6}_{0.1}$	36^{63}_{36}	13.1
04026	$5.05^{0.01}_{4.95}$	$5.05^{4.95}_{4.95}$	$3.6^{24.4}_{3.1}$	19^{86}_{19}	6.3
04165	$1.35^{0.01}_{1.25}$	$1.36^{6.64}_{1.26}$	$0.5^{0.3}_{0.1}$	0^{200}_{1}	3.2
04273	$1.14^{0.01}_{1.04}$	$1.16^{2.84}_{1.06}$	$4.1^{0.1}_{3.6}$	68^{37}_{58}	5.8
04284	$3.00^{0.01}_{2.90}$	$3.05^{2.95}_{2.95}$	$13.6^{0.1}_{13.1}$	14^{91}_{4}	5.6
04325	$2.17^{0.01}_{2.07}$	–	$6.3^{0.1}_{5.8}$	14^{91}_{4}	5.2
04456	$4.46^{0.01}_{4.36}$	$4.59^{3.41}_{4.49}$	$0.5^{7.5}_{0.1}$	0^{50}_{1}	2.6
04499	$0.70^{0.01}_{0.60}$	–	$4.8^{3.2}_{4.3}$	20^{85}_{10}	32.3
04555	$1.57^{0.01}_{1.47}$	$5.84^{2.16}_{5.75}$	$1.0^{2.0}_{0.5}$	196^{9}_{196}	1.1
04820	$4.46^{0.01}_{4.36}$	$4.59^{3.41}_{4.49}$	$0.5^{9.9}_{0.1}$	73^{76}_{63}	2.9
04936	$3.80^{0.01}_{3.70}$	$3.87^{4.13}_{3.77}$	$6.5^{0.1}_{6.0}$	32^{67}_{22}	4.2
05045	$9.55^{0.01}_{9.45}$	$18.00^{0.01}_{17.90}$	$0.5^{9.1}_{0.1}$	50^{50}_{50}	2.5
05228	$1.41^{0.01}_{1.31}$	–	$0.8^{0.3}_{0.3}$	227^{272}_{227}	3.0
05251	$1.57^{0.01}_{1.47}$	$1.61^{2.39}_{1.51}$	$4.6^{0.1}_{4.1}$	18^{87}_{8}	6.2
05253	$1.63^{0.01}_{1.53}$	$1.96^{1.42}_{1.86}$	$1.4^{2.4}_{0.9}$	280^{19}_{270}	3.6
05414	$3.08^{0.01}_{2.98}$	–	$9.2^{0.1}_{8.8}$	4^{101}_{4}	7.3
05510	$2.60^{0.01}_{2.50}$	$2.61^{5.39}_{2.51}$	$3.7^{0.2}_{3.2}$	31^{74}_{21}	14.1
05840	$10.22^{0.01}_{10.12}$	$10.27^{7.73}_{10.17}$	$0.5^{1.7}_{0.1}$	0^{406}_{1}	22.2
05842	$1.57^{0.01}_{1.47}$	$1.61^{2.39}_{1.51}$	$2.9^{0.1}_{2.4}$	21^{484}_{11}	2.2
05931	$0.86^{0.01}_{0.76}$	$0.90^{3.10}_{0.80}$	$4.9^{0.1}_{4.4}$	36^{69}_{26}	5.2
05982	$3.78^{0.01}_{3.68}$	$8.00^{0.01}_{7.90}$	$7.8^{0.1}_{7.3}$	6^{299}_{6}	6.4
06118	$0.59^{0.01}_{0.49}$	$0.63^{1.33}_{0.53}$	$1.2^{1.7}_{0.7}$	103^{2}_{93}	5.5
06277	$3.40^{0.01}_{3.30}$	$3.51^{4.49}_{3.41}$	$11.6^{6.4}_{11.1}$	117^{188}_{107}	2.3
06521	$4.53^{0.01}_{4.43}$	$5.84^{2.16}_{5.75}$	$0.5^{0.9}_{0.1}$	0^{750}_{1}	4.6
06537	$1.84^{0.01}_{1.74}$	$1.87^{2.13}_{1.77}$	$3.6^{0.1}_{3.1}$	46^{260}_{26}	23.5
06702	$2.55^{0.01}_{2.45}$	$2.55^{0.78}_{2.45}$	$3.4^{4.6}_{2.9}$	9^{96}_{9}	30.4
06778	$2.39^{0.01}_{2.29}$	$2.40^{1.60}_{2.30}$	$6.8^{0.1}_{6.2}$	50^{55}_{50}	7.1
07021	$0.80^{0.01}_{0.70}$	$0.82^{4.49}_{0.72}$	$1.4^{0.2}_{0.9}$	649^{100}_{639}	9.6

Continued . . .

Table B.3 – Continued from previous page

Galaxy	Maximum Disc Model				
UGC	M/L Disc	M/L Bulge	r_0	ρ_0	χ^2
(1)	(2)	(3)	(4)	(5)	(6)
07045	$3.20^{0.01}_{3.10}$	$6.92^{1.08}_{6.82}$	$5.1^{0.1}_{4.6}$	14^{91}_{14}	4.0
07154	$2.34^{0.01}_{2.24}$	$2.40^{1.60}_{2.30}$	$9.5^{0.1}_{9.0}$	4^{101}_{4}	6.9
07323	$2.28^{0.01}_{2.18}$	–	$3.3^{14.7}_{2.8}$	2^{103}_{2}	4.5
07766	$1.68^{0.01}_{1.58}$	$1.70^{2.30}_{1.59}$	$0.5^{4.1}_{0.1}$	0^{106}_{1}	5.7
07831	$1.74^{0.01}_{1.64}$	–	$0.5^{7.5}_{0.1}$	0^{106}_{1}	6.5
07861	$0.43^{0.01}_{0.33}$	$0.46^{0.27}_{0.35}$	$1.1^{26.9}_{0.6}$	9^{96}_{9}	2.3
07876	$1.34^{0.01}_{1.24}$	$1.34^{2.66}_{1.24}$	$1.5^{0.2}_{1.0}$	99^{106}_{89}	2.2
07901	$1.34^{0.01}_{1.24}$	$3.33^{4.67}_{3.23}$	$2.7^{0.1}_{2.2}$	90^{215}_{80}	4.1
07985	$0.86^{0.01}_{0.76}$	$0.90^{3.10}_{0.80}$	$0.7^{0.3}_{0.2}$	279^{26}_{269}	4.2
08334	$1.34^{0.01}_{1.24}$	$3.73^{0.27}_{3.63}$	$1.7^{0.1}_{1.2}$	153^{596}_{153}	5.8
08403	$0.26^{0.01}_{0.16}$	–	$6.5^{0.1}_{6.0}$	19^{86}_{19}	4.7
08490	$3.40^{0.01}_{3.30}$	$3.51^{4.49}_{3.41}$	$3.7^{0.1}_{3.2}$	43^{262}_{33}	2.8
08709	$4.53^{0.01}_{4.43}$	$4.53^{1.47}_{4.43}$	$5.8^{0.1}_{5.3}$	4^{101}_{4}	14.4
08852	$1.47^{0.01}_{1.37}$	$1.49^{2.51}_{1.39}$	$1.6^{0.5}_{1.1}$	158^{148}_{148}	9.4
08900	$1.52^{0.01}_{1.42}$	$1.52^{2.48}_{1.42}$	$8.0^{3.8}_{7.5}$	64^{41}_{54}	3.9
08937	$2.68^{0.01}_{2.58}$	$4.77^{3.23}_{4.67}$	$5.6^{2.4}_{5.1}$	34^{715}_{34}	7.9
09179	$2.28^{0.01}_{2.18}$	$2.32^{1.68}_{2.22}$	$2.4^{0.1}_{1.9}$	77^{228}_{67}	5.4
09248	$1.41^{0.01}_{1.31}$	$1.44^{4.56}_{1.34}$	$1.2^{0.5}_{0.7}$	272^{33}_{262}	7.0
09358	$2.20^{0.01}_{2.10}$	$7.64^{0.36}_{7.54}$	$18.6^{61.4}_{18.1}$	12^{93}_{2}	6.8
09363	$1.68^{0.01}_{1.58}$	$1.70^{2.30}_{1.59}$	$7.5^{0.1}_{7.0}$	12^{93}_{2}	3.8
09366	$1.96^{0.01}_{1.85}$	$2.94^{1.06}_{2.84}$	$0.7^{1.5}_{0.2}$	413^{336}_{403}	5.5
09465	$1.19^{0.01}_{1.09}$	–	$1.7^{0.1}_{1.2}$	66^{39}_{56}	2.2
09576	$1.25^{0.01}_{1.15}$	$1.25^{2.75}_{1.15}$	$5.4^{0.1}_{4.9}$	7^{98}_{7}	8.9
09649	$9.29^{0.01}_{9.19}$	$15.97^{2.03}_{15.87}$	$0.5^{37.5}_{0.1}$	0^{506}_{1}	22.5
09736	$3.54^{0.01}_{3.44}$	$8.00^{0.01}_{7.90}$	$0.5^{2.7}_{0.1}$	238^{511}_{238}	11.0
09753	$2.12^{0.01}_{2.02}$	$2.14^{1.86}_{2.04}$	$1.2^{0.1}_{0.7}$	220^{385}_{220}	11.8
09858	$5.65^{0.01}_{5.55}$	$5.67^{2.33}_{5.57}$	$2.4^{0.1}_{1.9}$	17^{732}_{17}	9.5
09866	$4.68^{0.01}_{4.58}$	$4.75^{4.25}_{4.65}$	$8.6^{19.4}_{8.1}$	18^{181}_{18}	2.8
09943	$1.30^{0.01}_{1.20}$	$1.34^{2.66}_{1.24}$	$2.8^{2.3}_{2.3}$	55^{50}_{55}	4.0

Continued . . .

Table B.3 – Continued from previous page

Galaxy	Maximum Disc Model				
UGC	M/L Disc	M/L Bulge	r_0	ρ_0	χ^2
(1)	(2)	(3)	(4)	(5)	(6)
09969	$3.84^{0.01}_{3.84}$	$4.54^{3.46}_{4.54}$	$1.9^{0.9}_{1.8}$	262^{43}_{232}	5.2
10075	$4.41^{0.01}_{4.31}$	–	$32.0^{0.1}_{31.5}$	4^{201}_{4}	7.6
10359	$0.60^{0.01}_{0.50}$	$5.31^{2.69}_{5.21}$	$3.7^{0.3}_{3.2}$	38^{67}_{38}	4.1
10521	$1.74^{0.01}_{1.64}$	$1.78^{2.22}_{1.68}$	$1.2^{1.4}_{0.7}$	58^{48}_{48}	6.4
10652	$0.97^{0.01}_{0.87}$	$1.00^{7.00}_{0.90}$	$1.8^{0.1}_{1.2}$	346^{403}_{336}	10.1
10757	$1.68^{0.01}_{1.58}$	$2.05^{1.95}_{1.95}$	$6.6^{1.4}_{6.1}$	23^{82}_{13}	2.3
10897	$0.32^{0.01}_{0.22}$	$0.37^{3.63}_{0.27}$	$1.7^{0.5}_{1.2}$	103^{2}_{93}	4.1
11283	$6.16^{0.01}_{6.06}$	$6.17^{2.83}_{6.07}$	$0.5^{2.7}_{0.1}$	0^{106}_{1}	14.1
11300	$2.96^{0.01}_{2.86}$	$3.13^{5.87}_{3.03}$	$3.1^{0.1}_{2.6}$	36^{69}_{26}	5.4
11597	$0.37^{0.01}_{0.27}$	$0.63^{2.66}_{0.53}$	$0.5^{2.2}_{0.1}$	0^{106}_{1}	7.7
11670	$1.18^{0.01}_{1.08}$	$1.25^{0.44}_{1.15}$	$6.6^{0.1}_{6.1}$	16^{89}_{16}	10.9
11707	$1.10^{0.01}_{1.00}$	$1.20^{3.30}_{1.10}$	$3.9^{0.1}_{3.4}$	14^{91}_{14}	3.5
11852	$0.59^{0.01}_{0.49}$	$0.63^{3.19}_{0.53}$	$2.4^{0.3}_{1.9}$	209^{190}_{159}	69.0
11861	$0.10^{0.01}_{0.01}$	–	$3.2^{3.6}_{2.7}$	49^{56}_{39}	5.5
11914	$0.81^{0.01}_{0.71}$	$0.90^{0.71}_{0.80}$	$0.5^{4.8}_{0.1}$	0^{106}_{1}	3.0
12060	$5.63^{0.01}_{5.53}$	–	$0.5^{7.5}_{0.1}$	0^{106}_{1}	13.6
12754	$1.63^{0.01}_{1.53}$	–	$2.7^{0.2}_{2.2}$	51^{54}_{41}	8.1

Table B.4: Parameters of mass models using the Best Fit Model (BFM) and fixed M/L techniques with the Navarro-Frenk-White model (NFW): (1) Name of the galaxy in the UGC catalogue; the columns (2) to (6) and (7) to (10) show respectively the BFM parameters, and the fixed M/L parameters for the NFW model. (2): M/L of the disc in $M_\odot/L_\odot$; (3): M/L of the bulge in $M_\odot/L_\odot$. (4) & (8): the central halo concentration index; (5) & (9): the halo velocity in km s^{-1}; (6) & (10): the reduced χ^2; (7): M/L derived using the B - V color in units of $M_\odot/L_\odot$.

Galaxy	**NFW (BFM)**					**NFW with fixed M/L**			
UGC	M/L Disc	M/L Bulge	c	V_{200}	χ^2	M/L	c	V_{200}	χ^2
(1)	(2)	(3)	(4)	(5)	(6)	(7)	(8)	(9)	(10)
00089	$1.68^{0.05}_{1.58}$	$1.70^{1.15}_{1.59}$	$5.1^{6.5}_{4.1}$	$500.0^{0.1}_{490.0}$	7.8	1.52	$6.9^{5.3}_{5.9}$	$455.5^{44.5}_{445.5}$	8.0
00094	$0.37^{1.15}_{0.27}$	$0.46^{7.54}_{0.36}$	$45.2^{4.3}_{35.2}$	$105.9^{94.1}_{85.9}$	3.8	1.41	$43.1^{1.1}_{33.1}$	$89.5^{110.5}_{69.5}$	4.0
00508	$0.59^{1.91}_{0.49}$	$2.14^{1.86}_{2.04}$	$20.5^{7.9}_{12.5}$	$390.9^{109.1}_{190.9}$	1.3	2.20	$14.6^{2.0}_{6.6}$	$397.7^{102.3}_{197.7}$	1.3
00528	$0.10^{0.01}_{0.01}$	$0.10^{0.35}_{0.01}$	$58.8^{19.3}_{57.8}$	$25.8^{74.2}_{24.8}$	2.3	0.78	$1.0^{106.0}_{0.1}$	$1.0^{0.1}_{0.1}$	177.7
00763	$0.26^{0.16}_{0.16}$	$0.28^{3.72}_{0.18}$	$11.0^{1.2}_{10.0}$	$89.1^{310.9}_{69.1}$	2.8	0.73	$4.0^{0.6}_{3.0}$	$175.5^{224.5}_{155.5}$	3.0
01317	$0.10^{0.05}_{0.01}$	–	$28.0^{0.1}_{27.0}$	$128.2^{171.8}_{108.2}$	4.1	1.15	$28.0^{0.1}_{27.0}$	$102.7^{197.3}_{82.7}$	5.4
01437	$1.30^{0.11}_{1.20}$	$2.05^{1.95}_{1.95}$	$2.3^{53.5}_{1.3}$	$159.1^{40.9}_{139.1}$	2.4	1.00	$44.3^{1.3}_{43.3}$	$77.3^{122.7}_{57.3}$	2.6
01736	$0.10^{0.01}_{0.01}$	$0.10^{3.90}_{0.01}$	$5.1^{3.5}_{4.1}$	$472.7^{27.3}_{372.7}$	5.9	0.84	$4.0^{0.6}_{3.0}$	$500.0^{0.1}_{400.0}$	7.3
01886	$0.41^{1.31}_{0.31}$	$0.64^{7.36}_{0.54}$	$31.5^{8.9}_{30.5}$	$149.5^{250.5}_{129.5}$	4.2	1.18	$18.8^{3.8}_{17.8}$	$149.5^{250.5}_{129.5}$	3.6
01913	$0.10^{0.01}_{0.01}$	$0.10^{3.90}_{0.01}$	$1.6^{0.1}_{0.6}$	$500.0^{0.1}_{480.0}$	21.2	0.89	$1.0^{0.1}_{0.1}$	$303.6^{0.1}_{283.6}$	37.4
02045	$0.10^{0.01}_{0.01}$	$1.16^{2.84}_{1.06}$	$10.0^{0.1}_{9.0}$	$286.4^{13.6}_{285.4}$	3.6	1.32	$55.0^{45.0}_{54.0}$	$1.0^{0.1}_{0.1}$	63.0
02080	$0.92^{0.82}_{0.82}$	$8.00^{0.01}_{7.90}$	$14.6^{7.3}_{13.6}$	$77.3^{122.7}_{57.3}$	2.2	1.29	$17.7^{0.1}_{16.7}$	$60.9^{139.1}_{40.9}$	2.2
02183	$0.10^{0.33}_{0.01}$	$0.72^{0.71}_{0.62}$	$54.5^{2.5}_{53.5}$	$64.5^{335.5}_{63.5}$	5.2	1.55	$1.0^{56.0}_{0.1}$	$1.0^{27.2}_{0.1}$	18.1

Continued . . .

Table B.4 – Continued from previous page

Galaxy	NFW (BFM)					NFW with fixed M/L			
UGC	M/L Disc	M/L Bulge	c	V_{200}	χ^2	M/L	c	V_{200}	χ^2
(1)	(2)	(3)	(4)	(5)	(6)	(7)	(8)	(9)	(10)
02193	$0.10^{0.71}_{0.01}$	$0.10^{3.90}_{0.01}$	$9.3^{11.8}_{8.3}$	$390.9^{109.1}_{290.9}$	2.1	1.03	$6.9^{5.3}_{5.9}$	$472.7^{27.3}_{372.7}$	2.2
02503	$0.10^{0.01}_{0.01}$	$0.10^{3.90}_{0.01}$	$21.1^{4.1}_{20.1}$	$201.4^{198.6}_{181.4}$	19.5	1.32	$9.3^{3.5}_{8.3}$	$158.2^{241.8}_{138.2}$	35.2
02800	$0.10^{0.05}_{0.01}$	–	$2.2^{1.8}_{1.2}$	$363.6^{36.4}_{163.6}$	6.9	0.69	$1.0^{0.1}_{0.1}$	$200.0^{0.1}_{0.1}$	103.9
02855	$0.10^{0.01}_{0.01}$	$0.10^{0.01}_{0.01}$	$1.0^{0.6}_{0.1}$	$69.0^{34.0}_{68.0}$	27.1	1.08	$27.0^{0.1}_{26.0}$	$1.0^{0.1}_{0.1}$	6891.3
03013	$0.10^{0.16}_{0.01}$	$0.10^{1.95}_{0.01}$	$32.8^{5.1}_{31.8}$	$121.8^{178.2}_{101.8}$	6.4	1.03	$13.7^{6.4}_{12.7}$	$70.9^{229.1}_{50.9}$	7.6
03334	$2.39^{0.11}_{2.29}$	$2.40^{1.60}_{2.30}$	$3.5^{28.0}_{2.5}$	$339.5^{60.5}_{319.5}$	9.4	1.09	$27.7^{0.1}_{26.7}$	$192.7^{207.3}_{172.7}$	9.8
03382	$0.10^{1.09}_{0.01}$	$0.10^{3.90}_{0.01}$	$23.9^{9.8}_{22.9}$	$236.4^{263.6}_{136.4}$	1.8	1.55	$5.1^{2.5}_{4.1}$	$481.8^{18.2}_{381.8}$	2.9
03463	$1.25^{0.33}_{1.15}$	$1.25^{2.75}_{1.15}$	$12.2^{7.1}_{11.2}$	$97.7^{302.3}_{77.7}$	2.5	1.18	$12.8^{0.6}_{11.8}$	$97.7^{302.3}_{77.7}$	2.4
03521	$0.97^{1.53}_{0.87}$	$0.99^{3.01}_{0.89}$	$14.0^{11.8}_{13.0}$	$115.0^{285.0}_{95.0}$	1.0	1.10	$14.6^{2.4}_{13.6}$	$106.4^{293.6}_{86.4}$	0.7
03528	$0.54^{1.96}_{0.44}$	$0.54^{3.46}_{0.44}$	$44.4^{28.9}_{43.4}$	$140.9^{259.1}_{120.9}$	9.3	1.41	$37.1^{12.0}_{36.1}$	$132.3^{267.7}_{112.3}$	6.7
03708	$0.10^{0.38}_{0.01}$	–	$13.4^{12.4}_{12.4}$	$409.3^{90.7}_{408.3}$	1.2	1.13	$27.0^{0.1}_{26.0}$	$1.0^{56.7}_{0.1}$	7.8
03809	$2.44^{0.06}_{2.34}$	$8.00^{0.01}_{7.90}$	$30.3^{5.1}_{29.3}$	$115.0^{285.0}_{95.0}$	5.8	0.87	$31.5^{0.1}_{30.5}$	$140.9^{259.1}_{120.9}$	6.4
03876	$0.81^{1.64}_{0.71}$	$0.81^{3.19}_{0.71}$	$8.7^{4.7}_{7.7}$	$155.0^{45.0}_{135.0}$	1.7	0.90	$8.7^{2.4}_{7.7}$	$150.9^{49.1}_{130.9}$	1.6
03915	$0.10^{0.11}_{0.01}$	$0.10^{3.90}_{0.01}$	$43.0^{2.5}_{42.0}$	$110.0^{90.0}_{90.0}$	2.5	1.12	$53.2^{0.1}_{52.2}$	$81.4^{118.6}_{61.4}$	3.7
04026	$4.41^{0.18}_{4.31}$	$4.41^{3.59}_{4.31}$	$3.2^{24.5}_{2.2}$	$412.7^{87.3}_{392.7}$	5.2	1.41	$46.7^{1.1}_{45.7}$	$129.1^{370.9}_{109.1}$	8.3
04165	$0.10^{0.22}_{0.01}$	$0.10^{3.90}_{0.01}$	$19.9^{2.4}_{18.9}$	$52.7^{47.3}_{32.7}$	2.5	1.00	$21.1^{5.9}_{20.1}$	$21.8^{78.2}_{1.8}$	2.6
04273	$0.43^{0.11}_{0.33}$	$0.46^{3.54}_{0.35}$	$12.2^{3.0}_{11.2}$	$190.9^{309.1}_{90.9}$	3.9	1.29	$4.0^{1.8}_{3.0}$	$454.5^{45.5}_{354.5}$	6.7

Continued . . .

Table B.4 – Continued from previous page

Galaxy	NFW (BFM)					NFW with fixed M/L			
UGC	M/L Disc	M/L Bulge	c	V_{200}	χ^2	M/L	c	V_{200}	χ^2
(1)	(2)	(3)	(4)	(5)	(6)	(7)	(8)	(9)	(10)
04284	$0.10^{0.05}_{0.01}$	$0.10^{3.90}_{0.01}$	$2.8^{0.6}_{1.8}$	$459.1^{40.9}_{259.1}$	4.8	0.62	$2.8^{0.1}_{1.8}$	$411.4^{88.6}_{211.4}$	5.0
04325	$2.50^{0.01}_{2.40}$	–	$1.0^{1.8}_{0.1}$	$200.0^{300.0}_{0.1}$	8.5	0.66	$1.6^{0.6}_{0.6}$	$404.5^{95.5}_{204.5}$	8.7
04456	$0.10^{2.40}_{0.01}$	$0.10^{3.90}_{0.01}$	$17.0^{10.0}_{16.0}$	$150.0^{150.0}_{50.0}$	1.9	0.97	$12.8^{8.3}_{11.8}$	$154.5^{145.5}_{54.5}$	1.8
04499	$0.10^{0.01}_{0.01}$	–	$1.0^{0.8}_{0.1}$	$413.6^{27.3}_{313.6}$	43.4	0.82	$1.0^{0.5}_{0.1}$	$318.2^{13.6}_{218.2}$	46.3
04555	$0.86^{0.98}_{0.76}$	$0.90^{3.10}_{0.80}$	$28.0^{42.8}_{27.0}$	$89.5^{110.5}_{69.5}$	0.7	1.18	$32.5^{6.8}_{31.5}$	$77.3^{122.7}_{57.3}$	0.6
04820	$1.26^{1.31}_{1.16}$	$3.33^{4.67}_{3.23}$	$36.6^{20.4}_{35.6}$	$161.4^{238.6}_{111.4}$	2.0	2.26	$54.5^{0.1}_{53.5}$	$121.6^{278.4}_{71.6}$	2.0
04936	$0.10^{0.44}_{0.01}$	$0.10^{3.90}_{0.01}$	$9.3^{1.2}_{8.3}$	$263.6^{136.4}_{113.6}$	3.5	0.75	$7.5^{1.2}_{6.5}$	$303.4^{96.6}_{153.4}$	3.5
05045	$4.17^{2.85}_{4.07}$	$4.17^{13.83}_{4.07}$	$51.7^{5.3}_{41.7}$	$175.0^{225.0}_{75.0}$	1.6	1.08	$51.7^{4.3}_{41.7}$	$209.1^{190.9}_{109.1}$	1.6
05228	$1.41^{0.11}_{1.31}$	–	$11.5^{6.0}_{6.5}$	$79.8^{20.2}_{78.8}$	4.1	1.08	$12.5^{1.0}_{7.5}$	$88.8^{11.2}_{87.8}$	4.4
05251	$0.48^{0.22}_{0.38}$	$0.54^{3.46}_{0.44}$	$5.7^{1.8}_{4.7}$	$160.0^{140.0}_{140.0}$	7.3	0.40	$6.9^{0.1}_{5.9}$	$140.9^{159.1}_{120.9}$	7.1
05253	$0.76^{0.33}_{0.66}$	$1.43^{1.95}_{1.33}$	$35.4^{21.6}_{34.4}$	$106.4^{293.6}_{46.4}$	2.7	1.48	$32.8^{1.3}_{31.8}$	$98.6^{301.4}_{38.6}$	3.2
05414	$1.03^{0.55}_{0.93}$	–	$1.0^{1.8}_{0.1}$	$391.4^{8.6}_{371.4}$	8.0	0.75	$1.6^{0.6}_{0.6}$	$305.0^{95.0}_{285.0}$	7.9
05510	$0.10^{0.01}_{0.01}$	$0.10^{3.90}_{0.01}$	$27.7^{1.3}_{26.7}$	$105.9^{94.1}_{85.9}$	6.3	0.95	$18.8^{0.1}_{17.8}$	$114.1^{85.9}_{94.1}$	7.6
05840	$0.10^{0.01}_{0.01}$	$0.10^{7.90}_{0.01}$	$66.2^{0.1}_{65.2}$	$115.5^{184.5}_{95.5}$	13.4	1.09	$64.0^{0.1}_{63.0}$	$109.1^{190.9}_{89.1}$	13.7
05842	$0.54^{0.71}_{0.44}$	$0.54^{3.46}_{0.44}$	$2.2^{4.1}_{1.2}$	$500.0^{0.1}_{300.0}$	2.5	0.99	$1.6^{2.4}_{0.6}$	$493.2^{6.8}_{293.2}$	2.4
05931	$0.10^{0.05}_{0.01}$	$0.10^{3.90}_{0.01}$	$4.0^{2.4}_{3.0}$	$427.3^{72.7}_{327.3}$	4.4	0.48	$2.8^{0.6}_{1.8}$	$463.6^{36.4}_{363.6}$	5.5
05982	$1.30^{0.60}_{1.20}$	$7.82^{0.18}_{7.72}$	$12.2^{11.0}_{2.2}$	$161.1^{88.9}_{141.1}$	4.5	1.09	$36.5^{0.1}_{26.5}$	$93.2^{156.8}_{73.2}$	7.0

Continued . . .

Table B.4 – Continued from previous page

Galaxy	NFW (BFM)					NFW with fixed M/L			
UGC	M/L Disc	M/L Bulge	c	V_{200}	χ^2	M/L	c	V_{200}	χ^2
(1)	(2)	(3)	(4)	(5)	(6)	(7)	(8)	(9)	(10)
06118	$0.26^{0.11}_{0.16}$	$0.63^{1.33}_{0.53}$	$11.6^{4.7}_{10.6}$	$132.2^{67.8}_{131.2}$	4.2	1.32	$5.1^{21.9}_{4.1}$	$1.0^{0.1}_{0.1}$	113.5
06277	$0.10^{1.09}_{0.01}$	$1.16^{2.84}_{1.06}$	$12.2^{7.7}_{11.2}$	$500.0^{0.1}_{400.0}$	2.1	1.08	$10.5^{4.1}_{9.5}$	$500.0^{0.1}_{400.0}$	2.1
06521	$2.44^{0.06}_{2.34}$	$2.49^{1.51}_{2.39}$	$37.8^{8.5}_{27.8}$	$95.5^{204.5}_{45.5}$	2.8	0.89	$38.8^{1.1}_{28.8}$	$123.9^{147.7}_{73.9}$	3.5
06537	$0.10^{0.01}_{0.01}$	$0.10^{3.90}_{0.01}$	$11.0^{0.6}_{10.0}$	$201.4^{198.6}_{181.4}$	22.1	0.75	$8.1^{0.1}_{7.1}$	$227.3^{172.7}_{207.3}$	22.8
06702	$0.10^{0.01}_{0.01}$	$0.10^{3.19}_{0.01}$	$57.0^{0.1}_{56.0}$	$97.7^{302.3}_{47.7}$	13.9	1.18	$55.7^{1.3}_{54.7}$	$73.9^{326.1}_{23.9}$	15.4
06778	$0.70^{0.16}_{0.60}$	$1.52^{2.48}_{1.42}$	$12.5^{6.4}_{11.5}$	$235.0^{5.0}_{215.0}$	5.6	1.08	$12.5^{0.1}_{11.5}$	$220.0^{20.0}_{200.0}$	5.9
07021	$0.10^{0.01}_{0.01}$	$0.10^{3.90}_{0.01}$	$30.8^{5.0}_{28.8}$	$154.5^{345.5}_{54.5}$	8.1	1.76	$7.0^{5.0}_{5.0}$	$472.7^{27.3}_{372.7}$	22.2
07045	$0.86^{0.38}_{0.76}$	$2.78^{3.22}_{2.68}$	$19.8^{6.5}_{18.8}$	$105.9^{94.1}_{85.9}$	2.6	1.40	$25.5^{0.1}_{24.5}$	$85.5^{114.5}_{65.5}$	2.9
07154	$0.92^{0.33}_{0.82}$	$1.07^{2.92}_{0.97}$	$4.0^{2.4}_{3.0}$	$184.1^{215.9}_{164.1}$	5.4	0.89	$4.5^{0.6}_{3.5}$	$166.8^{233.2}_{146.8}$	5.3
07323	$0.10^{0.11}_{0.01}$	–	$4.0^{1.8}_{3.0}$	$191.4^{208.6}_{190.4}$	2.7	1.00	$1.6^{1.2}_{0.6}$	$291.2^{108.8}_{290.2}$	3.2
07766	$0.37^{0.38}_{0.27}$	$2.05^{1.95}_{1.95}$	$10.0^{2.2}_{9.0}$	$89.5^{110.5}_{69.5}$	4.6	0.62	$14.5^{0.1}_{13.5}$	$65.0^{135.0}_{45.0}$	5.3
07831	$0.76^{0.05}_{0.66}$	–	$11.6^{1.2}_{10.6}$	$80.4^{419.6}_{79.4}$	4.3	0.78	$11.6^{0.1}_{10.6}$	$80.4^{419.6}_{79.4}$	4.3
07861	$0.10^{0.16}_{0.01}$	$0.10^{0.62}_{0.01}$	$1.0^{8.3}_{0.1}$	$432.0^{68.0}_{431.0}$	2.1	1.09	$1.0^{26.0}_{0.1}$	$1.0^{0.1}_{0.1}$	14.3
07876	$0.10^{0.33}_{0.01}$	$0.10^{3.90}_{0.01}$	$7.4^{0.1}_{6.4}$	$175.5^{24.5}_{155.5}$	3.3	0.90	$6.1^{0.1}_{5.1}$	$179.5^{20.5}_{159.5}$	3.6
07901	$0.21^{0.27}_{0.11}$	$0.46^{3.54}_{0.35}$	$51.9^{4.4}_{41.9}$	$105.9^{94.1}_{85.9}$	3.0	0.92	$38.7^{0.1}_{28.7}$	$101.8^{98.2}_{81.8}$	4.0
07985	$0.10^{0.05}_{0.01}$	$0.10^{3.90}_{0.01}$	$21.1^{0.1}_{20.1}$	$77.3^{122.7}_{57.3}$	3.2	0.82	$13.4^{0.6}_{12.4}$	$73.2^{126.8}_{53.2}$	3.9
08334	$0.15^{0.11}_{0.05}$	$2.40^{1.60}_{2.30}$	$37.1^{2.4}_{36.1}$	$114.1^{85.9}_{94.1}$	4.9	1.32	$37.1^{0.1}_{36.1}$	$77.3^{122.7}_{57.3}$	9.8

Continued . . .

Table B.4 – Continued from previous page

Galaxy	NFW (BFM)					NFW with fixed M/L			
UGC	M/L Disc	M/L Bulge	c	V_{200}	χ^2	M/L	c	V_{200}	χ^2
(1)	(2)	(3)	(4)	(5)	(6)	(7)	(8)	(9)	(10)
08403	$0.10^{0.01}_{0.01}$	–	$2.2^{0.1}_{1.2}$	$400.0^{100.0}_{300.0}$	13.2	0.73	$1.0^{0.1}_{0.1}$	$500.0^{0.1}_{400.0}$	25.3
08490	$1.41^{0.27}_{1.31}$	$1.43^{2.57}_{1.33}$	$4.0^{14.2}_{3.0}$	$368.2^{31.8}_{318.2}$	2.5	0.69	$12.2^{0.6}_{11.2}$	$113.6^{286.4}_{63.6}$	2.5
08709	$2.39^{0.11}_{2.29}$	$2.40^{1.60}_{2.30}$	$13.4^{9.5}_{12.4}$	$118.2^{81.8}_{98.2}$	12.8	0.73	$20.5^{0.1}_{19.5}$	$130.5^{69.5}_{110.5}$	14.7
08852	$0.27^{0.01}_{0.17}$	$0.38^{3.62}_{0.28}$	$26.7^{2.6}_{25.7}$	$120.0^{180.0}_{100.0}$	7.5	1.29	$11.3^{0.1}_{10.3}$	$160.0^{140.0}_{140.0}$	8.6
08900	$0.10^{0.05}_{0.01}$	$0.10^{3.90}_{0.01}$	$8.1^{0.1}_{7.1}$	$500.0^{0.1}_{300.0}$	7.1	1.22	$6.3^{0.6}_{5.3}$	$500.0^{0.1}_{300.0}$	8.8
08937	$0.65^{0.27}_{0.55}$	$4.00^{0.01}_{3.90}$	$26.5^{5.1}_{25.5}$	$172.7^{127.3}_{152.7}$	6.3	1.29	$55.7^{0.1}_{54.7}$	$121.8^{178.2}_{101.8}$	12.2
09179	$0.10^{0.01}_{0.01}$	$0.10^{3.90}_{0.01}$	$5.1^{2.4}_{4.1}$	$327.3^{172.7}_{227.3}$	4.8	0.80	$3.4^{0.1}_{2.4}$	$472.7^{27.3}_{372.7}$	5.3
09248	$0.10^{0.33}_{0.01}$	$0.10^{3.90}_{0.01}$	$24.6^{2.4}_{23.6}$	$110.0^{90.0}_{90.0}$	6.4	1.29	$20.5^{1.8}_{19.5}$	$93.6^{106.4}_{73.6}$	6.7
09358	$0.26^{0.33}_{0.16}$	$8.00^{0.01}_{7.90}$	$7.8^{2.2}_{6.8}$	$314.5^{185.5}_{294.5}$	5.6	1.29	$61.8^{2.2}_{60.8}$	$85.5^{414.5}_{65.5}$	18.9
09363	$0.10^{0.33}_{0.01}$	$0.19^{3.81}_{0.09}$	$8.1^{1.2}_{7.1}$	$172.7^{327.3}_{152.7}$	3.0	1.36	$1.6^{0.1}_{0.6}$	$434.5^{65.5}_{414.5}$	4.0
09366	$0.65^{0.33}_{0.55}$	$1.87^{2.13}_{1.77}$	$26.5^{5.1}_{25.5}$	$122.3^{77.7}_{102.3}$	4.5	1.03	$36.6^{3.8}_{35.6}$	$105.9^{94.1}_{85.9}$	4.5
09465	$0.15^{0.54}_{0.05}$	–	$8.1^{1.2}_{7.1}$	$108.6^{391.4}_{28.6}$	4.2	0.82	$5.7^{2.4}_{4.7}$	$137.3^{362.7}_{57.3}$	4.3
09576	$0.15^{0.16}_{0.05}$	$0.19^{3.81}_{0.09}$	$6.9^{1.2}_{5.9}$	$106.4^{293.6}_{86.4}$	7.6	1.06	$1.0^{0.6}_{0.1}$	$296.4^{0.1}_{276.4}$	9.0
09649	$0.10^{2.13}_{0.01}$	$18.00^{0.01}_{17.90}$	$25.2^{7.6}_{24.2}$	$63.2^{336.8}_{43.2}$	17.2	1.29	$27.7^{1.3}_{26.7}$	$54.5^{345.5}_{34.5}$	18.9
09736	$0.10^{1.08}_{0.01}$	$5.06^{0.94}_{4.96}$	$12.2^{4.5}_{11.2}$	$159.1^{40.9}_{139.1}$	8.7	1.18	$23.5^{2.2}_{22.5}$	$97.7^{102.3}_{77.7}$	8.4
09753	$0.81^{0.16}_{0.71}$	$0.81^{3.19}_{0.71}$	$38.7^{17.6}_{28.7}$	$73.4^{126.6}_{72.4}$	10.8	0.82	$38.7^{4.4}_{28.7}$	$73.4^{126.6}_{72.4}$	10.5
09858	$0.26^{1.25}_{0.16}$	$0.28^{3.72}_{0.18}$	$23.5^{2.2}_{22.5}$	$101.8^{98.2}_{81.8}$	7.7	1.18	$21.2^{0.1}_{20.2}$	$97.7^{102.3}_{77.7}$	7.4

Continued . . .

Table B.4 – Continued from previous page

Galaxy	NFW (BFM)					NFW with fixed M/L			
UGC	M/L Disc	M/L Bulge	c	V_{200}	χ^2	M/L	c	V_{200}	χ^2
(1)	(2)	(3)	(4)	(5)	(6)	(7)	(8)	(9)	(10)
09866	$0.81^{1.69}_{0.71}$	$0.81^{3.19}_{0.71}$	$6.3^{3.5}_{5.3}$	$500.0^{0.1}_{480.0}$	2.4	1.18	$6.3^{1.8}_{5.3}$	$456.4^{43.6}_{436.4}$	2.3
09943	$0.26^{0.16}_{0.16}$	$0.28^{3.72}_{0.18}$	$39.2^{5.1}_{38.2}$	$97.7^{302.3}_{77.7}$	2.6	1.32	$3.5^{0.1}_{2.5}$	$296.4^{103.6}_{276.4}$	4.5
09969	$0.15^{0.44}_{0.05}$	$0.19^{3.81}_{0.09}$	$27.1^{0.1}_{17.1}$	$198.2^{101.8}_{178.2}$	3.7	1.36	$25.0^{2.1}_{15.0}$	$185.5^{114.5}_{165.5}$	3.8
10075	$2.39^{0.11}_{2.29}$	–	$10.5^{8.9}_{9.5}$	$129.1^{370.9}_{109.1}$	6.9	0.89	$17.5^{0.1}_{16.5}$	$118.2^{381.8}_{98.2}$	7.3
10359	$0.10^{0.01}_{0.01}$	$8.00^{0.01}_{7.90}$	$3.4^{1.2}_{2.4}$	$380.0^{120.0}_{360.0}$	3.4	0.84	$1.6^{0.1}_{0.6}$	$467.3^{32.7}_{447.3}$	10.0
10521	$0.32^{0.27}_{0.22}$	$0.37^{3.63}_{0.27}$	$14.6^{2.4}_{13.6}$	$107.3^{392.7}_{87.3}$	5.1	0.71	$13.4^{0.1}_{12.4}$	$96.4^{403.6}_{76.4}$	5.0
10652	$0.10^{0.01}_{0.01}$	$0.10^{3.90}_{0.01}$	$8.1^{1.8}_{7.1}$	$472.7^{27.3}_{272.7}$	14.4	1.18	$6.3^{1.2}_{5.3}$	$465.9^{34.1}_{265.9}$	15.9
10757	$0.10^{0.76}_{0.01}$	$0.28^{3.72}_{0.18}$	$2.8^{3.0}_{1.8}$	$445.5^{54.5}_{245.5}$	1.9	0.99	$2.2^{1.8}_{1.2}$	$390.9^{109.1}_{190.9}$	2.0
10897	$0.10^{0.01}_{0.01}$	$0.10^{3.55}_{0.01}$	$3.4^{2.4}_{2.4}$	$418.2^{81.8}_{218.2}$	5.1	0.80	$1.6^{1.2}_{0.6}$	$418.2^{81.8}_{218.2}$	7.6
11283	$4.00^{0.01}_{3.90}$	$4.00^{0.01}_{3.90}$	$20.9^{8.2}_{10.9}$	$50.8^{149.2}_{49.8}$	11.4	0.89	$25.7^{2.0}_{15.7}$	$96.0^{104.0}_{95.0}$	12.3
11300	$0.10^{0.87}_{0.01}$	$0.10^{3.90}_{0.01}$	$11.0^{0.6}_{10.0}$	$129.1^{370.9}_{109.1}$	4.7	1.15	$2.8^{1.8}_{1.8}$	$489.1^{10.9}_{469.1}$	4.6
11597	$0.10^{0.01}_{0.01}$	$0.90^{2.39}_{0.80}$	$14.5^{0.1}_{13.5}$	$123.1^{76.9}_{122.1}$	5.8	0.67	$100.0^{0.1}_{99.0}$	$1.0^{0.1}_{0.1}$	82.5
11670	$0.10^{0.01}_{0.01}$	$0.90^{0.80}_{0.80}$	$43.8^{13.5}_{42.8}$	$84.2^{15.8}_{83.2}$	5.6	1.61	$1.0^{99.0}_{0.1}$	$1.0^{6.8}_{0.1}$	43.8
11707	$0.10^{0.22}_{0.01}$	$0.10^{3.90}_{0.01}$	$5.1^{1.2}_{4.1}$	$132.3^{267.7}_{112.3}$	3.7	0.82	$4.5^{0.6}_{3.5}$	$115.0^{285.0}_{95.0}$	3.9
11852	$0.10^{0.01}_{0.01}$	$0.10^{3.63}_{0.01}$	$7.5^{2.5}_{6.5}$	$463.6^{36.4}_{363.6}$	74.2	1.55	$2.6^{0.8}_{1.6}$	$500.0^{0.1}_{400.0}$	81.1
11861	$0.10^{0.01}_{0.01}$	–	$2.2^{0.1}_{1.2}$	$454.6^{45.4}_{453.6}$	7.5	0.82	$5.7^{21.3}_{4.7}$	$1.0^{0.1}_{0.1}$	302.5
11914	$0.10^{0.11}_{0.01}$	$0.72^{0.89}_{0.62}$	$44.1^{7.2}_{43.1}$	$123.1^{76.9}_{122.1}$	2.1	1.91	$80.0^{0.1}_{79.0}$	$1.0^{0.1}_{0.1}$	419.3

Continued . . .

Table B.4 – Continued from previous page

Galaxy	NFW (BFM)					NFW with fixed M/L			
UGC	M/L Disc	M/L Bulge	c	V_{200}	χ^2	M/L	c	V_{200}	χ^2
(1)	(2)	(3)	(4)	(5)	(6)	(7)	(8)	(9)	(10)
12060	$3.70^{0.50}_{3.60}$	–	$1.0^{10.0}_{0.1}$	$172.7^{127.3}_{152.7}$	12.3	0.75	$8.1^{1.2}_{7.1}$	$102.7^{197.3}_{82.7}$	14.4
12754	$0.10^{0.01}_{0.01}$	–	$9.9^{3.0}_{8.9}$	$181.8^{318.2}_{81.8}$	5.6	0.80	$3.4^{1.2}_{2.4}$	$472.7^{27.3}_{372.7}$	6.7

2 Surface brightness profile and mass models

We present the mass models of the 100 galaxies using the optical R_c-band photometry. The surface brightness profiles decomposition for the 27 galaxies from SDSS are shown in this work while we do not present the remaining 73 galaxies from OHP because they have already been published in Barbosa et al. (2015). Note that 4 of the 27 SDSS galaxies have not been decomposed, for these galaxies, we just show the observed surface brightness profiles.

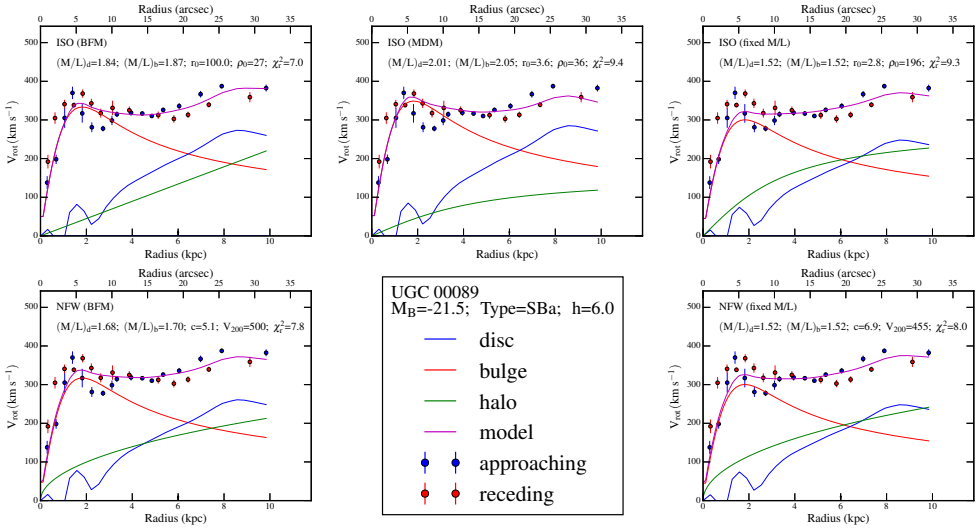

Figure B.1: Lines 1 and 2 - Mass models. First line: pseudo-isothermal sphere density profiles (ISO). Second line: Navarro, Frenk & White density profiles (NFW). First column: Best Fit Model (BFM). Second column: Maximum Disk Model (MDM) for line 1 (ISO model). Third column: Mass-to-Light ratio M/L fixed using the optical (B - V) color. The name of the galaxy, its B-band absolute magnitude, morphological type and disk scale length has been indicated in the insert located line 2-column 2. For each model, the fitted parameters and the reduced χ^2 have been indicated in each sub-panel. The legends are the same for Figs. B.2 – B.100. The surface brightness profiles decomposition for the 27 galaxies from SDSS are shown in this work while we do not present the remaining 73 galaxies from OHP because they have already been published in Barbosa et al. (2015). Note that 4 of the 27 SDSS galaxies have not been decomposed, for these galaxies, we just show the observed surface brightness profiles.

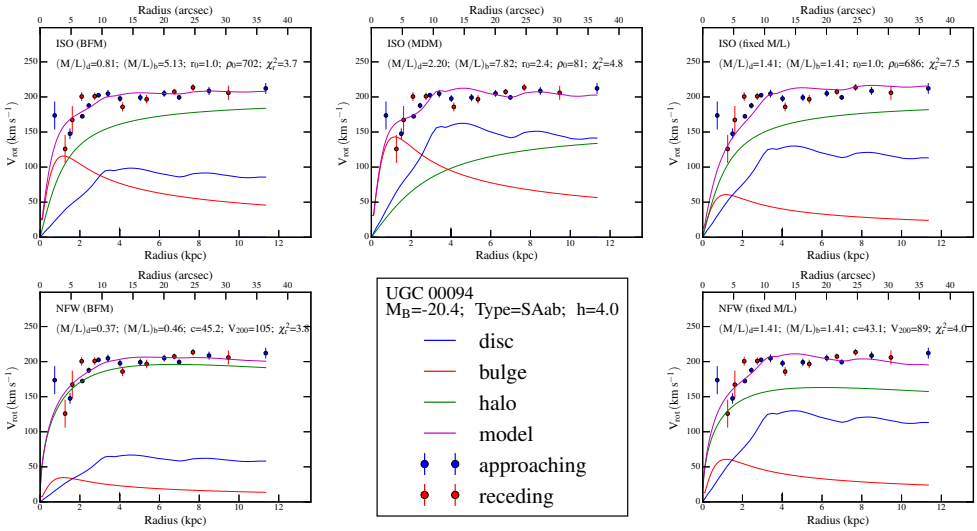

Figure B.2

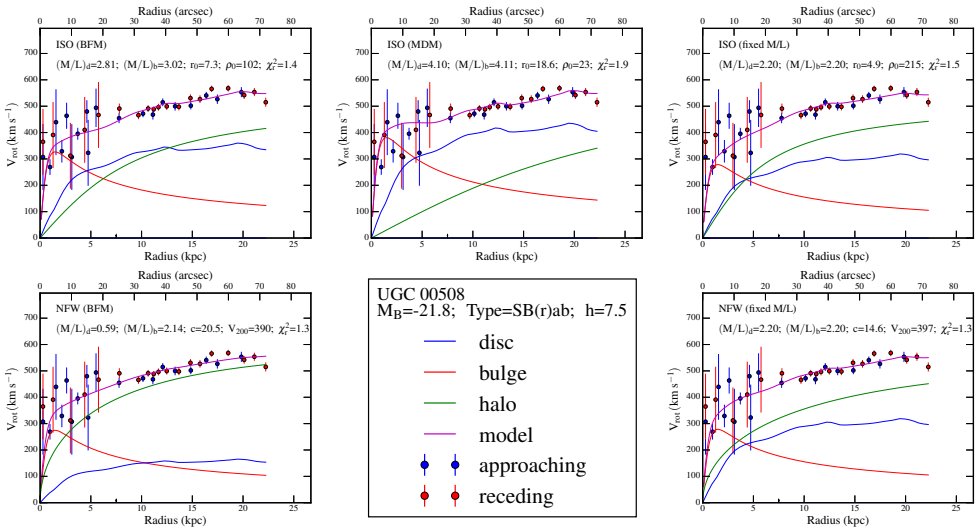

Figure B.3

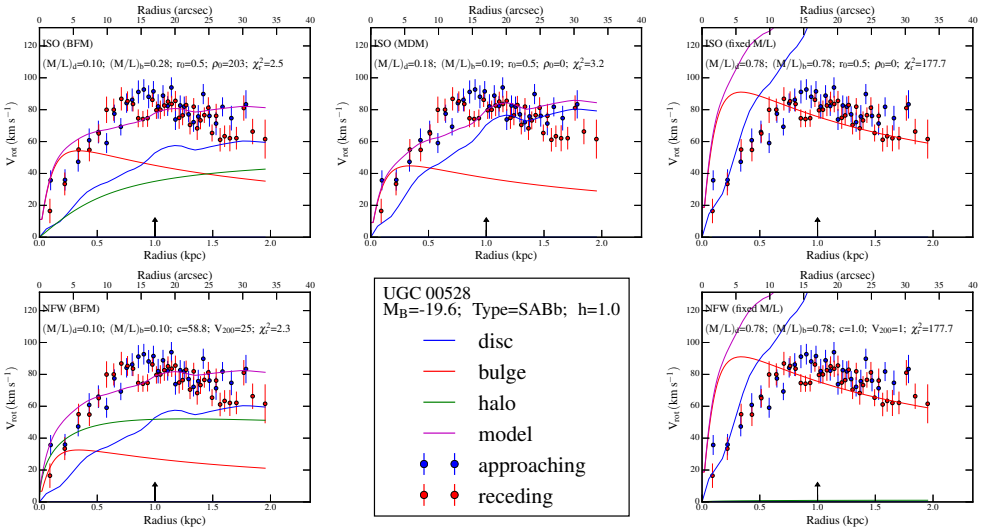

Figure B.4

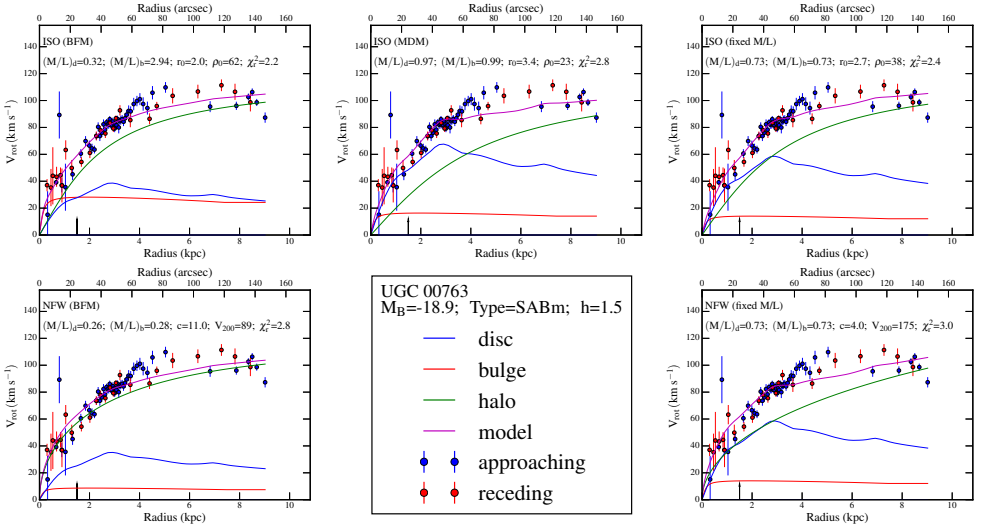

Figure B.5

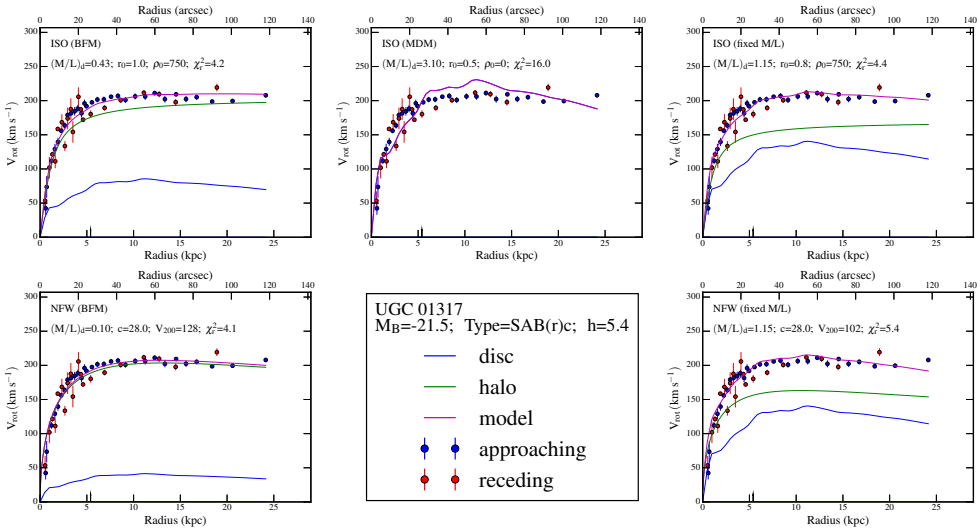

Figure B.6

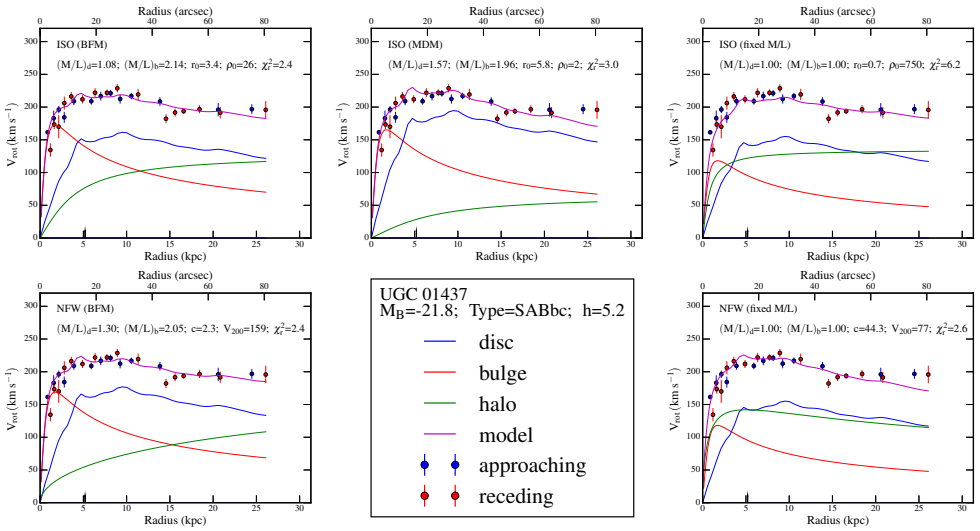

Figure B.7

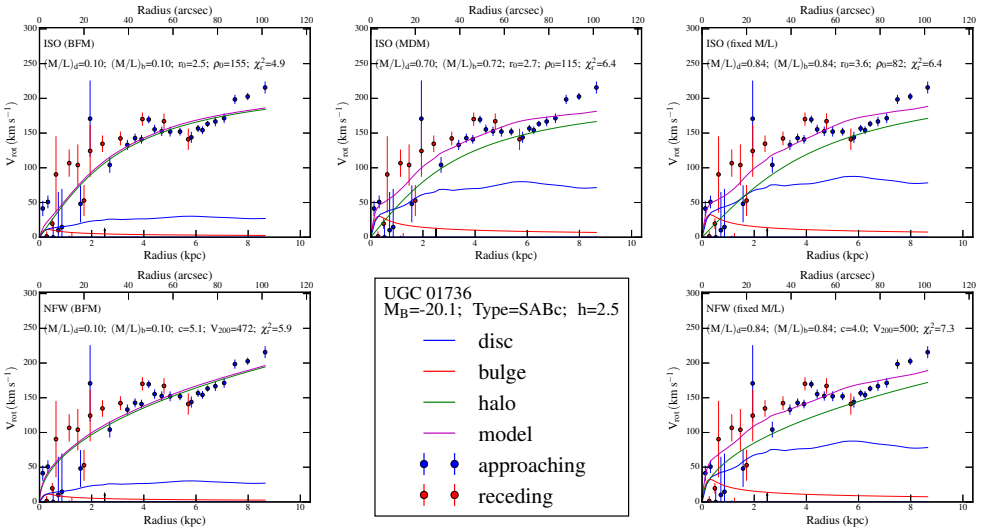

Figure B.8

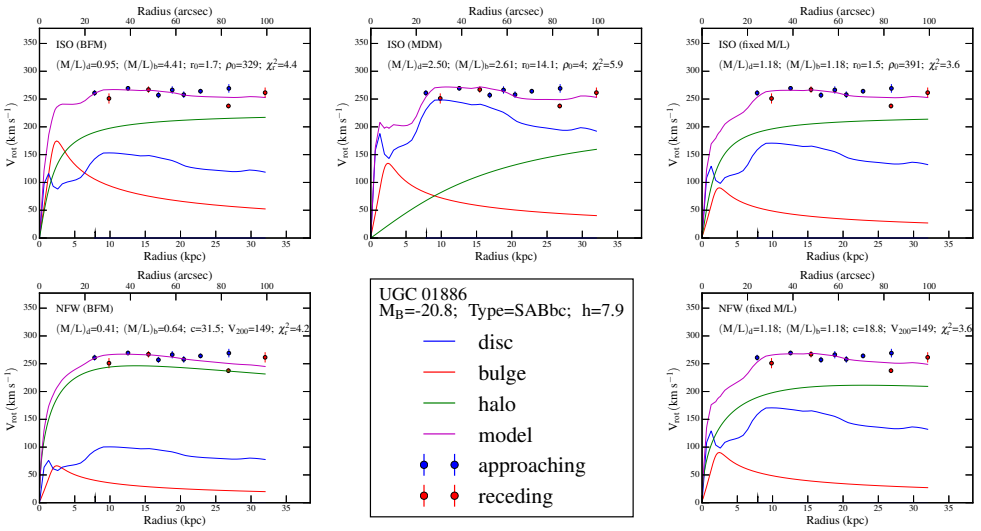

Figure B.9

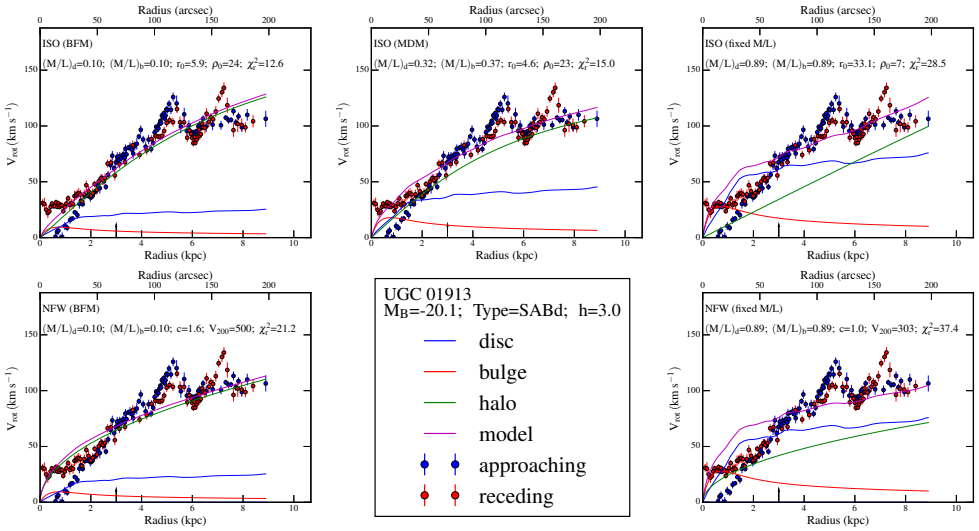

Figure B.10

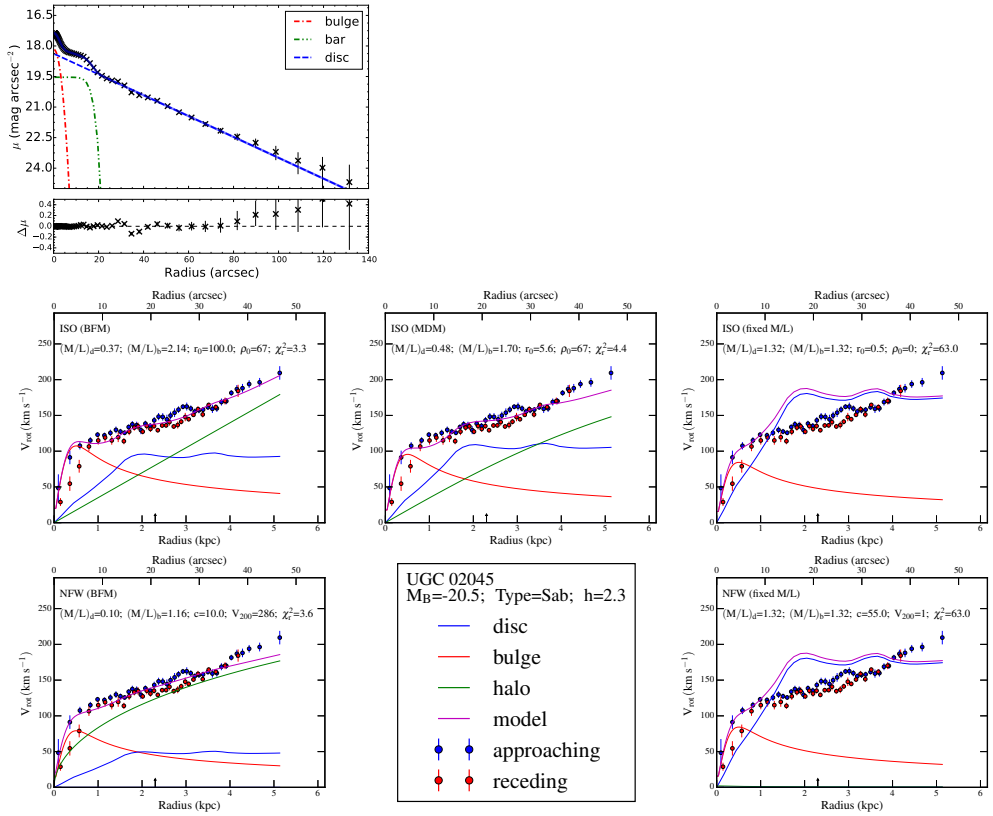

Figure B.11

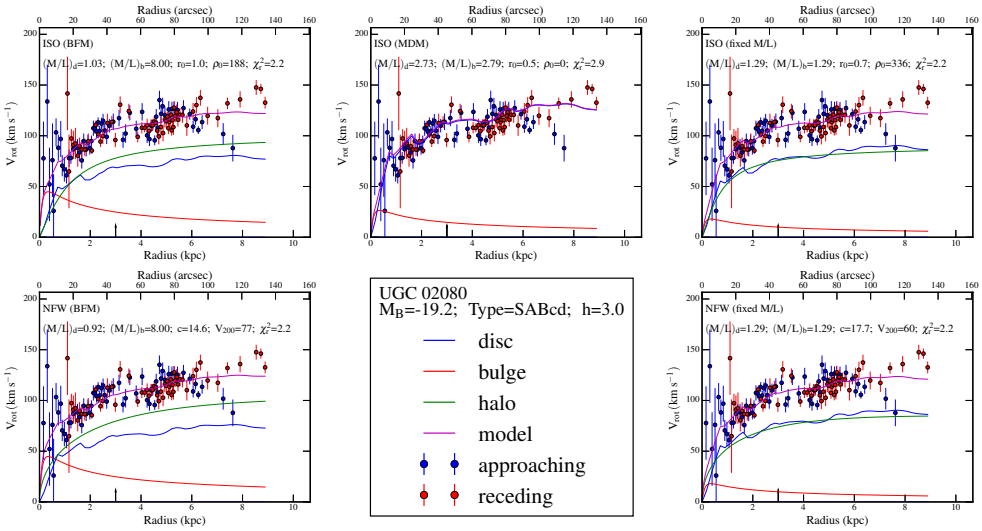

Figure B.12

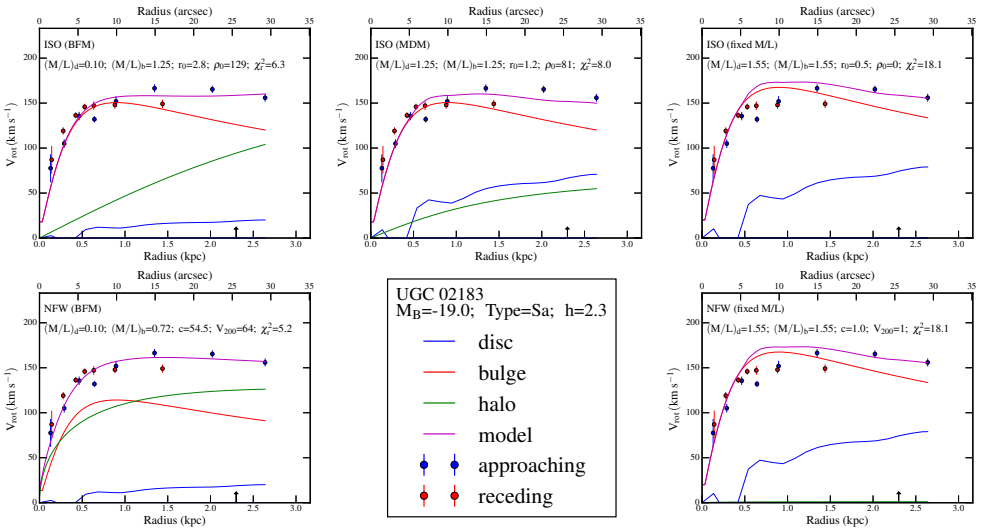

Figure B.13

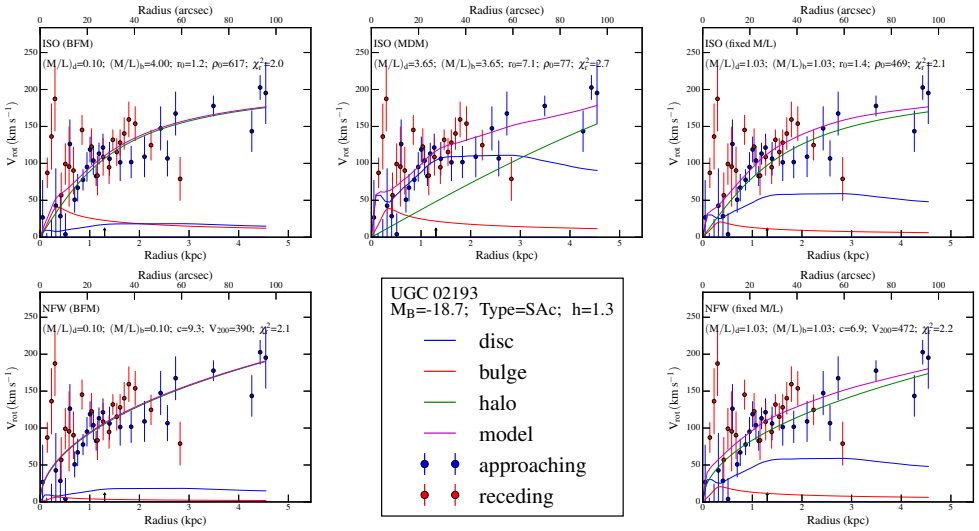

Figure B.14

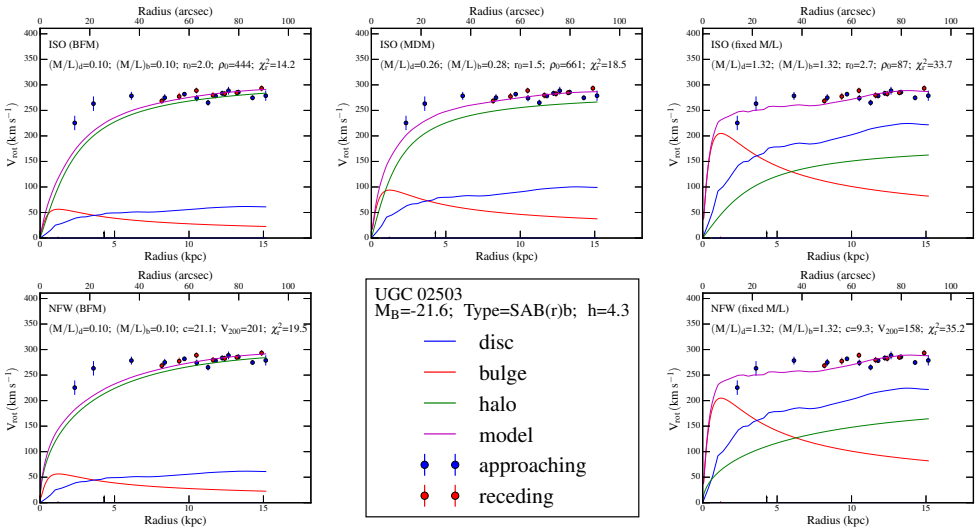

Figure B.15

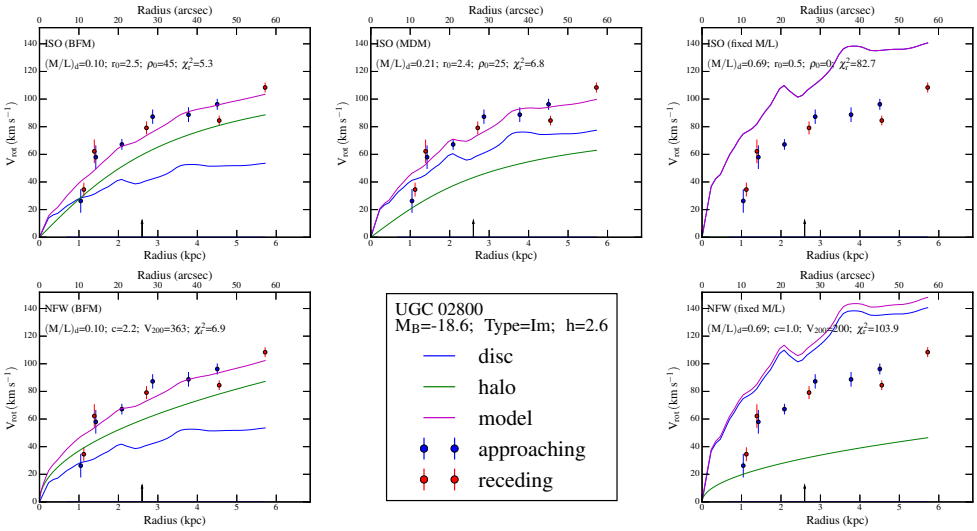

Figure B.16

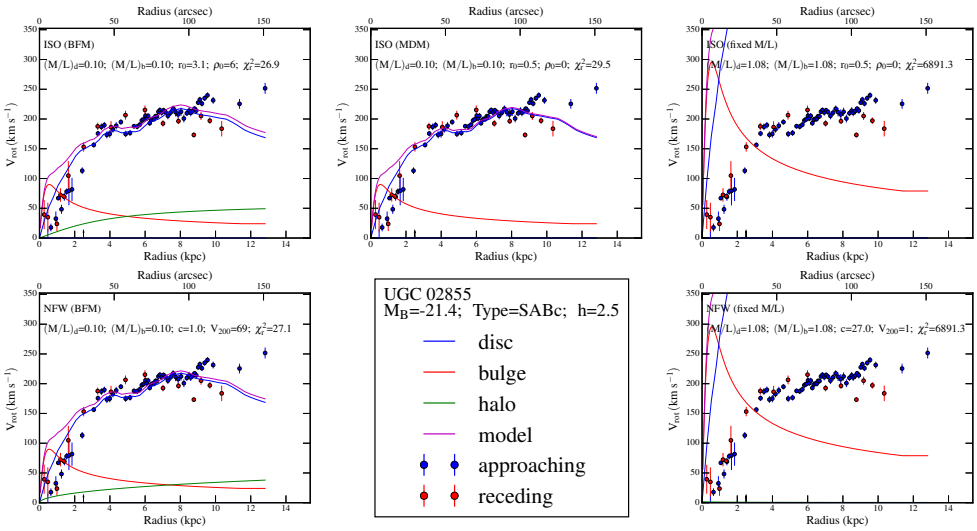

Figure B.17

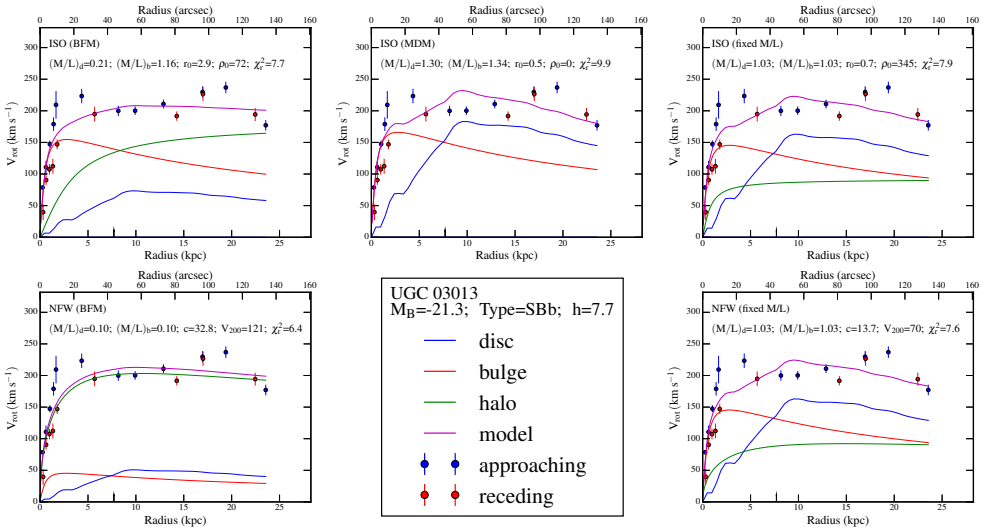

Figure B.18

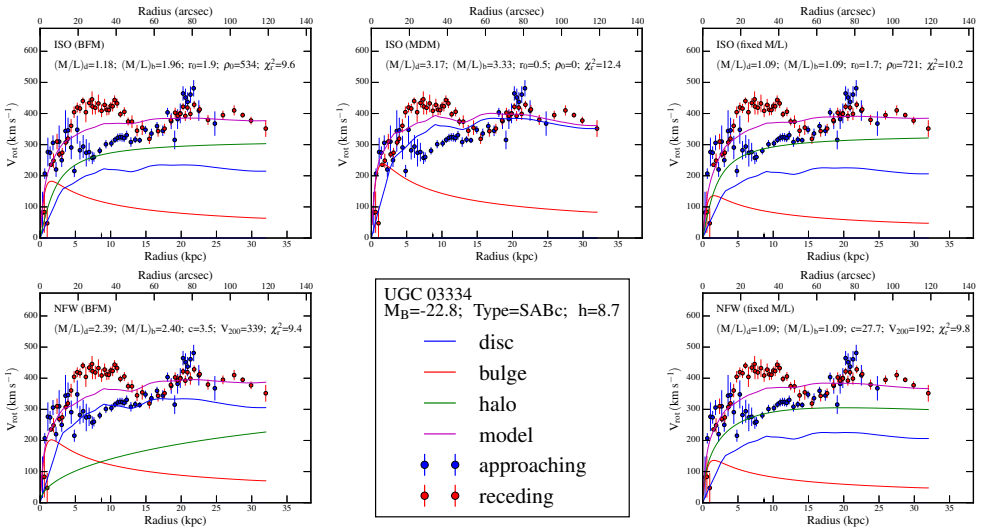

Figure B.19

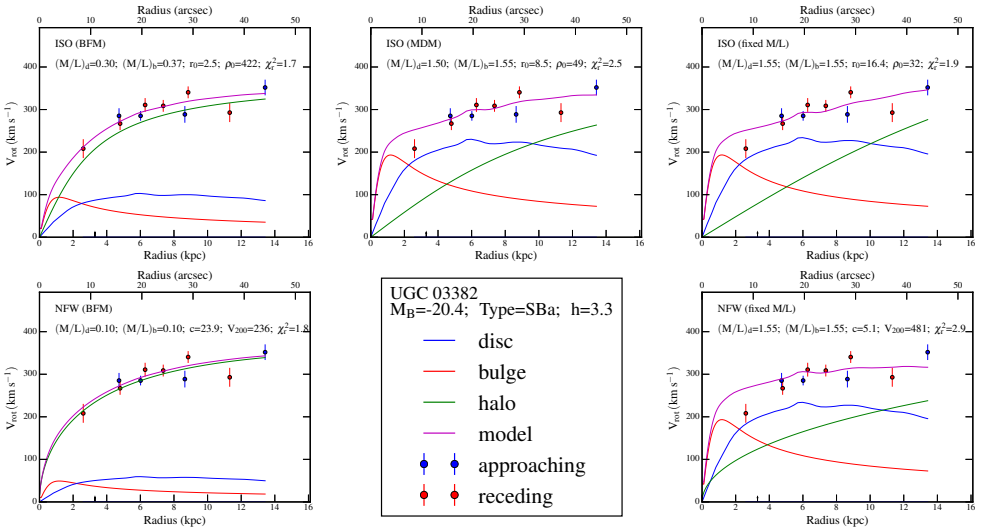

Figure B.20

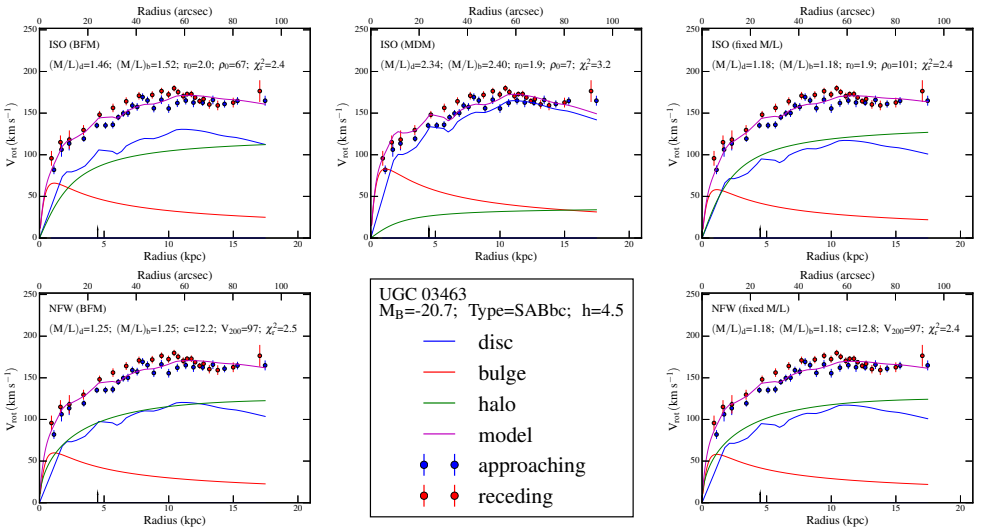

Figure B.21

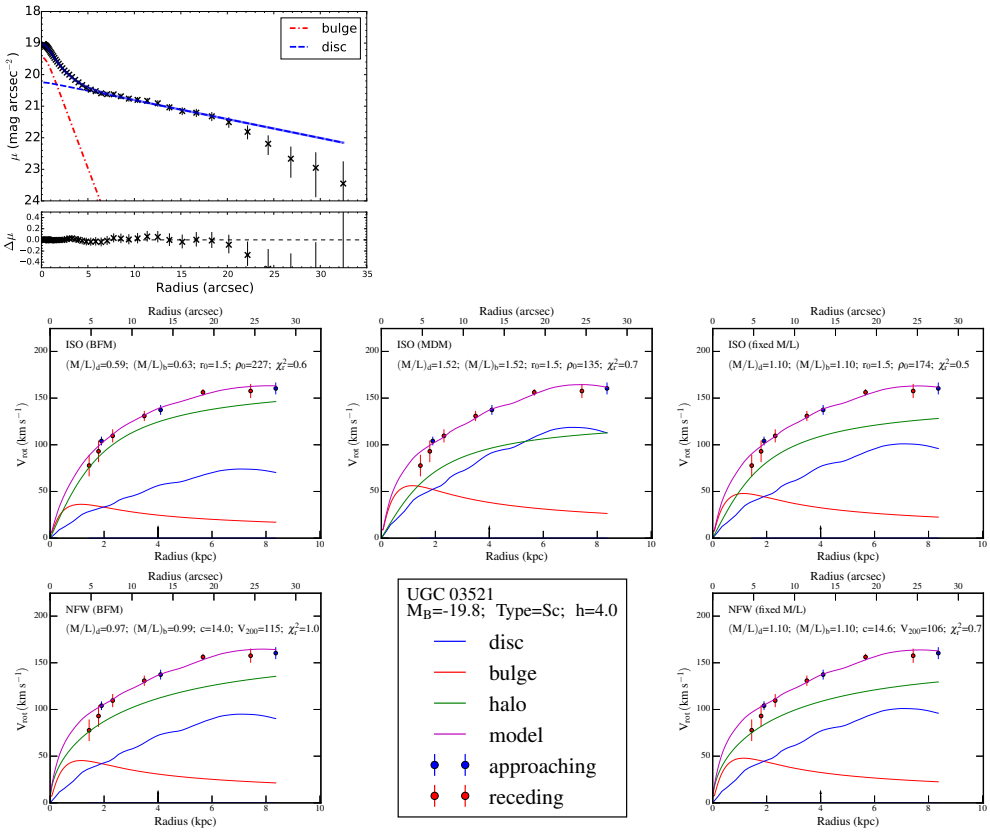
bulge
disc
μ (mag arcsec⁻²)
Δμ
Radius (arcsec)
ISO (BFM)
(M/L)d=0.59; (M/L)b=0.63; r0=1.5; ρ0=227; χr²=0.6
ISO (MDM)
(M/L)d=1.52; (M/L)b=1.52; r0=1.5; ρ0=135; χr²=0.7
ISO (fixed M/L)
(M/L)d=1.10; (M/L)b=1.10; r0=1.5; ρ0=174; χr²=0.5
NFW (BFM)
(M/L)d=0.97; (M/L)b=0.99; c=14.0; V200=115; χr²=1.0
NFW (fixed M/L)
(M/L)d=1.10; (M/L)b=1.10; c=14.6; V200=106; χr²=0.7
Vrot (km s⁻¹)
Radius (kpc)
UGC 03521
MB=-19.8; Type=Sc; h=4.0
disc
bulge
halo
model
approaching
receding

Figure B.22

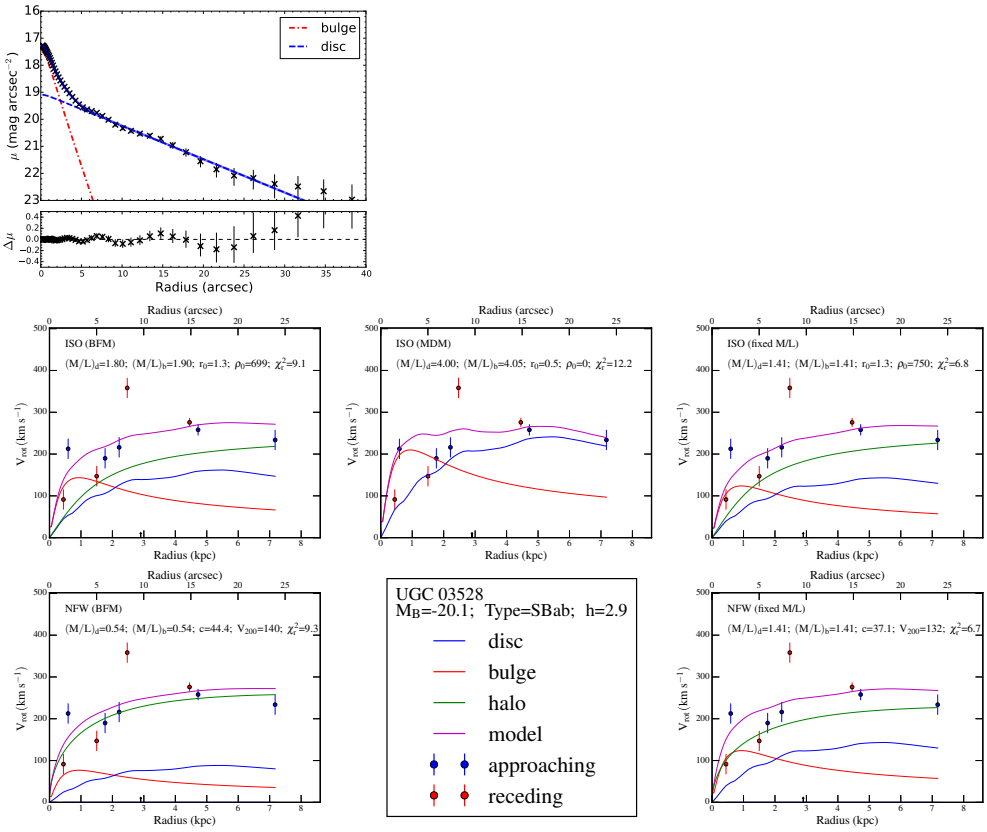

Figure B.23

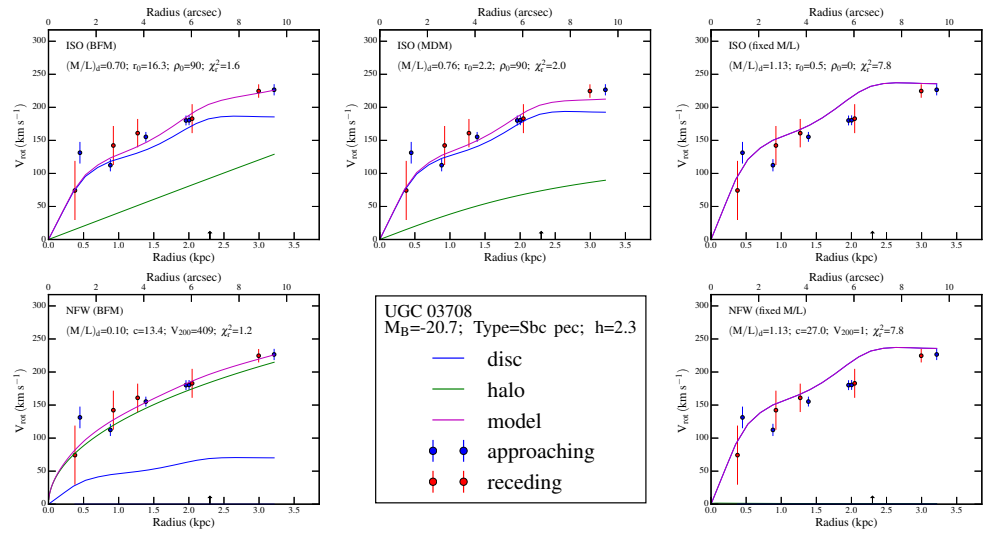

Figure B.24

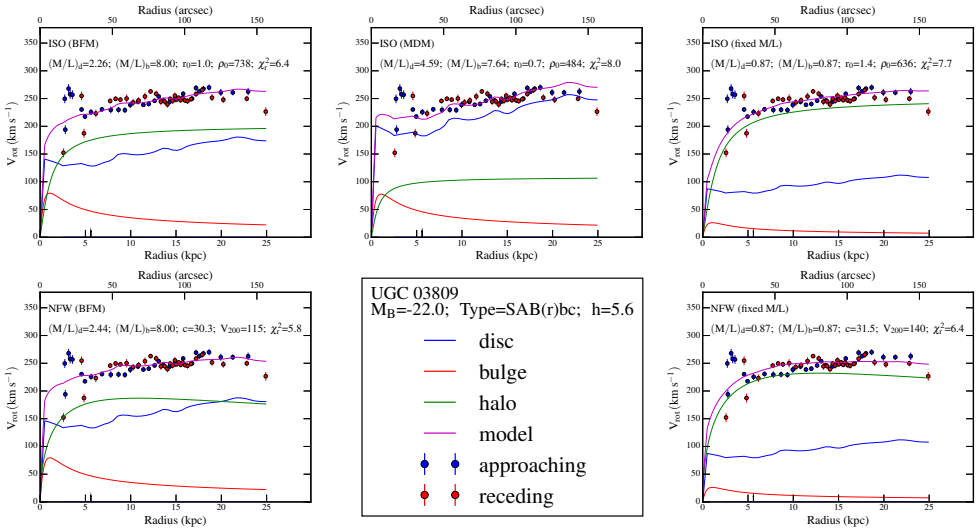

Figure B.25

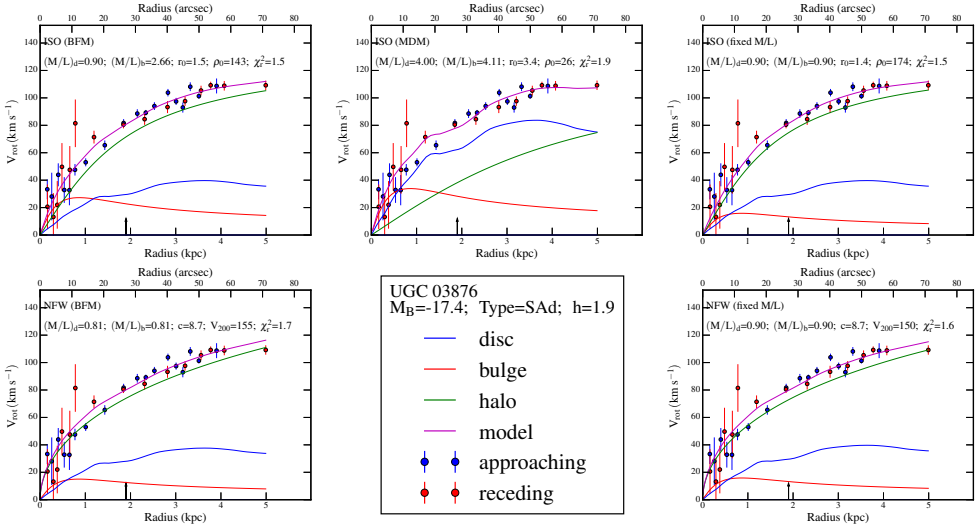

Figure B.26

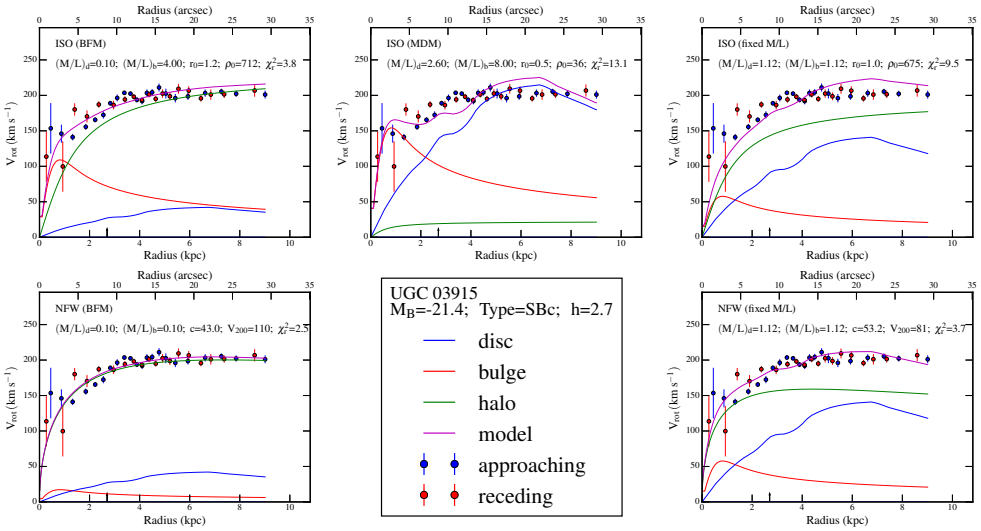

Figure B.27

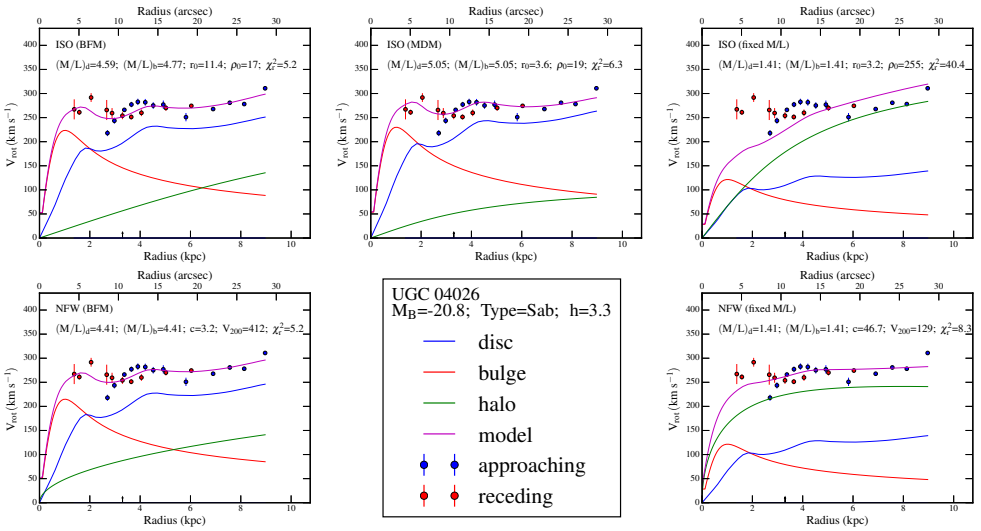

Figure B.28

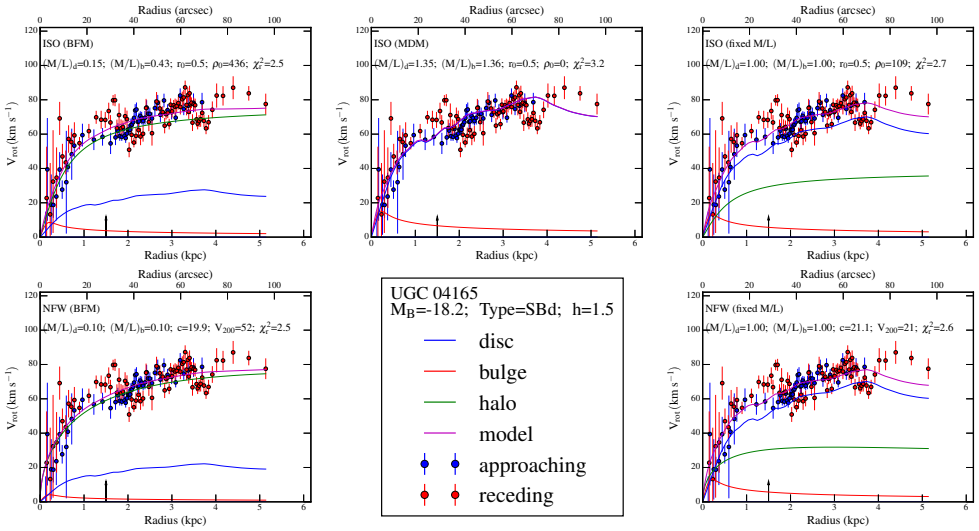

Figure B.29

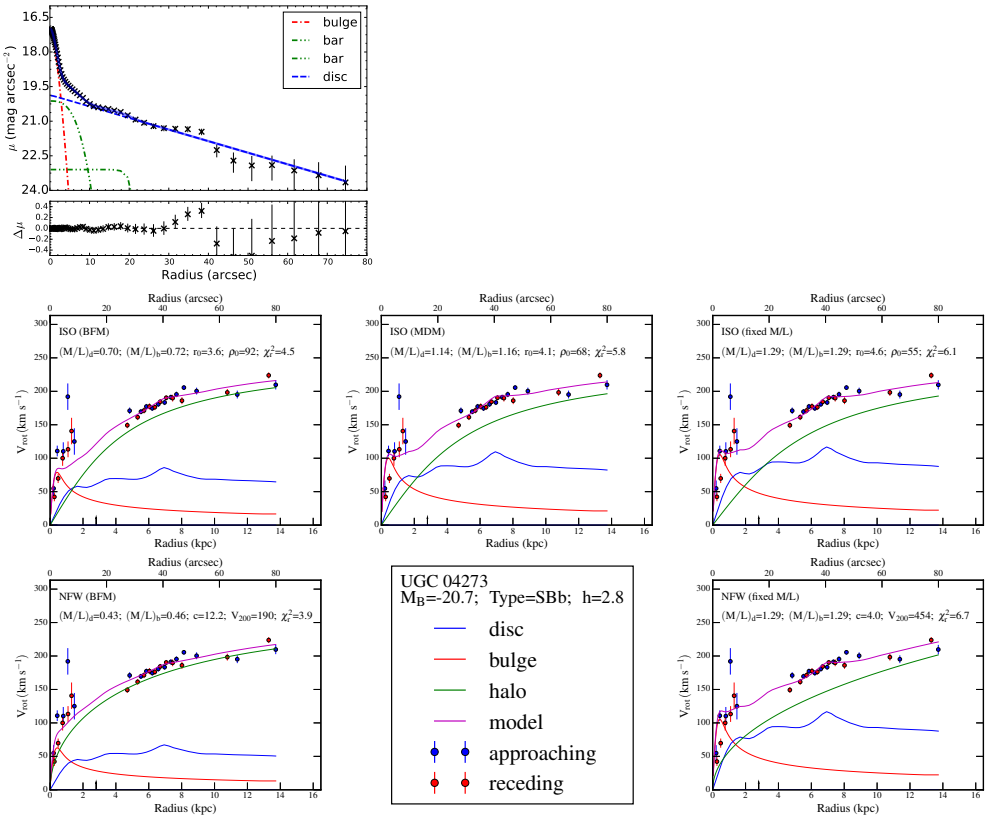

Figure B.30

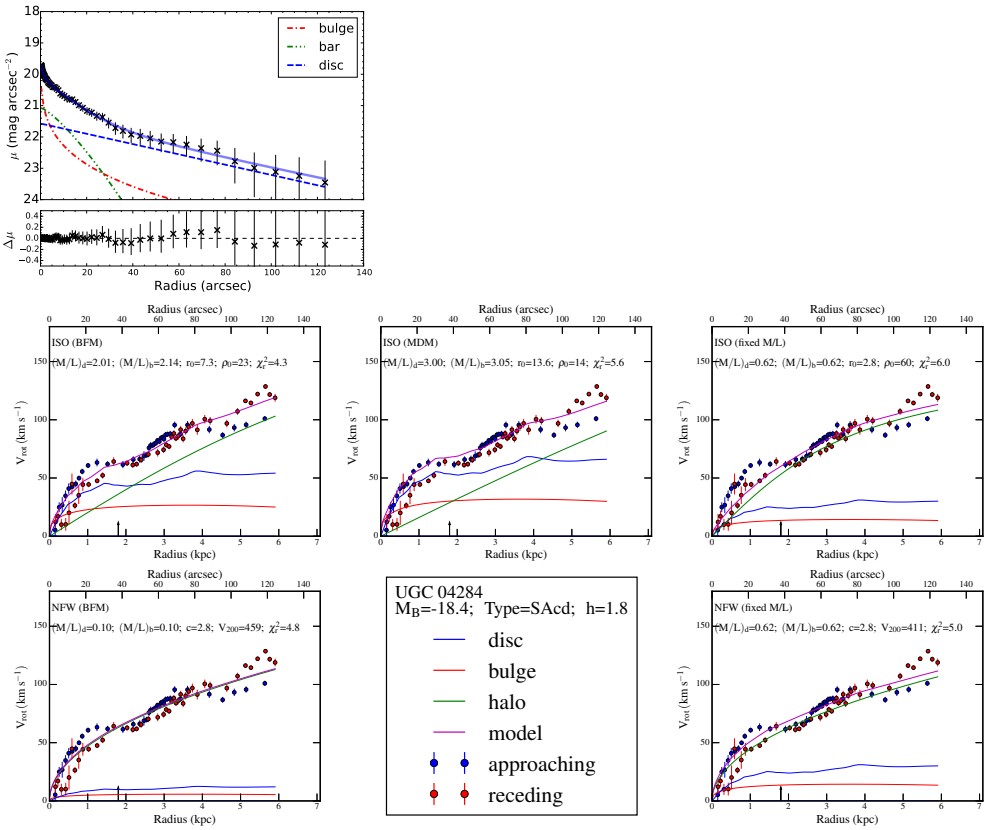

Figure B.31

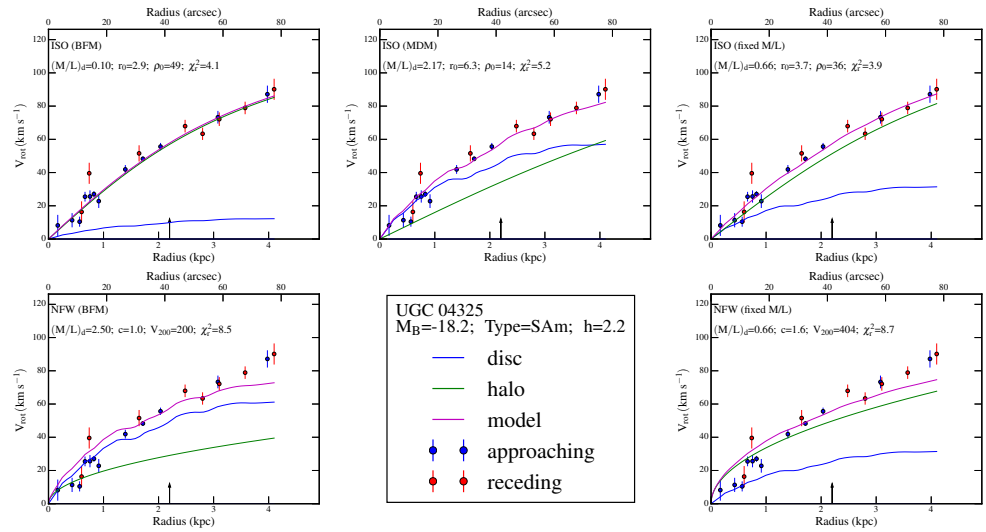

Figure B.32

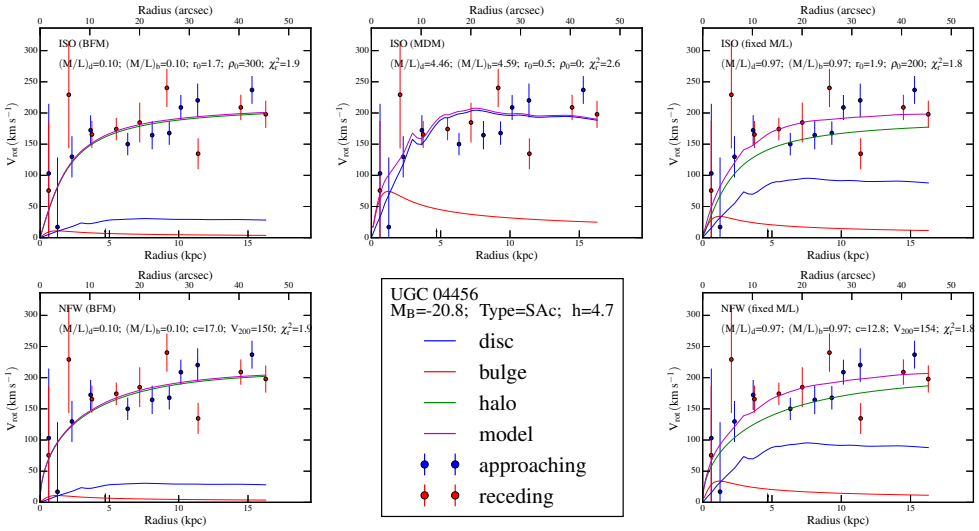

Figure B.33

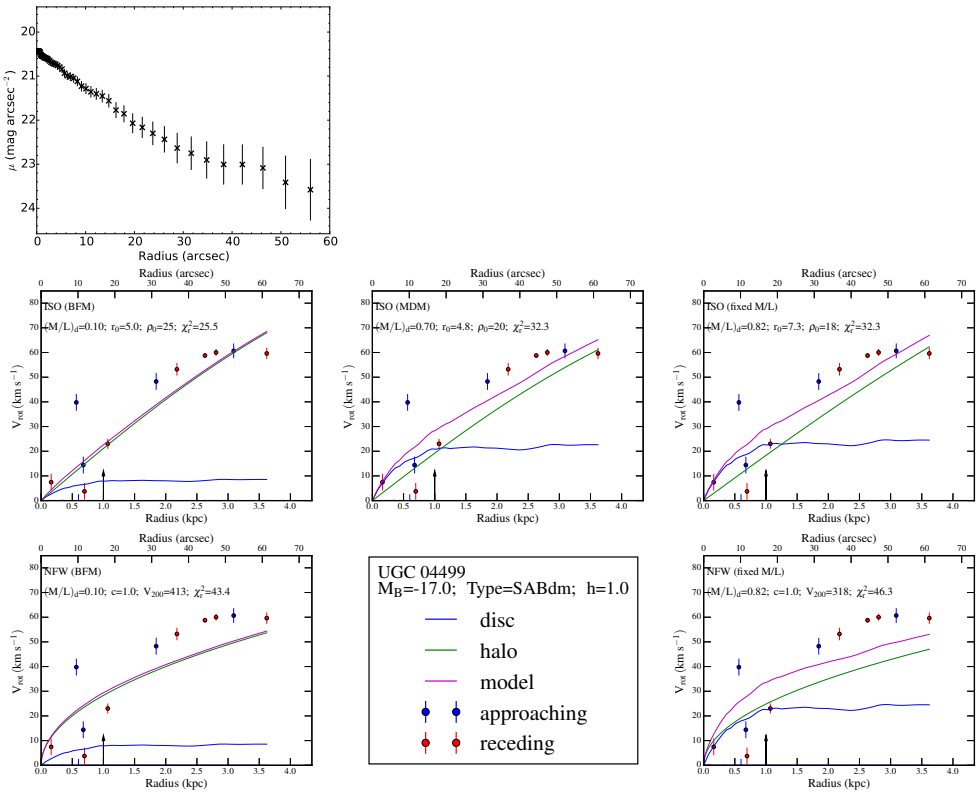

Figure B.34

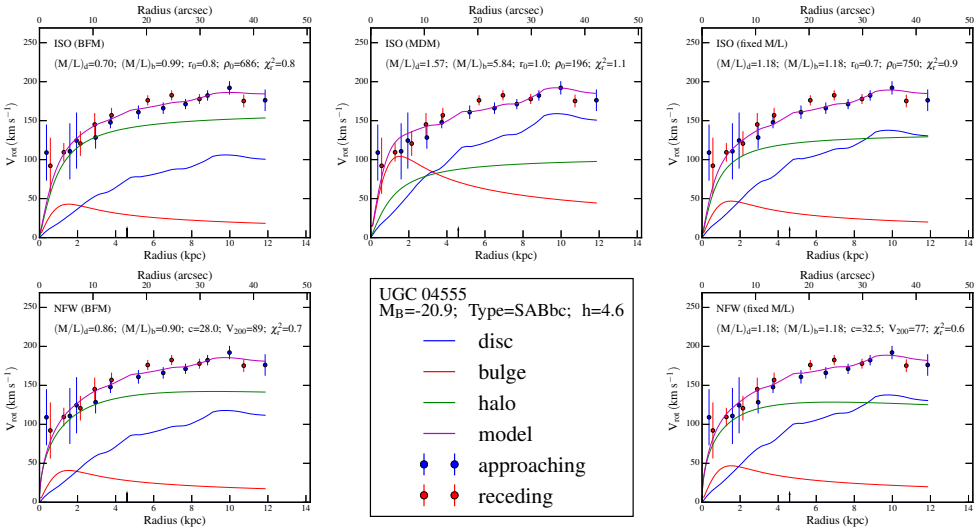

Figure B.35

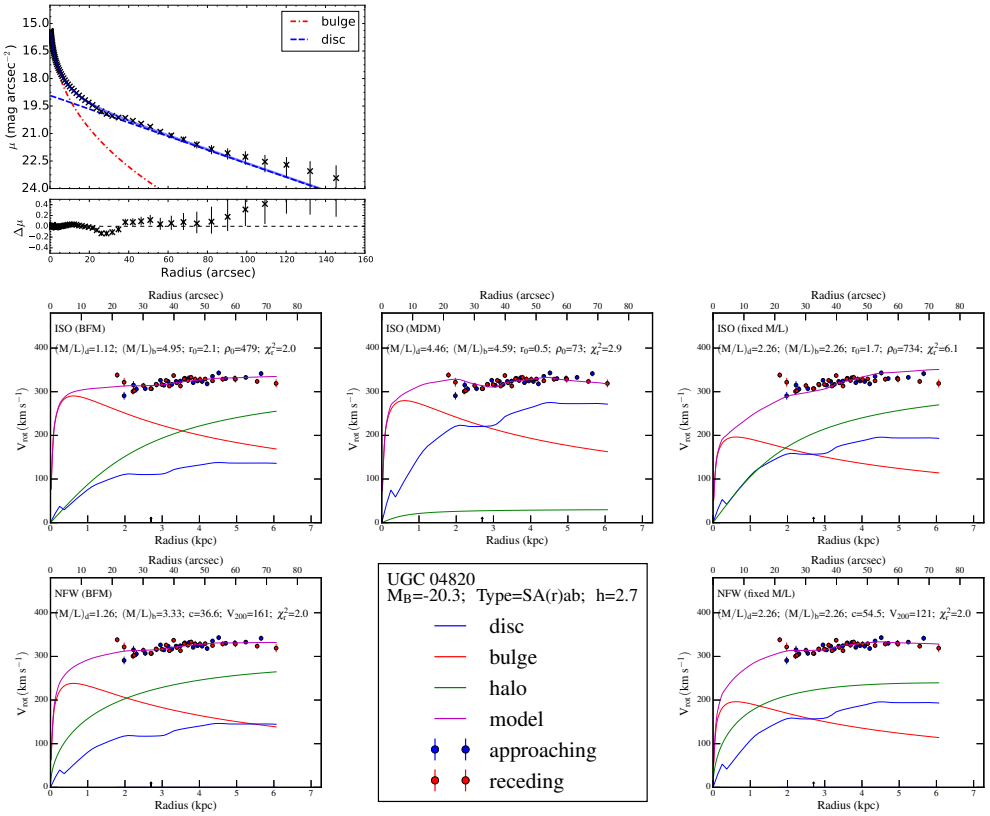

Figure B.36

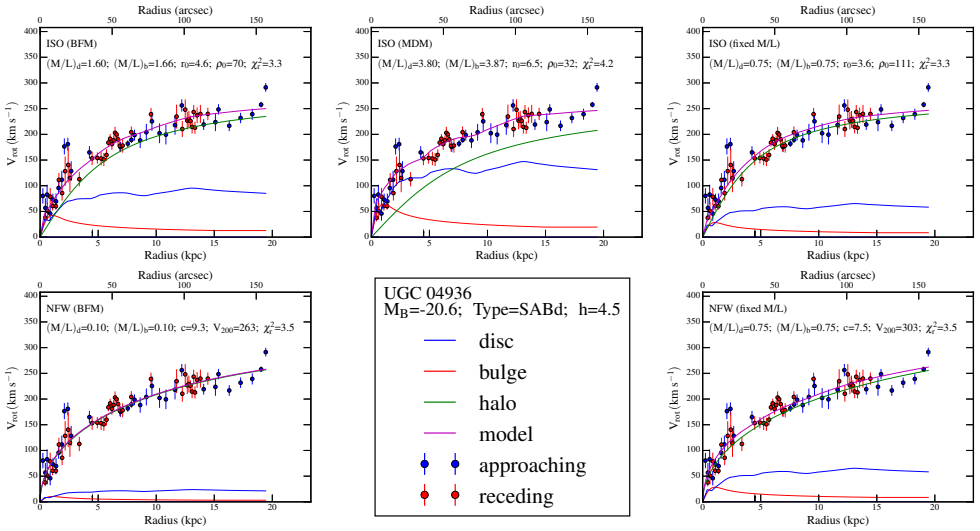

Figure B.37

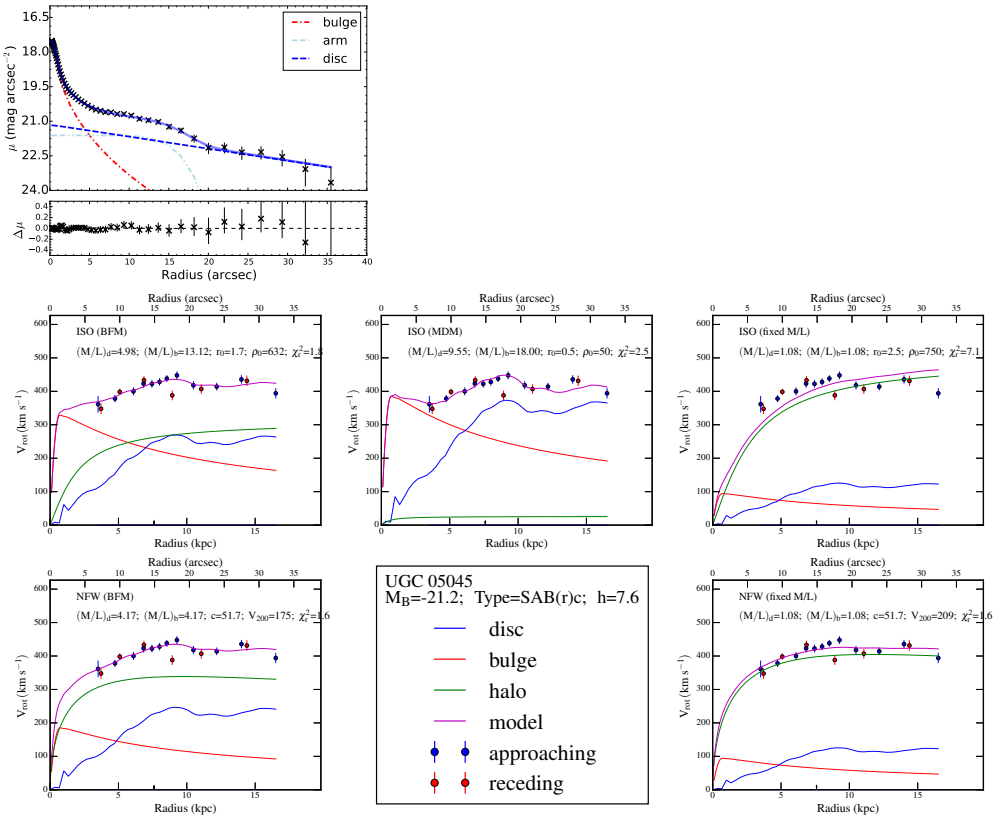

Figure B.38

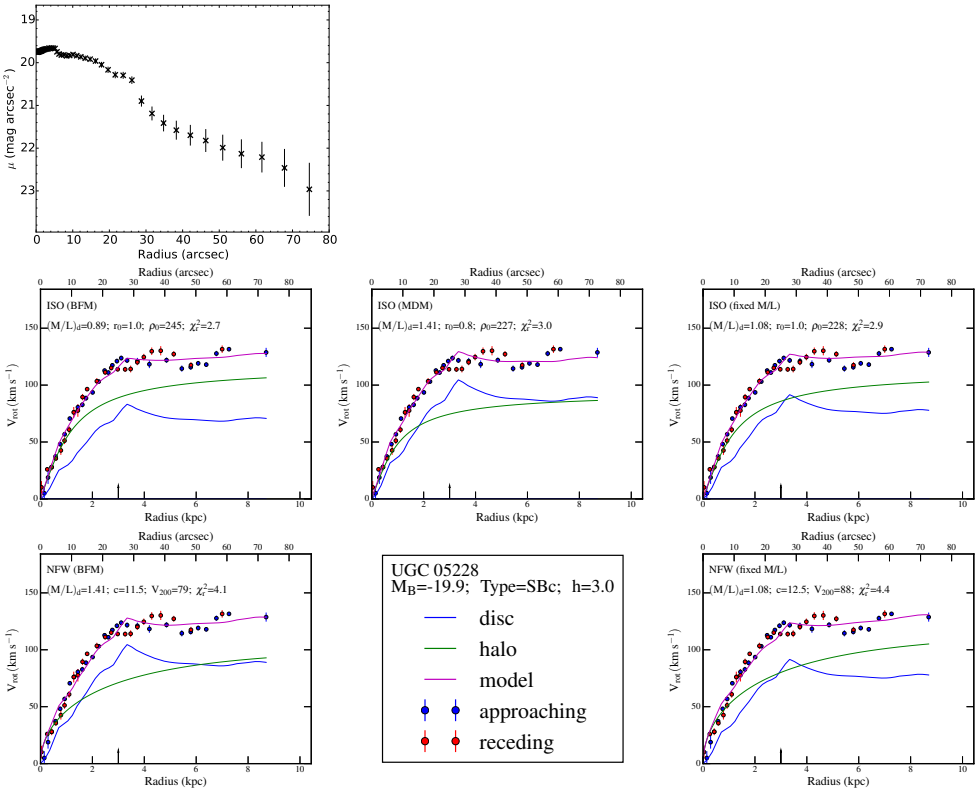

Figure B.39

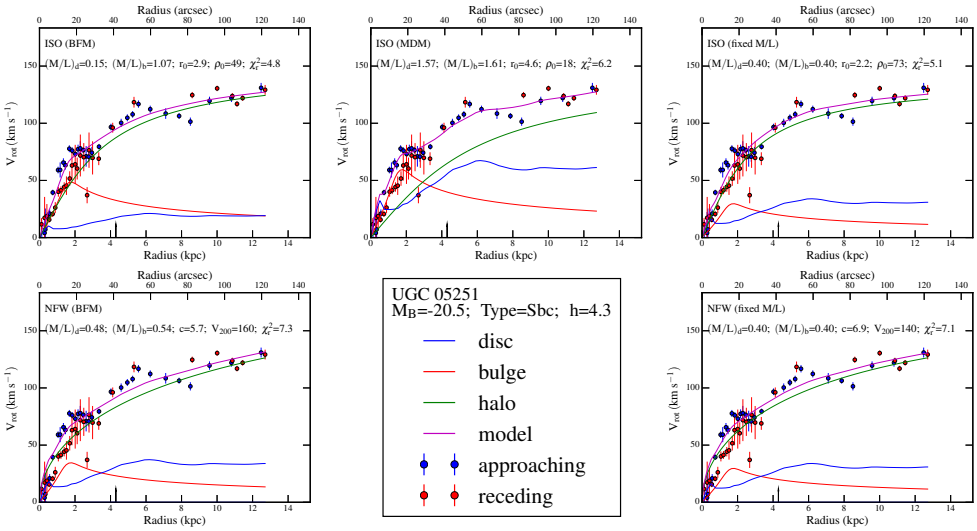

Figure B.40

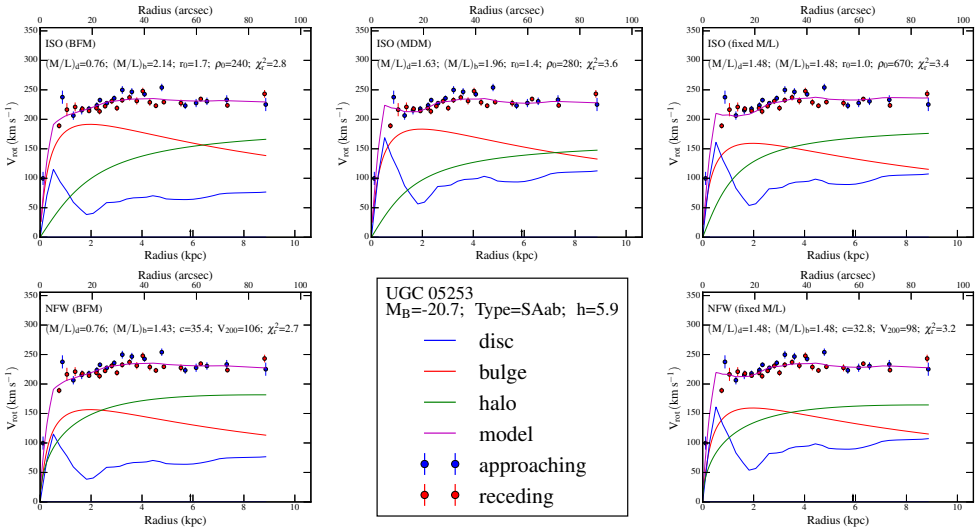

Figure B.41

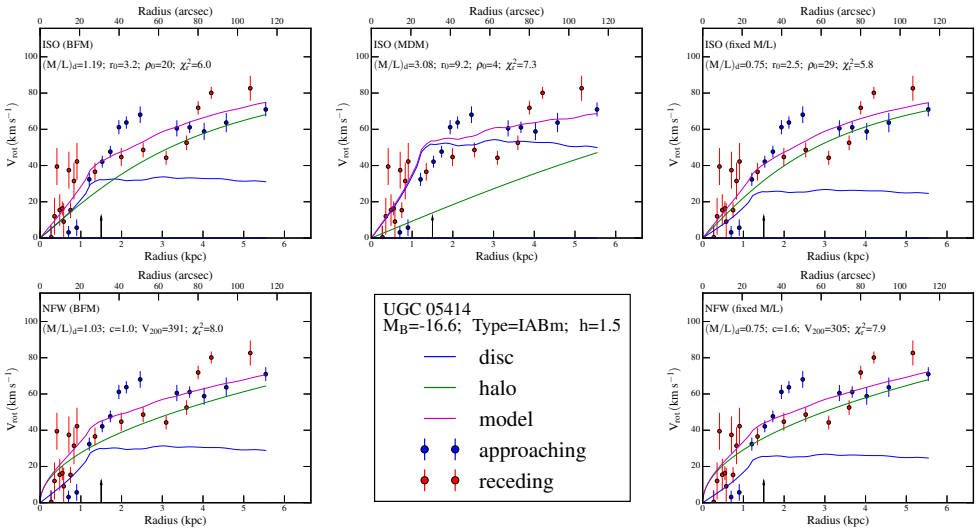

Figure B.42

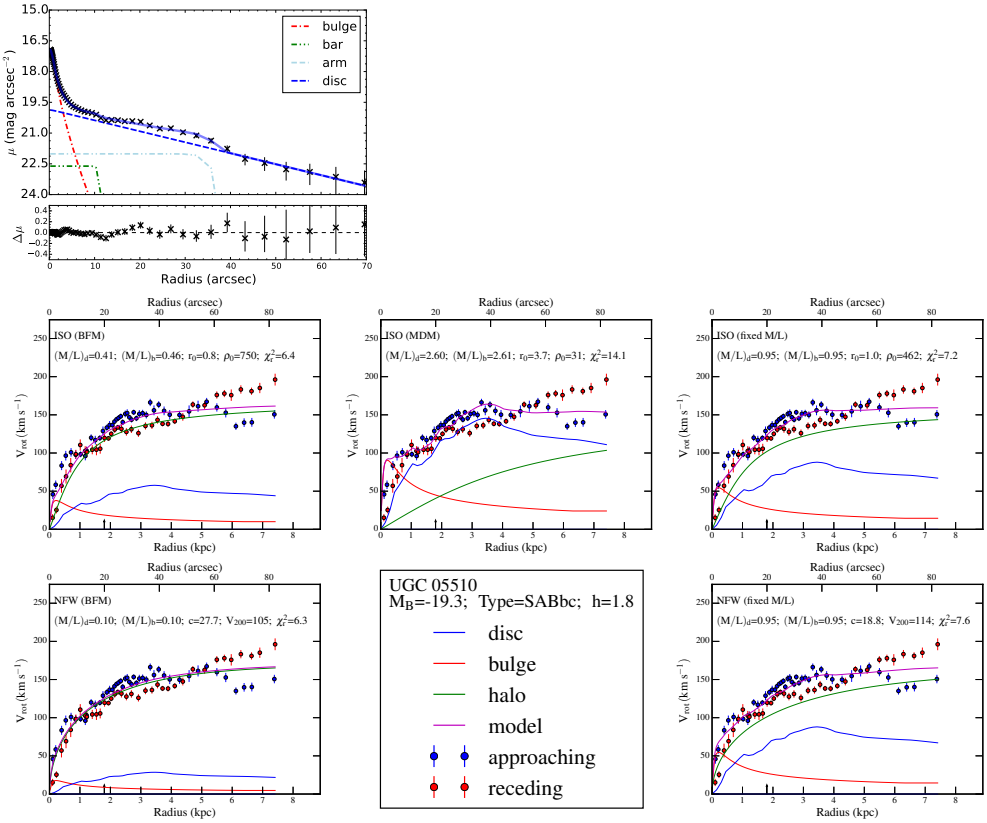
bulge
bar
arm
disc
μ (mag arcsec⁻²)
Δμ
Radius (arcsec)
ISO (BFM)
(M/L)d=0.41; (M/L)h=0.46; r0=0.8; ρ0=750; χ²r=6.4
ISO (MDM)
(M/L)d=2.60; (M/L)h=2.61; r0=3.7; ρ0=31; χ²r=14.1
ISO (fixed M/L)
(M/L)d=0.95; (M/L)h=0.95; r0=1.0; ρ0=462; χ²r=7.2
NFW (BFM)
(M/L)d=0.10; (M/L)h=0.10; c=27.7; V200=105; χ²r=6.3
NFW (fixed M/L)
(M/L)d=0.95; (M/L)h=0.95; c=18.8; V200=114; χ²r=7.6
Vrot (km s⁻¹)
Radius (kpc)
UGC 05510
MB=-19.3; Type=SABbc; h=1.8
disc
bulge
halo
model
approaching
receding

Figure B.43

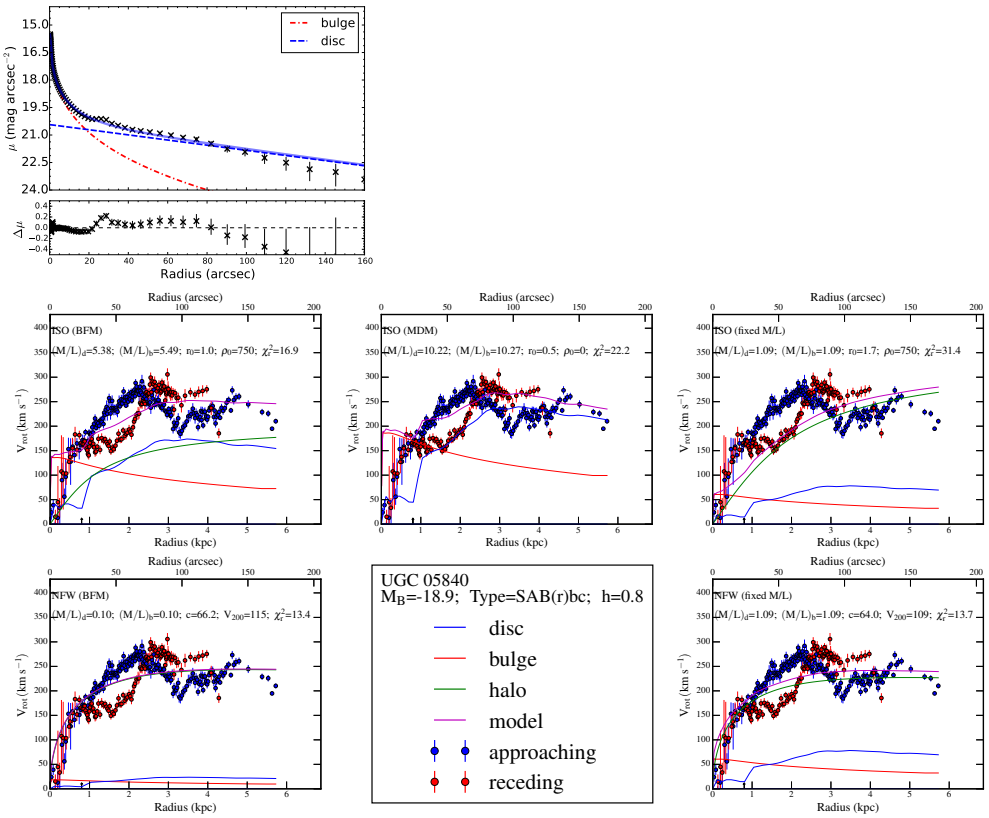

Figure B.44

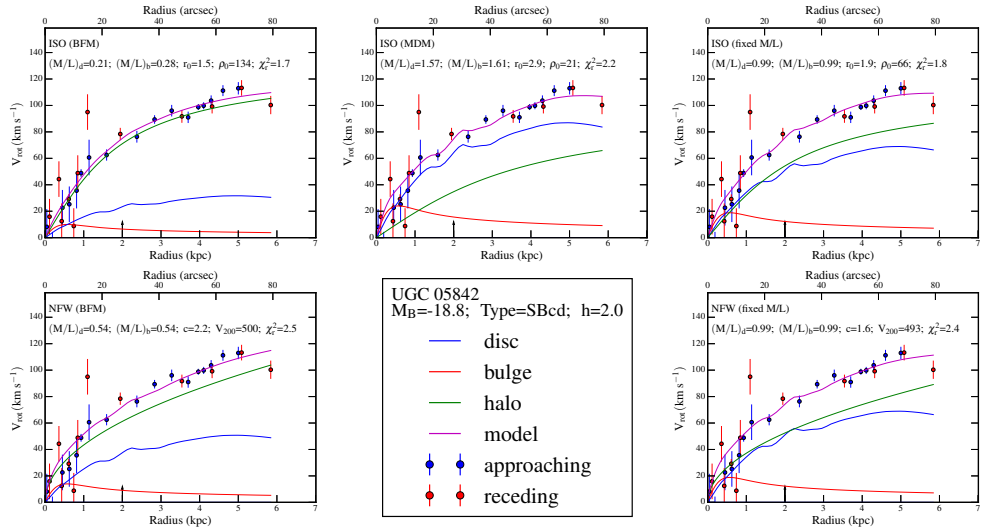

Figure B.45

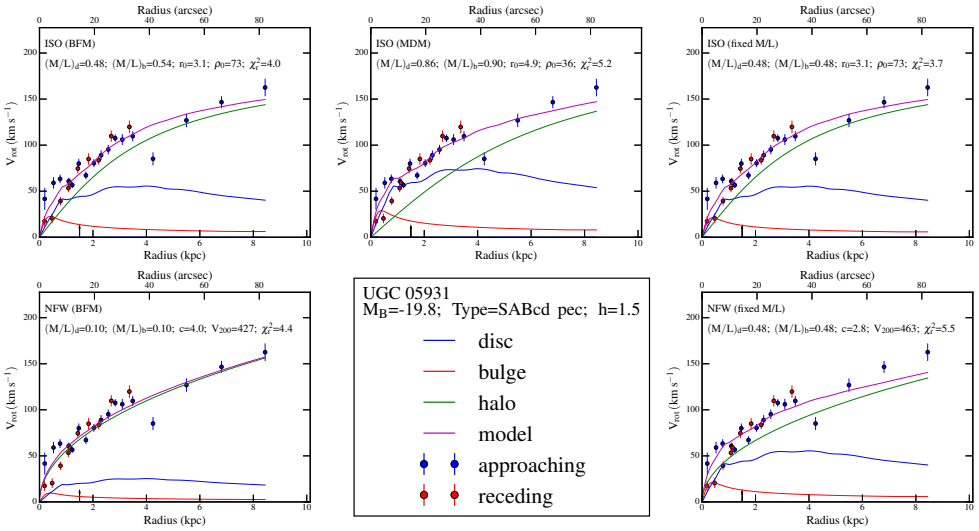

Figure B.46

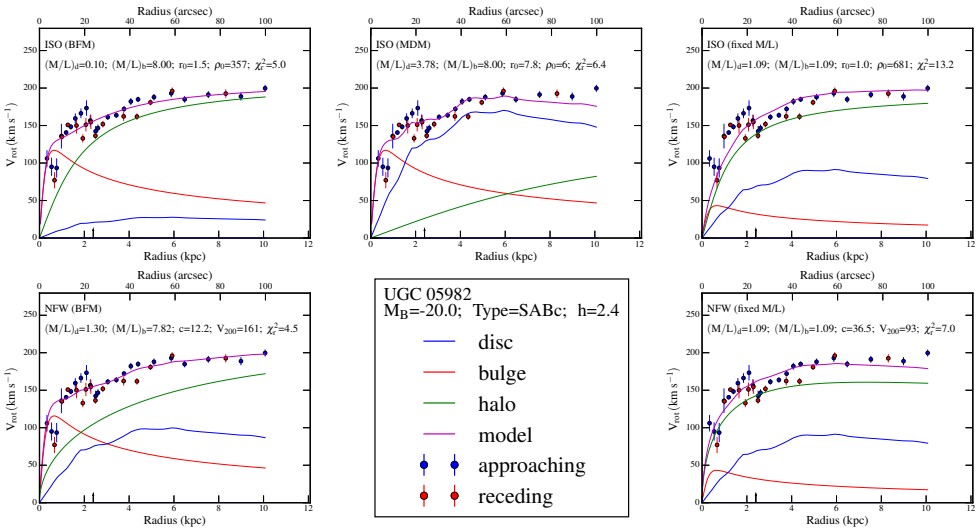

Figure B.47

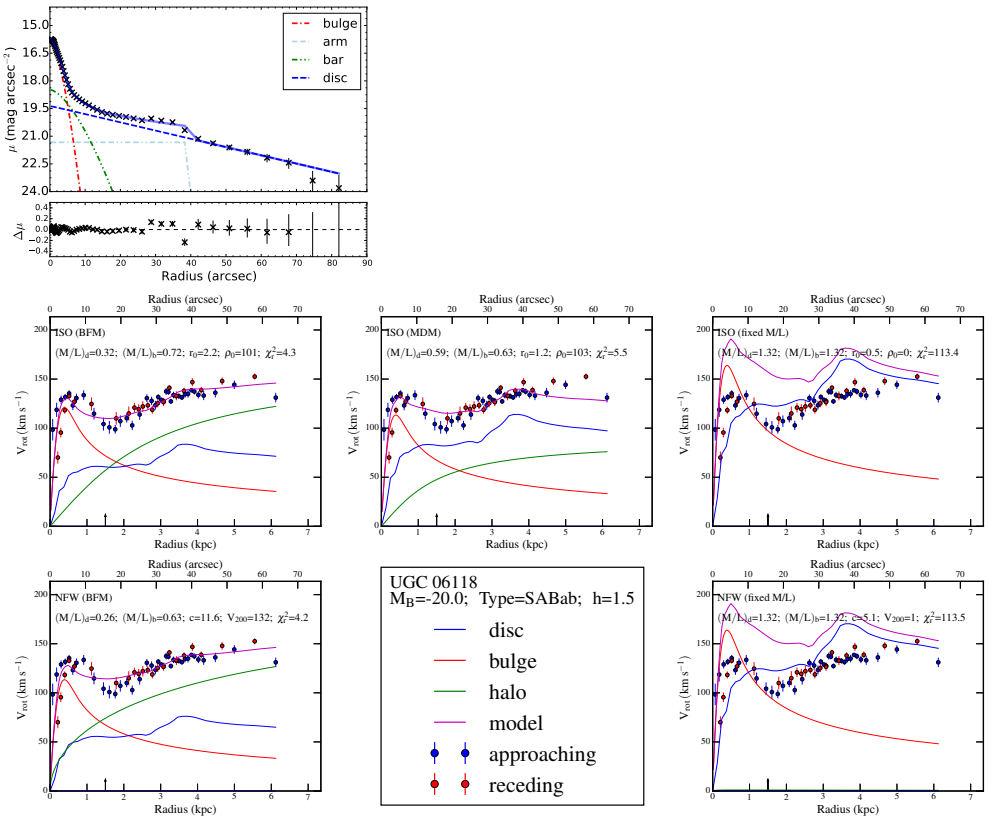
bulge
arm
bar
disc
μ (mag arcsec⁻²)
Δμ
Radius (arcsec)
ISO (BFM)
(M/L)d=0.32; (M/L)h=0.72; r0=2.2; ρ0=101; χ²r=4.3
ISO (MDM)
(M/L)d=0.59; (M/L)h=0.63; r0=1.2; ρ0=103; χ²r=5.5
ISO (fixed M/L)
(M/L)d=1.32; (M/L)h=1.32; r0=0.5; ρ0=0; χ²r=113.4
NFW (BFM)
(M/L)d=0.26; (M/L)h=0.63; c=11.6; V200=132; χ²r=4.2
NFW (fixed M/L)
(M/L)d=1.32; (M/L)h=1.32; c=5.1; V200=1; χ²r=113.5
Vrot (km s⁻¹)
Radius (kpc)
UGC 06118
MB=-20.0; Type=SABab; h=1.5
disc
bulge
halo
model
approaching
receding

Figure B.48

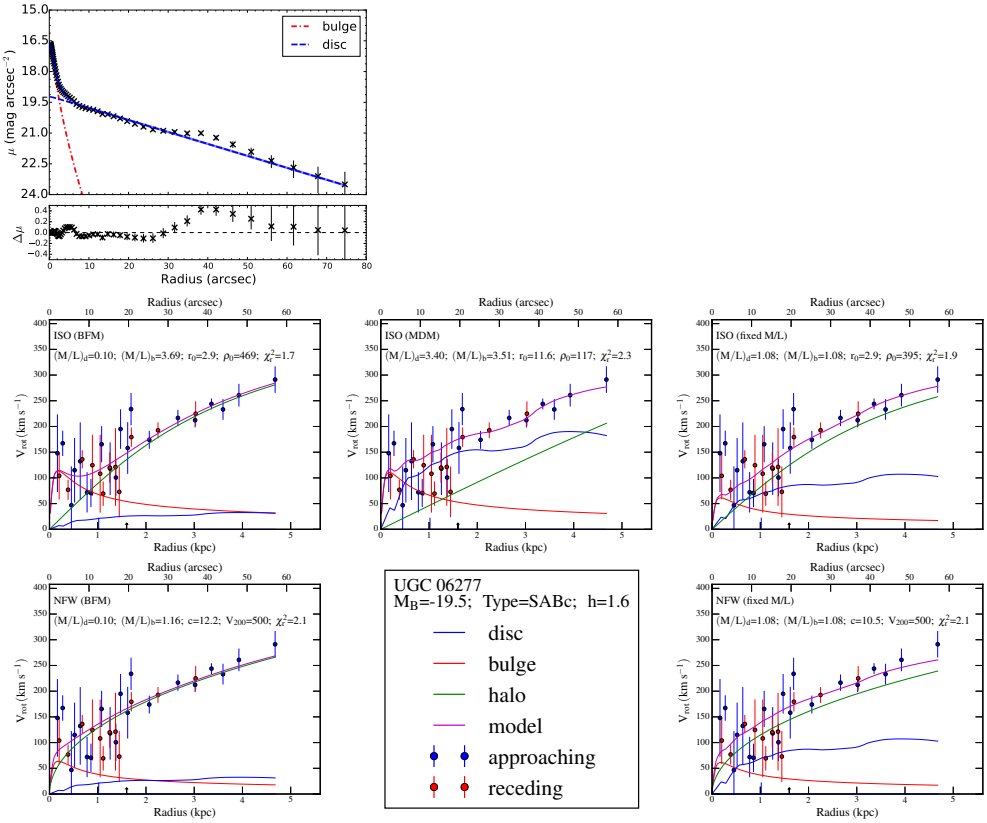
bulge
disc
μ (mag arcsec⁻²)
Δμ
Radius (arcsec)
ISO (BFM)
(M/L)d=0.10; (M/L)b=3.69; r0=2.9; ρ0=469; χ²r=1.7
ISO (MDM)
(M/L)d=3.40; (M/L)b=3.51; r0=11.6; ρ0=117; χ²r=2.3
ISO (fixed M/L)
(M/L)d=1.08; (M/L)b=1.08; r0=2.9; ρ0=395; χ²r=1.9
NFW (BFM)
(M/L)d=0.10; (M/L)b=1.16; c=12.2; V200=500; χ²r=2.1
NFW (fixed M/L)
(M/L)d=1.08; (M/L)b=1.08; c=10.5; V200=500; χ²r=2.1
Vrot (km s⁻¹)
Radius (kpc)
UGC 06277
MB=-19.5; Type=SABc; h=1.6
disc
bulge
halo
model
approaching
receding

Figure B.49

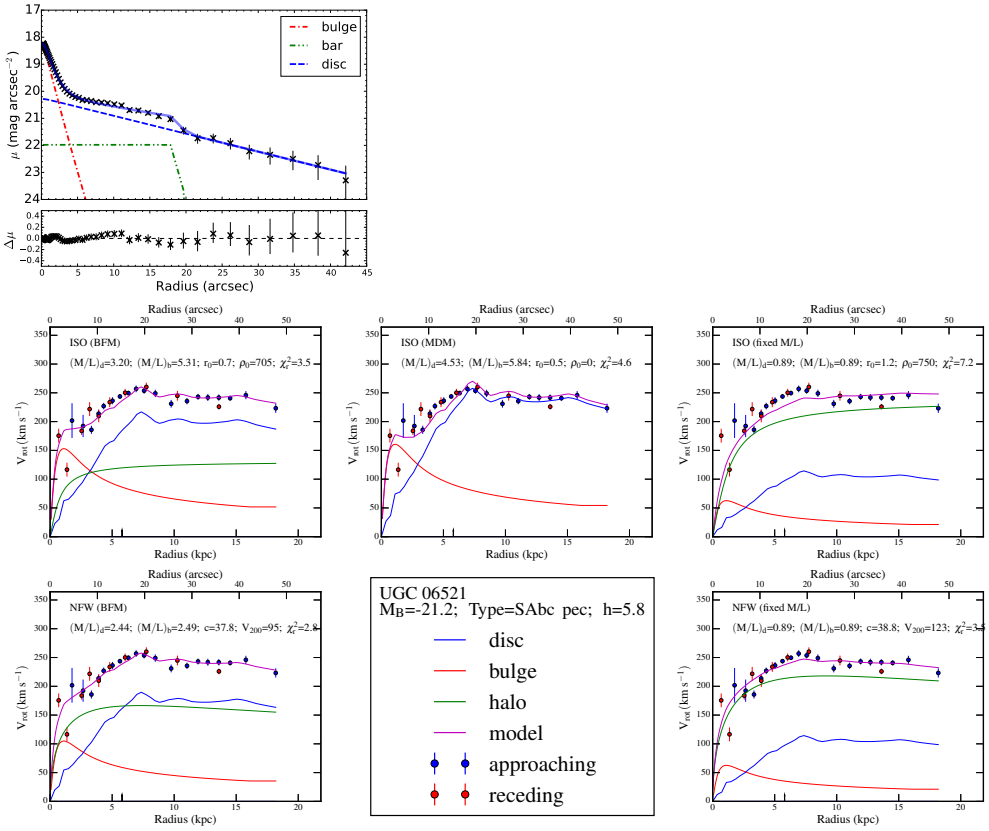

Figure B.50

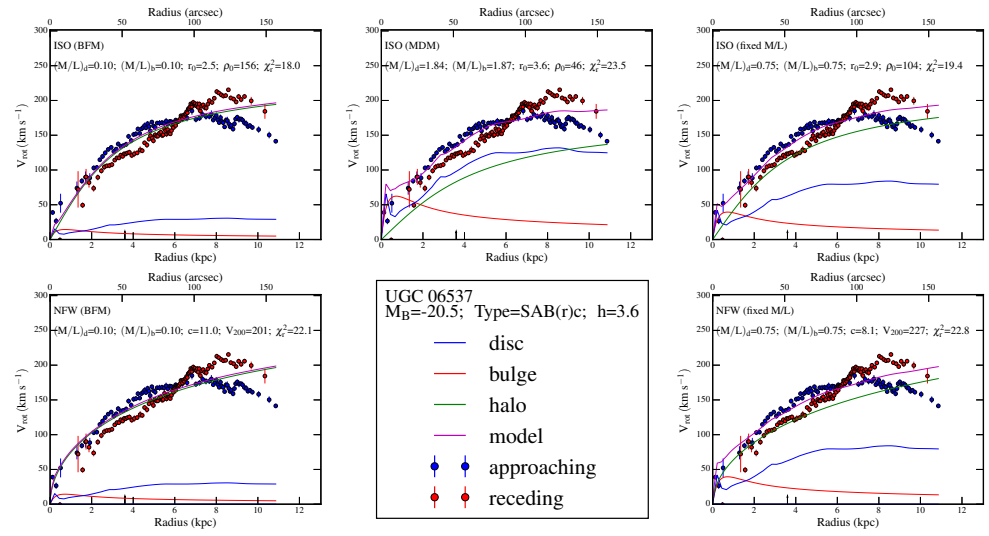

Figure B.51

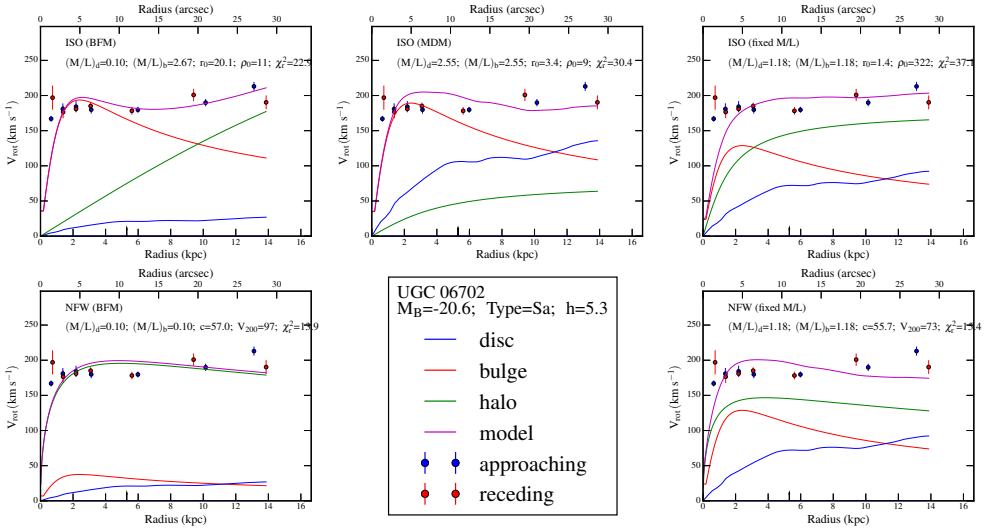
Radius (arcsec)
ISO (BFM)
ISO (MDM)
ISO (fixed M/L)
NFW (BFM)
NFW (fixed M/L)
Radius (kpc)
V_rot (km s^-1)
UGC 06702
M_B=-20.6; Type=Sa; h=5.3
disc
bulge
halo
model
approaching
receding

Figure B.52

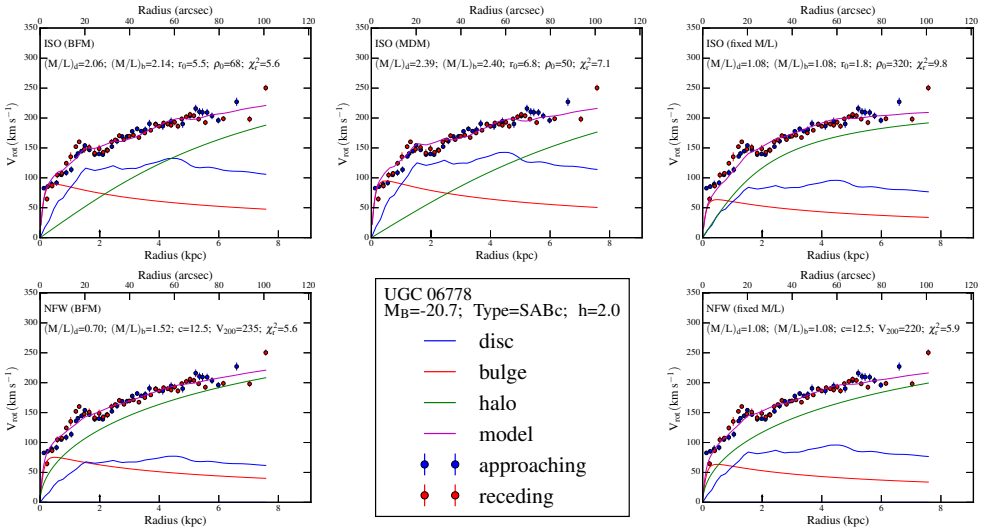

Figure B.53

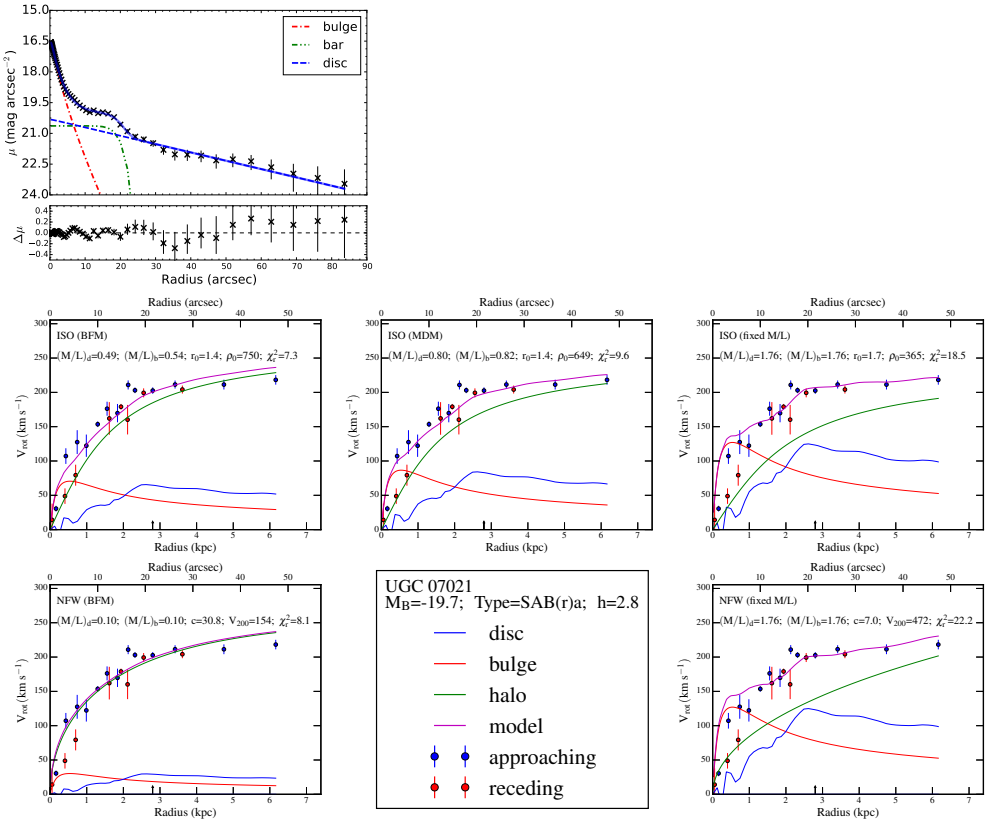

Figure B.54

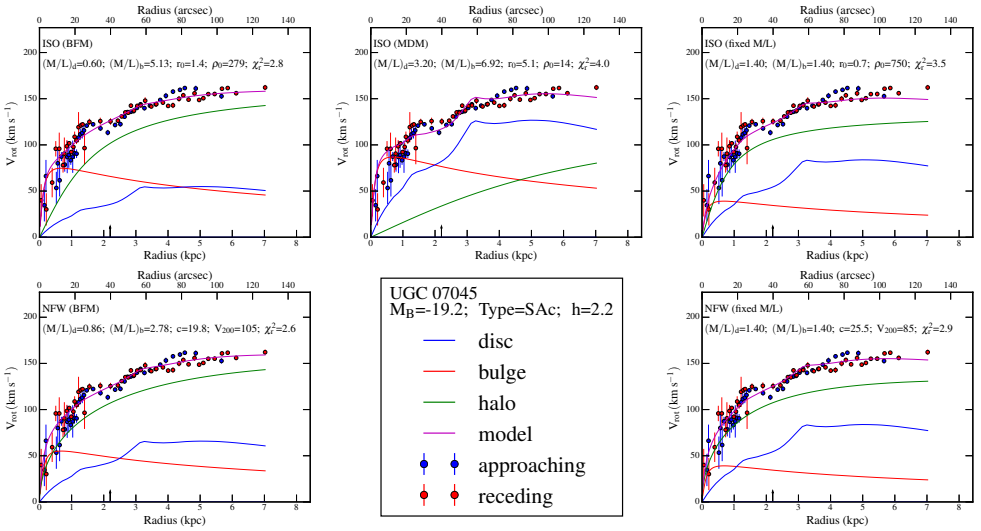

Figure B.55

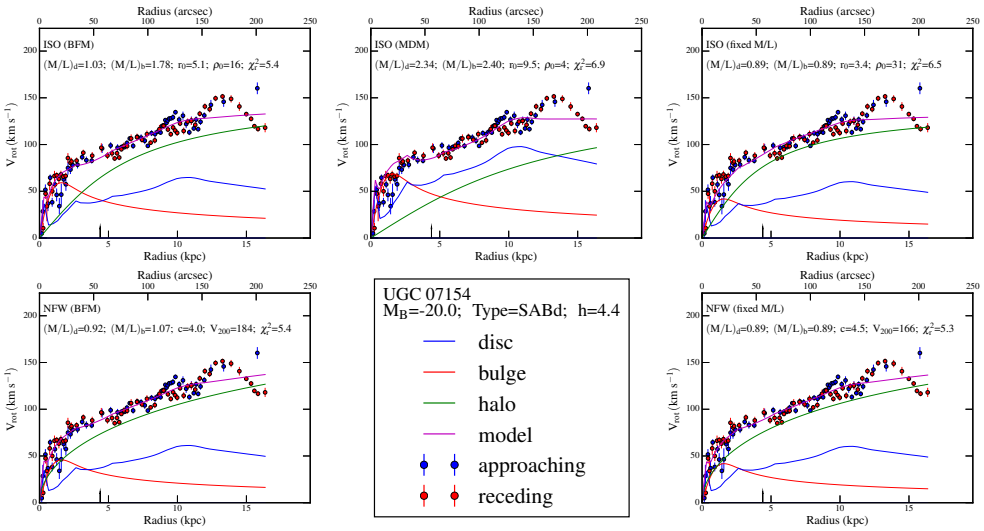

Figure B.56

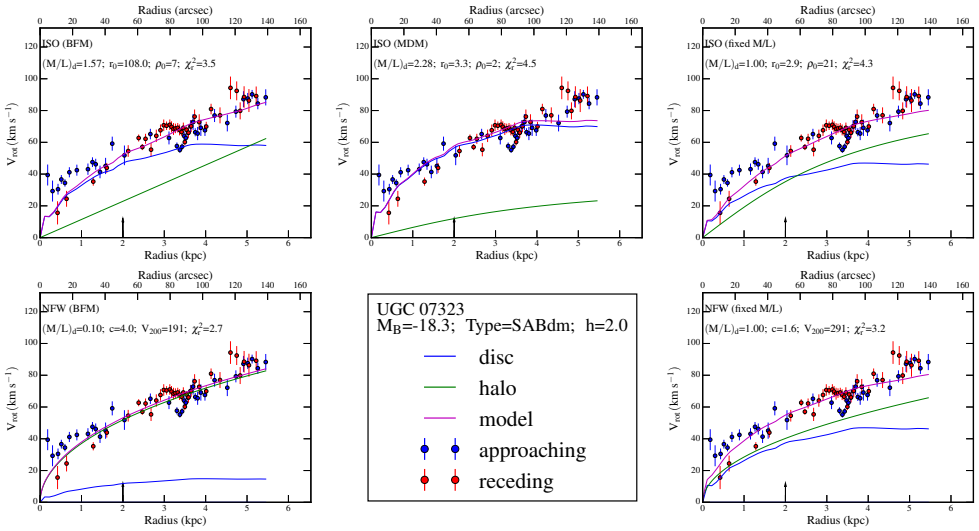

Figure B.57

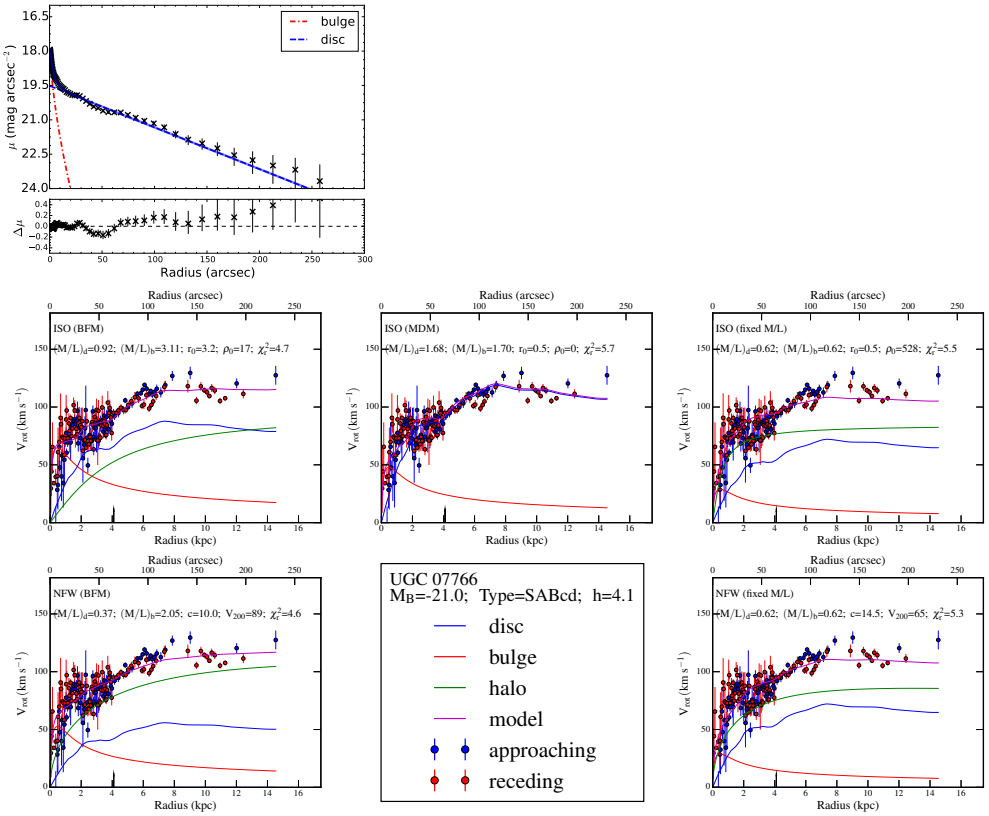

Figure B.58

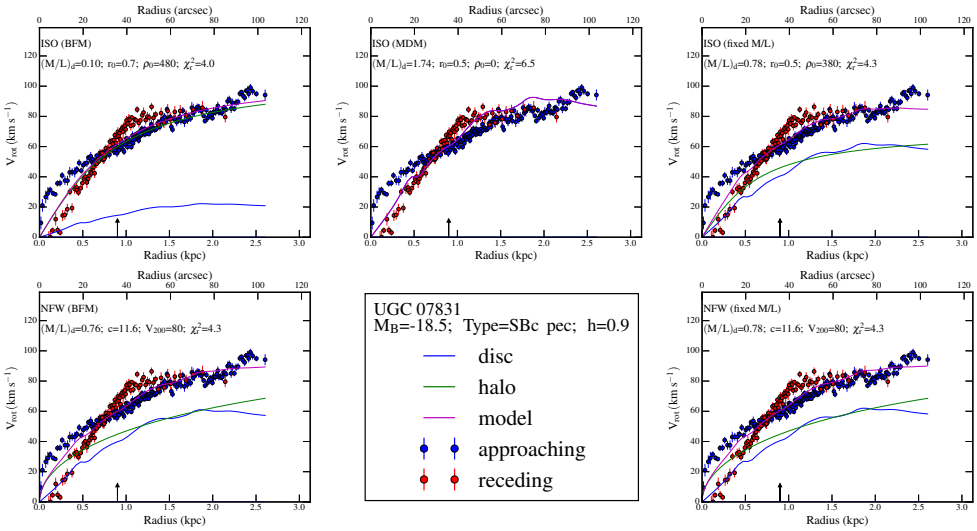

Figure B.59

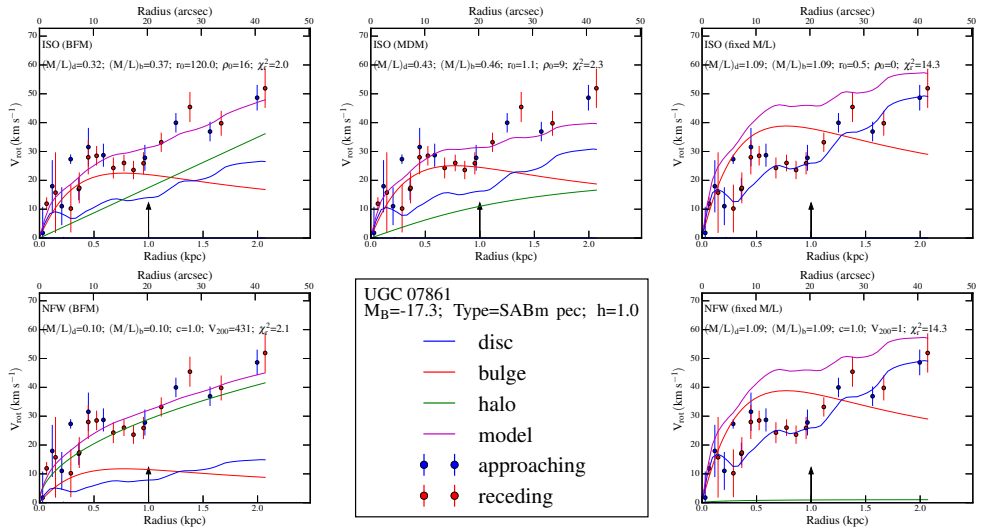

Figure B.60

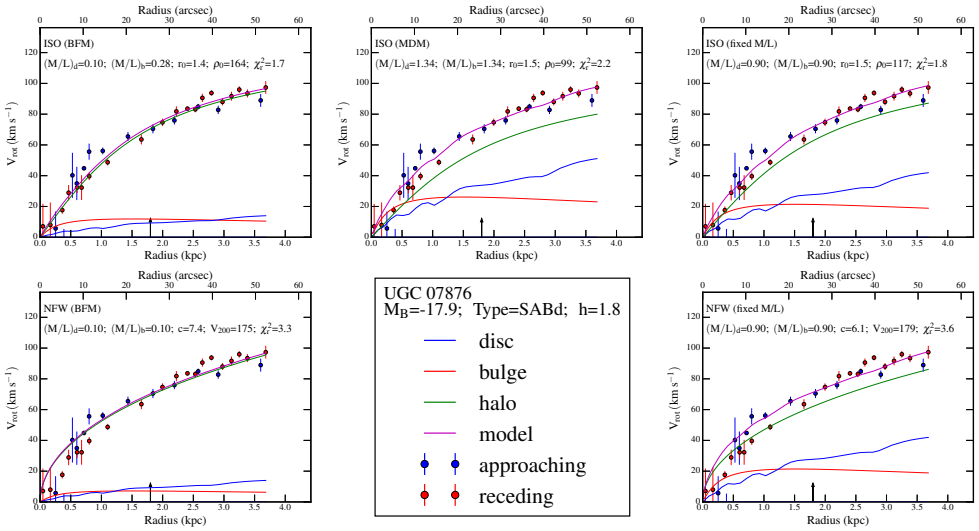

Figure B.61

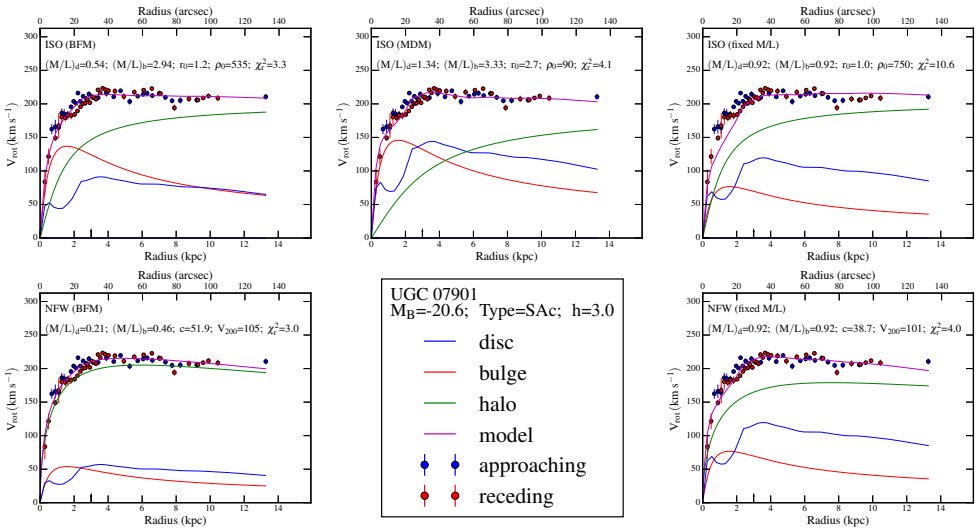

Figure B.62

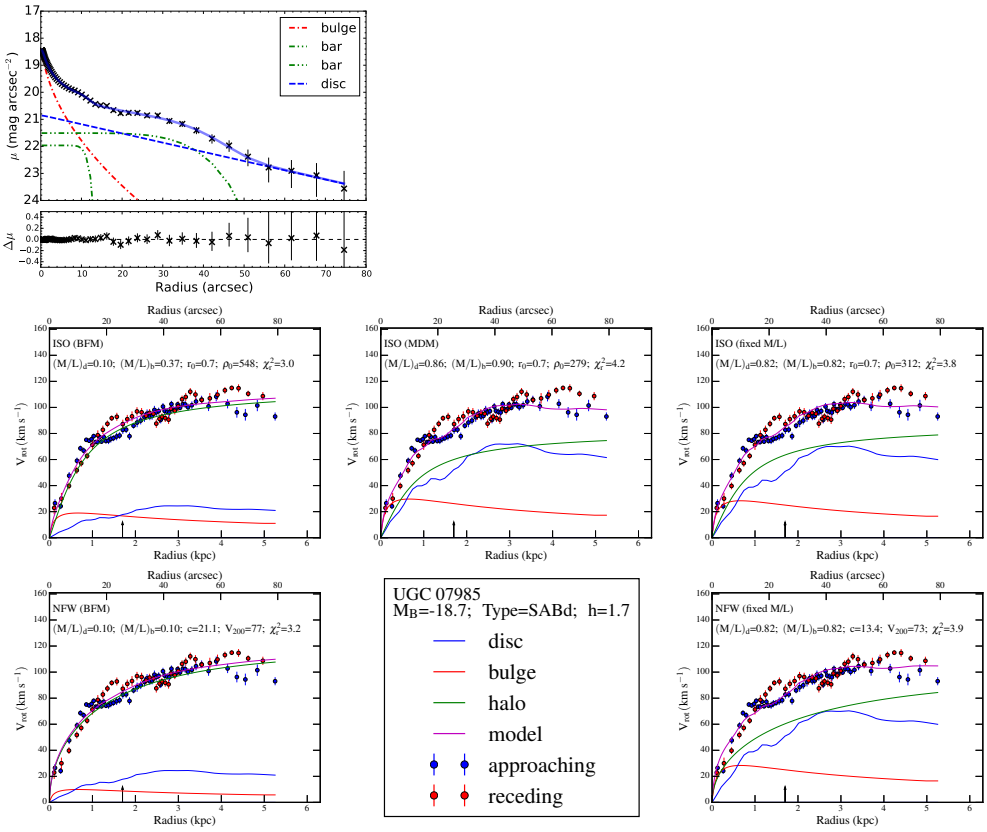

Figure B.63

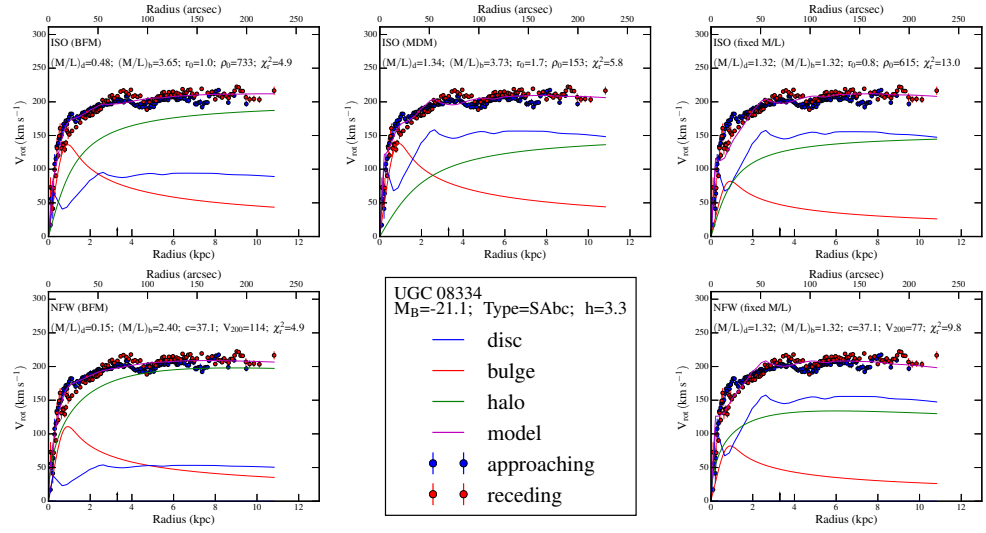

Figure B.64

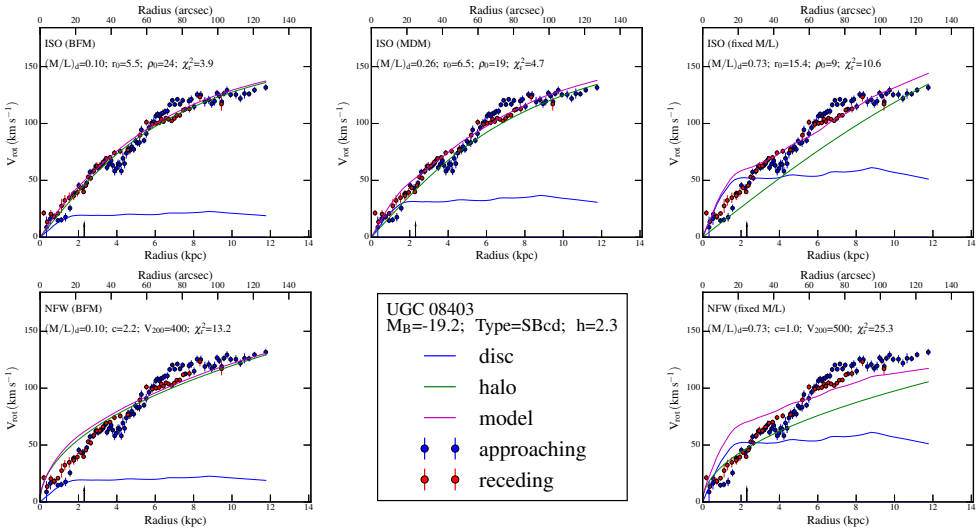

Figure B.65

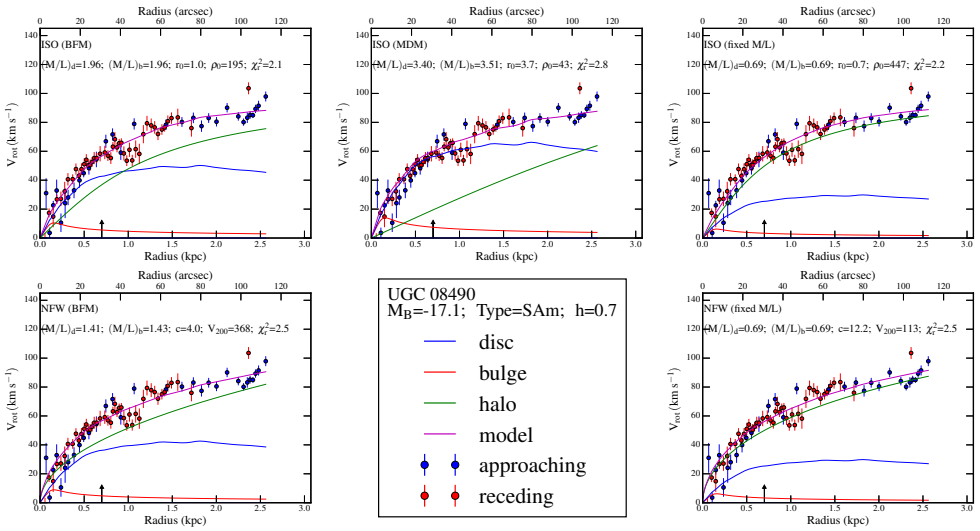

Figure B.66

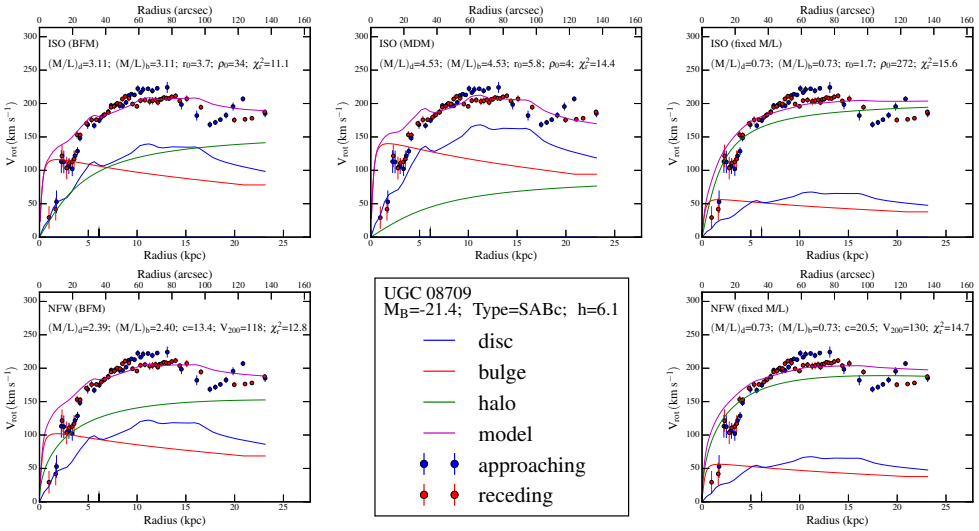

Figure B.67

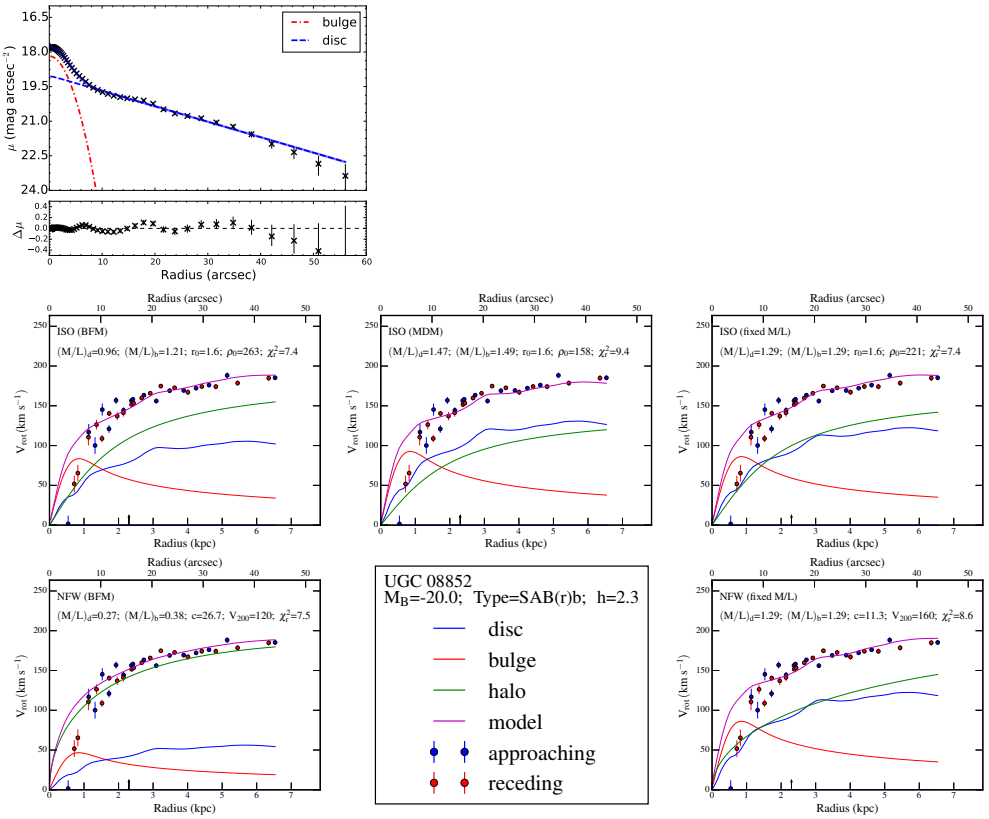

Figure B.68

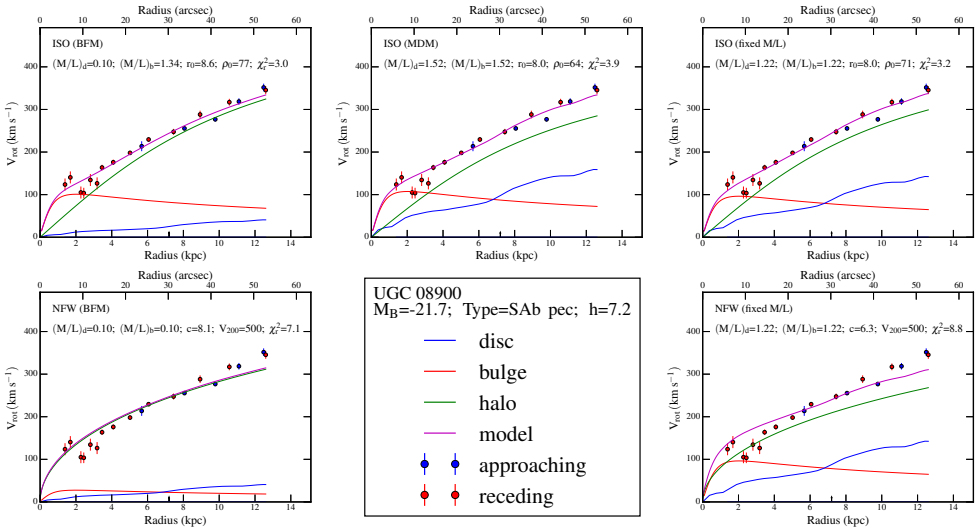

Figure B.69

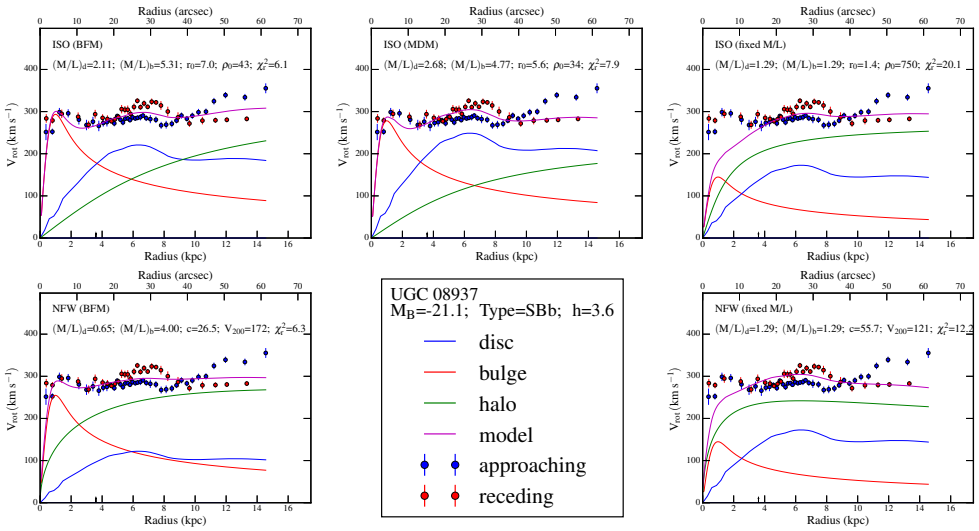

Figure B.70

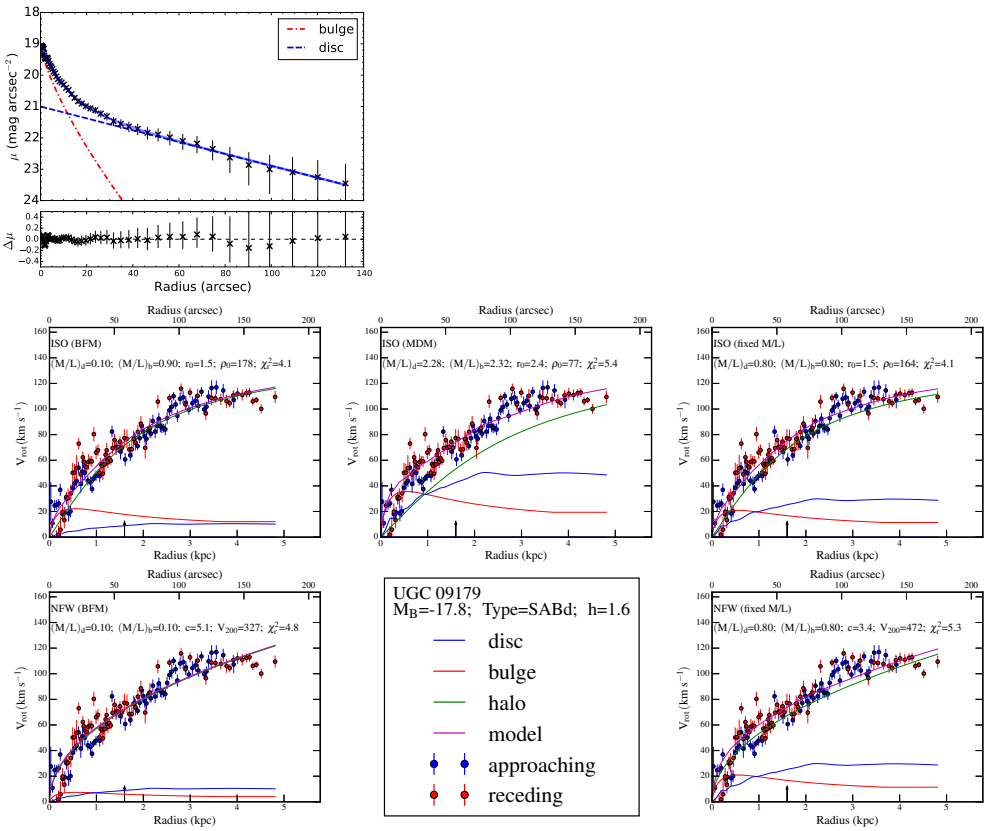
bulge
disc
μ (mag arcsec⁻²)
Δμ
Radius (arcsec)
ISO (BFM)
(M/L)d=0.10; (M/L)b=0.90; r0=1.5; ρ0=178; χ²r=4.1
ISO (MDM)
(M/L)d=2.28; (M/L)b=2.32; r0=2.4; ρ0=77; χ²r=5.4
ISO (fixed M/L)
(M/L)d=0.80; (M/L)b=0.80; r0=1.5; ρ0=164; χ²r=4.1
NFW (BFM)
(M/L)d=0.10; (M/L)b=0.10; c=5.1; V200=327; χ²r=4.8
NFW (fixed M/L)
(M/L)d=0.80; (M/L)b=0.80; c=3.4; V200=472; χ²r=5.3
Vrot (km s⁻¹)
Radius (kpc)
UGC 09179
MB=-17.8; Type=SABd; h=1.6
disc
bulge
halo
model
approaching
receding

Figure B.71

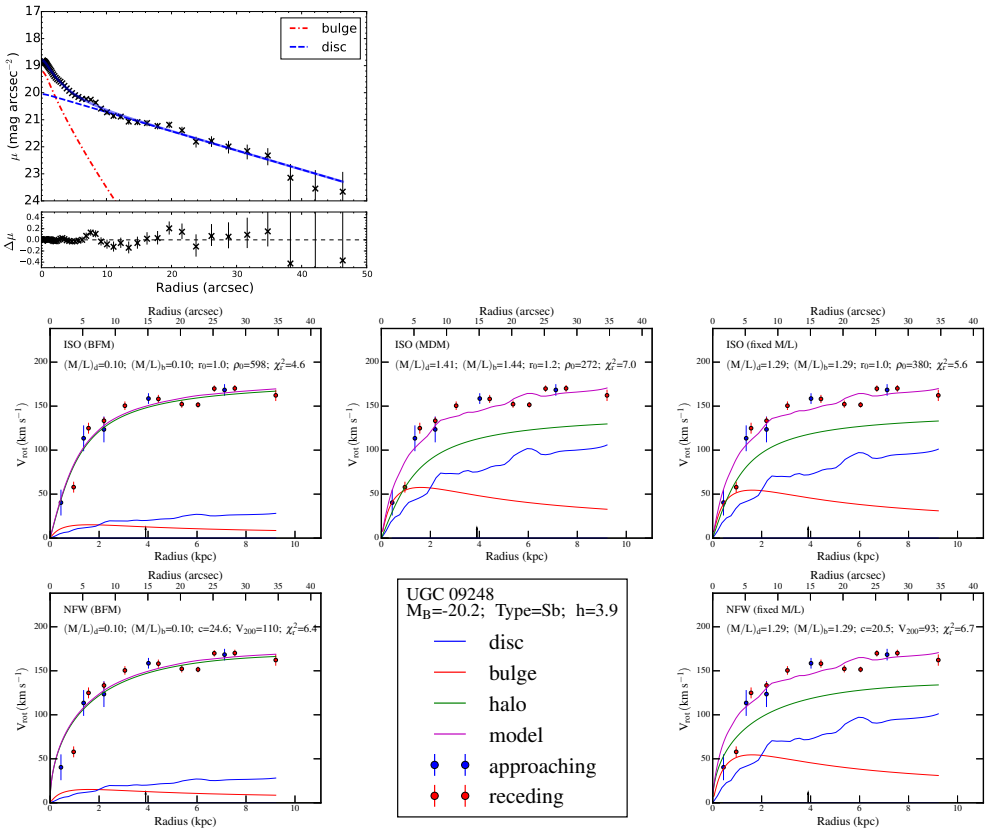
bulge
disc
μ (mag arcsec⁻²)
Δμ
Radius (arcsec)
ISO (BFM)
(M/L)d=0.10; (M/L)b=0.10; r0=1.0; ρ0=598; χ²r=4.6
ISO (MDM)
(M/L)d=1.41; (M/L)b=1.44; r0=1.2; ρ0=272; χ²r=7.0
ISO (fixed M/L)
(M/L)d=1.29; (M/L)b=1.29; r0=1.0; ρ0=380; χ²r=5.6
NFW (BFM)
(M/L)d=0.10; (M/L)b=0.10; c=24.6; V200=110; χ²r=6.4
NFW (fixed M/L)
(M/L)d=1.29; (M/L)b=1.29; c=20.5; V200=93; χ²r=6.7
Vrot (km s⁻¹)
Radius (kpc)
UGC 09248
MB=-20.2; Type=Sb; h=3.9
disc
bulge
halo
model
approaching
receding

Figure B.72

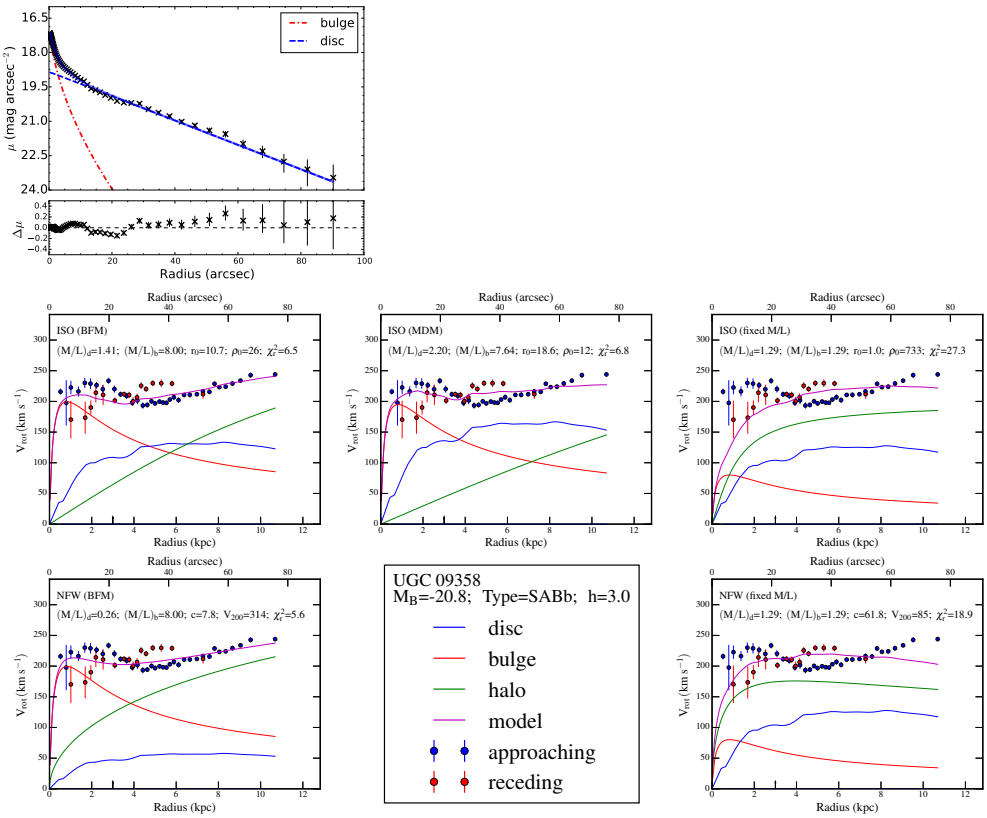

Figure B.73

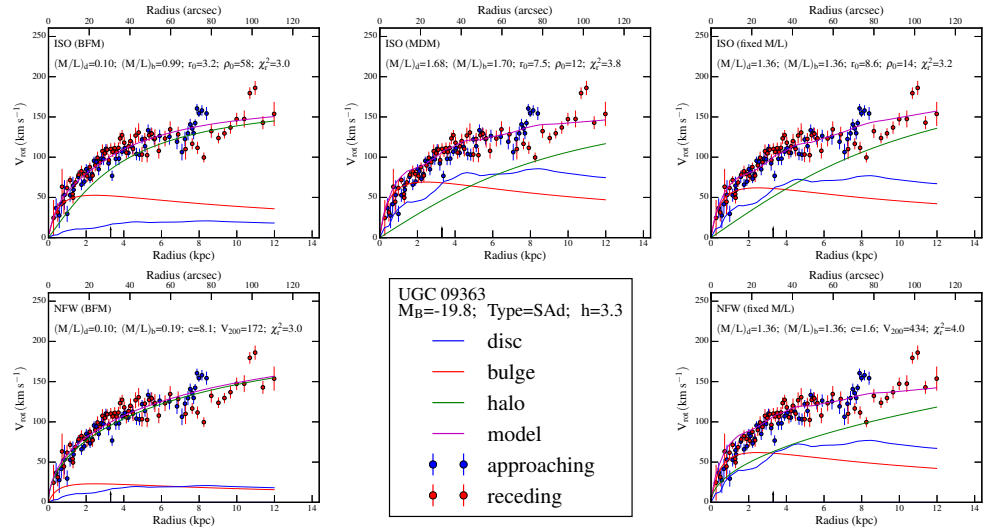

Figure B.74

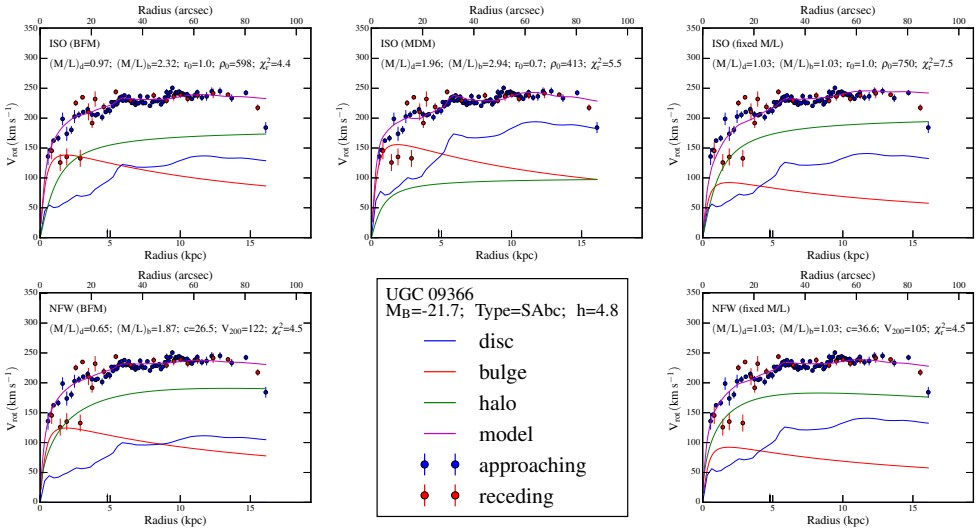

Figure B.75

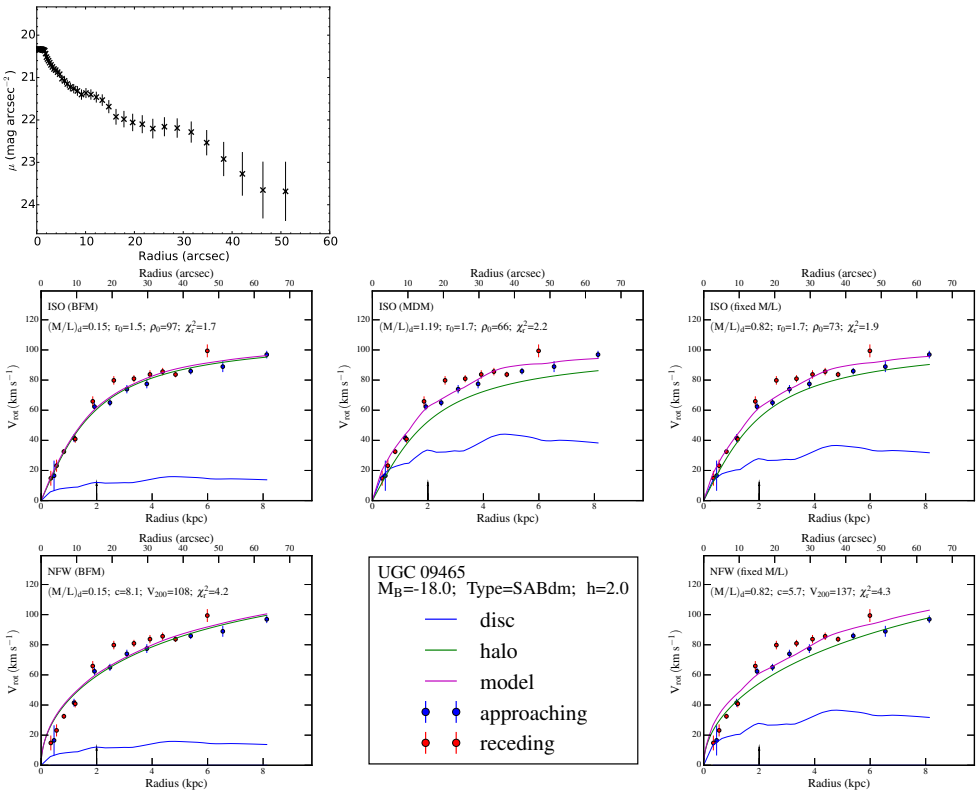

Figure B.76

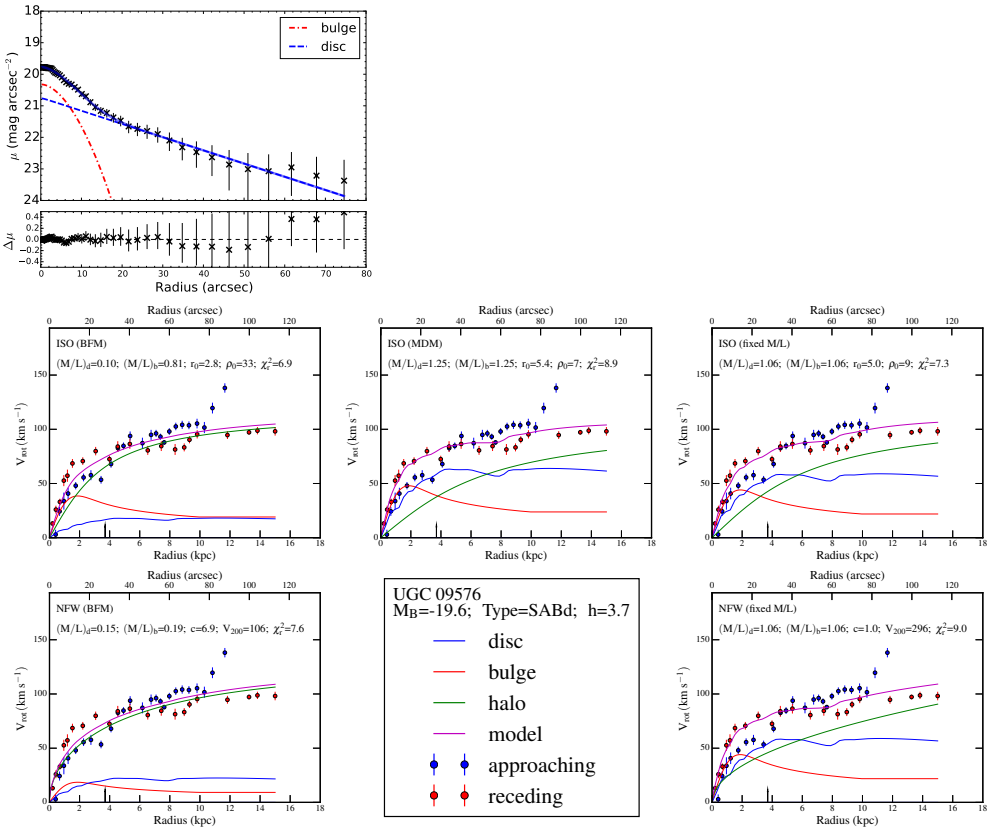

Figure B.77

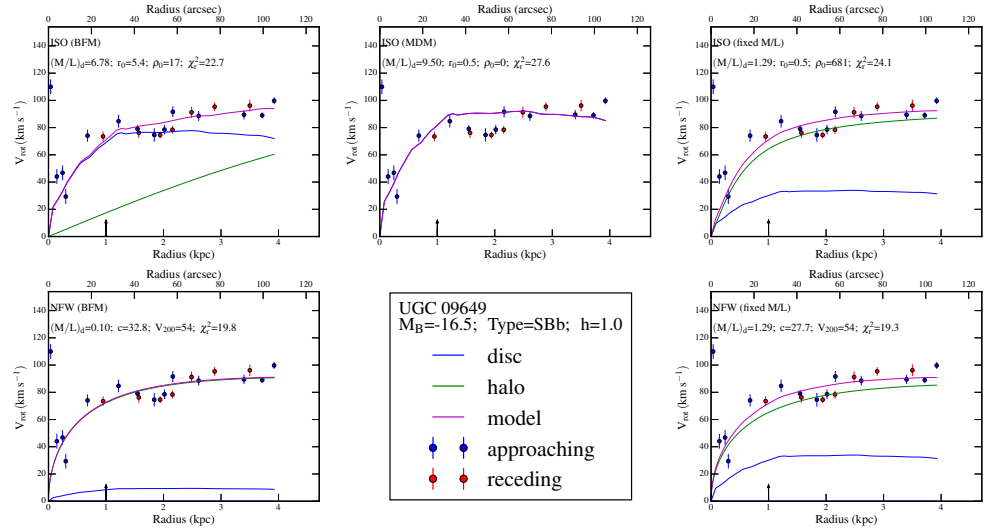

Figure B.78

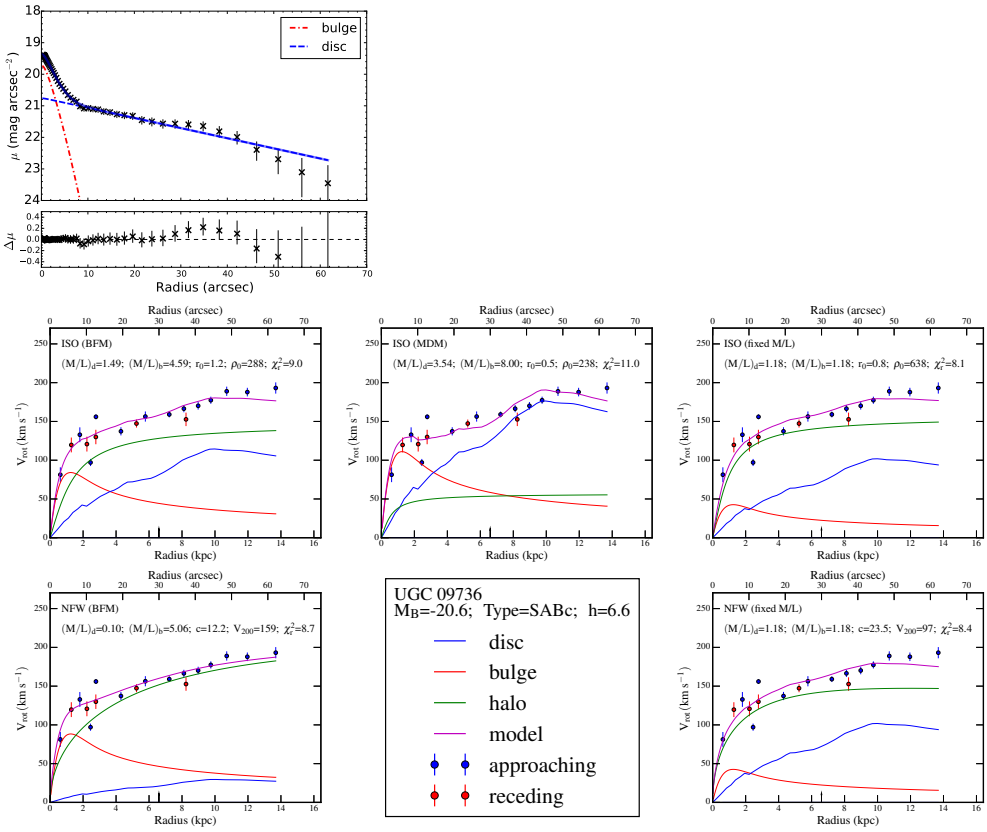

Figure B.79

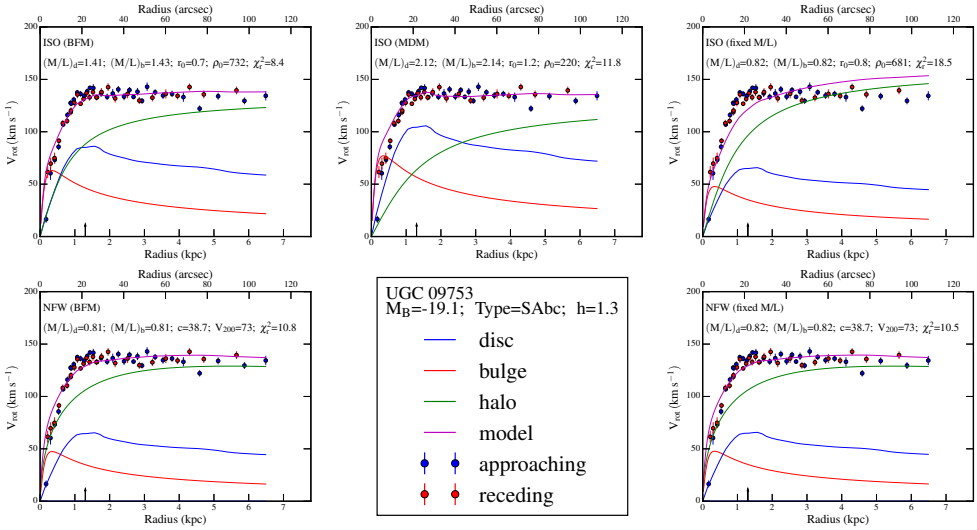

Figure B.80

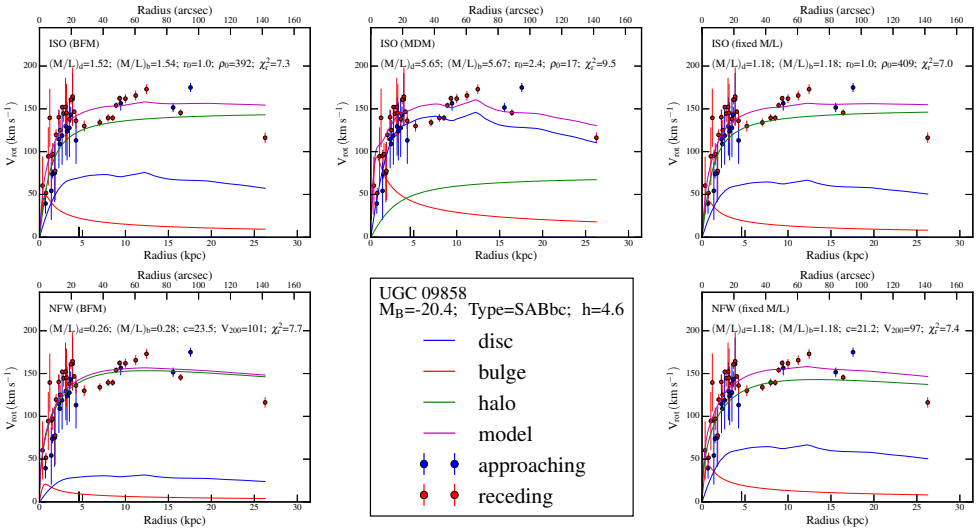

Figure B.81

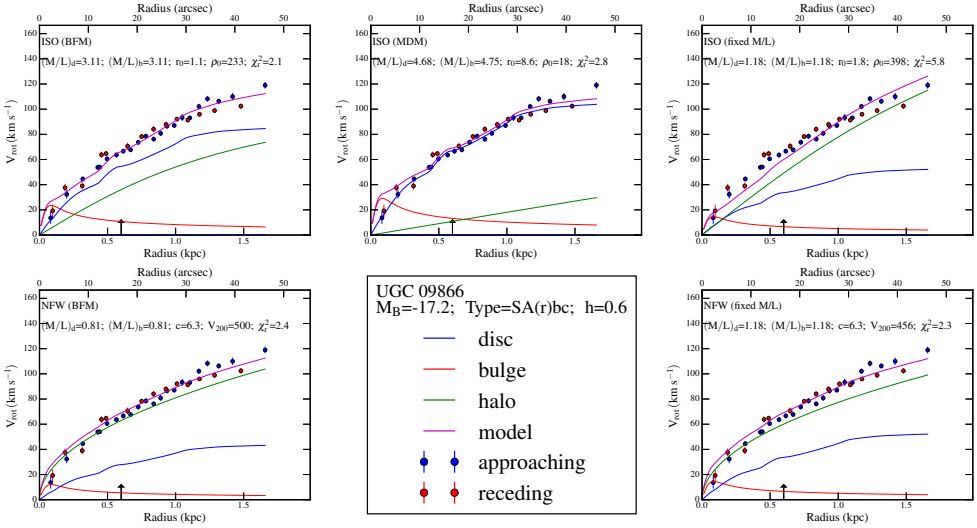

Figure B.82

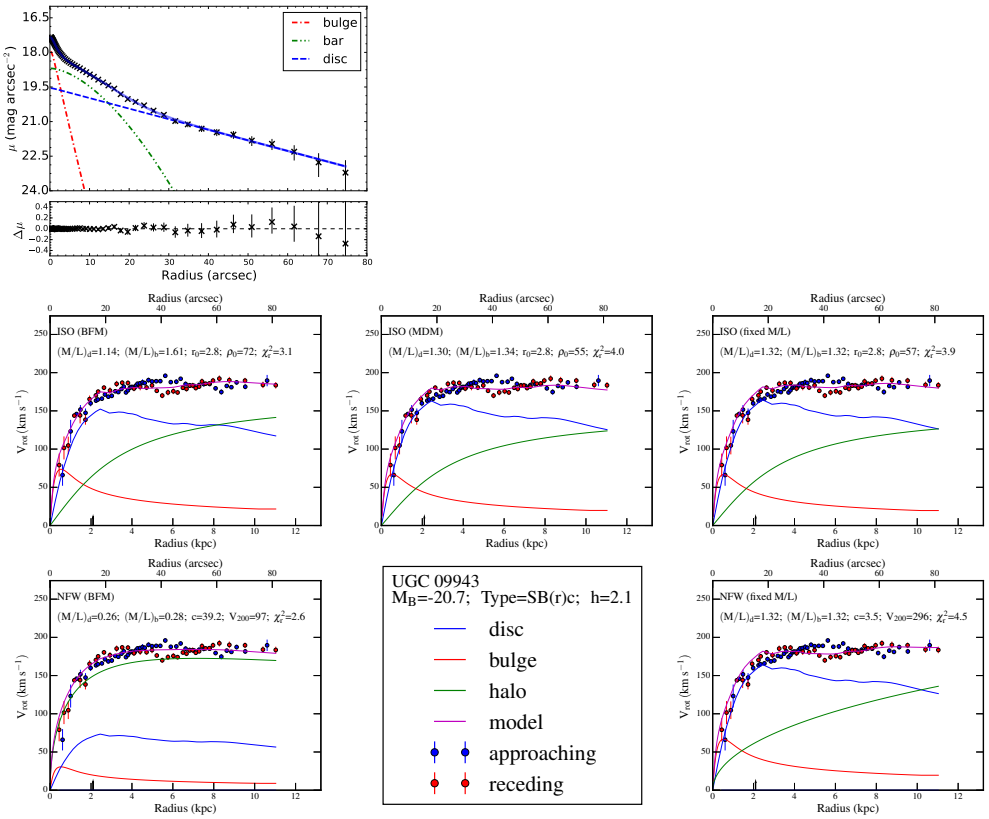

Figure B.83

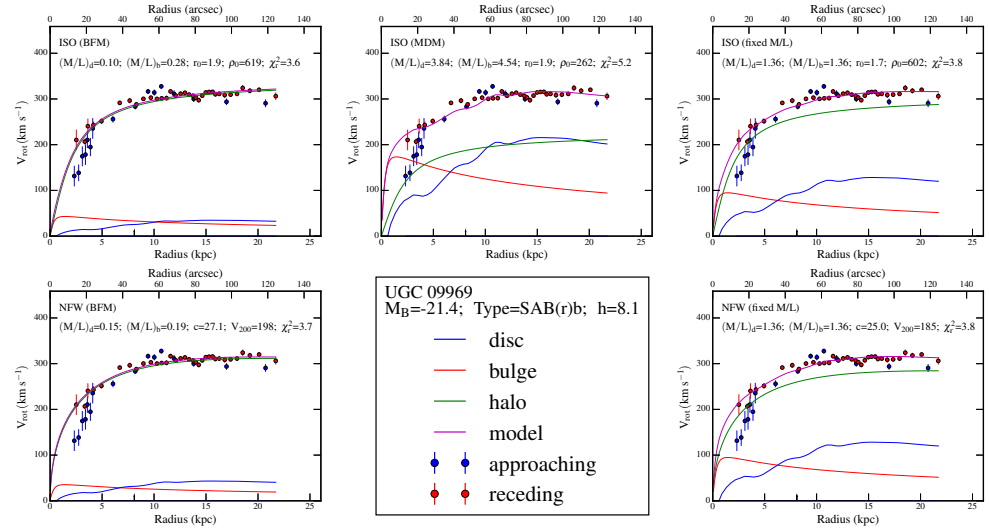

Figure B.84

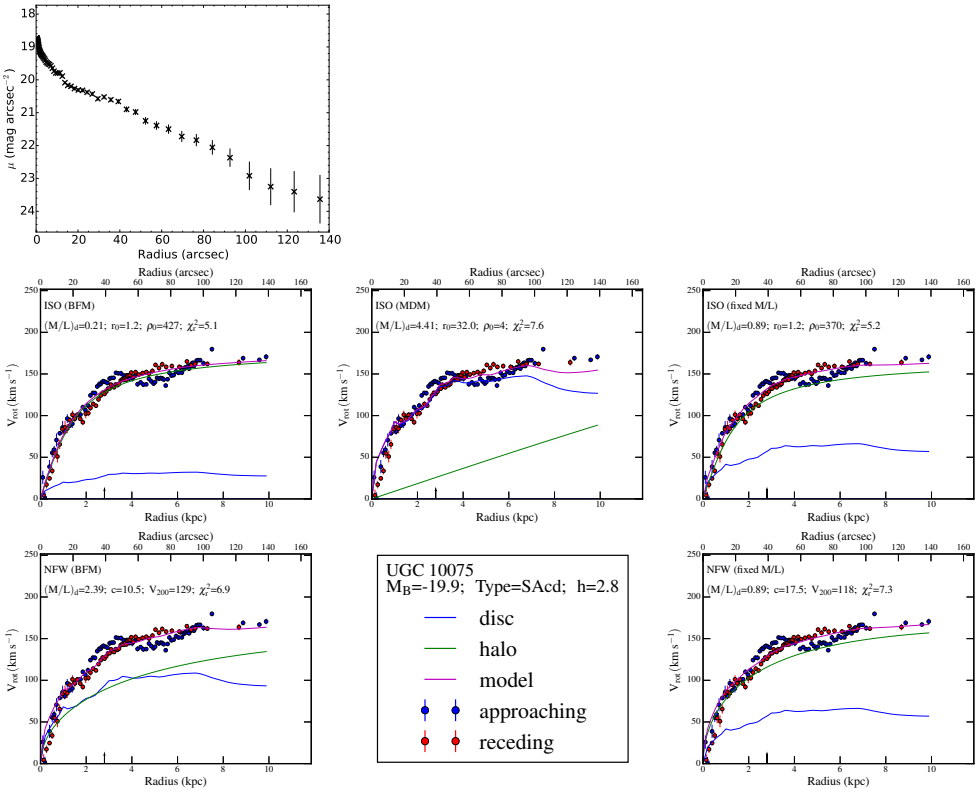

Figure B.85

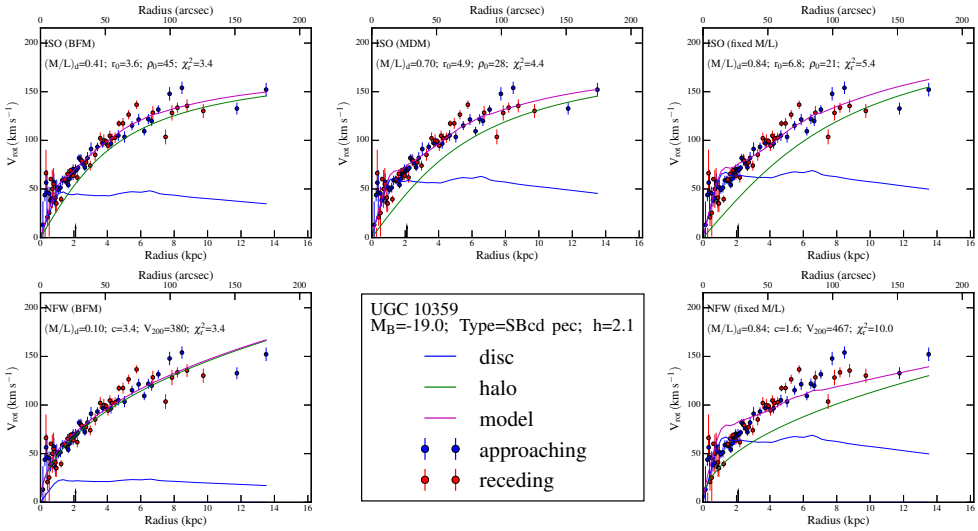

Figure B.86

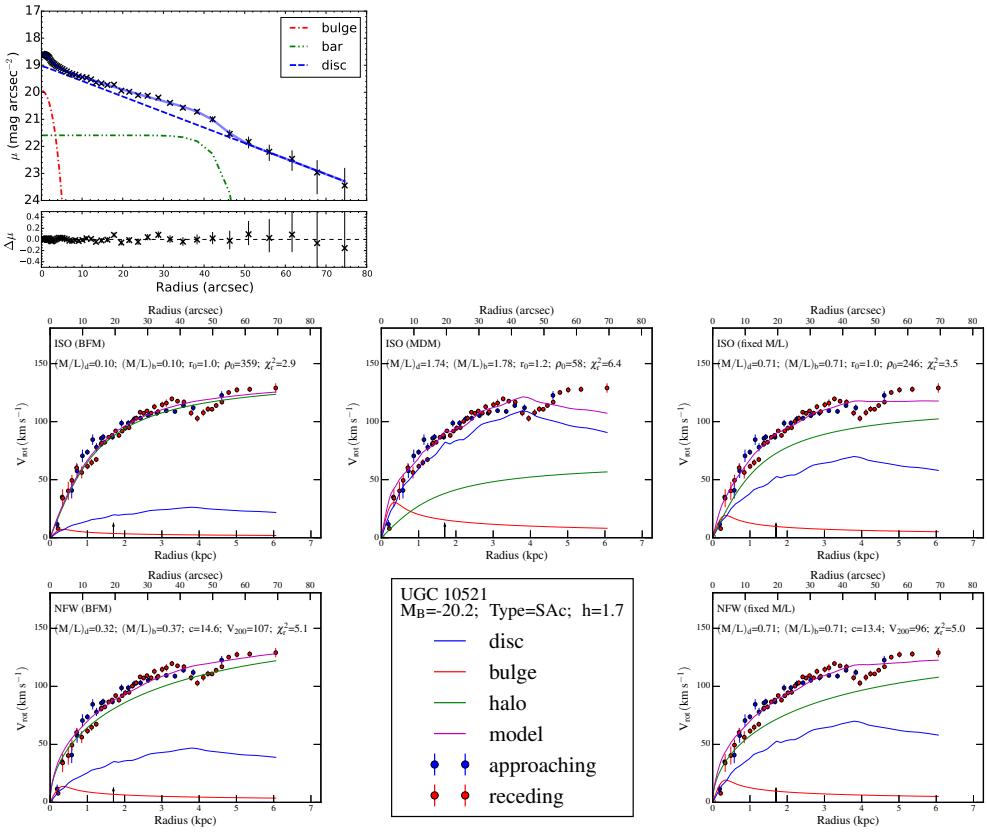

Figure B.87

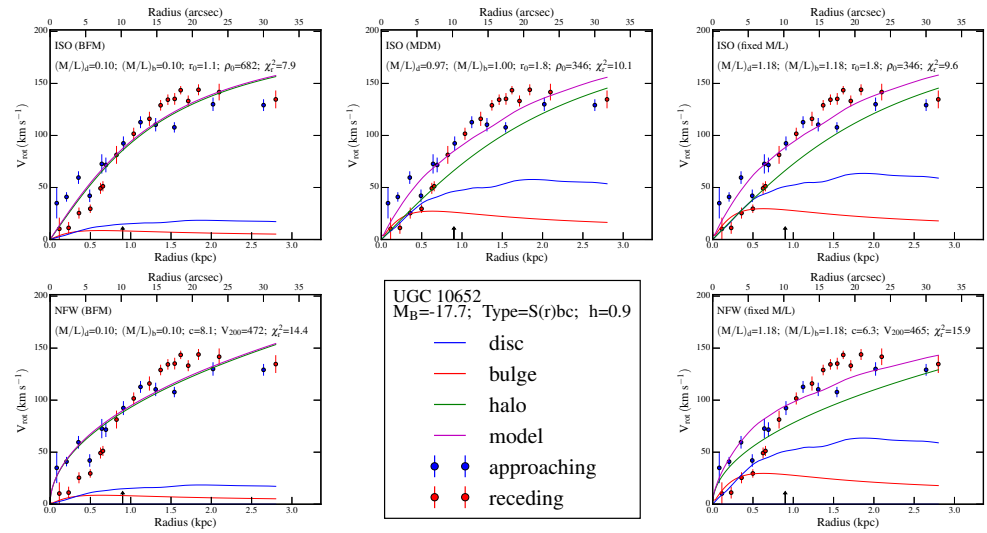

Figure B.88

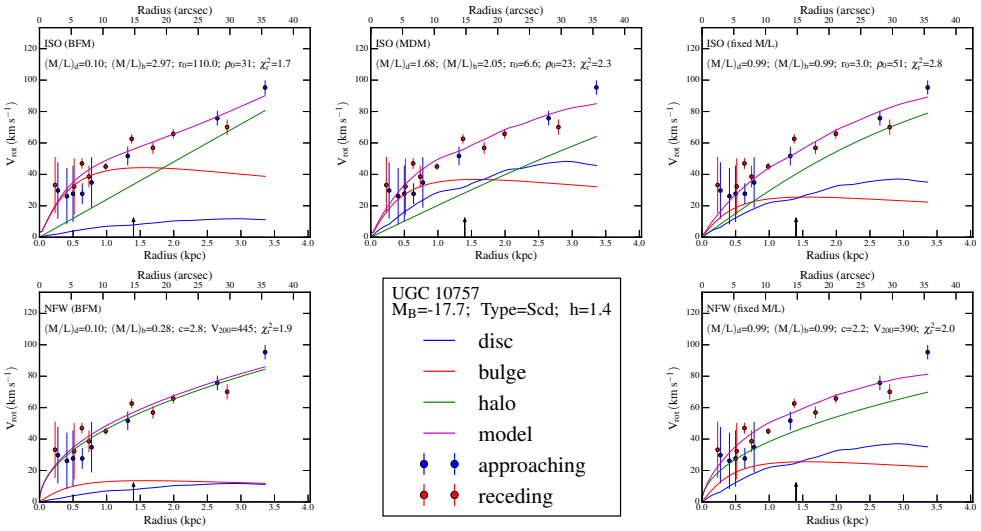

Figure B.89

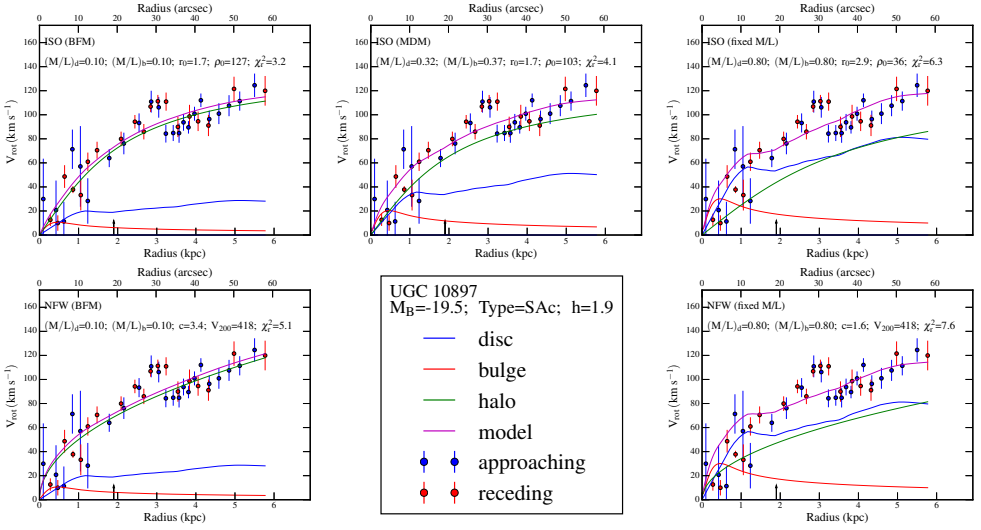

Figure B.90

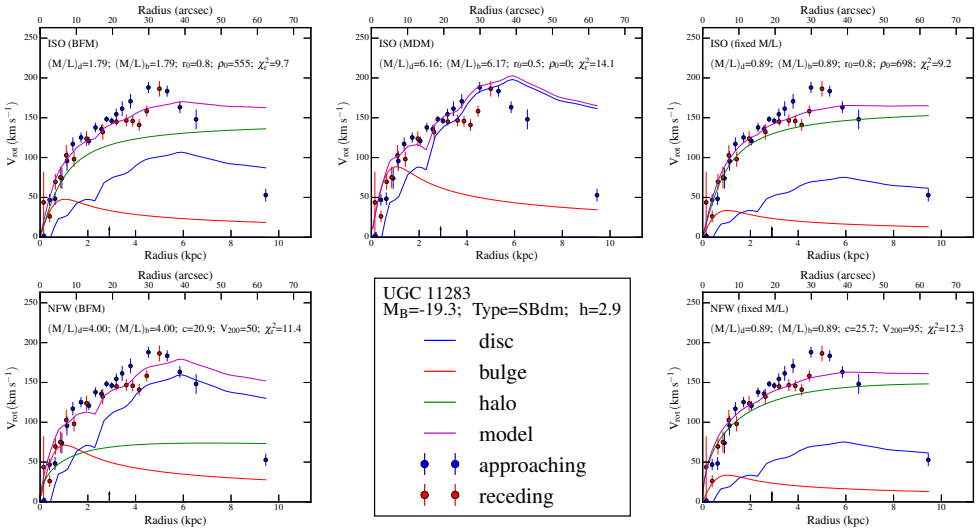

Figure B.91

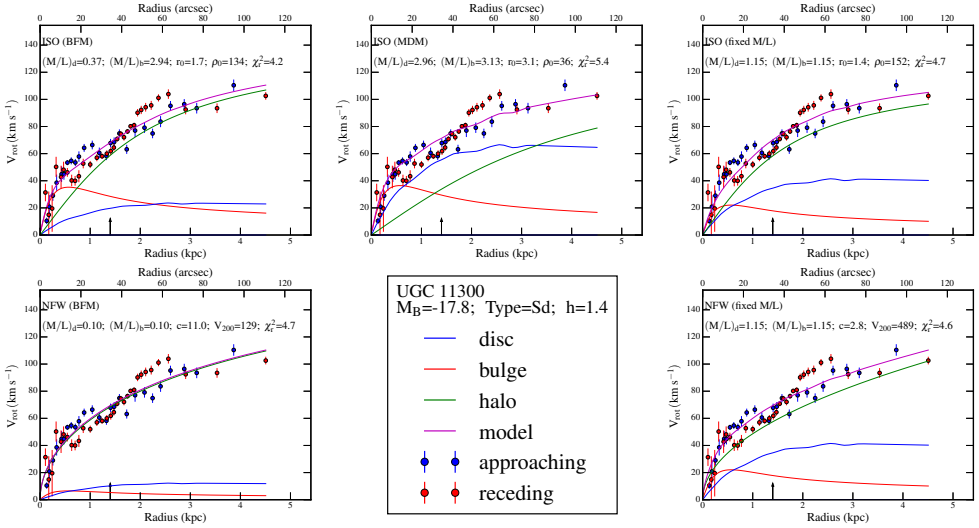

Figure B.92

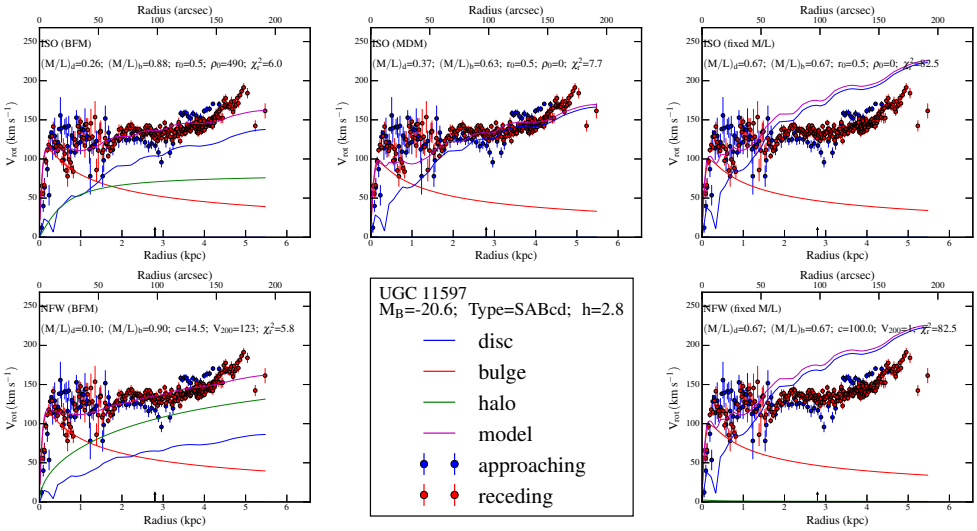

Figure B.93

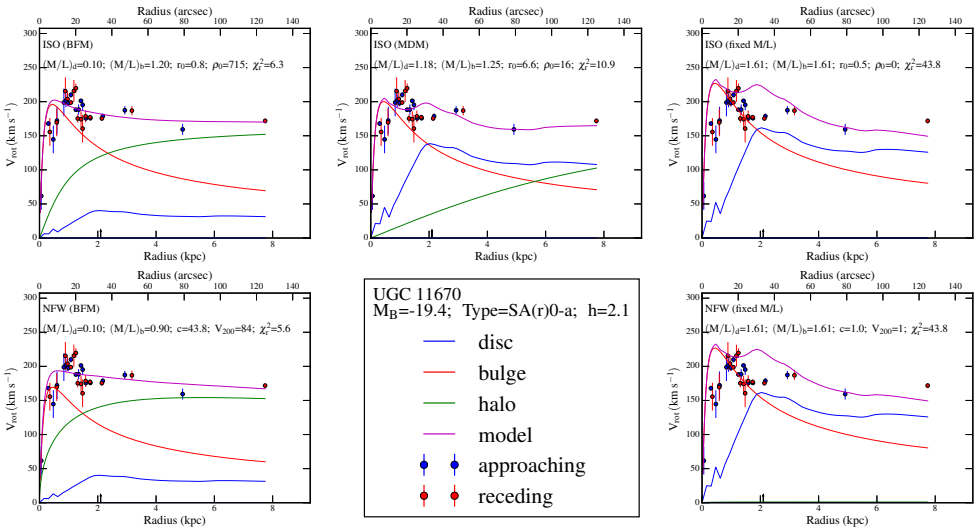

Figure B.94

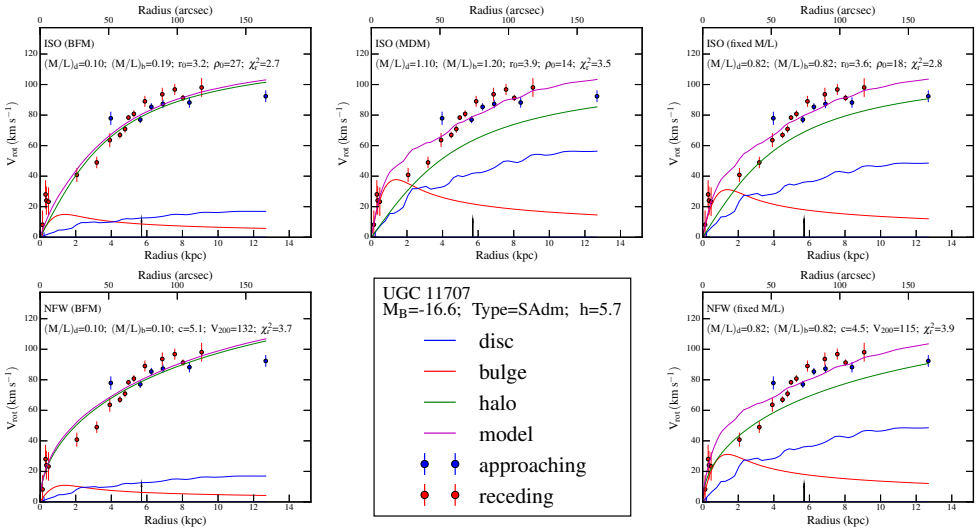

Figure B.95

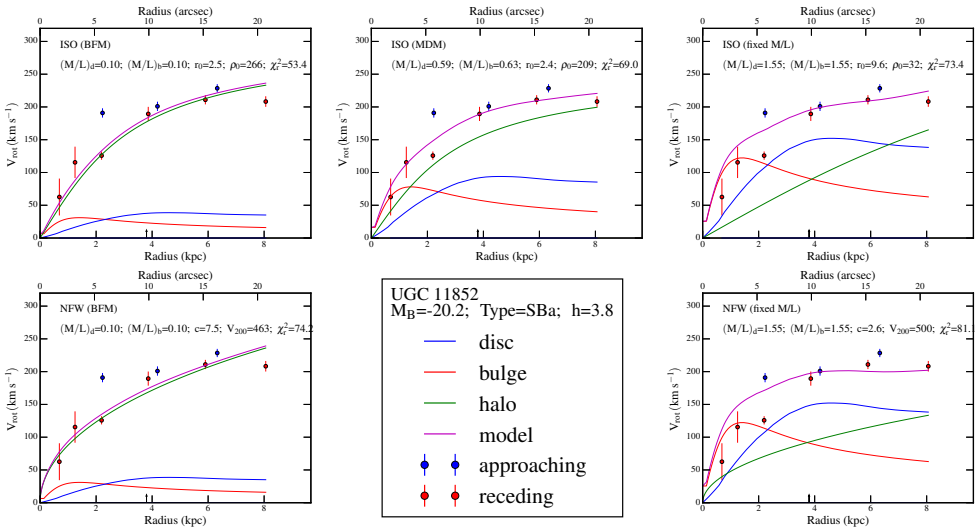

Figure B.96

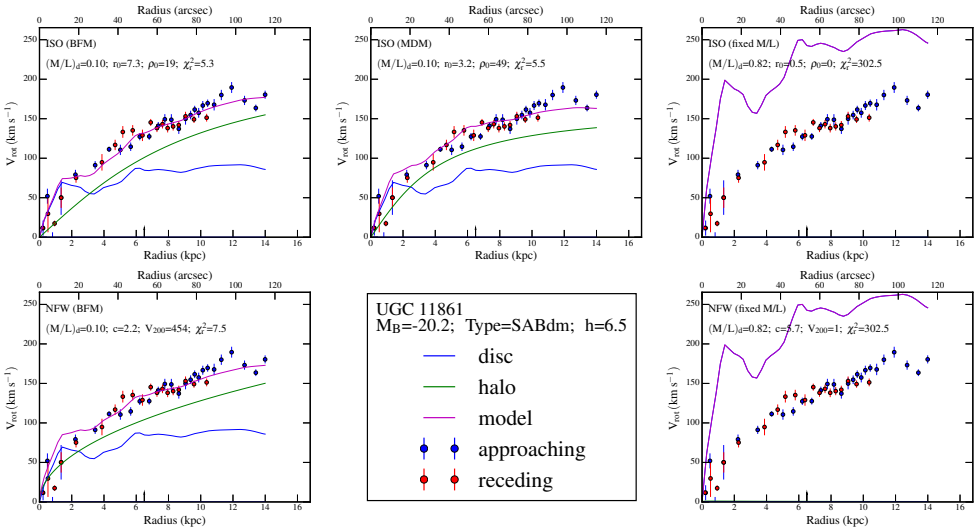

Figure B.97

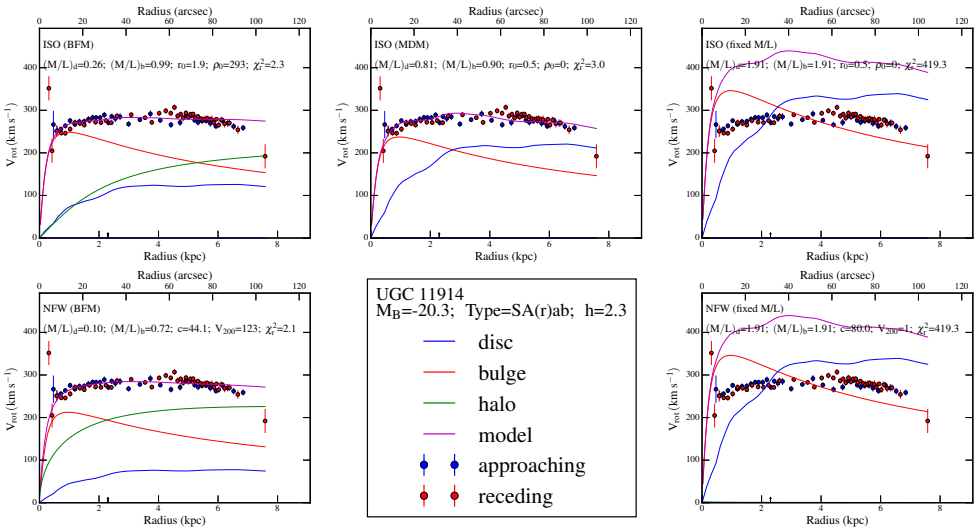

Figure B.98

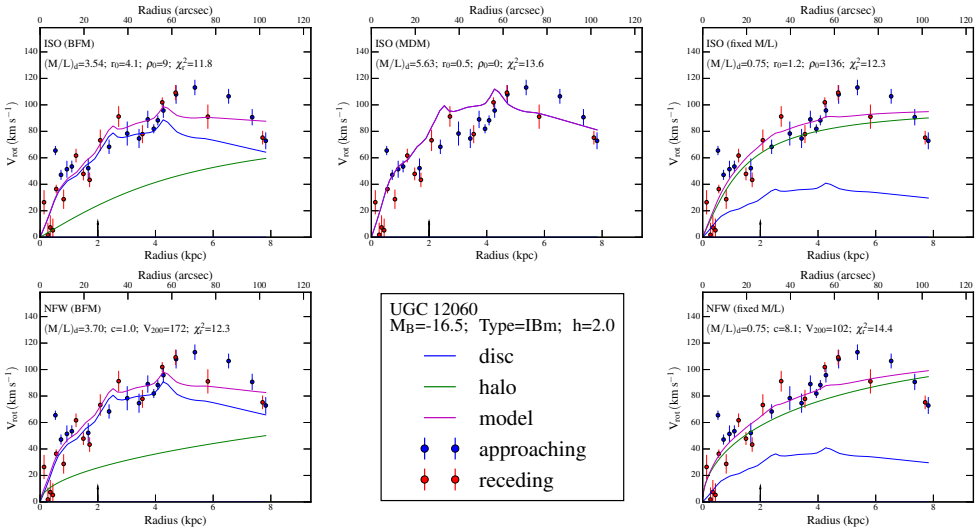

Figure B.99

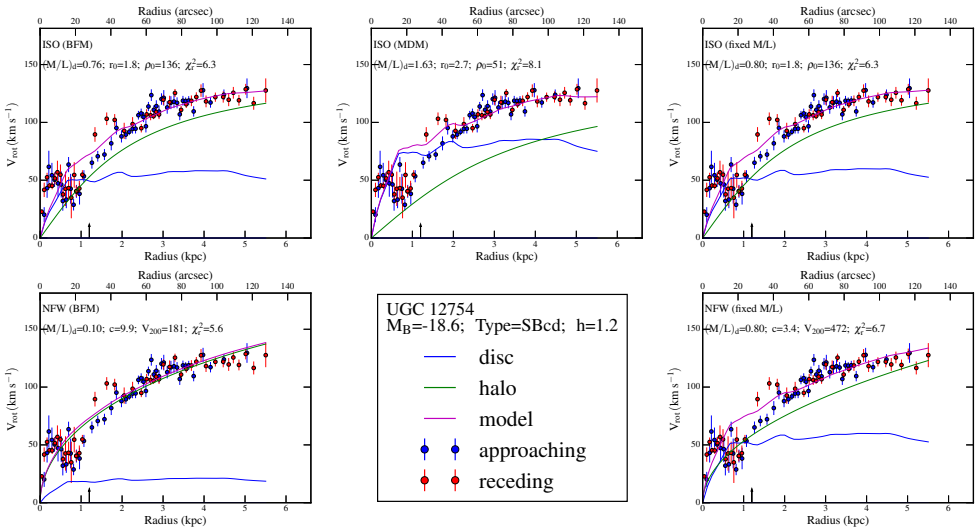

Figure B.100